Determination of space weather effects on the geomagnetic field : an automatic derivation of geomagnetic baselines containing quiet variations

Veronika Haberle

To cite this version:

Veronika Haberle. Determination of space weather effects on the geomagnetic field : an automatic derivation of geomagnetic baselines containing quiet variations. Earth and Planetary Astrophysics [astro-ph.EP]. Université Paul Sabatier - Toulouse III, 2023. English. NNT : 2023TOU30283 . tel-04573929

HAL Id: tel-04573929
https://theses.hal.science/tel-04573929v1

Submitted on 13 May 2024

THÈSE

En vue de l'obtention du

DOCTORAT DE L'UNIVERSITÉ DE TOULOUSE

Délivré par : *l'Université Toulouse 3 Paul Sabatier (UT3 Paul Sabatier)*

Présentée et soutenue le *13/11/2023* **par :**

Veronika HABERLE

Determination of Space Weather Effects on the Geomagnetic Field: An Automatic Derivation of Geomagnetic Baselines containing Quiet Variations

JURY

Mioara MANDEA	Rapporteuse
Monika KORTE	Rapporteuse
Roman LEONHARDT	Examinateur
Pierdavide COISSON	Examinateur
Vincent GENOT	Examinateur
Sébastien TRILLES	Examinateur
Aurélie MARCHAUDON	Directrice de thèse
Aude CHAMBODUT	Co-Directrice de thèse

École doctorale et spécialité :
SDU2E : Astrophysique, Sciences de l'Espace, Planétologie
Unité de Recherche :
Institut de Recherche en Astrophysique et Planétologie (UMR 5277)
Directeur(s) de Thèse :
Aurélie MARCHAUDON et *Aude CHAMBODUT*
Rapporteurs :
Mioara MANDEA et *Monika KORTE*

THÈSE

En vue de l'obtention du

DOCTORAT DE L'UNIVERSITÉ DE TOULOUSE

Délivré par l'Université Toulouse 3 - Paul Sabatier

Présentée et soutenue par

Veronika HABERLE

Le 13 novembre 2023

Dérivation des effets de la Météorologie de l'Espace sur le champ géomagnétique: dérivation automatique de la ligne de base géomagnétique incluant les variations calmes

Ecole doctorale : **SDU2E - Sciences de l'Univers, de l'Environnement et de l'Espace**

Spécialité : **Astrophysique, Sciences de l'Espace, Planétologie**

Unité de recherche :
IRAP - Institut de Recherche en Astrophysique et Planetologie

Thèse dirigée par
Aurélie MARCHAUDON et Aude CHAMBODUT

Jury
Mme Mioara MANDEA, Rapporteure
Mme Monika KORTE, Rapporteure
M. Roman LEONHARDT, Examinateur
M. Pierdavide COïSSON, Examinateur
M. Vincent GéNOT, Examinateur
M. Sébastien TRILLES, Examinateur
Mme Aurélie MARCHAUDON, Directrice de thèse
Mme Aude CHAMBODUT, Co-directrice de thèse

Contents

Abstract

With increasing dependence on technology, the effects of space weather are becoming a significant societal risk raising the need for real-time monitoring and forecasting. The geomagnetic field being affected directly by solar events is an important proxy which state is described by magnetic indices. These indices are based on magnetic observatory measurements which encompass contributions of various sources. The main challenge is thus the separation of these with the extraction of the storm-induced portion being a complex and time consuming task. The geomagnetic baseline contains the non-storm share - or the quiet sources - within magnetic field measurements and is a fundamental part to be taken into account for the derivation of any such index. Its determination is ideally done by a simple algorithm which captures quiet sources well, while being applicable to an extensive network of magnetic observatories independent of the considered epoch.

This thesis is concerned with the exploration of novel methodologies that determine such geomagnetic baselines suitable for near-real time applications. The horizontal components of magnetic field measurements from observatories situated in mid- to low latitudes are leveraged for this purpose. The first and main part of the present manuscript deals with the introduction of a baseline approach based on conventional methodologies while the second part investigates the utilisation of artificial intelligence.

In the main part, signal filtering techniques are leveraged to automatically determine quiet variations of the geomagnetic field - the filter baseline. An exhaustive physical analysis taking into account measurements between 1991 and 2019 confirms that the most important quiet sources in mid- and low-latitudes are accurately represented. These include the secular variation and the solar quiet current system. A significant finding is that the intrinsic day-to-day variability of the solar quiet current system is accurately contained within the filter baseline. However, the analysis also reveals that storm signatures are present. To overcome this drawback, the filter baseline is replaced during disturbances. First, an algorithm automatically detects disturbances with the aid of the filtering approach and the residuals using the filter baseline. Second, during the identified intervals a set of possible substitution baselines based on analytical models describing quiet variations is deduced. Comparisons suggest that using variations from days prior to disturbances hold suitable quiet variations. Using the substitution baseline during identified disturbances on the filter baseline holds the final geomagnetic baseline which shows good agreements with existing ones and thus can generally be used for mid- to low-latitude observatories. As the algorithm only uses magnetic field measurements and any of its steps is fully automated, it is adapted for operational near-real time applications and the deployment in now- and forecasting environments.

In the second part, the application of artificial intelligence for the determination of quiet variations is investigated. A random forest algorithm is used to identify important drivers of these variations, followed by the use of Long-Short Term Memory neural networks to reproduce them. First results show promising possibilities for the derivation of baselines with the support of AI and pave the way for future work.

Résumé (FR)

Avec la dépendance croissante à la technologie, les effets de la météorologie spatiale deviennent un risque sociétal non négligeable nécessitant surveillance en temps-réel et prévision. Le champ géomagnétique est directement affecté par les événements solaires. Son état est un indicateur important décrit par les indices d'activité magnétique. Ces indices sont dérivés des mesures des observatoires magnétiques or ces données englobent les contributions de diverses sources dont la proportion varie selon l'activité. Le principal défi est donc la séparation entre la part induite par les orages magnétiques et la ligne de base géomagnétique contenant les contributions des sources en périodes calmes. Cette tâche complexe et longue demeure une étape fondamentale pour la dérivation d'un indice et est idéalement réalisée par un algorithme simple. Celui-ci capture de façon satisfaisante les contributrions des sources en périodes calmes sur les séries temporelles d'un réseau étendu d'observatoires magnétiques quelle que soit l'époque.

Cette thèse porte sur l'exploration de nouvelles méthodologies de détermination de telles lignes de base géomagnétiques adaptées à des applications en temps quasi réel.

La première et principale partie du présent manuscrit décrit une nouvelle méthode de détermination des lignes de base géomagnétiques en suivant des méthodologies conventionnelles, tandis que la seconde partie étudie l'utilisation de l'intelligence artificielle. Dans la première partie, les techniques de filtrage du signal sont utilisées sur les séries temporelles pour déterminer automatiquement les contributions des sources en période calme - la ligne de base du filtre. Une analyse physique exhaustive prenant en compte les mesures effectuées entre 1991 et 2019 confirme que les plus importantes de ces contributions aux latitudes moyennes et basses sont représentées avec précision. Il s'agit notamment de la variation séculaire, du champ crustal rémanent et du système de courant solaire calme. Un résultat significatif est que la variabilité journalière intrinsèque du système de courant solaire calme est correctement contenue dans la ligne de base du filtre. Cependant, l'analyse révèle également la présence de signatures dues aux orages magnétiques. Tout d'abord, un algorithme détecte automatiquement les périodes perturbées à l'aide de l'approche de filtrage et des valeurs de résidus obtenues par soustraction de la ligne de base du filtre. Ensuite, pendant ces intervalles identifiés, un ensemble de lignes de base de substitution possibles, basées sur des modèles analytiques décrivant les variations des différentes sources en périodes calmes, est déduit. Les comparaisons suggèrent que l'utilisation simple des variations des jours précédant les perturbations permet d'obtenir des lignes de base appropriées. L'utilisation de cette ligne de base de substitution permet d'obtenir la ligne de base géomagnétique finale. Cette dernière montre de bonnes concordances avec les lignes de base existantes et peut être utilisée pour les observatoires situés à des latitudes moyennes ou basses. Comme l'algorithme n'utilise aucune information a priori mais uniquement les mesures du champ magnétique et que chacune des étapes est entièrement automatisée, la méthodologie est adaptée aux applications opérationnelles en temps quasi réel et au déploiement pour des applications de surveillance et prévision.

Dans la seconde partie, l'application de l'intelligence artificielle pour la détermination des variations en période calme est étudiée. Un algorithme de forêt aléatoire est utilisé pour identifier les facteurs et paramètres importants de ces variations, suivi par l'utilisation de réseaux de neurones à mémoire à long terme pour reproduire et retrouver ces paramètres. Les premiers résultats montrent des possibilités prometteuses pour la dérivation de lignes de base avec le soutien de l'intelligence artificielle et ouvrent la voie à de futurs travaux.

Overview of the Thesis and Research Question

Space weather refers to the dynamic conditions within the space environment that can impact technological systems and human activities in space and on Earth. Determining the impact of space weather events, like solar flares, coronal mass ejections and co-rotating interaction regions, is thus necessary and becomes more and more important in near real-time applications. Geomagnetic indices provide quantitative measures of the impact of space weather phenomena on the geomagnetic field. One of the key elements of these indices is the geomagnetic baseline that describes the complex, undisturbed geomagnetic field and forms the central feature of this doctoral thesis. The present manuscript is divided into four parts:

I. **Introduction**
In chapters 1 to 3 the theoretical background needed to adequately follow this thesis is presented. The opening chapter is dedicated to the theory of basic space plasma physics as it is the primary theory governing space weather. In the second chapter, an overview of space weather is given, with focus on the near-Earth space environment and the geomagnetic field. Geomagnetic indices are introduced in Chapter 3 and finally, geomagnetic baselines are discussed which leads to the motivation of the PhD thesis topic at hand.

II. **Baseline Derivation**
Chapter 4 is dedicated to the technical aspects of this work. We start by outlining the employed data set and applied methodology that allows us to introduce an automatic baseline derivation method referred to as the filter baseline. This is followed by a detailed analysis to which extent the filter baseline is able to resemble the undisturbed geomagnetic field. A large part of the work presented in chapters 4 and 5 has been published in **Haberle, Marchaudon, Chambodut, and Blelly (2022)** which can be found in the annex. Chapter 6 covers the treatment of undesirable storm signatures within the baseline. Eventually, the final baseline is compared with existing ones.

III. **Leveraging Artificial Intelligence**
Artificial intelligence has led to promising results in a wide range of applications and a short introduction of it is given in Chapter 7. In Chapter 8 we explore the application of the random forest method to determine the most important drivers of quiet variations of the geomagnetic field, which is followed by the use of a Long-Short Term Memory neural network to reproduce these variations in Chapter 9. The results are discussed in Chapter 10.

IV. **Conclusions and Perspective**
Last but not least, the conclusion and perspective of the presented work is outlined.

As such, this thesis addresses two research questions. The first one is concerned with the introduction of a new methodology to derive geomagnetic baselines for operational (near-)real time environments. The physical research question formulates as:

1. Is the derived baseline reflecting the quiet variations of the geomagnetic field?

The second one is concerned with the applicability of artificial intelligence for describing the undisturbed geomagnetic field. The physical research question formulates as:

2. To which extend can AI support the determination of the baseline with respect to conventional methods?

Part I

Introduction

Chapter 1

Basic Space Plasma Physics

The fundamental principles of physics that govern and give rise to the phenomena studied in this thesis are described within the framework of plasma physics. Plasma is the most abundant visible matter in the universe. Plasma physics, and especially space plasma physics, enables the understanding and description of many phenomena, observed in our solar system. It continues to enhance our understanding of the interaction between the Sun and Earth, including the solar atmosphere, the constant particle stream from the Sun - the solar wind, and plasma structures accompanied by complex current systems in the near-Earth space environment. Let alone, the field of plasma physics significantly contributed to the comprehension of phenomena and effects relating to space weather. In the following a brief introduction outlining the main results of space plasma physics is given that serves as a background for space weather phenomena. The objective of this thesis is not to study space plasma physics but to leverage its applications. Therefore, important and relevant concepts from plasma physics are presented to the scope as they are useful for a thorough understanding of succeeding chapters. For further and more elaborate treatment of the subject the interested reader is referred to books like Baumjohann and Treumann (2012) for a general overview with basic mathematical treatment and Cravens (1997) for a thorough mathematical treatment of solar system plasma.

1.1 Definition of a plasma

Plasma is an ionised gas of charged particles and is the most abundant state of matter in the universe with more than 99 % of known baryonic matter being in the plasma state. An ideal plasma is quasi-neutral, i.e. it has approximately the same numbers of positive and negative charges considering large enough scales. The characteristic Debye length λ_D describes the maximum distance at which charged particles are influenced by the electric field of other particles within a plasma. It depends upon the plasma temperature T_e and plasma density n_e:

$$\lambda_D = \left(\frac{\epsilon_0 k_B T_e}{n_e e^2} \right) , \tag{1.1}$$

whereby it is assumed that ions and electrons have similar temperatures and densities, i.e.: $T_e \approx T_i$ and $n_e \approx n_i$. ϵ_0 is the free space permittivity, k_B the Boltzmann constant and e the electron charge. Quasi-neutrality is actively aimed for by plasma and is guaranteed in systems which physical dimensions L fulfills

$$\lambda_D \ll L \, . \tag{1.2}$$

Collectively, the charged particles arrange themselves to mitigate the impact of external electrostatic fields. For this Debye shielding to occur, sufficiently enough charged particles need to be present within a Debye sphere of radius λ_D which is satisfied for plasma parameters Λ with

$$\Lambda = n_e \lambda_D^3 \gg 1\,. \tag{1.3}$$

In their efforts to maintain quasi-neutrality driven by the Coloumb force, the fully ionised plasma is characterised by its typical oscillation frequency. The electron plasma frequency ω_{pe} is defined as

$$\omega_{pe} = \sqrt{\frac{n_e e^2}{m_e \epsilon_0}}\,, \tag{1.4}$$

with m_e being the electron mass. In order to guarantee that the electrons are not affected by collisions with neutrals, the time between two electron-neutral collisions τ_n needs to be sufficiently larger than the plasma frequency, i.e.

$$\frac{\omega_{pe}}{\tau_n} \gg 1\,. \tag{1.5}$$

An ideal plasma satisfies the three plasma criteria (1.2), (1.3) and (1.5). Examples of such plasma are important drivers of phenomena studied in this thesis, like the solar wind which is a stream of charged particles expelled from the the Sun's atmosphere or the ring current which is a large-scale current flow that encircles Earth at around 3 to 8 Earth-radii (R_E) earth radii R_E in the equatorial plane (Daglis, Thorne, Baumjohann, & Orsini, 1999) which we will study later on in detail.

1.2 Single Particle Motion

Due to their electrically charged nature, the dynamics of plasmas are governed by their interaction with self-induced and external magnetic and electric fields. Assuming that particles do not directly interact with each other and their generated fields are much weaker than the external magnetic fields, their motions can be described by the single particle approach and, even though rarely directly applicable, provide a great insight into a plasma's dynamics.

The most important forces acting on a plasma are the Coulomb force

$$\mathbf{F_C} = q\mathbf{E}\,, \tag{1.6}$$

when the charged particles are at rest and the Lorentz force,

$$\mathbf{F_L} = q\left(\mathbf{v} \times \mathbf{B}\right) \tag{1.7}$$

when particles move as current elements with velocity $\mathbf{v}$ in a magnetic field $\mathbf{B}$. Such that, the equation of motion for a particle can be written as

$$m\frac{d\mathbf{v}}{dt} = q\left(\mathbf{E} + \mathbf{v} \times \mathbf{B}\right)\,. \tag{1.8}$$

In the absence of an electric field, the $\mathbf{E}$ term in (1.8) is dropped leading to a gyration motion of the particle with gyro- or cyclotron frequency

$$\omega_g = \frac{qB}{m}\,, \tag{1.9}$$

which results in opposite directions for electrons and protons. The gyro-radius writes as

$$r_g = \frac{mv_\perp}{qB} \,, \tag{1.10}$$

whereby $v_\perp$ is the constant speed perpendicular to $\mathbf{B}$ and B is the magnitude of the homogenous magnetic field. Note that the mass of the particle is in the numerator and thus the gyro-radius of the electron is significantly smaller than that of the ions. Such a particle describes a helicoidal trajectory, i.e. a circular orbit around the so-called guiding centre for $v_\perp$ and a helix when there is a velocity $v_\parallel$ parallel to the magnetic field lines. The pitch-angle of the helix is defined as

$$\alpha = \arctan\left(\frac{v_\perp}{v_\parallel}\right) \,. \tag{1.11}$$

In the presence of an electric field $\mathbf{E}$, the gyro-motion is joined by a drift motion of the guiding center as it is accelerated when it moves in the direction of $\mathbf{E}$ increasing its gyro-radius, and decelerated otherwise, decreasing the gyro-radius. This motion is caused by the $\mathbf{E} \times \mathbf{B}$ drift

$$\mathbf{v}_E = \frac{\mathbf{E} \times \mathbf{B}}{B} \,. \tag{1.12}$$

The direction of this drift does not depend upon the charge and thus no current is created.

Further motions are induced when the magnetic field $\mathbf{B}$ is not homogenous. In fact, often $\mathbf{B}$ has a gradient or is curved. An additional perpendicular gradient of the magnetic field ∇B results in a drift perpendicular to the magnetic field and the gradient due to the induced changing of the gyro-radius (1.10) as

$$\mathbf{v}_\nabla = \frac{mv_\perp^2}{2qB^3} \left(\mathbf{B} \times \nabla B\right) \,. \tag{1.13}$$

It is accompanied by the magnetic moment μ which is the ratio between perpendicular particle energy and magnetic field defined as

$$\mu = \frac{mv_\perp^2}{2B} \,. \tag{1.14}$$

When the magnetic field is curved the particle experiences a centrifugal force due to their parallel verocity $v_\parallel$, leading to the curvature drift around the local radius of the curvature $\mathbf{R_c}$ as

$$\mathbf{v_R} = \frac{mv_\parallel^2}{q} \frac{\mathbf{R}_c \times \mathbf{B}}{R_c^2 B^2} \,. \tag{1.15}$$

Both the gradient drift and curvature drift are in opposite directions for electrons and ions. When the magnetic field lines are curved and in the additional presence of a perpendicular gradient, they induce a total magnetic drift $\mathbf{v_B} = \mathbf{v_R} + \mathbf{v}_\nabla$ which is the main mechanism behind an important current system in the near-Earth environment: the ring current, which we will discuss in detail later on.

Together with the magnetic moment in (1.14), the magnetic flux Φ_μ through the surface encircled by a gyrating particle

$$\Phi_\mu = \frac{2\pi m}{q^2}\mu = const \tag{1.16}$$

are adiabatic invariants meaning that they vary slowly in comparison to their typical particle motion. Considering a particle that moves in an inhomogeneous magnetic field, equations (1.11) and (1.14) relate the pitch angle α to the magnetic field strength with the magnetic moment as

$$\frac{\sin^2 \alpha_2}{\sin^2 \alpha_1} = \frac{B_2}{B_1} \,. \tag{1.17}$$

Is the magnetic field also converging into stronger magnetic fields, the pitch angle of the particle will increase and at the point where it reaches $\alpha = 90^\circ$ it will be reflected at the mirror point. If the magnetic field configuration is that of a dipole, i.e. the field increases at the poles, two mirror points one in the magnetic's north pole and one in the south pole will cause particles to become trapped. This is a feature of the Earth's internal magnetic field and trapped particles partially make up the radiation belts and the ring current, which we will discuss later.

1.3 Collisions and Conductivity

When single particles move as governed by the introduced equations, they eventually also interact with other particles via binary collisions. When particles within a plasma have enough space to move around such that collisions occur rarely when compared to other relevant variations of the fields, the plasma is considered collisionless. However, when collisions occur frequently enough, particle interactions become important.

In fully ionised plasmas, the charged particles interact through electric Coulomb collisions with Coulomb cross-section σ_C. This cross-section is significantly enlarged through the particle's Coloumb field leading to frequent small angle deflections. When a much faster electron approaches an ion, that can be assumed at rest, and using the plasma parameter as introduced in (1.3), the collision frequency derives to

$$\nu_{ei} \approx \frac{\omega_{pe}}{16\pi} \frac{\ln \Lambda}{\Lambda} \,. \tag{1.18}$$

The associated mean free path can be defined as

$$\lambda_e = \frac{\langle v \rangle}{\nu_{ei}} \approx \frac{64\pi n_e}{\omega_{pe}^4 \ln \Lambda} \left(\frac{k_B T_e}{m_e} \right)^2 \,, \tag{1.19}$$

and due to the electron temperature T_e in the nominator, λ_e will be shorter in cold and longer in hot plasmas. Using the plasma parameter (1.3) to rewrite (1.19) holds

$$\frac{\lambda_e}{\lambda_D} \approx \frac{16\pi\Lambda}{\ln \Lambda} \gg 1 \,. \tag{1.20}$$

This implies that the mean-free path in plasmas is much larger than the Debye sphere, such that an electron passes by many Debye-spheres of ions before colliding with one. Fully ionised plasma can be considered collisionless when the mean-free path is much larger than the scale of the plasma system and collisional frequencies are much smaller than the plasma frequencies in the considered regions. This is the case for most geophysical plasmas.

In partially ionised plasmas, the main collision occurs between charged particles and neutrals while Coulomb collisions play a secondary role and can often be neglected. This is the case for example in the upper part of the terrestrial atmosphere, the so-called ionosphere, where collisions with ionised and neutral particles occur frequently due to increased neutral and plasma densities. Neutral-electron collisions can be simplified in a first approximation as head-on collisions with the neutral collision frequency ν_n, i.e. the number of collisions per second,

$$\nu_n = n_n \sigma_n \langle v \rangle \,, \tag{1.21}$$

with cross-section of an atom or molecule $n_n \sigma_n$, whereby n_n is the neutral particle density and $\sigma_n = \pi d_0^2$ is the molecular cross-section, and average velocity $\langle v \rangle$. The length a charged particle travelled before encountering a collision with neutrals is called the mean free path

$$\lambda_n = \frac{\langle v \rangle}{\nu_n} = (n_n \sigma_n)^{-1} \,. \tag{1.22}$$

Averages are used for the quantities to account for the thermal motion. Equation (1.22) is a first approximative description for neutral-electron collisions where electrons are assumed to be much smaller hard spheres than neutrals. As ions and neutrals may be similar in mass and momentum, their interaction becomes more complex. The interested reader finds further details in dedicated books, like Schunk and Nagy (2009).

For collisional plasma, the equation of motion (1.8) is enlarged with a collisional term that describes the momentum lost by charged particles to the bulk of plasma or to the neutrals (in case of partially ionised plasma)

$$m\frac{d\mathbf{v}}{dt} = q\left(\mathbf{E} + \mathbf{v} \times \mathbf{B}\right) - m\nu_c(\mathbf{v} - \mathbf{u}) \,, \tag{1.23}$$

whereby ν_C is the collision frequency and $\mathbf{u}$ is the bulk velocity.

In an unmagnetised plasma, when electrons move and their collision partners (ions and, if not fully ionised, neutrals) can be assumed to be at rest, they carry a current $\mathbf{j} = -en_e\mathbf{v}_e$, generating an electric field $\mathbf{E} = -\frac{m_e v_c}{e}\mathbf{v}_e$ resulting in Ohm's law,

$$\mathbf{E} = \eta\,\mathbf{j} = \frac{m_e \nu_c}{n_e e^2}\mathbf{j} \,, \tag{1.24}$$

with η being the plasma resistivity that depends upon the electron density and the collision frequency.

When the plasma is magnetised, the plasma may move across magnetic field lines, such that Ohm's law in (1.24) derives as

$$\mathbf{j} = \sigma_0\left(\mathbf{E} + \mathbf{v} \times \mathbf{B}\right) = \frac{n_e e^2}{m_e \nu_c}\left(\mathbf{E} + \mathbf{v} \times \mathbf{B}\right) \,, \tag{1.25}$$

with the scalar plasma conductivity σ_0. This is valid in fully ionised plasmas with extremely low collision frequencies and the conductivity may be approximated as infinite.

However, in a partially ionised and magnetized plasma where collisions are abundant as is the case in the terrestrial ionosphere, the scalar becomes a finite anisotropic conductivity tensor. Assuming a magnetized plasma at steady state with electrons moving at velocity $\mathbf{v}_e$ and ions and neutrals at rest, the equation of motion (1.23) writes as

$$\mathbf{E} + \mathbf{v}_e \times \mathbf{B} = -\frac{m_e v_c}{e}\mathbf{v}_e \tag{1.26}$$

Using the plasma conductivity σ_0 as defined in (1.25) and using $\mathbf{j} = -en_e\mathbf{v}_e$ to express $\mathbf{v}_e$ we get another form of Ohm's law:

$$\mathbf{j} = \sigma_0\mathbf{E} - \frac{\sigma_0}{n_e e}\mathbf{j} \times \mathbf{B} \,. \tag{1.27}$$

Assuming a magnetic field along the $z-$axis, i.e. $\mathbf{B} = B\hat{\mathbf{e}}_z$, the anisotropic conductivity tensor σ can be written as

$$\mathbf{j} = \sigma\,\mathbf{E} = \begin{bmatrix} \sigma_P & -\sigma_H & 0 \\ \sigma_H & \sigma_P & 0 \\ 0 & 0 & \sigma_{||} \end{bmatrix} \mathbf{E} \,. \tag{1.28}$$

The tensor elements are the following:

- The Pedersen conductivity σ_P determines the Pedersen currents in the direction $\mathbf{E}_\perp$ transverse to the magnetic field and writes as

$$\sigma_P = \sigma_0 \, \frac{\nu_c^2}{\nu_c^2 + \omega_{ge}^2} \,. \tag{1.29}$$

- The Hall conductivity σ_H governs the Hall currents in the direction perpendicular to electric and magnetic fields $-\mathbf{E} \times \mathbf{B}$ and writes as

$$\sigma_H = \sigma_0 \, \frac{\omega_{ge}\nu_c}{\nu_c^2 + \omega_{ge}^2} \,. \tag{1.30}$$

- And finally, the parallel conductivity $\sigma_{||}$ governs the magnetic field-aligned currents that are driven by the parallel electric component $E_{||}$ and is written as

$$\sigma_{||} = \sigma_0 = \frac{n_e e^2}{m_e \nu_c} \,. \tag{1.31}$$

The Hall conductivity σ_H and the Pedersen conductivity σ_P are perpendicular to the magnetic field. $\sigma_{||}$ is the conductivity that arises on the parallel direction of the magnetic field and is equal to the plasma conductivity in the unmagnetised case. Also note that Pedersen and Hall conductivities depend upon the ratio of the collision frequency and the gyrofrequency ω_{ge}. These effects become especially interesting in the ionosphere of Earth where the conductivities give rise to the dynamo region and relevant current systems for this work which are discussed later in chapter 2.3.1.

1.4 Magnetohydrodynamic Description of a Plasma

Often the individual particle motions are too detailed and the main interest lays on the plasma's bulk properties. For this purpose the plasma can be described as a fluid with macroscopic variables that characterise the bulk movement, such as the bulk velocity $\mathbf{v}$, density ρ, pressure p and average temperature T. Due to the electrically charged nature of the plasma, the fluid is subject to the presence of external and internal magnetic fields.

This subfield of plasma physics is called Magnetohydrodynamics (MHD). The Maxwell equations are the underlying governing equations

$$\nabla \cdot \mathbf{E} = \frac{\rho_c}{\epsilon_0} \tag{1.32}$$

$$\nabla \cdot \mathbf{B} = 0 \tag{1.33}$$

$$\nabla \times \mathbf{E} = -\frac{\delta \mathbf{B}}{\delta t} \tag{1.34}$$

$$\nabla \times \mathbf{B} = \mu_0 \mathbf{j} + \mu_0 \epsilon_0 \frac{\delta \mathbf{E}}{\delta t} \tag{1.35}$$

Using Ohm's generalised law (1.25) in Faraday's law (1.34) and together with Ampere's law (1.35), $\nabla \cdot \mathbf{B} = 0$ and dropping $\delta \mathbf{E}/\delta t$ yields the induction equation

$$\frac{\delta \mathbf{B}}{\delta t} = \underbrace{\frac{\eta \nabla^2 \mathbf{B}}{\mu_0}}_{Diffusion} + \overbrace{\nabla \times (\mathbf{v} \times \mathbf{B})}^{Convection} . \tag{1.36}$$

which describes the transport of magnetic field lines and plasma. Whether the plasma is governed by magnetic diffusion or by the convection of the bulk is determined by the Reynolds number

$$R = \frac{\mu_0 v L}{\eta} , \tag{1.37}$$

with L being the characteristic length. If $R \ll 1$ diffusion prevails and if $R \gg 1$ convection prevails.

For ideal MHD the following assumptions hold: 1) the plasma is a single fluid species such that electrons and ions are indistinguishable, 2) plasma is non-relativistic, i.e. the right term in (1.35) is zero and 3) the plasma is quasi-neutral. In an ideal collisionless plasma, when conductivity becomes infinite such that resistivity is zero, diffusion becomes negligible and convection is the only remaining term. This results in Ohm's law as

$$\mathbf{E} + \mathbf{v} \times \mathbf{B} = 0 . \tag{1.38}$$

and is themed the frozen-in flux theorem. The meaning of (1.38) is that the magnetic field lines and the plasma move together and are inseparable. As convection prevails

$$\frac{\delta \mathbf{B}}{\delta t} = \nabla \times (\mathbf{v} \times \mathbf{B}) \tag{1.39}$$

holds.

For length-scales that are too small to guarantee quasi-neutrality, ideal MHD breaks down. This is the requisite for an important process: magnetic reconnection (see e.g. Hesse and Cassak (2020) for a comprehensive review). Its basic principle is illustrated in figure 1.1. Reconnection occurs when opposite-directed magnetic field lines get sufficiently close. At the X line (or point), indicated by the white square, the magnetic field line topology changes. In the illustration, the leftward and rightward magnetic field lines merge to create a new closed magnetic field line on the left and the right (however opening of field lines is also possible). The creation of new field lines is accompanied by high-velocity plasma jets as plasma is heated and accelerated. Magnetic reconnection is a very efficient, short-lived process to transform magnetic energy to kinetic energy. It is an important process that allows energy from the solar wind to enter the near-Earth environment and leads to substorms and geomagnetic storms, which is elaborated in the following.

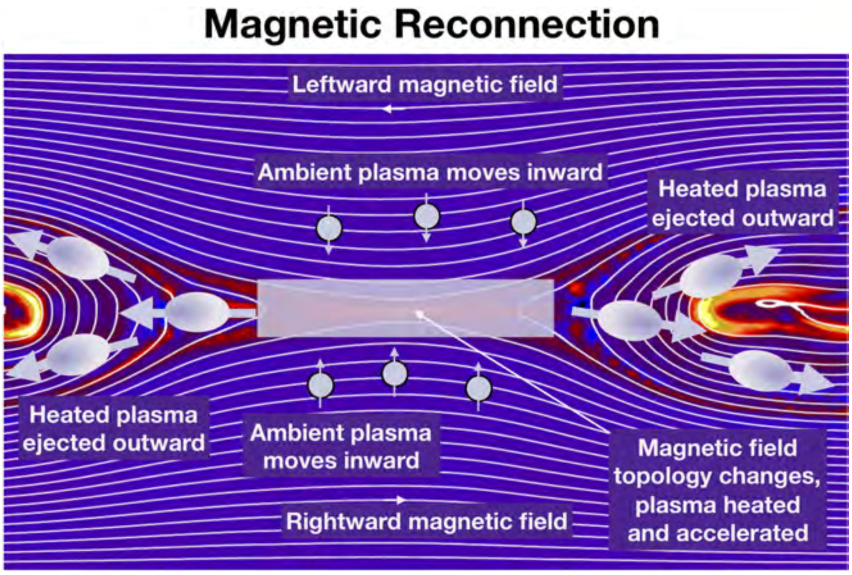

Figure 1.1: Conceptual principle of magnetic reconnection. Frozen-in plasma on opposite-directed field lines is convected into the white middle square where reconnection occurs, leading to newly created field lines and jets of heated and accelerated plasma. Taken from Hesse and Cassak (2020).

Chapter 2

Space Weather and the Geomagnetic Field

During the past century, technology and digitalisation have accelerated human progress which led to an increasing amount of our culture existing in digital form (Hodson, 2018). The digital revolution has brought humanity access to a wide range of new possibilities including global communication and navigation, as well as to a vast online database of knowledge. All of which is powered by electricity and thus demands for the expansion and development of power grid infrastructures all around the globe. The sky being not the limit, we have started populating our near-Earth space environment with technology to support our infrastructure and to explore the solar system in order to gain a better understanding of the world we live in. We have become dependent on these infrastructures and, consequently, have also learned about the threats they face. Especially in the past few decades the term *Space Weather* has emerged in order to describe the effects due to the interaction between our Sun and Earth on technological and human well-being. Space Weather is defined by the US National Science Foundation as (Wright et al., 1997):

> *"Conditions on the Sun and in the solar wind, magnetosphere, ionosphere, and thermosphere that can influence the performance and reliability of space-borne and ground-based technological systems and can endanger human life or health".*

As humanity expands and fosters its technological reaches, Space Weather is able to impact a wide variety of areas. Numerous socio-economical consequences are well documented in the literature (see e.g. Koskinen et al. (2001); Desmaris (2015); Wolfert, Ge, Verdouw, and Bogaardt (2017); Eastwood, Nakamura, Turc, Mejnertsen, and Hesse (2017)) including the following selected examples:

- **Scientific Payload on Spacecraft Missions**
  During space-missions, satellites and their payload built from sensible electronics have to withstand the harsh environment of space while performing their tasks. High energetic particles are able to penetrate the outer layers of satellites and harm fragile components by corrupting data or, in the worst case, destroying essential electrical components and instruments.
- **Communication and Positioning Systems**
  The ionosphere modulates the propagation of radio frequency signals. Variable conditions in the electron density due to increased solar activity can lead to loss of signals, affecting crucial communication and positioning systems. This can lead, for example, to significant positioning errors in precision agriculture and decreased directional drilling accuracy.

- **Power Grid Damage**
  Magnetospheric and ionospheric currents are enhanced during geomagnetic disturbances and lead to rapid and intense magnetic variations. Accompanied by geoelectric fields, they are responsible for geomagnetically induced currents (GIC) in electrical systems. GICs can lead to damages and malfunctioning on the power grid causing major power outages on wide-area scales.

Another more recent and comprehensive overview of space weather effects can be found in Coster, Erickson, Lanzerotti, Zhang, and Paxton (2021). Especially, strong space weather events called solar storms pose a significant risk. One of the first documented extreme events is the Carrington event that occurred in 1859. Richard Carrington observed intense white light flares above a large sunspot group on the surface of the Sun. Only 18 hours later, strong aurora were visible in the global night sky including mid- and low-latitudes. Back then, communication relied on telegraphs, connecting endpoints via kilometer long electrical cables. On a global scale, while some telegraph operators reported loss of messaging services, others had the possibility to send messages without active power supply. This was at a time, when technology was still in its early stages. A recent study on another intense event, the March 1940 Superstorm by Love et al. (2023), summarises the impacts from the unusually rapid geomagnetic field variations as *"severe for induced geoelectric fields on communication and power grid infrastructure at that time"*.

Even though, no comparable intense event has happened in the near past, there are many recordings of space weather impacts that demonstrate its present threat. In 2003, the so-called Halloween events were a series of storms accompanied by beautiful auroral displays, but led to major power outages in Lapland (Pulkkinen, Lindahl, Viljanen, & Pirjola, 2005). A recent example showed that not only very intense storms have the capability to disturb our operations: In 2022, a batch of communication satellites was launched but failed to reach orbit due to insufficient fuel reserves. The cause for which was a moderate solar storm that most probably led to just enough heating and thus expansion of the neutral atmosphere such that the satellite drag was stronger than the maximum thrust of their engines (Fang et al., 2022). Another interesting study considers the possible consequences of space weather conditions during the tragic case of the Titanic, affecting navigation and communication systems (Zinkova, 2020). These are but a few examples of the impacts of space weather illustrating its importance and the need for a better understanding and improved forecasting capabilities. As our society developed into a more technology-dependent civilisation, a global disruption in communication and infrastructure poses a substantial global threat. The discipline of space weather is devoted to the origin of such effects and deals with the investigation of phenomena arising on the Sun and their interactions and effects on Earth and in Earth's near-space environment. By nature it comprises a broad variety of domains, from heliophysics to geophysics. An overview of the main actors and related phenomena of space weather is presented in figure 2.1.

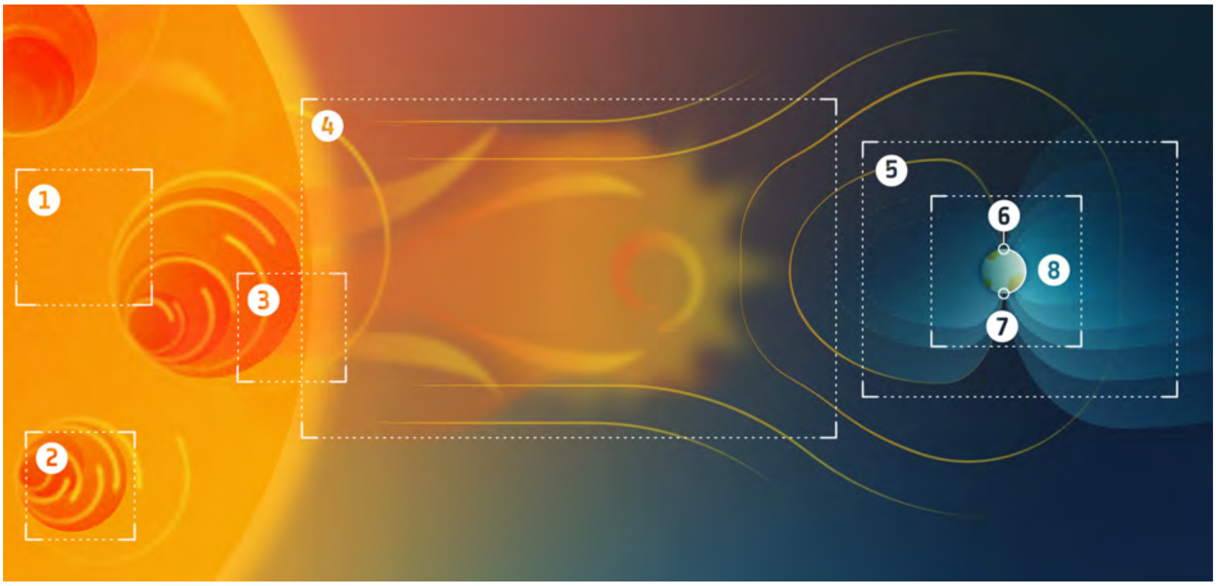

Figure 2.1: An overview of Space Weather depicting the main actors and associated phenomena, the Sun ①-③ and the Earth ⑤-⑧, and their interconnection via the solar wind ④. Image courtesy from ESA.

① **The Sun** is our nearest star and is the main driver and energy provider for space weather phenomena

② **Solar Flares** are strong bursts of electromagnetic energy that originate on the Sun's surface

③ **Coronal Mass Ejections** (CMEs) are large scale eruptions of solar material that are ejected into space

④ **The Solar Wind** is a constant stream of particles from the Sun's atmosphere carrying the solar magnetic field with it which is the cause for the Earth's particularly shaped magnetic environment

⑤ **The Magnetosphere** is formed as the solar wind compresses Earth's internal magnetic field on the day-side and elongates it on the night-side

⑥ **Substorms** are smaller-scale disturbances of the geomagnetic field which consequences are mainly confined to polar regions and are associated with auroral displays

⑦ **The Ionosphere** is a layer of ionised particles around Earth which coexists with Earth's neutral atmosphere, called the thermosphere

⑧ **Geomagnetic Storms**, accompanied by substorms, induce strong perturbations in the geomagnetic field which have consequences on a global scale, especially in the equatorial and radiation belt regions

The actors and associated phenomena related to space weather can mainly be described by plasma physics as presented in the previous chapter 1. In the following, each actor is presented in more detail, starting with the driver, the Sun. The magnetosphere as a large-scale structure is introduced and important current systems that support its shape are outlined. This is followed by a detailed discussion of the ionosphere with focus on mid-latitudes, given that its associated phenomena hold significant relevance for this work. Thereafter the geomagnetic field and its sources are presented. Last but not least, important measures in the field of space weather are introduced: magnetic activity indices. These condense geomagnetic information into a single (or sets of) indicator(s) that characterise the state of the geomagnetic field and act as important space weather proxies. The final chapter in the introduction covers geomagnetic baselines that are needed to determine the net effect of external drivers on the geomagnetic field, which represents the core of the presented work.

2.1 Our Sun

In astrophysics, the Sun, as illustrated in figure 2.2, is classified as a G-class main sequence star with luminosity class V (Gray et al., 2021), implying that it is an average star from the main sequence. It has a radius of around 700 000 km and a mass of 2×10^{30} kg. Its main constituent is Hydrogen, followed by around one fourth of Helium and traces of other, heavier elements. The immense power of the Sun is produced in its hot and high pressure core, burning Hydrogen to Helium. With helioseismology, it is possible to infer that the Sun is build up by a radiative zone, encapsulated within a convective zone. The transition area between those two, the tachocline, is believed to harbour the solar dynamo that generates the Sun's complex magnetic field which underlying processes are still actively debated (Charbonneau, 2020). The magnetic field of the Sun was first discovered by Hale (1908) after the discovery of the Zeeman effect.

The convective interior ot the Sun is cooled by radiating the largest portion of its total radiative output of 4×10^{26} W from its surface into space. The photosphere, the apparent visible surface of the Sun, is a thin layer of a few hundreds of kilometers at the base of the solar atmosphere with temperatures of around 5800 K. At a closer look, small scale structures are visible: the granulation. So-called granules are convection cells that origin in the lower convective zone. Hot plasma raises, to cool off through radiation and then sinks down again. Occasionally, darker regions are observable on the photosphere. These sunspots are regions with lower temperatures and thus appear darker, the umbra, surrounded by slightly brighter regions, the penumbra. Sunspots are characterised by strong magnetic fields and usually occur in pairs of opposing field directions. Solar flares are sudden and intense releases of electromagnetic energies that are associated with rapid reconfigurations of the Sun's magnetic field. Prominences are large and bright structures that emerge from sunspots with opposite polarity and extend from the Sun's surface out into its atmosphere and are often described as giant loops of plasma. On top of the photosphere, the Sun's atmosphere is distinguished into three layers. The chromosphere is about 2000 km high and can be observed in the UV spectrum. The transition region is a thin layer where the fastest temperature raise occurs: from several tens of thousands of K to a few million K that are found in the solar corona. Processes explaining such a steep temperature rise are still under hot debate (Cranmer et al., 2015). The Sun is too bright to observe its much fainter corona. During solar eclipses or with specialised instrumentation, so-called corona-graphs that occult the surface of the Sun, coronal features are made

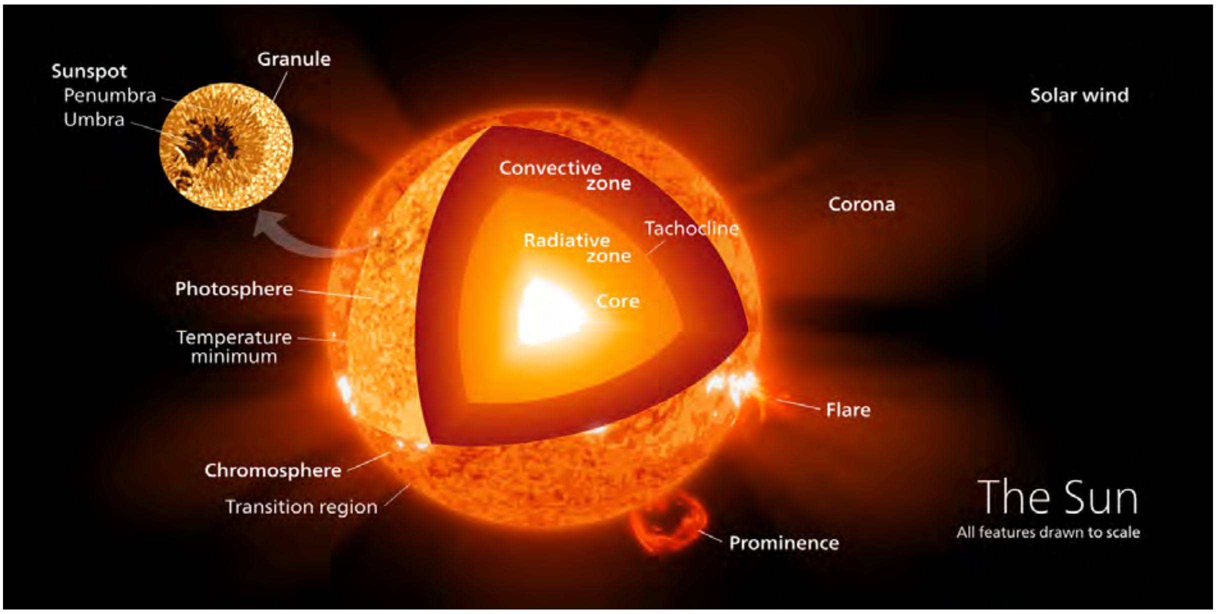

Figure 2.2: A scientifically informed artistic impression of the Sun and its components. Designed and provided by Wikimedia Commons User:Kelvin13

visible. These structures are made of plasma that travels on open and closed magnetic field lines. Coronal holes are surface regions with open magnetic fields on which plasma flows out into interplanetary space. Due to the outflow these regions are marked by less dense plasma and thus are darker.

As our closest star, the Sun provides our planet with life-sustaining energy through electromagnetic radiation. The solar spectrum can be described by a black-body spectrum of ~5800 K with additional contributions in the extreme ultra-violet (EUV) and X-ray regime originating in its chromosphere and corona. This contribution in the high energy part of the spectrum is the major source of heating and ionisation of the higher parts of Earth's atmosphere, creating the ionosphere which is discussed in detail in chapter 2.3. Additionally, the Sun's reach stretches far beyond the orbit of Pluto, creating a cavity within the interstellar space, called the Heliosphere, protecting us from high energetic galactic cosmic rays. This stretching of the Sun's influence is due to the extension of its atmosphere from the solar corona into space by what is known as the solar wind.

2.1.1 Solar Wind

Postulated in the early twentieth century by Birkeland, the first in-situ observations, and thus confirmation of the solar wind as a particle stream coming from the Sun, were conducted by the Mariner 2 mission (Neugebauer & Snyder, 1966). The solar wind is a fully ionised plasma which main constituents are protons H^+, alphas H_e^{2+} and electrons. Classically, two types of solar wind can be distinguished: The slow solar wind originates mainly from equatorial latitudes of the Sun, having average velocities of $\sim$300 to 400 $\mathrm{km\,s^{-1}}$ with densities of $\sim 7\,\mathrm{cm^{-3}}$. The fast solar wind has velocities of up to 500 to 800 $\mathrm{km\,s^{-1}}$ while having lower densities with $\sim 2.5\,\mathrm{cm^{-3}}$ and originates mainly from coronal holes in the Sun's polar regions. Here one foot of the magnetic field lines is attached to the Sun and the other one is stretched out into interplanetary space on which the plasma is accelerated to supersonic speeds into the heliosphere.

In MHD, the solar wind can be described as a magnetised fluid for which the frozen-in theorem (1.38) applies. This important result leads to the creation of the interplanetary magnetic field (IMF) as plasma being tied into the solar magnetic field is flowing into space. As the Sun rotates and plasma is expelled, together with the frozen-in magnetic field, an archimedian spiral structure is created, the so-called Parker Spiral (Parker, 1958). This topology leads to a big scale structure magnetic field that propagates through interplanetary space interacting with the solar system's bodies, especially the Earth's magnetic field. The Parker spiral in the equatorial plane (as looking from top down) is depicted in figure 2.3 by using the solar wind velocity from the model HelioCast (Réville et al., 2023). The black circle indicates a distance of one astronomical unit (AU), whereby 1 AU equals approximately 150 million km representing the average Sun-Earth distance.

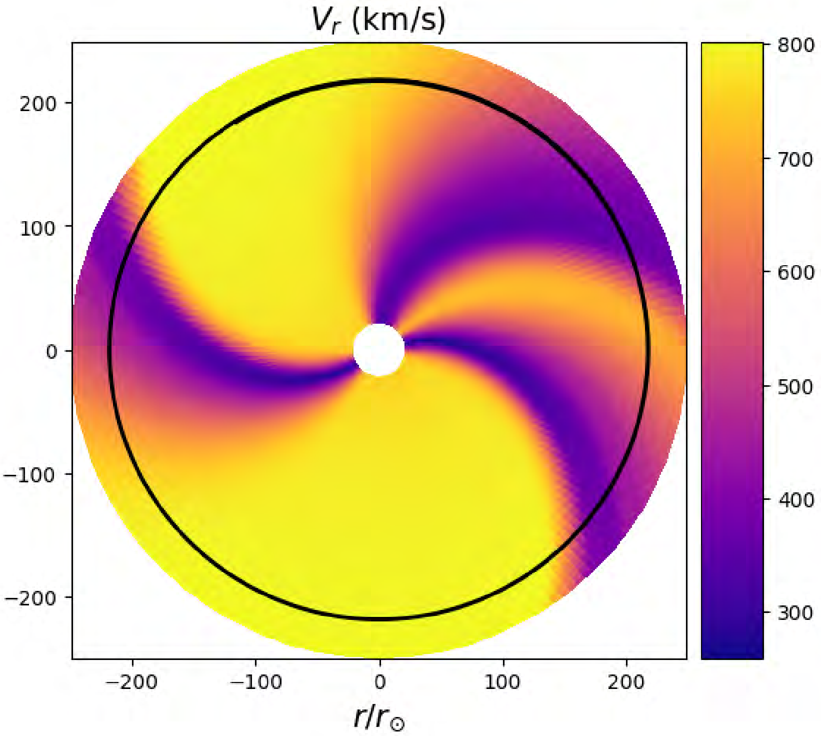

Figure 2.3: The Parker Spiral illustrated by the modelled solar wind velocity in the equatorial plane in top-down view as derived from HelioCast (Réville et al., 2023). The black circle indicates a distance of 1 AU and the white inner one the position of the Sun. The axes are given with respect to Sun's radius $r_\odot$.

2.1.2 Variability of the Sun

Driven by its internal dynamo, the Sun's activity is modulated during its typical 11-year Solar Cycle (SC). This cycle has already been recognised as early as 1848 due to its manifestation in the number of sunspots S_N with each cycle being individual with its own behaviour (Hathaway, 2015). However, general patterns can be deduced leading to four phases: the solar cycle minimum and maximum together with increasing and decreasing phases. During solar minimum, the quiet Sun has a dipole-like magnetic field with generally low magnetic activity and coronal holes that tend to occur mainly on the poles. The number of sunspots is at its minimum. While at solar maximum, magnetic activity is at its peak, leading to a complex magnetic field topology (McComas et al., 2003). The corona is highly structured and coronal holes occur more frequently, now also around the equator, increasing the occurrences of transient events like CMEs and flares. The sunspot numbers are at their peak. Currently we are in the increasing phase of solar cycle 25 (SC25). Not only the corpuscular emission is affected by the solar cycle, but also the electromagnetic radiation. UV and X-ray fluxes are significantly enhanced during solar maximum compared to minimum. Especially radio emissions that are recordable at Earth's surface are good proxies for the solar cycle and solar activity. The 10.7 cm solar radio flux, $F10.7$, has been reported and used since the first half of the twentieth century for measuring solar activity levels. It is expressed in solar flux units (sfu), with 1 sfu $= 10 \times 10^{-22}\,\mathrm{W\,m^{-2}\,Hz^{-1}}$. A detailed review of the measurements and derivation of the $F10.7$ index is given in Tapping (2013). Figure 2.4 shows the sunspot number S_N and the $F10.7$ index. Increased solar activity from transient events are readily distinguishable in $F10.7$.

Another important property of the Sun is its rotation period of 27 days which is connected to the recurrence of coronal holes and with associated patterns in the solar wind.

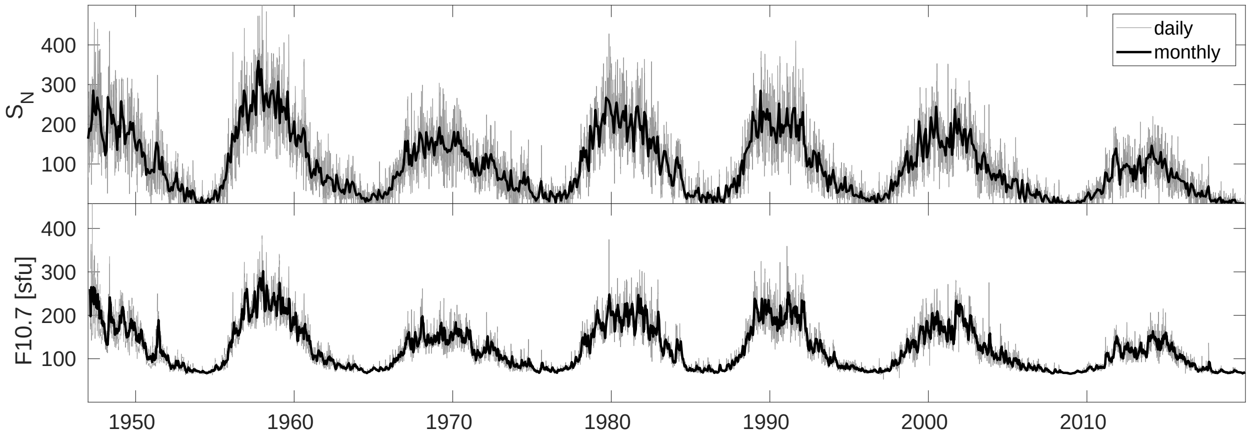

Figure 2.4: The daily and monthly averaged sunspot number S_N and $F10.7$ index in sfu since 1947. The data is taken from SILSO World Data Center (2023) and from LISIRD (LASP Interactive Solar Irradiance Datacenter)

On smaller timescales, transients often manifest themselves as sporadic and violent events. Solar flares as sudden locally confined brightening on the photosphere that can extend into the corona and increase the electromagnetic radiation in all wavelengths significantly. They are classified according to their soft X-ray energy flux in specific spectral bands: A, B, C, M, X, with X being the most intense and each class increases the intensity by a factor of 10 (Hudson, 2011). They are also clearly observable in $F10.7$. Coronal Mass Ejections (CMEs) are eruptive events in the lower corona that can be associated to magnetic reconfigurations of prominences. They blast high amounts of charged particles with speeds of up to $2000\,\mathrm{km\,s^{-1}}$ into interplanetary space, increasing IMF and solar wind parameters dramatically. When a CME expands into interplanetary space, and thus also when it arrives at Earth, it is commonly referred to as an Interplanetary Coronal Mass Ejection (ICME). CME occurrence rates are lower during solar minimum and higher during solar maximum, remaining high during the descending phase. Co-rotating interaction regions (CIRs) form when the fast solar wind catches up with the slower wind, creating high compression regions. These large-scale structures of transient solar events, when reaching Earth, may be highly geoeffective and consequently produce major geomagnetic storms (Denton et al., 2006; Kilpua, Balogh, von Steiger, & Liu, 2017).

2.2 The Magnetosphere

The solar wind with the frozen-in IMF encounters the Earth's magnetic field as an obstacle giving rise to a complex configuration of plasmas and magnetic fields that make up the so-called magnetosphere (Vasyliunas, 1983). As the plasma is slowed down upstream of Earth, a bow shock is formed, converting kinetic into thermal energy. This leads to the plasma having higher and more variable temperature, pressure and magnetic field strength with subsonic speeds in the magneto-sheath, situated just behind the bow shock. The magnetopause marks the boundary layer at which the external solar wind pressure is balanced with the internal magnetic pressure. In ram-direction, i.e. on the dayside, the Earth's magnetic field lines are compressed, while on the night-side the solar wind flow elongates field lines forming the magnetotail. The stand-off distance or subsolar point of the magnetopause has a typical value of 10 R_E with $1\,R_E \approx 6371\,\mathrm{km}$. This distance is highly variable as a function of solar wind properties. The magnetotail on the night-side is estimated to extend out up to 5000 R_E (Cowley, 1991). There is a reversal in direction of the magnetic field lines between the northern and southern lobes of the tail which are separated by the plasma sheet. The polar cusps are regions around Earth's magnetic poles that map into the outer magnetospheric regions close to the magnetopause. When they connect with the IMF, solar wind particles are able to penetrate inside the magnetosphere, down to the upper atmosphere in dayside auroral zones via these funnels.

The magnetosphere is populated with various distinct plasma populations (in terms of energy and density). For example, the toroidal-shaped radiation belts are located between 2 and 6 R_E, consisting of highly energetic particles that are trapped on magnetic field lines bouncing between the two hemispheres. The plasmasphere, a torus-shaped volume co-located with the radiation belts, consists of cool and dense plasma. The plasma comes from two main sources: the ionosphere and the solar wind. Plasma from ionospheric outflow is populating mainly the plasmasphere. Plasma from the solar wind first populates the outer regions of the magnetosphere, mainly in the plasma sheet, which can then be injected towards the inner magnetosphere in the radiation belts and ring current (Kronberg et al., 2021). The overall structure of the magnetosphere is supported by various current systems, see e.g. Ganushkina, Liemohn, and Dubyagin (2018) for a review.

- **Magnetopause and Magnetotail Currents**
  The magnetopause separates the low magnetic field strength regime of the solar wind from the high magnetic field strength regime of the magnetosphere. This configuration leads to $\nabla \times \mathbf{B} \neq 0$. As the solar wind particles encounter the much stronger magnetic field strength of the magnetosphere their gyration is influenced in the magnetopause layer. They perform half a gyration with ions having a larger gyroradius than electrons and the species are deflected in opposite directions. This leads to the generation of the magnetopause currents, also known as the Chapman-Ferraro currents, which flow on the surface of the magnetosphere as depicted in figure 2.6 in green. In the magnetotail, these currents close through the cross-tail current that flows in the equatorial plane from evening (dusk) to morning (dawn) sector. The shape and geometry of the current sheet is depending on a feature of the Earth's intrinsic magnetic field, the dipole tilt

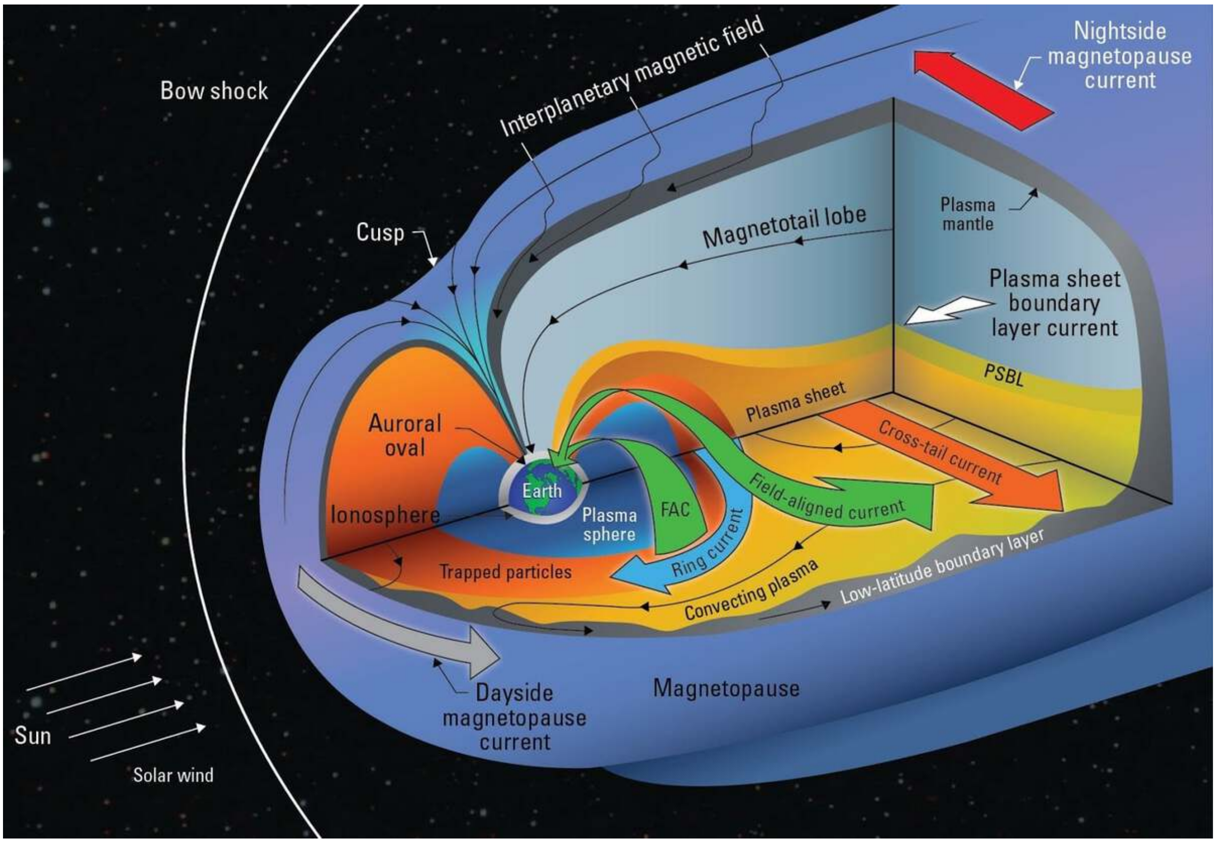

Figure 2.5: An illustration of the inner structure of the magnetosphere with its complex morphology of current systems. Image courtesy from the National Oceanic and Atmospheric Administration (NOAA).

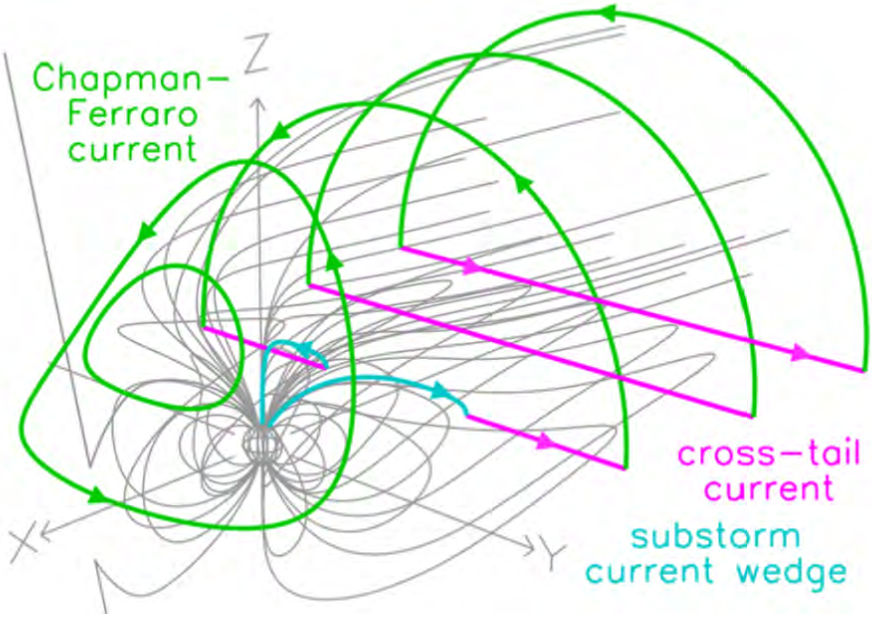

Figure 2.6: Schematics of the magnetopause current system (Chapman-Ferraro current in green) that closes via the cross-tail current (in pink) on the night-side. The substorm current wedge (in blue) is an important current system that arises during substorms. (Taken from Milan et al. (2017))

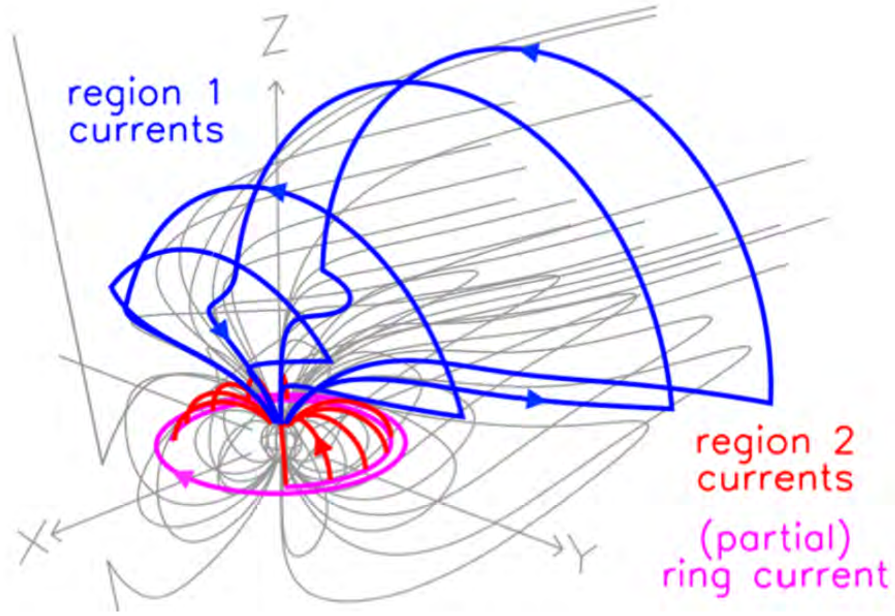

Figure 2.7: Schematics of the Region 1 (blue) and Region 2 (red) Field Aligned Currents (FAC) systems together with the Ring current (pink). (Taken from Milan et al. (2017))

(see chapter 2.5.1), and the conditions in the IMF (Tsyganenko, 1989; Tsyganenko & Stern, 1996).

- **Ring Current**
  The dipole configuration of Earth's internal magnetic field (i.e. a curved geometry with gradient magnetic field that is stronger towards the poles than at the equator) leads to two magnetic mirror points, as discussed in chapter 1.2. The particles undergo a bounce motion and become trapped, leading to increased particle fluxes inside of ∼6 R_E, forming the so-called radiation or Van Allen belts for the most energetic particles. Additionally to the bounce motion, the particles also experience a gradient and curvature drift due to the inhomogeneous dipole magnetic field, leading to an azimuthal drift. The drift, as in equation (1.15), is westward for ions and eastward for electrons, resulting in charge separation. The differential motion of the particles give rise to an important current flowing in the equatorial plane at around 2 - 9 R_E: the Ring Current (Cole, 1966). During geomagnetic storms, the partial ring current connects to the high latitude ionosphere as depicted in pink in figure 2.7. Moreover, further particles are injected following tail reconfiguration, leading to a significant increase in intensity of the ring current which is recorded by ground magnetometers (see chapter 2.4).

- **Field-Aligned Currents (FACs)**
  The field aligned currents (also referred to as Birkeland currents) connect the magnetosphere with the high-latitude ionosphere (Iijima & Potemra, 1978). Two types of FACs are distinguished: Region 1 FACs connect the high-latitude ionosphere into the dayside magnetopause and the magnetotail and are farther poleward (depicted in blue in figure 2.7) and Region 2 FACs that connect to the ring current farther equator-ward (depicted in red). They are a consequence of convection patterns driven by the solar wind and pressure gradients in the magnetosphere.

These current systems and the magnetosphere in general are not static. The Earth's rotation induces co-rotation of the atmosphere such that the plasma in the inner magnetosphere drags the magnetic field lines with it. The convection in the outer magnetosphere is due to the solar wind flowing around it through viscous interaction and is enhanced by reconnection processes at the magnetopause and in the tail. The steady-state magnetospheric convection is illustrated in figure 2.8 after Dungey (1961). The IMF that is frozen

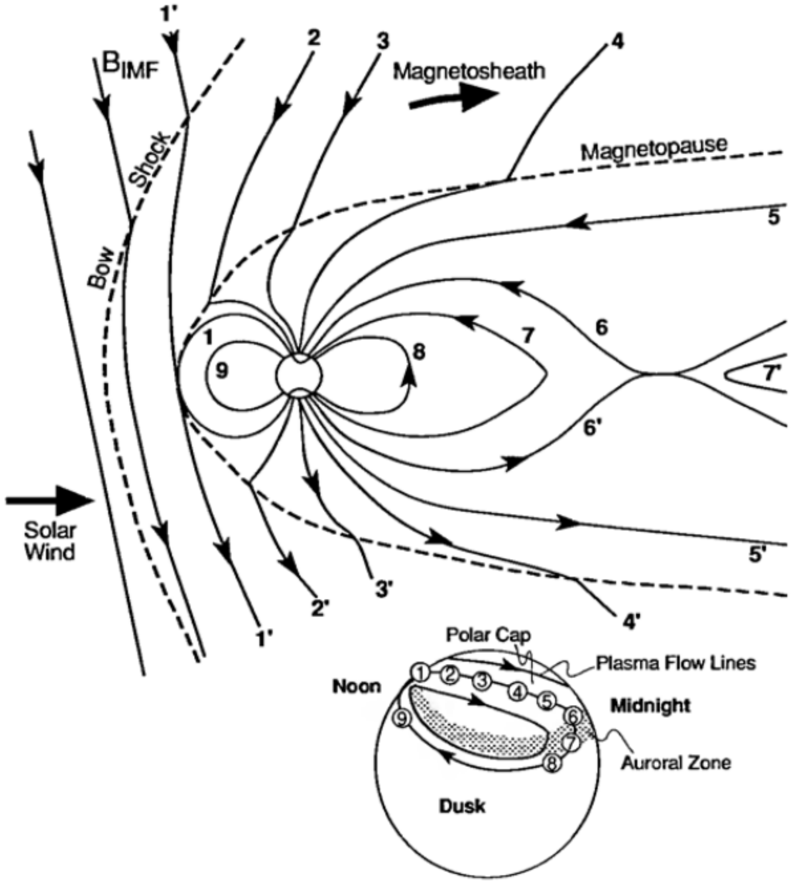

Figure 2.8: The steady-state magnetospheric convection that is initiated via magnetic reconnection of the IMF with Earth's magnetic field on the day-side after Dungey. The corresponding convection patterns in the high-latitude ionosphere are depicted on the lower right. (Taken from Kivelson and Russell (1995))

into the solar wind encounters the Earth's magnetic field. When the IMF is pointing in the opposite direction than the Earth's magnetic field, i.e. the IMF is pointing southward (also referred to as B_z negative), magnetic reconnection is enabled to take place on the day-side. This is the case for field lines **1** and **1'**. The previously closed field line **1** from Earth is opened up and connected to the solar wind **2**, **2'**. The solar wind drags the field line over the polar cap **3**, **3'** and into the magnetotail **4**, **4'**. In the tail lobes magnetic energy piles up, leading to convection of field lines towards each other from both hemispheres **5**, **5'**. Eventually, magnetic tension is high enough to trigger magnetic reconnection, forming a new, closed field line **6** and **6'** that is again connected to Earth. The other field line **7'** forms a magnetic island and is expelled into interplanetary space. Accelerated due to the conversion of magnetic energy into kinetic energy, the connected field line **7** together with the the particles moves towards Earth on the night-side. When magnetic pressure is higher than the kinetic pressure, field line **8** becomes dipolar-shaped again. The closed field line **9** is then transported back to the day-side. This cycle induces the typical convection patterns observed in the high-latitude ionosphere, as depicted in the lower part of figure 2.8 for which the numbers mark the associated magnetospheric field lines. The induced convection patterns are equivalent to an electric potential pattern with a total potential difference between dawn and dusk of about 50-100kV, also referred to as the polar cap potential. In practice, the convection is not steady. Though the reconnection rates on the day-side and night-side keep balance on longer time-periods, for shorter periods a strong imbalance can occur, which leads to the formation of substorms described in detail in chapter 2.4. This short introduction of the magnetosphere already suggests the complex coupling between the solar wind, magnetosphere and ionosphere. In fact, in order to understand and predict phenomena, it is needed to consider all these subsystems as one unified system with constant interaction.

2.3 The Ionosphere

The neutral atmosphere of Earth can be classified by distinct temperature profiles in dependence of altitude. The troposphere, which reaches from the ground to approximately 12 km, is the layer we live in and for which temperatures fall with raising height. The stratosphere, located between 12-50 km is characterised by a raise in temperature due to the absorption of solar UV light by ozone. Between 50 and 85 km, the mesosphere exhibits fast falling temperatures with increasing height due to effective CO_2 cooling. Above 85 km temperatures rise quickly in the thermosphere as solar UV and soft X-ray radiation can penetrate these heights easily, resulting in effective heating (de Pater & Lissauer, 2015). The solar radiation does not only increase temperatures but is energetic enough to invoke ionisation and plays an important factor in the creation of the ionosphere. As the neutral atmosphere is characterised by its temperature profile, the ionosphere can be characterised by its electron density profile as illustrated in figure 2.9. The upper neutral atmosphere overlaps with the lower ionosphere, leading to plasma-neutral interactions, especially in the D- and E-region. Detailed reviews including chemistry and transport mechanisms in the ionosphere, and treatment of its creation and variations can be found in e.g. Kelley (1989) and Schunk and Nagy (2009). In the following, the main ionisation and loss processes that are responsible for the distinct density profile of the ionosphere are briefly described.

- **Solar UV Ionisation**
  The main source of electron production in the ionosphere is direct irradiation from the Sun. The high energies needed to ionise atmospheric atoms and molecules, i.e. removing electrons from the atom's shell, come from above the UV regime of the solar radiation spectrum. The stronger the radiation, the deeper it can penetrate into the atmosphere as depicted in figure 2.9. When an atom or molecule is ionised, the incident radiation decreases its intensity as it spends energy on ionisation. The amount of decrease depends upon the initial intensity, the number density of the neutral gas, the absorption cross-section and the radiation's path length through the medium. According to the barometric law, the neutral density decreases with altitude and thus the radiation intensity increases with altitude. This leads to a pronounced electron density peak around 400 km, forming the so-called Chapman profile (Chapman, 1931).

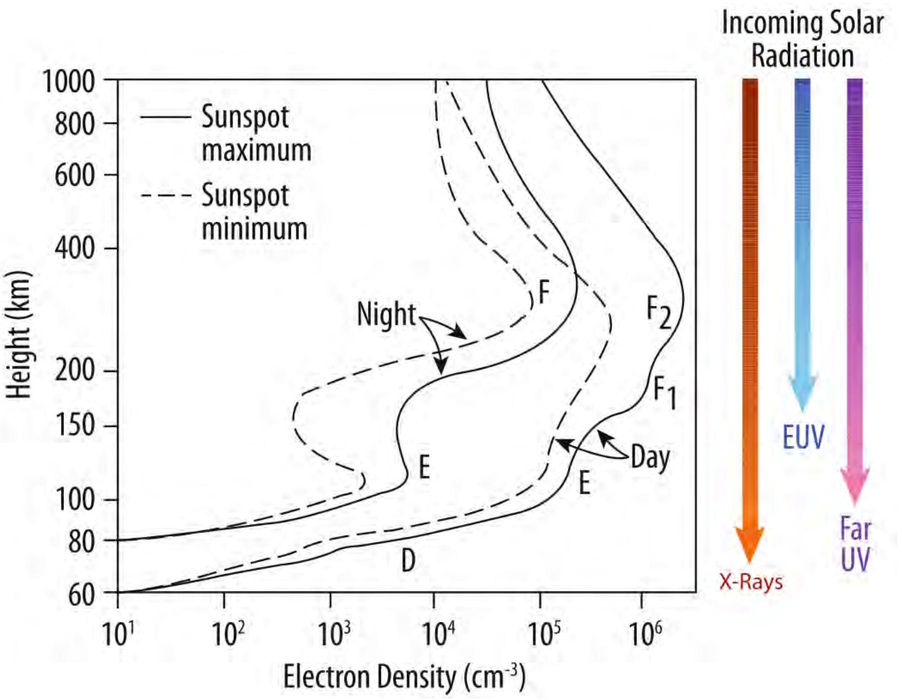

Figure 2.9: The electron density profile of the ionosphere with indications of the solar radiation penetration depths. Distinct profiles for night- and day-time during solar maximum and minimum are indicated. (Taken from Pfaff (2012))

- **Ionisation by Energetic Particles**
  Energetic particles essentially from the magnetopause and the tail that enter the atmosphere via magnetic field lines have enough energy to ionise atoms and molecules. This production process dominates during the night when the main source of ionisation, the solar radiation, ceases. This process is able to maintain the general profile of the ionosphere but to a weaker extent. The stopping height marks the height at which the incoming particle deposits the majority of its energy into the atmosphere, leading to the night peaks. Even though less energetic, this process is especially important at high latitudes where ionisation and conductivity is reinforced through precipitating particles from the solar wind via dayside and tail reconnection.

- **Recombination**
  An important loss process is recombination during which the positive ion gains an electron and forms a neutral atom. The recombination rate depends upon the number densities of ions and electrons, as well as the collision frequency. In the lower ionosphere recombination is dominant as collision frequencies are increased due to the high density of neutral atoms and molecules.

- **Charge Exchange**
  The process of exchanging electrons between interacting and colliding particles (e.g. neutral atoms with ions) is called charge exchange. This process changes the nature of the ions and is proportional to the electron number. This is an important loss process in the high altitude F-region of the ionosphere, converting hydrogen ions into oxygen ions and vice-versa.

The combination of these processes forms the characteristic density profile of the ionosphere as sketched for mid-latitudes in figure 2.9. It is common to divide the ionosphere according to this profile into three main layers: the D-, E- and F-regions.

- **The D-Region**
  The D-region is situated at an altitude of about 60 to 90 km. The main ionisation process is high-energy X-ray radiation which is able to penetrate these depths. Due to the relatively high density of neutral atoms and molecules from the atmosphere, high collision frequencies occur leading to a gas that is only weakly ionised. In this region, chemistry dominates and negative and complex ions can be formed. During night-time, the production source of solar irradiation ceases and loss processes dominate, such that the D-region vanishes. Temporarily the ionisation level in the D-region can be remarkably enhanced during events like solar flares.

- **The E-Region**
  At altitudes between 90 and 150 km, the E-layer forms due to the absorption of EUV to Far UV radiation with peak densities around 110 km. At these heights, substantial densities of neutrals are still present and the gas is partially ionised. This allows strong interactions due to differential motion between the ionised and neutral particles giving rise to the E-region dynamo that is the source of important current systems in the ionosphere. Generally, this layer is in balance between production, charge exchange and loss processes and thus in chemical equilibrium. Auroral particle precipitation is able to maintain the E-region during the night in higher latitudes.

- **The F-Region**
  The F-region can be classified into two sub-regions during daytime: The F1-region forms by absorption of shorter UV radiation at around 200 km followed by chemical formation of NO^+ ions which possesses a very low ionisation potential. It disappears during the night as this production source ceases. The F2-region located at an altitude of about 300 km is predominately populated by oxygen ions. During the day, O^+ is produced locally in the ionosphere and transported upward to the plasmasphere. This acts as a reservoir and the particles are transported downward maintaining the F-region during the night as recombination effects are also decreased due to low densities.

Each of these layers has a major dependency on solar radiation which creates the distinct day and night density profiles in figure 2.9. The solar radiation intensity varies with solar cycle and so does the ionisation profile. During solar maximum (and thus Sunspot maximum), the electron density is significantly higher as solar radiation is increased than during solar minimum (and thus Sunspot minimum). The difference is in the order of one to two magnitudes. Additionally, as solar illumination varies with season, densities are higher during summer than winter.

2.3.1 The E-Region Ionospheric Dynamo

At the altitudes of the E-region, abundances of charged and neutral particles co-exist and allow for strong interactions between these populations creating the so-called ionospheric dynamo. In turn, this dynamo gives rise to important current systems in the ionosphere. In this region, the plasma can be considered partially ionised and magnetised with densities allowing abundant collisions. The electron cyclotron frequency is higher than the electron-neutral collision frequency for the lighter electrons. Meanwhile, the ion cyclotron frequency of the heavier ions is lower than their collision frequency with neutrals. This leads to the electrons being frozen into the magnetic field, while the ions are governed by winds and tides from the neutral atmosphere. Consequently, in Ohm's law (1.25) the conductivity tensor becomes anisotropic as in (1.28) and writes as

$$\mathbf{j} = \sigma(\mathbf{E} + \mathbf{U} \times \mathbf{B}) \,, \tag{2.1}$$

with $\mathbf{U}$ being the neutral wind velocity and the anisotropic conductivity tensor σ with Pedersen conductivity σ_P, Hall conductivity σ_H and parallel conductivity $\sigma_{\|}$. The conductivities depend upon electron density and collision frequencies between electron-ions and ion-neutrals. The exact expressions are derived in K.-I. Maeda (1977) and Takeda and Araki (1985). Figure 2.10 illustrates a typical conductivity profile in the day-time ionosphere at mid-latitudes as generated by the IRAP plasmasphere-ionosphere model (IPIM) (Marchaudon & Blelly, 2015).

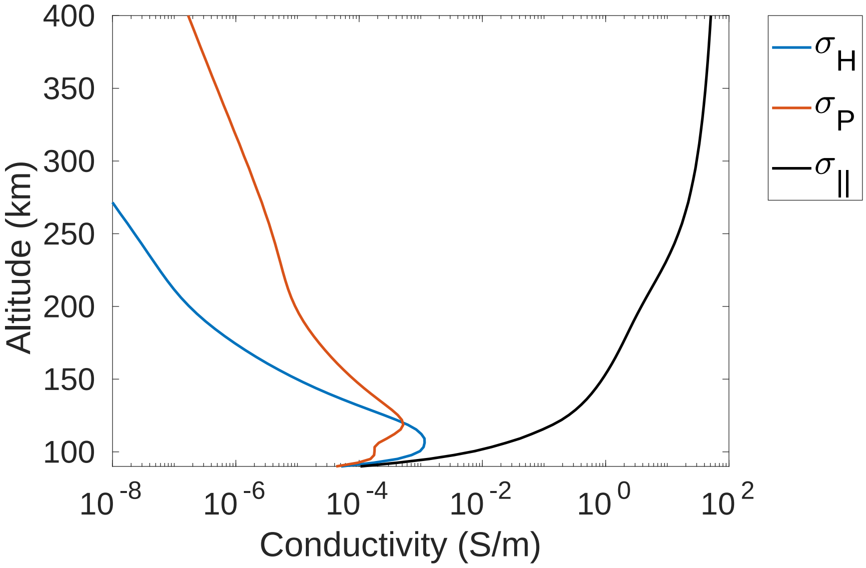

Figure 2.10: Conductivity profile of the E- and F-region in the mid-latitudinal ionosphere using IPIM (Marchaudon & Blelly, 2015).

The Hall conductivity σ_H (blue) peaks at lower altitudes with higher values than the Pedersen conductivity σ_P (in red). The parallel conductivity $\sigma_{\|}$ (in black) is always higher than σ_P and σ_H. These conductivities are the basis of ionospheric current systems as parallel (field-aligned), Pedersen and Hall currents are generated and coexist in this system. The differential motion between ions and electrons creates a Hall current through the electron motion perpendicular to the electric and magnetic fields, since ions are strongly slowed down by collisions with neutrals. At higher altitudes where the cyclotron and collision frequency of ions becomes comparable, the ions start moving in the direction of the electric field and they carry a Pedersen current. In the high-latitude ionosphere, the Pedersen currents have the role of closing FACs in the auroral oval and are associated with auroral displays (Baker, 2019).

2.3.2 Solar Quiet Current Systems

In low- and mid-latitudes the E-region dynamo is powering an important current system: the Solar Quiet (Sq) current system. The name solar quiet comes from their imprints on geomagnetic field measurements as they induce very smooth and characteristic diurnal variations in the absence of solar storms, i.e. during geomagnetically quiet periods.

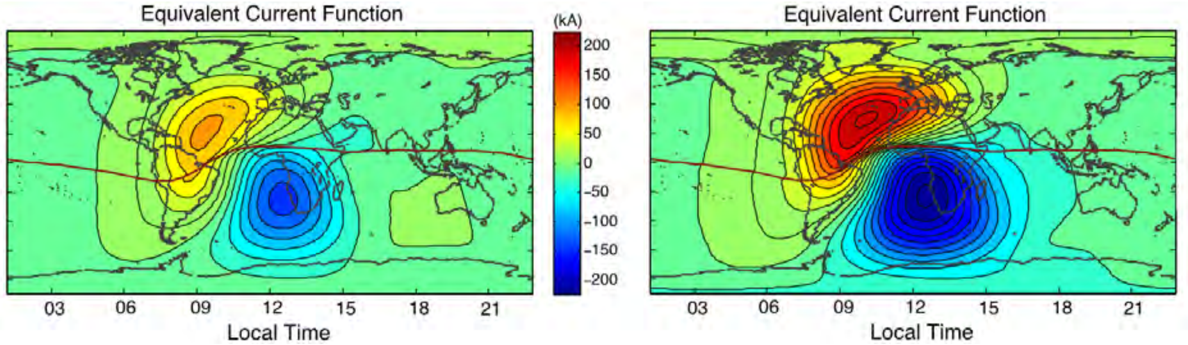

Figure 2.11: Simulation of the global intensity of the solar quiet current systems for low solar activity (left) and strong solar activity (right). (Taken from Yamazaki and Maute (2017))

The global shape of the Sq current systems is depicted in figure 2.11 and forms two vortex cells, one in each hemisphere. The direction of the currents is inverted in the two hemispheres, i.e. in the northern hemisphere (NH) the current cell is directed anti-clockwise and in the southern hemisphere (SH) clockwise. At the geomagnetic equator where the two cells meet a very strong zonal current is flowing reinforced by the specific magnetic configuration in this region: the Equatorial Electrojet (EEJ), see chapter 2.3.3.1. The Sq currents cannot be directly measured, but are indirectly derived from magnetic field data (see chapter 2.6.1). The typical patterns induced by the Sq current cells in magnetometer readings is depicted in figure 2.12 for a large set of magnetometer stations spread over latitude and aligned on one longitudinal sector. The magnetic field is given in geographic coordinates, N pointing towards North, E towards East and Z vertically down (see chapter 2.6.3). The North component indicates the position relative to the focus of the current cell. In the NH, it is negative when the station is situated above the focus and positive when it is situated below the focus. In the SH, it is the opposite as the current cell flows in the opposite direction. The East component shows a smooth sine signal that changes sign from NH to SH. The Z component seems mainly unaffected. In all three components the footprints of the equatorial electrojet is clearly visible around the dip equator.

As these cells are powered by the E-region dynamo which is depending on direct solar irradiation, these current systems are concentrated on the day-side. Due to the coupling to the neutral atmosphere in the dynamo region, the Sq currents are strongly modulated by atmospheric tides. Such tides are global-scale oscillations with harmonic periods of a day, i.e. 24 hours, 12 hours, 8 hours, 6 hours and so on of which the 24 hours tide is the primary driver of Sq currents (H. Maeda, 1955; Kato, 1957; Lindzen & Chapman, 1969). Through the absorption of infrared radiation in the troposphere and absorption by ozone in the stratosphere, the latent heat release generates upward-propagating tides. As they propagate upward they grow exponentially and when they reach the dynamo region they have amplitudes of several tens of meters per second in the horizontal wind. One third

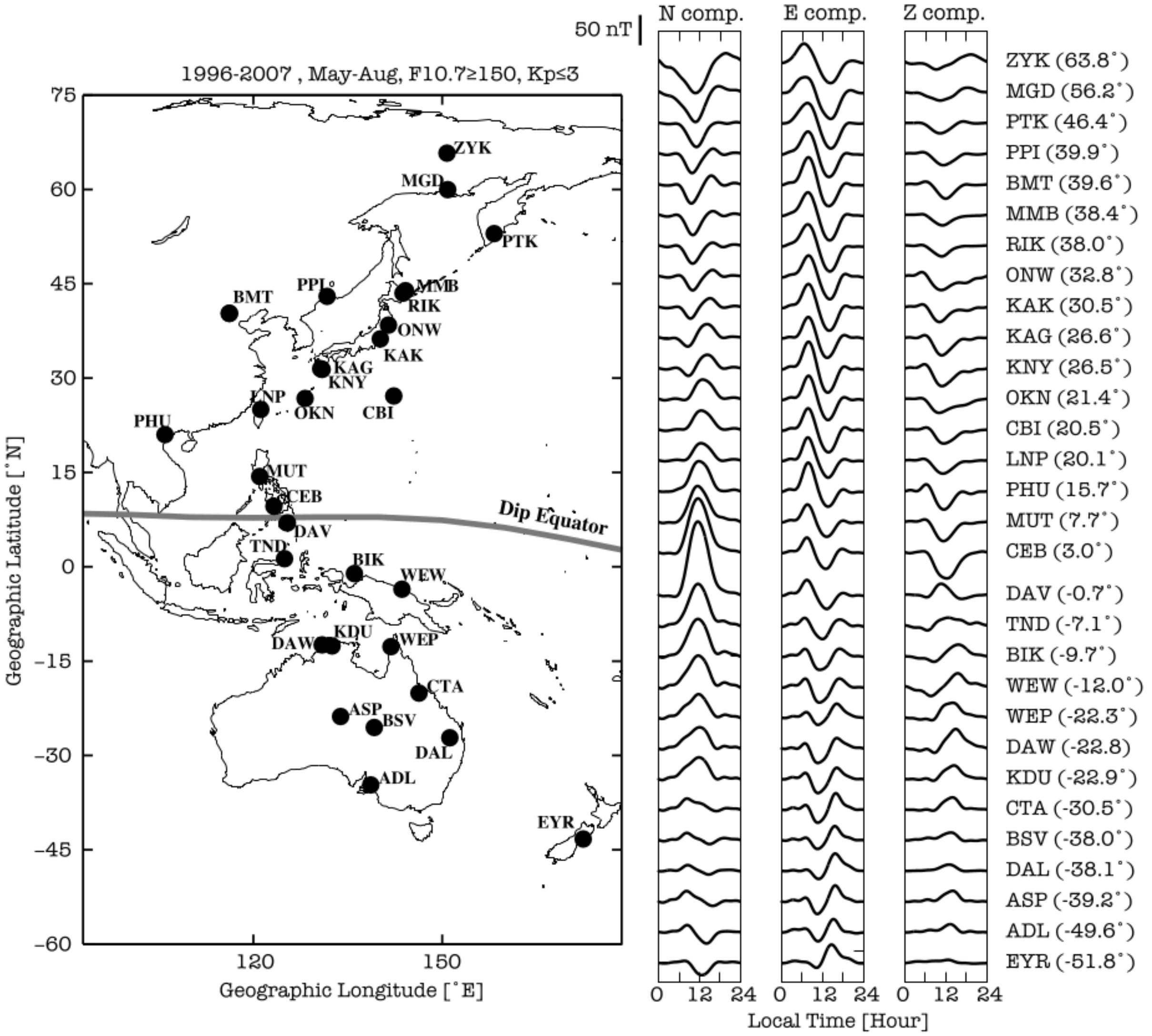

Figure 2.12: Average daily variations in magnetic field measurements in the three components North (N), East (E) and vertically down (Z) during May to August 1996-2007. (Taken from Yamazaki and Maute (2017))

of the total Sq currents are driven by such upward propagating tides (Yamazaki & Richmond, 2013; Yamazaki, Richmond, Maute, Wu, et al., 2014). Analysing magnetometer measurements from mid-latitudes, the spectra show distinct spikes at 24h, 12h, 8h and 6h which are a clear indicator of the Sq current system (Campbell, 1989).

As already noted before and as seen in figure 2.9, the electron density and thus conductivity is varying with the solar cycle and consequently modulates the solar quiet current system. Distinct solar cycle, seasonal and day-to-day variations of the Sq currents are well documented and outlined in the following. A detailed overview and description of the Sq currents together with the equatorial electrojet can be found in Yamazaki and Maute (2017).

- **Solar Cycle Dependency**
  The conductivity of the ionosphere is closely connected with solar activity. This affects the amplitude and the focus position of the Sq current cells. The amplitude is typically two times larger during solar maximum than during minimum (Takeda,

1999). Various studies suggest that the amplitude is highly linearly correlated with solar proxies like $F10.7$ (Yamazaki & Kosch, 2014; Yamazaki & Maute, 2017). Studies have shown that the amplitude of the 24h, 12h and 8h Fourier components are strongly dependent on $F10.7$ while the same holds for the phase for the 24h and 12h components and thus the location of the focus which shifts to later local times as solar activity increases (Olsen, 1988; Yamazaki & Kosch, 2014; Yamazaki & Maute, 2017).

- **Seasonal Dependency**
  In general, the Sq amplitude is higher during summer than winter at mid-latitudes due to prolonged solar irradiation. Peak amplitudes can be found during both equinoxes in low- and equatorial latitudes which can be related to the influences of the equatorial electrojet and possible equinoctial effects. The amplitudes during summer are around three times higher than during winter (Takeda, 1999; Yamazaki & Maute, 2017). Especially during winter, the currents can become so weak that the cell itself may disappear (Campbell, Arora, & Schiffmacher, 1993; Rastogi, Crandra, & James, 1996; Stening & Winch, 2013). The season also has a significant effect on the location of the focus. During summer the focus is shifted to earlier local times when compared to winter, which holds for both hemispheres (Campbell & Schiffmacher, 1987, 1988).

- **Day-to-Day Variability**
  The Sq current systems show strong day-to-day (D2D) variability in shape, amplitude and phase. This D2D variability is well documented while its driving mechanisms are yet to be fully understood, see e.g. Hasegawa (1960); Stening (2008). Figure 2.13 is an example of such variations for four stations in the Indian sector, spread over a small longitudinal band, covering mid- to low latitudes, see panel a. Panel b illustrates the average daily variation ΔH of the horizontal component of the geomagnetic field between March and April 2009. Similarly, the shape of this variation gives information about the observatory's location with respect to the

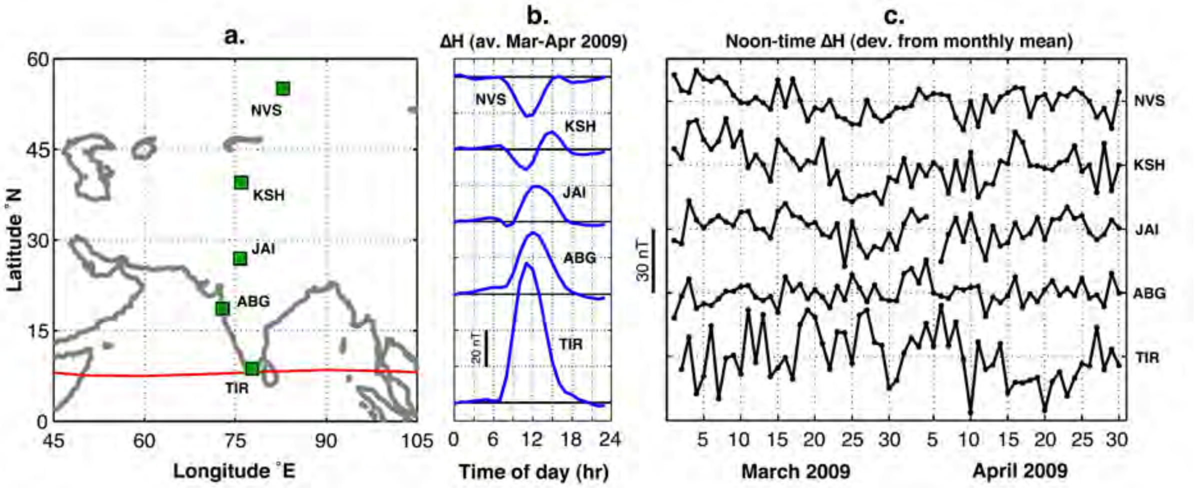

Figure 2.13: Daily variations of the northern cell of the solar quiet current system. Panel a indicates the location of the magnetic observatories. Panel b shows the average daily variation in the horizontal H component. Panel c shows the value of the H component at noon per day. (Taken from Yamazaki and Maute (2017))

cell's focus. Kashi (KSH) is close to the focus, such that when the cell is exactly above the station, ΔH is zero with changing signs before and after the crossing. Novosibirsk (NVS) is to the North of the current cell and thus is influenced by the top, westward portion of the Sq current. Jaipur (JAI) and Alibag (ABG) are south of the focus and thus are influenced by the eastward portion. Lastly, the spike observed in Tirunelveli (TIR) is induced by the stronger EEJ. Panel c shows the values of ΔH at noon during the same period for each station and each day. The amplitudes can vary highly irregularly from one day to the next at all latitudes. This is a persistent feature of the solar quiet current system which is present also during magnetically very quiet periods, as is the case for the period of figure 2.13 which is during the very quiet year of 2009 (during solar minimum). This suggests that the intrinsic D2D variation has its roots in winds and tides from the neutral atmosphere. Many studies and simulations have been conducted to highlight the importance of lower-atmospheric drivers, like e.g. Kawano-Sasaki and Miyahara (2008); Jin et al. (2011); Fang et al. (2013); Yamazaki, Richmond, Maute, Liu, et al. (2014). Further studies and investigations are needed for a better understanding of the causes for the D2D variability.

2.3.3 Electrojets

Besides the Sq current system, the ionospheric dynamo gives rise to further currents: the already mentioned equatorial electrojet and the auroral electrojets. These are themed jets due to their jet-like features.

2.3.3.1 Equatorial Electrojet

The Equatorial Electrojet (EEJ) is a strong zonal current that flows above the magnetic dip equator on the dayside of Earth (Chapman, 1951). Its effects are clearly present in geomagnetic field measurements as can be seen in figure 2.12 and 2.13. The physical phenomena associated with the EEJ is the so-called Cowling effect (Cowling, 1932). At the equator the magnetic field lines are horizontal and engulfed in the ionosphere while the ionospheric electric field points eastward in general, leading to an eastward Pedersen current and a downward Hall current. However, due to the poorly conducting layers surrounding the dynamo region, a charge accumulation occurs at the upper and lower boundaries of the ionosphere. In turn, this generates a vertical Pedersen electric field enhancing the conductivity parallel to the boundaries. Consequently, this generates an eastward Hall current, adding to the already existing eastward Pedersen current. Similar to the Sq currents, the EEJ exhibits distinct solar cycle, seasonal and day-to-day variabilities (Yamazaki & Maute, 2017). It is under debate if the EEJ is a current system on its own or a consequence of the Sq current systems. At the very least, the Sq current systems contribute to the EEJs amplitude. Typical latitudinal ranges for the EEJ are between -10° to 10° (Yamazaki & Maute, 2017).

2.3.3.2 Auroral Electrojets

While the Sq current systems and the EEJ are driven by the ionospheric wind dynamo, the auroral electrojets (AEJ) are driven by the ionospheric solar wind dynamo. They arise mainly due to the convection patterns of the magnetic field lines and are strongly modulated by energy input through the coupling with the solar wind. Through increased precipitation of particles, the conductivities of the auroral ionosphere are significantly enhanced and give rise to these strong Hall currents in the northern and southern hemispheres, flowing along the auroral ovals. Especially during storm conditions, these current systems are significantly enhanced.

2.4 Storm Activity

If the IMF in the solar wind points northward, the reconnection rate with the geomagnetic field is drastically lowered. If this condition holds for a longer period of time the magnetosphere may be considered to be in a quiet state (Moretto et al., 2021). However, if the incoming solar wind has a southward directed IMF (negative B_z), promoting dayside reconnection to take place, considerable amounts of energy and particles from the solar wind are injected into the magnetosphere-ionosphere system. This leads to increased convection and reconnection rates, enhances current systems and leads to further phenomena which play an important role for space weather. The general consensus discriminates between magnetospheric substorms and geomagnetic storms.

2.4.1 Magnetospheric Substorms

Rostoker et al. (1980) defines substorms as follows:

> *"A magnetospheric substorm is a transient process initiated on the nightside of the earth in which a significant amount of energy derived from the solar wind-magnetosphere interaction is deposited in the auroral ionosphere and in the magnetosphere."*

Enhanced reconnection during longer periods of southward IMF B_z lead to enhanced energy input that is transferred to the magnetotail, where reconnection rates increase as magnetic pressure increases. As indicated in figure 2.8, reconnection in the tail leads to enhanced amounts of newly created closed magnetic field lines that are pushed towards Earth. In this process a pair of FAC currents is formed referred to as the substorm current wedge as depicted in light-blue in figure 2.6. This system plays an important part for substorms as it diverts parts of the tail-current into the high latitude ionosphere. The supplied energy through this process enhances the auroral electrojets and leads to increased auroral display (Kepko et al., 2015). Typical timescales for substorms are around 2 to 4 hours and they can be divided into three phases: the growth, expansion and recovery phase. During the growth phase the magnetotail loads due to negative B_z enabled dayside reconnection and the polar cap expands. The two lobes act as energy storages as magnetic field lines are convected (Caan, McPherron, & Russell, 1973; Runov et al., 2021). During the expansion phase, the energy from the tail is released, intensifying the auroral electrojets, and augmenting auroral displays. The auroral oval expands equatorward due to increased reconnection at the magnetopause and tail. After the unloading process, the recovery towards the quiet state starts.

Substorm activity is strongly connected to auroral activity and is usually confined to high latitudes. Against the suggestion of the naming, substorms are not necessarily accompanied by storms. Generally, they do appear during global storms, but can occur independently. Thus, substorms are more abundant than geomagnetic storms and generally less intense.

2.4.2 Geomagnetic Storms

A geomagnetic storm is a magnetic disturbance observed worldwide that lasts for several hours to days and is not confined to high-latitudes but affects also low- and mid-latitudes. Thus it is said to be geoeffective. These global-scale disturbances of the geomagnetic field are induced by strong solar transients like CMEs accompanied by prolonged southward IMF B_z of several hours. The amount of energy that is deposited into the magnetosphere-ionosphere system and thus the level of geoeffectiveness depends greatly on the solar wind parameters like velocity, density as well as strength and orientation of the IMF. Due to the increased energy deposition during geomagnetic storms the current systems are significantly enhanced. This includes increased substorm activity and intensifying of auroral electrojets. The most prominent feature is the enhancement of the ring current which experiences elevated particle injection from increased reconnection in the tail (Kistler et al., 2016) and with protons and oxygen ions fed by FACs from auroral regions (see figure 2.7). This increase is also referred to as the storm-time ring current which can last for hours and days. Its clearest signature can be found in geomagnetic field measurements. As the storm-time ring current flows westward in the equatorial plane, its induced magnetic field is in opposite direction of the Earth's dipole field, leading to a clear depression of the horizontal H component as is indicated in figure 2.14.

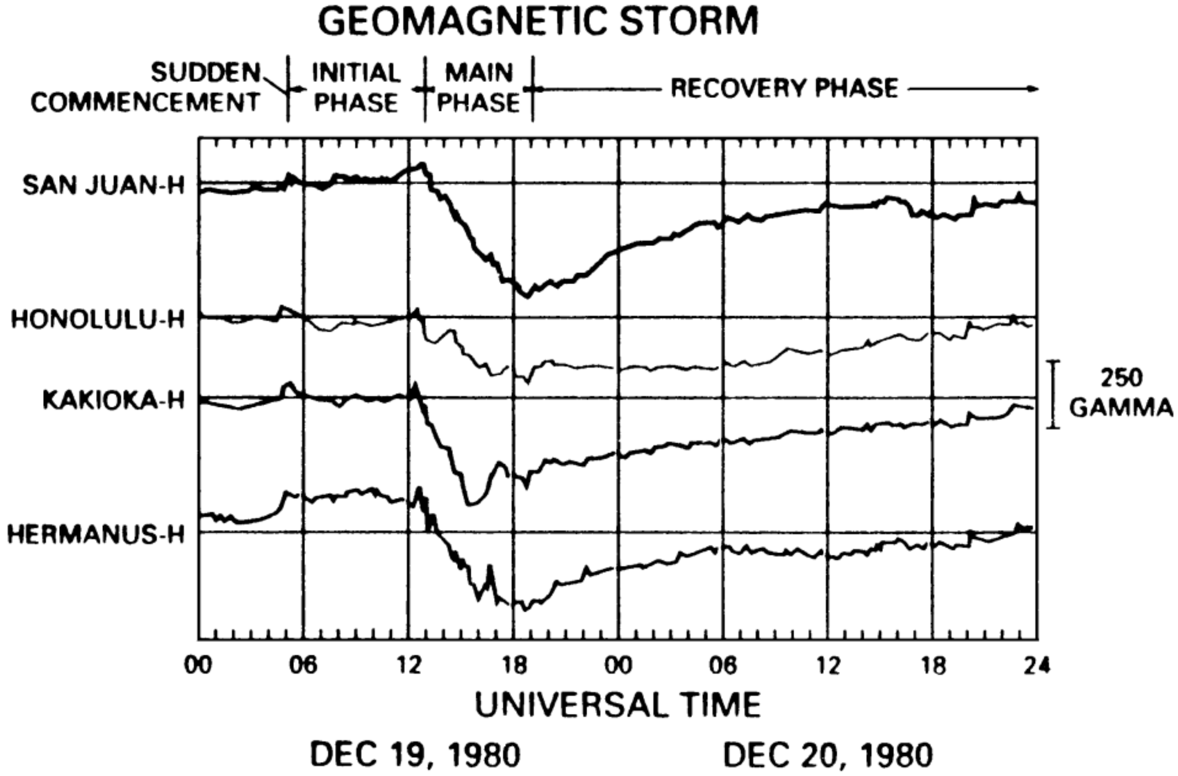

Figure 2.14: Geomagnetic storm effects on the horizontal component of geomagnetic field measurements at four low-latitude observatories. The typical phases of the storm are indicated. 1 GAMMA corresponds to 1 nT. (Taken from Campbell (2003))

Geomagnetic storms can be divided into three phases: the initial, main and recovery phase. The initial phase is marked by a positive increase that is associated with the compression of the dayside magnetic field due to increased solar wind pressure. When the compression is especially strong, a Storm Sudden Commencement (SSC) can be observed as a strong positive deflection. The main phase is indicated by a strong negative deflection due to the enhancement of the ring current. The recovery phase encompasses the decay of the storm-time current (Hutchinson, Wright, & Milan, 2011). The disturbance field in low- and mid-latitudes is generally not axisymmetric. During the main phase of the storm, the ring current is usually asymmetric as injected ions are mainly present in the evening and afternoon sectors. When injection finishes and the recovery phase starts, the ring current becomes more symmetric (Sugiura & Chapman, 1960; Akasofu & Chapman, 1964; Weygand & McPherron, 2006).

It is common to characterise geomagnetic storms according to the global deflection of the magnetic H component induced by the enhanced ring current. This deflection is summarised in the disturbance storm-time (Dst) index derived from the four magnetic observatories from figure 2.14. Gonzalez et al. (1994) defines geomagnetic storms as

> *"... an interval of time when a sufficiently intense and long-lasting interplanetary convection electric field leads, through a substantial energization in the magnetosphere-ionosphere system, to an intensified ring current strong enough to exceed some key threshold of the quantifying storm time Dst index."*

As such, the 1-hour Dst index and nowadays also its 1-minute version the SYM-H index, have been used in many studies to define and classify geomagnetic storms (see chapter 3.1.3 for further details on these indices). While strong CMEs can cause severe storms with associated Dst values well below $-100\,\mathrm{nT}$, CIRs can cause moderate storms especially during the declining and low solar activity phases (Allen et al., 2020).

Geomagnetic storms on a global and substorms on a local level can induce unwanted and harmful effects in our technology and pose a threat to human health and safety, as discussed in the introduction of this chapter. Enhancing our capabilities for their accurate forecasting is an important and active field which also started to leverage artificial intelligence methods (Camporeale, 2019; Nitti et al., 2022).

2.5 Geomagnetic Field

The geomagnetic field is a superposition of numerous magnetic sources, with the Earth's internally-generated magnetic field being the predominant contributor, commonly referred to as the main field. The previously introduced phenomena and concepts arise due to solar radiation, the atmosphere and the interaction of the solar wind with the Earth's main field, leading to a complex and coupled system of currents within the ionosphere and magnetosphere. According to Amperes Law in equation (1.35), each of these currents induces a magnetic field and as such contributes to the overall geomagnetic field.

Sources are classified into external and internal origin. Figure 2.15 illustrates some prominent sources of the geomagnetic field. They are classified into external and internal origin. External sources include current systems like Sq, FACs and EEJ. Internal sources include the main field and are discussed in the following.

2.5.1 Earth's Main Magnetic Field

Within the depths of our Earth, pressure and temperature levels are so high that rock, iron and nickel melt,constituting the fluid outer core. These fluids are in motion via

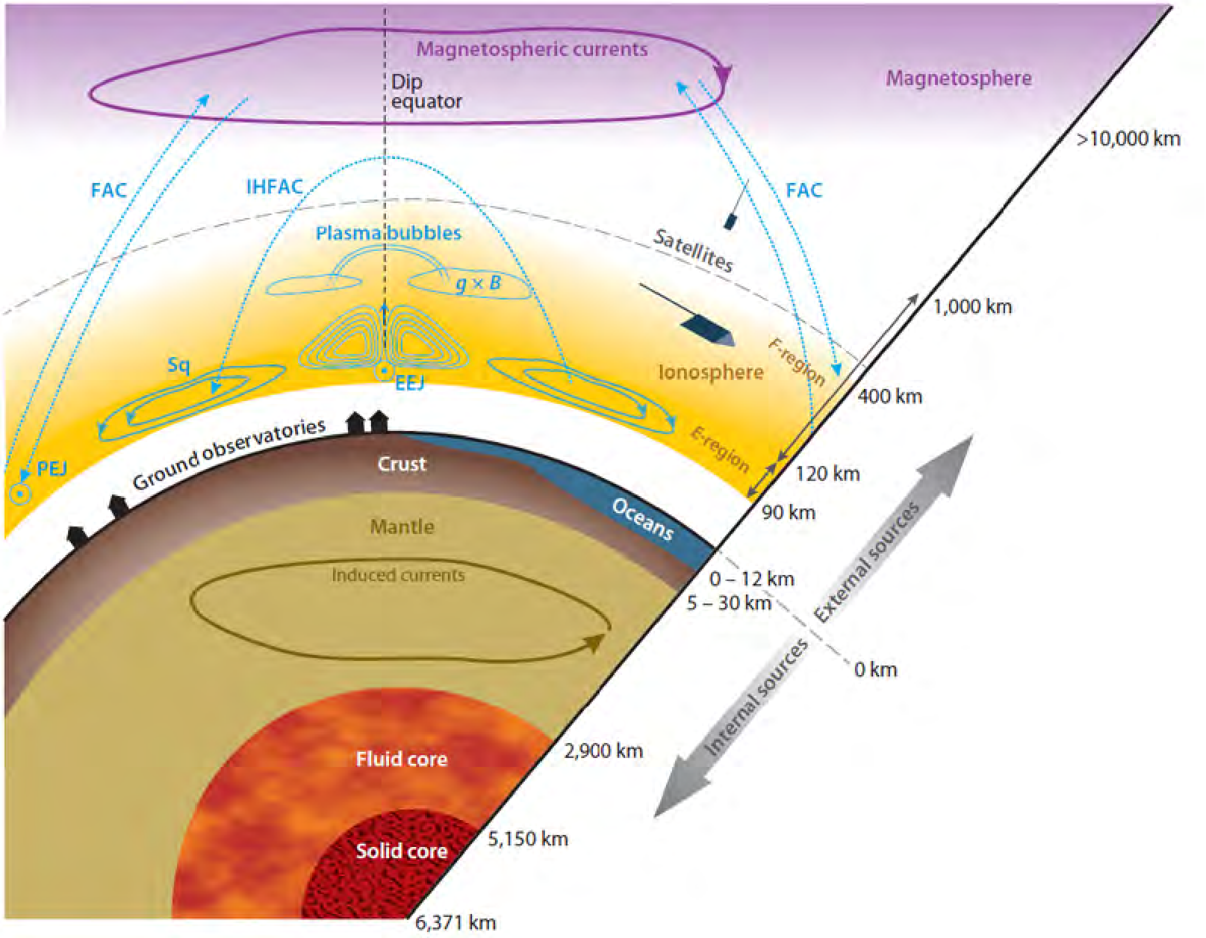

Figure 2.15: Overview of internal and external sources of the geomagnetic Field. (Taken from Olsen (2016))

convection and, together with the rotation of Earth, generate an electric current that induces a powerful magnetic field. This process is referred to as the geomagnetic dynamo and is thought to be the reason for Earth's intrinsic magnetic field (Gauss, 1877; Landeau, Fournier, Nataf, Cébron, & Schaeffer, 2022). Within around $6R_E$ this field can be approximated by a dipole magnetic field with strengths of ∼60 000 nT at the poles and ∼25 000 nT at the equator. The dipole geometry is responsible for the magnetic mirrors that lead to the formation of the radiation belts and ring current, as discussed earlier in chapter 2.2. The dipole axis is tilted with respect to Earth's rotation axis of approximately 11° and the magnetic south pole is located in the northern hemisphere, while the magnetic north pole is located in the southern hemisphere.

The dynamo process is not stable such that the magnetic field's intensity and direction are slowly but continuously changing. The timescales involved in this smooth drift range from years to millennia. Paleomagnetism is the field of study that uses specialised techniques to extract magnetic field information from very old samples to understand these extended long-term changes of the main field (Gilder & Lhuillier, 2019). The most dramatic events are pole reversals whereby the field strength declines for a few thousand years until the reversal takes place, with a succeeding strengthening of the field in the following thousand years (Gubbins, 2008). Currently, the magnetic south pole moves with up to 60 km per year from Canada towards Siberia and the magnetic north pole with around 5 km per year from Antarctica towards Australia (Olsen & Mandea, 2007). These gradual changes are referred to as secular variation which is an active field of study (Bloxham & Gubbins, 1985; Finlay, Olsen, Kotsiaros, Gillet, & Tøffner-Clausen, 2016; Finlay et al., 2020). Though gradual, they are important factors for space weather as changing field configurations can directly accentuate its effects (Mandea & Chambodut, 2020).

In order to describe the ever-changing magnetic field, sophisticated models are generated that are based on geomagnetic field measurements. The International Geomagnetic Reference Field (IGRF) model is produced and maintained by the International Association of Geomagnetism and Aeronomy (IAGA). The model represents the geomagnetic field in terms of spherical harmonics which coefficients are determined every five years to account for the temporal changes of the secular variation. The spherical harmonic expansion shows that the contribution of the 1st order degree (the dipole part) accounts for approximately 93 % of the total magnetic field. The latest model is IGRF-13 and is valid for the years 1990 to 2025 (Alken et al., 2021).

2.5.2 Further Internal Sources

Within Earth's crust, remanent and induced magnetisation of magnetic minerals like magnetite and titanium are found within the lithosphere. The space era enabled the mapping of the lithospheric field with satellite surveys (Thébault, Vigneron, Langlais, & Hulot, 2016). The associated field strengths are location-dependent and in general are not much more than 100 nT, but can reach several hundreds of nanotesla for major anomalies in regions like Kursk and Bangui (Taylor & Frawley, 1987; Njiteu Tchoukeu et al., 2021). Crustal bias averages and respective variances for geomagnetic observatories is given in e.g. Verbanac, Mandea, Bandic, and Subasic (2015) of which a selection is summarised in table 2.1. The variation around the mean is of oscillatory nature and can be related to errors in the input data and influences from external fields.

Another internal source is the ocean circulation that generates a magnetic field that can be sensed at locations nearby the oceans and coastal regions. The associated electric current is generated by salt ions that are deflected by the Lorentz force in different directions due to their polarity (Petereit, Saynisch-Wagner, Morschhauser, Pick, & Thomas, 2022).

2.5.3 Variability of the Geomagnetic Field

When recording the geomagnetic field, the resulting signal is a composition of all internal and external sources, resulting in a wide amplitude-frequency spectrum as depicted in figure 2.16. The crustal field is virtually constant and not represented in the spectrum. The variations induced due to the internally-generated magnetic field happen gradual and over extended periods of time. They are associated with high amplitude changes on the low frequency part of the spectrum. This includes pole reversals that stretch over millions of years and the secular variation that consistently changes the amplitude which can be recognised within months to years. External sources act on shorter time-scales and are associated with smaller amplitude variations. The solar cycle with its period of around 11 years induces amplitudes in the range of 10-20 nT. In mid-latitudes the solar quiet current systems can induce diurnal and sub-diurnal variations of 20-50 nT. Substorms are responsible for field changes of up to 1000 nT in polar regions lasting for

Table 2.1: Selected averages and respective variances of crustal biases for selected magnetic observatories given by Verbanac et al. (2015).

Code	X (nT)		Y (nT)		Z (nT)	
ABK	6.19	± 12.42	63.02	± 3.35	42.95	± 11.29
CLF	-82.09	± 9.67	-13.00	± 2.9	124.78	± 7.48
ESK	1.09	± 8.21	-32.52	± 3.27	-35.81	± 10.71
FRD	56.86	± 10.09	-51.35	± 1.41	137.9	± 7.47
HAD	-51.70	± 8.74	18.34	± 2.62	91.28	± 7.88
HON	-185.19	± 12.97	80.8	± 3.1	-320.61	± 3.91
KAK	-14.80	± 13.01	10.07	± 1.56	-86.22	± 4.54
MEA	92.31	± 13.96	15.67	± 3.72	-33.67	± 8.18
NGK	-31.60	± 9.42	0.99	± 2.77	-62.28	± 8.32
OTT	122.46	± 10.14	-133.92	± 1.58	149.54	± 7.24
PPT	-922.02	± 15.29	-1039.73	± 8.72	-398.55	±5.16
SBA	-2204.59	± 8.93	-970.29	± 11.05	-3748.76	± 33.56
THL	-58.33	± 10.1	98.36	± 4.29	37.65	± 24.64
WNG	43.76	± 9.38	46.63	± 2.54	-53.22	± 8.86

several hours, while geomagnetic storms can disrupt the global geomagnetic field in the order of hundreds of nanotesla, even in mid-latitudes for several days. Lightning induces electromagnetic resonances between the Earth's surface and the ionosphere. These are referred to as Schumann resonances and are found in the high frequency regime (Price, 2016). On the very end of the high frequency spectrum, human-made noise generators can be found which include powerline noise and radio emissions (Mandea, Korte, Yau, & Petrovský, 2019).

2.6 Data Acquisition and Coordinate Systems

Data acquisition, just as in any other field, plays an important role in the understanding of space weather. The advancements in technology have revolutionized measurement techniques, allowing for more accurate, precise, and efficient data acquisition over the past decades. Nowadays, we are able to measure magnetic fields with up to seconds resolution and deploy instruments not only on ground but also in space. This chapter is dedicated to the recording of the geomagnetic field and solar wind. The representation of data in space, i.e. in vector format, depends upon the selected underlying coordinate system, of which the most common ones for space weather are briefly presented.

2.6.1 Geomagnetic Field Measurements

The sources of the geomagnetic field come in a high spatial and temporal variety as indicated in 2.16. Geomagnetic field changes that occur over geological timescales, like pole reversals, are determined with paleo-magnetism techniques (Gilder & Lhuillier, 2019). For other, shorter variations, dedicated instruments that record ambient magnetic fields are used. In the advent of the space age, it is not only possible to collect data from the ground, but to measure the magnetic field configuration also in space (Marchaudon, 2019).

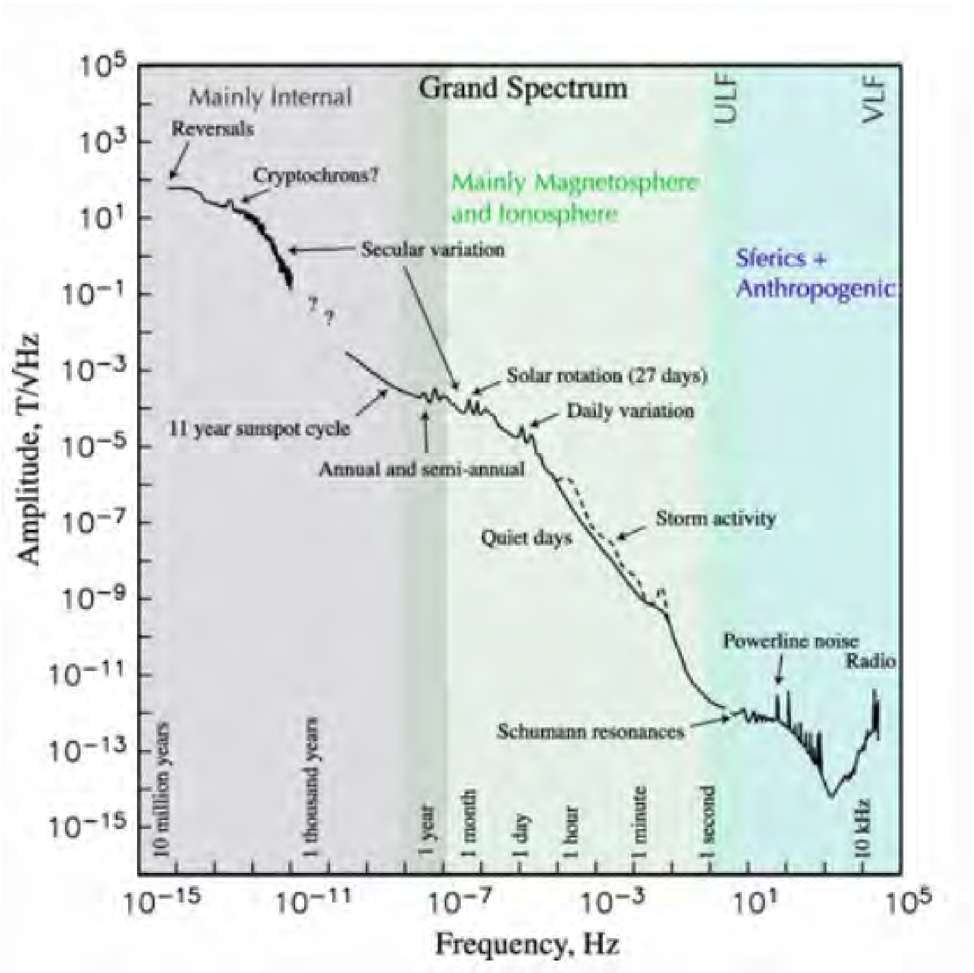

Figure 2.16: The amplitude-frequency spectrum of the geomagnetic field with indications of associated sources. (Taken from Constable (2016))

2.6.1.1 Instrumentation

Historically, analogue magnetograms produced by magnetic variometers were used to record the geomagnetic field. Such historic and abundant geomagnetic field records hold highly valuable information and it is an important task to make these records digitally available (see e.g. Kärhä and Tanskanen (2022)). Nowadays magnetometers are dedicated to measure the ambient magnetic field in digital form. As it is a vector field, it consists of a magnitude and direction. A single instrument is not able to record the entire vector and thus combinations of magnetometers are needed to accurately measure the geomagnetic field. The most commonly used magnetometers are Fluxgate Magnetometers which measure field variations in one or more directions and Scalar Magnetometers which measure the magnitude of the field (Jankowski & Sucksdorff, 1996).

Fluxgate Magnetometers have a core made up of a highly magnetically permeable material in rod or ring shape. Two windings are wrapped around the core: the excitation coil and the sensing coil. The excitation coil is powered by an alternating current, saturating the ferromagnetic core periodically. When there is no external magnetic field, no change of magnetic flux is noticed at the sensing coil. However, when there is an external field, a net change in flux induces a voltage in the sensing coil which gives information about the ambient magnetic field. With this instrument the magnetic field variations are detected in one direction (Primdahl, 1979).

Scalar Magnetometers measure the magnitude of the magnetic field and are based on magnetic resonance. A typical scalar magnetometer to measure Earth's magnetic field is the proton precession magnetometer (PPM) (Cahill & van Allen, 1956). The PPM consists of a proton rich liquid placed within a coil. A current is applied on the coil. Once the current is switched off, the precession of the protons is measured as it is proportional to the ambient magnetic field strength.

Combining fluxgate magnetometers with scalar magnetometers allows the recording of the absolute geomagnetic field.

2.6.1.2 Ground Observations

On Earth's surface, magnetic observatories are facilities at stable, geographic locations that host magnetometers and provide high-quality, long sequence, absolute geomagnetic field measurements, with the longest continuous records being over 150 years. Nowadays, an increasing number of magnetic observatories are able to deliver high quality magnetic field data with temporal resolutions of up to seconds. A list of such observatories is maintained by IAGA, together with their official three letter designator e.g. the French observatory Chambon-la-Forêt has the abbreviation CLF. The Real-time Magnetic Observatory Network (INTERMAGNET)[1], ensures quality minute-resolution data of its member observatories and facilitates the free data exchange between nations and the creation of geomagnetic data products. Data from the INTERMAGNET network comes in vector format with a resolution of 0.1 nT and 1 minute cadence. 41 magnetic observatories were involved in the creation of this network in 1991. Since then, the amount of member observatories has been continuously rising, although also some stations opted out completely or for a limited amount of time due to malfunctioning or stopping of data production (Kerridge, 2001; Gilder & Lhuillier, 2019). Appendix A provides details on INTERMAGNET observatories between 1991 to 2019. The global distribution of observatories is also depicted in figure 4.1.

Other ground facilities include magnetometer arrays that are deployable in a flexible manner. These are usually used during measurement campaigns that aim at investigating dedicated magnetic phenomena for a short period of time.

While these options work well on solid ground, they are less suited for magnetic measurements on water bodies. As two thirds of our planet is covered by oceans, this poses tight restrictions on magnetic field measurements. Dedicated marine and airborne magnetic surveys are conducted on water and in airspace to cover these parts of the world over a limited range and for a limited amount of time (Gilder & Lhuillier, 2019).

2.6.1.3 Satellite Missions in Space

With the launch of the space age in the 1960s, new opportunities arose including the recording of the geomagnetic field from space. Since then, almost all satellites harbour fluxgate and scalar magnetometers. Various dedicated space missions with explicit science goals regarding the geomagnetic field have been conducted by national space research centres, as well as international space agencies like the European Space Agency (ESA) and National Aeronautics and Space Administration (NASA). The CHAMP mission from the German Aerospace Center (DLR) launched in 2010 was dedicated to investigate the

---

[1] intermagnet.github.io

Earth system with focus on its gravitation and magnetic field, as well as the atmosphere and ionosphere. During its more than 10 year mission it helped expand our knowledge of the geomagnetic field including the crustal field (Hemant, Maus, & Haak, 2005), the secular variation (Golovkov, Zvereva, & Chernova, 2005; Holme & Olsen, 2005), as well as neutral thermospheric waves (Park et al., 2014). The SWARM mission by ESA launched in November 2013 consists of three identical satellites and is dedicated to investigations of Earth's magnetic field and its accompanying electric currents. Since its launch, it has enabled progress in understanding ionospheric current systems (Chulliat, Vigneron, & Hulot, 2016), modeling of the internal magnetic field (Tozzi, Mandea, & De Michelis, 2016) and the mapping of the lithospheric field (Thébault et al., 2016), just to name a few. Another example is the Magnetospheric Multiscale Mission (MMS) launched in March 2015 that is dedicated to enhance our knowledge of the still poorly understood process of magnetic reconnection in the Earth's near-space system.

2.6.2 Solar Wind Measurements

Not only gave the rise of the space era opportunities for in-situ studies of our near-Earth space environment, it also opened up interplanetary space to our instrumentation. Several missions with the goal of uncovering mysteries of the Sun and the solar wind have been launched since. A recent example is the mission Parker Solar Probe (PSP) launched in 2018 which is dedicated to study the Sun's atmosphere. By flying through the Sun's corona it is possible for the first time to probe this interesting region in-situ and to expand our knowledge of the origin and evolution of the solar wind (Raouafi et al., 2023).

The knowledge of real-time solar wind conditions is essential, especially for now- and forecasting of space weather. On the Earth-Sun line, an important location, the so-called Lagrange L1 point, arises from gravitational balance. At this point, a spacecraft is quasi-stable, needs minimum propulsion to remain there and keeps the same angular velocity as Earth. Additionally, this position is, for normal conditions, approximately 1 hour upstream of the solar wind from Earth and thus can give important in-situ information about incoming solar wind conditions. Therefore, this point is strategically taken by several missions to observe the solar wind. Important examples include the Solar and Heliospheric Observatory (SOHO), the Advanced Composition Explorer (ACE), the Deep Space Climate Observatory (DSCOVR) and since 2020 also Wind. The main parameters that are measured and provided by these missions include the solar wind velocity, the interplanetary magnetic field B_{IMF} and plasma temperatures and densities. Solar wind data from ACE and DSCOVR can be found on the OMNI web interface omniweb.gfsc.nasa.gov and are complemented with other solar wind missions such as Wind. The highest temporal resolution for the solar wind data is 5 minutes (Papitashvili & King, 2020).

2.6.3 Coordinate Systems

Coordinate systems are used to locate objects in space and to give vector fields a reference frame. Usually coordinate systems are adapted for the phenomena and conditions of interest. For the geomagnetic field, various adapted magnetic coordinate systems are in place. An extensive review including definitions of the most widely used ones can be found in Laundal and Richmond (2016).

Geomagnetic field measurements on ground are typically given in a local geographic coordinate system which x-axis points towards geographic North, y-axis to geographic

$$D = \arctan\left(\frac{Y}{X}\right)$$

$$I = \arctan\left(\frac{Z}{H}\right)$$

$$F = \sqrt{X^2 + Y^2 + Z^2}$$

$$H = \sqrt{X^2 + Y^2}\,.$$

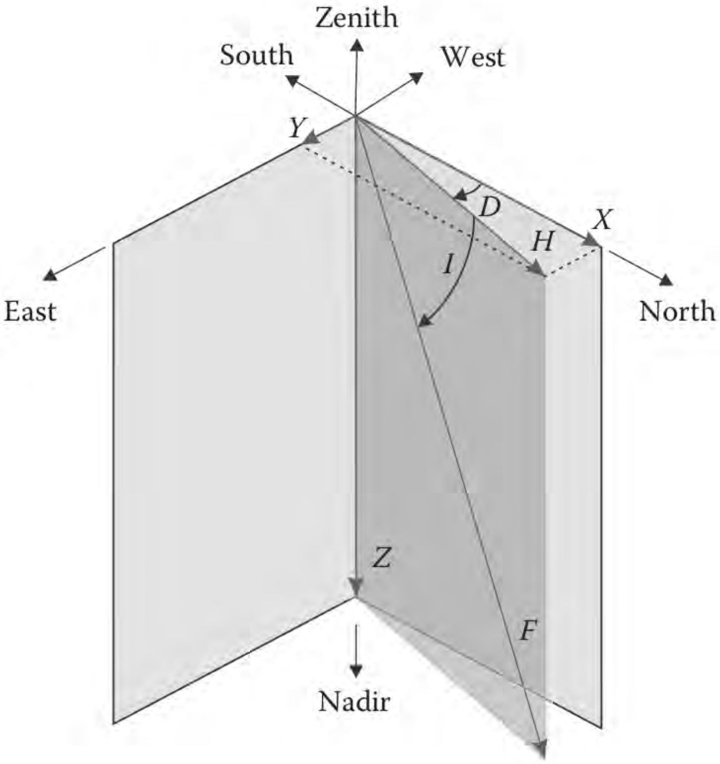

Figure 2.17: Local NED coordinate system with magnetic elements X, Y, Z and definition of derived elements declination D, intensity I, field intensity F and horizontal intensity H. (Taken from Olsen (2016))

East and z-axis vertically down, hence it is also referred to as NED system. The components $B = (X, Y, Z)$ are illustrated in figure 2.17. Data from the INTERMAGNET network is provided in this NED frame. Derived magnetic elements are the declination D which is the angle between geographic and magnetic North, the inclination I which is the angle between the local horizontal plane and the field vector and the total and horizontal field intensities, F and H. The expression of these quantities together with their visualisation is presented in figure 2.17.

Up to now, we used expressions like polar, mid-latitudes and equatorial to refer to certain latitudinal regions of Earth. As the magnetic dipole axis is tilted by approximately 11° from the Earth's rotation axis, these regions do not coincide in the magnetic and geographical frames. To describe magnetic phenomena which depend upon the dipole-axis, it is more convenient to choose a magnetic reference frame rather than a geographic one. Such a coordinate system depends upon the internally generated magnetic field of Earth, implying its magnetic coordinates will change together with the secular variation. In a first approximation the magnetic field can be described by a dipole that is tilted from the rotation axis of 11° and originates in the center of Earth using the Centered Dipole coordinate (CD) system. For a more accurate description, the Eccentric Dipole (ED) coordinate system is based on a dipole representation with its origin shifted from the center. Its Cartesian z-axis is aligned with the dipole axis, positively towards North, and is shifted about 500 km from the center of Earth, thus *eccentric* dipole. Its y-axis is perpendicular to the plane containing the dipole axis and the rotation axis of Earth. The x-axis completes the right-hand system. Eccentric Dipole coordinates may be expressed in spherical coordinates (r, θ, ϕ) with r corresponding to the Earth's radius, θ to the

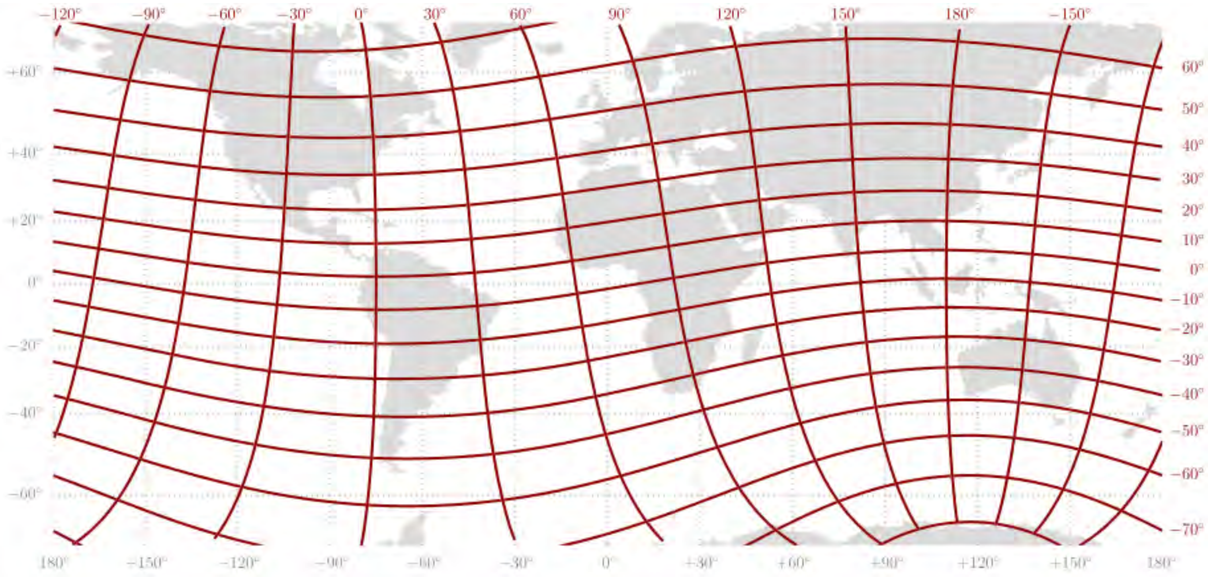

Figure 2.18: Eccentric Dipole Coordinates projected on the Earth's geographic surface map. (Taken from Laundal and Richmond (2016))

magnetic latitude and ϕ to the magnetic longitude. An example of how this magnetic coordinate system describes locations on Earth's geographic surface is illustrated in figure 2.18.

For phenomena that are farther away from Earth, the geomagnetic field itself as a reference frame may not be ideal anymore. Especially for solar wind observations, the Geocentric Solar Magnetospheric (GSM) coordinate system is convenient. Its x-axis points from the centre of Earth (which is also its origin) to the Sun. The y-axis is perpendicular to the magnetic dipole axis and the Earth-Sun line. The z-axis completes the right-hand coordinate system.

The angle μ, sometimes called the dipole tilt angle, is the angle between the geomagnetic dipole axis and the geocentric solar magnetospheric (GSM) z-axis. This angle changes as a function of time of the day (due to the tilt of the dipole axis) and season (due to the inclination of Earth's equatorial plane). In the northern hemisphere, μ has its maximum at the summer solstice and its minimum at the winter solstice, which is vice-versa for the southern hemisphere. At the equinoxes, it is equal to zero (Cnossen, Wiltberger, & Ouellette, 2012).

Another practical quantity is the solar longitude L which describes the position of the Earth around the Sun and provides information on the season. It is defined as 0° at spring equinox, and thus is 90° at summer solstice, 180° at autumn equinox and 270° at winter solstice. For further information on its derivation please relate to Bretagnon and Francou (1988) and Meeus (1998).

For phenomena that are driven by direct solar illumination, the solar zenith angle χ can be used which is 90° when the Sun is directly above the location of interest.

The Magnetic Local Time (MLT) combines information on magnetic longitude and solar position. Its midnight magnetic meridian is defined as the meridian that is 180° magnetic longitude away from the subsolar point. An hour, where 1 h corresponds to 15° magnetic longitude, is positive towards magnetic east. The MLT/magnetic latitude system rotates with respect to the Earth at the rate at which the subsolar point crosses magnetic meridians.

Chapter 3

Geomagnetic Indices

The identification and quantification of storm signatures from solar forcing is an important subject in space weather. It has been long recognised that storm signatures are distinctly present in geomagnetic field measurements and thus can be used for the characterisation of the resulting disturbances. Geomagnetic indices or magnetic activity indices as based on magnetic field measurements are designated measures to quantify magnetic activity. Indices are traditionally derived from data coming from a network of stable ground observatories and generally represent external disturbance sources of the geomagnetic field. The common derivation strategy is to divide the signal into contributions from quiet and disturbed sources. When looking above the low frequency regime of the geomagnetic field and in the absence of strong external solar drivers (see figure 2.16), the geomagnetic field exhibits smooth variations during the course of a day on top of a longer trend that are induced from sources like the solar quiet current system and the secular variation. Contrarily, disturbances induce non-periodic, to some extent shorter-lived variations, like the prominent H depression for geomagnetic storms, see figure 2.14. The determination of the quiet sources leads to a theoretical quiet magnetic field signal, the so-called geomagnetic baseline. Subsequently, this baseline is subtracted from the recorded magnetic signal, leaving the disturbance information within the residual.

One of the first indices derived in such a manner are the K-indices as introduced by Bartels in 1939. During this epoch, trained observers identified baselines on magnetograms printed on paper. The general idea of these indices has persisted to the present day. However, since this first attempt, significant improvements have been made in terms of our understanding of the geomagnetic field and associated space weather effects. Especially, within the past few decades, entering and embracing the digital age, it has been increasingly easier to access geomagnetic field data and the possibility to use computers to analyze and manipulate geomagnetic field signals. This advancement led to the definition of further indices which play a crucial role in the description of the Sun-Earth relationship and act as an important proxy for Space Weather models and forecasts (Liemohn et al., 2018). Significant effort has been put into the creation and derivation of magnetic indices with the goal of improving our understanding of the solar impacts on the geomagnetic field. While some indices are created for the purpose of evaluating the overall state of the geomagnetic field, others are dedicated to the quantification of specific physical phenomena like current systems and activities over certain regions. The International Service of Geomagnetic Indices (ISGI) as a service of the International Association of Geomagnetism and Aeronomy (IAGA) is dedicated to validate and provide access to geomagnetic indices that fulfil certain quality standards. As the derivation of magnetic indices can take a considerable amount of time and in order to provide values as soon as possible, they can be marked as quick-look or provisional. This indicates that the index value is not final and may differ from its definitive (and thus final) value. In the following, examples of well-established and broadly-used geomagnetic indices along with their derivation methods are given. Comprehensive discussions about geomagnetic indices can be found in Menvielle, Iyemori, Marchaudon, and Nosé (2011). As will become clear, the determination of the baseline is an important part, as it defines which source contributions are contained within an index. Baseline derivation methods for selected indices are presented in addition to other methodologies that extract the quiet variations from geomagnetic field measurements. The last part of this chapter is concerned with the caveats and improvement opportunities of existing geomagnetic baselines and motivates the present work.

3.1 Examples

As already mentioned, one of the very first introduced indices are the K-indices. Several planetary indices that are meant to describe the overall state of the geomagnetic field are based on these early versions and are still in use nowadays. We start with the introduction of these and continue to more recently proposed ones which evolved as a consequence of our improved understanding of the geomagnetic field and the availability of data.

3.1.1 K-Indices and K-derived Indices

The K-indices were introduced by Bartels, Heck, and Johnston (1939) with the goal of quantifying irregular variations within geomagnetic field measurements. In general, they are derived and provided by the magnetic observatories themselves following standards recommended by IAGA.

For their derivation the irregular variations for each of the two horizontal components X and Y of the geomagnetic field are determined. This is done by removing the so-called non-K variations from the measurements. The non-K variations are defined to comprise all quiet source contributions of the geomagnetic field. Further details on this initial idea of a baseline is given in chapter 3.2. For each 3 hour UT interval, 0-3 UT, 3-6 UT, etc., and for each of the two components X, Y, the maximum difference of the determined irregular variations is calculated. From these two values, the maximum is used to quantify the level of irregularity in numbers between 0 to 9. A level of 0 corresponds to a very quiet state of the geomagnetic field, while 9 indicates an extremely disturbed state. The mapping between maximum value in nanotesla and class 0-9 was fixed for the Niemegk observatory (NGK) in a non-linear scale, see table 3.1. As amplitudes from magnetic disturbances depend strongly on location, this scale cannot be directly applied to other observatories, when assuming that the same disturbance produces the same class at each observatory. Therefore, grids are used to define the appropriate proportionality per observatory. These grids depend upon the so-called K9 lower limit (K9LL) which is determined for each observatory by ISGI (Mayaud, 1968). The local K-indices are used to define more global indices, referred to as K-derived geomagnetic indices.

Table 3.1: Mapping between the amplitude of determined irregular variation and K level class at Niemegk observatory.

Range (nT)	0-5	5-10	10-20	20-40	40-70	70-120	120-200	200-330	330-500	> 500
K-level	0	1	2	3	4	5	6	7	8	9

3.1.1.1 Kp Index

One of the most-widely used indices is the Kp (K-planetary) index. The idea of the Kp index is to quantify the overall planetary state of the geomagnetic field and was introduced by Bartels (1949). It is derived from standardised K-indices, the Ks-indices, from 13 geomagnetic observatories. The standardisation process is needed to remove seasonal and local time artifacts from the K-indices for which empirical and complex conversion tables are employed (Bartels, 1957a, 1957b). The Kp itself is defined as the simple average of the Ks-indices from the 13 stations and as such comes in a time-resolution of 3 hours and at a scale from 0 to 9. The classes and thus the Kp index are non-linear, although linearity is a desirable characteristic for indices in general. Therefore the *ap* index was introduced in *ap units*, whereby 1 ap unit corresponds to approximately 2 nT (Bartels & Veldkamp, 1954). The Kp index is used in many space weather models and is popular in the broad public, where it finds application in aurora forecasts. The generally accepted consent is that Kp below 2 is considered as low to quiet geomagnetic activity, whereby Kp above 7 is considered very strong activity. It needs to be pointed out here that the observatories used for Kp are located in mid-latitudes and are heavily weighted towards Europe, see figure 3.4 upper left panel. Hence, the Kp indices are a more appropriate proxy for these regions.

Kp is a historical index endorsed by IAGA, see Matzka, Stolle, Yamazaki, Bronkalla, and Morschhauser (2021) for a recent review. Since its beginning, the Kp time-series is derived by the German institute in charge of the Niemegk observatory, nowadays the GeoForschungsZentrum (GFZ) Potsdam being the ISGI collaborating institute. The full dataset is available at doi.org/10.5880/Kp.0001.

3.1.1.2 Classification of Disturbed and Quiet Days

Johnston (1943) introduced the most quiet and most disturbed days per month based on the Kp index. Each day of a month is assigned a number derived as the mean of

1. the sum of all eight Kp values
2. the sum of the squares of the eight Kp values
3. the maximum of the eight Kp values

This allows the ranking of the days: the ten quietest Q-days are the days with the lowest values, and the five most disturbed D-days are the ones with the highest values. The main issue with this definition is that the Q and D days are defined relative for each month. This implies that during a very disturbed month, even the quiet days may be disturbed and vice-versa for very quiet months.

3.1.1.3 *am*, *an* and *as* Indices

The *am*, *an* and *as* indices as proposed by Mayaud (1968) are formally endorsed by IAGA and are routinely produced by a French institute, nowadays the École et Observatoire des Sciences de la Terre (EOST) being the ISGI collaborating institute in charge. The main improvement of these indices is that a total of 24 observatories are used, see figure 3.4 lower left panel. They are located in subauroral regions, covering five longitude sectors in the NH and four in the SH, see Mayaud, Berthelier, Menvielle, and Chambodut (2023) for an overview of former observatories. Each sector contains two to three stations. This distribution enables investigations of local time and longitudinal dependencies of irregular variations. For each 3 hour interval and sector a K_i value is derived by averaging the K-indices of the associated observatories. The value is converted to an amplitude a_i in nanotesla and normalised to represent activity at 50° magnetic latitude. The *an* index is then the weighted mean of the five sectors in the NH and *as* is the weighted mean of the four sectors in the SH. The weights account for balancing the longitudinal distribution. The *am* index is the mean of *as* and *an*, $am = (an + as)/2$. The full dataset is available at doi.org/10.25577/et43-6h78.

3.1.1.4 $a\sigma$ Index

The *am* index, using a global network of observatories, describes the overall state of the geomagnetic field. In order to provide a more localised characterisation of geomagnetic activity, the $a\sigma$ index family was introduced by Chambodut, Marchaudon, Menvielle, El-Lemdani Mazouz, and Lathuillére (2013). They are based on the same network as the *am* index and are derived analogously. The observatories are divided into four MLT sectors which are used to derive $a\sigma_{Dawn}$ for 03-09 MLT, $a\sigma_{Noon}$ for 09-15 MLT, $a\sigma_{Dusk}$ for 15-21 MLT and $a\sigma_{Midnight}$ for 21-03 MLT. They are available in nanotesla and have a time-resolution of 3 hours. The full dataset is available at isgi.unistra.fr/indices_asigma.php.

3.1.1.5 *aa* Index

The *aa* index was introduced to provide simple means of monitoring and determining global geomagnetic activity back to 1868 (Mayaud, 1972). It is produced from the K-indices of two antipodal magnetic observatories in England and in Australia, see Mayaud, Menvielle, and Chambodut (2023) for an overview of former observatories and figure 3.4 middle left panel for current observatories. The K-indices are converted back to amplitudes in nanotesla and standardised to represent activity at magnetic latitude of 50° by using the mid-class amplitudes of the Niemegk grid. This index is a rough measure of geomagnetic activity with a long-term homogenised series and is formally endorsed by IAGA and derived by EOST. The full dataset is available at doi:10.25577/9z05-v751.

3.1.1.6 Classification of Really Quiet Days

The really quiet and quiet days over 24 hours and 48 hours (CK24 and CK48 days) were introduced by Mayaud (1972) to indicate magnetically very quiet periods. They are based on 1) the mean of the *aa* index values and 2) the p-sum which is the transformed and weighted sum of the *aa* values, centered on the UT day. The key for the p-sum is shown in table 3.2.

Table 3.2: Key for transformation of *aa* into p-values for the classification of really quiet days.

$\sum aa$ in nT	$aa \leq 17$	$17 < aa \leq 21$	$21 < aa \leq 28$	$28 < aa \leq 32$	$32 < aa$
p-value	0	1	2	4	6

The classification into "C" and "K" days is as follows:

- CK24: quietest days over 24-hours with mean(aa) < 13 nT
    - "C" indicates a really quiet C-day with Sum(p) < 4

  - "K" indicates a quiet K-day with Sum(p) >= 4
- CK48: quietest days over 48-hours with mean(aa) < 13 nT
  - "C" indicates a really quiet C-day with Sum(p) < 6
  - "K" indicates a quiet K-day with Sum(p) >= 6

The amount of CK24 and CK48 days per year is depicted in figure 3.1 and is not evenly distributed as it follows solar activity. Note that the time period starts as early as 1868, due to the long-term availability of the *aa* index.

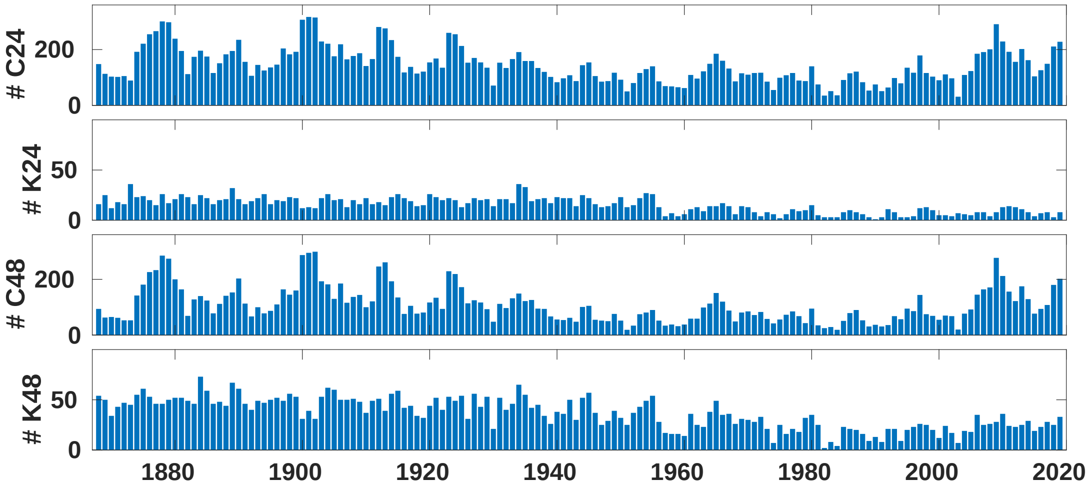

Figure 3.1: The amount of quiet days per year between 1868 and 2020. From top to bottom: The number of C24, K24, C48 and K48 days. Note that the vertical scale is smaller for K24 and K48 (between 0 and 100) than for C24 and K24 days (between 0 and 360).

3.1.1.7 Hpo Indices

The Kp index has, though widely used, some obvious deficiencies. These include a low time resolution of 3 hours and a fixed upper limit, which is 9. Temporal storm features below 3 hours are not resolved, nor is it possible to classify very intense events. To overcome these issues and while guaranteeing compatibility with the Kp indices, Yamazaki et al. (2022) introduced the Hpo indices. The Hpo indices are derived from 1-minute data of the same 13 observatories in a very similar manner as for the Kp indices. Especially, the baseline determination for each of the two horizontal components is the same as for the K indices. The main addition of the Hpo indices opposed to the 3 hour Kp-index is that they come in 30-minutes and 1-hour cadence, the Hp30 and Hp60 and are open-end such that any value above 9 is possible. As for the Kp indices, the Hpo indices are not linear, and have their linear equivalents in nanotesla, the *ap*30 and *ap*60 indices.

3.1.2 Auroral and Polar Indices

The Auroral Electrojet (AE) index family was introduced to track the strength of the auroral electrojets (Davis & Sugiura, 1966). They are endorsed by IAGA and made available through the World Data Center for Geomagnetism Kyoto, Japan as an ISGI collaborating institute. For its derivation the 1-minute horizontal H measurements from 12 observatories is used, see figure 3.4 upper right panel. The stations have a relatively uniform spatial distribution along auroral and sub-auroral latitudes in the northern hemisphere. The baseline is derived by averaging the measurements from the five quietest days (Q-days) of each month for each individual station. The residual H components of all stations are superposed. The upper and lower envelopes define the AU and AL indices, respectively. The AE index is derived as the difference between AU and AL, i.e. AE = AU - AL, and the AO index as the mean AO = (AU+AL)/2. As such, the AE index family comes in units of nanotesla. The full dataset is available at dx.doi.org/10.17593/15031-54800.

In general, the AU and AL indices represent the maximum eastward and westward electrojet currents, respectively, and can be used as energy dissipation proxies for the auroral ionosphere. Therefore, they are often used for substorm studies. Some considerations have to be kept in mind when using the AE indices. The distribution of stations is not fully uniform, such that substorm onsets and underestimation of magnitudes may occur. The sources included in the AE indices are not solely due to the auroral electrojets but they can also contain contributions from other magnetospheric currents. Finally, no counterpart exists for the southern hemisphere.

The polar cap indices, PCN for the northern and PCS for the southern polar cap, were introduced to characterise the magnetic activity in the polar caps as it is directly connected to the convection and thus energy input from the solar wind (Troshichev, Dmitrieva, & Kuznetsov, 1979). They reflect the cross polar potential in millivolt per meter (mV/m) and are derived from H and D magnetic field measurements at one observatory situated in each of the polar caps, Qaanaaq (THL, former Thule) in the northern and Vostok (VOS) in the southern one. The PC indices as described in Troshichev and Janzhura (2012) are endorsed by IAGA. The ISGI collaborating institutes are the National Space Institute at the Technical University of Denmark (DTU Space) for PCN and the Arctic and Antarctic Research Institute (AARI) of the Russian Federation for PCS. The full dataset for PCN is available at doi.org/10.11581/DTU:00000057.

Each PC index can be calculated in near real-time as it only needs data from one station and its baseline derivation is optimised for this purpose (as described in section 3.2.3). Though it is well correlated with solar wind parameters, various sources can contribute to the PC index.

3.1.3 Ring Current Indices

The Disturbance Time Index (Dst) was introduced by Sugiura (1964) to monitor the axially symmetric part of the ring current that induces the depression of the horizontal magnetic component. It is endorsed by IAGA and derived from the four observatories in figure 2.14 that are sufficiently far from the EEJ and auroral zones, see figure 3.4 middle right panel. The full dataset is available at dx.doi.org/10.17593/14515-74000. Its baseline derivation takes into account the main field and the solar quiet variations derived during the five quietest days of the month, the Q-days (see section 3.2.2). However, with its time resolution of one hour, it does not allow studies for shorter lived phenomena and related features.

The provisional SYM-H index with time resolution of 1-minute is based on 6 observatories, see figure 3.4 lower right panel, with the idea to provide a better description of the symmetric part of the ring current. Analogously, the ASY-H is proposed to track the asymmetric part of the ring current. Their derivation is described in Iyemori (1990) and in the technical report Iyemori, Takeda, Nose, Odagi, and Toh (2010). The baseline includes the main field and the Sq field, similar to that of the Dst index. The SYM-H is commonly accepted and used as the high-temporal resolution Dst index. Naturally, some differences arise and need to be kept in mind when doing so, especially for stronger disturbances (Wanliss & Showalter, 2006).

As the main feature of geomagnetic storms is the enhancement of the ring current, the Dst index is used in its definition (see section 2.4.2) and together with the SYM-H index they act as some of the most used proxies for space weather studies. Though similar, the definition of storm phases and corresponding start- and end-times of geomagnetic storms vary from study to study, some of which are presented in the following.

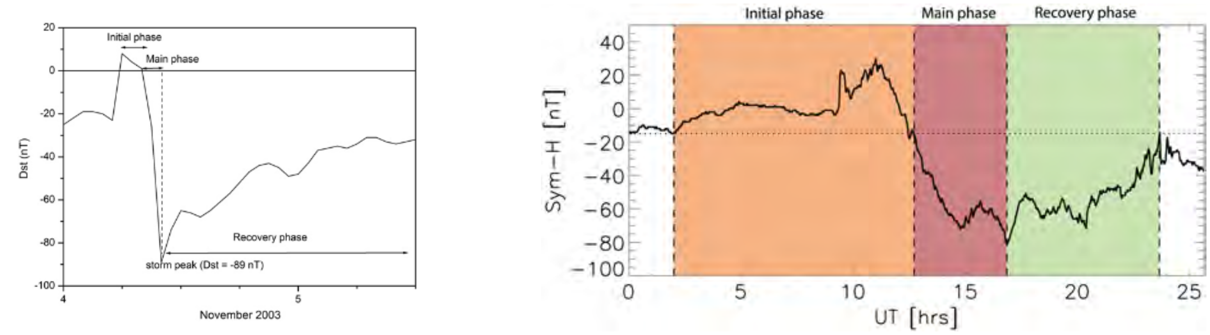

Figure 3.2: Left: Definition of geomagnetic storm phases with the Dst index from Echer et al. (2011). Right: Definition of geomagnetic storm phases with the SYM-H index from Walach and Grocott (2019).

1. **Echer et al. (2011)**
   The catalogue of Echer et al. (2011) covers a total of 1377 storms with peak Dst below −50 nT between 1957 and 2008. They are used to investigate storm intensity dependencies on solar cycle, annual variations and season to derive occurrence probabilities. By analysing each storm manually, they separate individual storms from complex events. Their initial phase starts at the highest positive value before the minimum Dst and ends when Dst crosses zero. This zero-crossing also marks the beginning of the main phase. The minimum Dst marks the end of the main phase. As their study is concerned with the strengths of storms, they did not define the end of recovery phases. Complex events are excluded, such that only single storm signatures are in the catalogue. The full storm list is available on-demand from the authors. On request, I received a catalogue with a total of 1516 storm entries covering the years 1957 to 2019, of which 599 storms are between 1991 to 2019.

2. **Ji, Moon, Gopalswamy, and Lee (2012)**
   The catalogue of Ji et al. (2012) covers a total of 63 geomagnetic storms with peak minimum Dst below −100 nT between 1998 to 2006. They use this set of events and solar wind data from the satellite ACE to compare several Dst forecast models focusing on intense events with regards to amplitude and time of minimum Dst. They define the start of the storm when there is a noticeable decrease of Dst after an identified corresponding interplanetary shock in the solar wind data. The storm end is defined as the time when Dst recovers above −50 nT.

3. **Lu, Peng, Wang, Gu, and Zhao (2016)**
   The catalogue of Lu et al. (2016) covers a total of 80 intense geomagnetic storms

with Dst below -100nT between 1995 to 2014. Similar to the one of Ji et al. (2012), they use these events as the data set for Dst forecasts with artificial intelligence algorithms. They define the start-time of the storm as the significant decrease of the Dst value from a relatively stable state and the end-time as the recovery of Dst above $-50\,\mathrm{nT}$.

4. **Li and Yao (2020)**
   The catalogue of Li and Yao (2020) covers a total of 95 storms with minimum peak Dst below $-30\,\mathrm{nT}$ between 1998 and 2011. From satellite data, they identify ICMEs and their properties to study associated geoeffectiveness. The storm list contains events with the corresponding geomagnetic response in Dst. Complex events are excluded. The start time of the main phase is defined as the maximum Dst value occurring between the ICME shock and the minimum Dst Dst_{min}. No initial phase is determined as they argue that not all ICMEs show a clear initial phase in Dst. The end of the main phase and the start of the recovery phase is determined by the minimum Dst. In this study, the recovery phase end is defined as the Dst recovering above 10% of Dst_{min} for storms with $Dst_{min} > -60\,\mathrm{nT}$ or 30% for $Dst_{min} \leq -60\,\mathrm{nT}$.

5. **Walach and Grocott (2019)**
   The catalogue of Walach and Grocott (2019) contains a total of 48 storms between 1997 to 2008 with the condition of SYM-H being below $-80\,\mathrm{nT}$. They use this list of storms to study ionospheric convection during extreme storm conditions. The minimum SYM-H value marks the beginning of the recovery phase and the end of the main phase. The end of the recovery phase is marked by the crossing of the quiet level which is chosen as $-15\,\mathrm{nT}$. The beginning of the main phase is defined as the last point when SYM-H crosses the quiet level prior to the main phase end. The beginning of the initial phase is marked as the point when SYM-H crosses the quiet level, coming from positive values.

For both indices it cannot be excluded that they contain contributions from other current systems. As they are averaged over longitude, they do not give information about local variations. When used as a proxy for ring current energy, the SYM-H has shown to overestimate the energy input by up to a factor of 4 and shifts of the maximum energy content by 3 to 9 hours due to included contributions of tail currents and substorm activity (Sandhu, Rae, & Walach, 2021).

Due to their importance in characterising storm activity, the literature shows increased interest in the forecast of both, the Dst and SYM-H indices, also with artificial intelligence methods, see e.g. Ji et al. (2012); Lu et al. (2016); Bhaskar and Vichare (2019); Laperre, Amaya, and Lapenta (2020); Siciliano et al. (2021).

3.1.4 Further Indices

Within the last decade, the availability of magnetic data has been significantly enlarged. Ground infrastructure has been updated, leading to an increasing amount of observatories that provide high quality and high cadence magnetic data, while space observations have been continuously improving to provide data in a reliable and more pertinent way. The consequence of this progress is reflected in the numerous studies that propose indices with higher temporal and spatial resolutions. Some examples include the SuperMAG based auroral electrojet (SME) and ring current indices (SMR) (Newell & Gjerloev, 2011, 2012) with time resolution of 1-minute. The initial idea of tracking the corresponding current systems holds, with the difference that the number of magnetic observatories used for the derivation is increased and further indices for the description of local time zones are provided. The baseline derivation differs from that of its traditional counterparts (see section 3.2.5 for details). With the magnetic data provided by the SWARM mission, the space-based indices Swarm-Dst, Swarm-ap and Swarm-AE were introduced recently (Balasis, Papadimitriou, & Boutsi, 2019; Papadimitriou et al., 2021). As satellites provide a latitudinal coverage, the data used to produce each of the indices needs to be constrained to the appropriate latitudinal ranges. The removed baseline contains the main field as derived from the CHAOS-6 model (Finlay et al., 2016) and a low-pass filter with cut-off frequency of 4 hours. These space-derived indices show very good linear correlations with ground-based indices and act as good addition to the description of the geomagnetic field's state.

3.1.5 The St. Patrick's Day Storm of 2015 as Recorded by Magnetic Indices

The St. Patrick's Day storm that occurred between 17th and 18th of March 2015 was one of the most intense space weather events of SC24. It is classified as 'Severe' according to the U.S. National Oceanic and Atmospheric Administration (NOAA)[1] (Poppe, 2000). A strong CME with southward IMF, together with a high-speed stream led to severe effects on Earth. The event is well-studied in the literature (e.g. Wu et al. (2016)) including the documentation of severe effects on the ionosphere (e.g. Nava et al. (2016); Astafyeva, Zakharenkova, and Förster (2015); De Michelis et al. (2020)) and significant impacts on satellite positioning (e.g. Jacobsen and Andalsvik (2016); Zakharenkova, Astafyeva, and Cherniak (2016); Yang et al. (2020)). Aurora sightings were documented even in mid-latitudes with Aurorasaurus[2] (Case & MacDonald, 2015).

Figure 3.3 illustrates how this event manifested itself in various magnetic index responses showing the period between 14th to 22nd of March 2015, from top to bottom (with their extreme value): Kp (8); *am* and *aa* (241 nT and 284 nT); Hp30 and Hp60 (8 and 8); AU and AL (664 nT and −2300 nT); AE and SME (2298 nT and 2877 nT); PCN and PCS (15.5mV/m and 15mV/m); Dst, SYM-H and SMR (−222 nT, −234 nT and −249 nT). The K-derived, polar cap and ring current indices indicate geomagnetically calm days during March 14th and 15th, though elevated substorm activity is recorded in the auroral electrojet index family and SME. On March 16th, a moderate event can be identified that leads to slightly higher values in all indices. On 17th of March, at around 5am UT, all indices show a rapid increase, with the ring current indices indicating a clear SSC followed by the storm-typical H depression. Strong values across all indices remain for around 24 hours until 18th of March at midnight, which marks the end of the storm's main phase which features high substorm activity (AE) and a clear intensification of the ring current (Dst, SYM-H). The auroral, polar cap and ring current indices show two distinct peaks in activity during the main phase, the first one peaking at around 9.30am UT with a succeeding calming of around 30 minutes. During March 18th, the ring current indices indicate a slow recovery phase which is accompanied by slowly decreasing substorm activity. The K-derived indices show a consistent decrease accordingly. The slow recovery continues further until March 21st.

---

[1] swpc.noaa.gov/noaa-scales-explanation

[2] aurorasaurus.org/

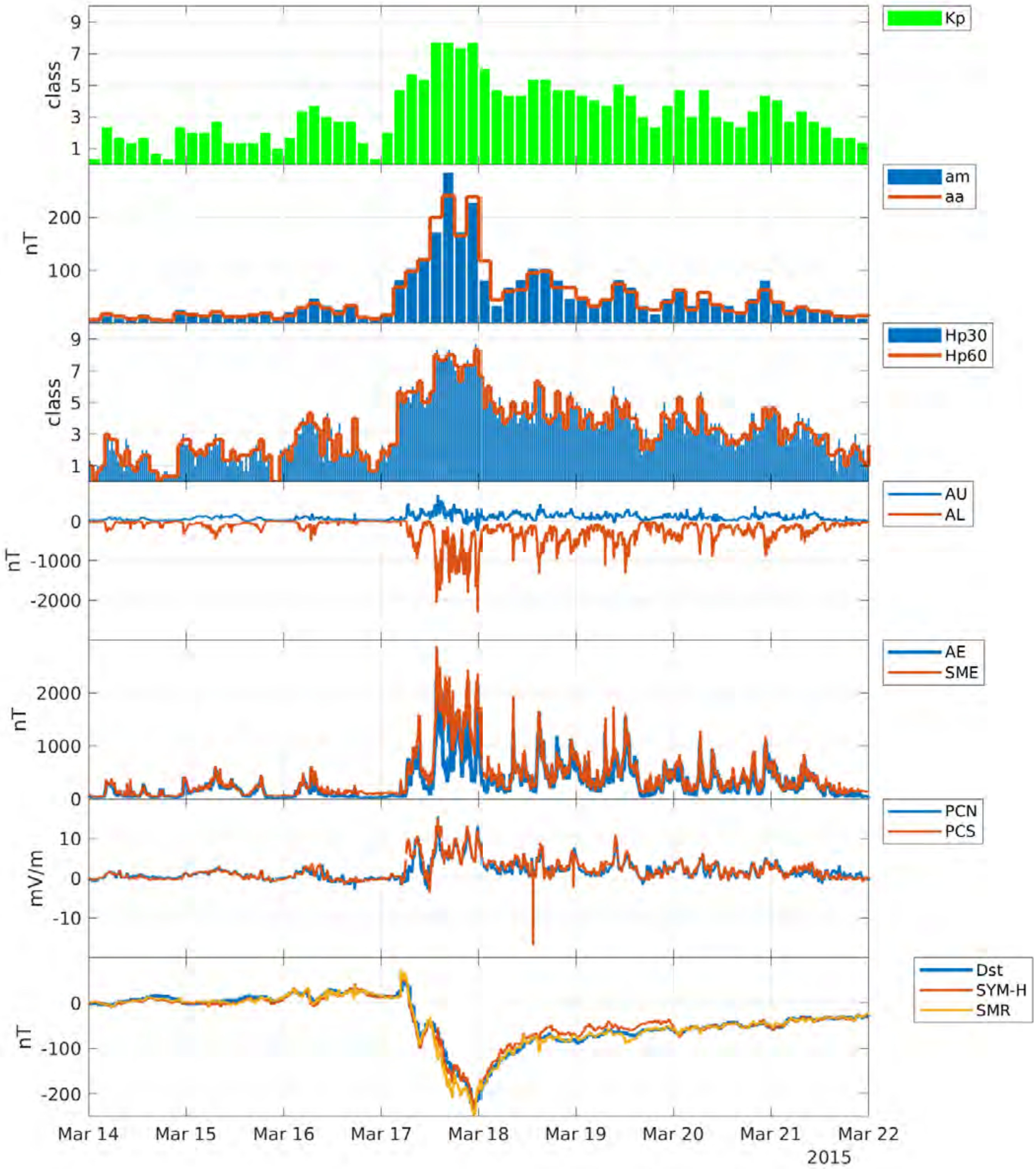

Figure 3.3: Illustration of magnetic index responses to the St. Patrick's Day Storm in 2015 during the period of 14th to 22nd of March. From top to bottom the indices are Kp; *am* and *aa*; Hp30 and Hp60; AU and AL; AE and SME; PCN and PCS; Dst, SYM-H and SMR.

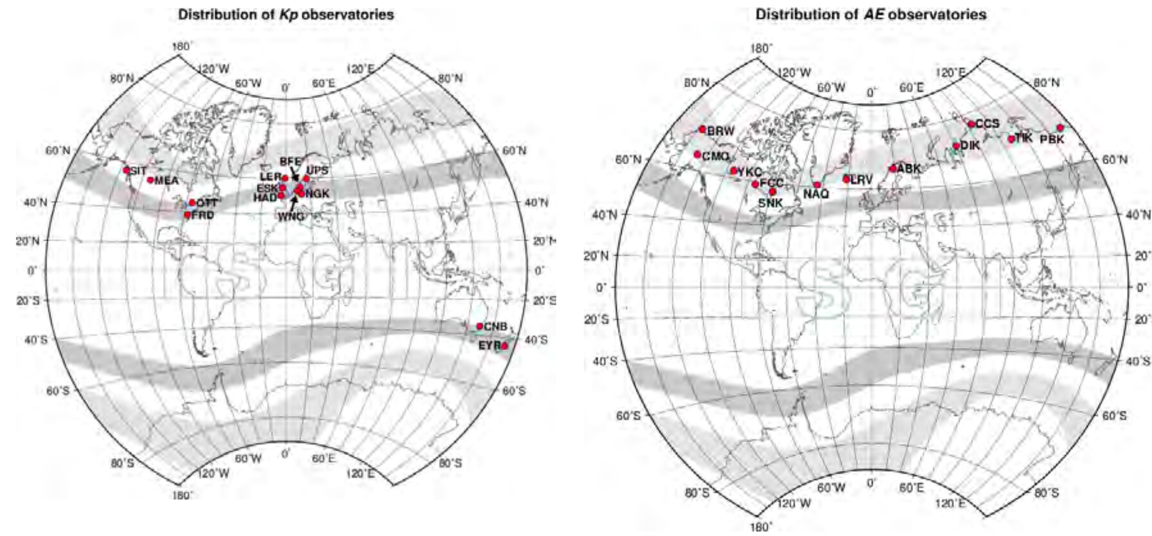

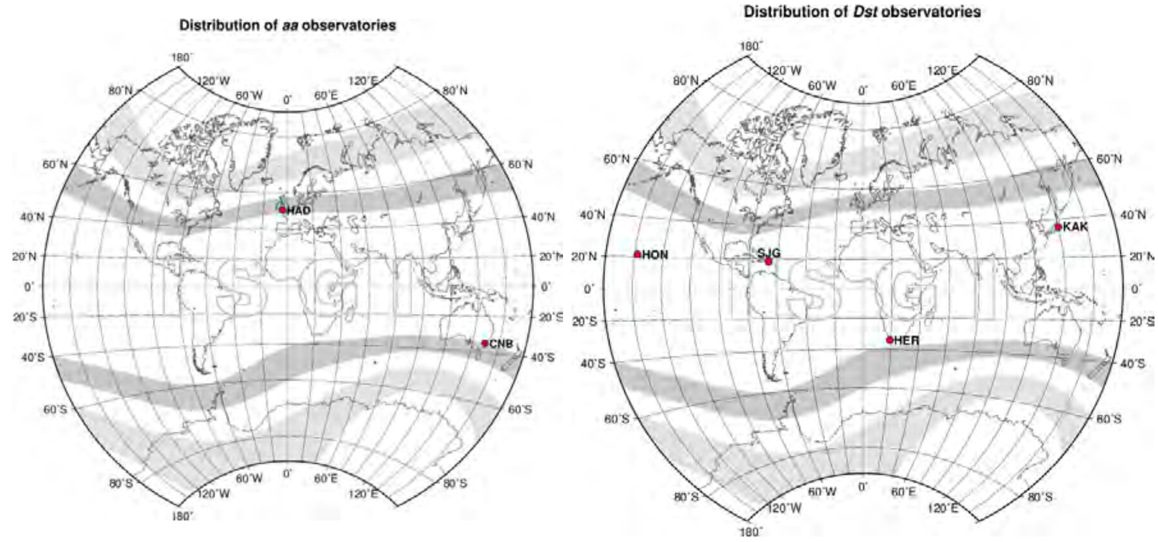

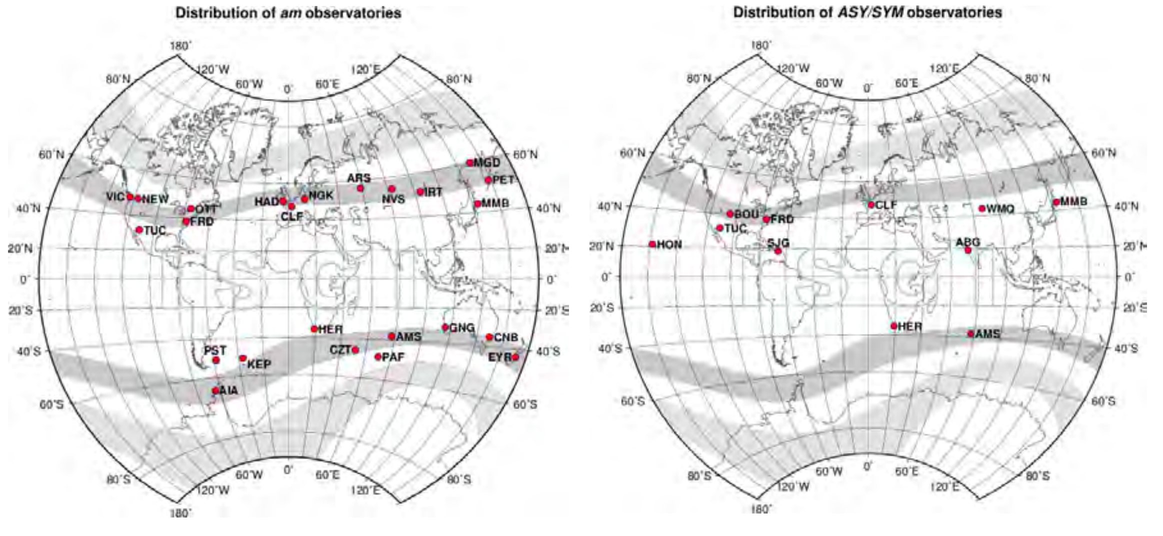

Figure 3.4: Location of observatories of networks for several indices: Kp, AE, aa, Dst, am and $SYM - H$. (Taken from ISGI)

This example illustrates how magnetic indices are essential for the quantification and description of space weather events, in particular the responses of the various magnetospheric and ionospheric current systems.

3.2 Geomagnetic Baselines

Whether tracking the intensity of a dedicated current system or describing the general state of the geomagnetic field, all indices have in common that they characterise the corresponding irregular variations within field measurements. To do so, the contribution from the source of interest has to be isolated within the geomagnetic field signal. Generally, this is achieved by removing the geomagnetic baseline. Such a baseline is supposed to contain all contributions from stable and quiet magnetic field sources and none from the source of interest. Thus, after removing, the residuals contain solely information on the source of interest, e.g. disturbances. In 1939, Bartels (1939) referred to this source separation as K-variations, that contain the quiet sources and non-K variations, that contain disturbance - or irregular - source contributions. Bartels et al. (1939) defines the geomagnetic baseline as

> *"... a smooth curve (a regular daily variation) to be expected for that element on a magnetically quiet day, according to the season, the sunspot-cycle, and, in some cases, the phase of the Moon"*

which is assumed to encompass the solar daily variation, the lunar daily variation and the after-effects of disturbances like recovery phases of the ring current. At the time, trained observers identified these quiet curves on analogue magnetograms by hand. This rather subjective definition was later made more concrete into a set of 7 practical rules by Mayaud (1980) to support the objectivity of the baseline determination. The identification of solar quiet current systems for mid-latitudinal observatories was explicitly included within these rules. In particular due to the space era, our understanding of the near-Earth environment and the associated current systems, together with their coupling to the solar wind enhanced our understanding of the sources contributing to the geomagnetic field. Nowadays, it is commonly accepted that a geomagnetic baseline includes the secular variation, solar cycle induced variations and the solar quiet variations. However, up to this date there is no qualitative ground truth on the shape of geomagnetic baselines and the general guidelines from the past are still widely employed to justify baseline derivations. As has been briefly indicated, each of the introduced index families uses a different method for the determination of the baseline. This also implies, that each method will produce different baselines, that lead to differences in the disturbance fields (i.e. the residuals after removal of the dedicated baseline method). Ultimately, this results in differences in the actual disturbance classification which needs to be taken into account when using the indices. In the following some frequently used baseline methods are introduced.

3.2.1 Computer-produced Baseline Derivation for the K-Indices

Since their introduction in 1939, the K-indices still form the base in the production of widely used K-derived geomagnetic indices for low- to mid-latitudes. With increasing digitalisation, the need for faster, computer-aided production of the K-indices rose and as a direct response a variety of algorithms were introduced. In 1991, at the International

Union of Geodesy and Geophysics (IUGG) meeting in Vienna, available algorithms were systematically investigated with regards of their accuracy in producing K-indices and corresponding baselines (Menvielle, Papitashvili, Hakkinen, & Sucksdorff, 1995). The algorithm from Sucksdorff, Pirjola, and Häkkinen (1991), referred to as the FMI method (the abbreviation coming from Finnish Meteorological Institute), produced good enough results for the continuation of computer-based K-indices[3].

The baseline according to the FMI method is based on a regression over a sliding window centred on the 24h UT day. For each UT hour with start-time t_0 and end-time t_1, the mean over the interval $(t_0 - m, t_1 + n)$ is calculated, with m and n being minutes. The resulting 24 values (one per hour) are fitted by a 5th order harmonic curve which is the baseline.

m is a fixed number of minutes, that depends upon the local time (LT): from 0-3 LT $m = 90$min, from 3-6 LT $m = 60$min, from 6-18 LT $m = 0$min, from 18-21 $m = 60$min and from 21-0LT $m = 90$min. n is derived in two steps:

1. Step: For each 3 hour UT interval (0-3UT, 3-6UT, etc.) the maximum and minimum of the horizontal components are used to derive an initial K-value K_{init}. With $n_{init} = K_{init}^{3.3}$, the hourly mean values for the intervals $(t_0 - m, t_1 + n_{init})$ are fitted with a 5th order harmonic which gives the preliminary baseline.
2. Step: The preliminary baseline is then removed from the measurements. Per 3 hour interval, the maximum and minimum of the residuals are used to determine the preliminary K-index K_{prelim}. The final n value used for the actual interval length of the K baseline derivation is defined as $n := K_{prelim}^{3.3}$.

To deploy this method, measurements from the full UT day need to be available.

3.2.2 Baseline Derivation for the Dst Index

The baseline for the final Dst index takes into account the secular variation $H_{secular}$ and the Sq variations H_{sq}. The two values are based upon the corresponding variations on the five quietest days of each month, the Q-days (see chapter 3.1.1.2).

$H_{secular}$ is estimated by least-square fitting of the annual mean values of all Q-days, during epoch τ that includes also the past four years as

$$H_{secular}(\tau) = A + B\tau + C\tau^2 \,. \tag{3.1}$$

For each month, an Sq average is calculated based on the 5 Q-days per month. For a year, this set of 12 Sq averages is expanded in a double Fourier series taking into account the local time LT and the month M as

$$H_{sq}(\mathrm{LT}, \mathrm{M}) = \sum_j \sum_k A_{jk} \cos\left(j\mathrm{LT} + \alpha_j\right) \cos\left(k\mathrm{M} + \beta_k\right) \,. \tag{3.2}$$

Therefore, to derive the final Dst index at time-step t, the measurements from at least the 4 years prior to t have to be available. This leads to long delays in the production of Dst. The World Data Center for Geomagnetism in Kyoto provides provisional and real-time (quicklook) Dst values. It needs to be kept in mind that these are derived from unverified raw data and thus may contain inaccuracies.

---

[3] The computer script in C is available at space.fmi.fi/MAGN/K-index/FMI_method/K_index.h

3.2.3 Baseline Derivation for the PC Indices

Janzhura and Troshichev (2008) introduced an automatic method for the determination of the baseline for the two polar cap stations used for the PC indices. They use data from quiet days to generate a statistical quiet variation H_q that is based on a 30-days running window. Per UT hour, 120 sample quiet minutes are identified from the running window and the mean of these represents H_q. The quiet samples are determined by two criteria:

1. $dB/dt < \gamma$ for each 20-minute interval
2. $|B(dt) - \overline{B(dt)}| < \beta$ for the mean of the 20-minute $B(dt)$ and the mean of the 20min intervals $\overline{B(dt)}$ within the previous 3 hours

The determination of the thresholds γ and β depends upon the amount of points available to determine H_q. Starting at $\gamma = 2\,\mathrm{nT/min}$ and $\beta = 2\,\mathrm{nT}$, γ and β are iteratively increased until 120 such quiet samples are found. The final mean is weighted according to the number of iterations needed to achieve the threshold of 120 samples. This mean is used as a baseline on days from which it is generated. On other and thus disturbed days, the baseline from the identified quiet days is interpolated. This approach makes it possible to project the baseline up to 20 days in advance by extrapolating H_q in amplitude. The phase is taken as constant, as no important phase changes were found in their observations.

Therefore the PC method can be used as a running method to provide near-real time baselines for the two polar cap stations.

3.2.4 IMAGE Method

Van De Kamp (2013) introduced a baseline derivation for observatories that are part of the International Monitor for Auroral Geomagnetic Effects (IMAGE) in Scandinavia with the goal of studying high-latitude ionospheric currents, especially auroral electrojets. The network contains a total of 32 magnetometers with geographic latitudes ranging from 58° to 79° which deliver data in 10-seconds resolution.

This baseline does not only include the long-term trend and diurnal variations, but also discontinuities in magnetometer measurements. When magnetometer data does not come from well-controlled and stable instrumentation, occasional artificial discontinuities may occur that can affect the baseline. In the first step of the IMAGE method, automatically identified jumps are investigated and removed manually accordingly. The long-term trend and the daily variations are based on identified quiet and disturbed days. To identify quiet days, each UT hour is fit by a straight line which is removed from the measurements. From these residuals the standard deviation σ is calculated. The maximum σ_{max} of all the hourly σs is used to describe the level of disturbance for the corresponding UT day. The day with the smallest σ_{max} is marked as the quietest day of the month. To guarantee real quietness, the smallest σ_{max} has to additionally be below an empirically identified threshold. The optimal threshold is derived by visual inspection from the station Abisko (ABK), nearby Kiruna in Sweden, and then adjusted empirically for other stations in relation to ABK. The diurnal baseline for a quiet day consists of the 7 lowest harmonics of the fast-fourier transform (FFT) applied on the data from the quiet day. For non-quiet days, the curves from adjacent quiet days are interpolated. This can also be applied when there is no quiet day found in a month or for longer periods. The long-term baseline is taken as the simple median of the UT day if the day is not disturbed. The categorisation with disturbed is done analogously to the quiet determination: σ_{max} has to be above an empirically threshold. In this case the long-term trend for the UT day is interpolated from adjacent non-disturbed days. The full baseline is then the superposition of the jump, long-term and diurnal baselines.

The baseline is derived for each station and each component separately, and thus each of the manual steps listed above (jump verification, threshold determination) have to be done per station and per component. This leads to the baseline determination being time-consuming and only applicable for the considered time-interval. Hence, it is not applicable for real-time applications. However, by removing the jump baseline, the IMAGE method gives access to data from remote and therefore harder to maintain equipment, which is a common condition in auroral latitudes. This increases spatial distribution of measurements for space weather studies.

3.2.5 SuperMAG Method

Gjerloev (2012) introduced a baseline derivation method that is used for the SuperMAG indices. The very first step of this method is to rotate magnetometer measurements into a specific local magnetic coordinate system. The rotation angle is determined by an arbitrarily defined time-dependent declination angle based on the horizontal field components, smoothed over 17 days.

The long-term trend and the diurnal variations are included in the baseline. For the diurnal variations, the mode (i.e. the value with the highest occurrence rate) for each day is removed from the measurements. For each 30 minute interval, the mode of the residuals of the day in question, together with its preceding and succeeding days is determined. The amount of days surrounding the day of interest depends upon the fluctuations within components X, Y, Z and magnetic latitude of the employed magnetometer. A cubic convolution interpolation method is applied on the weighted half hourly mode values to derive the diurnal variations. The weights depend upon the amount of days used. For the yearly trend the mode over the past 17 days for each day is generated. A weighted smoothing procedure is then applied on the series of modes to determine the long-term trend. The weighted smoothing procedure depends upon the fluctuations in the instantaneous measurements and from the previous eight days and differs for each of the components. Lastly, from the residuals (difference between measurements and diurnal variations and yearly trend) a station specific offset is determined. This offset is derived as the mode of the residuals during Q-days and shows clear dependencies on magnetic latitude.

The final SuperMAG baseline is comprised of the diurnal variations, the yearly trend and the residual offset.

For the SuperMAG method, no manual steps have to be performed. However, as it needs information from surrounding days, it cannot be applied in real-time, nor is it clear how many following days are needed to produce the mode for the 30min interval. Additionally, the knowledge of the magnetic coordinates of the measurements are a prerequisite.

3.3 Motivation for this Work

Each of the introduced baseline methods are being actively used with each of them bringing their own advantages and disadvantages.

With the somewhat loose definition of what a geomagnetic baseline actually is, it is not trivial to quantify differing baselines and tell whether one is more correct than another. One justification for a baseline is given by Van De Kamp (2013) comparing the IMAGE method with the SuperMAG method and argues that both are very similar and thus can both be employed. The common consensus that seems to have been establishing itself over the past years is, however, that a baseline is made up of the quiet sources that comprise the long-term trend and some typical diurnal variations. This approach is explicitly followed by the Dst, IMAGE and SuperMAG methods. Though, each of these motivates its own way of derivation to ultimately contain the quiet sources, detailed investigations of the actually contained sources is widely absent. Gjerloev (2012) and Van De Kamp (2013) show the spectra of the baseline and argue that the 24h harmonics are sufficiently represented and thus include the diurnal quiet variations. Many of the methods actually use some kind of statistical averaging to describe quiet variations. In the case of methods applied to mid-latitudes, this leads to an averaging of the Sq current footprints fully neglecting its intrinsic D2D variability.

A common challenge faced by all methods is the identification of measurements from quiet variations that are used as proxies for the baseline. Using the official Q-days as derived from the K-indices as described in chapter 3.1.1.2 or any other arbitrarily chosen UT quiet days come with a series of limitations and caveats that have been extensively discussed in e.g. Mayaud (1980); Joselyn (1989); Menvielle et al. (1995); Janzhura and Troshichev (2008); Gjerloev (2012); Van De Kamp (2013). Some of these include

- Disturbances can be locally and temporally confined such that they are missed when looking at the UT day
- Quiet days that are based on indices which need some kind of quiet criteria is a circular argumentation
- Using the average of any number of quiet UT days within a certain range in order to derive statistical properties of quiet variations is arbitrary

Thus, methods that make use of and produce baselines per UT day like the K-, Dst and PC method, may not be able to accurately describe disturbance influences.

The idea of having a computer-based derivation of baselines for the K-indices came from the need to provide them in a timely and automatic manner without manual intervention. Certainly, for any near real-time application this requirement has to hold too. This implies that the usage of future measurements or further input parameters like magnetic locations cannot be incorporated into the baseline derivation, as is the case for K, Dst and SuperMAG methods. Any manual intervention that is needed for baseline derivation steps like the removal of outliers or the derivation of thresholds are also not suitable for real-time applications.

The ultimate goal of this work is to present a baseline which contains the sources of the quiet geomagnetic field and which implementation is fully automated and thus may be employed in near real-time, overcoming the discussed short-comings. For such a baseline derivation the following chapters

1. describe the automatic derivation of the baseline during quiet periods
2. investigate and analyse associated sources that contribute to the quiet baseline
3. introduce an algorithm to deduce quiet variations during disturbed periods for the baseline
4. explore the deployment of artificial intelligence for baseline derivation.

Part II

A Novel Geomagnetic Baseline

Chapter 4

Generation of the Filter Baseline

The ultimate goal is to derive a geomagnetic baseline that can be used for magnetic indices in mid-latitudinal regions. The main purpose of a geomagnetic baseline is to separate long-term and recurrent contributions from short-lived and sporadic magnetic activity within geomagnetic field data. Based on certain frequencies, the contributions can be related to certain sources as was shown and discussed in figure 2.16. With this premise, we introduce the approach of temporal filters to determine baselines in an automatic manner.

At first, the description of and considerations about the leveraged data-set used in this work is given, followed by a short excursion of using temporal filters for signal analysis. This enables us to define a baseline resulting from temporal filtering, which we will refer to as the *Filter Baseline*. Finally, we discuss some computational aspects of this approach.

4.1 Usage of Magnetic Observatory Data

In chapter 3, we saw that magnetic indices are usually derived from ground magnetic field measurements. For this work, data provided by the INTERMAGNET network ensuring high quality data that is delivered in minute resolution is used. To recall, the data comes as a vector in the local NED coordinate system with components X, Y, Z (see chapter 2.6.3). As they hold the most important magnetospheric and ionospheric information and as is common for most indices, we use the horizontal components X and Y. The considered time span covers 29 years and starts in 1991 when the network was founded and ends in 2019 as definitive data was available at the start of this PhD work. During this period a total of 149 observatories delivered data for at least one year to the INTERMAGNET database. The location of these observatories is depicted in figure 4.1. The detailed list of observatories and their participation in INTERMAGNET can be found in appendix A together with an enlarged map of their geographic locations.

We want to derive a baseline for observatories in mid-latitudinal regions at which the auroral and equatorial electrojets only play a secondary role. Therefore, the used observatories are constrained to magnetic latitudes from 20° to 60° degrees in both hemispheres, using magnetic ED coordinates (see chapter 2.6.3). In figure 4.1 stations at magnetic mid-latitudes in the northern hemisphere are indicated in blue and in the southern hemisphere in red. Stations that are outside of the boundaries are indicated in grey. From this map, it is clear that the distribution is heavily weighted towards central Europe.

Presenting the results of this work for each of the considered stations, which includes the generation of the filter baseline and the subsequent analysis, would result in a storybook that bursts the page limits of a doctoral thesis. Rather, the results for all considered stations have been exhaustively analysed and reviewed and are available upon request. Further in this work, the performed analysis and investigations will be illustrated by a set of carefully selected observatories. The choice is based on the length of availability, homo-

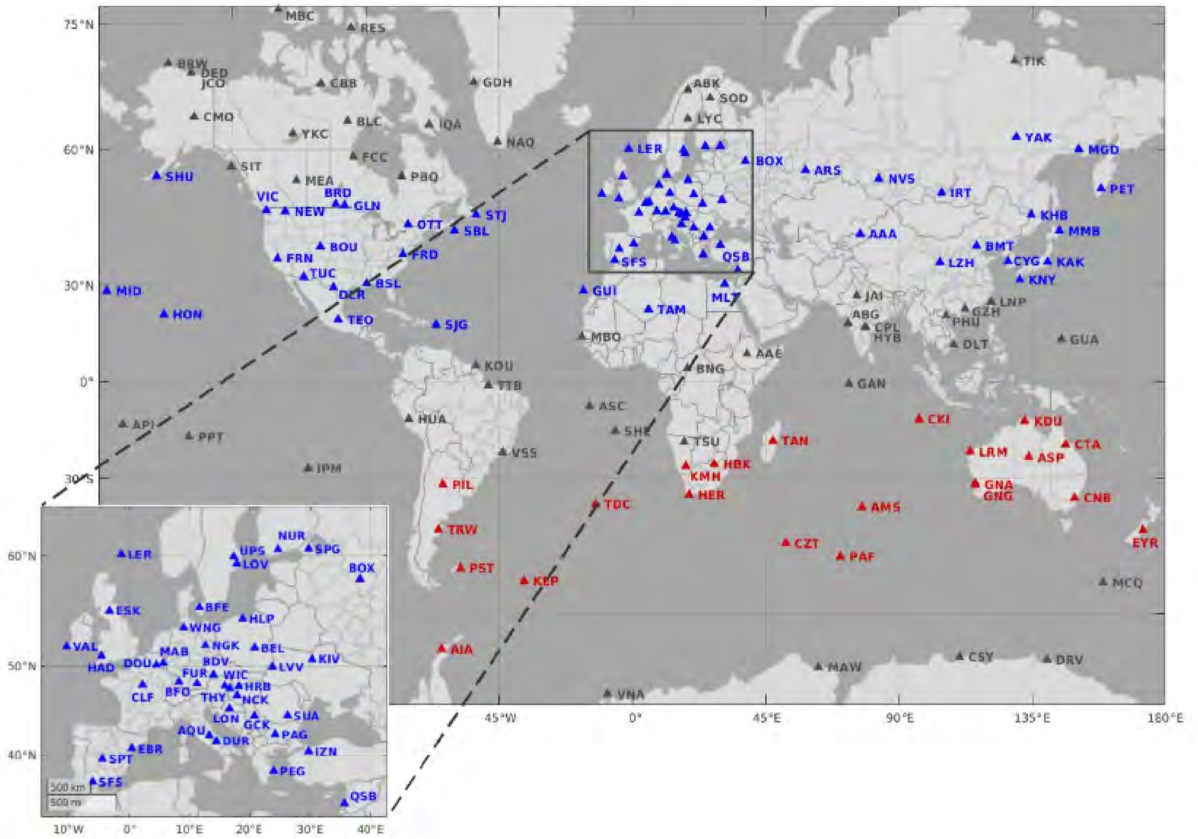

Figure 4.1: A geographic map showing INTERMAGNET stations which delivered data for at least one year between 1991 - 2019. Blue and red corresponds to stations with absolute magnetic ED latitude between 20° and 60° in the northern (blue) and southern (red) hemispheres, respectively. Grey corresponds to stations outside of these boundaries, i.e. equatorial and polar regions.

geneity of the data and on the location within the mid-latitudinal range. The magnetic observatory Chambon-la-Forêt (CLF) in France, Europe, is part of INTERMAGNET for the entire considered 29 years period having minor down-times (total of 0.66‰). It is located at 48.025°N which corresponds to magnetic ED latitude 43.3° to 42.7° between 1991 and 2019 and is thus centrally positioned within the considered latitude range of 20° to 60°. Furthermore, CLF is close to several other magnetic observatories. Comparison with them enables the identification and ruling-out of potential local effects. Thus, the main observatory to illustrate results is CLF in this work. When larger scale phenomena are investigated, additional observatories are illustrated when appropriate. Their choice is based on similar criteria and additional criteria are outlined when applicable. The definitive dataset from CLF can be accessed under the BCMT Data Repository (BCMT, 2023).

4.2 Time Domain Filtering

Temporal or time-domain filtering is a type of digital signal processing that modifies time-series according to frequencies. They are used to selectively amplify or attenuate specific frequency components of a signal. Filters are used for e.g. the removal of noise, enhancement of signal clarity or extraction of specific features and patterns.

A filter consists of an input signal, an output signal (the response) and a unit sample response (transfer function). In practice, ideal filters are not realisable and numerical filters that approximate the ideal ones as closely as needed are designed.

A temporal filter is realised by the convolution of a signal with a filter kernel that defines desired temporal characteristics. The filter kernel specifies the weights to be applied to the signal at each time step, and can be designed to achieve a variety of objectives, such as low-pass, high-pass, band-pass, or band-stop filtering. Some examples of time-domain filters include moving average filters, which smooth a signal by averaging neighbouring samples, or digital Butterworth filters, which are designed to provide a flat frequency response in the passband and steep roll-off in the stopband. The finite impulse response (FIR) filters are digital signal processing filters that operate on discrete-time signals. These are characterized by their impulse response, which is a weighted sum of the input signal and its past values, where the weights are defined by a finite-length sequence of coefficients. One of the key advantages of FIR filters is that they are always stable, meaning that their output will not grow indefinitely or oscillate over time. They can also be designed to have linear phase response, which means that the filter introduces a constant time delay across all frequency components of the input signal which preserves the signal's phase relationships.

Designing filters with the desired frequency response and multiplying it with a rectangular window sequence yields relatively large oscillations and ripples near the band edge of the filter. The choice of an appropriate window function that decays toward zero gradually can help this problem. Several windows exist, among which the Hamming window is used to extract single channels, as signals close to the edge of the passband are already well suppressed. Filtering is a standard signal analysis tools and details about these methods can be found in various textbooks, e.g. Hamming (1977); Proakis and Manolakis (2006).

4.3 Definition of the Filter Baseline

Magnetic field measurements can be treated as discrete time signals and as such they can be represented in the time-domain, as well as in the frequency domain. The amplitude-frequency spectrum of geomagnetic field measurements of both components, X and Y at CLF for the entire period between 1991 to 2019 is presented in the upper panels of figure 4.2 in dark blue. The lower panels show the spectra of five filters, that are introduced shortly. The main external quiet-time contributions in mid-latitudes are due to the solar quiet current systems which operate on periods of 24h, 12h, 8h and 6h, which effect is clearly observed as peaks in figure 4.2. Additionally to these (sub-)diurnal variations, a smooth change of the Earth's magnetic field is induced by sources acting above the 24 hours timescales (including Earth's dynamo that is responsible for the secular variation). In previous chapters and figure 2.16, we saw that it is possible to assign main frequency regimes to the various sources of the geomagnetic field. Using this assumption, we perform a frequency analysis of the signal with the goal of isolating source contributions. This can be accomplished by temporal filters as introduced in the previous section. Temporal filters have been employed in various studies to remove the diurnal recurrent variations from ground measurements, see for example Behannon and Ness (1966a, 1966b); Bhargava and Yacob (1970); Jadhav, Rajaram, and Rajaram (2002). Please note, that a complete separation of sources cannot be achieved by considering exclusively frequency regimes. Its limitation will be discussed at a later point (see chapter 5.3 and 5.4).

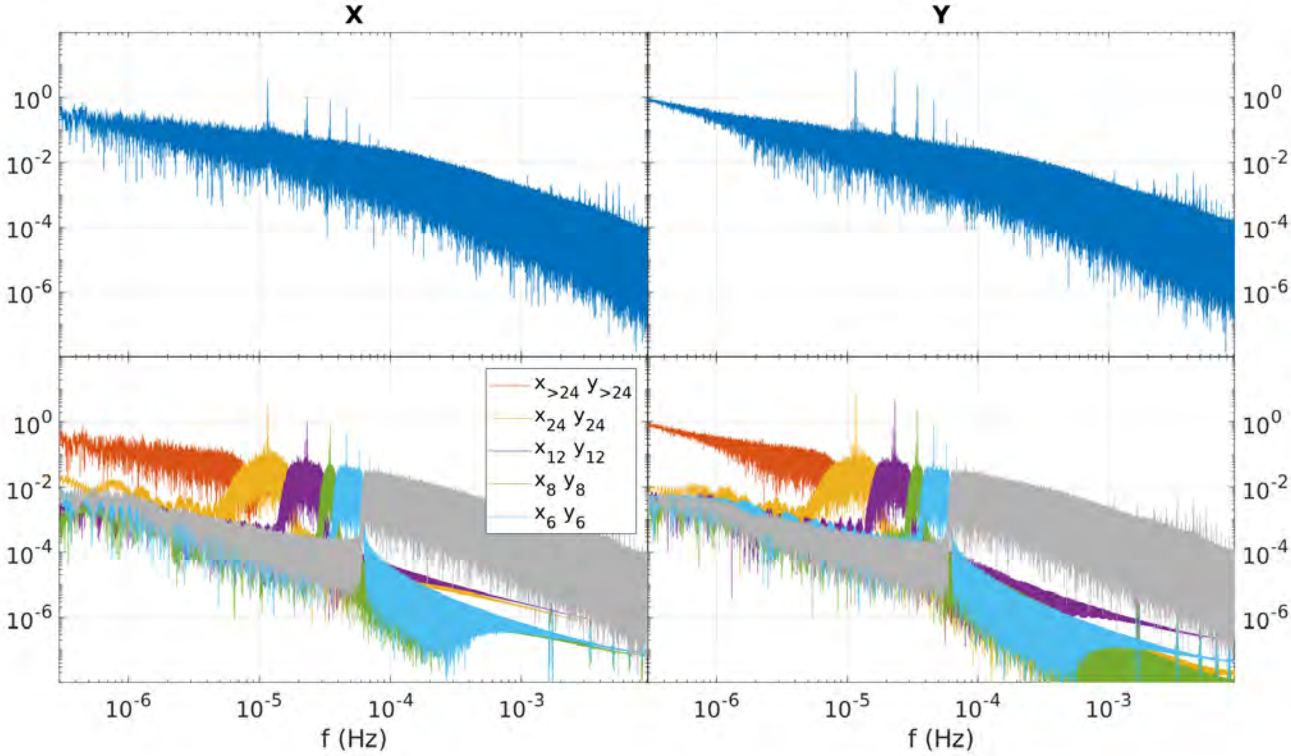

Figure 4.2: Amplitude-frequency spectra of the filters for the X and Y components at CLF for the entire period between 1991 to 2019 in dark-blue in the upper two panels. The lower two panels show the spectra of each of the temporal filter responses: Long-term filters (orange), diurnal (yellow), semi-diurnal (violet), 8h (green), 6h (bright blue) and the remaining signal (residuals in grey).

For the separation of sources, we use FIR filters with Hamming window on a centered three-days data sample, i.e. for timestep t data from $t - 1.5$days to $t + 1.5$days is taken. Five filters are defined: one low-pass and four band-pass as summarised in table 4.1. The frequency regimes for the five filters are determined according to the following considerations, see also Haberle et al. (2022). To extract long-term variations, we use a low-pass filter with cut-off frequency of 7.716×10^{-6} Hz corresponding to variations above 36 hours within the signal. For the four (sub-)diurnal frequencies, we eventually use band-pass filters that are implemented with the help of low-pass filters. To extract the 24-hour variations, we apply a low-pass filter with cut-off frequency of $1/24\text{h} = 1.1574 \times 10^{-5}$ Hz on the signal, from which we subtract the output of the long-term filter. The 12-hour variations are then computed as the difference between the low-pass filter with cut-off frequency of $1/12\text{h} = 2.3148 \times 10^{-5}$ Hz applied on the signal from which we substract the sum of the outputs of the 24h band-pass and the long-term filter. The 8h and 6h band-pass filters are implemented analogously.

The filters are applied separately to each of the horizontal components X and Y of the geomagnetic field measurements. In the following, we label the magnetic observatory measurements in capital X, Y, and the filter responses in lower-case x, y with the corresponding period range as subscript as indicated in table 4.1. The lower panels of figure 4.2 show the amplitude-frequency spectrum of each of the filters during 1991-2019. As designed, each (sub-)diurnal filter contains the related peak frequencies, e.g. the semi-diurnal filter in violet contains the peak at 12 hours, and the long-term filter contains lower frequencies. Please take notice of the soft edges for the (diurnal) band-pass filters which is achieved by applying the Hamming window.

Table 4.1: Finite impulse response (FIR) filters, corresponding passing frequencies and their notation. The sum of the five filter responses forms the baselines x_{FB} and y_{FB}. (Haberle et al., 2022)

Signal Contribution	Pass Frequencies	Notation	
Long-Term	below 7.716×10^{-6} Hz	$x_{>24}$	$y_{>24}$
Diurnal	7.716×10^{-6} to 1.1574×10^{-5} Hz	x_{24}	y_{24}
Semi-Diurnal	1.1574×10^{-5} to 2.3148×10^{-5} Hz	x_{12}	y_{12}
8 hours	2.3148×10^{-5} to 3.4722×10^{-5} Hz	x_8	y_8
6 hours	3.4722×10^{-5} to 4.6296×10^{-5} Hz	x_6	y_6

Returning to the assumption that these frequency regimes are the main contributions to the measured quiet magnetic field and knowing that sources superpose each other, we can define a baseline based on the filter responses:

$$x_{FB} = x_{>24} + x_{24} + x_{12} + x_8 + x_6 \text{ for } X\text{, and} \tag{4.1}$$

$$y_{FB} = y_{>24} + y_{24} + y_{12} + y_8 + y_6 \text{ for } Y \tag{4.2}$$

We will refer to (4.1) and (4.2) as the *Filter Baseline*. The filter responses in the time-domain are demonstrated in figure 4.3 of X and Y at CLF in the five upper panels. The filter baseline is demonstrated in the sixth panel (in red) plotted together with the measurements (in black). The residuals are calculated as the difference between the measurements and the filter baseline, illustrated in the bottom panel.

4.4 Computational Aspects

4.4.1 High Performance Computing

Generating one filter value at time-step t, i.e. applying one of the five filters introduced before on the centred 3-days window around t, takes 0.7 s using an off-the-shelf computer (COTS) with Intel(R) Core(TM) i9-9880H CPU with 2.30GHz. This results in a total of $5 \times 0.7\,\text{s} = 3.5\,\text{s}$ that is needed to generate the full filter baseline at time-step t. Implications for real-time applications are discussed in the next subsection.

In order to evaluate and analyse the introduced filter approach, a statistically significant amount of data needs to be available. For the purpose of this thesis, the data from 149 observatories within 1991 to 2019 was used and for each time-step t (in minute resolution) each of the five filters had to be applied. These are more than 15 million filter operations for a station that delivered 29 years worth of data. A standard CPU is just not fast enough to treat the entire database in a practicable manner. In order to provide remedy to this issue, high performance computing was leveraged. Graphical Processing Units (GPUs) that are equipped with powerful cores can be used for more general tasks than only graphics rendering. Being equipped with a large number of cores and on-board memory capacity, they are used for tasks that can be parallelised. Libraries for the usage

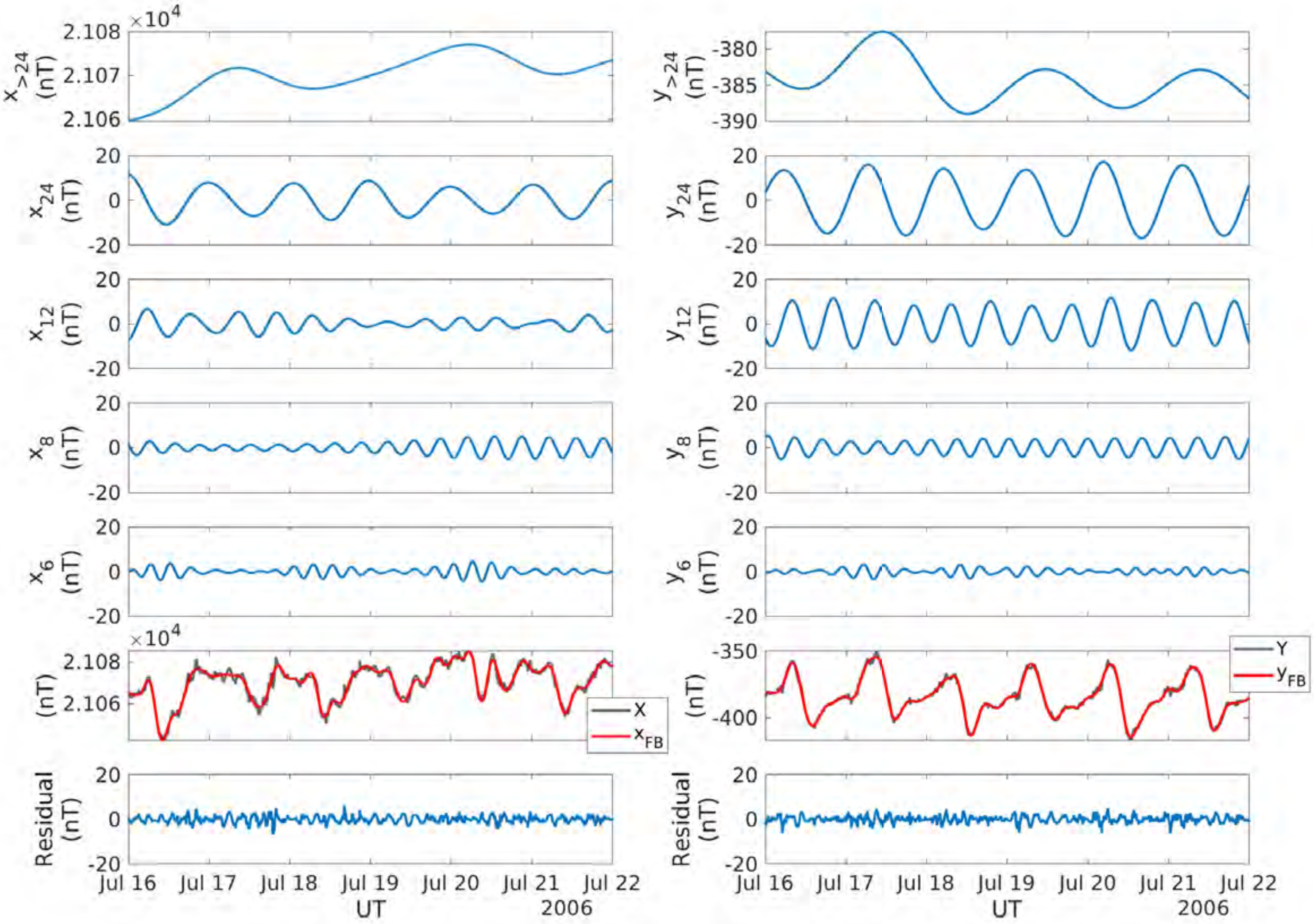

Figure 4.3: Decomposition of X (left) and Y (right) measurements at CLF over 6 CK-days between 16th to 22nd of July 2006. From top to bottom: the five consecutive FIR filter responses; comparison of measured magnetic field component (black) with the determined quiet baseline (red); residuals calculated as difference between measurements and filter baseline. (Haberle et al. (2022))

of GPUs are mainly written in CUDA (Compute Unified Device Architecture) for Nvidia cards and OpenCL (Open Computing Language) for both AMD and Nvidia cards and are based on *C* or Fortran. By parallelising the task at hand, a GPU can treat multiple operations at a fraction of time than a standard CPU would need. Applying filters to signals is a flagship example of processes that can be parallelised, as the filter can be applied at each time-step independently. Therefore, the filtering of the database is done on a GPU, more precisely an Nvidia Quadro 2000T and programmed in its native language CUDA fortran. This application of high performance computing allows to generate the entire filtered database within 4 hours. This enables the extension of the database with additional magnetic field data in the future and also provides the option of re-computation for differing filter designs (e.g. enlarging the three days filter window).

4.4.2 Real-time Applications

As already stated, generating one filter value at time-step t_0, i.e. applying one of the five filters introduced before on the centered 3-days window around t_0, takes $0.7\,\mathrm{s}$ using the aforementioned COTS. This makes a total of $5 \times 0.7\,\mathrm{s} = 3.5\,\mathrm{s}$ that is needed to generate the full filter baseline at t_0. No further information like location of the observatory or handled time-period needs to be provided in order to generate the frequency responses. This means that for the computation of the filter baseline, the architecture and power of the used machine is the deciding factor. As we use minute data, the $3.5\,\mathrm{s}$ from COTS, however, do not pose strong restrictions on the potential real-time application. The more relevant limitation for any real-time application is the fact that a centered window of 3 days is used. Such that, in order to generate a filter value at time-step t, not only the past 1.5 days of the signal need to be known, but also the future 1.5 days.

On a more physical note, as we will also see later: using only the filter approach doesn't separate sources fully. A single source can act on various frequency regimes of the spectrum. Disturbances, like geomagnetic storms, have an inhomogeneous duration in time which can exceed the chosen three-days filter window and in general disturbances that last more than 6 hours can influence any of the filter responses. Further details on these limitations is discussed in succeeding chapters.

Chapter 5

Sources within the Filter Baseline

In the previous chapter, we motivated the derivation of the filter baseline to contain sources of the quiet geomagnetic field, i.e. long-term and solar quiet variations. This chapter is devoted to the identification of sources which contributions can actually be recognised within the baseline. I present the behaviour of the filter outputs (responses) and investigate their variations, giving thorough analysis. I start with the discussion of sources within the long-term filter and then continue to the diurnal and sub-diurnal filters. Eventually, I discuss disturbance signatures.

5.1 Long-term Filter

The long-term filter is a low-pass filter with cut-off period of 36 hours, i.e. it preserves variations with periods above 36 hours. The spectrum of its output is depicted in 4.2 (orange) and the variations in the time domain in figure 5.1. The upper two panels show the filter output for the X and Y components at CLF over the entire period of 29 years and the lower two panels present a zoomed-in view on 3-months. Starting with the upper panels, $x_{>24}$ shows a steady increase from approximately 20 700 to 21 270 nT which is a total increase of 570 nT, with shorter fluctuations of up to 300 nT. Similarly, $y_{>24}$ shows a steady, but steeper increase of 1500 nT (from around -1100 to 400 nT), transitioning from negative to positive values around 2014, with shorter fluctuations in the order of tens of nanotesla.

From previous chapters we learned that the configuration of Earth's internal magnetic field slowly changes over time. This smooth drift can be also observed in the filter outputs. As the magnetic pole moves closer to Europe, we expect the magnetic field strength at CLF to slowly increase accordingly as it drifts towards higher magnetic latitudes. This increase in field strength can be observed in each component of the magnetic field measured at CLF and in particular here in both $x_{>24}$ and $y_{>24}$ (see the upper panels of Figure 5.1). The magnitude of $y_{>24}$ is lower than that of $x_{>24}$ as the magnetic meridian is close to geographic North (equal in 2014 when $Y = 0$ and thus declination was zero at that point). To see if the outputs are in agreement with the observed and modeled secular variation, we compare them with the latest IGRF-13 model (Alken et al., 2021). In figure 5.2 the results for two observatories that are in mid-latitudes, CLF in Europe and Fredericksburg (FRD) in North America, are presented. The IGRF evolution of both horizontal magnetic components is depicted in red and its general trend follows that of the filter outputs. For most of the components, however, a fairly constant offset can be observed. As described in chapter 2.5.2, the crust induces a certain, constant magnetic field bias that depends upon the local properties of the ground. Adding the mean biases from Verbanac et al. (2015) from table 2.1 for CLF and FRD to the IGRF model results in the yellow line in figure 5.2. We see that, now, the long-term filters are

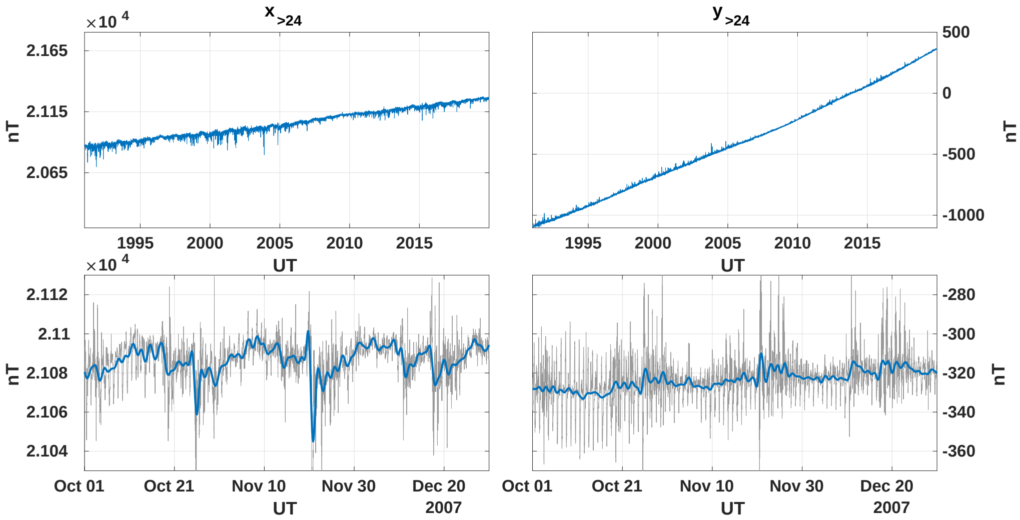

Figure 5.1: Responses of the long-term filters $x_{>24}$ and $y_{>24}$ for CLF. The upper panels depict the general trend between 1991 and 2019, the lower panel presents a zoomed-in view of 3 months, whereby the grey indicates the magnetic field components X and Y

in good agreement with the model including the crustal bias. However, the filter output is less smooth than the IGRF-13 model. To quantify the linear correlation between the filter output and the IGRF-13 model plus crustal bias, we use the Pearson correlation coefficient. The Pearson correlation coefficient is a statistical measure that assesses the linear relationship between two continuous variables. It ranges from -1 to 1. A value of -1 indicates a perfect negative linear relationship between the two variables, where as one variable increases, the other decreases by a similar amount. A value of 1 indicates a perfect positive linear relationship between the two variables, where as one variable increases, the other increases by a similar amount. A value of 0 indicates no linear relationship between the two variables. The Pearson correlation coefficient is calculated by dividing the covariance between the two variables by the product of their standard deviations. For each station and each component the linear correlation is above 0.99, from which we can infer that the secular variation and the crustal bias are contained within the long-term filter response.

Apart from the general trend, the long-term filter also contains shorter variations. A clear seasonal dependency can be recognised. The lower panels of 5.1 present the zoomed-in view on a three-months period and display variations with periods of 27-days. These variations are very clear for the X component, and less, but still present, for the Y component. The observed 27-days variation is in agreement with Briggs (1984); Jakowski, Fichtelmann, and Jungstand (1991); Van De Kamp (2013); Poblet and Azpilicueta (2018) who attribute these to either the solar rotation period or tidal variations that arise from the interaction between solar-quiet and lunar tides. However, we cannot exclude the possibility that these variations are a superposition of sources enhancing each other within the same frequency range. Furthermore, $y_{>24}$ shows less short-time variability than $x_{>24}$, as it is proportionally less affected by fluctuations from external sources. Here I would like to point out that signatures of geomagnetic storms are identifiable within the long-term filters. For example, the famous Halloween storms can be clearly identified in both $x_{>}24$ and $y_{>}24$ as strong dips at the end of 2003. In fact, the long-term filter can be associated

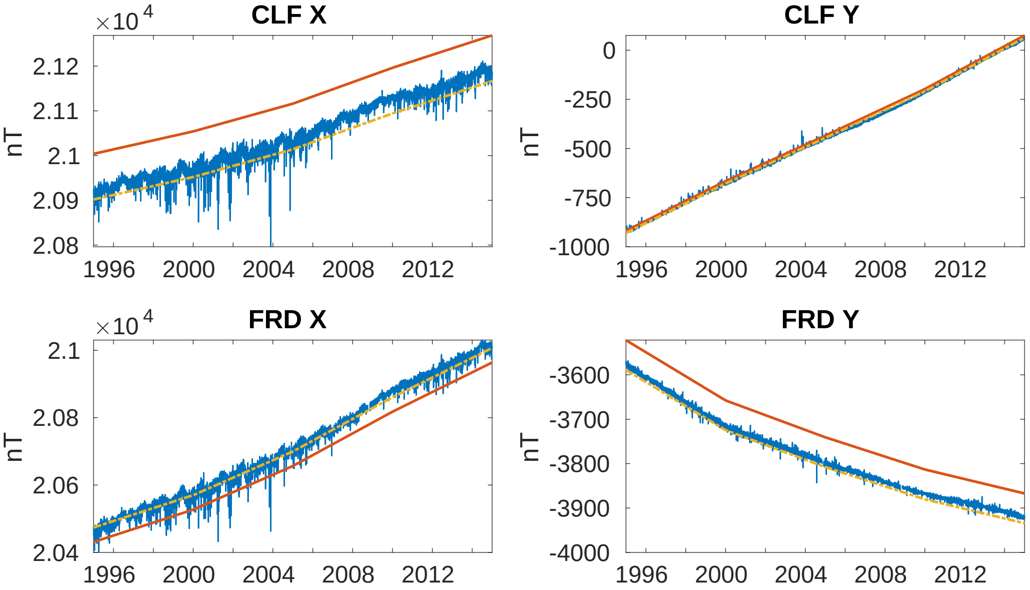

Figure 5.2: Comparison of the long-term filter (in blue) with the IGRF model (in red) for two stations CLF (top) and FRD (bottom). The crustal bias is added to the IGRF model in yellow.

with the Dst index to a certain extent, as we will see in chapter 6.1.1.

5.2 Diurnal and Sub-Diurnal Filters

This section presents an extensive analysis of the diurnal and sub-diurnal filters. To commence with, the (sub-)diurnal filter responses are discussed individually in relation to solar cycle, season and local time. This is followed by further analysis with the purpose of identifying the footprints of the Sq current system within the combination of the diurnal and sub-diurnal responses. Subsequently, we will try to anticipate and reproduce the quiet variations on the basis of observed solar cycle-, seasonal- and local time dependencies and the filter responses themselves. We will see that the key for the description of quiet variations steams from a pertinent consideration of the day-to-day variability.

5.2.1 Variations within the (Sub-)Diurnal Filter Responses

In this subsection, we look at global patterns of the 24h, 12h, 8h and 6h filter responses of the X and Y components at CLF and the combined (sub-)diurnal signal containing the sum of the four filters:

$$x_D = x_{24} + x_{12} + x_8 + x_6 \tag{5.1}$$

$$y_D = y_{24} + y_{12} + y_8 + y_6 \, . \tag{5.2}$$

They are presented in Figures 5.3 and 5.4 with respect to local time and day of year, alongside the $F10.7$ index in the first panel to facilitate comparisons with solar cycle phases. We superimposed the occurrence of sunrise and sunset at 110 km altitude on corresponding panels as (lower and upper) black dashed lines. For demonstration purposes, we illustrate dependencies on local time, season and solar activity corresponding to variable solar irradiation conditions over the solar cycle 23 from 1998 to 2008. The analogue figures for the entire period 1991-2019 can be found in appendix B.

Let us start with the individual filter responses. They are presented in the four central panels of Figures 5.3 and 5.4. Periodical patterns can be observed with respect to day-of-year and, more specifically, season and local time. Each filter response is a sinus like function with period P and thus has one maximum and one minimum per period. This can be clearly observed as the filter responses of x_{24}, y_{24} have one maximum and minimum per day, the 12h filters have two, the 8h have three and the 6h filters have four.

For the X component (figure 5.3), the filter with the highest amplitude is clearly x_{24}, followed by x_{12}, while x_8 and x_6 have a noticeably smaller amplitude in comparison. The intensity of all filters follows the solar cycle smoothly. Generally, during solar maximum (around 2002) amplitudes are the highest and decrease to lower values during solar minimum (around 2008). Moving on to seasonal dependencies, the intensity of the filters is higher during summer than during winter months. For x_8 and x_6 the amplitude almost diminishes to values below $\pm 5\,\mathrm{nT}$. In x_{24}, we see a clear morning crest phased with the local sunrise (transition from positive to negative values near the lower dashed line) and enhanced activity during summer months after sunset (transition of negative to positive values near the upper dashed line). Also the sub-diurnal filters respond to sunrise (lower dashed lines), around which each of them features positive activity. In general, they seem rather unaffected by sunset (upper dashed lines).

For the Y component in figure 5.4, the diurnal y_{24} and semi-diurnal y_{12} are rather comparable in intensity and y_8, y_6 play a secondary role. Again, the intensity of all filters follows the solar cycle smoothly with higher amplitudes during solar maximum than minimum. Likewise, the seasonal dependency is very dominant. For y_{24}, y_{12} and y_8 the amplitudes are significantly higher during summer than during winter months. The amplitudes during winter reduce considerably, especially for y_8 and y_6. Interestingly, y_6 has elevated amplitudes during equinoxes. In contrast to x_{24}, y_{24} activity is phased with sunset, marking more or less the end of negative values (transitioning from negative to values around and above zero near the upper dashed line) and enhanced activity during summer sunrise (lower dashed line). The semi-diurnal y_{12} shows similarities to x_{24}: it is phased with sunrise (transition from negative to positive values near the lower dashed line) and increased positive values during summer months during sunset (upper dashed line). Some connection between sunrise and activity in y_8 and y_6 can be identified, but their amplitudes are consistently smaller, as discussed before.

I would like to draw the attention to the colour-scales of the two figures. For the Y component in figure 5.4 it ranges from -30 to 30 nT, whereby the one of the X component in figure 5.3 ranges from -15 to 15 nT. Thus, the filter outputs contributing to the X component are in general twice as less intense as the ones contributing to the Y component. Overall, $x_{24} > x_{12} > x_8 > x_6$ and $y_{24} \geq y_{12} > y_8 > y_6$ can be deduced as a rule of thumb.

As already stated, comparisons to $F10.7$ (depicted in top panels) show that the general trend of amplitudes for each filter response is aligned with the solar cycle phases. However, the general trend can be disturbed from one day to the other by magnetospheric processes enhancing the level of magnetic activity, especially during the maximum of the solar cycle. Looking closely, the effects of the Halloween storms in the end of 2003 are in fact identifiable (among others). This observation also holds for the combination of all (sub-)diurnal filters x_D and y_D presented in the lowest panels of Figure 5.3 and 5.4 which I will review now.

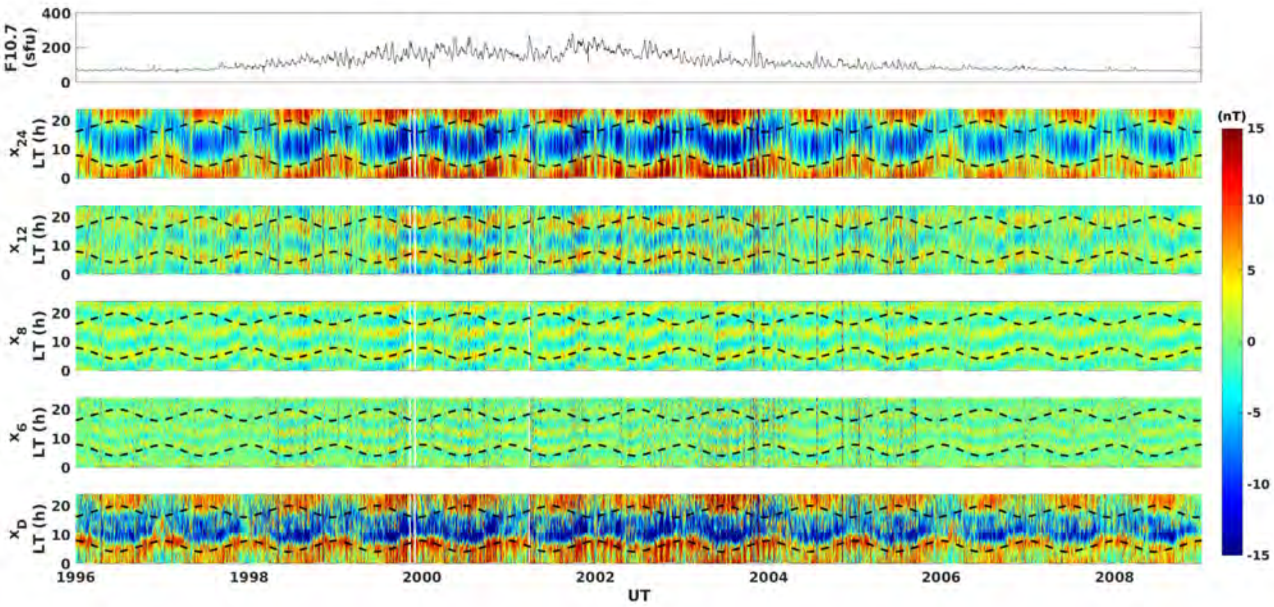

Figure 5.3: Filter responses for SC23 (1998 to 2008) as function of solar local time (LT) for the X component at CLF. From top to bottom: the $F10.7$ daily values in sfu; x_{24}; x_{12}; x_8; x_6 and x_D in nT. Dashed black lines indicate local time for sunrise (morning hours) and sunset (evening hours). Periods with unavailable data are not represented and appear as white vertical stripes. Note that the limits of the colour-scale range from $-15\,\mathrm{nT}$ to $15\,\mathrm{nT}$.

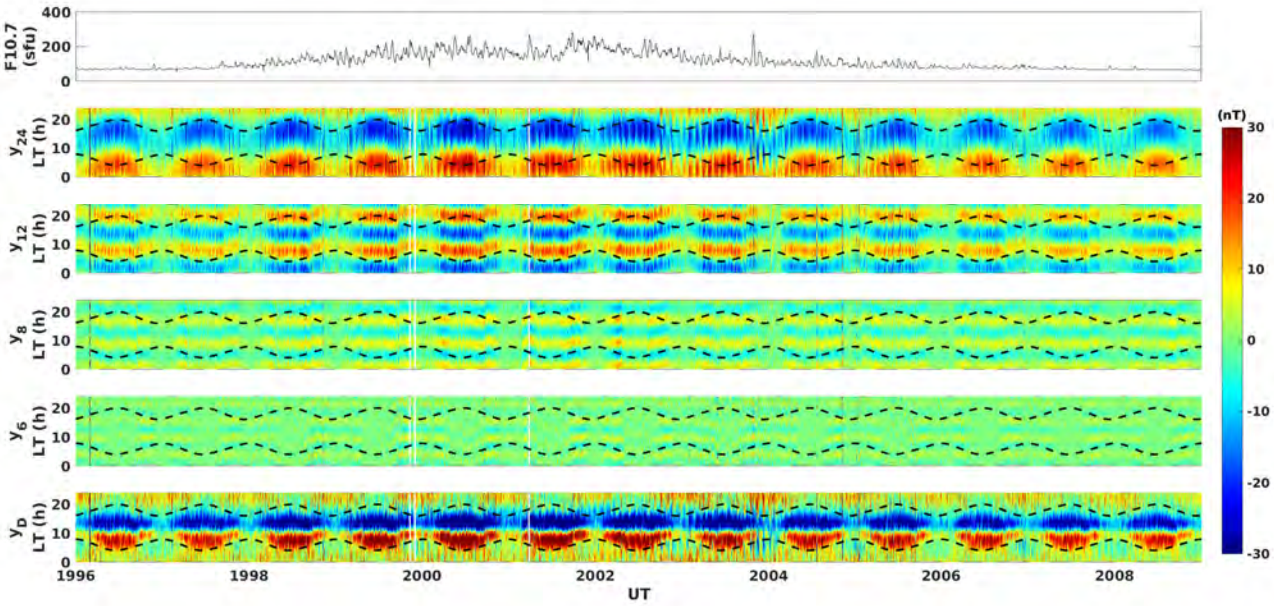

Figure 5.4: Analogue to Figure 5.3 for the Y component at CLF. From top to bottom: the $F10.7$ daily values in sfu; y_{24}; y_{12}; y_8; y_6 and y_D in nT. Note that the limits of the colour-scale range from $-30\,\mathrm{nT}$ to $30\,\mathrm{nT}$.

Similar to the individual filter outputs, y_D is twice as intense as x_D. For both, the recurring patterns remain clear and highlight solar cycle and seasonal variations with enhanced activity during solar maximum (around 2002) and summer months.

x_D has a seasonal-dependent minimum around local noon which is surrounded by two positive crests of activity around dawn and dusk (at least during summer). y_D has a maximum followed by a minimum, with the zero-crossing centred around local noon, which shows no clear dependency on season. The activity increase is well phased with sunrise (lower dashed line) for both combined signals, while the activity decrease is more complex to associate with sunset (upper dashed line). The combined signal x_D still displays night-side activity especially during solar maximum, but also in summer nights during solar minimum. A clear reduction of the activity is observed in the night time for y_D where it almost reaches zero, implying that all filter outputs added together cancel out, showing that only the combination of the individual filters is physically meaningful. Therefore, we will investigate further on x_D and y_D in the following.

To get an understanding of the dominant seasonal and local time variations of the combined diurnal signal, we will use the method of superposed epoch analysis (SEA). It is used to extract overarching characteristics within datasets and was first used by Chree (1913) to investigate the relationship between sunspot occurrence and geomagnetic field variations. First, individual events or periods are defined, aligned via a commonly defined reference point and averaging gives information about general trends and patterns. We generate one SEA per magnetic observatory and per component, x_D and y_D, in dependence of solar local time and day of year (season) for magnetically quiet periods. Data on magnetically very quiet CK48-days between 1991 and 2019, which total 3040 days, are used to generate SEA, see chapter 3.1.1.6. Be reminded that the season can be described by the solar longitude $L \in (0°, 360°)$ which is derived from the position of Earth around the Sun, whereby $L = 0°$ defines spring equinox in the NH. The data is arranged into bins of $\Delta L = 10°$ (vertical axis) and $\Delta LT = 10\,\mathrm{min}$ (horizontal axis). The value per bin is derived as the average of all values that belong to the specific bin.

Here, I present four representative observatories at low and mid-latitudes, where the signatures of equatorial and auroral electrojets are minimized. Additional to the criteria from chapter 4.1, the stations are selected according to their location with respect to the to-be-expected solar quiet current cells in both hemispheres. The SEA of further stations with corresponding detailed discussions may be found in Haberle et al. (2022) and additional stations are presented in appendix E.1.

Figure 5.5 presents the resulting SEA for two European observatories: CLF and San Fernando (SFS), and two Australian observatories: Alice Springs (ASP) and Canberra (CNB). Note that they are located in latitude from North to South in this order. The black lines indicate the mean local sunrise (morning hours) and sunset (evening hours) at an altitude of 110 km between 1991 and 2019. The upper left panels show the SEA for CLF. The combined filter output y_D describes a maximum during morning and a minimum during afternoon hours, almost vanishing during night times throughout the year. The increase in activity during morning hours strictly follows local sunrise, appearing earlier during summer than during winter, while the activity decreases rather constantly in the afternoon around 15h LT, except during winter solstice. In addition to the prolonged activity, the signal intensity is stronger during summer (in NH $L = 90°$) than during winter (in NH $L = 270°$). One of the most striking features is the relatively constant zero-crossing of the activity around noon for y_D. The pattern of x_D is less clear. As noted in the global patterns before, the dawn crest of activity is well phased with sunrise and

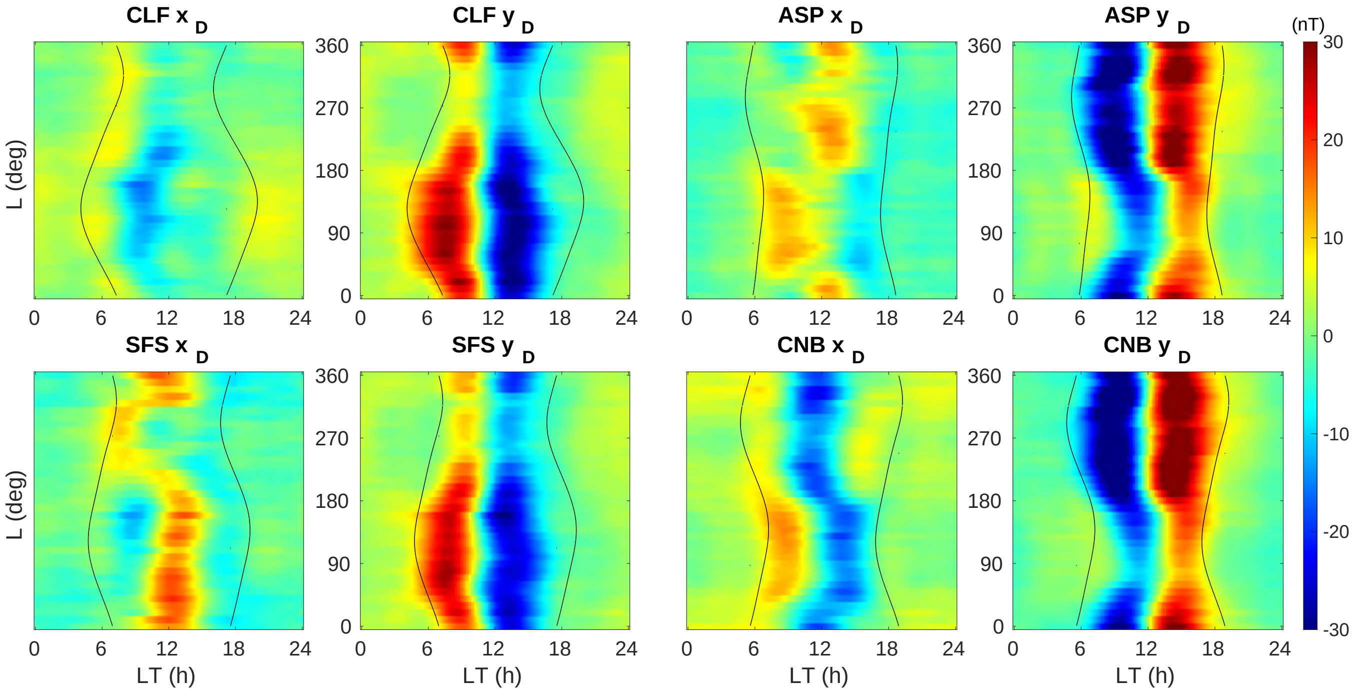

Figure 5.5: Super-posed epoch analysis of the combined (sub-)diurnal filter responses x_D and y_D, depending on local time and season for two European observatories (CLF, SFS) and two Australian observatories (ASP, CNB), during magnetically quiet days. Black lines indicate local sunrise (morning hours) and sunset (evening hours). Note that the colour-scale is the same for all panels.

is present throughout the solar longitude, while the minimum and the dusk crest that extends into the pre-midnight hours, are mainly observed during summer and autumn.

The magnetic observatory San Fernando (SFS) is located South of CLF at 36.7°N, 5.9°W (second row). Its y_D shows a remarkably similar pattern as CLF, being well phased with sunrise and to a lesser extent with sunset. The main difference to CLF lies within its x_D which describes a maximum around local noon from spring to autumn. Around autumn equinox ($L = 180°$), the maximum abruptly shifts to morning hours and returns to noon hours shortly after winter solstice ($L = 270°$). On the other hand, no clear activity is observed during night, at dawn, or at dusk and only a rather limited minimum is observed after dawn during summer.

The solar longitude describes the season reversely in each hemisphere, e.g. summer in SH is at $L = 270°$ and winter at $L = 90°$. ASP is located in the SH at -23.76°S and 133.88°E nd its SEA is presented in the top right panels of Figure 5.5. The combined signal y_D describes a minimum in the morning hours and a maximum during afternoon hours, as opposed to NH stations, with stronger amplitudes during summer. As for NH observatories, y_D is well phased with sunrise and additionally with sunset. The only exception is during winter at sunrise, when a local and fainter maximum can be observed. The combined signal x_D is not as clearly phased with sunrise. During spring ($L = 180°$) and autumn equinox ($L = 0°$), x_D shows a maximum around noon. Similar to SFS in the NH, the maximum shifts to morning hours shortly after autumn equinox and returns to noon hours at spring equinox.

CNB is situated south of ASP at -35.32°S and 149.36°E and analogously shows a remarkably similar behaviour in y_D. x_D has a minimum during day-light hours that shifts to later LT between autumn and spring equinox. During local winter, x_D shows also a local maximum in the morning hours. The analysis presented in Figure 5.5 is in good agreement with the magnetic footprints one expects from the solar quiet current cells flowing at an altitude of about 110 km above the magnetic observatories, i.e. the increase of activity at sunrise, the inversion of the x_D variations for locally close observatories (e.g. CLF vs SFS, ASP vs CNB) and the inversion of the y_D variations between observatories located in different hemispheres (e.g. CLF vs CNB). This implies that the combined filter output from the 24h, 12h, 8h and 6h filters are the major contributors to the Sq currents. While the overall day-side patterns of x_D and y_D are clearly related to the Sq currents, some further, but minor contributions can be attributed to other sources. These are discussed in Haberle et al. (2022).

5.2.2 Reproducing the Quiet Variations from Diurnal and Semi-Diurnal Filters

The previous results confirm that the (sub-)diurnal filters capture the signal of the Sq current well which is one of the sources that we would like to be included in our baseline. We also saw that there are strong dependencies of each individual filter response on solar cycle, season and local time. We now pose the question whether it is possible to model and anticipate the quiet variations with the help of the observed dependencies and the individual filter responses.

As briefly mentioned and further discussed later (see chapter 5.3), storm signatures are present in all filter responses and thus in the filter baseline, albeit these should not be included. Additionally to an enhanced understanding of the quiet variations, reconstructions will be useful during storm-time, as considered in later chapters (see chapter 6).

Before we start modelling, let us take into account two more considerations. The 24h and 12h components, together with the 8h and 6h component are the major frequency contributors to the solar quiet currents. The 8h and 6h component, however, account for about half of that of the 24h and 12h component (see e.g. Campbell (2003)). This is in agreement with our findings from the first part of 5.2.1 and figures 5.3, 5.4, where we deduced that the main amplitude contributions are within diurnal and semi-diurnal filter responses. Furthermore, a model can only be valid for one component of one observatory. In the scope of this work, we will present and discuss the results for the magnetic observatory Chambon-la-Forêt, as discussed in 4.1.

As such, we restrict the following modelling efforts to diurnal and semi-diurnal filter responses, i.e. x_{24}, x_{12} and y_{24}, y_{12} and the resulting superposition

$$x_{24+12} = x_{24} + x_{12} \tag{5.3}$$

$$y_{24+12} = y_{24} + y_{12} \tag{5.4}$$

from measurements at CLF. It will become evident that this choice does not impact the primary conclusion drawn from this subchapter. By convention, I will introduce the general filter response z that covers both components and filter responses, and mark respective models with this letter.

5.2.2.1 Seasonal and Local Time Dependencies during Quiet Periods

The SEA presented in figure 5.5 gives a statistical view on the quiet variations. Hence, our first approach to reproduce the quiet variations will be based on a similar SEA of the diurnal and semi-diurnal filter responses. The resulting model will depend upon local time LT and season L. Accordingly, we conduct the superposed epoch analysis (SEA) on the sum of the two frequency contributions per observatory and per magnetic component, i.e. $x_{24}+x_{12}$ and $y_{24}+y_{12}$, during CK-days between 1991 and 2019 in the same manner as in 5.2.1. The first row of figure 5.6 presents the SEA results for the magnetic observatory CLF. The black lines indicate the mean sunrise (morning hours) and sunset (evening hours) times between 1991 and 2019. There is a clear trend in activity with sunrise and sunset. The $y_{24}+y_{12}$ component describes a maximum in the morning hours and a minimum in the afternoon hours, almost vanishing during night times throughout the year. The signal is stronger during summer (in NH $L=90°$) than during winter (in NH $L=270°$). The $x_{24}+x_{12}$ component is not as clearly phased with sunrise/sunset and describes a minimum around local noon. These observations are in agreement with the general Sq footprints in 5.2.1 and support the choice of constraining the modelling to diurnal and semi-diurnal responses.

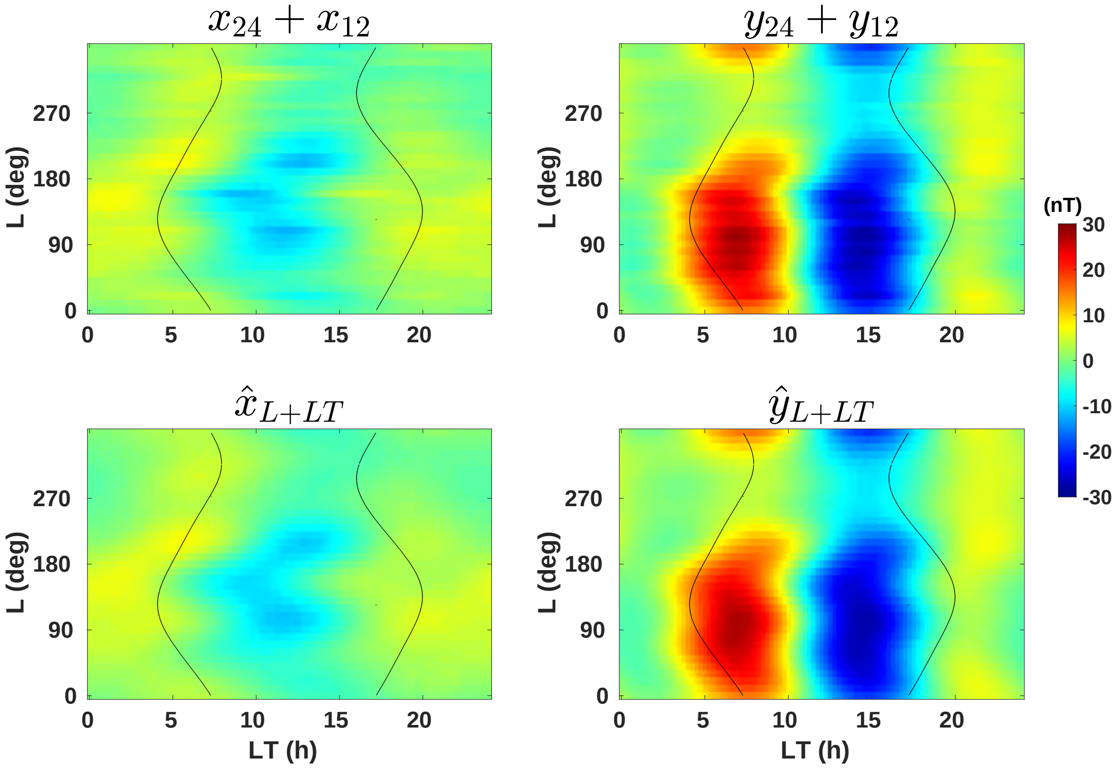

Figure 5.6: SEA of diurnal and semi-diurnal components for magnetically quiet days between 1991-2019 at the magnetic observatory CLF in the upper two panels. The lower panels show the results of the analytical model from equation (5.5). Sunrise and sunset local times are indicated as black lines.

We use these SEA results to derive a qualitative description of the variations within the diurnal and semi-diurnal contributions in dependence of the season and local time. The statistical trend evidently exhibits a sinusoidal relationship in both dimensions, i.e. local time and solar longitude. Thus, a two dimensional harmonics model may be used per component:

$$\hat{z}_{L+LT} = \left(\sum_{i=0}^{k} \alpha_i \cos(iL) + \beta_i \sin(iL)\right) \left(\sum_{j=0}^{k} \gamma_j \cos(jLT) + \delta_j \sin(jLT)\right) \tag{5.5}$$

where L is the solar longitude, LT is the local time, k is the order of the harmonics with coefficients α_i, β_i, γ_j and δ_j for $i, j = 0, 1..k$. The coefficients are determined by fitting this model with order $k = 4$ to retrieve $\hat{x}_{L+LT}$ and $\hat{y}_{L+LT}$. The values of the coefficients can be found in appendix C.1. There was no significant difference found between fitting each frequency response separately and adding them, or directly fitting the sum of the two frequency responses. The SEA generated models $\hat{x}_{L+LT}$ and $\hat{y}_{L+LT}$ at CLF are illustrated in the lower panels of figure 5.6 and clearly replicate the statistical features of the original filter responses. This implies that the season and local time dependencies are sufficient to explain the overarching variation of the 24h and 12h signal.

5.2.2.2 Solar Cycle and Seasonal Dependencies

The model in equation (5.5) is derived from statistical binning, whereby a bin does not hold information on the solar cycle phase, i.e. $F10.7$. As quiet days tend to occur more frequently during solar minima and therefore during lower values of $F10.7$ (compare figure 2.4 with figure 3.1) this model is biased towards lower solar cycle phases and may lead to underestimation of amplitudes during years with higher solar activity.

To avoid this bias, let us seek a description of the variations in dependence of $F10.7$. Remember that the filter responses are periodic functions in nature and thus can be described by an amplitude and phase, whereby the phase is determined by the period P of each filter. However, it is not excluded that phase shifts occur which themselves may depend upon solar activity and season. Indeed, phase shifts are clearly observable in figures 5.3 and 5.4 that depend upon season, e.g. the minima of x_{24} occur earlier in summer than during winter and the minima of y_{24} later in summer than in winter. Therefore, it makes sense to look for a description of the amplitude and phase in dependence of L and $F10.7$, such that a filter response z may be described by

$$z = \hat{A}_z(L, F10.7) \cos\left(\phi_z + \hat{\phi}_z(L, F10.7)\right) , \tag{5.6}$$

whereby $\hat{A}_z$ denotes the dependent amplitude, ϕ_z the filter's phase and $\hat{\phi}_z$ the dependent phase shift. Note that the information on local time LT is already coded into the phase using this description.

As before, I use a harmonic model for L, but here with order $k = 2$, for both, amplitude and phase. Additionally, I add a linear dependency on $F10.7$ to account for its influence. The linear relationship with solar activity, which also varies with season, is in agreement with Shinbori, Koyama, Nosé, Hori, and Otsuka (2017) and may also be inferred from figure 5.15 which will be discussed later. To avoid extreme solar forcing events, we will restrict the data-set to CK48-days only, as has been done before. The mathematical description for the model is as follows. First, the filter response is separated in its cosine c and sine s components. These are then used to define the amplitude $a = \sqrt{c^2 + s^2}$ and the phase $p = \arctan(s, d)$, which are illustrated in figure 5.9 in blue for CK-days and in grey for non-CK-days. The full model describes as

$$\widehat{A}_{zp}(L, F10.7) = a_z(L) + b_z(L)F10.7 \tag{5.7}$$

$$\widehat{\phi}_{zp}(L, F10.7) = c_z(L) + d_z(L)F10.7 \tag{5.8}$$

$$\widehat{z}_{p,L+F10.7} = \widehat{A_z} \cos\left(\phi_z - \widehat{\phi_z}\right) \tag{5.9}$$

where $\widehat{A}$ and $\widehat{\phi}$ are the modeled amplitude and phase, a, b, c, d are the harmonic models depending on L which write as

$$a(L) = \sum_{i=0}^{2} \alpha_i \cos(iL) + \beta_i \sin(iL)\,, \tag{5.10}$$

and analogously for $b(L)$, $c(L)$, $d(L)$ for which the corresponding coefficients α_i and β_i are given in appendix C.2.

In practice, the amplitude and phase are separated into intervals of 10° solar longitude L. Each interval I_{Li} is then linearly fitted according to solar activity $F10.7$, i.e. $h_{Li} = g_i + f_i \times F10.7$, for $i = 1, .., 36$. Figure 5.7 illustrates this process for the amplitude of x_{24}. All of the 36 intervals I_{Li} are plotted, each being a scatter plot of $F10.7$ and the amplitude. The linear fit per interval is indicated in red. We observe that the linear fit differs for each I_{Li}. First of all, the majority of the $F10.7$ values is concentrated towards lower values, beneath 100 to 120. This means that the slope f_i of the fit is based on fewer values. In fact, at several intervals the slope is close to zero (e.g. intervals from $L: 60$ to $L: 100$). Other intervals show rather steep slopes like $L: 330 - 340$. In general, we can deduce, that the linearity relationship signifies rather a trend here. Eventually, this leads to 36 times 2 coefficients (one for the offset and one for the slope) for each, the amplitude and phase.

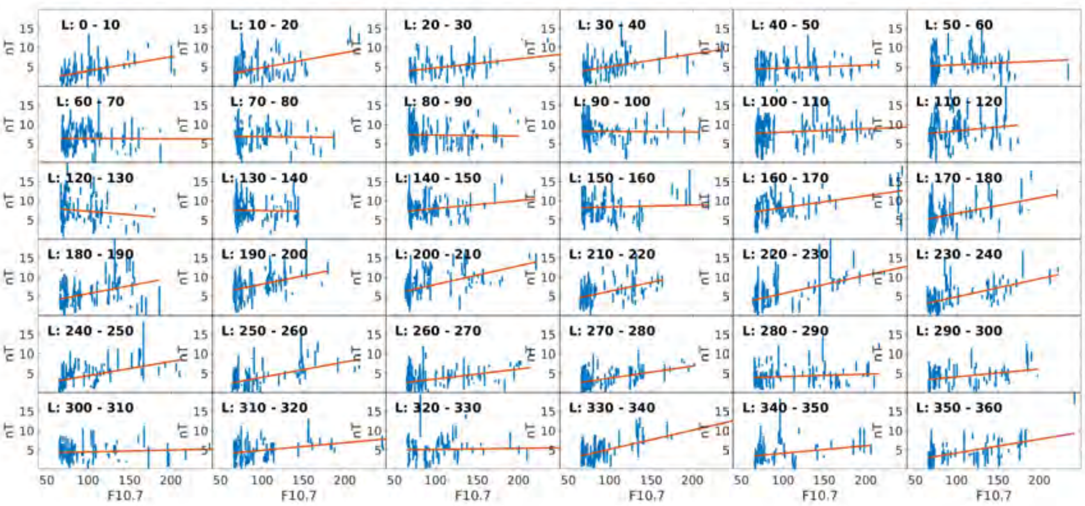

Figure 5.7: Fitting the amplitude of x_{24} in linear dependence to solar activity F10.7 for quiet days in intervals of 10° solar longitude L.

These sets of coefficients are then used to for the harmonic models $a(L)$, $b(L)$, $c(L)$, $d(L)$. The coefficients g_i and f_i correspond to the blue dots, and the red line is the fitted harmonic model in figure 5.8. According to (5.7) and (5.8), b and d are the coefficients that express the dependence on $F10.7$. Comparing the values for b and d with a and c, we see that there are two magnitudes of difference for the amplitudes and three for the phase. This implies, that in the model the dependence on solar activity is rather small and becomes only important for very high values of $F10.7$.

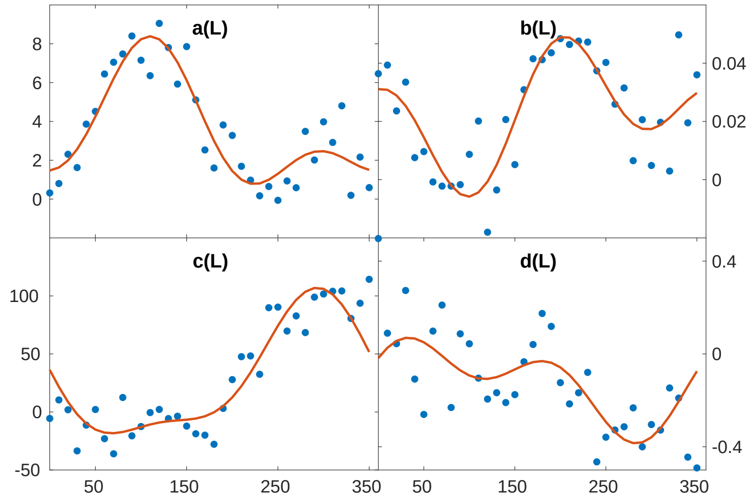

Figure 5.8: Fitting the amplitude and phase coefficients derived from figure 5.7 with the harmonic model of equation (5.10) with order k=2.

In figure 5.9 the resulting models for $\widehat{A_{24}}$ from (5.7) and $\widehat{\phi}_{24}$ from (5.8) (in yellow) for the amplitude and phase (in blue for CK-days and grey otherwise) of x_{24} are presented. The resulting coefficients α_i and β_i for each a, b, c and d are given in appendix C.2.

For $\widehat{A}_{24}$ in the upper panel, we see that the general, seasonal and solar cycle trend of the amplitude is followed. Clear spikes are visible which correspond to elevated $F10.7$ values. For example, the spike due to the Halloween storm is clearly visible. It is also clear from this plot, that the amplitudes are in general quite underestimated and small scale structures are not really resolved.

For $\widehat{\Phi_{24}}$, we can draw similar conclusions as it follows the general, seasonal trend well. Unsurprisingly, variations in $F10.7$ are not as pronounced as for $\widehat{A}_{24}$. Also here, small scale structures are not really resolved.

Overall, the general trend of the amplitude and phase is contained within the models but they struggle when it comes to resolving more granular day-by-day features. The full model for the diurnal and semi-diurnal components added together derives as

$$\hat{x}_{L+F10.7} = \hat{x}_{24,L+F10.7} + \hat{x}_{12,L+F10.7} \tag{5.11}$$

$$\hat{y}_{L+F10.7} = \hat{y}_{24,L+F10.7} + \hat{y}_{12,L+F10.7} \tag{5.12}$$

Further details of these are discussed in chapter 5.2.2.5.

5.2.2.3 Forward Propagation of Filter Responses

The previous two models are derived by attempting to fit the data on the entire available period from 1991 to 2019. Even though both capture general trends, they struggle to resolve day by day features. For this third model, I will follow a different strategy.

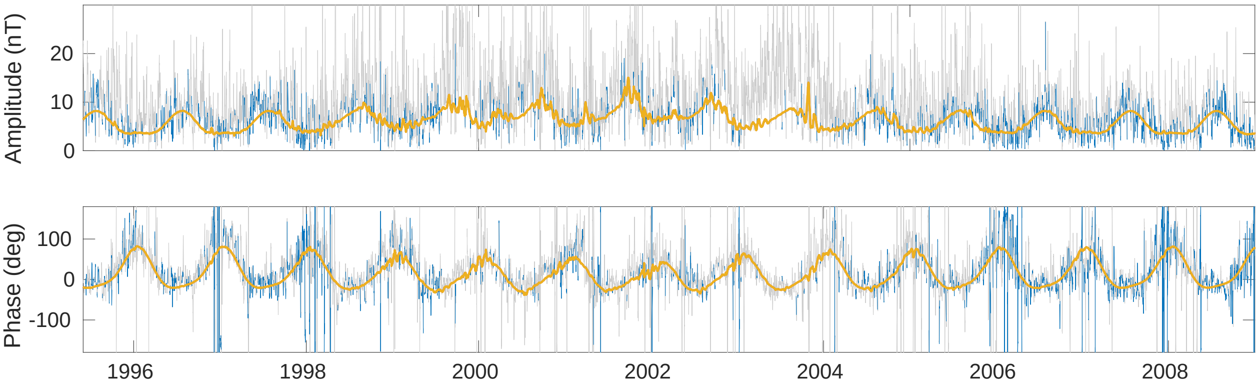

Figure 5.9: Amplitude and phase for x_{24} at CLF with its corresponding model results (in yellow) for $\widehat{A}$ and $\widehat{\phi}$. Note that the data in blue is the amplitude and phase of x_{24} during CK48 days. Non-CK days are indicated in grey.

In order to anticipate the signal of the filter responses, I assume that they do not change significantly from one day to another, at least not during quiet days. With this assumption, the signal can be forward propagated, which means that the signal is time-shifted from the past to represent the signal in the future. The used time-shift δt hereby depends upon the period P of the filter. For the diurnal filter this would be 24 hours, i.e. the signal is time-shifted into the future for 24 hours. Analogously, the semi-diurnal filter reconstruction is time-shifted 12 hours into the future. In terms of implementation this is achieved by a simple data shift of the corresponding δt. We end up with two reconstructions per filter and component:

$$\hat{z}_{24,shift}(t) = z_{24}(t - 24h) \tag{5.13}$$

$$\hat{z}_{12,shift}(t) = z_{12}(t - 12h) \tag{5.14}$$

Their superposition results in the reconstruction with forward propagation

$$\widehat{x}_{shift} = \widehat{x}_{24,shift} + \widehat{x}_{12,shift} \tag{5.15}$$

$$\widehat{y}_{shift} = \widehat{y}_{24,shift} + \widehat{y}_{12,shift} \tag{5.16}$$

Figure 5.10 demonstrates this method on ten consecutive CK days in the beginning of 2010. For the X component (upper panel), we notice discrepancies in the beginning of the period and a rather good agreement towards the end, though the phase is not always well met. On the second half of January 7th, the forward propagation is very accurate. The extrapolation of Y is in good agreement with the actual data and the phase is generally well met. Between the second half of January 2nd and January 5th, the strongest amplitude and phase discrepancies occur, which are smaller compared to the X component. I would like to point out, that the local extrapolation is not exactly equal at t and $t - 24h$, e.g. $\hat{x}(t) \neq x(t - 24h)$. This is due to the fact that its 12h component is taken at $t - 12h$ and not at $t - 24h$. An important implication for this method is that its foreseeing capability is limited to the period of the filter. In practice this means that at time-step t_0 only the following 24h, $t_0 + 24$h, can be modelled for the 24h filter, the following, $t_0 + 12$h, for the 12h filter, and so on.

In general, we can infer that the forward propagation works well to reproduce quiet variations, when there is little to no change from one day to the next.

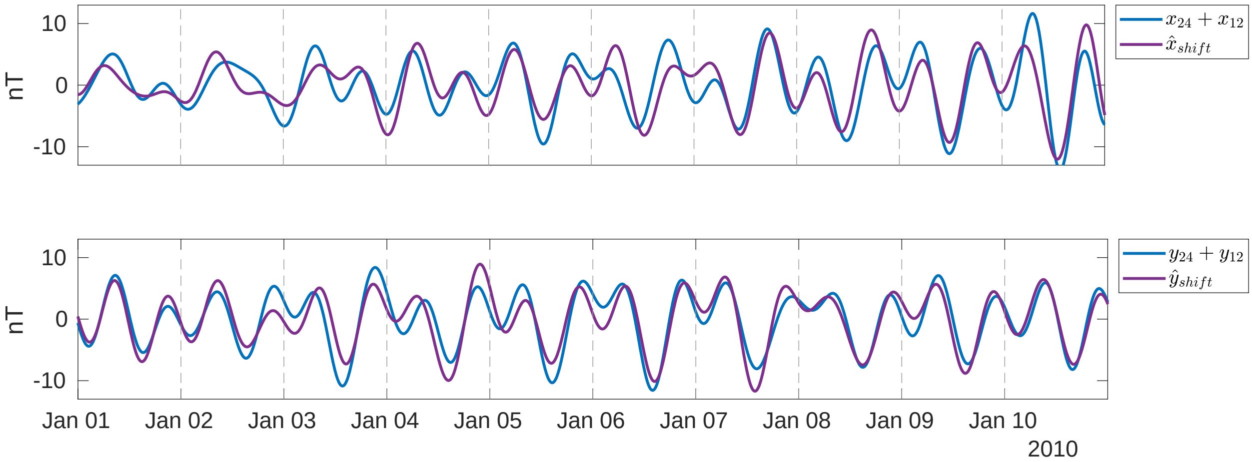

Figure 5.10: Comparison of the local extrapolation for the combination of diurnal and semi-diurnal filter responses for CLF. The extrapolation is in purple and the sum of the filter values is in blue. All days are CK-days. The y-axis is in nanotesla.

5.2.2.4 Further Reconstructions

Both, $L + LT$ and $L + F10.7$ models, reproduce general trends very well but fail to anticipate more granular variations. Further considerations on how to catch these have been conducted. I briefly outline some of these models here. Unfortunately, even though some work a little better than others, all of them fail to catch more granular variations appropriately.

- Moon phase
  If we observe the spectrum of the semi-diurnal filter responses x_{12} and y_{12} closely in figure 4.2, we identify a second peak just to the left of the frequency peak at 12h. In fact, this peak is associated to the moon which induces a signal at a period of 12.4h. As it is so close to the 12h one, it can induce a smooth shift of the phase in the 12h filter responses. To account for it, I added the 12.4h amplitude and phase in (5.6) and fitted it accordingly. For x_{12} the resulting reconstruction performs similar to the SEA fit $\hat{x}_{12,L+LT}$. However, it introduces strong phase-lags for y_{12}, making it unusable.
- Energy deposited into the atmosphere
  Another idea is to base the model upon the energy deposited within the system. The energy can be estimated by the duration of exposure to sunlight times the intensity per day. The solar zenith angle can be used to describe the duration and $F10.7$ the intensity. This quantity is then used to fit the amplitude and phase of each filter response. The resulting reconstructions struggle to reproduce amplitudes and phases, which may imply that the deposited energy alone is not sufficient to explain the observed variations or that the response is not linear.

One reason for these models to not perform well can be related to the used parameters. All parameters are external ones. What I mean by that is that solar cycle phases, solar zenith angles and seasons and moon phases influence the system and the ionosphere from the top. However, the ionosphere is also driven from below, and actually heavily influenced from the underlying neutral atmosphere. Whereby the season L and energy deposited in the system do play a role in heating of the neutral atmosphere, no other parameter describing the complex tide interactions is used in any of these models.

5.2.2.5 Comparison of Reconstructions

With equations (5.5) and (5.9) we have two analytical descriptions of the diurnal and semi-diurnal variations that depend upon season and local time, and season and solar activity, respectively. The third model in (5.13) and (5.14) is based on local properties of the signal. Let us discuss their performances a bit further.

Figure 5.11 shows the three models versus the actual filter responses for solar cycle 23. The models for x_{24+12} are on the left and for y_{24+12} on the right. From top to bottom there is the season and local time model in orange, the season and solar activity model in yellow and finally the forward propagation model in purple.

As the model based on season and local time $\hat{z}_{L+LT}$ in orange is derived from the SEA, it does not change from one year to the next and thus we see the unchanging repeating patterns in both components. It is evident that this model is insensitive to any solar cycle variations and performs worse during stronger solar activity, e.g. around solar maximum in 2002. The superposition of filter responses x_{24+12} shows a high degree of variability. From this it is hard to discern seasonal patterns and it is difficult to relate it to the clear seasonal patterns of its model $\hat{x}_{L+LT}$. What we can agree to is, that during winter, generally, amplitudes are lower than during summer. The superposition of filter responses y_{24+12} shows a clear seasonal pattern that is well matched by its model $\hat{y}_{L+LT}$, apart from the mentioned solar cycle variations.

Looking at the middle panels, the model based on season and solar activity $\hat{z}_{L+F10.7}$ in yellow clearly changes amplitudes with solar cycle phases and shows seasonal patterns for both components. $x_{L+F10.7}$ has an under-laying seasonal pattern that has clear higher amplitudes during summer than winter during low solar cycle phases, e.g. around 1997 and 2007. This seasonal pattern is clearly modulated by stronger and more frequent solar activity during solar maximum, around 2002. $y_{L+F10.7}$ shows the seasonal patterns clearly with according adaption to solar activity.

The forward propagation model $\hat{z}_{shift}$ in purple is almost indistinguishable on this (extended) time-scale as it basically resembles the activity from the previous day and local differences as seen on shorter timescales (like in figure 5.10) are not apparent anymore.

Summarising the greater picture we can say the following. For the model not taking into account the solar activity, it is clear (and not surprising) that tit does not resemble well periods with strong solar activity. Taking into account the solar activity $F10.7$ yields solar cycle trends and thus is better in reproducing general trends. The forward propagation model is following the components indiscriminately on the scale of a solar cycle. Let us compare the models on shorter time-scales to see differences on a more granular level.

Figure 5.12 shows the results for x_{24+12} and y_{24+12} (left and right, respectively) for three CK-days during solar maximum in the upper panels (a) and during solar minimum in the lower panels (b). Each panel has three sub-panels that show the component in blue together with each of the three models in the same color-coding as in figure 5.11. The solar activity for the days in November 2001 was $F10.7 > 200$ and for the days in November 2009 $F10.7 < 80$ (see figure 2.4).

To start the more granular comparison, let us begin by considering x_{24+12} in the left panels. Looking at $\hat{x}_{L+LT}$ in orange, we observe the clear underestimation of the amplitude during maximum in 2001 (a) and intriguingly a slight overestimation thereof

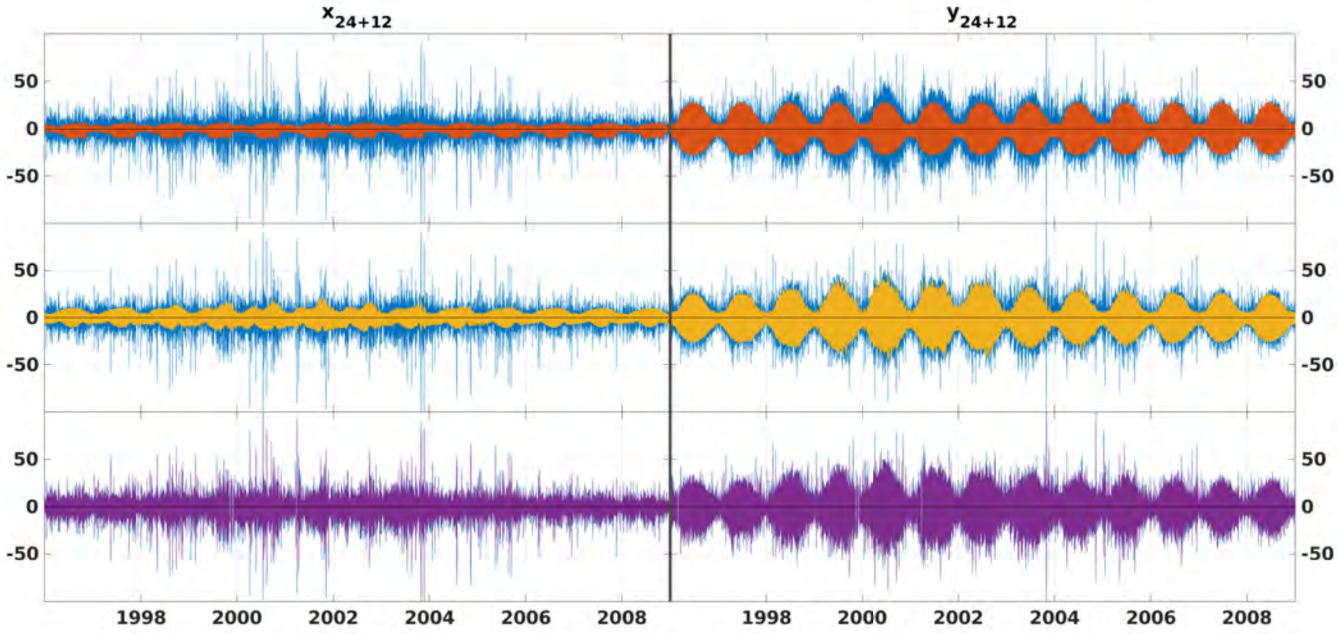

Figure 5.11: Comparison of the models over solar cycle 23 for CLF. The left panels show the X component and the right panels the Y component. From top to bottom the models are $\hat{z}_{L+LT}$ (in orange), $\hat{z}_{L+F10.7}$ (in yellow) and $\hat{z}_{shift}$ (in purple). All vertical axes are in nanotesla.

during 2009 (b). The phase is reasonably well reproduced for both SC phases. $\hat{x}_{L+F10.7}$ in yellow performs very poorly during maximum and minimum. During solar maximum (a), the phase is not very well met, while the amplitude is not resembled at all. During solar minimum (b), the phase of the reconstruction lags behind for a few hours, while the amplitude is slightly overestimated. The poor performance on the phase may be related to the missing of the local time information. The forward propagation model $\hat{x}_{shift}$ is reasonably in phase and amplitudes are fairly well resembled for both solar cycle (SC) phases.

For y_{24+12} in the right panels of (a) and (b), all models are remarkably well in phase and match the amplitudes pretty well, except for $\hat{y}_{L+LT}$ which does not match the solar maximum amplitude.

Utilising the standard deviation σ, we can get a more quantitative assessment of the performance of the models. First, we compute the standard deviation for each superposition of filter responses x_{24+12} and y_{24+12}. Second, we compute the standard deviation for the component minus the model (residuals), e.g. on $z_{24+12} - \hat{z}_{L+LT}$. A standard deviation of zero, $\sigma = 0$ for the residuals would imply that the component is perfectly reconstructed. This means the lower the standard deviation of the residuals the better the signal is reconstructed. Table 5.1 summarises these values for the components and the residuals for all three models. Please note that only data from quiet days is used for the calculation of the standard deviation.

The lowest σ for X is found to be from the forward propagation model which reduces the spread by around a third. This is slightly better than the $L+LT$ model. The $L+F10.7$ model performs very poorly, having almost the same σ as X which can be partially related to the model being out-of-phase. For Y, we see how each of the models performs a little

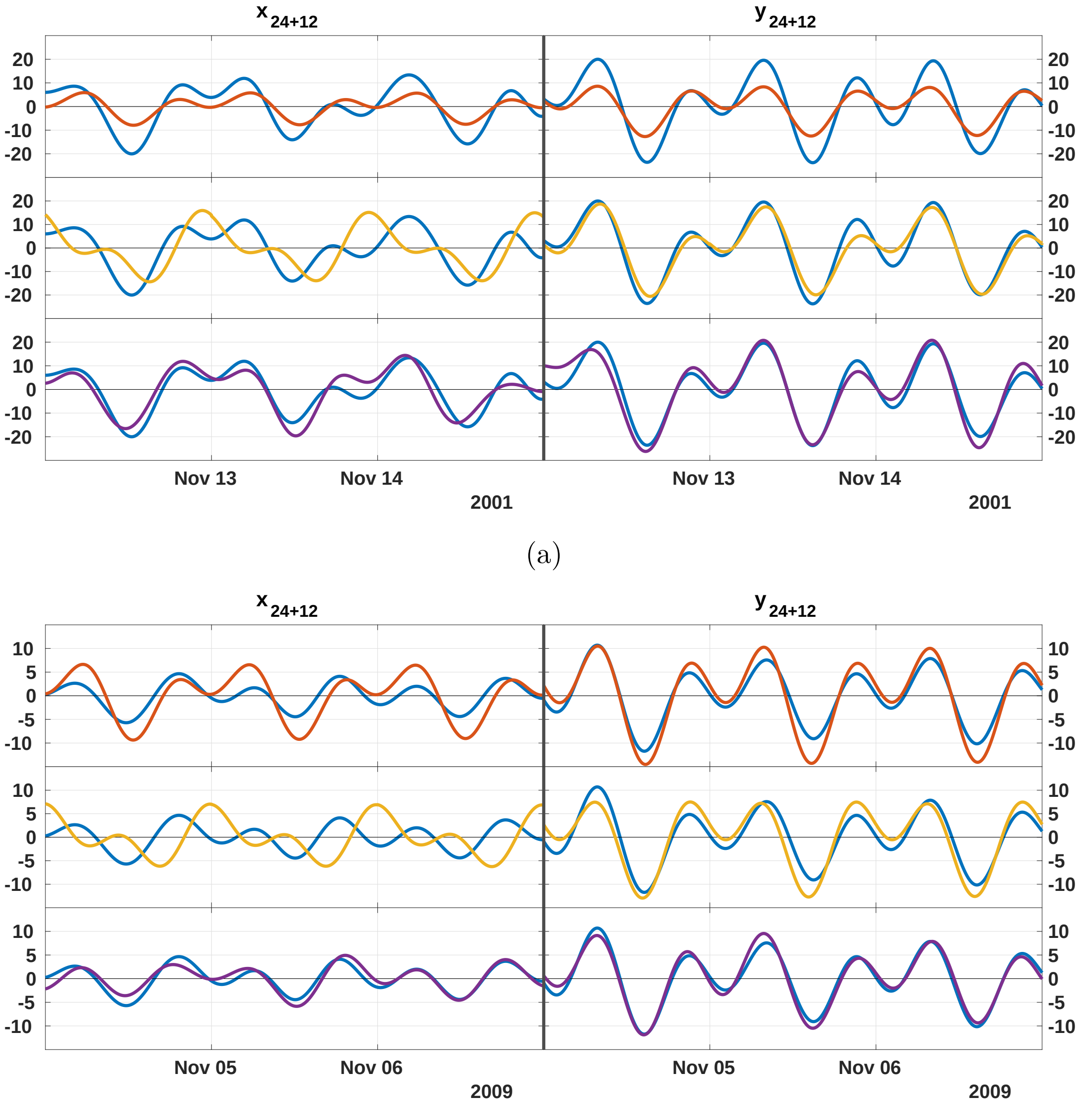

(a)

(b)

Figure 5.12: Demonstration of the three models compared to the actual signal in blue for (a) high and (b) low solar activity at CLF. The left panels show the X component and the right panels the Y component. From top to bottom the models are $\hat{z}_{L+LT}$ (in orange), $\hat{z}_{L+F10.7}$ (in yellow) and $\hat{z}_{shift}$ (in purple). All vertical axes are in nanotesla.

Table 5.1: Standard deviations for the initial filter response x_{24+12}, y_{24+12} and the residuals after removing each of the corresponding models.

	σ		σ
x_{24+12}	5.58 nT	y_{24+12}	12.27 nT
res $\hat{x}_{L+LT}$	3.84 nT	res $\hat{y}_{L+LT}$	3.95 nT
res $\hat{x}_{L+F10.7}$	5.33 nT	res $\hat{y}_{L+F10.7}$	3.74 nT
res $\hat{x}_{shift}$	3.62 nT	res $\hat{y}_{shift}$	3.22 nT

better: the best is also the forward propagation model, followed by the $L + F10.7$ model and then by the $L + LT$ model. The forward propagation model reduces the spread by almost a factor of 4.

In conclusion, we can infer that the $L + LT$ and $L + F10.7$ models may be used to depict general trends in quiet variations. However, the used physical parameters are not sufficient to accurately reproduce day-to-day behaviour, which especially for the X component shows complex patterns. We have found that the best method to overcome this challenge is to use local prior information of the signal with the forward propagation model.

At last, while the y_{24+12} is well matched in general, the volatility and high fluctuations of x_{24+12} pose a serious challenge for the task of physical modelling here. The question remains in which way the presented models may be improved. The $L + LT$ model is derived on statistics which are performed exclusively on quiet days. As mentioned and observed, this implies that it is weighted towards lower $F10.7$, explaining the observed under-performance even during quiet days during solar maximum. The $L + F10.7$ model adapts amplitudes according to solar cycle phase but performs quite poorly especially when it comes to reproducing the phase in x_{24+12}. This may imply that the linearity in equation (5.9) is not sufficient to capture the real, under-lying relationship. Combining the two, for example generating the SEA per solar cycle phase and then adapting it with $F10.7$ can be one path to improve the modelling. Additionally, both models are derived based on the entire considered period from 1991 to 2019. It is well-known, however, that solar cycles can differ significantly from one to another. One possibility to take this into account would be to adapt the model per solar cycle, i.e. derive them only over data belonging to one solar cycle.

The forward propagation model reproduces the observed variations best among the three analysed ones, but still there are considerable differences. This means that the observed discrepancies have a different origin than from the sole dependence of the parameters LT, L or $F10.7$.

5.2.3 Day-to-Day (D2D) Variability

From the results of the previous modeling sub-section, we can infer a pertinent day-to-day (D2D) variability within the (sub-)diurnal filter responses. Further investigations on this variability are the subject in the following. We start with looking at the diurnal and semi-diurnal filter responses individually for CLF as has been done in the previous chapter 5.2.2. As the D2D variability is a characteristic feature of Sq currents (see chapter 2.3.2), we will then investigate the combined diurnal filter responses x_D and y_D (see equations (5.1) and (5.2)) more closely.

5.2.3.1 D2D in the Individual Diurnal and Semi-Diurnal Filters

In order to gain a better understanding of the D2D variability of the individual filters, let us examine their amplitude and phase evolution from one day to another. To do so, I determine local maxima and minima and their corresponding local solar time LT occurrences. The peak-to-peak amplitude is derived as the difference between the value at maximum and the value at the consecutive minimum in nT. The delay is the time in hours that has passed to reach the consecutive minimum from the maximum. Figure 5.13 demonstrates these D2D variables for the diurnal filter response y_{24} during winter 2009. The 14th of December was the only non CK-day during this period. Up until the 28th of December the LT occurrences and delay of the extrema follow a smooth course. After that, both can vary up to 4 hours from one day to another. The amplitude varies from below 5 to up to 15nT throughout the period. This example already demonstrates that there is a distinct day-to-day variability within the diurnal component. Indeed, this holds true for all the other (sub-)diurnal components and in particular for y_{12}, x_{12} and x_{24}. Note that for the semi-diurnal filter responses with period of 12h, there are two maxima and two minima, and thus two amplitudes and two delays per day.

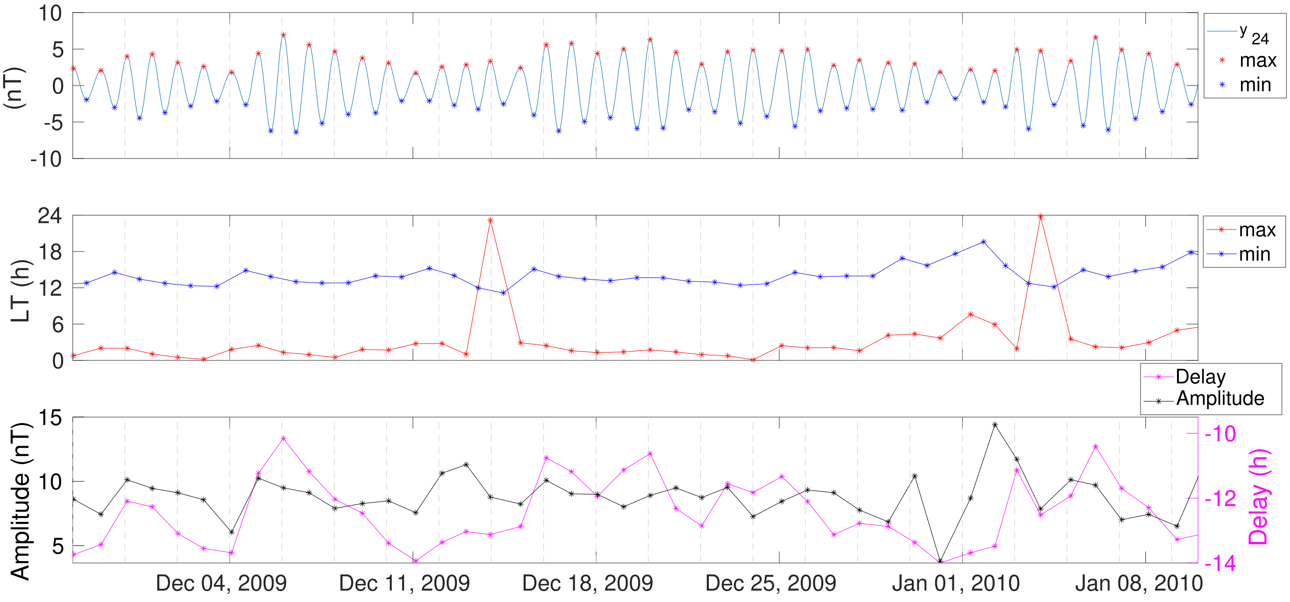

Figure 5.13: Temporal evolution of the diurnal filter response y_{24} during winter 2009-2010 at CLF. Indicated are the extrema with their local time occurrences, as well as the amplitude and delay among them. The dashed vertical lines mark midnight of every second UT day.

From figures 5.3 and 5.4 and the reconstruction of the diurnal and semi-diurnal quiet variations in chapter 5.2.2, we already deduced and confirmed a general seasonal and solar cycle dependency. Let us investigate the extend of these dependencies on the D2D variables.

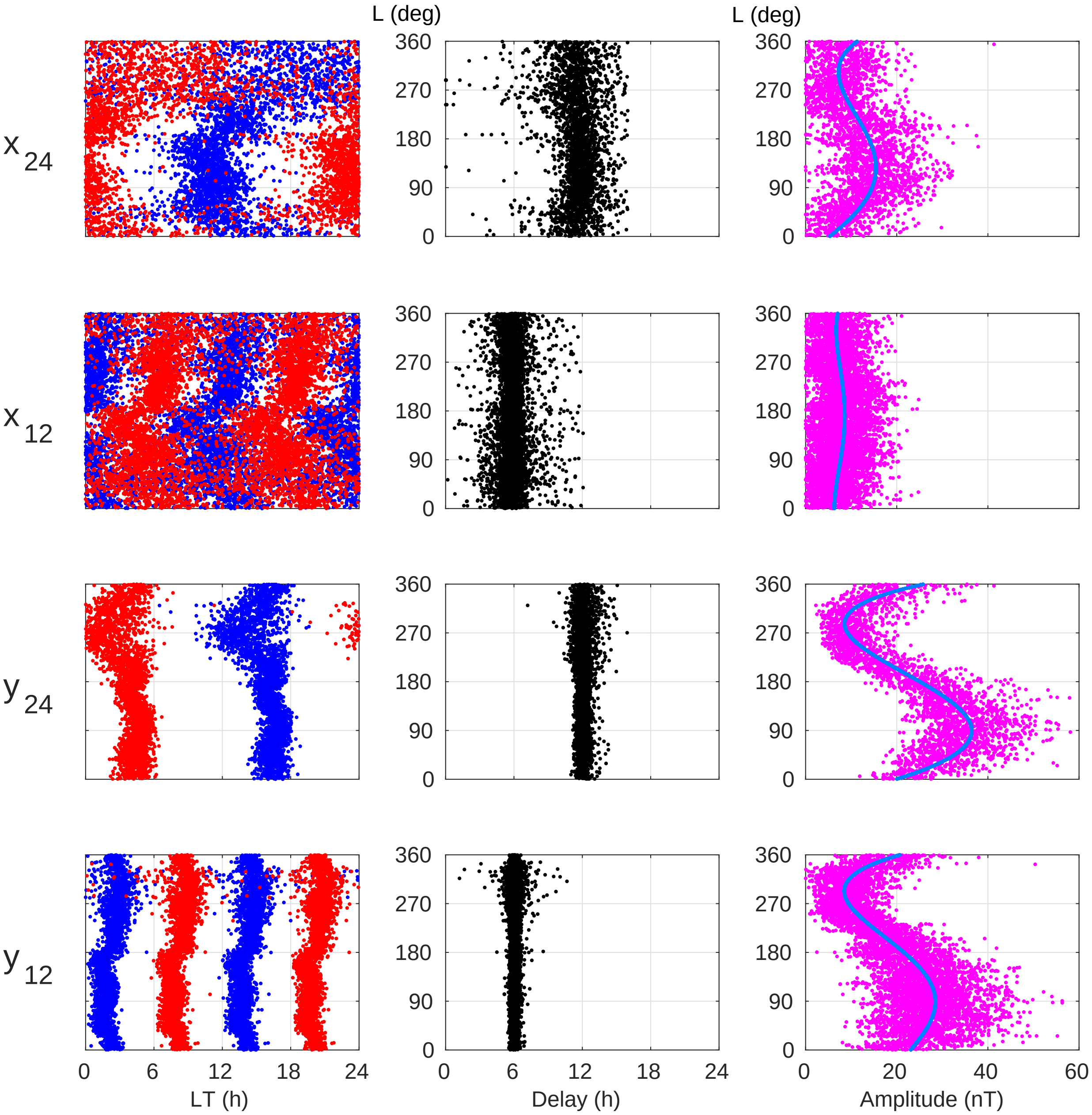

Figure 5.14: Local Time Occurrence (maxima in blue and minima in red), Delay (in black) and Amplitude (in magenta) of the diurnal and semi-diurnal filter responses in dependence of L for CLF. A polynomial fit to describe the amplitude variations in season is indicated in bright blue. Each vertical axis shows the solar longitude L in degree.

Figure 5.14 illustrates the D2D variables for the diurnal x_{24}, y_{24} and semi-diurnal x_{12}, y_{12} filter responses in dependence of season L during CK48 days between 1991 to 2019 (total of 3040 days). The left panels shows the local time occurrences, maxima in red and minima in blue. It is possible to identify the general trend in the LT occurrences of the extrema of x_{24} and x_{12} (earlier in summer than in winter), even though there is a significant scatter. For y_{24} the extrema occur earlier in winter than in summer, while it is vice-versa for y_{12} where extrema rather occur earlier in summer than in winter. For both scattering is almost non-existent during summer and increases slightly during winter. The delay is shown in the middle panels. As for the occurrences, the delays for the X filters have a higher dispersion than the ones of the Y filters. The LT occurrences and the delay are closely related to the phase of the filter responses. The strong dispersion in X implies that the signal is prone to changing phase rather rapidly, already during quiet days and seasonal dependencies are rather secondary. The dispersion in Y is rather low and seasonal dependencies are clearer. This can be one explanation to why the models perform worse for the X component than for the Y component.

The right panels show clear trends and dispersion in amplitudes. We can have a quantitative view on the amplitudes by fitting a polynomial p of order 4, which is indicated by the blue line. The coefficients of these fits can be found in appendix C.3. The peak amplitude in summer, the minimum amplitude in winter and the mean amplitude during equinoxes is listed in table 5.2. The seasons are divided into four intervals of each 90° solar longitude, centred at $L = 0°$ for spring, $L = 90°$ for summer, $L = 180°$ for autumn and finally $L = 240°$ for winter. The amplitude of x_{24} is twice as large during summer than during winter. The dispersion varies only slightly and is lowest in winter $\sigma = 4.83$ and highest in autumn $\sigma = 6.09$. For x_{12}, the amplitude or around 8 nT does not vary very much depending on the season, with values slightly smaller during winter and spring 6.6 nT to 6.8 nT than during summer and autumn 8.3 nT to 8.4 nT. The dispersion is constant for all seasons at around 4 nT. While x_{24} has some dependence, the dispersion is quite high and x_{12} is rather unaffected by season. For both Y filter responses, the amplitude has a clear dependency on season with highest amplitudes during summer and significantly lower amplitudes during winter. The dispersion is highest during summer and lowest during winter. The amplitudes of the Y filters show a very strong dependence on L.

Again these insights support our findings that the models for the Y component are more accurate, while the X component shows a higher level of complexity, especially for the phase.

Table 5.2: The mean amplitude and corresponding dispersion of the diurnal and semi-diurnal filter responses in dependence of season for CLF. All values are in nanotesla.

	spring	summer	autumn	winter
x_{24}	8.73 ±5.35	15.42 ±5.85	13.61 ±6.09	7.21±4.83
x_{12}	6.62 ±3.84	8.35 ±3.94	8.43 ±4.32	6.75 ±3.68
y_{24}	22.70 ±6.05	36.44 ±6.62	24.81 ±6.20	8.53 ±4.15
y_{12}	20.01 ±6.33	28.46 ±7.17	21.30 ±5.90	8.46 ±4.01

Analogously to figure 5.14, the dependencies of the day-to-day variables on the solar flux $F10.7$ during magnetically quiet days are shown in figure 5.15. Here, the overall dependencies on $F10.7$ are considerably less prominent, or even non-existent.

Starting with the local time occurrences of the extrema and their corresponding delay, it is very hard to decipher any clear trend. It seems that their spreading during low $F10.7$ is higher than during high $F10.7$. Please be reminded that quiet days are biased towards lower solar cycle phases, occurring more frequently than during higher SC phases, which contributes to the increased number of values around low $F10.7$. This implies that $F10.7$

has very little influence on the day-to-day variability of the phase, which is reflected in the small coefficients b and d in (5.7) and (5.8), see also figure 5.8.

For the amplitude one may surmise a tendency with increasing solar flux for which a very weak linear dependency may be deduced for x_{24}, y_{12} and y_{24}. No dependency of x_{12} on $F10.7$ may be deduced from this figure which is consistent with the model coefficients as they are the smallest for x_{12} dependence on $F10.7$ (see appendix table C.3).

These findings underline the challenges the $L + F10.7$ model encounters to reproduce the signal on a day by day basis. We can conclude that the simple linear dependence on $F10.7$ is not able to describe the relationship.

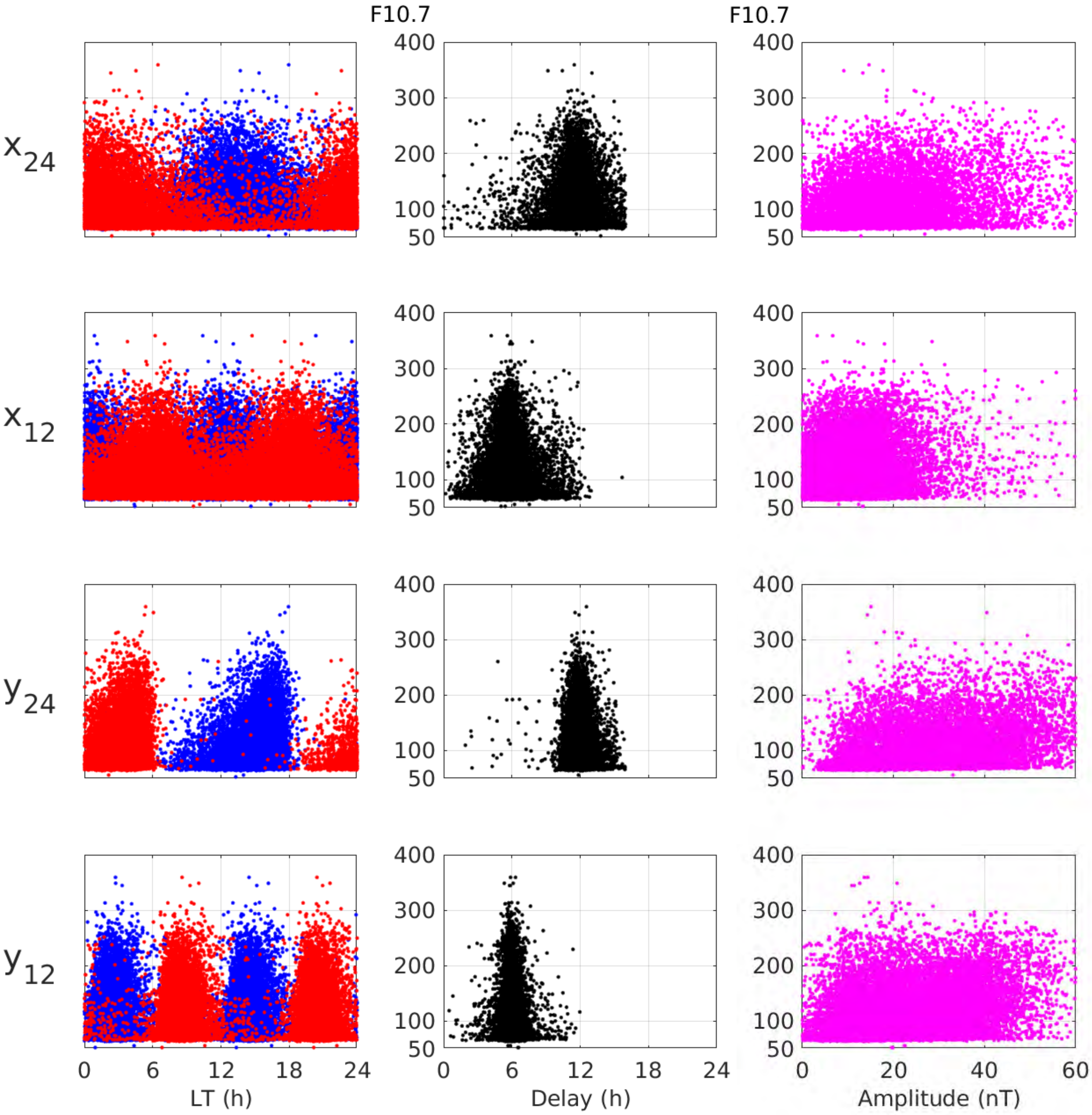

Figure 5.15: Local Time Occurrence (maxima in blue and minima in red), Delay (in black) and Amplitude (in magenta) of the diurnal and semi-diurnal filter responses in dependence of $F10.7$ for CLF. Each horizontal axis shows the solar activity index $F10.7$ in sfu.

5.2.3.2 D2D Variations within the Combined (Sub-)Diurnal Filters

We expect the combined (sub-)diurnal filter responses x_D and y_D to inherit the individual filter responses' D2D variability. Additionally, they hold Sq information as we have seen in chapter 5.2.1 and an inherent day-to-day variability is characteristic for the Sq current systems. This behaviour can be followed on Figure 5.16 where CLF's x_D and y_D are plotted over consecutive CK48 days during summer 2009.

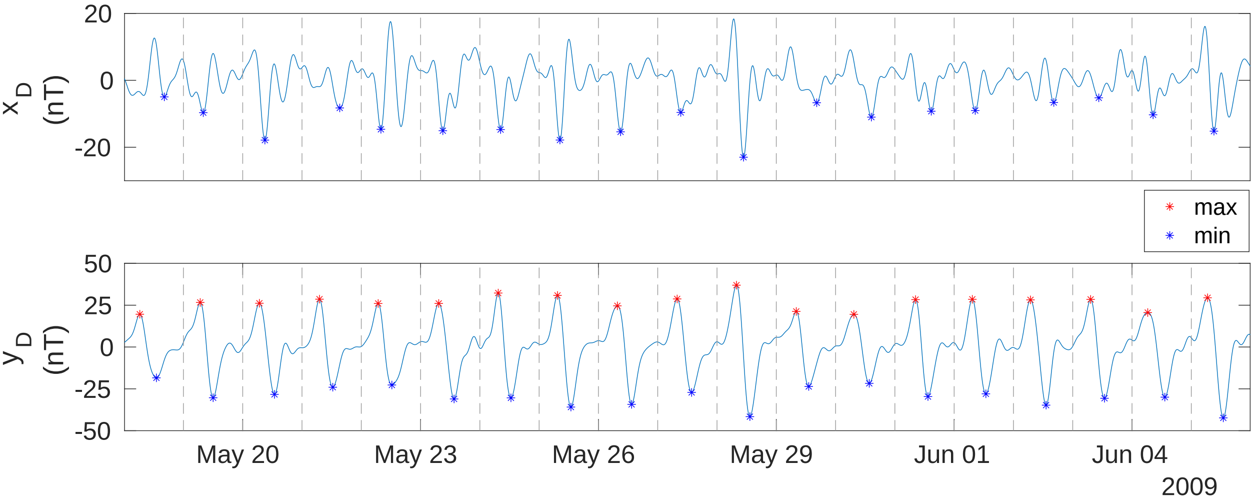

Figure 5.16: Day-to-day variability of x_D and y_D at CLF over a period of consecutive CK-days. The upper panel presents the evolution of x_D with the daily minimum (blue stars) and the lower panel the daily evolution of y_D with daily maximum / minimum marked by red and blue stars.

For x_D, the definition of a maximum and minimum (and successively delay and amplitude) during sunlit hours is not applicable. Its trend generally has only one minimum during the day (see also Figure 5.5). Therefore I investigate the occurrences of the minimum and their associated amplitude in dependence of season L in figure 5.17. We see that the timing of its minimum at CLF shows a distinct shift of approximately 2 hours around equinox (starting around 08h LT between spring and summer, and around 10h LT during autumn and winter). Apart from this general pattern, we see clear dispersion of the occurrences for all seasons. This is another indicator that the phase of x_D, even though having a general trend with season, can vary significantly from one day to the next. The amplitude of the minimum (on the right in pink) has a principal variation with season, on top of a persistent dispersion. As before, we can use a polynomial fit of order 4 to describe its variations quantitatively. The coefficients of the fit are given in appendix C.3. Table 5.3 summarises the mean and dispersion of the amplitude for each season. The summer minimum is around $-16\,\mathrm{nT}$ and the winter maximum is around $-9\,\mathrm{nT}$, indicating that the winter amplitude is about 2/3 times smaller than during summer. The dispersion instead is constantly around $5\,\mathrm{nT}$ for all seasons.

For y_D in figure 5.18, we see a recurrent sinusoidal pattern during sunlit hours for which we can deduce the three D2D variables LT occurrence of maxima, their delay and amplitude as was done for the individual filter responses before. In this example, the amplitude varies significantly on a daily basis between $20\,\mathrm{nT}$ and $80\,\mathrm{nT}$. In the same manner, I compute the D2D variables for y_D at CLF for all quiet days between 1991 and 2019 and present them as scatter-plots against solar longitude in Figure 5.18. It is clear

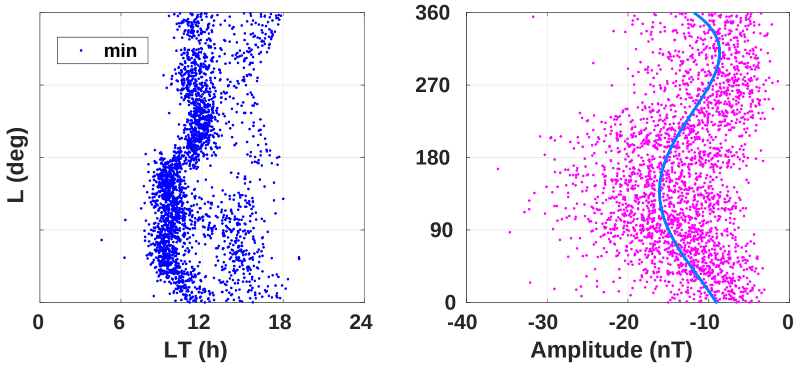

Figure 5.17: Statistics of seasonal and day-to-day variability of x_D at CLF during quiet days between 1991 and 2019. The left panel shows local time occurrence of minima, and the right the amplitude of the minima.

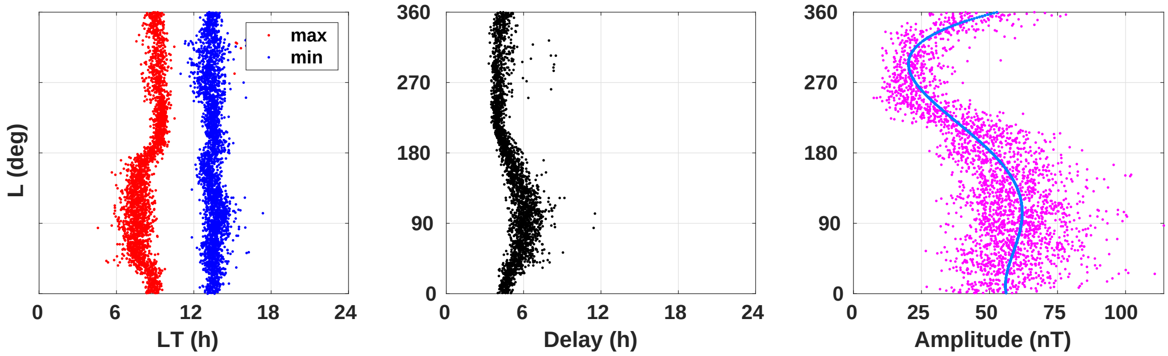

Figure 5.18: Statistics of seasonal and day-to-day variability of y_D at CLF during quiet days between 1991 and 2019. From left to right, the panels show local time occurrence of extrema, delay and amplitude between them. Taken from Haberle et al. (2022).

that the day-to-day variability has a strong seasonal dependency. For the maximum, two regimes can be distinguished: during summer months the maxima occur around 06-09h LT, while they occur later at around 09-10h LT during winter, which is directly related to the LT sunrise shift with season. The transition between these two regimes happens abruptly around $L = 10^\circ$ and $L = 180^\circ$. On the other hand, the timing of the minimum is more constant over time, which, too, is related to the decrease of activity observed constantly around 15h LT in Figure 5.5. The central panel shows that the delay between maximum and consecutive minimum is longer during summer (around 6-7 hours) than during winter (around 5 hours) with more dispersion in summer. This implies that the phase of y_D is rather robust compared to x_D. The right panel shows a clear sinusoidal dependency of the amplitude on the season. As for x_D, table 5.3 gives the numbers of the 4th order polynomial fit for the observed amplitude of y_D. The coefficients are given in appendix C.3. Summer maximum is 62 nT, while the winter minimum is around 20 nT, indicating that the amplitude during summer is about 3 times larger than during winter.

Returning to the day-to-day variability of the signal, it is clear from Figures 5.17 and 5.18 that, for any given L, dispersion is observed in the D2D variables parameters. For y_D this spread is comparable during during solstices than during equinoxes and is almost doubled during summer with respect to winter. For the amplitude, the standard deviation is 12.27 nT for the summer period ($45^\circ < L < 135^\circ$) and 7.72 nT during win-

Table 5.3: Quantification of amplitude mean and spread in dependence of season for CLF. All values are in nanotesla.

	x_D	y_D
spring	-10.45 ± 4.56	48.48 ± 11.94
summer	-16.09 ± 4.98	62.02 ± 12.27
autumn	-14.98 ± 5.43	50.03 ± 11.10
winter	-8.65 ± 4.57	20.23 ± 7.72

ter ($225° < L < 315°$), suggesting that the spread during summer increases by over 60 % compared to winter. For x_D amplitude, the standard deviation, however, is rather constant, with maximum differences of 20 %. Overall, we see a total day-to-day variability in amplitude for y_D of about 20 % to 30 % and for x_D of about 20 %.

The results presented here demonstrate a non-negligible day-to-day variability of the combined filter outputs x_D and y_D which is more pronounced during summer. This phenomenon has been observed in the majority of physical and electro-dynamical parameters of the ionosphere for more than 40 years and is well documented for Sq currents in the literature (see e.g. Schlapp (1968); G. M. Brown and Williams (1969); Greener and Schlapp (1979); Takeda and Araki (1985); Yamazaki and Maute (2017)). Simulations from Yamazaki, Häusler, and Wild (2016) showed that variations within the Sq current can be attributed to 75 % to solar illumination and to 25 % to atmospheric and magnetospheric drivers. Forbes, Palo, and Zhang (2000) found that around 25 % to 30 % of the plasma peak density variations in the 1-2 hours to days range in the F-region can be attributed to meteorological phenomena. The day-to-day variabilities found in our study are in the order of 20 % to 30 % for the amplitude of x_D and y_D, which is consistent with these previous studies. Additionally, the results presented in figures 5.17 and 5.18 reveal two intriguing properties of the day-to-day variability:

- The occurrence in local time of the maxima and minima, as well as the delay among them has a clear dependency on season.
- The spread of the amplitude is clearly dependent on season.

Our analysis minimises magnetospheric influences by taking into account only very quiet magnetic conditions. However, on such quiet days, solar flares may still occur and disturb the signal. To investigate on this, we excluded all quiet days on which X and M class solar flares were recorded during daylight hours and re-ran our analysis. Expectedly, the percentages of day-to-day variability did not change significantly. Flares can have very strong effects on the ionospheric ionization and thus on the associated currents, but their influences are only present for a very limited time (J. Y. Liu, Chiu, & Lin, 1996).

For the individual filter responses, the spread in local time occurrences of extrema and associated delays is clearly narrower during high solar activity than during quieter days while no clear dependence on $F10.7$ was identifiable, as indicated in figure 5.15. This suggests that solar flux variations due to solar cycle phases are not impacting the day-to-day variability appreciably.

These considerations lead us to conclude that the majority of the observed day-to-day variability may be attributed to atmospheric drivers only, which underlying processes become stronger with increasing solar illumination, confirming the neutral atmosphere as a key role.

Gravity waves and tides within the neutral atmosphere are known to exhibit complex interference behaviour that can drastically change from one day to another (Stening, Reztsova, & Minh, 2005; H. L. Liu et al., 2018). For example, the lunar tide induced by the revolution of the moon around Earth has a period of 12.4 hours which is very close to that of the solar semi-diurnal one. The small difference in period may lead to a smooth drift of the contributions of x_D and y_D, leading to amplification or reduction of the global signal over a course of a few days. Attempts to model such a lunar tide effect did not reproduce the variations of amplitude within the combined daily contributions x_D and y_D. This tends to conclude that several sources of tides and waves (like e.g. the well-known 5-days planetary waves (King, Wheeler, & Lane, 2015; Day, Taylor, & Mitchell, 2012) are involved in this phenomenon which remains challenging to model.

5.3 Storm Contributions

Signatures of strong geomagnetic storms are evidently present in all presented figures that illustrate the filter responses over the entire solar cycle. For example contributions of the famous Halloween storms in the end of 2003 are distinctly recognisable within the long-term filter responses $x_{>24}$ and $y_{>24}$ in figures 5.1 and 5.2. For the (sub-)diurnal filter responses and their combination in figures 5.3 and 5.4, the Halloween storms are identifiable as vertical lines of strong values which occur at the same time as the peak in $F10.7$ in late 2003.

Let us emphasize on the storm contributions with the concrete example of the most intense event of SC24: the St. Patrick storm in 2015 (see section 3.1.5). The X and Y components at CLF during the St. Patrick storm together with the filter baseline in red are shown in the first panels of Figure 5.19. From this it is very clear that the filter baseline follows the storm-induced deflection of both components closely. The second panels indicate the long-term filter responses, which clearly extracted the main storm features. Before and after the event, the combined (sub-)diurnal filter responses x_D and y_D (in the third panels from top) follow smooth patterns that are in agreement with the quiet variations we saw in chapter 5.2. This pattern is majorly distorted during the main phase of the storm and still influenced during its recovery phase. In the bottom panels, I depict the residuals, i.e. component minus the full filter baseline. A part of the storm influence is still clearly contained within these but underestimated as some of its effects are already removed by the filter baseline.

5.4 Conclusion for the Filter Baseline

In chapter 4 I introduced the filter baseline which is made up of the responses of five temporal filters. The filters are designed to operate on frequency ranges related to known quiet geomagnetic field sources in mid-latitudes, i.e. one long-term filter for the secular variation and four (sub-)diurnal filters containing the harmonics of 24h for the solar quiet current systems.

In order to determine the sources that effectively contribute to the filter baseline I presented and analysed the filter responses in detail in chapter 5. In section 5.1, and especially 5.2, we concluded that the secular variation is effectively captured within the

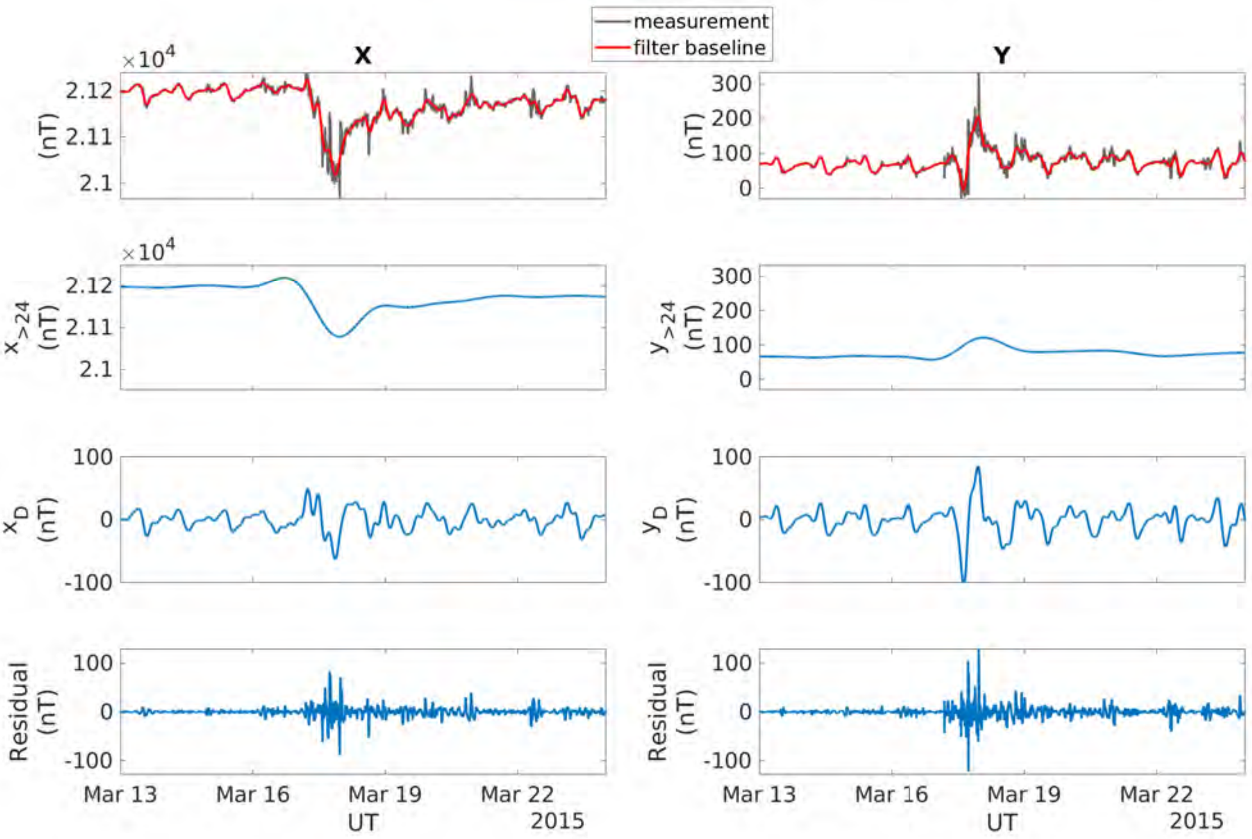

Figure 5.19: Magnetic field measurements and filter responses during the St. Patrick's Storm in 2015 at CLF. The X component is on the left and the Y component on the right. From top to bottom: measurements (black) with overlaid filter baseline (red); long-term filter responses; combined (sub-)diurnal filter responses; residuals by removing the filter baseline from the measurements. Storm signatures are evident in all panels.

long-term filter responses. A more thorough analysis was necessary to identify the solar quiet patterns within the (sub-)diurnal filter responses. We identified the statistical properties of the Sq current by using the superposed-epoch analysis on the combined (sub-)diurnal filter responses. Three analytical models were presented to describe the observed quiet variations within the 24h and 12h filter responses in section 5.2.2 for which the forward propagation model in 5.2.2.3 performed the best. In chapter 5.2.3 we were able to attribute the challenges encountered during the modelling to the intrinsic day-to-day variability within the individual filter responses. Furthermore, the day-to-day variability within the combined (sub-)diurnal filter responses is very similar to that of the Sq currents. This confirms that not only the Sq current system is an important contributor to the filter baseline but that even its intrinsic D2D variability which is significantly influenced by the neutral atmosphere is accounted for. We conclude that the filter baseline contains relevant quiet sources of mid-latitudes as published in Haberle et al. (2022).

In the last part of this chapter, in section 5.3, I elaborated on further contributions within the filter baseline which confirms that the filter baseline contains significant storm contributions. While the filter baseline can safely be deployed during geomagnetically quiet periods, all levels of filters can be strongly modified during non-quiet periods, making the filter baseline not directly applicable outside quiet periods. In the latter case, the filter baseline tends to contain a considerable amount of storm influences as indicated by figure 5.19. Further discussions of the filter baseline and comparisons with other methods during quiet periods can be found in Haberle et al. (2022). For the derivation of the final baseline this implies that further steps are necessary to remove the storm signatures. This is the challenge we will tackle in chapter 6.

Chapter 6

Adapting the Filter Baseline during Disturbances

The filter baseline is well suited to follow typical variations during geomagnetically quiet periods and captures quiet sources accurately, including the intrinsic day-to-day variability. However, disturbance contributions within the filter baseline are still present during non-quiet periods, especially during storm-time. This indicates that using the filter baseline directly will tend to underestimate the strength of storms and disturbances. Thus, we acknowledge that the filter baseline is not directly applicable for all time periods. This chapter explores possible solutions to address this issue. The strategy is to substitute the baseline during disturbance-time with representative quiet variations such as explored in chapter 5.2.2. As has been done in 5.2.2 and 5.2.3, we will present and discuss the results for the magnetic observatory Chambon-la-Forêt, as discussed in 4.1. Keeping in mind that our goal is to deploy this baseline in an operational, possible near-real time context, we pose the requirement that the identification of disturbance intervals and the corresponding replacement baseline are achieved without further manual intervention.

In order to adapt the baseline during disturbance-time, we need two ingredients: I) the knowledge of when the filter baseline fails, meaning time-intervals when the baseline would underestimate effects and thus needs to be replaced and II) how to replace the baseline during the identified time-interval. We start with the investigation of proxies that hold disturbance information and how to quantify their suitability for determining on when to replace the baseline. With significant parameters at hand, we develop an algorithm that identifies disturbance intervals. We will then discuss which replacement options best represent quiet variations during the identified storm intervals leading to the definition of the full baseline. We will put the results in perspective by comparing it to other baseline derivation methods and provide further discussions about the presented methodology.

6.1 Disturbance Proxies

In the first instance we look at parameters that are able to provide insights about when the baseline leads to residuals that tend to underestimate the effects of disturbances. In order to develop an understanding of such effects, we will consider a prolonged period and investigate the behaviour of the magnetic components and filter responses during identified events. Figures 6.1 and 6.2 show the evolution of the X and Y components at CLF with their respective filter baselines, the responses of all filters and the resulting residuals. The first panel depicts the component in black with overlaid filter baseline in red. The following panels show the filter responses of the long-term filter, the combined diurnal filter, the 24h-, 12h-, 8h-, and 6h-filters separately and finally the residuals (derived as component minus filter baseline). The orange indicates filter responses during CK days and blue non-CK days.

For X in the top panel of figure 6.1 four events (1-4) are marked. Two storm-like events can be identified: one at the end of April/beginning of May marked as (1) and one at the end of May/beginning of June marked as (3). For both, the deflection of X is strongly pronounced which is closely followed by the filter baseline. During these two events we expect the residuals derived with the filter baseline to underestimate the effects of the storm, leading to the need to replace it. Event (4) can be identified by a deflection in X which is less pronounced than in (1) and (3). The rather smooth variations from previous days are perturbed nonetheless, such that a substitution would be desirable. Event (2) does not exhibit a deflection, but clearly interrupts the rather smooth X variations from previous days such that a substitution of the baseline may be applicable. The goal is to relate variations within the filter responses and residuals to the events (1-4) and to compare them between CK days and non-CK days as displayed in figure 6.1.

- The long-term filter response $x_{>24}$ (second panel from top) inherits the deflections for the two storms (1) and (3). Event (4) shows a much weaker signature and event (2) a positive deflection, but it is not straight-forward to discern them from previous CK variations.
- The combined (sub-)diurnal filter response x_D in the third panel from top shows rather unstructured patterns such that differences in modulation on CK, non-CK days and event (2) are unclear. The stronger the event the stronger the corresponding modulation in pattern and amplitude for events (1), (3) and (4).
- The diurnal filter response x_{24} (in the fourth panel from top) shows comparable amplitude variations during CK, non-CK days and the weak event (2), while enhancements occur depending on the strength for events (1),(3) and (4). Especially during the strong event (3) the amplitude rises significantly.
- The semi-diurnal filter response x_{12} (fifth panel from top) shows rather clear differences between CK days and disturbed non-CK days, being modulated clearly during events (1), (2) and (3). Intriguingly, its amplitude during event (4) is substantially decreased.
- For filter response x_8 (sixth panel from top) it is challenging to distinguish variations during CK days and non-CK days.
- Looking at x_6 (seventh panel from top), amplitudes clearly vary between CK and non-CK days. The strong event (3) manifests itself in a clear amplitude increase, whereby events (1) and (4) to a lesser extent but still identifiable. Signatures of event (2) are not present.
- Last but not least, the residuals (bottom panel) show consistently low values during CK-days (orange) and clearly elevated amplitudes during disturbances. All four events have clear signatures.

Turning our attention towards figure 6.2, the same four disturbance events (1-4) are indicated for the Y component (top panel). Contrarily to X, event (1) influences the amplitude of Y clearer than event (3). The smooth variations are perturbed for both events and the substitution of the baseline is favourable. The effects of event (4) are rather subtle, though it modifies the smooth pattern such that a baseline replacement may be considered. Event (2) has no noteworthy signature in Y that would raise the need to substitute the baseline. On June 4th there is a subtle disturbance, that modifies the smooth day-to-day variations slightly which the filter baseline follows. It may be debated

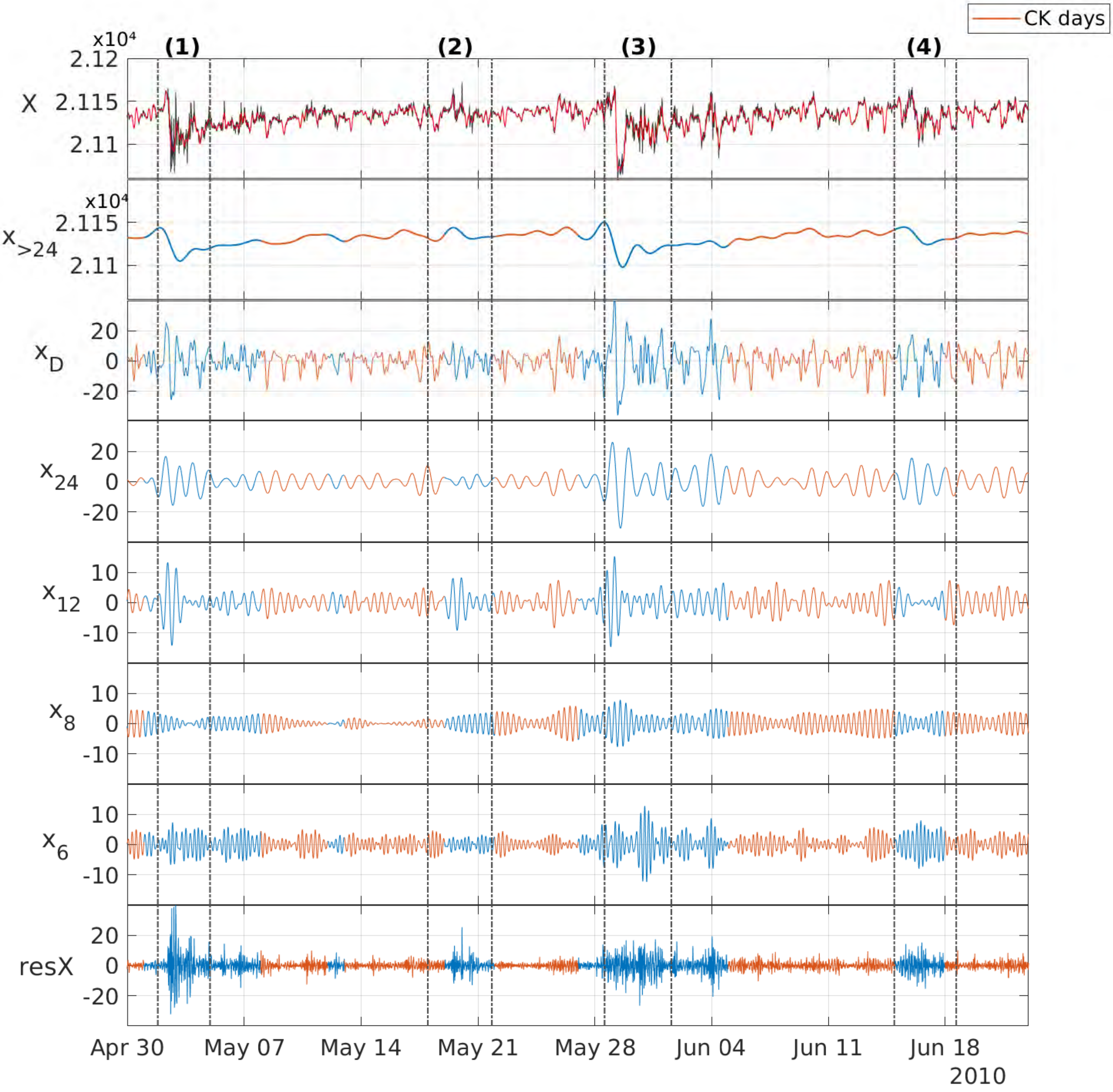

Figure 6.1: The variations of the filter responses for the X component at CLF. Panels from top to bottom: X (black) with filter baseline y_{FB} (red); long-term filter responses $x_{>24}$; combined (sub-)diurnal filter response x_D; 24h-; 12h-; 8h-; 6h filter responses x_{24}, x_{12}, x_8, x_6 ; residuals res$X$ derived as $X - x_{FB}$. Orange indicates CK days, i.e. magnetically very quiet days. All vertical axes are in nanotesla.

if this event needs replacement or not. In general, the Y component is less perturbed than the X component during the considered period, mainly because its amplitude is smaller than X and also because Y is orthogonal to the magnetic meridian, while X is collinear to the field lines and thus more affected and dynamic. This characteristic is also reflected in its filter responses as displayed in figure 6.2.

- For $y_{>24}$ (second panel from top), although signatures of event (1) are present, the identification of the other disturbances is difficult as their variations are rather smooth during the considered period.
- The combined (sub-)diurnal filter y_D (third panel from top) follows smooth patterns during the entire period which are modulated and increased during events (1) and (3).
- In panels four to six from top, there are no striking differences for CK and non-CK days, as well as during the events (1-4) for the filter responses y_{24}, y_{12} and y_8. Solely a small increase in y_{24} and y_{12} occurs in the beginning of event (1) and (3). This can be related to the Y component being rather stable and less perturbed during the illustrated period and these filter responses are more robust to disturbances in general.
- The 6h filter response y_6 (seventh panel from top) shows clear signatures of event (3) and to a lesser extent in event (1), even though a bit delayed. No clear, isolated signature can be found for event (1). Intriguingly, the disturbance on June 4th is clearly recognisable.
- Aligned with the residuals of X, the residuals of the Y component (bottom panel) have clear signatures of event (1), (3) and (4). As for y_6 the disturbance on June 4th is clearly pronounced.

As a summary, during this exemplary period the parameters with the clearest signatures of disturbances, for which the residuals as derived from the filter baseline would underestimate their effects, are found to be within the following three parameters: the long-term filter response for X, the 6h filter response and the residuals for both components X and Y. This leads us to the hypothesis that these are the parameters that hold the most valuable information on when to replace the baseline, at least for CLF, which is a representative observatory in mid-latitudes. This example also demonstrates that disturbances modulate the X component more profoundly than the Y component at CLF, implying that the determination for when to replace the baseline has to be ascertained for each of the components separately and may not need to be done always simultaneously for both. In the following we will investigate the three identified parameters more thoroughly.

6.1.1 Storm Information within the Long-term Filter Responses

In chapter 5.1, we concluded that the main source contributing to the long-term filter responses $x_{>24}$, $y_{>24}$ is the secular variation that induces the observed smooth trend on top of recurrent seasonal and 27-days oscillations. In addition to these variations, we observe distinct storm signatures during the entire period from 1991 to 2019, see also figures 5.1 and 5.2. To isolate and highlight the storm signatures from the general trend and recurrent variations, we remove the moving average over the past 27-days to obtain the de-trended long-term filter responses. This enables us to compare them with storm indices (see chapter 3.1.3). As a reminder, the Dst and SYM-H indices are commonly accepted proxies for geomagnetic storms as they track the ring current that is significantly

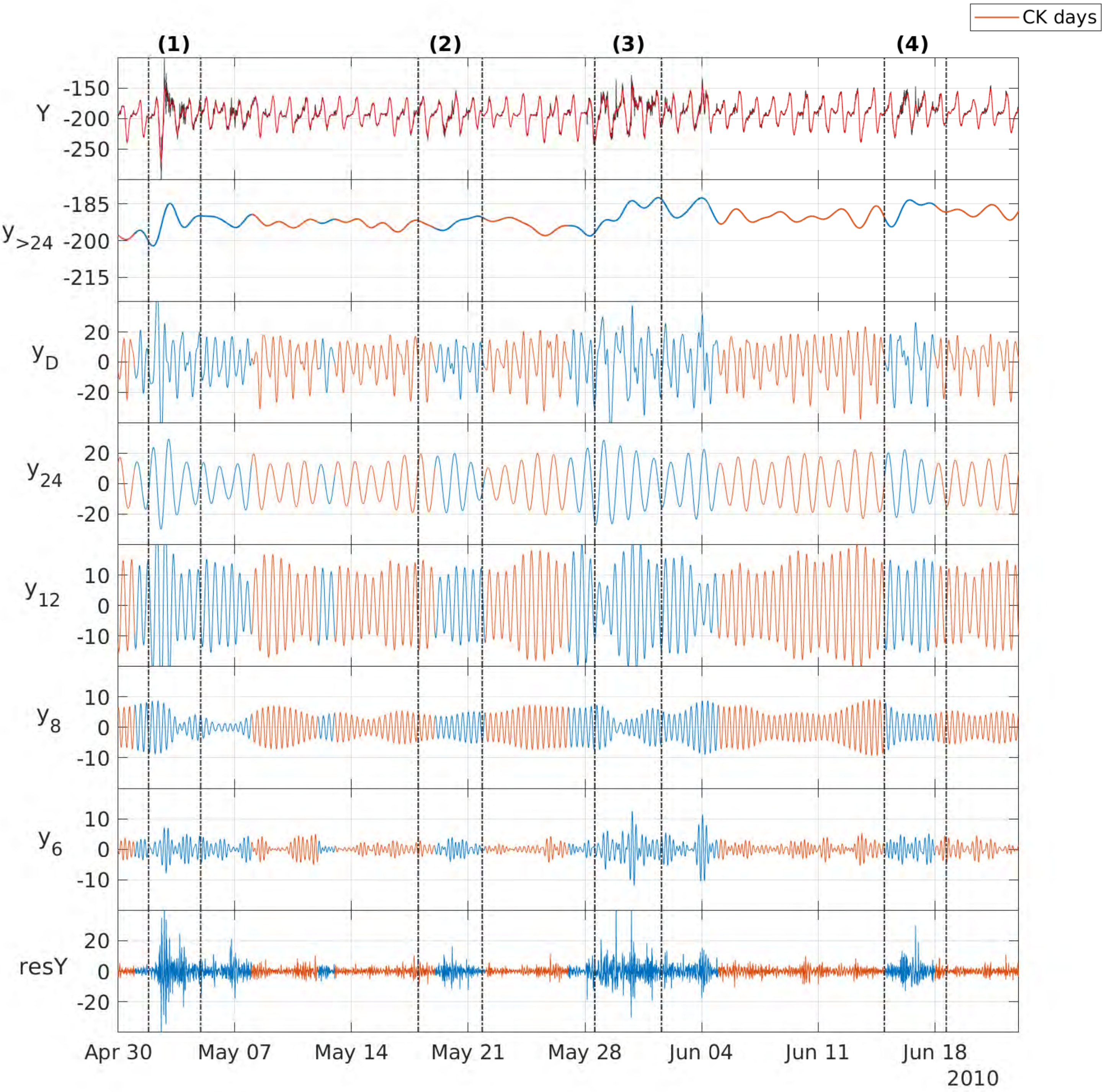

Figure 6.2: The variations of the filter responses for the Y component at CLF. Panels from top to bottom: Y (black) with filter baseline y_{FB} (red); long-term filter responses $y_{>24}$; combined (sub-)diurnal filter response y_D; 24h-; 12h-; 8h-; 6h filter responses y_{24}, y_{12}, y_8, y_6 ; residuals res$Y$ derived as $Y - y_{FB}$. Orange indicates CK days, i.e. magnetically very quiet days. All vertical axes are in nanotesla.

intensified due to enhanced particle fluxes in the radiation belts during storm-time. The SYM-H comes in a time-resolution of one minute, identical as the filter values, and is derived from the horizontal component H from six low to mid-latitudinal observatories, including CLF. In fact, the SYM-H index is derived from the horizontal component and in order to get a more accurate view on its relationship with the long-term filters, we introduce the 27-day de-trended long-term horizontal intensity $\bar{h}_{>24}$, defined as

$$\bar{h}_{>24}(t_0) = \sqrt{x(t_0)^2_{>24} + y(t_0)^2_{>24}} - \frac{1}{27d} \sum_{t=t_0-27d}^{t_0} \sqrt{x(t)^2_{>24} + y(t)^2_{>24}}\,, \tag{6.1}$$

A window of 27-days guarantees the smoothing of the 27-days variation and the removal of seasonal and longer-term variations.

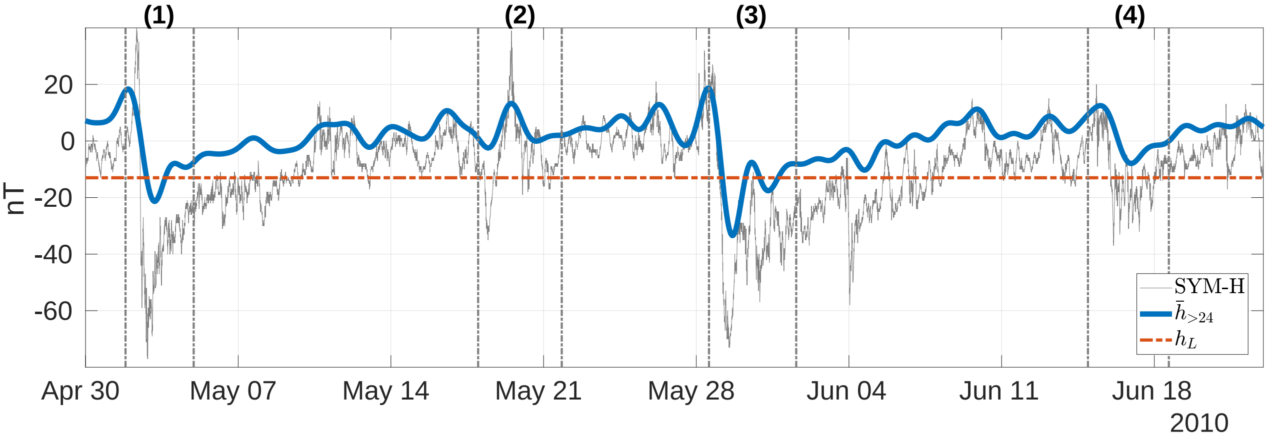

Figure 6.3: Evolution of the 27-day de-trended long-term horizontal intensity $\hat{h}_{>24}$ (in blue) together with the limit h_L (in orange) at CLF. The SYM-H index is indicated in grey. The same events as in figures 6.1 and 6.2 are marked by horizontal dash-dotted lines. The vertical axis is in nanotesla.

In figure 6.3, we see that the de-trended $\bar{h}_{>24}$ is in remarkable agreement with the general patterns of SYM-H. Indeed, $\bar{h}_{>24}$ is linearly correlated with SYM-H having a Pearson coefficient of 0.79, indicating strong linear correlation. We can leverage this characteristic to derive a threshold h_L for storm identification, indicated by the orange horizontal line. Using the (minute resolution) data for the entire period between 1991 to 2019, we apply a linear fit for CLF to obtain the relationship

$$\bar{h}_{>24} \approx 0.47\ \times \text{SYM-H} + 6.34\,. \tag{6.2}$$

The question remains which SYM-H value is best to be used for defining the threshold h_L. In the literature it is common to define storms by their minimum Dst and SYM-H, e.g. the conditions Dst $< -50\,$nT and SYM-H $< -50\,$nT are commonly used to define strong storms, see chapter 2.4.2. Instead of using such an arbitrary limit, let us come back to our findings from chapter 5.2 where we attributed the statistical variations of the combined (sub-)diurnal filter response x_D to y_D to the Sq current system and try to leverage this information.

We saw that, when looking at the super-posed epoch analysis, the x_D and y_D resemble closely those of the Sq current system with distinctive day patterns as seen in figure 5.5. In order to derive a threshold, we can partition the SEA from section 5.2.1 into activity levels of SYM-H and analyse until which level the traces of the Sq current systems are preserved. For one UT day, the SYM-H level is determined by taking the mean of all SYM-H values during that day. A common threshold for low and quiet geomagnetic activity is given by SYM-H $> -20\,\mathrm{nT}$, which we will define as the first level (Gonzalez et al., 1994). From there, we continue in 10nT steps down to -70nT. Really strong storms are then in the last level for Dst $< -70\,\mathrm{nT}$. The SEA based on days sorted per SYM-H level is given in figure 6.4. For very low activity, the patterns of the Sq currents are dominant. Though, the values are slightly increased in general in comparison to figure 5.5. For SYM-H levels between -20nT and -30nT, the general patterns of the Sq current system are generally preserved. However, increased levels of activity is observable everywhere. Especially night-time enhancements are starting to increase for both components. Continuing to higher levels, for x_D at SYM-H $> -40\,\mathrm{nT}$, its typical patterns are still recognisable, though enhancements are apparent while for y_D we could distinguish them until SYM-H $< -50\,\mathrm{nT}$. From that on, the traces of Sq patterns melt within a general pattern from which they are hardly distinguishable anymore.

This analysis suggests that Sq patterns in x_D and y_D prevail until SYM-H $> -40\,\mathrm{nT}$ at CLF. Using this information in (6.2) holds the threshold $h_L = -13\,\mathrm{nT}$, as is marked by the orange line in figure 6.3. Each time-step t that satisfies $\bar{h}_{>24}(t) < h_L$ is then marked as a disturbance for both of the components, i.e. both $x_{FB}(t)$ and $y_{FB}(t)$ would need to be replaced. In relation to the four events (1-4), the strong events (1) and (3), in particular their main phases, are identified. The moderate event (4), however is too weak to fall below the derived limit. Contrarily, event (2), which manifests itself with a positive peak, is obviously missed as only negative values are taken into account by h_L. This method is thus intended to identify strong events for which the likelihood is high, that the filter baseline for both components needs to be replaced.

One more thought on this method is that we need to be careful comparing the de-trended filter responses with SYM-H. First of all, SYM-H is a global index derived by combining measurements of six low to mid-latitude observatories while the de-trended filter response is derived from one individual magnetic observatory. In the demonstrated case, we look at data from the station CLF which is situated centrally in mid-latitudes. Although being part of the SYM-H's network, it is still possible that local characteristics within $\bar{h}_{>24}$ are less pronounced or even not at all represented within SYM-H and vice versa. This fact can be one explanation for the rather strong SYM-H around June 4th (below $-50\,\mathrm{nT}$) not being quite as present within $\bar{h}_{>24}$ at CLF. Interestingly enough, this disturbance is however clearly recognisable in Y. Secondly, even though we motivated the choice of the 27days de-trending window, any changes in its length will ultimately also affect the relationship (6.2) in SYM-H.

Nevertheless, SYM-H is a commonly accepted proxy for geomagnetic storms and the stronger a storm the more geoeffective it is, increasing the likelihood that stations independent of latitude and longitude are affected. During such geoeffective disturbances, the filter baseline tends to follow its effect closely and we can still make use of the linear correlation with SYM-H and apply it to detect periods of strong storms.

6.1.2 Disturbance Information within the 6h Filter and the Residuals

In the beginning of this chapter we deduced from figures 6.1 and 6.2 that the 6h-filter and the residuals are parameters that hold valuable disturbance information. During the two

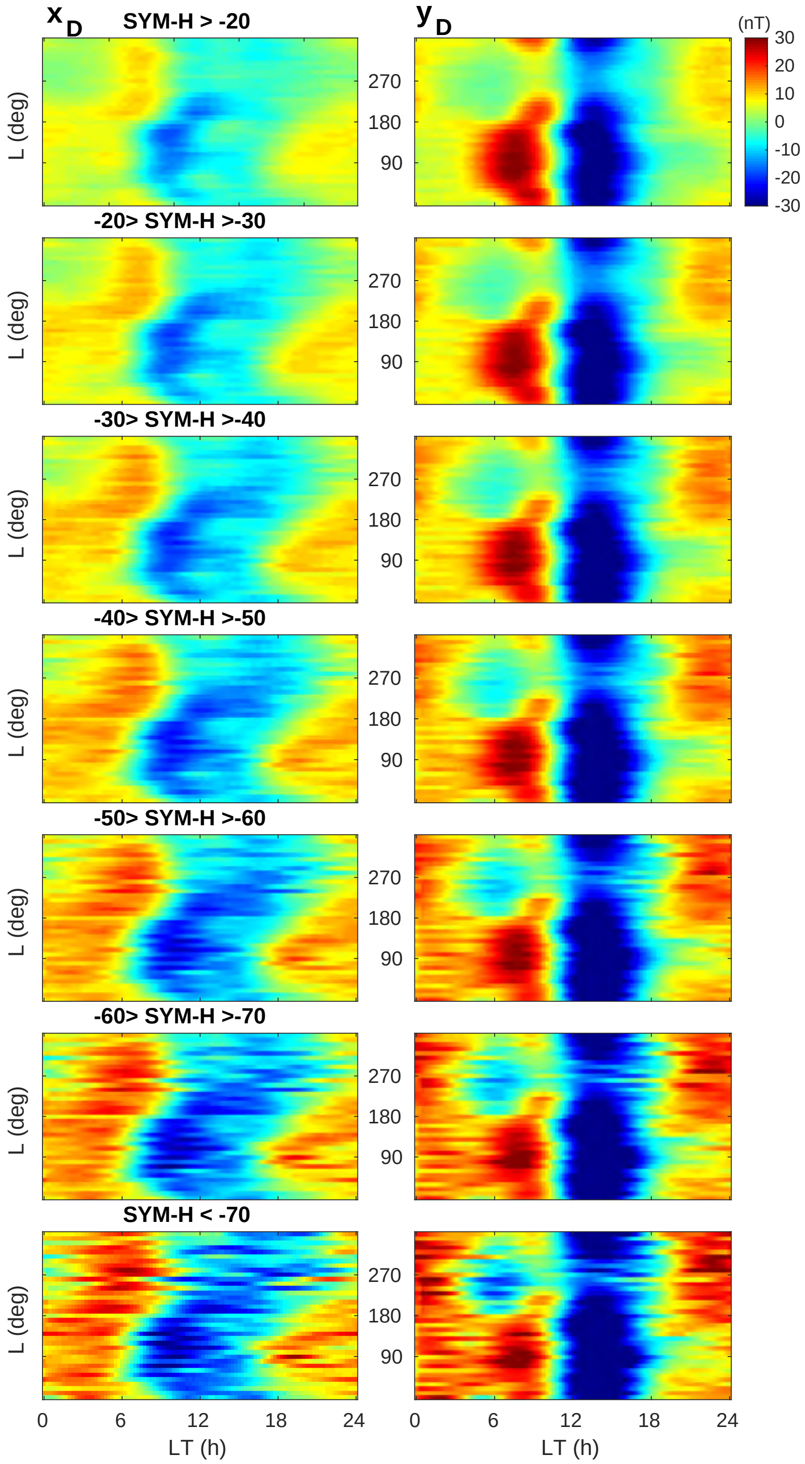

Figure 6.4: The super-posed epoch analysis for the combined (sub-)diurnal filter responses x_D (left) and y_D (right) at CLF for corresponding SYM-H levels.

strong events (1) and (3), for which baseline replacement is required, both feature significantly elevated amplitudes from a general background/quiet level. Hence it is reasonable to characterise the background level by identifying upper and lower boundaries.

Assuming that a significant increase in amplitude marks disturbance-time and that occurrences of increased amplitudes are less frequent than the general background/quiet level, we can treat disturbance amplitudes like outliers. The mean μ and standard deviation σ of a given distribution can be used to determine confidence intervals, e.g. in the case of a normal distribution, 68% of values are between $\mu \pm \sigma$, 95% are between $\mu \pm 2\sigma$ and 99% are between the $\mu \pm 3\sigma$ confidence interval. Thus, outliers can be characterised by their associated $i\sigma$th confidence interval and upper and lower boundaries can be defined as $b_{U/L} = \mu \pm i\sigma$. Identifying outliers by deriving boundaries from the mean and standard variation in this manner is commonly referred to as sigma-clipping.

Before we can apply this approach to identify disturbance-time, we need to know more about the underlying distributions of the 6h-filter values and the residuals and see if their μ and σ are suitable parameters. Figure 6.5 presents relative-count histograms in percentages for the two parameters during CK days (upper panels) and non-CK days (lower panels) during the considered time period from figures 6.1 and 6.2. The best-fit normal distribution and its corresponding mean μ and standard deviations $\pm\sigma$ are indicated.

Starting with the parameters for X on the left, we see that the fitted distributions are aligned well for x_6. The peak of the distribution of the residuals X on CK days is more pronounced, while the distribution on non-CK days has a steeper slope than their best-fit Normal distributions. Analogous observations hold for y_6 and residuals Y, whereby additionally the peaks are more pronounced in general for these 3 parameters. A striking feature is that during non-CK days, the distributions are farther spread than during CK days, which is reflected in their σ. The difference between disturbed σ and quiet σ is significantly more pronounced for the residuals. While the mean, indicated by the solid vertical burgundy line, is around zero for all distributions, the standard deviation, indicated by the dashed vertical burgundy lines, is sensitive for discriminating quiet from disturbed periods. This also holds for the residuals even though their distribution is not fully aligned with their best-fit Normal distribution. We can conclude that the sigma values are suitable to define upper and lower boundaries.

The 6h-filter and the residuals are time-dependent variables that are influenced by various external and internal factors. This implies for example that we cannot exclude changes in the background variation during solar cycle phases, seasons or other factors. Therefore using a standard deviation derived on a fixed time-interval will not be sufficient. To allow for this variability, we compile the running mean μ and running standard deviation σ over a sliding window of the past 6 days for each of the two parameters which in turn enables us to define a running upper and lower boundary $b_{u/l} = \mu \pm \sigma$. Six days will account for any long-term effects from solar cycle phases or seasons, but also account for periods which are very disturbed due to a strong event increasing background levels for several days even after the end of such an event. The resulting boundaries are illustrated in figures 6.6 for X and 6.7 for Y. Note that we apply this method on both, the 6h-filter and the residuals. We see that the boundaries describe the general background field accurately during quiet periods. As expected, the boundaries are broadened during disturbances, as σ increases and stay broadened for the following days due to the disturbance being kept within sliding window (after 6 days the disturbance has moved out of this window).

Coming back to the four events (1-4) we identified before, it is evident that the residuals X and the residuals Y overshoot the background boundaries during each of the events. While some of the values from the 6h-filter are outside of the defined boundaries, they cross the boundaries less often and less clearly. This brings us to the conclusion that the residuals hold stronger and clearer disturbance information and thus are better suited for

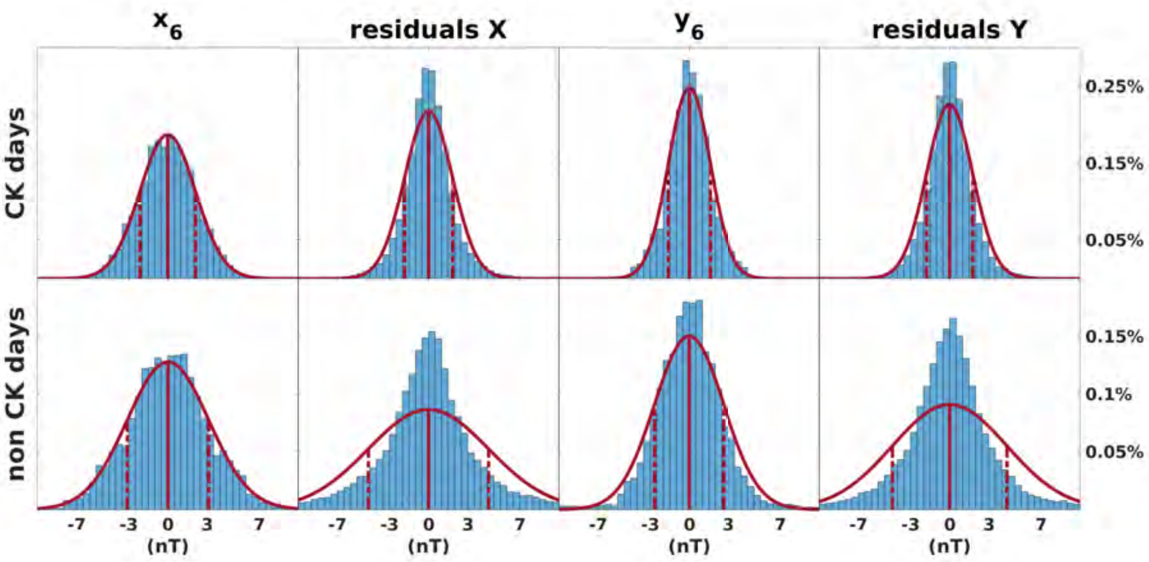

Figure 6.5: Probability distribution functions for CK and non-CK days during April to June 2010 of the residuals and 6h filter for X and Y. The burgundy curve indicates the best-fit Normal distribution together with its mean (solid) and standard deviation (dashed).

disturbance detection than the 6h-filter responses. In the next chapter, we will support this conclusion quantitatively.

6.1.3 Disturbance Detection Qualifiers

The illustrated sample periods in figures 6.1 and 6.2 suggest that the long-term filter and the residuals contain the most promising disturbance information. The valid question remains whether this statement holds for the entire considered period between 1991-2019. In the following, we introduce and discuss objective criteria that can aid us in evaluating the quality of the detection.

It should be emphasized that the disturbance determination is evaluated in the same time resolution as the available data, that means for each minute. Also note, that each parameter was presented together with a dedicated method, i.e. we used a derived limit for the long-term filter value and sigma-clipping for the residuals.

- **Total amount of identified disturbance minutes**
  Considering the entire period of 28 years, the total amount of minutes that are identified as disturbed provides information on how sensitive an algorithm is. For example, if more than 50% of the time is identified, the method may be too relaxed marking too many minutes. If on the other hand less than 5% are marked it may be too restrictive. Rigorous empirical investigations indicated that around 25-35% is a legit range to guarantee that not too little, nor too many minutes are marked.

- **Ring current indices below a certain threshold**
  The stronger a storm, the more likely the need for substituting the filter baseline is. In the literature, see storm lists in the introduction, a threshold of $Dst < -50\,\mathrm{nT}$ is frequently used to identify strong storms. We can evaluate algorithms based on how

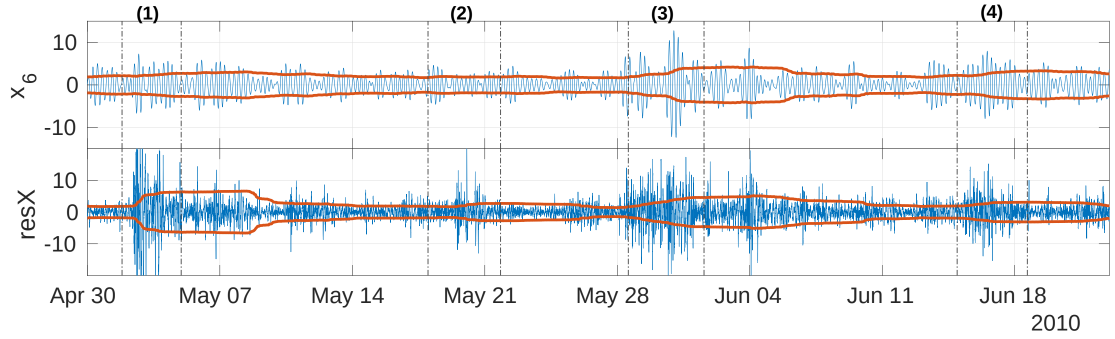

Figure 6.6: The upper panel shows the evolution of x_6 and the lower one the residuals of X. The upper and lower boundaries as derived by sigma-clipping are indicated in orange. The vertical axes are in nanotesla.

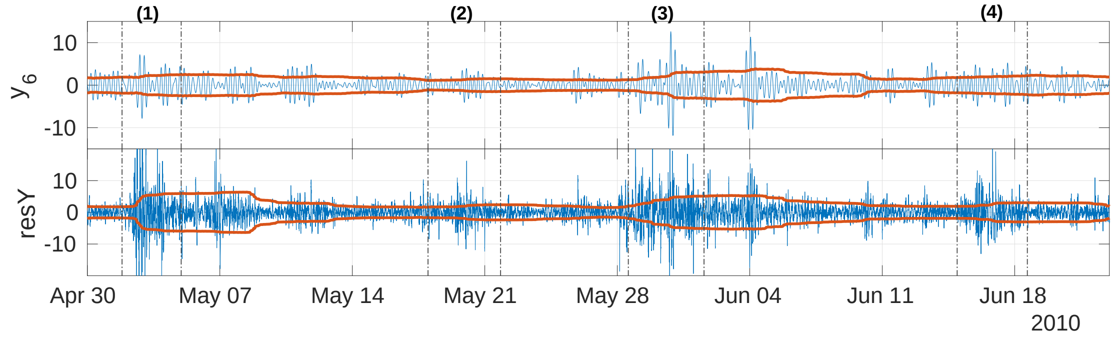

Figure 6.7: The upper panel shows the evolution of y_6 and the lower one the residuals of Y. The upper and lower boundaries as derived by sigma-clipping are indicated in orange. The vertical axes are in nanotesla.

many minutes are marked of the total minutes that satisfy Dst or SYM-H below this threshold. Such qualifiers can give information about how much of the main phase and beginning of recovery phases for strong storms are successfully identified.

- **Minutes during very quiet days**
  As the baseline is capturing quiet sources well, the likelihood that the filter baseline needs to be replaced during such quiet periods is very small. Therefore any algorithm should ideally not mark minutes during CK48 days.

As quantitative measures, these qualifiers can give a first glimpse upon the performance of an algorithm. However, they give no information about the location and concentration of the marked minutes, e.g. for a strong event with Dst$< -50\,$nT we do not know how many minutes of the individual event is eventually marked as a disturbance. Geomagnetic storm studies, as discussed in the introduction, provide lists of strong storms detailing their strength, start and end-times, chosen by certain aspects like isolated events and minimum Dst or SYM-H. However, as we have seen before, not all periods for which we want to replace the baseline are associated with strong Dst/SYM-H and not all storms with clear Dst/SYM-H have strong enough signatures to motivate a baseline replacement. At this point, I would like to remind the reader, that Dst and SYM-H are derived from four and six magnetic observatories, respectively, distributed over longitude. Even though the storms from the storm lists are quite intense, local variations in the deflection of the H component can still occur due to the complex morphology of storms and related current systems within the magnetosphere. This can lead to events, that have clear signatures in Dst and SYM-H, but are almost non-existent in measurements from specific other observatories, even if they are part of the index network. One of these examples is the storm from 27th July 1999 as listed in the storm catalogue of Li and Yao (2020). Even though it is quite intense in Dst, the components of X and Y at CLF are only marginally affected. The related figure can be found in appendix D.1. During these types of storms, the filter baseline actually would appropriately describe the long-term and quiet variations and would not need to be replaced. This implies that we cannot directly adopt these storm lists as appropriate storm qualifiers for the baseline replacement decision. Therefore, to get a better qualitative insight for the performance of an algorithm, we will need a tailor-made list of disturbances for which we would like to replace the baseline. It should be pointed out that such a list is valid only for the station for which it is derived and is not automatically usable for other stations. Although, the likelihood that such a disturbance list is applicable for geographically nearby stations is high.

To establish a disturbance list for CLF, we can use the storm list provided by Li and Yao (2020) as a basis. It contains 95 storms during 1998 to 2011, covering most of SC23. The storms originate from geoeffective ICMEs and have a consistent definition provided by the authors for the end of their recovery phases. For each year between 1998 and 2011, three storms are chosen, one per each quadrimester to evenly distribute them (January to April, May to August, September to December). If during a particular year and a particular trimester no storm is recorded in the storm list or no clear signatures were present within the measurements of CLF, a disturbance with a clear signature is manually identified within the period, independent of the Dst intensity. This results in a storm catalog of 39 events during which the filter baseline is supposed to be replaced at CLF. The full list of start and end times, minimum Dst and signatures in CLF can be found in appendix D.3. This list covers various morphologies and intensities of disturbances that we expect an algorithm to detect but we cannot claim that it is complete. We can now add further qualifiers, namely how many of the events from the disturbance list are detected and to which extend. We consider an event detected if at least 90% of it is marked as a disturbance and missed if less than 10% is marked. Events marked in-between 10% and 90% is considered as partially detected. This allows to see how well an algorithm performs in detecting the individual events.

Altogether, we can deduce 7 key performance indicators (KPIs) that can support the evaluation of algorithms with respect to disturbance identification:

1. **TOT:** Percentage of total minutes marked, should be between 25-35%
2. **Dst:** Percentage of total minutes marked with Dst below $-50\,\mathrm{nT}$, should be close to 100%
3. **SYM-H:** Percentage of total minutes marked with SYM-H below $-50\,\mathrm{nT}$, should be close to 100%
4. **CK:** Percentage of total minutes marked during CK-days, should be close to 0%
5. **Detected:** Amount of events from disturbance list which are detected, i.e. more than 90% of the individual event is marked, should be ideally 39
6. **Partially Detected:** Amount of events from disturbance list which are partially detected, i.e. between 10% and 90% of the individual event is marked, should be 0
7. **Missed:** Amount of events from disturbance list which are missed, i.e. less than 10% of the individual event is marked, should be ideally 0

We derive this set of disturbance detection qualifiers for the long-term filters together with the derived limit method and for the 6h-filter responses and residuals together with the sigma-clipping method and summarise them in table 6.1. The first thing we notice is that only a fraction of between 1991 and 2019 is marked as a disturbance. For the sigma-clipping method that can be related to the fact that only individual minutes are marked, as it looks for outliers and not full intervals. For the derived limit method which does mark intervals, this can be related to the detection of only very strong events which are not that frequent. As can be seen in the percentage of strong Dst and SYM-H values, it catches already around 80% of these. The percentage of marked CK-day minutes is reasonably low for all methods. Coming to the disturbance list, $\bar{h}_{>24}$ is able to detect 4 events and partially detects 28 and thus performs the best in comparison to the sigma-clipping method. Still, it misses 7 events. This can be related to the fact that these events do not have a strong enough signature in $\bar{h}_{>24}$. The performance for the sigma-clipping is generally low. However, it is evident that it performs better for the residuals than the 6h-filter for both components. These considerations re-assures the decision of preferring the residuals over the 6h-filter for disturbance detection. However, it also suggests that the presented methods need further considerations.

Table 6.1: KPIs for the derived limit method applied on the long-term filters $\bar{h}_{>24}$ and standard sigma-clipping on the 6h-filter responses x_6, y_6 and residuals for X and Y. In the header the ideal value is indicated beneath each KPI.

	TOT	Dst	SYM-H	CK	Detected	Partially Detected	Missed
ideal value	25-30%	100%	100%	0%	39	0	0
$\bar{h}_{>24}$	8.17	79.67	84.31	0.21	4	28	7
x_6	1.59	6.63	7.61	0.23	0	10	29
res$X$	2.63	9.23	10.58	0.39	0	11	28
y_6	1.30	5.62	6.55	0.18	0	6	33
res$Y$	2.69	9.71	11.20	0.46	0	11	28

6.1.4 Further Parameters for Disturbance Identification

The previous subsections focused on filter responses and corresponding residuals for the identification of disturbances. Several other parameters, including all filter responses and derivatives thereof, different representations of the information and the signals themselves were evaluated with the help of the KPIs and eventually discarded. The following list briefly introduces each of the considered parameters.

- Residuals of Filters and Models
  In chapter 5.2.2 we introduced three models to reproduce the quiet variations. Assuming that these provide a sufficiently good description of the actual quiet variations, we expect the difference between the filter response and the respective model to be significantly higher during disturbances than during quiet periods. Due to strong, intrinsic day-to-day variability and general performance of the models, however, there are consistent offsets within the residuals that can be partly related to phase shifts between the actual data and the models. This leads to high amplitudes within the residuals, even during quiet days and thus are not suitable to identify disturbances.

- Extrema of Filters
  Assuming that disturbances increase amplitudes significantly, we can apply sigma clipping to the running maxima and minima of the individual (sub-)diurnal filter responses and apply sigma-clipping to identify days or periods which exceed typical values. However, again, due to the strong day-to-day variability, the overlap between weak-to-moderate and quiet extrema is consistently obliterated. For the combined diurnal filter responses x_D and y_D, we saw that the day-to-day variability is in the order of 20% to 30% from one day to another. Using the maximum (or minimum) of x_D, y_D and comparing it to the consecutive maximum (or minimum), we can mark it as a disturbance when the difference exceeds the 30% boundary. Similar to the individual filters, this method did not produce convincing results. The main issue with this approach is that the maximum may be quite small during one very quiet day and may be relatively large on the next, still, quiet day, leading to overwhelmingly many quiet days being marked.

- Envelope and Phase of the Signals
  Each of the filter responses z are periodic functions that can be written as

  $$z(t) = A\cos\left(\omega t + \phi\right)\,,$$

  Developing the signal around $t \pm \delta t$ and using trigonometric identities, we obtain the envelop of its amplitude A:

  $$z(t-\delta t) - z(t+\delta t) = 2A\sin\left(\omega t + \phi\right)\sin\left(\omega \delta t\right)$$
  $$\iff A = \sqrt{\underbrace{s(t)^2}_{=:a} + \underbrace{\left(\frac{s(t-\delta t) - s(t+\delta t)}{2\sin(\omega\delta t)}\right)^2}_{=:b}} =: \sqrt{a(t)^2 + b(t)^2}\,,$$

  and the sine and cosine components of the phase

  $$\sin\phi(t) = -\frac{a}{||a+b||}\sin(\omega t) + \frac{b}{||a+b||}\cos(\omega t)$$
  $$\cos\phi(t) = -\frac{a}{||a+b||}\cos(\omega t) + \frac{b}{||a+b||}\sin(\omega t)\,.$$

  The envelop and phase, as well as their combinations was then analysed for each of the filter responses with the sigma-clipping method. Especially for the phase, the strong intrinsic day-to-day variability overshadows variations.

  Additionally, we investigated the interaction among the individual filters (including their phase and amplitude) to see if any collective behaviour can be leveraged to detect disturbances. While very intense events are clearly identifiable, the collective activity is fully overlapping for quiet periods and moderate events. The same was done to compare the filter responses of both components to investigate potential interactions between X and Y, giving similar results.

- Horizontal Field H and Total Field F
  Each component of the magnetic vector field $B = (X, Y, Z)$ is a projection of the total magnetic field and thus implies information compression and loss. To avoid missing potentially important information by considering each component alone, we investigated the horizontal field H and the total field F, as well as the respective filter responses. No further information has been found.

- Clockangle between X and Y
  Many magnetic indices are build on the H component as it is prone to storm signatures. This means that its components X and Y and their directions are influenced too. Thus, the phase between them defined as $\phi = atan(Y, X)$ may hold significant information. Additionally, the phase of each of the filters was analysed with no proper results.

- Coordinate Transformation
  In all our analysis we have been using the measurements in the local geographic NED frame as defined in chapter 2.6.3. To exclude missing storm information due to the coordinate system, we transformed the data into the IGRF magnetic frame and re-ran the analysis. No striking differences have been observed.

- Time Derivative of the Magnetic Field
  In GIC studies, the time-derivative dB/dt of the geomagnetic field is analysed and thresholds are derived, like has been done e.g. to determine strong SSC in Bailey and Leonhardt (2016). With the knowledge that storms introduce a stronger dB/dt, we may attempt to characterise storms and quiet variations by their time derivatives similarly. This can be done for the components themselves, as well as for the long-term filters. Unfortunately, as weak-to-moderate storms have amplitude signatures in the order of typical quiet variations, this approach is not giving good results for these regimes. However, strong storms can be detected with this method.

Many of the above mentioned approaches have in common, that the level of perturbation induced by weak-to-moderate storms and disturbances is in the order of the level of the typical quiet variation. Due to this tight overlap, it is almost impossible to find meaningful, global thresholds. This also implies that whatever method and parameter is used, also the ones we eventually use, the results will never be black and white, but a grey-zone in-between.

6.2 Algorithm to Detect Disturbed Periods

With the disturbance proxies, i.e. the long-term filters and residuals, we can attempt the creation of an algorithm that identifies periods during which the filter baseline will be replaced. Table 6.1 was useful to support the decision of using the residuals over the 6h-filter. Apart from that the main conclusion to be drawn from it is that the basic methods of derived limit and sigma-clipping are not reasonable to detect coherent periods of disturbances. The derived limit method does not take into account parts of the main phase and onsets but at least produces continuous intervals of disturbances. The sigma-clipping identifies individual minutes above and below a certain threshold. Therefore, we will adapt these two methods and use its combination to determine disturbance intervals during which we would like to replace the filter baseline.

6.2.1 Adapted Method for the Long-term Filter

Using a derived limit for the de-trended horizontal intensity $\bar{h}_{>24}$ results in the identification of parts of the main and recovery phases of stronger events. In the upper panel of figure 6.8, $\bar{h}_{>24}$ and h_L is illustrated as discussed in chapter 6.1.1. All values beneath h_L are marked as a disturbance t_D, indicated in orange. The lower two panels indicate the resulting disturbance intervals t_D on the components X and Y (also in orange). It is clear that the onset and parts of the main phase are missed. To overcome this issue, the most recent local maximum t_{max} is identified marking the start-time of the event(indicated by the yellow triangle). Looking for the onset in this manner is in agreement with typical definition of storms, where the local maximum before a Dst minimum is used as start-time, see chapter 2.4.2. As the shape of the long-term filter response is a wave, such a maximum can always be found, even if the storm is not accompanied by a clear SSC. The time-interval t_O (in yellow) up until t_{max} is appended to t_D. The algorithm defined in this manner produces the disturbance intervals $t_O + t_D$ as illustrated in the lower panels of figure 6.8 for the X (left) and the Y (right) components. Please note, that the intervals for both components are the same and this method is limited to identifying strong storms.

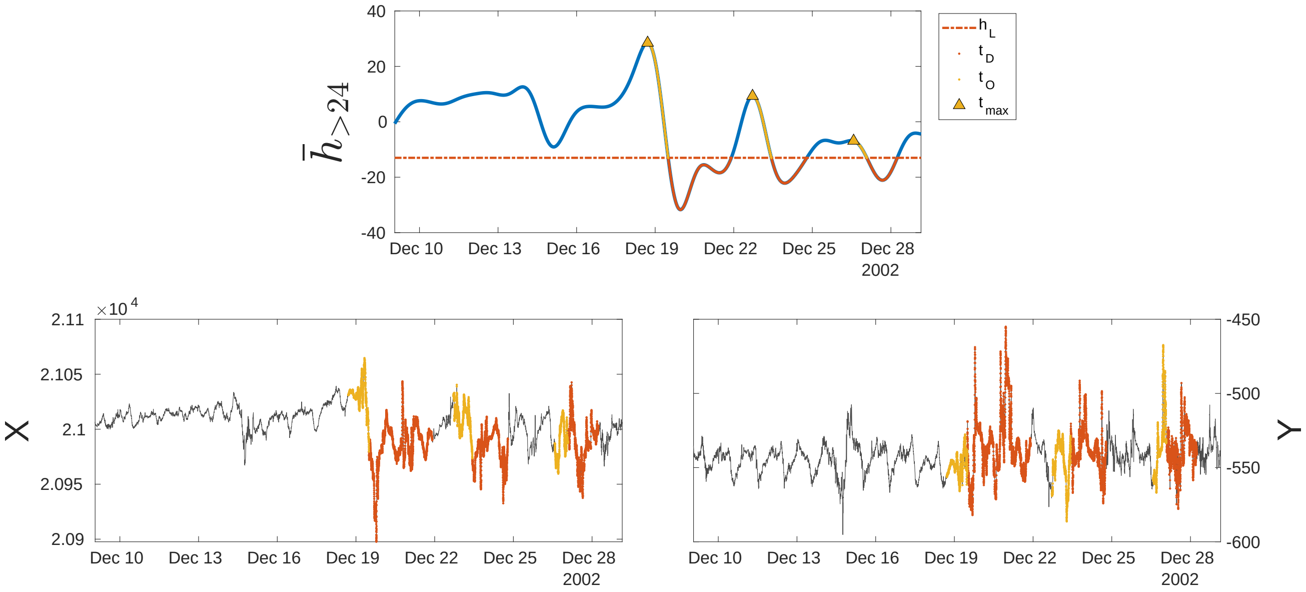

Figure 6.8: Illustration of the algorithm to detect strong storms with the de-trended horizontal intensity $\bar{h}_{>24}$ from chapter 6.1.1 in the upper panel. The lower panels show the corresponding identified intervals on the X (left) and the Y (right) components. All vertical axes are in nanotesla.

Using the KPIs from section 6.1.3, we can compare the initial method of derived limit with its adapted counterpart as summarised in table 6.2. For the adapted derived limit method on $\bar{h}_{>24}$, the KPIs are consistently better, catching even more of the strong Dst and SYM-H values while detecting very few quiet minutes. Still, this method alone misses 6 of the events, which can be related to the fact that only very intense events are identified.

6.2.2 Adapted Method for the Residuals

In figures 6.6 and 6.7 the upper and lower boundaries are derived using the 1σ confidence interval of the sigma-clipping on the residuals for X and Y. These cut-offs are quite tight and narrow-down significantly during extended quiet periods. Furthermore, disturbances are associated with boundary broadening which holds the risk that beginnings of and subsequent disturbances are hidden and remain unnoticed. The nature of the residuals, similar to the (sub-)diurnal filter responses, is to oscillate from negative to positive values crossing the zero-line in-between. Defining upper and lower boundaries enable the identification of single outliers, but misses values that occur when the residuals fluctuate from a positive to a negative outlier and vice-versa, meaning the identification of full intervals. It only makes sense to replace full intervals within the filter baseline rather than isolated minutes. We will now introduce a 2-step algorithm based on sigma-clipping that addresses these issues. Step 1 covers the determination of an appropriate boundary that catches as many disturbances as possible and step 2 deals with the issues of the zero oscillations. Supporting illustrations for these steps are found in figure 6.9, showing the X component on the left and the Y component on the right.

- **Step 1: Determining quiet levels**
  The sigma-clipping enables the definition of quiet level boundaries. As pointed out, the 1σ interval is too constrained and disturbances may be missed due to the featured broadening. Therefore we will adapt the quiet level boundary by combining a loose and a tight boundary, b_L, b_T.

  - **Step 1.1: Definition of loose and tight boundaries**
    To allow for a more relaxed border, we apply the sigma-clipping with 3σ on each of the residuals res$X$ and res$Y$, i.e. the boundaries are defined by the moving average μ_1 and moving standard deviation σ_1 over the past 6 days: $b_1 = \mu_1 \pm 3\sigma_1$, keeping the same window-length as in chapter 6.1.2. This boundary b_1 is derived on, and thus contains, influences of very strong outliers. We re-calculate the moving average μ_2 and moving standard deviation σ_2 only on the 3σ constrained values i.e. for $-b_1 < \text{res} < b_1$, providing us with the loose boundary $b_L = \mu_2 + \sigma_2$.
    For the tight boundary, we remove once more the outliers from the data, i.e. $-b_L < \text{res} < b_L$ and generate the weighted, moving mean $\hat{\mu}$ and standard deviation $\hat{\sigma}$. The weight function is half a cosine which, for $t = t_0$, is 0 at $t = t_0 - 6d$ and 1 at $t = t_0$. This ensures that disturbances that are farther in the past influence the tight boundary less than disturbances that are closer in time. The tight boundary then writes at $b_T = \hat{\mu} \pm 3\hat{\sigma}$. Both boundaries ($b_L$ in yellow and b_T in purple) are indicated in panels (a) in figure 6.9.

  - **Step 1.2 Combination of b_L and b_T**
    By default, we assume quiet time and apply the loose boundary b_L. As soon as a value above b_L is detected, the tight boundary is applied for the successive 12 hours. The resulting quiet level boundary b is depicted in panels (b) of figure 6.9 in orange. Each residual that is above (or below) this boundary is considered a disturbance candidate minute t_C. The resulting candidates on each of the components are indicated as orange dots labelled t_C in panels (c) of figure 6.9.

- **Step 2: Defining disturbance intervals**
  The result of Step 1 leaves us with an irregular collection of storm candidate minutes t_C. Unsurprisingly and from panels (c) in figure 6.9, it is evident that occurrences of t_C are clustered. We will first create full disturbance candidate intervals by adding values that belong to oscillations around zero, i.e. when the values oscillate in between the upper and lower quiet level boundaries b. We then check if these intervals belong to a disturbance by defining the minimum disturbance length Δt_{min}.

- **Step 2.1 Incorporation of oscillations**
  The typical disturbance event induces residuals that fluctuate from above to below the quiet boundaries b, implying that values within the quiet boundaries are missed although they belong to the same event. Such that, during the event's duration Δt, the values inside $|b|$ should be incorporated within disturbance candidates. Therefore, we define the maximum event time Δt_{CI} that relates two disturbance candidate minutes t_{C1} to t_{C2}. If the duration Δt between t_{C1} and t_{C2} is less than Δt_{CI} then t_{C1} and t_{C2} are considered to belong to the same event. All minutes t_{CI} (in yellow in panels (d)) within Δt are then added to the storm candidates, resulting in full disturbance candidate intervals (or events). By experience and empirical refinement, we determined $\Delta t_{CI} = 8hours$.
- **Step 2.2 Final Disturbance intervals**
  It is possible that the method of using a maximum Δt_{CI} between two disturbance candidates marks quiet periods. This is the case for e.g. the interval around 16th of December on the X component in panel (d) right after the moderate event. For the identification of such intervals, we define a minimum disturbance time $\Delta t_{min} = 15h$. Any disturbance candidate interval that is longer in duration than Δt_{min} is considered a final disturbance interval, otherwise it is removed. The time of 15h corresponds to a typical duration of shorter storms and agrees well with empirical refinement.

The final disturbance intervals t_D produced by this algorithm are illustrated in panels (e) for the X component (left) and the Y component (right) in figure 6.9. We can note here, that the marked intervals are not necessarily identical for both components and do not need to be geoeffective storms as is the case for the detection with the long-term filters. Rather this method identifies intervals for which the filter baselines show consistent discrepancies, not following quiet variations for longer periods.

Using the KPIs from section 6.1.3, we can also here compare the initial method of residuals with its adapted counterpart as summarised in table 6.2. The adapted method for the residuals of X and Y performs significantly better than the initial method in terms of catching strong Dst and SYM-H values. Also when it comes to detecting specific events, we clearly see an improvement, as the number of detected events raises from 0 to 16 for X and to 20 for Y while the number of partially detected events raises from 11 to 22 for X and to 16 for Y. This clear improvement can be related to the fact, that through the sigma-clipping individual outliers are marked, while the adapted method generates intervals of at least 15 hours. Still, the adapted method misses 1 event for X and even 3 for Y.

6.2.3 Combining the Adapted Methods

As a resume, we conclude that the adapted residuals method is able to catch weak and medium, as well as strong events, and the derived limit method to detect strong events. Directly combining these methods holds the final disturbance interval detection. Its outcome is illustrated in figure 6.10. Please note, that the method for the residuals of X are combined with the derived limit method on $\bar{h}_{>24}$ to give the intervals for the X component, and the method for the residuals of Y is combined with the derived limit method on $\bar{h}_{>24}$ to give the intervals for the Y component, as indicated by the caption of figure 6.10 and notation in table 6.2 by res$X$+$\bar{h}_{>24}$ and res$Y$+$\bar{h}_{>24}$.

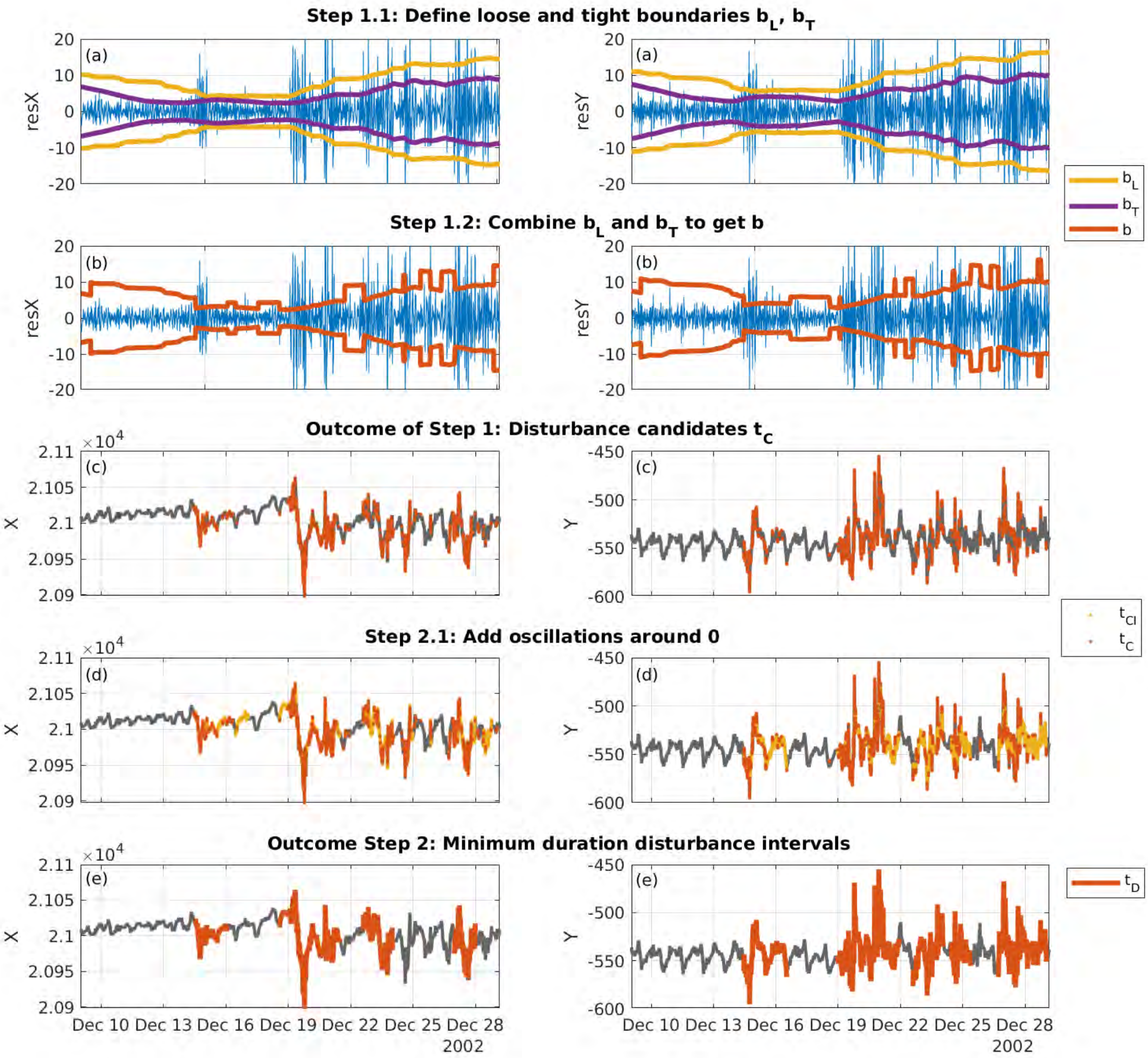

Figure 6.9: Visualisation of the two-step algorithm that is used to identify disturbance intervals for the residuals of X on the left and Y on the right. Residuals are in blue and components are in black. Panels (a) show the loose and tight boundaries b_L and b_T in yellow and violet, respectively, as defined in step 1.1. Panels (b) show the final upper and lower boundaries b (in orange) as defined by the combination of b_L and b_T in step 1.2. Panels (c) show the identified disturbance candidate minutes t_C (in orange dots) on the component (black) as outcome of step 1. Panels (d) indicate the added minutes t_{CI} (in yellow dots) during the residuals' oscillations around zero, as defined in step 2.1. Panels (e) show the outcome of Step 2, and thus the final disturbance intervals t_D (in orange), after removing intervals with lengths below the minimum duration as defined in step 2.2. All vertical axes are in nanotesla.

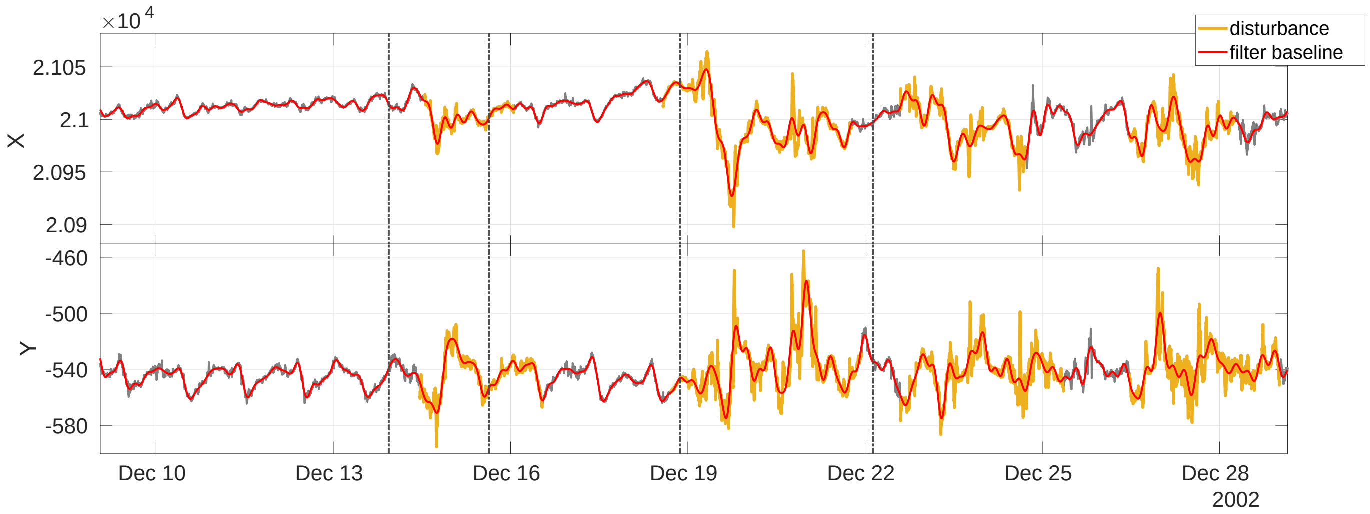

Figure 6.10: Full identification of disturbance intervals as produced by combining the adapted methods (res$X$+$\bar{h}_{>24}$ and res$Y$+$\bar{h}_{>24}$) for which the filter baseline should be replaced for the X (upper panel) and Y (lower panel) component. The intervals are marked in orange, and the filter baseline in black. The X and Y components are in grey in the background. The vertical lines mark a moderate and a strong events that occur during this time interval. The vertical axes are in nanotesla.

In figure 6.10, during the first days of the displayed period between 9th and 29th of December 2009, we observe a quiet period. The filter baseline follows the smooth X and Y variations as expected. Between 13th and 16th of December, a moderate event occurs which would be underestimated by applying the filter baseline. It is detected by both residuals, but slips through the derived limit for the long-term filter. The onset of this event is missed by a few hours, whereby the recovery phase was identified appropriately. Afterwards, another rather quiet period of a few days is observed until a second, stronger event occurs on December 19th and disturbs the components significantly for several days. Most of this period is identified as disturbed by both algorithms and results in a prolonged disturbance interval. For the onset and main phase of this storm, it is clear that using the filter baseline would result in underestimation of its strength. However, with regards to the event's recovery phase, it is not entirely apparent up until which point in time the filter baseline produces reliable results again, as no obvious quiet pattern can be determined. The answer is not trivial as we do not have a ground truth for how a baseline should look like, especially after a strong event and thus during its recovery phase. It is not obvious whether these succeeding, slightly disturbed variations are still within or already outside the limits of the typical day-to-day variations.

In order to get a more quantitative view on the algorithms, we look at their KPIs in table 6.2. The two combined methods do not miss any of the events in the list and both identify more than 90% of strong Dst and SYM-H. The amount of detected events is increased. However, the 13.25% of quiet minutes is marked as a disturbance and the total identified minutes (TOT) is rather high for Y.

All in all, the adapted methods and their combination are a clear improvement to the initially presented methodologies as we have seen qualitatively and quantitatively. However, there are still some caveats of the methods. By deriving upper and lower boundaries for the residuals, we had to overcome the issue of the zero oscillations. We

Adapted Method ideal value	TOT 25-30%	Dst 100%	SYM-H 100%	CK 0%	Detected 39	Partially Detected 0	Missed 0
$\bar{h}_{>24}$	13.18	85.44	89.51	0.54	15	18	6
res$X$	31.42	68.51	73.60	8.92	16	22	1
res$Y$	35.35	71.68	76.50	12.36	20	16	3
res$X$+$\bar{h}_{>24}$	35.55	90.98	94.36	9.33	24	15	0
res$Y$+$\bar{h}_{>24}$	39.16	91.95	94.84	12.82	27	12	0

Table 6.2: KPIs from section 6.1.3 for the adapted derived limit method applied on the long-term filter $\bar{h}_{>24}$ and the adapted sigma-clipping on the residuals for X and Y, as well as their combination. In the header the ideal value is indicated beneath each KPI.

did so by defining two durations: a minimum duration for the effects of a disturbance Δt_{CI} and a minimum duration of a disturbance to be considered Δt_{min}. This implies that any disturbance that manifests itself beneath 15h is missed, as well as events that cause zero-oscillations with recurrences above 8h. whereby the latter case seems to be less likely to happen, the minimum disturbance time puts a real restriction on the identified intervals. This should be kept in mind.

6.3 Quiet Variation Replacement during Disturbance-time

The combined, adapted algorithms from the previous chapter, i.e. res$X$+$\bar{h}_{>24}$ for X and res$Y$+$\bar{h}_{>24}$ for Y, provide intervals during which the filter baseline follows the disturbance induced variations closely, which leads to an underestimation of its effects. To avoid this, we look for a possible substitution of the filter baseline during the identified intervals. As discussed in the introduction, up to this date there is no ground truth on how quiet variations are supposed to look like quantitatively during disturbances and storm-time. The very least we will impose on the substitution, is that it incorporates typical quiet variations. As has been a common strategy up until now, we will split the substitution baseline into long-term and (sub-)diurnal variations and treat each of them separately.

Starting with the substitution of the long-term filter response, we will use the moving average over the past 3 days and denote it $\tilde{x}_{>24}$ and $\tilde{y}_{>24}$. This smooths disturbance variations and accounts for shorter trends that can be induced by disturbances that would be concealed in longer moving windows.

We will now look at how we can replace the combined (sub-)diurnal variations x_D and y_D. In chapter 5.2.2 we introduced three models that aimed at reconstructing observed quiet variations for the diurnal and semi-diurnal filter responses x_{24}, y_{24} and x_{12}, y_{12}. While the two analytical models, based on parameters like the solar longitude, local time and solar activity, reproduce general trends well, the shift model that is based on the filter responses themselves reproduces the intrinsic day-to-day variations the closest (also see table 5.1). To expand this model for the full combined (sub-)diurnal variations we develop it for the 8h- and 6h-filter analogously to what has been done in (5.13) and (5.14).

The full model then writes as

$$\hat{x}_{D,shift} = \hat{x}_{24,shift} + \hat{x}_{12,shift} + \hat{x}_{8,shift} + \hat{x}_{6,shift} \tag{6.3}$$

$$\hat{y}_{D,shift} = \hat{y}_{24,shift} + \hat{y}_{12,shift} + \hat{y}_{8,shift} + \hat{y}_{6,shift} \tag{6.4}$$

for both components. There is one important limitation we need to consider: at time-step t_0 we can only use this model up until $t_0 + 6$h, as we develop it also for the 6h filter. Assuming that a disturbance starts at t_0, after $t_0 + 6$h this model would be generated on disturbed information, namely the disturbance-affected 6h-filter response x_6. To avoid this issue, we do not use the model directly, but take its daily variation two days before the disturbance start t_0, i.e. $t_0 - 48$h to $t_0 - 24$h. Using the 48-24 hours instead of the 24-0 hours before, ensures that potential disturbance onsets are not included in the replacement. This gives us a 24-hour template with quiet daily variations. As disturbances may last longer, we repeat this template and extend it to fit the full disturbance length. The obtained replacement for the combined (sub-)diurnal variations with the shift model is denoted as $\tilde{x}_{D,shift}$ and $\tilde{y}_{D,shift}$.

We know that the combined (sub-)diurnal filter responses x_D and y_D follow the quiet variations well during quiet periods. Another possibility to replace them during disturbances is thus to use their variations from a previous, quiet interval. We can derive such intervals as we have done for the shift model by taking the variations from the previous 48h to 24h as a template and extend it to the length of the disturbance. We denote it as

$$\tilde{x}_D(t) = x_D(t - 24h) \tag{6.5}$$

$$\tilde{y}_D(t) = y_D(t - 24h)\,. \tag{6.6}$$

With this approach we obtain two substitution baselines by the superposition of the long-term filter replacement with the two combined (sub-)diurnal filter replacements. The baselines write as, for the X component

$$\tilde{x}_{B,shift} = \tilde{x}_{>24} + \tilde{x}_{D,shift} \tag{6.7}$$

$$\tilde{x}_B = \tilde{x}_{>24} + \tilde{x}_D\,, \tag{6.8}$$

and for the Y component

$$\tilde{y}_{B,shift} = \tilde{y}_{>24} + \tilde{y}_{D,shift} \tag{6.9}$$

$$\tilde{y}_B = \tilde{y}_{>24} + \tilde{y}_D\,. \tag{6.10}$$

To ensure smooth transitions, we apply a spline on 3 hours before and after the start and end of each disturbance. Figures 6.11 and 6.12 illustrate the filter baseline with both incorporated substitutions. Overall we can say that both replacements are quite similar and differ mainly on smaller scales. The differences manifest in small-scale ripples within the shift model $\tilde{x}_{B,shift}$ and $\tilde{y}_{B,shift}$ (in orange) compared to the smoother $\tilde{x}_B$ and $\tilde{y}_B$ (in green). For the moderate event between 13th to 16th of December both replacements show smooth variations. The possible onset of this event is not fully detected, such that the peak in X is preserved and will not be present in the residuals (after removing each baseline from the measurements). For the intense event between 19th to 22th December, the variations are also smooth for both replacements and we see that the general trend of both components, especially the one of X, are systematically followed. As for the disturbance detection, the period after the strong event is quite complex. The baseline is

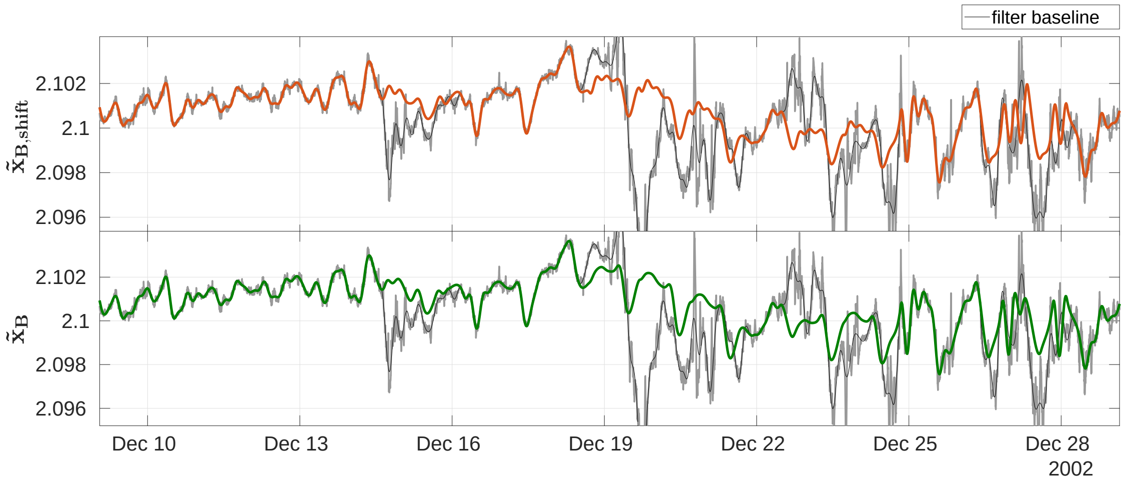

Figure 6.11: X Component: Comparison between the two baseline replacements. The component is in grey, the filter baseline in black. The shift model replacement $\tilde{x}_{B,shift}$ is in orange and the combined (sub-)diurnal replacement $\tilde{x}_B$ is in green. The vertical axes are in nanotesla.

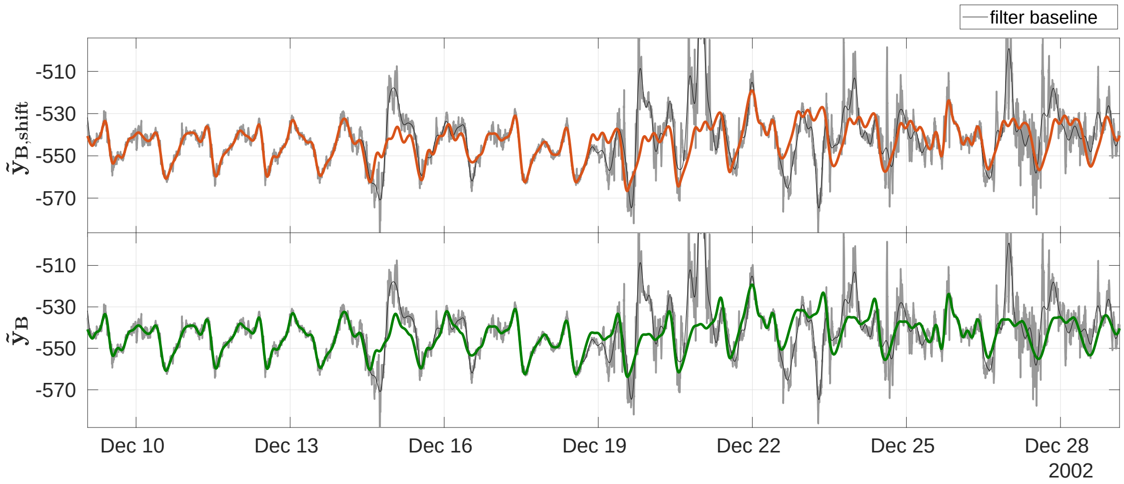

Figure 6.12: Y Component: Comparison between the two baseline replacements. The component is in grey, the filter baseline in black. The shift model replacement $\tilde{y}_{B,shift}$ is in orange and the combined (sub-)diurnal replacement $\tilde{y}_B$ is in green. The vertical axes are in nanotesla.

replaced according to the identified intervals and smooth, recurrent patterns are hard to identify for both baseline replacements. As mentioned before, it is not trivial to determine an appropriate baseline during this period.

Based on the two examples, we can make the qualitative choice of using $\tilde{x}_D$ and $\tilde{y}_D$ as they incorporate less small-scale features which are not necessarily present in the typical quiet variations. Further examples of this final baseline for the moderate event of mid-December 2002 is given in appendix E.2.

The problem of choosing a baseline is somewhat badly conditioned as we do not know the ground truth. A thorough investigation would be appreciated that analyses these baselines for sets and types of various events, ideally covering all solar cycle phases and seasons and tailored for specific purposes (global/local effects, certain physical phenomena like ring current or FACs, etc). Such an investigation is ideally done by involving the corresponding communities accompanied by transparent result discussions, including advantages and drawbacks of each baseline method.

6.4 Comparison with Existing Baselines

As there is no ground truth of quiet variations during geomagnetic storms and other disturbances, the applicability and validity of baselines is hard to determine, such as for the variations we observed after the 25th of December in figure 6.11 and 6.12. Van De Kamp (2013) uses a spectral analysis to show that only sources acting on interesting frequencies are contained within the baseline. Naturally, as the filter baseline is based on frequency regimes, only the fast variations that are most likely related to storms are part of the residuals. All the other, above 6 hour variations, are retained in the baseline. This is evident in Figure 4.2. Additionally, chapter 5 gives a detailed analysis on what sources make up the quiet-time filter baseline and we adapted the baseline during storm-time.

What Van De Kamp (2013) did and what we aim for here, is to compare the derived baseline with other baselines, namely the SuperMAG one from Gjerloev (2012) and the FMI one from Sucksdorff et al. (1991). The method from Van De Kamp (2013) and the one for the PC indices from Troshichev and Janzhura (2012) are designed for auroral and polar observatories and thus are out of range for low- and mid-latitudes considered in this work.

To determine the baseline, the FMI method performs a 5^{th} degree harmonic fit to hourly means, which are determined taking into account apriori information such as magnetic latitude and local time (Sucksdorff et al., 1991). The original software written in C is made available through the long-term ISGI repository. The method used by the SuperMAG service consists of rotating the magnetic data into an arbitrary magnetic coordinate system, followed by determining a daily baseline, annual trend and residual offset that differs for each of the magnetic field vector components (Gjerloev, 2012). Their baseline data is not directly accessible and several steps had to be executed to make them available for this work. SuperMAG provides the actual and baseline removed data in a magnetic local frame that uses an arbitrary declination. In order to compare them to the original data as provided by observatories from INTERMAGNET, SuperMAG data needs to be transformed to the local geographic frame first, followed by subtracting the baseline removed data from the measurements in order to retrieve the baseline. Hereafter we compare our method to the FMI method, referred to as x_K, y_K; and to the SuperMAG method, referred to as x_S, y_S. As such, Figure 6.13 demonstrates our baseline (green) in comparison with the X, Y components (grey), the FMI (blue) and the SuperMAG (red) baselines, whereby grey shaded time intervals indicate non-CK48 days.

During magnetically quiet days (white background), our and FMI baselines closely follow the magnetic activity, capturing the day-to-day variability smoothly and showing little discrepancies between them. The SuperMAG baseline x_S, y_S shows some distinct differences, especially for the X component. The actual measurements are not always followed closely, e.g. there is a clear positive and negative offset between the magnetic observatory data and SuperMAG estimation of the quiet baseline for the X component during the afternoon / night of December 10th and 13th. In general, the SuperMAG method follows a rather steady pattern showing minor differences from one day to another. As shown before, there is a non-negligible day-to-day variation within the signal, which is most likely induced by atmospheric drivers. These variations are well captured by x_B, y_B and x_K, y_K, but less with x_S, y_S indicating that it may lead to overestimation of

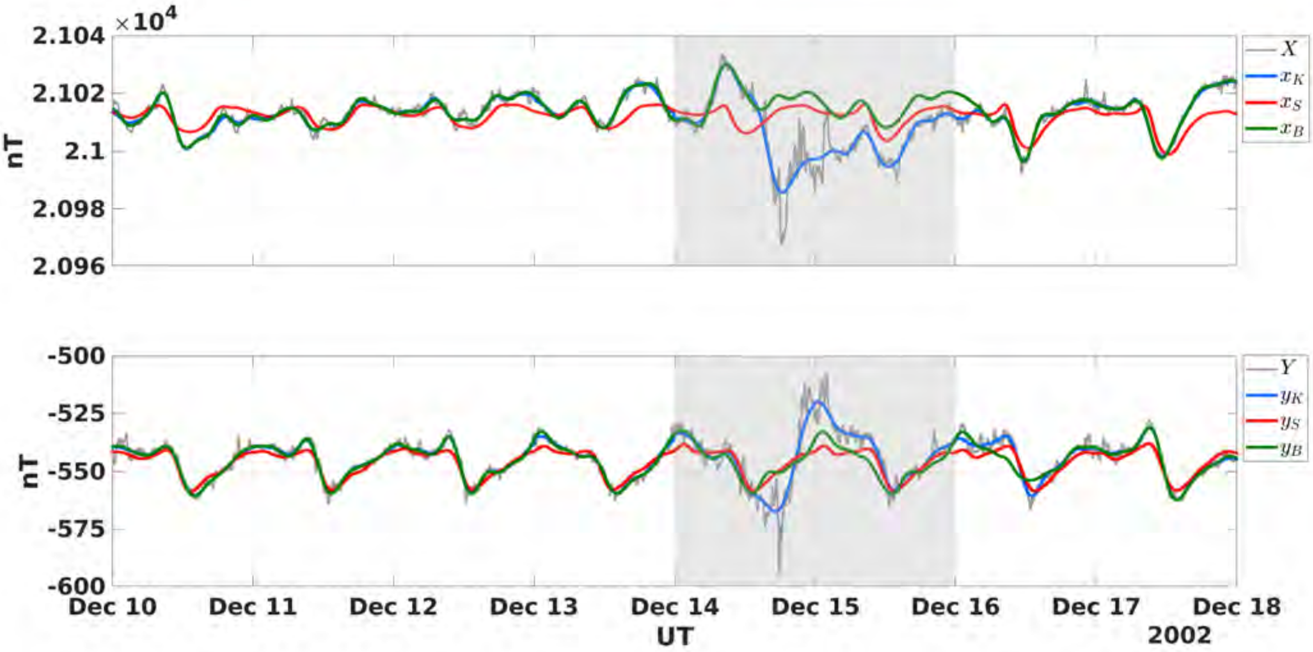

Figure 6.13: Comparison of baseline methods. The methods of the introduced baseline (green), FMI (blue) and SuperMAG (red) for X, Y components (grey) at CLF during winter 2002 are presented. The grey shaded areas indicate non-CK48 days. All vertical axes are in nanotesla.

magnetospheric drivers during quiet days with increased day-to-day variability. To be able to quantitatively compare baselines, we calculate the difference between ours and each of the two other methods for all CK48 days of 2009, during a minimum of solar activity. We make the simple assumption that this difference can be described by a Gaussian distribution, using its variance to quantify deviations. For the X component, we find a variance of 1.6 nT, and for the Y component 1.7 nT between our baselines and the FMI ones; and 6.2 nT, and 4.6 nT between our baselines and SuperMAG ones. This implies that our determination of baselines can be used instead of the FMI method without causing major changes in the baseline reconstruction during magnetically quiet days. Additionally, the filtering method together with the replacement during disturbances is able to produce baselines without any further information than the magnetic measurements themselves, whereas the SuperMAG method needs the magnetic latitude as an input, which is evolving over time and not trivial to be determined in real-time. This property gives the introduced method the main advantage of being directly applicable, i.e. as soon as the geomagnetic field data is available.

Let us now come to the disturbed period. During non-CK48 days, indicated by the grey shaded area in Figure 6.13, clear differences between the three baseline methods are evident. Our filter method follows the activity very closely during the start of the event and then continues with similar variations as during the quiet days before. The FMI method on the other hand follows the storm signatures clearly, reacting to the strong deflection. The SuperMAG baseline simply continues it's course. As we do not know the ground truth for these variations we can only discuss possible errors. For the FMI method, as it closely follows the activity, it would suggest that the storm is underestimated, rather similar to using the original filter baseline. For the SuperMAG baseline, the quiet variations do not closely follow the magnetic field's variations. For our adapted filter baseline, as it follows the onset of the storm rather closely, this implies that it underestimates the onset which effects may not be reflected in the residuals.

6.5 Discussion

The first two parts of this chapter deal with the identification of intervals for which the filter baseline is not appropriate. This is followed by the replacement with an adapted baseline containing quiet variations during the identified interval. We then compared the full baseline with existing ones, showing that the presented one can be used as an appropriate baseline in general. Additionally, the introduced procedure can be executed in real-time as it works only on the filter data itself. No further input is required to derive the full baseline. As there is no ground truth in what a baseline has to look like, the user of a baseline needs to be aware of how it is derived and where the caveats are. In the following we provide a discussion that should be kept in mind.

The identification of when to replace the filter baseline is a complex problem. First of all, periods and conditions need to be determined for which the filter baseline underestimates disturbance impacts. To answer this question a set of events needs to be determined for which underestimation happens, implying that the effects are known. Whereby this may be easier for geomagnetic storms and events with high geoeffectiveness, effects of weak to moderate events are not as clear to be determined accurately. In the course of this chapter, we encountered such problems with e.g. event (4) in figure 6.7 or for the prolonged disturbed period after 25th of December in figure 6.10. To some extent, choices have to be made here which the user needs to take into account. We can conclude that the disturbance determination as introduced here is at least consistent as it is derived on fixed, unchangeable rules that treat each data point the same way. For the presented methodology we saw that e.g. onsets of weak to moderate storms are not fully reflected within the residuals when applying the full baseline. Other caveats include that the derived-limit on the long-term filters is based on the horizontal intensity and as it is indiscriminately used for both components it may lead to false-positive intervals. The sigma-clipping method is build on the premise that the quiet variations make up the majority of the signal and that storm variations are stronger and occur less frequently. While this is certainly true during solar minimum, we cannot guarantee this holds during solar maximum when external driving is significantly increased. For the adapted sigma-clipping, a parameter-tuning with the help of the KPIs can help in identifying ideal values for e.g. the minimum duration of disturbances Δt_{min} and minimum duration of disturbance effects Δt_{CI}. Other caveats may be overcome by investigating further methods, in addition to the sigma-clipping such as discussed in 6.1.4. Even though the presented KPIs are a good start, more refined KPIs including extended storm and disturbance lists, as well as more granular detection classes can help improve methods more quantitatively.

The used replacement during disturbances is based on variations from two days before the start and then duplicated for the duration of the disturbance. This implies that the baseline assumes the same variations of this interval during the entire disturbance length. We have seen that there is an intrinsic day-to-day variability within quiet variations. Such a variability is not taken into account by the introduced replacement. Fair enough, as there is no knowledge of a baseline during storm-time, we may choose to leave out day-to-day variability during storm-time. Such an approach has been also followed by Gjerloev (2012) and Van De Kamp (2013). Additionally, Van De Kamp (2013) improves his templates by using variations from before and after the event. For an operational, real-time determination we have no information about conditions after a disturbance event and cannot apply similar strategies. However, for post-processing such methods should be considered. As pointed out on several occasions, the biggest challenge in quantifying baselines is that there is no ground truth. The concept of a baseline was introduced by Bartels et al. (1939). Since then Mayaud (1980) tried to concretise this concept. Up to today, there is no commonly accepted way of how a baseline has to look like. Their guidance still is preserved. The baseline should be a smooth curve that is composed of the quiet sources of the geomagnetic field. For the filter baseline this is exhaustively showed in chapter 5. Furthermore, the fact that there is no quantitative way to validate quiet curves remains especially true during storm times. For example, in Figure 6.13 the adapted filter baseline x_B, y_B and the SuperMAG baseline x_S, y_S during the two disturbed days are very similar to their quiet curve of the preceding day, which can be interpreted physically as a fully developed Sq current cell. However such a full system does not necessarily form during a disturbance event (Le Huy & Amory-Mazaudier, 2008) which may be even the case in this example, as the actual measurements are very different from the expected Sq current signature. In order to support the choice of which quiet variations should be used to replace the baseline during disturbance-time, the actual derivation of the index with different baselines may be helpful. This way, a set of possible indices is created, which can be used to evaluate effects of known events and support the decision of which baseline performs better.

It is important to keep such considerations in mind when employing this baseline, especially for index derivation purposes. All in all, the presented baseline is consistent and contains quiet variations appropriately, for CLF.

According to chapter 4.1, we chose CLF to illustrate the methodology and results because it is a representative station for mid-latitudes and provides ready access to considerably good data quality. The question remains if the presented method is applicable for other stations such that the results hold.

In fact, the limit h_L needs to be derived for each station separately. Investigations show that $\bar{h}_{>24}$ is reasonably well correlated with all stations in mid-latitudes considered in this work, see figure 4.1. The corresponding determination of the SYM-H limit is, on the other hand, more tedious. For each station, the Sq current patterns need to be investigated according to SYM-H level, as has been done in figure 6.4. Ideally, objective criteria should be put into place to decide at what point the Sq patterns are too disturbed and thus define the SYM-H limit. Once such a limit is defined, it may be applied for periods over a few years but then would need re-calibration as the secular variation moved the station to different magnetic latitude, changing the Sq patterns at the specific station. Such a re-calibration, however, does not impact the near real-time operability. As this method is supposed to mark strong events, it may be also appropriate to use a SYM-H limit that is commonly associated with strong events, like SYM-H$< -50\,$nT. Such a threshold would need to be discussed and elaborated with the community.

The adapted sigma-clipping works as long as residuals react clearly to disturbances which is largely guaranteed by the signal filtering itself. The residuals are generated by removing all variations above 6 hours from the measurements. This means, that all faster variations, below 6h, are contained within the residuals. Disturbances act on such timescales independent of location and thus are supposed to be contained, in a first order, within the residuals. Therefore the residuals together with the sigma-clipping may be applied to other stations.

This implies that the introduced baseline derivation should be applicable to other mid-latitude observatories, in general. Extended analysis of the baseline for each of the observatories certainly would be supportive.

Part III

Geomagnetic Variations with Artificial Intelligence

Chapter 7

Introduction to AI

The field of Artificial Intelligence (AI) is a rapidly advancing field that seeks to develop intelligent machines capable of simulating human-like cognition and decision-making. It involves the creation of algorithms and systems that can learn from data, recognize patterns, and make predictions, enabling machines to perform tasks that traditionally required human interaction. AI has found applications across various industries, including healthcare, finance, transportation, and entertainment, revolutionizing the way we live and work. As research and development in AI continue to progress, its potential to transform our world and address complex challenges is becoming increasingly evident. In contrast to traditional algorithms that use pre-defined set of procedures by developers, AI algorithms use input data (experience) to derive procedures themselves (deriving statistical decisions based on experience).

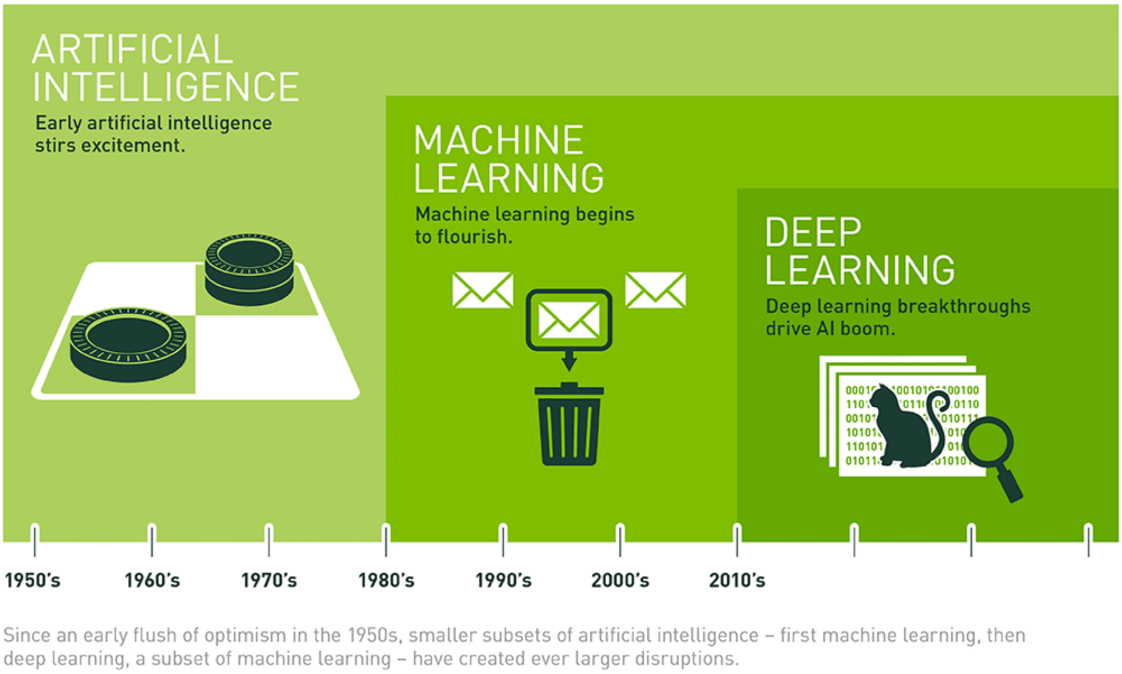

Figure 7.1: An overview of the time-line and development of AI, ML and DL. Taken from nvidia.com.

As a discipline of AI, Machine Learning (ML) uses large quantities of input data that are used to train algorithms. These algorithms learn on how to produce desired output by themselves without further interaction of the developer. The fundamentals of ML were introduced by McCulloch and Pitts (1943) who, inspired by the human brain, introduced the first mathematical models of neural networks. Since then the methods of ML have been increasingly developed and made accessible to a ever growing userbase. Especially during the past decade, ML techniques that leverage several layers of neural networks, so-called deep neural networks, have demonstrated successful applications across a wide array of domains and gave birth to the sub-domain of Deep Learning (DL). Very good high-level introductions to ML and DL are given by Serrano (2021) and Trask (2019) and the standard literature covering DL techniques in a more mathematical way is Goodfellow, Bengio, and Courville (2016).

As such, ML and especially DL techniques have been considered in a wide range of space weather problems (Camporeale, 2019). Successful AI applications include flare forecasting, coronal hole detection and magnetospheric condition determination, as well as solar wind speed determination from solar images (E. J. Brown, Svoboda, Meredith, Lane, & Horne, 2022). Especially magnetic index forecasting with ML has shown promising results. Such models include solar wind data from satellites situated at L1 and are trained to forecast responses of geomagnetic indices, as well as geomagnetic perturbations on ground (Keesee et al., 2020; Coughlan et al., 2023). Other approaches take a further complexity step and apply ML techniques to forecast geomagnetic perturbations from solar disk images (Bernoux, Brunet, Buchlin, Janvier, & Sicard, 2022). The promising AI results in the domain of space weather motivate this second part of the thesis which is dedicated to leveraging artificial intelligence methods for the description and understanding of quiet variations. This introductory chapter gives a brief overview of artificial intelligence, machine learning and deep learning, outlining the most important concepts and techniques needed for its application. The models and results of these techniques are presented in chapters 9 and 8 and discussed in chapter 10.

7.1 Machine Learning

As humans, we make decisions based on experience. Experience for a machine is data. As such, machine learning describes the field of artificial intelligence for which the computer is able to make decisions based on data without further interaction of the developer.

In order to solve a given problem, the computer uses data to build a **model** which is basically a set of rules that represent the data. Models are build by training **algorithms** which are procedures or sets of steps that solve certain problems and perform computations on available input data. Trained models can then be used to make decisions or predictions on new, not yet encountered input data. **Features** are any properties or characteristics of the data that the model can leverage to make predictions. The desired output data, which is referred to as the **label**, are the variables to be predicted. Depending on the properties of the label, two types of supervised learning models are distinguished:

1. Regression models that predict numerical data, such that the output can be any number
2. Classification models which output are concrete states, categories or classes.

The branch of machine learning that uses labeled data is called supervised machine learning. In this case, the features which are of interest for the prediction (=labels) are pre-determined and explicitly fed to the computer. Two other types of machine learning use unlabeled data: unsupervised machine learning, in which the computer finds patterns on its own (like e.g. clustering or dimensional reduction), and reinforcement learning, in which the computer learns from unlabeled data on its own while desired behaviours are rewarded and negative ones are punished (which is successfully applied in e.g. video games and management of resources). In this work we consider supervised machine learning.

Let us consider a basic problem (adapted from Serrano (2021)) to get acquainted with the basic nomenclature of machine learning. Sometimes, an email friend from work, Sandra, sends us spam emails, which we would like to avoid. Most of the time, however, she sends us emails that are highly relevant, which we will relate to as ham[1]. The tracked information of received emails is summarised in table 7.1 as labeled data. In this example the features are 'Day of the week', 'Attachment size in kilobyte (KB)' in column 1 and 2 and the label is 'Spam or Ham' in column 3. As the label has two classes, namely 'Spam' and 'Ham', we are faced with a classification problem. From this data, we would like to build a model that tells us if we should read the next email from Sandra or not. By human-eye it is possible to scan this table and come up with rules according to the two first columns and we can derive two models.

Table 7.1: Table summarising data from received emails which are classified as spam or ham.

Day of the week	Attachment size in KB	Spam or Ham
Monday	1	Ham
Tuesday	2	Ham
Saturday	16	Spam
Sunday	20	Spam
Sunday	18	Spam
Wednesday	3	Ham
Friday	5	Ham
Saturday	25	Spam
Saturday	3	Ham
Tuesday	1	Ham
Thursday	3	Ham

1. Model: According to 'Day of the week', an email is generally spam when it is received during week-ends
2. Model: According to 'Attachment size in KB', an email is ham when it has an attachment smaller than 15KB.

The question is how a computer is able to learn independently from this data. Let us therefore consider the well-known linear regression algorithm. Reformulating the classification problem from before, the label could be e.g. the probability that an email from Sandra is spam to render it a regression problem for which we would like to find a linear equation that describes the probability. Also, linear regression has been applied several times throughout this thesis, e.g. to determine the threshold for the long-term filters in chapter 6.1.1.

The linear regression algorithm is a common and easy-to-understand method to describe data. Using this example, further mathematical concepts and operating principles

---

[1] Monty Python Flying Circus, 1970

that are leveraged in machine learning algorithms can be introduced and easily made accessible. In fact, a linear regression can be realised with ML techniques. However, in practice ML methods are computationally too expensive compared with its simplicity. The equation of linear regression writes as

$$y = wx + b \tag{7.1}$$

with x being the features, w being the weight for feature x and b being an offset or bias. The label is y which we would like to predict. For the one dimensional case in graphical sense, w is the slope and b is the y-intercept. A change in the slope equals a rotation and change of b equals a translation of the line.

Iteratively, the regression algorithm adjusts the weight and bias until an optimal solution is found. An iteration is referred to as an **epoch** during which the weight and bias are adjusted by a small number called the **learning rate** η. Number of epochs and learning rate are usually fixed before training a model. In figure 7.2, the outcome after each epoch are visualised on a dataset including 6 two-dimensional data-points. The algorithm starts with an initial guess for w and b as depicted in the left panel 'Starting point'. During each epoch, the weight and bias are adjusted by the learning rate η to move closer to the points. During the first 10 epochs in panel 2 a considerable change is observed, moving the line consistently closer to fitting the points. During the following 40 epochs in the third panel, the line is still adapted but in smaller steps. Finally in the fourth panel, during epochs 51-10000, the line changes marginally and eventually is well fitted to the points.

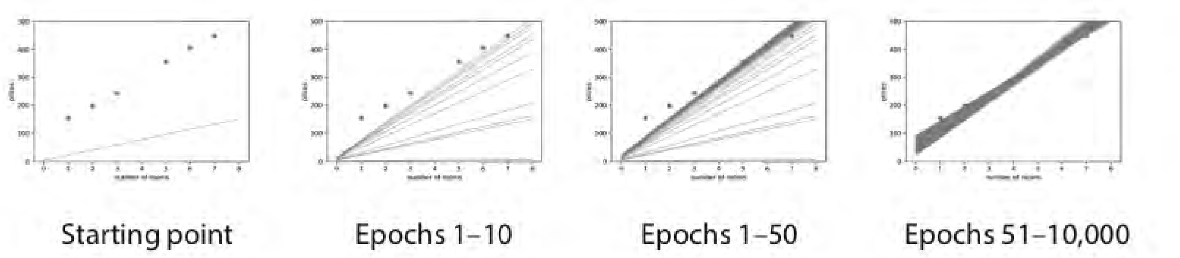
Starting point Epochs 1–10 Epochs 1–50 Epochs 51–10,000

Figure 7.2: The linear regression improvement with increasing iterations (epochs). From left to right: the resulting line with randomly initialised weight and bias at the starting point; the adapted lines during epochs 1 to 10; the adapted lines during epochs 1 to 50; the adapted lines during epochs 51 to 10000. Taken from Serrano (2021)

At the end of each epoch, the **loss function** is calculated to measure the results of the algorithm. One of the most common loss functions are the Root Mean Square Error (RMSE) which is defined as

$$RMSE = \sqrt{\frac{\sum_{i=1}^{N} (\hat{y}_i - y_i)^2}{N}} \tag{7.2}$$

with $\hat{y}_i$ being the predicted label. The smaller the RMSE, the closer the model describes the data, and thus finding the optimal RMSE is a minimisation problem. **Gradient Descent** is one of the most commonly used methods for solving it. Gradient Descent works by calculating the gradient (derivative) of the loss function with respect to each parameter. The gradient points in the direction of the steepest increase of the loss function and by taking its negative steepest decrease of the loss function is obtained. The learning rate η gives the amount of change and thus is a crucial for the convergence of the gradient descent. If the learning rate is too large, the algorithm may overshoot the optimal solution and fail to converge and if the learning rate is too small, the convergence may be very slow. The algorithm may end after a preset number of epochs, but flexible ending criteria may be used as well. Such criteria include thresholds for the absolute value or rate of change of the loss function. Crucial parameters like the number of epochs or the learning rate, that are part of the algorithm are referred to as **hyperparameters**. Their choice can significantly influence model performance. Ideal values can be found with hyperparameter-tuning techniques, like grid search or random search, during which models are trained with different values of hyperparameters and their performance is compared. In the case of the basic linear regression in equation (7.1), w and b are referred to as **trainable parameters**. For polynomial regressions, such as the amplitude description in figure 5.14, all the weights w_i and the bias b are trainable parameters.

Common problems in machine learning are **overfitting** and **underfitting**. Figure 7.3 illustrates a set of data points that form a parabola and three polynomial models with varying degrees. Model 1 has degree 1 and fits a line. This is a clear underfit of the data, i.e. the model is too simple to describe the data's general shape. Model 2 fits a polynomial of degree 2 which describes the data well, while having some error (noise). Model 3 on the other hand fits the observations perfectly by a polynomial of degree 10. This is a clear example of overfitting. The model is not able to predict new observations adequately as it is too complex. Ideally, any trained model generalises the available data without describing too few (too simple) nor too many (too complex) details. In order to overcome the problem of underfitting and overfitting, i.e. to choose the model that gives the best generalisation, the available data is split into three, non-overlapping sets:

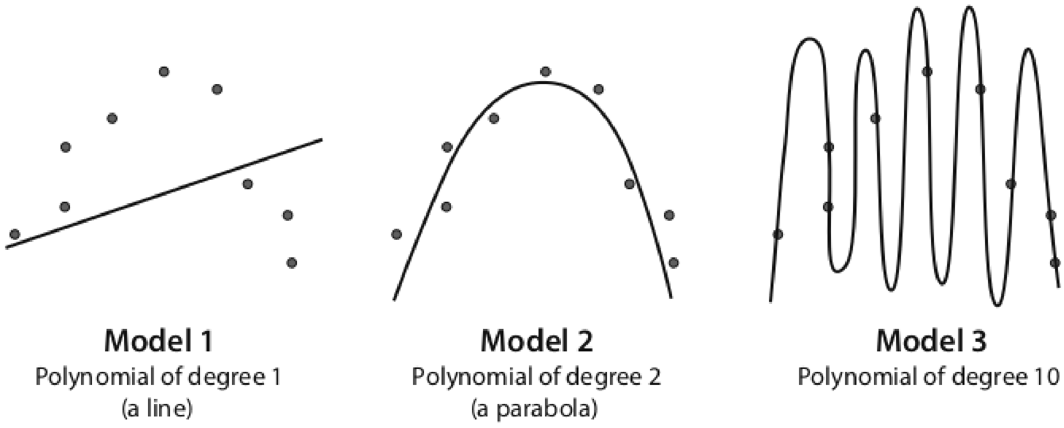

Figure 7.3: Examples of polynomials with degree 1 (left), degree 2 (middle) and degree 10 (right) for fitting a set of points. Model 1 illustrates underfitting, while model 3 illustrates overfitting. Taken from Serrano (2021)

- The **Training Set** is used to train the model and learn patterns and relationships within the data, like adapting the weights and bias of the polynomial regression.
- The **Validation Set** is generally used to understand if models under- or overfit and to tune hyperparameters with the goal of finding ideal values of a model.
- The **Testing Set** is used to provide an unbiased final evaluation of a model.

In general, when the model performs poorly on the training and validation sets, it is underfit, while when it performs well on the training set but poorly on the validation set, it is overfit. An adequate model will perform well on both the training and validation sets. Depending on the size of the inital dataset, the ratio between training, validation and testing sets may vary (Guyon, 1997). In practice, the rule of thumb is to split the data into 60-20-20% or 80-10-10% for training, validation and testing set, respectively. The **Complexity Graph** is an effective tool that can help choosing the right model complexity to avoid over- and underfitting. It visualises the training error, which is supposed to be a downward curve, and the validation error, which is a curve that shows some downward trend before an upward trend. An example of the complexity graph of a best-fit degree polynomial is depicted in figure 7.4. The number of degrees is on the horizontal axis and the error on the vertical axis. For degrees smaller than 4, the training and validation errors keep falling, and thus the model improves which indicates underfitting. Above degree 4, even though the training error goes down, the validation error increases, which indicates overfitting. In this special case the best model minimises the training error according to the validation error at degree 4. For real applications, these curves may get very complex and it depends upon the problem to find appropriate trade-offs. Another possibility to avoid overfitting is **Regularisation** which introduces a measure of complexity for the model. Two typical measures based on the weights of the model are the L1 norm, as the sum of the absolute weights of the model, and L2 norm, as the sum of the squares of the weights. L1 tends to remove features (e.g. sets the weight to 0) which may be beneficial when a lot of features are available, referred as to lasso regression (Tibshirani, 1996). L2 tends to provide lower weights in general, which may be

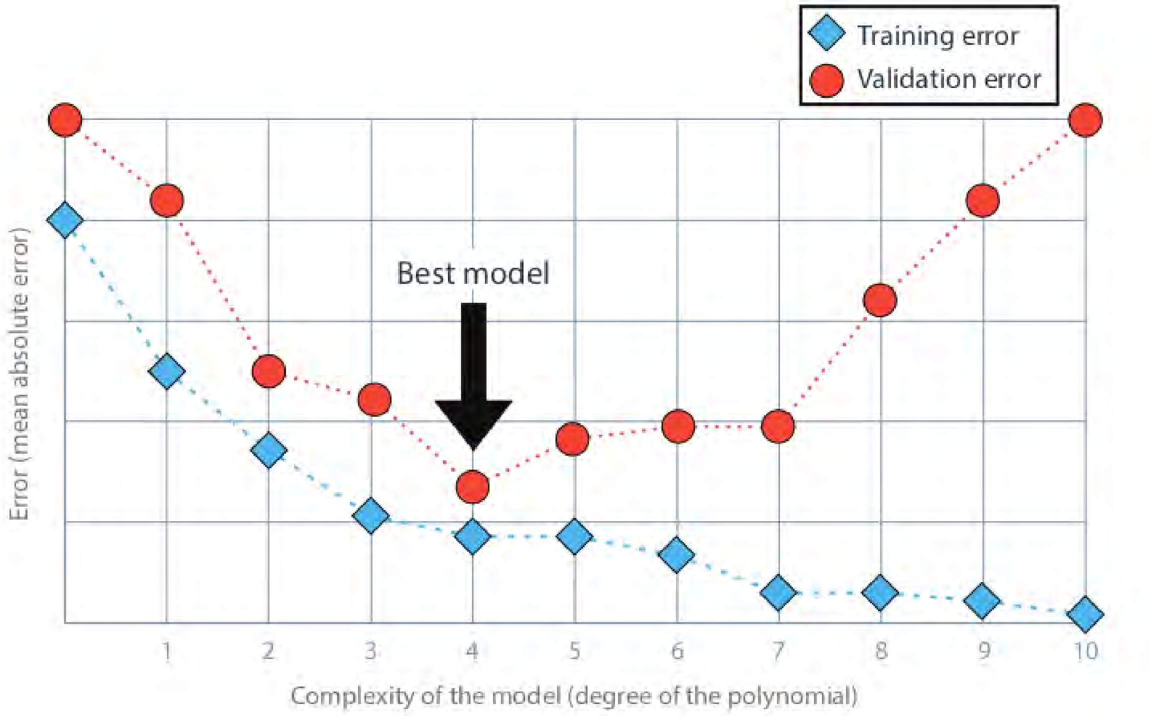

Figure 7.4: An example of a complexity graph that visualises the error for the training and validation sets of polynomial models with degrees 0 to 10. The best model is indicated by a black arrow. Taken from Serrano (2021)

beneficial when few features are available or all features are of similar importance, referred to as ridge regression (Tibshirani, 1996). Together with the loss function or regression error, like the RMSE in equation (7.2), the regularisation term (L1 or L2 norms) can be leveraged to find the least complex model with the best performance by minimising either

$$\text{Lasso regression error} = \text{regression error} + \text{L1 norm} \tag{7.3}$$

$$\text{Ridge regression error} = \text{regression error} + \text{L2 norm} \tag{7.4}$$

Figure 7.5 shows a polynomial models with and without regularisation. In the left panel, no regularisation was applied, leading to an overfit. In the middle panel, the L1 regularisation was applied which favours the removal of features by setting the weights to zero. This leads to an underfit of the model in this case, as all features are of equivalent importance. In the right panel, the L2 regularisation was applied, adjusting weights appropriately to find the correct degree. It is also possible to describe how important regularisation is by multiplying the regularisation term by the hyperparameter λ. For $\lambda = 0$ no regularisation is applied and thus highly complex models may be favoured, while a high λ favours simpler models. The regularisation parameter is commonly chosen as powers of 10, like 10, 1, 0.1, 0.01. As a hyperparameter, ideal values for λ can also be determined during hyperparameter-tuning.

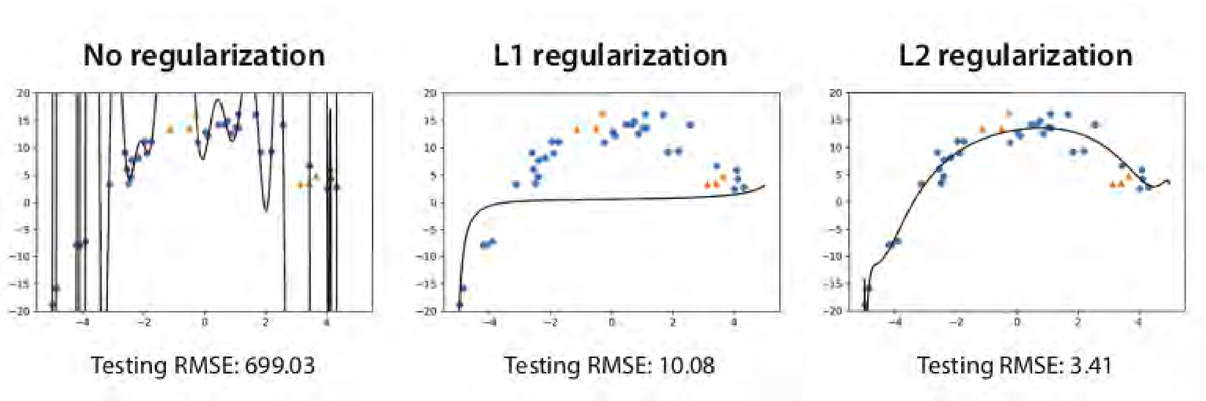

Figure 7.5: Examples of models with and without regularisation including the root mean square error (RMSE) on the testing set. The left panel shows the model without, the middle with L1, and the right with L2 regularisation. Taken from Serrano (2021)

Having familiarised ourselves with the terminology, let us now introduce one of the most commonly known machine learning algorithms: Random Forests. These allow for an intuitive approach of the basic concepts of machine learning and, apart for model derivation, are often used for feature selection purposes. This is followed by the introduction of very successful deep learning techniques that leverage neural networks for the specific case of sequential time-series data.

7.1.1 Random Forest

A Random Forest is a supervised machine learning method that can be used for both classification and regression problems and was introduced by Breiman (2001). It is a powerful algorithm that combines the predictions of multiple decision trees to improve accuracy, reduce overfitting, and enhance generalisation on new data. A decision tree is a tree-like structure where each internal node represents a feature, each branch represents a decision based on that feature, and each leaf node represents the predicted output or class label. An example of a decision tree is depicted in figure 7.6. A decision tree is based on yes-or-no questions (boundaries) and is represented by a binary tree with root node (the start), decision node, leaf nodes (a node which has no branch emanating from it), branches (edges that emanate from a decision node). The **depth** of a decision tree is the length of the longest path from a root to a leaf, e.g. the decision tree in figure 7.6 has a depth of 2. The building of decision trees is done by determining the most important features, i.e. the feature and associated boundary that split the data the best. For regression problems, the root mean square error is commonly used. To evaluate the performance of classification models, three commonly used measures are:

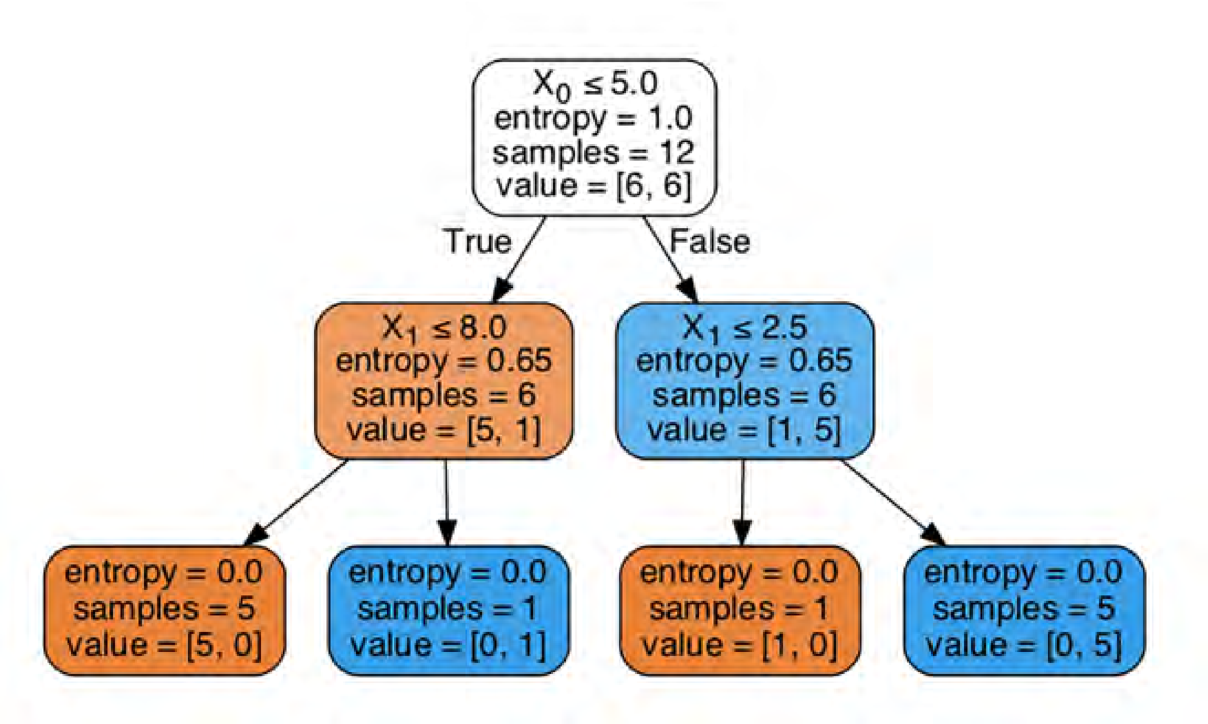

Figure 7.6: An example of a decision tree based on two variables x_0 and x_1 into two categories (e.g. squares and triangles) for a total of 12 samples. Each nodes indicates the decision criteria, the entropy, the number of samples and their classification. The two-dimensional visualisation of this split is illustrated in figure 7.7. Taken from Serrano (2021)

- **Accuracy** tells how often the model classified the data correctly. An accuracy of 100% indicates that all data are classified correctly.

$$Accuracy = \frac{\text{correct classifications}}{\text{total classifications}} \tag{7.5}$$

- The **Gini Impurity Index** is a measure of how diverse a dataset is. It is defined as

$$Gini = 1 - p_1^2 - p_2^2 - \cdots - p_n^2\,, \tag{7.6}$$

  with $p_i = \frac{a_i}{m}$, whereby m is the amount of elements in the dataset, n is the number of classes and a_i is the number of elements belonging to the ith class. The lower the Gini index, the purer the dataset, i.e. the classes contained in a leaf-node are similar, and thus the better the model.

- The **Entropy**, similar to the Gini index, is a measure of the diversity of a dataset and is defined as

$$Entropy = p_1 \log_2(p_1) - p_2 \log_2(p_2) - \cdots - p_n \log_2(p_n)\,, \tag{7.7}$$

with p_i being the same as in (7.6). The lower the entropy, the more similar the elements of the dataset. The entropy criteria tends to give better results but comes at a higher computational cost compared to the Gini index.

When building a decision tree, decision stumps (decision trees with depth 1) consisting of one node and two leaves per feature are created. Each leave is evaluated by the three measures and an index for each stump is calculated that is used to build the tree. Starting from the root node, the data is split according to the best feature into two leafs. The resulting samples of each leave are evaluated. If the samples are not ideally split, the leave is turned into a decision node with two further leaves. This procedure is iterated until a stopping condition is reached. Such conditions may be a minimum amount of change in accuracy, the reaching of a threshold for Gini impurity index or entropy or the reaching of the maximum depth of the tree. All of these are hyperparameters of a decision tree and thus of the random forest. They are set before training and optimum values may be found by hyperparameter tuning methods. For two features x_0 and x_1 and corresponding labels 'square' and 'triangle' a two dimensional plane can be used to visualisation, as depicted in the left panel of figure 7.7. During the first iteration depicted in the middle panel, the feature x_0 is determined as best split, drawing the vertical line at $x_0 = 5$. This creates a decision tree with two leaves. Each of the leaves contain one wrong classification and thus are turned into decision nodes. In the second iteration, depicted in the right panel, the best split of the left node is found to be feature x_1 with boundary $x_1 \leq 8$ and the right node by $x_1 \leq 2.5$. Each datapoint is accurately classified and the decision tree is build. The corresponding decision tree with depth 2, including decision criteria, entropy values, number of samples in each node and the value describing the amount of data points for label in each node is illustrated in figure 7.6.

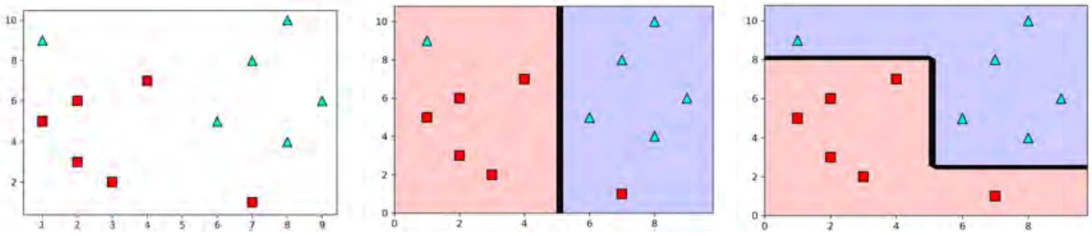

Figure 7.7: Two-dimensional illustration of domain splitting for the decision tree in figure 7.6. The left panel shows the distribution of the samples. The middle panel, after the first split (depth 1 in the decision tree) and the right panel the final split (final split at depth 2). Taken from Serrano (2021)

A random forest algorithm is an ensemble method consisting of many decision trees. It is categorised as a bagging method. Ensemble models, also called strong learners, are a collection of models, or also referred to as weak learners, joined together to improve predictions. Bagging includes the training of several models by using randomly drawn subsets of the input data (with replacement) which are the weak learners. The other ensemble method is called boosting and starts by training a first random model (first weak learner) and builds following models by improving poor predictions of the previous ones by focusing on mislabeled data (succeeding weak learners).

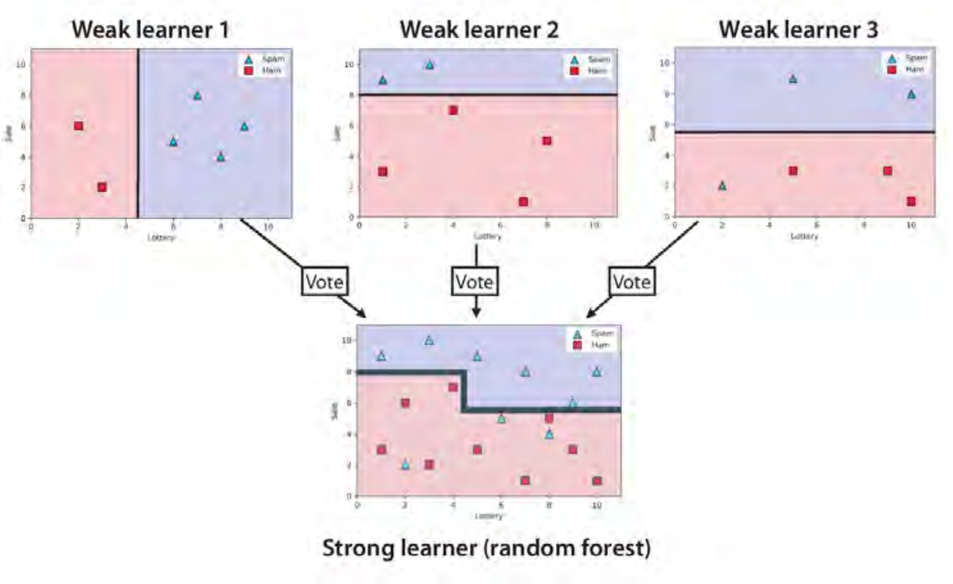

Figure 7.8: An example of random forest as a bagging ensemble method. Through voting of each weak learner (simple decisions trees), a strong learner is derived (random forest). Taken from Serrano (2021)

For both methods, the final output of classification problems is generated by voting of all weak learners, while in regression problems the final output is derived as the average of the weak learners. An example of a random forest for a classification problem (ham or spam email according to the features 'number of words lottery' and 'number of words sale') is depicted in figure 7.8. Each weak learner 1, 2 and 3 is based on a subset of the total input points and in general a simpler model. The final strong learner is then created by counting the votes of each of the weak learners, i.e. by majority.

7.2 Deep Learning

Deep Learning (DL) is a discipline of ML that makes use of Artificial Neural Networks (ANNs) that are based on cognitive functions of the human brain. ANNs have been successfully applied in a wide variety of fields leading to promising results (Sarker, 2021). The building blocks of an ANN, or for short Neural Network (NN), are **perceptrons** which simulate neurons of the human brain (McCulloch & Pitts, 1943). Figure 7.9 illustrates the functionality of a perceptron, indicating the neuron's equivalent. The perceptron consists of input variables x_i (axons), weights w_i (synapses) and a bias b, an activation function f and an output $\hat{y}$ (output axon). Per perceptron, there are $i = 1, ..., n$ inputs and corresponding weights and one bias b. The mathematical description of the perceptron (cell body) is given in equation (7.8) on the left of figure 7.9. The output of a perceptron can act as input for other perceptrons. Neural networks are build by combining layers of perceptrons, as depicted in figure 7.10. Features make up the input layer and labels the output layer. In between, layers of perceptrons are referred to as **hidden layers**.

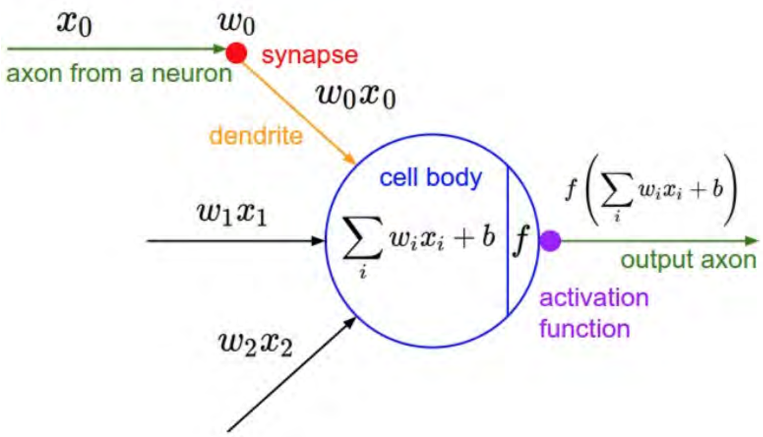

$$\hat{y} = f\left(\sum_i w_i x_i + b_i\right) \tag{7.8}$$

Figure 7.9: Illustration of the functionality of a perceptron (neuron) with the equivalent of a human brain cell. The perceptron receives input features (axons), weights (synapses) and a bias over which it creates the sum. The output is the activation function applied on the sum (within the cell body) and is written in equation (7.8). Taken from Serrano (2021)

The **depth** of a neural network is the number of hidden layers plus 1 (the output layer). The **size** of a layer depends upon the number of perceptrons contained in that layer. For example, the depth of the NN in figure 7.10 has a depth of 4 and the first hidden layer has a size of 6. The trainable parameters of a neural network are the weights and biases of its neurons. The training of the neural network is referred to as back-propagation (Rumelhart, Hinton, & Williams, 1986). The weights and biases are initialised and according to a loss function optimised. As for other ML methods, the mean square error is a common loss function for regression problems. At each epoch, the loss function and

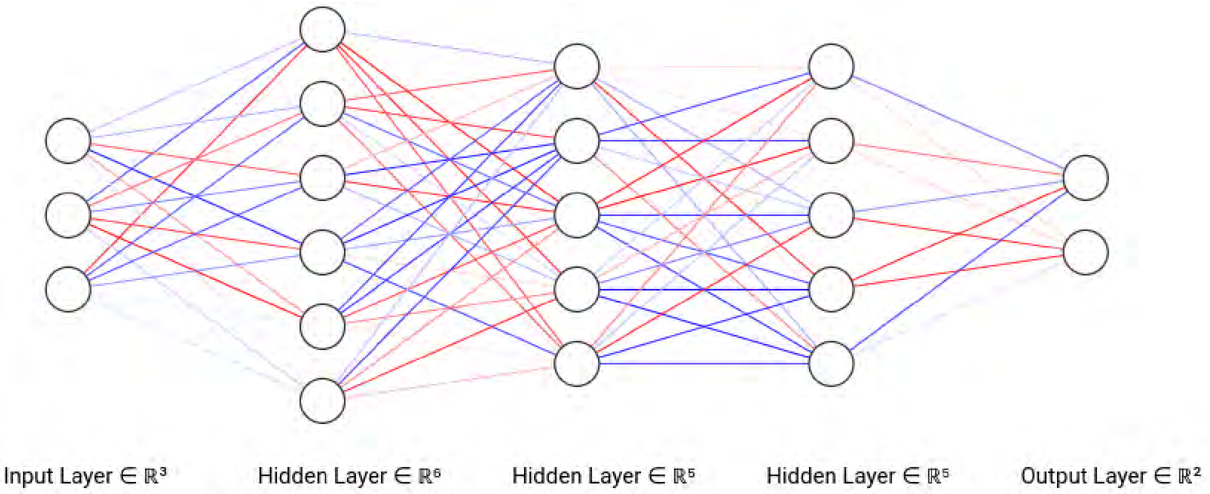

Figure 7.10: An example of a fully connected, trained neural network of depth 4 with three input features and two output labels. The first hidden layer has a size of 6, the second and third layers a size of 5 (number of neurons). The colour of the edges indicates the relative value of the corresponding weight for illustration purposes, with blue being negative and red positive weights and the more saturated, the higher the weight. This NN example was created with https://alexlenail.me/NN-SVG/.

corresponding gradients (the derivatives with respect to each of the weights and biases) are calculated. Then gradient descent is used to adapt the weights and biases according to the pre-set learning rate η to improve the model output. For a detailed treatment of back-propagation algorithm see also e.g. (Williams & Zipser, 1995). During the training two important problems arise which need to be taken care of: overfitting and vanishing gradients.

- **Overfitting:**
  Large architectures of neural networks are powerful, but run into the risk of memorizing the data instead of generalising it. One way of preventing overfits is to use regularisation. Similar to the introduced regularisation in machine learning (see figure 7.5), overfitting can be reduced by punishing higher weights. As in equations (7.3) and (7.4), a regularisation term is added to the loss function.

  Another way is to use **Dropout**. During the training, neurons run into the risk of learning patterns from statistical noise. Other neurons in the same network may then learn how to counterbalance such mistakes. This co-adaptation results in poor generalisation of the data. Dropout addresses this issue by preventing neurons from correcting mistakes of others by randomly removing some during the training. At each epoch, every neuron is dropped by a small probability, the drop-out rate p, and the network is trained only on the remaining ones.

- **Vanishing Gradient:**
  Backpropagation is based on the calculation of gradients and adapting weights accordingly. The gradients are calculated according to the chain rule of partial derivatives which leads to the multiplication of gradients from all the activation functions (see Williams and Zipser (1995) for further mathematical details). If these gradients are then very small, their product tends to vanish, which in turn does not lead to weight updates and eventually does not allow the network to learn. The choice of the activation function plays a crucial part in dealing with vanishing gradients. Typical activation functions include the sigmoid function σ, the hyperbolic tangent tanh and the rectified linear unit (ReLU) defined as

  $$\sigma(x) = \frac{1}{1+e^{-x}} \tag{7.9}$$

  $$\tanh(x) = \frac{e^{x} - e^{-x}}{e^{x} + e^{-x}} \tag{7.10}$$

  $$\mathrm{ReLU}(x) = \max(0, x) \tag{7.11}$$

  and plotted in figure 7.11. As tanh is steeper and thus its derivative is also steeper, it is better suited than the sigmoid function for solving the vanishing gradient problem. The popular ReLU function has the desirable property of being always, having no upper threshold and thus is often used.

As for ML algorithms, neural networks come with a set of hyperparameters that have direct impact on the model performance. Here too, hyperparameter tuning can help finding optimised values. Some of the most important hyperparameters include:

- Learning rate η

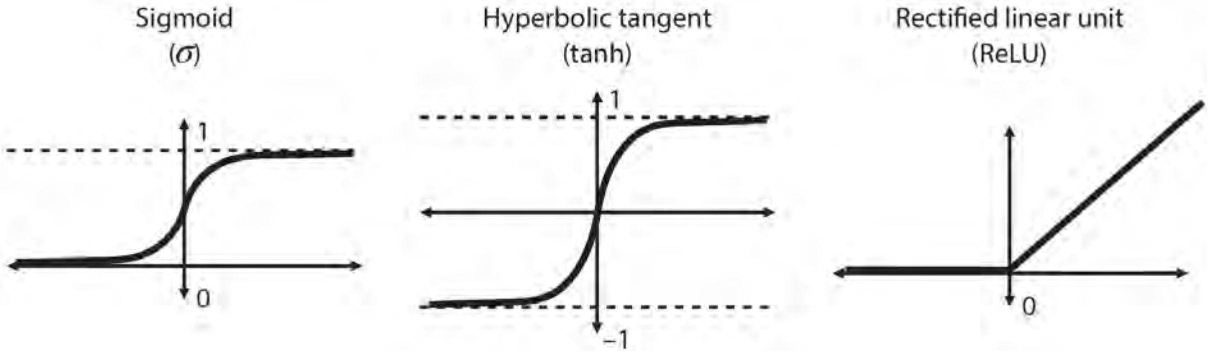

Figure 7.11: Examples of standard activation functions for perceptrons. Form left to right: the sigmoid σ from equation 7.9, hyperbolic tangent tanh from 7.10 and the rectified linear unit. Taken from Serrano (2021)

- Number of epochs
- The amount of input data that enters the training process at a given time (subsets of input data) which is referred to as batch or mini-batch
- Architecture of the network: number of layers, number of neurons per layer, as well as activation functions
- Regularisation parameters, L1, L2, or regularisation term λ
- Dropout-rate p

The architecture in figure 7.10 is referred to as a fully connected, feed-forward neural network or Multilayer Perceptron (MLP) network. Feed-forward relates to the fact that past input has no influence on the current prediction. Further architectures of neural networks are available that are specifically adapted for different classes of problems. For example a Convolutional Neural Network (CNN) is a class of deep neural networks that are extensively used in computer vision tasks such as image recognition, object detection and segmentation. The neural network introduced in the following section is specialised for time-series data.

In the following a neural network class is introduced that specialises on time-series.

7.2.1 Long-Short Term Memory (LSTM)

Recurrent Neural Networks (RNN) are neural networks that are specialised on problems that use data-series in which the sequence and order of the data is important, such as language processing and time-series. They come with an integrated memory, that uses information from prior inputs to influence current input and output. Such memory loops allow information to persist and to be passed on to the next time-step. So-called **hidden states** C act as memory within the network that contain relevant information from previous time-steps. On the top left of figure 7.12, a neural network A receives the input x_t and produces the output h_t at step t. The loop guarantees the passing of information from one step to the next. This visualisation is referred to as rolled. Unrolling the RNN, as is done on the top right of figure 7.12, reveals that the loop can be viewed as a temporal copies of the same network A per step $t = 0, 1, 2, ..., t$. At each time-step, the cell-state C of previous steps is used to generate the current output.

In practice, the vanishing gradient problem causes major issues during the training of RNNs, especially when trying to capture long-term dependencies in sequences. The gradient descent algorithm becomes easily unstable and does not converge anymore (Bengio, Simard, & Frasconi, 1994). A special case of neural networks are Long-Short Term Memory (LSTM) networks introduced by Hochreiter and Schmidhuber (1997). These overcome the problem by adapting the repeating module of the RNN. While the RNN has a simple layer that takes into account previous steps, the LSTM memory cell itself is made up of neurons that allow to selectively keep relevant information. This operating principle is realised by gates that decide upon which information enters the cell state and output and which does not. An LSTM cell consists of three gates: the forget, input and output gate. Each of these use the sigmoid activation function. The schematics of the LSTM cell is depicted on the bottom of figure 7.12. The functionality of the LSTM cell is based on the cell state C_t which is controlled by gates for limiting the amount of past information. Figures 7.13 to 7.16 illustrate the workflow of the LSTM cell and its gates with corresponding equations and description in the caption.

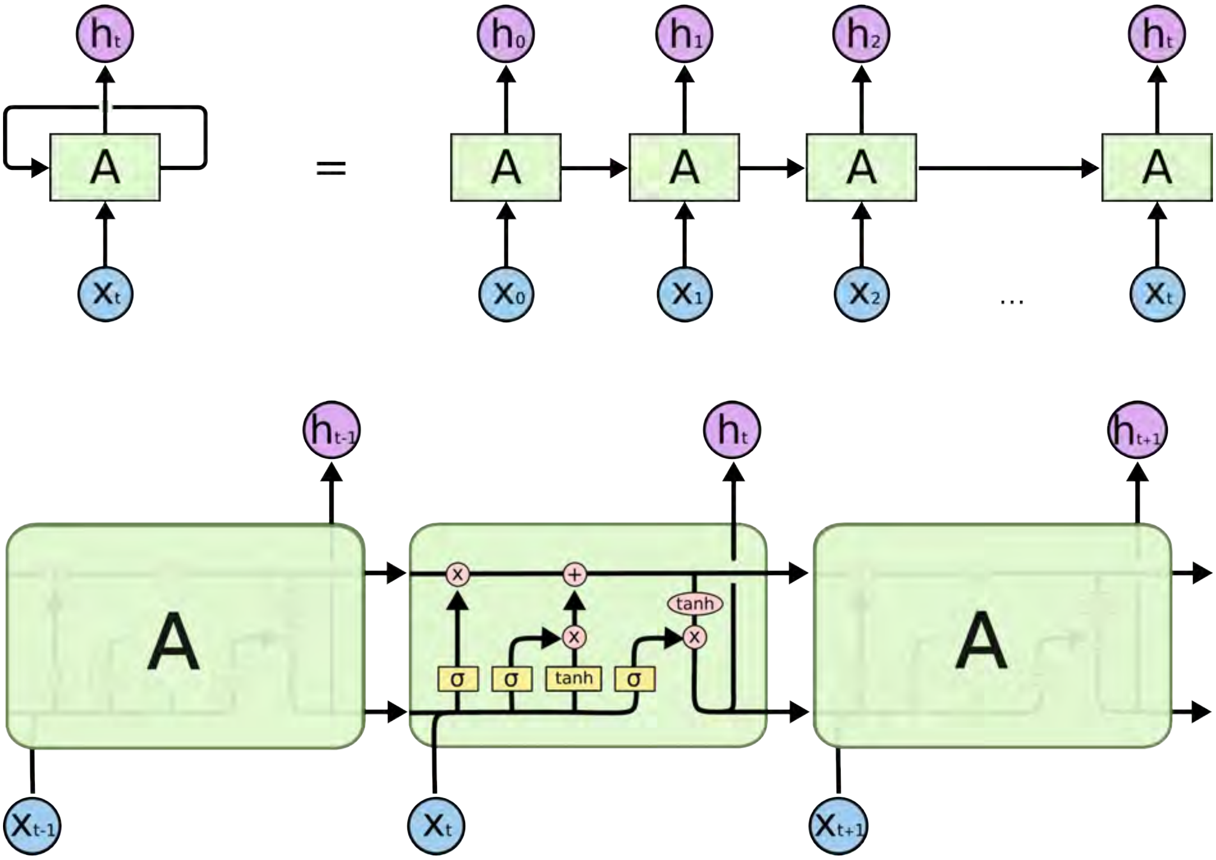

Figure 7.12: The top illustrates the schematics of the LSTM architecture in rolled (left) and unrolled version. The time dependence in the rolled version is indicated as a loop. In the unrolled version, the network is illustrated at several timesteps (indicated in the subscript). The lower figure depicts the details of the repeating cell A at timestep t including input and outputs for preceeding and succeeding time-steps. Taken from Colah (2015).

Based on the initial approach, further versions of LSTM exist. Some of these include the LSTM version introduced by Gers and Schmidhuber (2000) that adds a peephole connection such that the gate layers have access to the cell state, or Gated Recurrent Unit (GRU) as introduced by (Cho et al., 2014) that combines forget and input gates into one single update gate. The LSTM from Hochreiter and Schmidhuber (1997) is

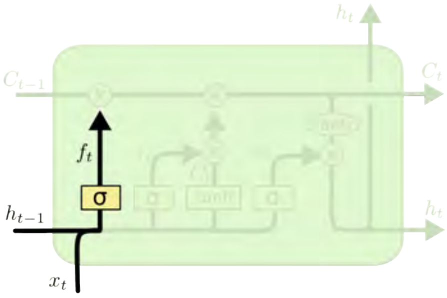

$$f_t = \sigma \left(W_f \cdot [h_{t-1}, x_t] \ + \ b_f\right)$$

Figure 7.13: **Forget gate.** The first step of the LSTM cell is to decide which information is irrelevant and may be forgotten by the network, i.e. information removed from the cell state. Therefore, the output of the previous step h_{t-1} and the input of the current step x_t are multiplied by the weight w_f and a bias b_f is added. This is then passed through the sigmoid function and makes up the forget gate's output f_t. Taken from Colah (2015).

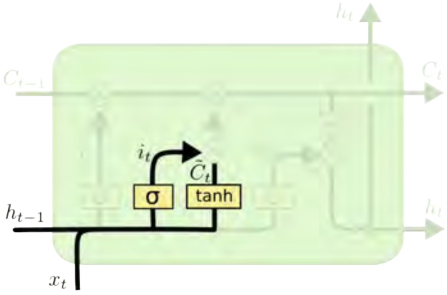

$$i_t = \sigma \left(W_i \cdot [h_{t-1}, x_t] \ + \ b_i\right)$$
$$\tilde{C}_t = \tanh(W_C \cdot [h_{t-1}, x_t] \ + \ b_C)$$

Figure 7.14: **Input gate.** Next, the input gate decides on which information to store in the cell state. The sigmoid layer chooses the values to update i_t and the tanh layer creates candidate values $\tilde{C}_t$ that may be added to the cell state. Taken from Colah (2015).

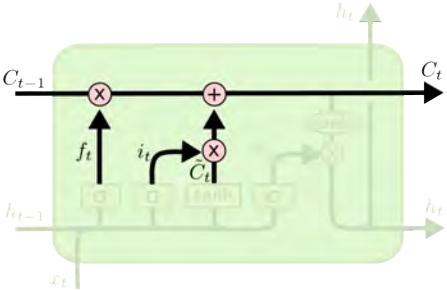

$$C_t = f_t * C_{t-1} + i_t * \tilde{C}_t$$

Figure 7.15: **Cell state.** With the forget and input gates, the new cell state C_t is derived by multiplying the output of the forget layer f_t with the old cell state C_{t-1} and adding the output of the input gate $i_t * \tilde{C}_t$. The final cell state C_t at timestep t is written on the right. Please not that this equations contains the three weights W_f, W_i, W_C, as well as the biases b_f, b_i, b_C. Taken from Colah (2015).

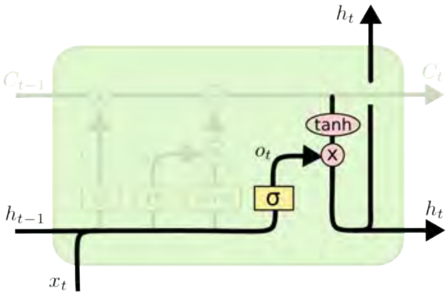

$$o_t = \sigma \left(W_o \ [h_{t-1}, x_t] \ + \ b_o\right)$$
$$h_t = o_t * \tanh\left(C_t\right)$$

Figure 7.16: **Output gate.** The output of the LSTM is based on the current cell state C_t and the output of the previous step passed through the sigmoid layer o_t. The cell state is run through a tanh function to give values between -1 and 1 and multiplied by o_t. The equations for the final output h_t are written on the right. Taken from Colah (2015).

considered shallow as it only contains one hidden layer. A stacked or deep LSTM network is made up several layers stacked together. The deep design allows for a higher degree of complexity by enabling nonlinear mapping between inputs and outputs for hierarchical learning (Hermans, in neural Information, & 2013, 2013; Pascanu, Gulcehre, Cho, & Bengio, 2014; Yu, Qu, Gao, & Tian, 2019). Deep LSTM models have demonstrated increased performance in various applications (Guan & Plötz, 2017; Althelaya, El-Alfy, & Mohammed, 2018; Ghimire et al., 2022). An example of a deep LSTM is illustrated in figure 7.17. The left shows a 3 layer unrolled RNN which indicates the influence of the layers at the previous time-steps to the current time-step. This relationship is indicated as feedback loops on the right in rolled visualisation. The choice of RNN architecture depends heavily on the problem to be solved. Several studies are dedicated to find the best architectures for different problems, see e.g. Jozefowicz, Zaremba, and Sutskever (2015).

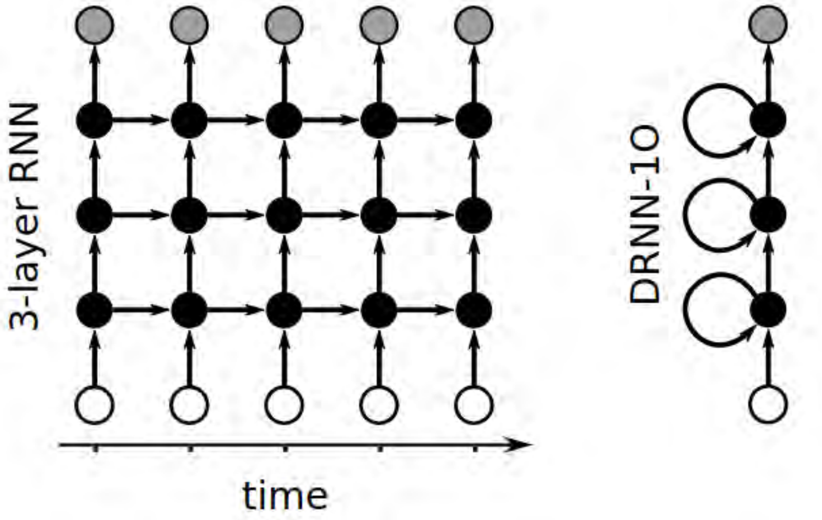

Figure 7.17: Schematics of a deep LSTM example with three hidden layers. The left figure depicts the unrolled network with indicated influence of past layers on the current layer. The right figure depicts the rolled version of the deep LSTM with indicated feedback loop. Adapted from Hermans et al. (2013)

Chapter 8

Feature Importance with Random Forest

Before we attempt to model diurnal variations, we will evaluate which input parameters are best to use. The ML concept of feature (or variable) importance provides information on the capability of individual features to influence model predictions. It answers the question of which features are the most influential ones in making predictions and decisions in the model.

A common criticism and highly debated topic of machine learning techniques is their *black box* approach as they do not directly provide information about which input features and to what extent they influence model results (Rudin, 2019). In fact, interpretabiliy and explainability of machine learning is a highly debated topic that receives increasing attention as these techniques are used for scientific insights and discoveries (Roscher, Bohn, Duarte, & Garcke, 2020; Burkart & Huber, 2021; Marcinkevičs & Vogt, 2023). Feature importance provides means to identify most important variables that are highly related to the output variables for interpretation purposes.

In chapter 7.1.1, we introduced the concept of decision trees and the ensemble method random forest. Random forests have been shown to be very efficient in determining feature importance (Genuer, Poggi, & Tuleau-Malot, 2010). When training a random forest model, an ensemble of decision trees are generated. At every node of each of these trees, the dataset is split according to the feature that leads to the lowest gini impurity index. The better a split, the lower this index. For each feature, the decrease in impurity is recorded and the average over all trees gives the feature importance. Features that frequently appear within the higher nodes of the decision trees tend to have higher importances. In general, feature importance is presented in relative values (in %) over all input features, such that the total equals 100%. One of the advantages of this method is its low computation cost as all the relevant information is already computed during model training.

In the following, we will investigate the feature importance for the two labels x_D and y_D, the combined (sub-)diurnal filters as defined in table 4.1 and equations (5.1) and (5.2). In accordance with the rest of this thesis, we will employ measurements and properties of the magnetic observatory Chambon-la-Foret.

8.1 Input Parameters and Training Sets

Explained in chapter 2.3.2 and as we have also seen in chapter 5.2.2, the solar quiet variations show strong dependencies on the local time LT, the solar longitude L and solar activity $F10.7$. Additionally, in figures 5.3 and 5.4, the activity of x_D and y_D suggest dependencies on the local time of sunrise LT_R and sunset LT_S. The solar zenith angle

χ being connected to solar illumination is another parameter that may influence diurnal variations. Furthermore, as described in chapter 5.3, the filter responses include variations induced by changing solar wind conditions, including solar storms (see also chapters 2.1.2, 2.4 and 2.5.3). Therefore we expect dependencies on solar wind parameters like the IMF orientation B_x, B_y and B_z, the velocity v, the density n and the temperature T. The solar wind data is taken from the OMNI web interface[1] which includes satellite data from ACE, Wind and DSCOVR at the L1 position (Papitashvili & King, 2020). This leads to a set of 12 input parameters, i.e.:

1) LT
2) χ
3) L
4) LT_R
5) LT_S
6) $F10.7$
7) B_x
8) B_y
9) B_z
10) v
11) n
12) T

When evaluating feature importance with random forest, some limitations need to be kept in mind (Genuer et al., 2010; Gregorutti, Michel, & Saint-Pierre, 2017). This method is known to give equal or similar importance to correlated features, but will give overall reduced importance when compared to the same tree without correlated counterparts. Another issue can occur that only one of the correlated features is selected, while the other ones are neglected. Therefore, let us have a look at the correlation between the 12 identified features. Figure 8.1 shows a heatmap of the pearson coefficients for each of the input features. Unsurprisingly, there is a high (anti-)correlation between L and LT_R (0.8) and L and LT_S (-0.73), as well as LT_R and LT_S (-0.98). Another high correlation is found for v and T of 0.68. Further, notable low to moderate correlations include L and χ (0.34), v and n (-0.36), as well as B_x and B_y (-0.41). To avoid known issues with random forest feature importance, we will only keep one feature of each of the correlation pairs with a pearson coefficient higher than 0.5. This leads to a set of 9 input parameters, as summarised in table 8.1.

Table 8.1: Input Parameters for the Random Forest models for the determination of the feature importance.

LT	$F10.7$	B_x
χ	v	B_y
L	n	B_z

We define three different datasets for which we want to derive feature importance for x_D and y_D. The first once covers the entire period between 2001 and 2010 which includes a very strong solar maximum and a very weak solar minimum. As we do not exclude dependency changes on parameters during different phases of the solar cycle, we define two further training sets: One during solar maximum between 2001 and 2002, and one during solar minimum between 2008 to 2009. To reduce computational costs we use a time-resolution of 1 hour for all features and labels. Additionally we normalise all values between 0 and 1 as we apply the random forest on a regression problem. This avoids the problem of features with high absolute values being favoured over those with low values in regression models.

---

[1] omniweb.gfsc.nasa.gov

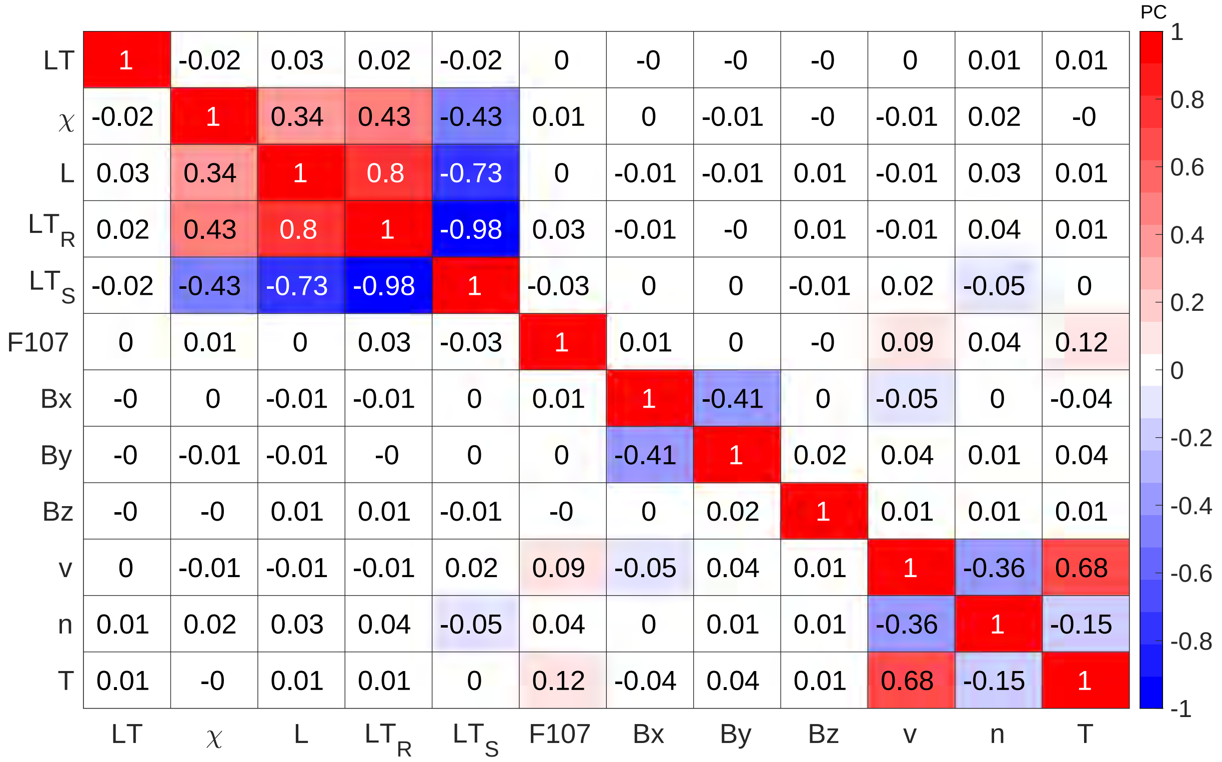

	LT	χ	L	LT_R	LT_S	F107	Bx	By	Bz	v	n	T
LT	1	-0.02	0.03	0.02	-0.02	0	-0	-0	-0	0	0.01	0.01
χ	-0.02	1	0.34	0.43	-0.43	0.01	0	-0.01	-0	-0.01	0.02	-0
L	0.03	0.34	1	0.8	-0.73	0	-0.01	-0.01	0.01	-0.01	0.03	0.01
LT_R	0.02	0.43	0.8	1	-0.98	0.03	-0.01	-0	0.01	-0.01	0.04	0.01
LT_S	-0.02	-0.43	-0.73	-0.98	1	-0.03	0	0	-0.01	0.02	-0.05	0
F107	0	0.01	0	0.03	-0.03	1	0.01	0	-0	0.09	0.04	0.12
Bx	-0	0	-0.01	-0.01	0	0.01	1	-0.41	0	-0.05	0	-0.04
By	-0	-0.01	-0.01	-0	0	0	-0.41	1	0.02	0.04	0.01	0.04
Bz	-0	-0	0.01	0.01	-0.01	-0	0	0.02	1	0.01	0.01	0.01
v	0	-0.01	-0.01	-0.01	0.02	0.09	-0.05	0.04	0.01	1	-0.36	0.68
n	0.01	0.02	0.03	0.04	-0.05	0.04	0	0.01	0.01	-0.36	1	-0.15
T	0.01	-0	0.01	0.01	0	0.12	-0.04	0.04	0.01	0.68	-0.15	1

Figure 8.1: Colour-coded correlation matrix for the 12 input features of the random forest models. Blue values correspond to negative and red values to positive correlation. The higher the opacity the higher the absolute correlation.

8.2 Random Forest Models

The random forest model is built with the scikit-learn framework in python (Pedregosa et al., 2011), leveraging its default implementation with 100 decision trees and using the mean squared error as loss-function. We do not implement any customised stopping function, such that the building of each tree is finished only once the leave has a sample size of 1. This guarantees that the random forest model is able to describe the data-set well. As we do not use this model to make accurate predictions of future data, but to see which features influence the given dataset, we want a high score for the training set. The performance on the test set is not of significant importance in this case.

We generate a total of 6 models which share the same 9 input features but differ by the considered time-interval (data-sets for entire period, solar minimum and solar maximum) and output label (x_D or y_D). The resulting six models and their details are summarised in table 8.2, showing the output label per model and the training set with the corresponding time-interval. The training duration is defined as the amount of time the computer needed to train/build the random forest. For regression models the R2 score represents the proportion of the dependent variable's variance that is explained by the independent variables, i.e. it gives information about how well the trained model is able to represent the training data. It is defined as

$$R2 \text{ Score} = 1 - \frac{\text{sum of squares of the residual errors}}{\text{total sum of the errors}} . \tag{8.1}$$

For our models it indicates how well the input features were able to describe the variations within x_D and y_D.

Table 8.2: Overview of the six random forest models, detailing the output label, the specific training set and corresponding time-interval in years, as well as the time needed for the training of the model (training duration) and the $R2$ score on the training set.

#	Output Label	Training Set	Time-Interval	Training Duration	$R2$ Score
1	x_D	entire period	2001-2009	49.6 s	0.9405
2	x_D	solar maximum	2001-2002	9.2 s	0.9422
3	x_D	solar minimum	2008-2009	8.19s	0.9481
4	y_D	entire period	2001-2019	44.3 s	0.9769
5	y_D	solar maximum	2001-2002	8.57 s	0.9815
6	y_D	solar minimum	2008-2009	7.92 s	0.9819

8.3 Results

As a first observation in the column 'Training Duration' in table 8.2, we recognise that the time needed to train the random forest models is well below one minute, making this algorithm very efficient. The $R2$ score in the last column is comparable across each training set per component x_D and y_D. The score of around 0.98 is high for y_D, suggesting that its variance is well captured within the model. For x_D the score of around 0.94 is less but it still ensures that the main part of the variance is encapsulated within the model.

A word of caution needs to be kept in mind here. The $R2$ scores indicate very good performances and may give the impression that the corresponding models are well suited to describe diurnal variations. However, the $R2$ score can be interpreted as how much better the model performs with respect to a model that is a simple straight line. Therefore, while these scores may be used to compare the ability of models on how well they describe the used training set, it is not advisable to use them as sole quality marker and/or decision criteria.

From the six models, we extract the feature importance as depicted in figure 8.2 for x_D on the left and y_D on the right. The feature importance is given in % relative to all 19 parameters. The results for solar minimum are coloured in blue, for solar maximum in red and for the entire period from 2001 to 2010 in yellow.

Several interesting observations can be derived. Starting with x_D, the solar zenith angle χ seems to be the most important feature with around 25% for all three time-periods, followed by the local time LT and solar longitude L, except during solar minimum when L has a higher importance than LT. The components of the IMF B_x, B_y and B_z have a higher relevance during solar maximum and during the entire period than during solar minimum, whereby B_z has the highest relative feature importance of the three. The solar wind velocity v has a higher importance during solar minimum and the entire period than during solar minimum. The solar wind density n, $F10.7$ and B_x are assigned the lowest importance in general.

Turning to y_D, we see that the most important feature during solar maximum and the entire period is the local time LT with over 55%, followed by the solar zenith angle χ with less than 20%. During solar minimum, χ is slightly more important than LT. Intriguingly, all the other input features are of much lower importance, with less than 10%, including the solar longitude L describing the season.

While for x_D the solar zenith angle is of higher importance, for y_D the local time LT is more important, at least during solar maximum and when considering the entire period. Note that the vertical axes have different ranges, suggesting that x_D is influenced by a

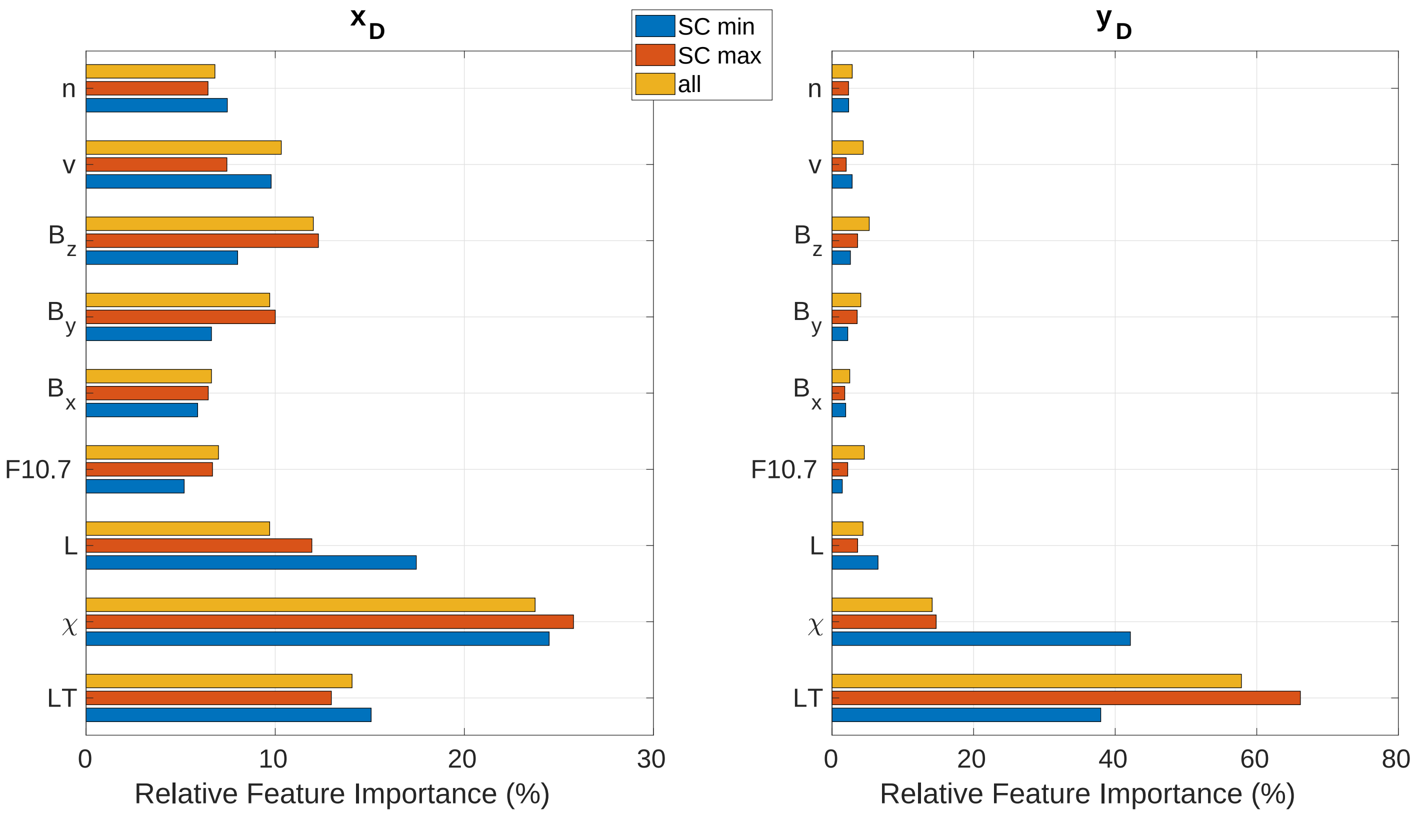

Figure 8.2: Relative feature importance in % as derived from the random forest models summarised in table 8.2. The results for each parameter and corresponding period (solar cycle minimum, solar cycle maximum and the total period) is illustrated for x_D on the left and y_D on the right.

higher number of features than y_D.

Let us name some discrepancies of the results in figure 8.2 and the previous work in this thesis. We know that the solar quiet variations depend strongly on direct solar illumination during the day, which has an approximate cycle of 24 hours, explaining the local time importance. The solar zenith angle is closely related to the local time LT and shows a linear correlation of 0.34. This may explain its elevated importance in the random forest feature importance method, even though it did not hold significant results when used in conventional modeling (see chapter 5.2.2.4). From the $L + LT$ model in chapter 5.2.2.1 and the amplitude dependencies found in figures 5.17 and 5.18, we know that both, x_D and y_D have clear dependencies on the solar longitude L. Although, this relationship is somewhat caught for x_D, it is almost non-existent for y_D. A similar reasoning can be used for the $F10.7$ index. The derived feature importance results also suggest that solar wind conditions impact mainly, and almost solely, the variations in x_D, but leave y_D fairly unaffected. It needs to be stated that random forests also tend to give preference to features with higher cardinality. This may add to the underestimation of the importance of the $F10.7$ index, as it comes in a one hour cadence. An important limitation for our application is also that random forests are not well-suited for sequential, time-series problems and do not capture any time dependencies.

Chapter 9

Diurnal Variations with LSTM

Chapter 5.2.2 was devoted to the description of quiet variations of the geomagnetic field and to which extent certain parameters influence them. This led to three analytical models, which are based on the local time LT, the solar longitude L, the solar activity index $F10.7$ and the signal itself. Their performance is discussed in section 5.2.2.5. In this chapter, our focus lies in exploring AI methods for the description of diurnal variations of the geomagnetic field, namely the combined (sub-)diurnal filters x_D and y_D as defined in equations (5.1) and (5.2). In accordance with the rest of this thesis, we will employ measurements and properties of the magnetic observatory Chambon-la-Foret. Due to the sequential nature of geomagnetic field measurements and the resulting filter responses, we will employ Long Short-Term Memory (LSTM) models, which are explicitly designed for handling such sequential data. In studies of ground perturbations and magnetic index forecasting, LSTM models have been widely explored and successfully applied, showing higher performances than feed-forward ANNs, see e.g. Tan, Hu, Wang, and Zhong (2018); Keesee et al. (2020); Siciliano et al. (2021); Collado-Villaverde, Muñoz, and Cid (2021); Pinto et al. (2022).

As for any modeling task, the first step is data preparation. For DL methods, this includes the splitting of data into training, validation and test sets. We then describe the architecture of a deep LSTM network. We will use it to derive two models that are build upon the same architecture but differ in their input features. One model, model 1, focuses on the quiet variations by taking into account a set of features derived from the feature importance and the physics-informed models. The other model, model 2, additionally takes into account solar wind parameters to include ground perturbations. These models are then trained and their training performance is analysed. Finally, the results of model 1 and model 2 are presented, compared and discussed.

9.1 Data Preparation

The first step when deploying any ML technique is data preparation which includes defining output labels (what do we predict) and input features (which parameters influence the prediction), as well as the splitting of the dataset (what periods do we consider for the training, validation and testing).

As mentioned, we are interested in the diurnal variations x_D and y_D of CLF which make up the two labels per model.

We consider two sets of input features: one for quiet variations and one for diurnal variations, leading to two models with the same architecture but with different input features. The input features to describe the quiet variations for model 1 are LT, χ, L and $F10.7$. The input features for the diurnal variations of model 2 are LT, χ, L, $F10.7$ plus the solar wind parameters B_x, B_y, B_z, v and n. The motivation for the choice of these input parameters and the adapted architectures are given below in chapter 9.3.1 and 9.3.2.

The larger the initial dataset, the more expensive the training becomes in terms of computational costs. This is especially true for neural networks. To keep computational resources economical, while ensuring an adequate mapping of diurnal variations, we use a time-resolution of one hour for all input and output variables and limit the full dataset to nine years from 2001 to 2009. To ensure sequential data, we will use all days within this period. This implies that the model will be trained on quiet days, as well as on disturbance-influenced periods.

Figure 9.1: Visualisation of the dataset-splits for solar maximum and minimum into training (blue), validation (yellow) and test (green) sets. The data is split according to the 80-10-10 rule.

With guidance of the 80-10-10 rule, we split the data into 7 years of training set (2001-2007) and one year of validation (2008) and test (2009) sets. The split is illustrated in figure 9.1. As has been done for the random forest algorithm, we normalise all values between 0 and 1.

9.2 Model Architecture

We use the original cell architecture of LSTMs as introduced by Hochreiter and Schmidhuber (1997) deployed in a deep LSTM network to reach a higher order of complexity compared to its shallow version. In our model, the first LSTM layer is made out of 100 neurons (or cells) that receives the input features, followed by 4 hidden LSTM layers with each 50 neurons. Each of these layers use the ReLU activation function. The output layer is a dense layer with the size of the to-be predicted labels. A dropout of 20% in between the last hidden layer and the output layer is added to prevent overfitting. An important hyperparameter of LSTMs is the look-back variable which sets the maximum amount of time for which past values can influence the current output. We use a look-back variable of 48 hours, allowing the LSTM to use information from two days ago for its predictions. As the prediction of diurnal variations is a regression problem, we use the mean square error (MSE) as loss-function and the mean absolute error (MAE) as the metric. The training runs for 20 epochs. We use a learning rate of $\eta = 0.001$.

The development and training of the models is done using the TensorFlow-Keras framework for Python (Abadi et al., 2016) and the scikit-learn toolkit (Pedregosa et al., 2011). These frameworks include a collection of state-of-the-art machine and deep learning methods, that allow, among others, to use high-level language for creating neural networks and implement efficient optimisation algorithms for the training. Figure 9.2 shows the architecture as build with Tensorflow-Keras.

One more property of machine learning methods that is important in practice should be noted at this point. The training of neural networks (or any other ML algorithm) is a stochastic process. This implies that no two trained models will be identical nor will their results be exactly the same. In order to receive reproducible results and be able to compare models with varying (hyper-)parameters, it is important to use a so-called

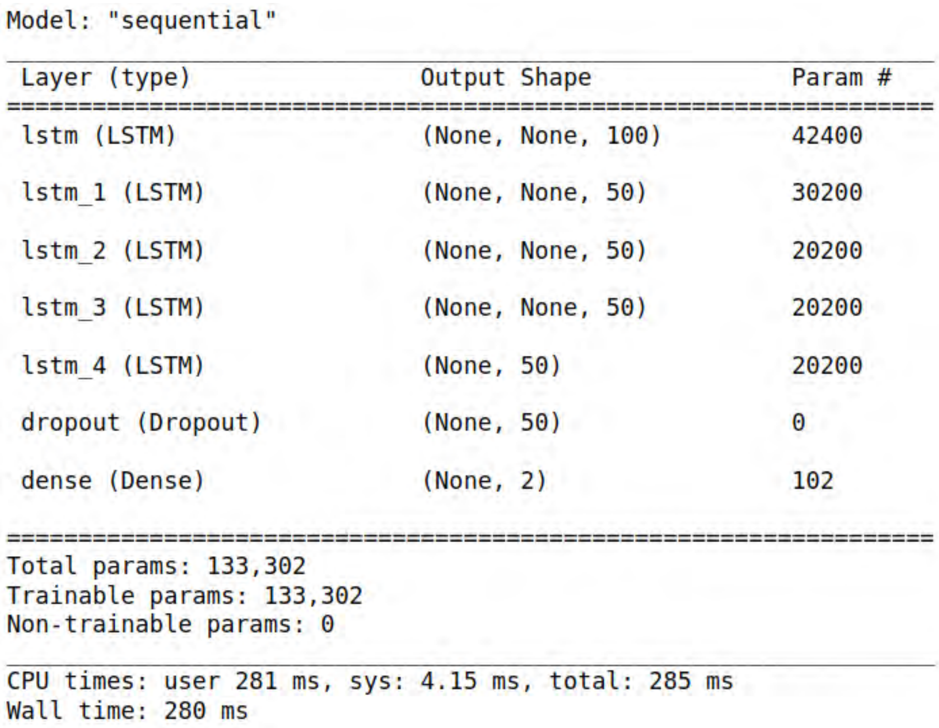

```
Model: "sequential"
_________________________________________________________________
 Layer (type)                Output Shape              Param #
=================================================================
 lstm (LSTM)                 (None, None, 100)         42400

 lstm_1 (LSTM)               (None, None, 50)          30200

 lstm_2 (LSTM)               (None, None, 50)          20200

 lstm_3 (LSTM)               (None, None, 50)          20200

 lstm_4 (LSTM)               (None, 50)                20200

 dropout (Dropout)           (None, 50)                0

 dense (Dense)               (None, 2)                 102

=================================================================
Total params: 133,302
Trainable params: 133,302
Non-trainable params: 0
_________________________________________________________________
CPU times: user 281 ms, sys: 4.15 ms, total: 285 ms
Wall time: 280 ms
```

Figure 9.2: The deep LSTM model architecture as build and summarised by the Tensorflow-Keras framework. The final dense layer has output shape 2.

random-seed. This random-seed describes the initialisation of the start conditions and guarantees reproducible results.

9.3 Two LSTM Models

Based on the prepared data-set and defined architecture, we derive two regression models. The first model, similar to the analytical models derived in chapter 5.2.2, predicts the quiet variations of the combined (sub-)diurnal variations based on the four parameters LT, L, χ and $F10.7$. With the second model, we explore the architecture to reproduce the full combined (sub-)diurnal variations including disturbance signatures by taking into account additionally the solar wind parameters B_x, B_y, B_z, v and n. In both cases, the same data-set covering the period from 2001 to 2009 is used, as described in section 9.1. Each of these models predict both labels, x_D and y_D simultaneously.

9.3.1 Model 1: Describing Quiet Variations with LT, L, $F10.7$ and χ

In chapter 5.2.2, we deduced physical models using the parameters local time LT, solar longitude L and solar activity index $F10.7$. From the data-driven feature importance in figure 8.2, we found that the solar zenith angle χ has a high importance for both, x_D and y_D. Combining the physical with the data-informed approach, we use these four parameters as input features for the first LSTM model. The corresponding architecture is depicted in figure 9.3 and we refer to it as *model 1*.

Assuming no external influences, except the solar cycle phase, the four parameters

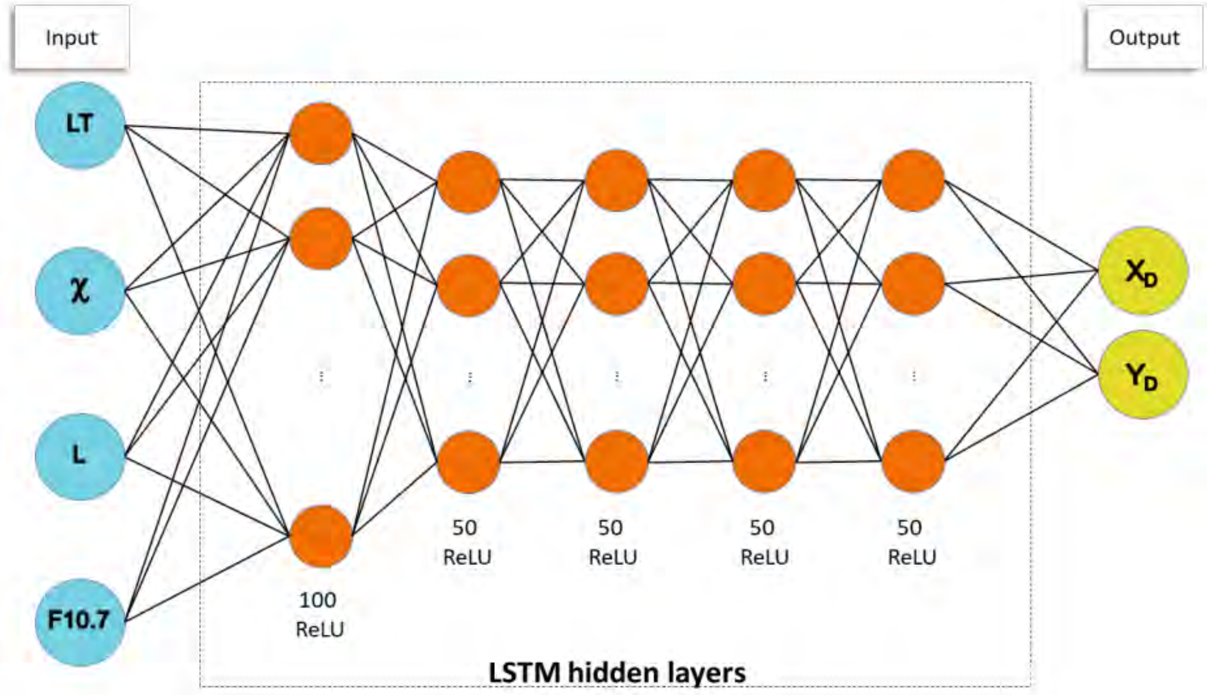

Figure 9.3: LSTM architecture of model 1. Its input features are the local time LT, solar zenith angle χ, solar longitude L and solar activity index $F10.7$. The LSTM network consists of five hidden layers. The temporal feedback loop and drop-outs are not indicated.

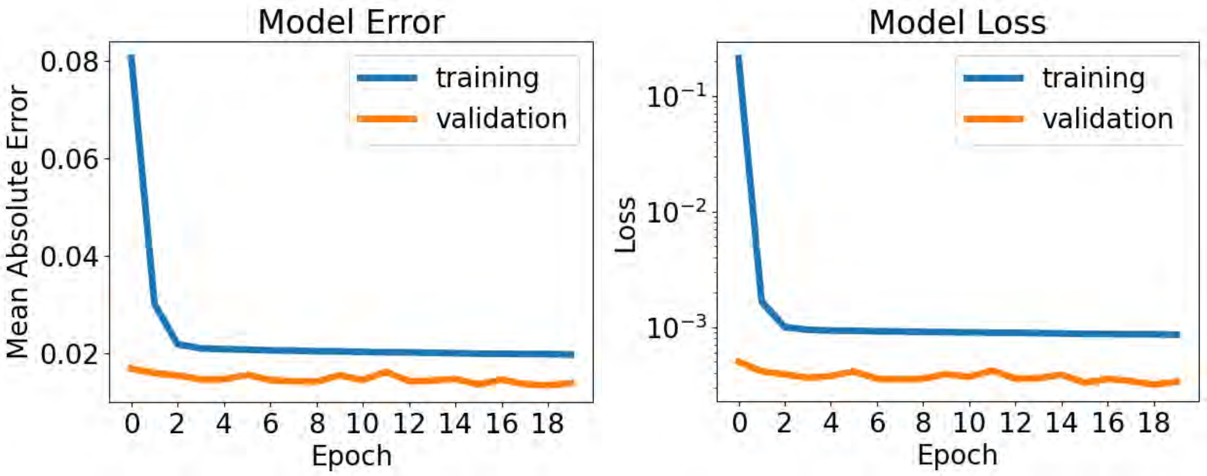

Figure 9.4: The training progression for the quiet variation model. The model error is illustrated on the left and the model loss on the right for both, the training (blue) and validation sets (orange) per epoch.

hold relevant drivers that are associated for variations of the solar quiet current systems (see also chapter 2.3.2). The training set for the LSTM model covers the full period from 2001 to 2007 which includes a strong solar maximum and the start of a weak solar minimum. This implies that a considerable amount of disturbed periods are included which the LSTM will train on. However, the only indicator for disturbed periods is the $F10.7$ index, which - even though being connected to solar storms - does not give further information, like duration or intensities of storms. Therefore, the disturbed periods within the training set may be viewed as noise.

The training of model 1 took 1 hour and 37 minutes. In figure 9.4 the progression of the model error (MAE) and model loss (MSE) for the training (blue) and validation (orange) sets during the 20 epochs are visualised. For the error and loss of the training set, we see a steep improvement during epoch 1 and 2, after which it stagnates. The validation curves, on the other hand, improve marginally during the first epochs and then fluctuate slightly. From the training error we deduce that after epoch 2 the neural network does not learn new patterns anymore and does not improve anymore.

There is a pool of possibilities that may explain this training behaviour, which may include:

- During gradient descent, the solution ends up in a local minimum (or a saddle point) and is no longer able to improve. This is a common issue faced with neural networks. The hyperparameter controlling the stepsize, the learning rate η, plays an important role. If it is too high, the optimal solution may be overshot, while if it is too small, the model may converge very slowly.
- Another possibility is underfitting: the model is too simple to learn the complex dependencies between the input features and output labels. In this case the model is not able to generalise on the training data.
- In order for models to learn effectively and finally to converge, the input data needs to be correctly preprocessed. Input data that includes high numbers of outliers or high levels of noise may significantly slow down and impede convergence.

9.3.2 Model 2: Describing Diurnal Variations including Solar Wind Parameters

We know that the entire training period between 2001 and 2007 includes disturbance events that may be viewed as noise in model 1. These events are closely related to solar wind conditions, as they influence geomagnetic field variations, and thus the combined (sub-)diurnal filters x_D and y_D. *Model 2* takes into account the solar wind parameters B_x, B_y, B_z, n and v in addition to the four features of model 1. The corresponding architecture is depicted in figure 9.5. In this case, the model is fed by parameters that influence geomagnetic disturbances and thus is aware of them.

The training of model 2 took 1 hour and 42 minutes. In figure 9.6 the progression of the model error (MAE) and model loss (MSE) for the training (blue) and validation (orange) sets during the 20 epochs are visualised. The curves of the training and validation errors have a falling trend for the first six to to seven epochs. During epoch 3, an increase of both occurs. While the validation error continuously decreases, the training error spikes at epoch 14. After that both start a slightly more pronounced decline. Analogue observations can be made for the model loss. Both, training and validation loss, spike at epoch 3, while the training loss spikes again at epoch 14.

Between epochs seven and twelve, the neural network does not learn very fast, however after epoch 13 it seems to pick up learning speed again. This may indicate that the model was able to get out of a local minimum (or a saddle point) and afterwards the model may converge. This would imply to increase the number of epochs for model 2. Spikes like the ones observed at epoch 13 may also imply that the data is very hard to generalise and further investigations on the dataset should be considered.

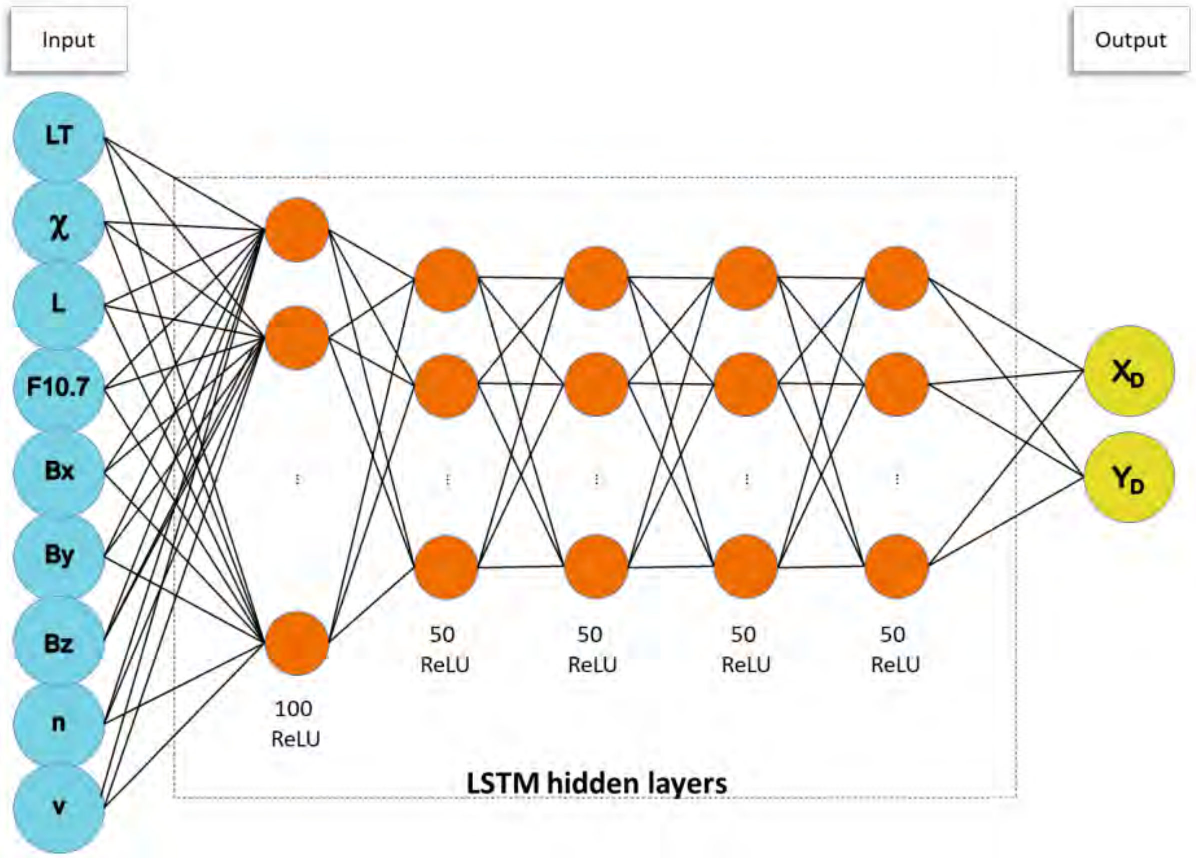

Figure 9.5: LSTM architecture of the quiet variation models with the input features local time LT, solar zenith angle χ, solar longitude L and the solar activity index $F10.7$. The LSTM network consists of five hidden layers. The temporal feedback loop and drop-out are not indicated.

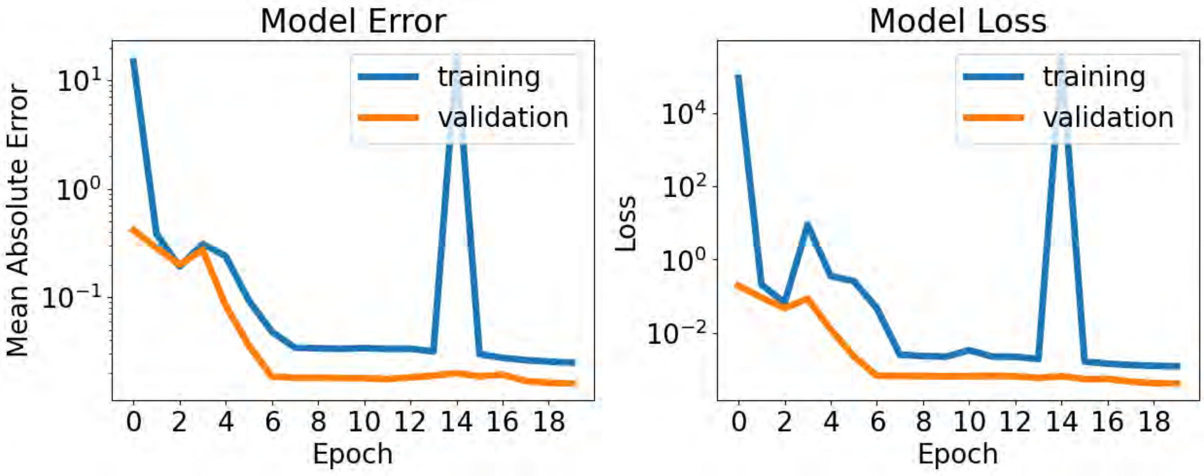

Figure 9.6: The training progression for the sw variation model. The model error is illustrated on the left and the model loss on the right for both, the training (blue) and validation sets (orange) per epoch.

9.4 Results

The final step in using the LSTM models is to apply them to the test set. The details of the models and their training, followed by their performance on the test set are summarised in table 9.1. Both took a comparable time of around 1.75 hours to train during 20 epochs on the training set. The time needed to apply them to the test set of one year (to make predictions) is in the order of seconds and thus much faster than the amount of time needed for training. The mean absolute error for the test set of model 1 is slightly better than that of model 2, which holds for the mean square error too. According to these two metrics, model 1 performs better than model 2 in predicting the two output labels.

Table 9.1: Details of the LSTM models including time needed for training and testing (prediction), the mean absolute error and the mean square error per label for the test set.

#	LSTM model	input features	Training Duration	Test MAE	Test MSE per label
1	quiet	$LT, \chi, L, F10.7$	1h 37min	0.0147	3.5979×10^{-4} 3.8546×10^{-4}
2	solar wind	$LT, \chi, L, F10.7$ B_x, B_y, B_z v, n	1h 42min	0.0174	5.3525×10^{-4} 4.6827×10^{-4}

To gain a more qualitative understanding of the model predictions, let us consider a concrete test period in the first two weeks of May. In the upper six panels of figure 9.7 the corresponding solar wind parameters and $F10.7$ are indicated. We see a clear increase of solar wind speed v around and after May 8th, while the other solar wind parameters are rather low, describing quiet conditions. The $F10.7$ index slightly increases after the 8th of May.

The model outputs are depicted in the two bottom panels in figure 9.7. The combined (sub-)diurnal filters x_D and y_D are shown in grey, model 1 taking into account the quiet variations is in blue and model 2 taking into account the solar wind parameters is in yellow. The first two weeks of May 2009 included mainly CK days with 4 non-CK days on the 7th, 8th, 9th and 14th of May.

In x_D on the upper panel, we see some stronger spikes between May 8th and 10th. It is striking that both models significantly deviate from the actual variations and do not describe x_D very well. In the beginning of May, the models partially catch the timing of the rising and falling edges in x_D to a certain extent. Although model 2 includes solar wind data, it does not show strong differences to model 1, merely the amplitude is slightly increased. In y_D (grey) in the lower panel, wee see that some variations occur around the 8th of May, which are not reproduced by any of the two models. Otherwise, both models describe the variations in y_D well. Model 1 and model 2 show high similarities for y_D.

The presented period, and in general the test set, covers the year 2009 which is known to be a very quiet year considering solar activity. Additionally, during the presented time interval, the solar wind conditions are mainly very quiet and do not change very much. This may be one reason for the similarity of the two model predictions.

The very bad performance of the models to predict variations in x_D, both in shape and amplitude, is partly related to the general volatility of the X component which already posed a significant challenge for the analytical models. Additionally, due to the definition of the split of the dataset, the trained models do not include any information on minimum solar cycle phase. However, this does not seem to impact the prediction of y_D too much for the presented time-interval.

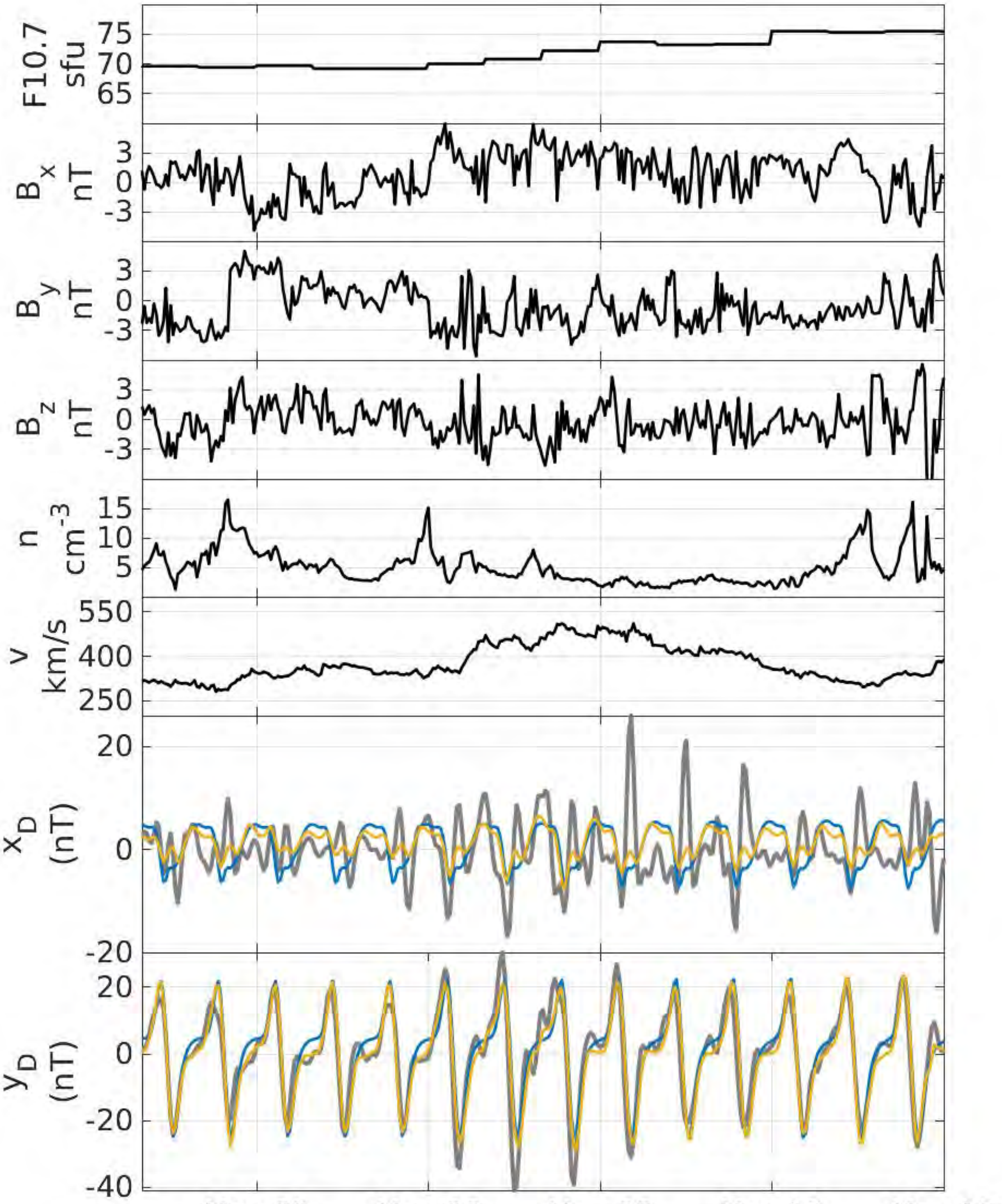

Figure 9.7: Solar wind parameters and model results from 1st to 15th of May 2009. From top to bottom: $F10.7, B_x, B_y, B_z, v$, n, x_D and y_D (in black). Model 1 is depicted in blue and model 2 in yellow. Non-CK days are from 7th to 9th of May and on the 14th of May.

Chapter 10

Discussion

This chapter gave a first introduction into AI methods and showed their application to problems addressed in this thesis. We introduced a popular machine learning algorithm, random forest, and a popular deep learning technique, LSTM. We applied the random forest method for feature importance and the LSTM for the description of the variations of the combined (sub-)diurnal filters x_D and y_D.

We deployed the random forest algorithm to find the variables that drive the majority of the variations among the input features: $LT, \chi, L, F10.7, B_x, B_y, B_z, v$ and n. We trained a total of six models, one per filter x_D, y_D and each with three different training periods: one during solar minimum, one during solar maximum and one covering almost a whole solar cycle. The resulting feature importance, though agreeing overall, showed several conflicting aspects in comparison with other physical data and interpretation. Reasons include known issues with inter-dependent input features when using random forest and the fact that this method does not consider the sequential nature of time series data. Though the initial results are controversial, they form first experiences for the identification of further drivers of diurnal variations of the geomagnetic field. Future work should deploy other, more suitable methods to determine feature importance. These include techniques to extract feature importance from RNNs and LSTMs, as is done in e.g. Olden, Joy, and Death (2004); Freeborough and van Zyl (2022); Stevens, De Smedt, and Peeperkorn (2022).

To predict the variations in x_D and y_D we trained two LSTM models. Model 1 that takes into account only four input features that do not hold significant storm information ($LT, \chi, L, F10.7$) and model 2 that uses additional solar wind data as input features (B_x, B_y, B_z, n, T). For y_D these models showed good results for the considered test period in figure 9.7, while the models were not able to reproduce variations in x_D. When attempting to describe general diurnal variations by using solar wind data in model 2, no major improvements for x_D nor y_D are found (c.f. Coughlan et al. (2023)). In fact both models produce very similar variations. Model 2 learns very fast until epoch 6 and at the end of epoch 20 the model still keeps on learning (see figure 9.6). This implies that further improvements are ongoing and further training should be done. However, ending the training of model 2 at epoch 20 may imply that it was only able to pick up similar patterns as model 1. One reason for this may be that the main drivers are indeed to be found in the input parameters of model 1. Another possibility may be that the architecture of both LSTMs are too simple for the complexity of the problem and thus both struggle to generalize the data in a similar manner. Both models predict x_D and y_D simultaneously and their final mean absolute error indicates that the models work well. Still, both models perform poorly in describing the variations in x_D. On one hand this means that the final mean absolute error is not a good metric to describe model performance and on the other hand it implies that future modeling efforts should consider the prediction of each component separately as x_D is so much more complex than y_D.

The initial idea for the LSTM models is to use them for the baseline determination. In section 6.3, the analytical shift model $\tilde{x}_{B,shift}$, $\tilde{y}_{B,shift}$ and the diurnal variations from previous days $\tilde{x}_B$, $\tilde{y}_B$ was used to replace the filter baseline during identified disturbance intervals, see equations (6.7) to (6.10). We can follow the same strategy and derive a baseline based on the preliminary results of the LSTM models. The two LSTM models produce very similar curves, however as the baseline should ideally contain quiet variations, we use model 1 as it is not learning from solar wind variations. With $\tilde{x}_{D,\text{model1}}$ and $\tilde{y}_{D,\text{model1}}$ denoting the results on the test-set of LSTM model 1 (section 9.3.1), the LSTM substitution baseline writes as

$$\tilde{x}_{LSTM} = \tilde{x}_{>24} + \tilde{x}_{D,\text{model1}} \tag{10.1}$$
$$\tilde{y}_{LSTM} = \tilde{y}_{>24} + \tilde{y}_{D,\text{model1}} \tag{10.2}$$

with $\tilde{x}_{>24}$ and $\tilde{y}_{>24}$ being the smoothed long-term filters over three days as defined in section 6.3. We use these to replace the filter baseline during identified disturbance intervals. In figure 10.1, the resulting LSTM baseline (in green) is compared to the baseline using previous diurnal variations (equations (6.9) and (6.10)) for X (top) and Y (bottom) component. The measurements are in grey and the filter baseline is in black.

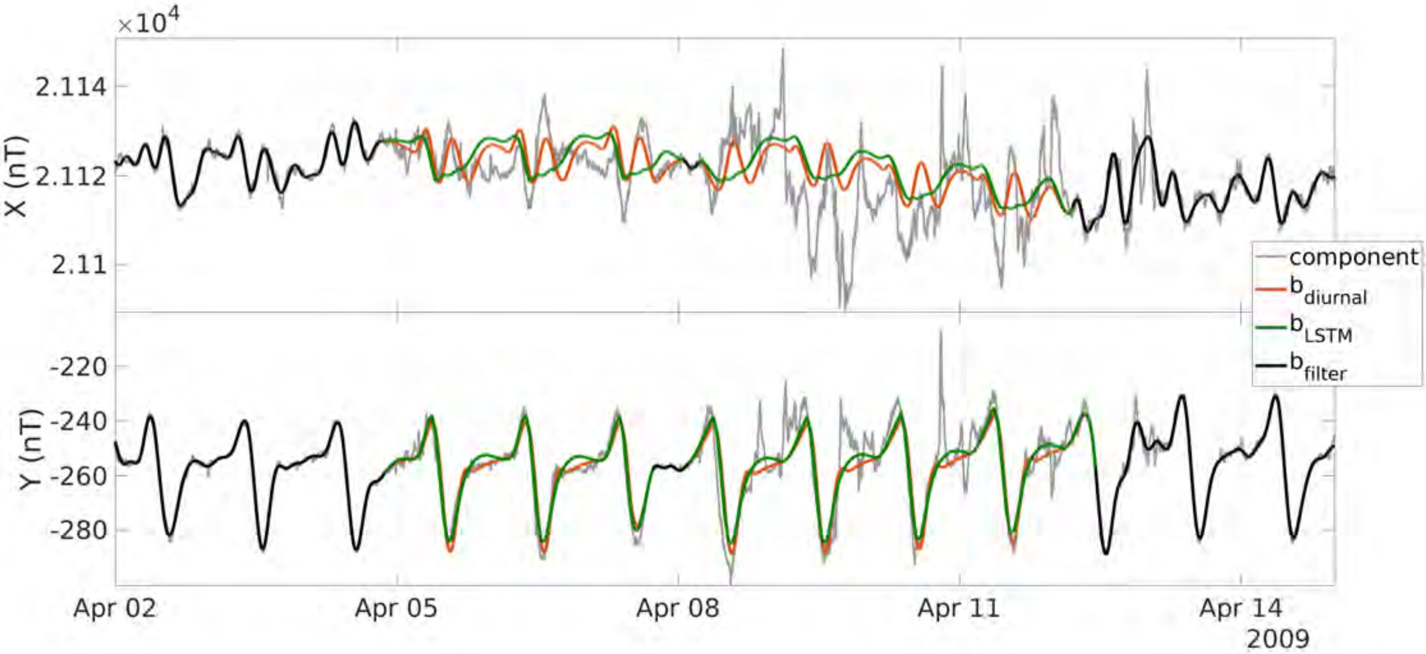

Figure 10.1: Comparison of the baseline using the diurnal model (orange) from equations (6.9) to (6.10) and the LSTM model (green) during 2nd to 15th of April 2009 for the X (upper panel) and Y (lower panel) component. The measurements are in grey and the filter baseline is in black.

In the upper panel of figure 10.1, the LSTM baseline b_{LSTM} for X in green shows a typical quiet pattern which is, however, very different from the variations of the previous quiet days (in black). In particular, a secondary smaller peak is not present while it is observed in the diurnal baseline b_{diurnal} in orange. In general the diurnal baseline captures the local variations from previous days well. This strongly suggests that the LSTM model for x_D requires further improvements with respect to more conventional methods.

For the Y component in the lower panel, both the LSTM and the analytical model describe possible quiet variations well. The location of the maxima and minima are well captured, together with the amplitudes. The only difference is that the LSTM baseline describes a small crest in-between minima and maxima. During this exemplary period, we can conclude that the LSTM model 1, though not ideal, produces a passable baseline, especially for the Y component, and motivates further work in this direction.

As such the introduced LSTM models may be used as a benchmark model for future improvements. From the training insights, one of the first improvement steps is to increase the number of epochs and increase the complexity of the model for x_D. In general, a dedicated hyperparameter tuning should be conducted to optimise the hyperparameters like the learning rate, number of hidden layers and their amount of neurons and the look-back time. Apart from using a fixed amount of epochs, flexible stopping conditions may be put in place to avoid over- and underfitting. Additionally, further validation techniques can be leveraged to improve model accuracy and input biases. For example, the walk-forward validation method is based on the training of several models by using different splits of the training and validation sets.

Furthermore, both models were trained on the basis of a ten year period and their prediction were presented on a specific, limited time-interval. Further investigations of model predictions for varying solar cycle phases and solar wind parameters, as well as seasons should be conducted. In fact, the data in the training, test and validation sets is continuous. Different splits of these sets can lead to generalisation improvements. Also expanding the training set to include a wider range of time can help the model improve. For describing quiet variations, one step would be to change the input data to contain only CK days as has been done in chapter 5.2. In this case, however, the data is no longer continuous. Other neural network architectures may be deployed, that take into account the duration disturbances between quiet days.

Once the model is trained, predictions can be calculated within milliseconds, which makes any of these models suitable for baselines in real-time applications from this point of view. Further efforts should be put into feature selections, comparing different methods and closely discussing them. From the considerations in this chapter, it is also clear, that AI models are only as good as their input data and, that though they offer very powerful and promising tools, the provided results still need close investigations and analysis, as is the case for any modeling effort.

Part IV

Conclusion and Perspective

Final Conclusion and Perspective for Future Work

In the very beginning of this thesis I formulated two research questions which I motivated and tried to answer over the course of this thesis. In the following I summarise the found answers.

1. Is the derived baseline reflecting the quiet variations of the geomagnetic field?

Magnetic indices condense geomagnetic field information into a few values that aim to describe the complex state of the near-Earth system driven by space weather (chapters 2 and 3). The response of the geomagnetic field to space weather events is an important measure for their severity. As the geomagnetic field is a superposition of sources, the storm signatures need to be extracted from other, quiet variations. This separation of sources is achieved by geomagnetic baselines, that describe the quiet variations and build the basis of magnetic indices. Various baseline methods exist, but are not applicable for (near-)real time applications (chapter 3.2). Furthermore, while the steps for the derivation of the baseline for most methods is well described, the demonstration of contained sources is widely missing.

In chapter 4, I introduce a methodology to extract the quiet variations of the geomagnetic field in an automatic and efficient way by using temporal filters with suitable frequency characteristics. In chapter 5, the resulting filter responses are thoroughly analysed with respect to geomagnetic field source contribution and the identification of quiet sources. Three analytical models are proposed to describe the observed variations. Through detailed discussions and physical analysis I concluded that the filter method is suitable to capture the quiet sources of the geomagnetic field. I refer to this preliminary baseline as the filter baseline.

At this point, the answer to the first research question was presented. The thorough analysis and physical interpretation of the filter baseline showed that it is able to automatically extract and describe the sources that contribute to the quiet geomagnetic field in mid-latitudes, the main ones being the secular variation and the solar quiet current systems. An important result of the analysis is, that the filter baseline is able to capture the intrinsic day-to-day variability of the Sq current systems which is not the case for the majority of existing baseline methods. Furthermore, the derived models and the investigation of the day-to-day variability improves our understanding of the climatology of the solar quiet current systems.

However, the filter baseline is only preliminary, because the temporal filters do contain disturbance contributions during non-quiet periods as outlined in chapter 5.3. Using the filter baseline directly would thus lead to underestimation of disturbances within residuals. I address this issue in chapter 6. The solution comprises two steps: step 1 identifies periods during which a disturbance is underestimated and in step 2 I infer possible quiet variations during the identified disturbance period. The initial filter baseline is adapted during the disturbance periods to lead to the proposition of several final baselines. In chapter 6.4, I compare the results of the introduced baseline method with existing ones.

The main conclusion I can draw from this work is that the introduced baselines may be used for dedicated magnetic index derivation as each of them describes the quiet geomagnetic field variations satisfyingly well. Additionally, the proposed baseline derivation does not rely on further input parameters than the magnetic field measurements themselves and as such may be used in near-real time applications. Nonetheless, several aspects remain that may be of interest for future work:

1. **Real-time applications.**
   The filtering method is based on a centred 3-days window and thus the final baseline will only be available with a delay of one and a half days. In an operational context this leads to two products: 1) the quick-look baseline, that is based on either the filtering of the previous 3 days or that takes into account some kind of forward propagation of filter values and 2) the final baseline that is available after one and a half days. Studies that quantify the differences between the quick-look and final baseline would support the applicability of such an approach.

2. **Source separation in geomagnetic field measurements.**
   Highly complex models taking into account a wealth of magnetic field measurements from all around the globe including satellite data are employed to describe and understand the geomagnetic field. These models are doing very good jobs in source separation and the determination of various contributions, but cannot be deployed in near-real time due to their complexity. Although the filtering method is able to extract the quiet sources sufficiently well, it is not able to perform a full source separation like those models. With the growing availability of reliable data streams from several observatories, it may be possible to enhance the filtering method with a spatial component by e.g. comparing the signal between neighbouring stations to improve the source separation in near-real time.

3. **Disturbance detection.**
   The introduced disturbance detection would also benefit from a spatial component. This would enable the identification and propagation of disturbance events including local anomaly detection. Additionally, further parameters would support the identification of full periods during which the filter baseline needs to be replaced, e.g. to fully include onsets of events. In any case, the introduced disturbance detection may be leveraged for further applications which require automatic identification of storm and disturbance signatures.

4. **The influence of the neutral atmosphere.**
   It is well known, and we also encountered this fact when deriving the models, that the neutral atmosphere plays an important part in the day-to-day variability of the solar quiet current systems as it directly influences the dynamo region through tides and winds. Several highly sophisticated modelling efforts are actively pursued to describe the neutral atmosphere and to gain insights into the ionospheric dynamo, which would lead to a better description of the day-to-day variations and drivers of the solar quiet current systems. Additional parameters that describe and characterise winds and tides within the neutral atmosphere may also be leveraged to improve the baseline description and replacement. Even a first useful step would be to study the thermospheric density, temperature and winds at the location of the

magnetic observatories. Such an approach can be realised by equipping observatories with suitable instruments like e.g. the Fabry-Perot interferometer.

5. **The involvement of the community.**
   As mentioned throughout this thesis, the identification of the baseline has no objective ground truth (at least at the time of this work). In the future sophisticated geomagnetic field models and advances in research linked to Sun-Earth relationships and geomagnetic field variations can help to identify such a ground truth. Until then, it is important to involve the community, including users that have an interest in the baseline (and derived indices) during the baseline derivation process. Together, feasible and measurable criteria for baselines and related baseline-testing procedures should be discussed and introduced.

6. **Derivation of magnetic indices.**
   The introduced baseline options may be used in geomagnetic index derivation. Such indices are not limited in their real-time derivation when using the introduced baseline. Further studies should be conducted, demonstrating the baselines' behaviour and characteristics, as well as outline contained sources for additional geomagnetic observatories in various longitudinal and latitudinal ranges. Such a study can also support users in choosing the ideal baseline for their specific application and shed light on advantages and disadvantages that need to be kept in mind. These aspects are ideally discussed with the specific community (e.g. internal field modelling would benefit from different properties than space weather forecasts).

2. To which extent can AI support the determination of the baseline with respect to traditional methods?

The main focus of this thesis lays in the determination of the baseline with conventional methods. However, in the second part I explored well-established machine and deep learning methodologies to determine quiet variations with limited success. As has been a common challenge, the neural network faced difficulties in describing the variations in the X component while the Y component was depicted fairly well. Though limited, the baseline substitution with the preliminary LSTM model is a promising start and the results pave the way for future improvements that provide a variety of possibilities:

1. **One model per component.**
   As X is so much more complicated than Y, one model per component, one that is more complex and one that is simpler, should be used. Additionally, a model for the third component Z that has not been considered in this work may allow the mapping of induction effects.

2. **Understanding the black box.**
   Once an appropriate model is found for the ground perturbations or quiet variations, dedicated feature importance methodologies based on the type of model should be deployed. Further parameters for the neutral atmosphere should be considered as input for these models. This will enhance our understanding of the main drivers within the results and thus of diurnal variations.

3. **Disturbance detection.**
   Chapter 6 is dedicated to the identification of disturbance intervals. It would be of

interest to know to which extend machine learning is able to identify such intervals. As a first step, a supervised model can be used to reproduce the methodology deployed in this thesis which then can be further improved. Another possibility would be to deploy unsupervised methods for which the computer will derive its own classifications of disturbances.

4. **Now- and Forecasting capabilities.**
   The results from this thesis motivate the generation of (analytical or AI) baselines for a number of observatories within a very short delay as this is possible as soon as the magnetic field measurements are available. As an increasing number of observatories provides near-real time and high quality data, the now-casting of the geomagnetic field state becomes evermore possible and accurate. Adding solar wind data, sophisticated AI models can be derived and leveraged to enhance forecasting capabilities.

In total, this thesis introduces a novel baseline derivation for near-real time applications which results are extensively discussed and presented in an unprecedented way. For the first time the application of AI for baseline derivations was deployed, delivering promising results.

Still, this thesis opens up more questions than it was able to close. Each of the above listed perspectives would deserve a doctoral study on its own for which I hope the current work may be of support. Especially future work that derives new families of magnetic indices with the help of the introduced baseline concepts is an exciting part I would be happy to contribute to. The application of AI shows promising results and I am excited to see further applications, especially in the support of baseline and magnetic index derivation. With this thesis I am proud to have contributed to the understanding of space weather.

The End

References

Abadi, M., Agarwal, A., Barham, P., Brevdo, E., Chen, Z., Citro, C., … Zheng, X. (2016). Tensorflow: Large-scale machine learning on heterogeneous distributed systems. *arxiv.org*. doi: doi.org/10.48550/arXiv.1605.08695

Akasofu, S.-I., & Chapman, S. (1964). On the asymmetric development of magnetic storm fields in low and middle latitudes. *Planetary and Space Science*, *12*, 607–626. doi: 10.1016/0032-0633(64)90008-X

Alken, P., Thébault, E., Beggan, C. D., Amit, H., Aubert, J., Baerenzung, J., … Zhou, B. (2021). International Geomagnetic Reference Field: the thirteenth generation. *Earth, Planets and Space*, *73*(1). doi: 10.1186/s40623-020-01288-x

Allen, R. C., Ho, G. C., Jian, L. K., Mason, G. M., Vines, S. K., & Lario, D. (2020). Predictive Capabilities and Limitations of Stream Interaction Region Observations at Different Solar Longitudes. *Space Weather*, *18*(4). doi: 10.1029/2019SW002437

Althelaya, K. A., El-Alfy, E. S. M., & Mohammed, S. (2018). Stock Market Forecast Using Multivariate Analysis with Bidirectional and Stacked (LSTM, GRU). *21st Saudi Computer Society National Computer Conference, NCC 2018*. doi: 10.1109/NCG.2018.8593076

Amory-Mazaudier, C. (1983). Contribution à l'étude des courants électriques, des champs électriques et des vents neuters ionospheriques des moyennes latitudes, variation régulière et variations perturnées : Etudes de cas à partir des observations du sondeur à diffusion incohérente de saint-santin, en relation avec les observations du champ magnétique terrestre. *PhD Thesis at Universite de Paris VI*.

Astafyeva, E., Zakharenkova, I., & Förster, M. (2015). Ionospheric response to the 2015 St. Patrick's Day storm: A global multi-instrumental overview. *Journal of Geophysical Research: Space Physics*, *120*(10), 9023–9037. doi: 10.1002/2015JA021629

Bailey, R. L., & Leonhardt, R. (2016). Automated detection of geomagnetic storms with heightened risk of GIC. *Earth, Planets and Space*, *68*(1), 1–13. doi: doi.org/10.1186/s40623-016-0477-2

Baker, D. N. (2019). Geomagnetic field sources: From earth's core to the sun. In M. Mandea, M. Korte, Y. Andrew, & E. Petrovsky (Eds.), *Geomagnetism, aeronomy and space weather: A journey from the earth's core to the sun* (pp. 41–47). Cambridge University Press. doi: 10.1017/9781108290135.005

Balasis, G., Papadimitriou, C., & Boutsi, A. Z. (2019). Ionospheric response to solar and interplanetary disturbances: a Swarm perspective. *Philosophical Transactions of the Royal Society A: Mathematical, Physical and Engineering Sciences*, *377*(2148), 20180098. doi: 10.1098/rsta.2018.0098

Bartels, J. (1939). *Terrestrial Magnetism and Electricity* (J. A. Fleming, Ed.). Dover.

Bartels, J. (1949). *The standardized index, Ks, and the planetary index, Kp* (Tech. Rep. No. IATME Bulletin 12b). Paris: International Union of Geodesy and Geophysics.

Bartels, J. (1957a). The geomagnetic measures for the time-variations of solar corpuscular radiation, described for use in correlation studies in other geophysical fields. *Annals of the International Geophysical Year,*(4), 227–236. doi: 10.1016/B978-1-4832-1304-0.50007-5

Bartels, J. (1957b). The technique of scaling indices K and Q of geomagnetic activity. *Annals of the International Geophysical Year*(4), 215–226.

Bartels, J., Heck, N. H., & Johnston, H. F. (1939). The three-hour-range index measuring geomagnetic activity. *Journal of Geophysical Research*, *44*(4), 411. doi: 10.1029/te044i004p00411

Bartels, J., & Veldkamp, J. (1954). International data on magnetic disturbances, first quarter, 1954. *Journal of Geophysical Research*, *59*(3), 423–427. doi: 10.1029/jz059i003p00423

Baumjohann, W., & Treumann, R. A. (2012). *Basic space plasma physics (revised edition).* Imperial College Press. doi: 10.1142/P850

BCMT. (2023). Bureau central de magnetisme terrestre. *Magnetic Definitive Data Repository*. doi: 10.18715/BCMT.MAG.DEF

Behannon, K. W., & Ness, N. F. (1966a). *The design of numerical filters for geomagnetic data analysis - NASA Technical Reports Server (NTRS).* Work of the US Gov. Public Use Permitted.

Behannon, K. W., & Ness, N. F. (1966b). Magnetic storms in the Earth's magnetic tail. *Journal of Geophysical Research*, *71*(9), 2327–2351. doi: 10.1029/JZ071I009P02327

Bengio, Y., Simard, P., & Frasconi, P. (1994). Learning Long-Term Dependencies with Gradient Descent is Difficult. *IEEE Transactions on Neural Networks*, *5*(2), 157–166. doi: 10.1109/72.279181

Bernoux, G., Brunet, A., Buchlin, É., Janvier, M., & Sicard, A. (2022). Forecasting the Geomagnetic Activity Several Days in Advance Using Neural Networks Driven by Solar EUV Imaging. *Journal of Geophysical Research Space Physics*, *127*(10), 10. doi: 10.1029/2022JA030868

Bhargava, B. N., & Yacob, A. (1970). The secular variation of the magnetic field and its cyclic components. *Journal of Atmospheric and Terrestrial Physics*, *32*(3), 365–372. doi: 10.1016/0021-9169(70)90008-5

Bhaskar, A., & Vichare, G. (2019). Forecasting of SYMH and ASYH indices for geomagnetic storms of solar cycle 24 including St. Patrick's day, 2015 storm using NARX neural network. *Journal of Space Weather and Space Climate*, *9*, A12. doi: 10.1051/swsc/2019007

Bloxham, J., & Gubbins, D. (1985). The secular variation of Earth's magnetic field. *Nature*, *317*(6040), 777–781. doi: 10.1038/317777a0

Breiman, L. (2001). Random forests. *Machine Learning*, *45*(1), 5–32. doi: 10.1023/A:1010933404324

Bretagnon, P., & Francou, G. (1988). Planetary theories in rectangular and spherical variables: Vsop87 solution. *A&A*, *202*, 309.

Briggs, B. H. (1984). The variability of ionospheric dynamo currents. *Journal of Atmospheric and Terrestrial Physics*, *46*(5), 419–429. doi: 10.1016/0021-9169(84)90086-2

Brown, E. J., Svoboda, F., Meredith, N. P., Lane, N., & Horne, R. B. (2022). Attention-Based Machine Vision Models and Techniques for Solar Wind Speed Forecasting Using Solar EUV Images. *Space Weather*, *20*(3). doi: 10.1029/2021SW002976

Brown, G. M., & Williams, W. R. (1969). Some properties of the day-to-day variability of Sq(H). *Planetary and Space Science*, *17*(3), 455–470. doi: 10.1016/0032-0633(69)90076-2

Burkart, N., & Huber, M. F. (2021). A Survey on the Explainability of Supervised Machine Learning. *Journal of Artificial Intelligence Research*, *70*, 245–317. doi: 10.1613/jair.1.12228

Caan, M. N., McPherron, R. L., & Russell, C. T. (1973). Solar wind and substorm-related changes in the lobes of the geomagnetic tail. *Journal of Geophysical Research*, *78*(34), 8087–8096. doi: 10.1029/ja078i034p08087

Cahill, L. J., & van Allen, J. A. (1956). High altitude measurements of the Earth's magnetic field with a proton precession magnetometer. *Journal of Geophysical Research*, *61*(3), 547–558. doi: 10.1029/JZ061i003p00547

Campbell, W. H. (1989). An introduction to quiet daily geomagnetic fields. *Pure and Applied Geophysics PAGEOPH*, *131*(3), 315–331. doi: 10.1007/BF00876831

Campbell, W. H. (2003). *Introduction to Geomagnetic Fields.* Cambridge University Press. doi: 10.1017/cbo9781139165136

Campbell, W. H., Arora, B. R., & Schiffmacher, E. R. (1993). External Sq currents in the India-Siberia region. *Journal of Geophysical Research: Space Physics*, *98*(A3), 3741–3752. doi: 10.1029/92ja02552

Campbell, W. H., & Schiffmacher, E. (1987). Quiet Ionospheric Currents and Earth Conductivity Profile Computed from Quiet-time Geomagnetic Field Changes in the Region of Australia. *Australian Journal of Physics*, *40*(1), 73. doi: 10.1071/ph870073

Campbell, W. H., & Schiffmacher, E. R. (1988). Quiet ionospheric currents of the southern hemisphere derived from geomagnetic records. *Journal of Geophysical Research*, *93*(A2), 933. doi: 10.1029/ja093ia02p00933

Camporeale, E. (2019). The Challenge of Machine Learning in Space Weather: Nowcasting and Forecasting. *Space Weather*, *17*(8), 1166–1207. doi: 10.1029/2018SW002061

Case, N. A., & MacDonald, E. A. (2015). Aurorasaurus and the St Patrick's Day storm. *Astronomy & Geophysics*, *56*(3), 3.13–3.14. doi: 10.1093/astrogeo/atv089

Chambodut, A., Marchaudon, A., Menvielle, M., El-Lemdani Mazouz, F., & Lathuillére, C. (2013). The K -derived MLT sector geomagnetic indices. *Geophysical Research Letters*, *40*(18), 4808–4812. doi: 10.1002/grl.50947

Chapman, S. (1931). The absorption and dissociative or ionizing effect of monochromatic radiation in an atmosphere on a rotating earth. *Proceedings of the Physical Society*, *43*(1), 26–45. doi: 10.1088/0959-5309/43/1/305

Chapman, S. (1951). The equatorial electrojet as detected from the abnormal electric current distribution above Huancayo, Peru, and elsewhere. *Archiv für Meteorologie, Geophysik und Bioklimatologie Serie A*, *4*(1), 368–390. doi: 10.1007/BF02246814

Charbonneau, P. (2020). Dynamo models of the solar cycle. *Living Reviews in Solar Physics*, *17*(1), 4. doi: 10.1007/s41116-020-00025-6

Cho, K., Van Merriënboer, B., Gulcehre, C., Bahdanau, D., Bougares, F., Schwenk, H., & Bengio, Y. (2014). Learning phrase representations using RNN encoder-decoder for statistical machine translation. In *Emnlp 2014 - 2014 conference on empirical methods in natural language processing, proceedings of the conference* (pp. 1724–1734). Association for Computational Linguistics (ACL). doi: 10.3115/v1/d14-1179

Chree, C. (1913). Some Phenomena of Sunspots and of Terrestrial Magnetism at Kew Observatory. *RSPTA*, *212*(484-496), 75–116. doi: 10.1098/RSTA.1913.0003

Chulliat, A., Vigneron, P., & Hulot, G. (2016). First results from the Swarm Dedicated Ionospheric Field Inversion chain Swarm Science Results after two years in Space 1. Geomagnetism. *Earth, Planets and Space*, *68*(1), 1–18. doi: 10.1186/s40623-016-0481-6

Cnossen, I., Wiltberger, M., & Ouellette, J. E. (2012). The effects of seasonal and diurnal variations in the Earth's magnetic dipole orientation on solar wind-magnetosphere-ionosphere coupling. *Journal of Geophysical Research: Space Physics*, *117*(11). doi: 10.1029/2012JA017825

Colah. (2015). *Understanding LSTM Networks.* Github. Retrieved from https://colah.github.io/posts/2015-08-Understanding-LSTMs/

Cole, K. (1966). Magnetic storms and associated phenomena. *Space Science Reviews*, *5*(6). doi: 10.1007/BF00173103

Collado-Villaverde, A., Muñoz, P., & Cid, C. (2021). Deep Neural Networks With Convolutional and LSTM Layers for SYM-H and ASY-H Forecasting. *Space Weather*, *19*(6). doi: 10.1029/2021SW002748

Constable, C. (2016). Earth's Electromagnetic Environment. *Surveys in Geophysics*, *37*(1), 27–45. doi: 10.1007/s10712-015-9351-1

Coster, A. J., Erickson, P. J., Lanzerotti, L. J., Zhang, Y., & Paxton, L. J. (2021). Space Physics and Aeronomy Collection: Space Weather Effects and Applications. *Space Physics and Aeronomy Collection: Space Weather Effects and Applications*, 1–225. doi: 10.1002/9781119815570

Coughlan, M., Keesee, A., Pinto, V., Mukundan, R., Marchezi, J. P., Johnson, J., ... Hampton, D. (2023). Probabilistic Forecasting of Ground Magnetic Perturbation Spikes at Mid-Latitude Stations. *Space Weather*, *21*(6). doi: 10.1029/2023SW003446

Cowley, S. W. (1991). The structure and length of tail-associated phenomena in the solar wind downstream from the Earth. *Planetary and Space Science*, *39*(7), 1039–1043. doi: 10.1016/0032-0633(91)90110-V

Cowling, T. G. (1932). The Electrical Conductivity of an Ionised Gas in the Presence of a Magnetic Field. *Monthly Notices of the Royal Astronomical Society*, *93*(1), 90–97. doi: 10.1093/mnras/93.1.90

Cranmer, S. R., Asgari-Targhi, M., Miralles, M. P., Raymond, J. C., Strachan, L., Tian, H., & Woolsey, L. N. (2015). *The role of turbulence in coronal heating and solar wind expansion* (Vol. 373) (No. 2041). doi: 10.1098/rsta.2014.0148

Cravens, T. E. (1997). *Physics of Solar System Plasmas.* Cambridge University Press. doi: 10.1017/cbo9780511529467

Daglis, L. A., Thorne, R. M., Baumjohann, W., & Orsini, S. (1999). The terrestrial ring current: Origin, formation, and decay. *Reviews of Geophysics*, *37*(4), 407–438. doi: 10.1029/1999RG900009

Davis, T. N., & Sugiura, M. (1966). Auroral electrojet activity index AE and its universal time variations. *Journal of Geophysical Research*, *71*(3), 785–801. doi: 10.1029/jz071i003p00785

Day, K. A., Taylor, M. J., & Mitchell, N. J. (2012). Mean winds, temperatures and the 16- and 5-day planetary waves in the mesosphere and lower thermosphere over Bear Lake Observatory (42° N, 111° W). *Atmospheric Chemistry and Physics*, *12*(3), 1571–1585. doi: 10.5194/acp-12-1571-2012

De Michelis, P., Pignalberi, A., Consolini, G., Coco, I., Tozzi, R., Pezzopane, M., ... Balasis, G. (2020, aug). On the 2015 St. Patrick's Storm Turbulent State of the Ionosphere: Hints From the Swarm Mission. *Journal of Geophysical Research: Space Physics*, *125*(8). doi: 10.1029/2020JA027934

Denton, M. H., Borovsky, J. E., Skoug, R. M., Thomsen, M. F., Lavraud, B., Henderson, M. G., ... Liemohn, M. W. (2006). Geomagnetic storms driven by ICME- and CIR-dominated solar wind. *Journal of Geophysical Research: Space Physics*, *111*(A7), 7–07. doi: 10.1029/2005JA011436

de Pater, I., & Lissauer, J. J. (2015). *Planetary sciences, updated second edition.* Cambridge: Cambridge University Press. doi: 10.1017/CBO9781316165270

Desmaris, G. (2015). Cosmic radiation in aviation: radiological protection of Air France aircraft crew. *Annals of the ICRP*, *45*(1_suppl), 64–74. doi: 10.1177/0146645316636009

Dungey, J. W. (1961). The steady state of the Chapman-Ferraro problem in two dimensions. *Journal of Geophysical Research*, *66*(4), 1043–1047. doi: 10.1029/jz066i004p01043

Eastwood, J. P., Nakamura, R., Turc, L., Mejnertsen, L., & Hesse, M. (2017). *The Scientific Foundations of Forecasting Magnetospheric Space Weather* (Vol. 212) (No. 3-4). Springer Netherlands. doi: 10.1007/s11214-017-0399-8

Echer, E., Gonzalez, W. D., & Tsurutani, B. T. (2011). Statistical studies of geomagnetic storms with peak Dst<=-50nT from 1957 to 2008. *Journal of Atmospheric and Solar-Terrestrial Physics*, *73*(11-12), 1454–1459. doi: 10.1016/j.jastp.2011.04.021

Fang, T. W., Akmaev, R., Fuller-Rowell, T., Wu, F., Maruyama, N., & Millward, G. (2013). Longitudinal and day-to-day variability in the ionosphere from lower atmosphere tidal forcing. *Geophysical Research Letters*, *40*(11), 2523–2528. doi: 10.1002/grl.50550

Fang, T. W., Kubaryk, A., Goldstein, D., Li, Z., Fuller-Rowell, T., Millward, G., ... Babcock, E. (2022). Space Weather Environment During the SpaceX Starlink Satellite Loss in February 2022. *Space Weather*, *20*(11), e2022SW003193. doi: 10.1029/2022SW003193

Finlay, C. C., Kloss, C., Olsen, N., Hammer, M. D., Tøffner-Clausen, L., Grayver, A., & Kuvshinov, A. (2020). The CHAOS-7 geomagnetic field model and observed changes in the South Atlantic Anomaly. *Earth, Planets and Space*, *72*(1), 1–31. doi: 10.1186/s40623-020-01252-9

Finlay, C. C., Olsen, N., Kotsiaros, S., Gillet, N., & Tøffner-Clausen, L. (2016). Recent geomagnetic secular variation from Swarm and ground observatories as estimated in the CHAOS-6 geomagnetic field model. *Earth, Planets and Space*, *68*(1), 112. doi: 10.1186/s40623-016-0486-1

Forbes, J. M., Palo, S. E., & Zhang, X. (2000). Variability of the ionosphere. *Journal of Atmospheric and Solar-Terrestrial Physics*, *62*(8), 685–693. doi: 10.1016/S1364-6826(00)00029-8

Freeborough, W., & van Zyl, T. (2022). Investigating Explainability Methods in Recurrent Neural Network Architectures for Financial Time Series Data. *Applied Sciences 2022, Vol. 12, Page 1427*, *12*(3), 1427. doi: 10.3390/APP12031427

Ganushkina, N. Y., Liemohn, M. W., & Dubyagin, S. (2018). Current Systems in the Earth's Magnetosphere. *Reviews of Geophysics*, *56*(2), 309–332. doi: 10.1002/2017RG000590

Gauss, C. F. (1877). *Werke.* Berlin, Heidelberg: Springer Berlin Heidelberg. doi: 10.1007/978-3-642-49319-5

Genuer, R., Poggi, J.-M., & Tuleau-Malot, C. (2010). Variable selection using random forests. *Pattern Recognition Letters*, *31*(14), 2225–2236. doi: 10.1016/j.patrec.2010.03.014

Gers, F. A., & Schmidhuber, J. (2000). Recurrent nets that time and count. In *Proceedings of the international joint conference on neural networks* (Vol. 3, pp. 189–194). IEEE. doi: 10.1109/ijcnn.2000.861302

Ghimire, S., Deo, R. C., Wang, H., Al-Musaylh, M. S., Casillas-Pérez, D., & Salcedo-Sanz, S. (2022). Stacked LSTM Sequence-to-Sequence Autoencoder with Feature Selection for Daily Solar Radiation Prediction: A Review and New Modeling Results. *Energies*, *15*(3), 1061. doi: 10.3390/en15031061

Gilder, S. A., & Lhuillier, F. (2019). Can Paleomagnetism Distinguish Dynamo Regimes? In M. Mandea, M. Korte, Y. Andrew, & E. Petrovsky (Eds.), *Geomagnetism, aeronomy and space weather* (pp. 48–53). Cambridge University Press. doi: 10.1017/9781108290135.006

Gjerloev, J. W. (2012). The SuperMAG data processing technique. *Journal of Geophysical Research: Space Physics*, *117*(9), 9213. doi: 10.1029/2012JA017683

Golovkov, V. P., Zvereva, T. I., & Chernova, T. A. (2005). Secular variation of the geomagnetic field from satellite data. In *Earth observation with champ: Results from three years in orbit* (pp. 323–328). Berlin/Heidelberg: Springer-Verlag. doi: 10.1007/3-540-26800-6

Gonzalez, W. D., Joselyn, J. A., Kamide, Y., Kroehl, H. W., Rostoker, G., Tsurutani, B. T., & Vasyliunas, V. M. (1994). What is a geomagnetic storm? *Journal of Geophysical Research*, *99*(A4), 5771. doi: 10.1029/93ja02867

Goodfellow, I., Bengio, Y., & Courville, A. (2016). *Deep Learning.* MIT Press.

Gray, R. O., Corbally, C. J., Burgasser, A. J., Hanson, M. M., Kirkpatrick, J. D., & Walborn, N. R. (2021). *Stellar Spectral Classification.* Princeton University Press. doi: 10.2307/j.ctv1nxcw72

Greener, J. G., & Schlapp, D. M. (1979). A study of day-to-day variability of Sq over Europe. *Journal of Atmospheric and Terrestrial Physics*, *41*(2), 217–223. doi: 10.1016/0021-9169(79)90014-X

Gregorutti, B., Michel, B., & Saint-Pierre, P. (2017). Correlation and variable importance in random forests. *Statistics and Computing*, *27*(3), 659–678. doi: 10.1007/s11222-016-9646-1

Guan, Y., & Plötz, T. (2017). Ensembles of Deep LSTM Learners for Activity Recognition using Wearables. *Proceedings of the ACM on Interactive, Mobile, Wearable and Ubiquitous Technologies*, *1*(2), 1–28. doi: 10.1145/3090076

Gubbins, D. (2008). Earth science: Geomagnetic reversals. *Nature*, *452*(7184), 165–167. doi: 10.1038/452165a

Guyon, I. M. (1997). A Scaling Law for the Validation-Set Training-Set Size Ratio.

Haberle, V., Marchaudon, A., Chambodut, A., & Blelly, P. L. (2022). Direct Determination of Geomagnetic Baselines During Quiet Periods for Low- and Mid-Latitude Observatories. *Journal of Geophysical Research: Space Physics*, *127*(8), e2022JA030407. doi: 10.1029/2022JA030407

Hale, G. E. (1908). On the Probable Existence of a Magnetic Field in Sun-Spots. *The Astrophysical Journal*, *28*, 315. doi: 10.1086/141602

Hamming, R. W. (1977). *Digital filters.* Prentice-Hall.

Hasegawa, M. (1960). On the position of the focus of the geomagnetic S q current system. *Journal of Geophysical Research*, *65*(5), 1437–1447. doi: 10.1029/jz065i005p01437

Hathaway, D. H. (2015). The solar cycle. *Living Reviews in Solar Physics*, *12*(1), 4. doi: 10.1007/lrsp-2015-4

Hemant, K., Maus, S., & Haak, V. (2005). Interpretation of CHAMP crustal field anomaly maps using geographical information system (GIS) technique. In *Earth observation with champ: Results from three years in orbit* (pp. 249–254). Berlin/Heidelberg: Springer-Verlag. doi: 10.1007/3-540-26800-6

Hermans, M., in neural Information, B. S. A., & 2013, U. (2013). Training and analysing deep recurrent neural networks. *proceedings.neurips.ccM Hermans, B SchrauwenAdvances in neural information processing systems, 2013 • proceedings.neurips.cc.*

Hesse, M., & Cassak, P. A. (2020). Magnetic Reconnection in the Space Sciences: Past, Present, and Future. *Journal of Geophysical Research: Space Physics*, *125*(2). doi: 10.1029/2018JA025935

Hochreiter, S., & Schmidhuber, J. (1997). Long Short-Term Memory. *Neural Computation*, *9*(8), 1735–1780. doi: 10.1162/neco.1997.9.8.1735

Hodson, R. (2018). Digital revolution. *Nature*, *563*(7733), S131. doi: 10.1038/d41586-018-07500-z

Holme, R., & Olsen, N. (2005). The spectrum of the magnetic secular variation. In *Earth observation with champ: Results from three years in orbit* (pp. 329–334). Berlin/Heidelberg: Springer-Verlag. doi: 10.1007/3-540-26800-6

Hudson, H. S. (2011). Global Properties of Solar Flares. *Space Science Reviews*, *158*(1), 5–41. doi: 10.1007/s11214-010-9721-4

Hutchinson, J. A., Wright, D. M., & Milan, S. E. (2011). Geomagnetic storms over the last solar cycle: A superposed epoch analysis. *Journal of Geophysical Research: Space Physics*, *116*(9), n/a–n/a. doi: 10.1029/2011JA016463

Iijima, T., & Potemra, T. A. (1978). Large-scale characteristics of field-aligned currents associated with substorms. *Journal of Geophysical Research*, *83*(A2), 599. doi: 10.1029/ja083ia02p00599

Iyemori, T. (1990). Storm-time magnetospheric currents inferred from mid-latitude geomagnetic field variations. *Journal of geomagnetism and geoelectricity*, *42*(11), 1249–1265. doi: 10.5636/jgg.42.1249

Iyemori, T., Takeda, M., Nose, M., Odagi, Y., & Toh, H. (2010). *Mid-latitude Geomagnetic Indices "ASY" and "SYM" for 2009 (Provisional)* (Tech. Rep.). Kyoto: Data Analysis Center for Geomagnetism and Space Magnetism, Graduate School of Science, Kyoto University.

Jacobsen, K. S., & Andalsvik, Y. L. (2016). Overview of the 2015 St. Patrick's day storm and its consequences for RTK and PPP positioning in Norway. *Journal of Space Weather and Space Climate*, *6*, A9. doi: 10.1051/swsc/2016004

Jadhav, G., Rajaram, M., & Rajaram, R. (2002, aug). A detailed study of equatorial electrojet phenomenon using Ørsted satellite observations. *Journal of Geophysical Research: Space Physics*, *107*(A8), SIA 12–1. doi: 10.1029/2001JA000183

Jakowski, N., Fichtelmann, B., & Jungstand, A. (1991). Solar activity control of ionospheric and thermospheric processes. *Journal of Atmospheric and Terrestrial Physics*, *53*(11-12), 1125–1130. doi: 10.1016/0021-9169(91)90061-B

Jankowski, J., & Sucksdorff, C. (1996). *Guide for Magnetic Measurements and Observatory Practice* (Tech. Rep.).

Janzhura, A., & Troshichev, O. (2008). Determination of the running quiet daily geomagnetic variation. *Journal of Atmospheric and Solar-Terrestrial Physics*, *70*(7), 962–972. doi: 10.1016/j.jastp.2007.11.004

Ji, E. Y., Moon, Y. J., Gopalswamy, N., & Lee, D. H. (2012). Comparison of Dst forecast models for intense geomagnetic storms. *Journal of Geophysical Research: Space Physics*, *117*(3), 3209. doi: 10.1029/2011JA016872

Jin, H., Miyoshi, Y., Fujiwara, H., Shinagawa, H., Terada, K., Terada, N., … Saito, A. (2011). Vertical connection from the tropospheric activities to the ionospheric longitudinal structure simulated by a new Earth's whole atmosphere-ionosphere coupled model. *Journal of Geophysical Research: Space Physics*, *116*(1), 1316. doi: 10.1029/2010JA015925

Johnston, H. F. (1943). Mean K-Indices from Twenty-one Magnetic Observatories and Five Disturbed Days for 1942. *Journal of Geophysical Research*, *48*(4), 219. doi: 10.1029/TE048i004p00219

Joselyn, J. A. (1989). Geomagnetic quiet day selection. *Pure and Applied Geophysics PAGEOPH*, *131*(3), 333–341. doi: 10.1007/BF00876832/METRICS

Jozefowicz, R., Zaremba, W., & Sutskever, I. (2015). An empirical exploration of recurrent network architectures. In *Icml'15: Proceedings of the 32nd international conference on international conference on machine learning* (pp. 2342–2350). Lille: JMLR.org. doi: dl.acm.org/doi/10.5555/3045118.3045367

Kärhä, O., & Tanskanen, E. I. (2022). Newly Digitized Data From Scandinavian Magnetometer Array Network Shows Large Regional Differences in Magnetic Environment. *Journal of Geophysical Research: Space Physics*, *127*(5), e2022JA030311. doi: 10.1029/2022JA030311

Kato, S. (1957). Horizontal wind systems in the ionospheric E region deduced from the dynamo theory of the geomagnetic Sq variation part IV. *Journal of geomagnetism and geoelectricity*, *9*(2), 107–115. doi: 10.5636/jgg.9.107

Kawano-Sasaki, K., & Miyahara, S. (2008). A study on three-dimensional structures of the ionospheric dynamo currents induced by the neutral winds simulated by the Kyushu-GCM. *Journal of Atmospheric and Solar-Terrestrial Physics*, *70*(11-12), 1549–1562. doi: 10.1016/j.jastp.2008.05.004

Keesee, A. M., Pinto, V., Coughlan, M., Lennox, C., Mahmud, M. S., & Connor, H. K. (2020). Comparison of Deep Learning Techniques to Model Connections Between Solar Wind and Ground Magnetic Perturbations. *Frontiers in Astronomy and Space Sciences*, *7*, 72. doi: 10.3389/fspas.2020.550874

Kelley, M. C. (1989). *The Earths Ionosphere - Plasma Physics and Electrodynamics* (2nd ed.). Academic Press.

Kepko, L., McPherron, R. L., Amm, O., Apatenkov, S., Baumjohann, W., Birn, J., … Sergeev, V. (2015). Substorm Current Wedge Revisited. *Space Science Reviews*, *190*(1-4), 1–46. doi: 10.1007/s11214-014-0124-9

Kerridge, D. (2001). *INTERMAGNET: Worldwide near-real-time geomagnetic observatory data* (Tech. Rep.). Edinburgh: British Geological Survey.

Kilpua, E. K., Balogh, A., von Steiger, R., & Liu, Y. D. (2017). Geoeffective Properties of Solar Transients and Stream Interaction Regions. *Space Science Reviews*, *212*(3-4), 1271–1314. doi: 10.1007/s11214-017-0411-3

King, M. J., Wheeler, M. C., & Lane, T. P. (2015). Association of Convection with the 5-Day Rossby–Haurwitz Wave. *Journal of the Atmospheric Sciences*, *72*(9), 3309–3321. doi: 10.1175/JAS-D-14-0316.1

Kistler, L. M., Mouikis, C. G., Spence, H. E., Menz, A. M., Skoug, R. M., Funsten, H. O., … Lanzerotti, L. J. (2016). The source of O+ in the storm time ring current. *Journal of Geophysical Research: Space Physics*, *121*(6), 5333–5349. doi: 10.1002/2015JA022204

Kivelson, M. G., & Russell, C. (1995). *Introduction to Space Physics.* Cambridge University Press. doi: 10.1017/9781139878296

Koskinen, H., Tanskanen, E., Pirjola, R., Pulkkinen, A., Dyer, C., Rodgers, D., … Boscher, D. (2001). *Space Weather Effects Catalogue, ESWS-FMI-RP-0001* (Tech. Rep. No. 14069). ESTEC.

Kronberg, E. A., Daly, P. W., Grigorenko, E. E., Smirnov, A. G., Klecker, B., & Malykhin, A. Y. (2021). Energetic Charged Particles in the Terrestrial Magnetosphere: Cluster/RAPID Results. *Journal of Geophysical Research: Space Physics*, *126*(9). doi: 10.1029/2021JA029273

Landeau, M., Fournier, A., Nataf, H. C., Cébron, D., & Schaeffer, N. (2022). Sustaining Earth's magnetic dynamo. *Nature Reviews Earth and Environment*, *3*(4), 255–269. doi: 10.1038/s43017-022-00264-1

Laperre, B., Amaya, J., & Lapenta, G. (2020). Dynamic Time Warping as a New Evaluation for Dst Forecast With Machine Learning. *Frontiers in Astronomy and Space Sciences*, *7*. doi: 10.3389/fspas.2020.00039

Laundal, K. M., & Richmond, A. D. (2016). Magnetic Coordinate Systems. *Space Science Reviews*, *206*(1-4), 27–59. doi: 10.1007/s11214-016-0275-y

Le Huy, M., & Amory-Mazaudier, C. (2008). Planetary magnetic signature of the storm wind disturbance dynamo currents: Ddyn. *Journal of Geophysical Research: Space Physics*, *113*(2). doi: 10.1029/2007JA012686

Li, D., & Yao, S. (2020). Stronger Southward Magnetic Field and Geoeffectiveness of ICMEs Containing Prominence Materials Measured from 1998 to 2011. *The Astrophysical Journal*, *891*(1), 79. doi: 10.3847/1538-4357/ab7197

Liemohn, M. W., McCollough, J. P., Jordanova, V. K., Ngwira, C. M., Morley, S. K., Cid, C., … Vasile, R. (2018). Model Evaluation Guidelines for Geomagnetic Index Predictions. *Space Weather*, *16*(12), 2079–2102. doi: 10.1029/2018SW002067

Lindzen, R. S., & Chapman, S. (1969). Atmospheric tides. *Space Science Reviews*, *10*(1), 3–188. doi: 10.1007/BF00171584

Liu, H. L., Bardeen, C. G., Foster, B. T., Lauritzen, P., Liu, J., Lu, G., … Wang, W. (2018). Development and Validation of the Whole Atmosphere Community Climate Model With Thermosphere and Ionosphere Extension (WACCM-X 2.0). *Journal of Advances in Modeling Earth Systems*, *10*(2), 381–402. doi: 10.1002/2017MS001232

Liu, J. Y., Chiu, C. S., & Lin, C. H. (1996). The solar flare radiation responsible for sudden frequency deviation and geomagnetic fluctuation. *Journal of Geophysical Research: Space Physics*, *101*(A5), 10855–10862. doi: 10.1029/95JA03676

Love, J. J., Rigler, E. J., Hartinger, M. D., Lucas, G. M., Kelbert, A., & Bedrosian, P. A. (2023). The March 1940 Superstorm: Geoelectromagnetic Hazards and Impacts on American Communication and Power Systems. *Space Weather*, *21*(6), e2022SW003379. doi: 10.1029/2022SW003379

Lu, J. Y., Peng, Y. X., Wang, M., Gu, S. J., & Zhao, M. X. (2016). Support Vector Machine combined with Distance Correlation learning for Dst forecasting during intense geomagnetic storms. *Planetary and Space Science*, *120*, 48–55. doi: 10.1016/j.pss.2015.11.004

Maeda, H. (1955). Horizontal Wind Systems in the Ionospheric E Region Deduced from the Dynamo Theory of the Geomagnetic Sq Variation. *Journal of geomagnetism and geoelectricity*, *7*(4), 121–132. doi: 10.5636/jgg.7.121

Maeda, K.-I. (1977). Conductivity and drifts in the ionosphere. *Journal of Atmospheric and Terrestrial Physics*, *39*(9-10), 1041–1053. doi: 10.1016/0021-9169(77)90013-7

Mandea, M., & Chambodut, A. (2020). Geomagnetic Field Processes and Their Implications for Space Weather. *Surveys in Geophysics*, *41*(6), 1611–1627. doi: 10.1007/s10712-020-09598-1

Mandea, M., Korte, M., Yau, A., & Petrovský, E. (2019). Geomagnetism, aeronomy and space weather: A journey from the earth's core to the sun. In M. Mandea, M. Korte, A. Yau, & E. Petrovsky (Eds.), *Geomagnetism, aeronomy and space weather: A journey from the earth's core to the sun* (pp. 1–332). Cambridge University Press. doi: 10.1017/9781108290135

Marchaudon, A. (2019). New insights in far-space measurements: Large-scale structures and processes in the solar wind and terrestrial magnetosphere. In M. Mandea, M. Korte, Y. Andrew, & E. Petrovsky (Eds.), *Geomagnetism, aeronomy and space weather: A journey from the earth's core to the sun* (pp. 98–112). Cambridge University Press. doi: 10.1017/9781108290135.009

Marchaudon, A., & Blelly, P. L. (2015). A new interhemispheric 16-moment model of the plasmasphere-ionosphere system: IPIM. *Journal of Geophysical Research: Space Physics*, *120*(7), 5728–5745. doi: 10.1002/2015JA021193

Marcinkevičs, R., & Vogt, J. E. (2023). Interpretable and explainable machine learning: A methods-centric overview with concrete examples. *Wiley Interdisciplinary Reviews: Data Mining and Knowledge Discovery*. doi: 10.1002/widm.1493

Matzka, J., Stolle, C., Yamazaki, Y., Bronkalla, O., & Morschhauser, A. (2021). The Geomagnetic Kp Index and Derived Indices of Geomagnetic Activity. *Space Weather*, *19*(5). doi: 10.1029/2020SW002641

Mayaud, P. N. (1968). *Índices Kn, Ks et Km* (Tech. Rep. No. IUGG Publication Office). Paris: C.N.R.S.

Mayaud, P.-N. (1972). The aa indices: A 100-year series characterizing the magnetic activity. *Journal of Geophysical Research*, *77*(34), 6870–6874. doi: 10.1029/ja077i034p06870

Mayaud, P. N. (1980). *Derivation, Meaning, and Use of Geomagnetic Indices* (Vol. 22). Washington, D. C.: American Geophysical Union. doi: 10.1029/GM022

Mayaud, P.-N., Berthelier, A., Menvielle, M., & Chambodut, A. (2023). *am geomagnetic index.* EOST.

Mayaud, P.-N., Menvielle, M., & Chambodut, A. (2023). *On-going time series of IAGA-endorsed geomagnetic index aa.* EOST.

McComas, D. J., Elliott, H. A., Schwadron, N. A., Gosling, J. T., Skoug, R. M., & Goldstein, B. E. (2003). The three-dimensional solar wind around solar maximum. *Geophysical Research Letters*, *30*(10). doi: 10.1029/2003gl017136

McCulloch, W. S., & Pitts, W. (1943). A logical calculus of the ideas immanent in nervous activity. *The Bulletin of Mathematical Biophysics*, *5*(4), 115–133. doi: 10.1007/BF02478259

Meeus, J. (1998). *Astronomical algorithms* (2nd ed.). Willmann-Bell, Inc.

Menvielle, M., Iyemori, T., Marchaudon, A., & Nosé, M. (2011). *Geomagnetic Observations and Models.* Dordrecht: Springer Netherlands. doi: 10.1007/978-90-481-9858-0

Menvielle, M., Papitashvili, N., Hakkinen, L., & Sucksdorff, C. (1995). Computer production of Kindices: review and comparison of methods. *Geophysical Journal International*, *123*(3), 866–886. doi: 10.1111/j.1365-246X.1995.tb06895.x

Milan, S. E., Clausen, L. B., Coxon, J. C., Carter, J. A., Walach, M. T., Laundal, K., … Anderson, B. J. (2017). Overview of Solar Wind–Magnetosphere–Ionosphere–Atmosphere Coupling and the Generation of Magnetospheric Currents. *Space Science Reviews*, *206*(1-4), 547–573. doi: 10.1007/s11214-017-0333-0

Moretto, T., Hesse, M., Kuznetsova, M., Rastätter, L., Vennerstrøm, S., & Tenfjord, P. (2021). How does the magnetosphere go to sleep? *Journal of Atmospheric and Solar-Terrestrial Physics*, *220*, 105626. doi: 10.1016/j.jastp.2021.105626

Nava, B., Rodríguez-Zuluaga, J., Alazo-Cuartas, K., Kashcheyev, A., Migoya-Orué, Y., Radicella, S. M., … Fleury, R. (2016). Middle- and low-latitude ionosphere response to 2015 St. Patrick's Day geomagnetic storm. *Journal of Geophysical Research: Space Physics*, *121*(4), 3421–3438. doi: 10.1002/2015JA022299

Neugebauer, M., & Snyder, C. W. (1966). Mariner 2 observations of the solar wind: 1. Average properties. *Journal of Geophysical Research*, *71*(19), 4469–4484. doi: 10.1029/jz071i019p04469

Newell, P. T., & Gjerloev, J. W. (2011). Evaluation of SuperMAG auroral electrojet indices as indicators of substorms and auroral power. *Journal of Geophysical Research: Space Physics*, *116*(A12). doi: 10.1029/2011JA016779

Newell, P. T., & Gjerloev, J. W. (2012). SuperMAG-based partial ring current indices. *Journal of Geophysical Research: Space Physics*, *117*(A5). doi: 10.1029/2012JA017586

Nitti, S., Podladchikova, T., Hofmeister, S. J., Veronig, A. M., Verbanac, G., & Bandić, M. (2022). Geomagnetic storm forecasting from solar coronal holes. *Monthly Notices of the Royal Astronomical Society*, *519*(2), 3182–3193. doi: 10.1093/MNRAS/STAC3533

Njiteu Tchoukeu, C. D., Basseka, C. A., Djomani, Y. P., Rousse, S., Etame, J., Llubes, M., … Eyike Yomba, A. (2021). Crustal thickness, depth to the bottom of magnetic sources and thermal structure of the crust from Cameroon to Central African Republic: Preliminary results for a better understanding of the origin of the Bangui Magnetic Anomaly. *Journal of African Earth Sciences*, *179*, 104206. doi: 10.1016/j.jafrearsci.2021.104206

Olden, J. D., Joy, M. K., & Death, R. G. (2004). An accurate comparison of methods for quantifying variable importance in artificial neural networks using simulated data. *Ecological Modelling*, *178*(3-4), 389–397. doi: 10.1016/j.ecolmodel.2004.03.013

Olsen, N. (1988). The solar cyle variability of lunar and solar daily geomagnetic variations. *Annales geophysicae (1988)*, *11*(4), 254–262.

Olsen, N. (2016). Earth's Magnetic Field. In G. V. Khazanov (Ed.), *Space weather fundamentals* (pp. 35–45). Taylor & Francis Group.

Olsen, N., & Mandea, M. (2007). Will the magnetic north pole move to Siberia? *Eos*, *88*(29), 293. doi: 10.1029/2007EO290001

Papadimitriou, C., Balasis, G., Boutsi, A. Z., Antonopoulou, A., Moutsiana, G., Daglis, I. A., … Trenchi, L. (2021). Swarm-Derived Indices of Geomagnetic Activity. *Journal of Geophysical Research: Space Physics*, *126*(11), e2021JA029394. doi: 10.1029/2021JA029394

Papitashvili, N. E., & King, J. H. (2020). OMNI 5-min Data [Data set]. *NASA Space Physics Data Facility.* doi: https://doi.org/10.48322/gbpg-5r77

Park, J., Lühr, H., Lee, C., Kim, Y. H., Jee, G., & Kim, J. H. (2014). A climatology of medium-scale gravity wave activity in the midlatitude/low-latitude daytime upper thermosphere as observed by CHAMP. *Journal of Geophysical Research: Space Physics*, *119*(3), 2187–2196. doi: 10.1002/2013JA019705

Parker, E. N. (1958). Dynamics of the Interplanetary Gas and Magnetic Fields. *The Astrophysical Journal*, *128*, 664. doi: 10.1086/146579

Pascanu, R., Gulcehre, C., Cho, K., & Bengio, Y. (2014). How to construct deep recurrent neural networks. *2nd International Conference on Learning Representations, ICLR 2014 - Conference Track Proceedings.*

Pedregosa, F., Michel, V., Grisel, O., Blondel, M., Prettenhofer, P., Weiss, R., … Duchesnay, É. (2011). Scikit-learn: Machine learning in Python. *jmlr.org*, *12*, 2825–2830.

Petereit, J., Saynisch-Wagner, J., Morschhauser, A., Pick, L., & Thomas, M. (2022). On the characterization of tidal ocean-dynamo signals in coastal magnetic observatories. *Earth, Planets and Space*, *74*(1), 67. doi: 10.1186/s40623-022-01610-9

Pfaff, R. F. (2012). The near-earth plasma environment. *Space Science Reviews*, *168*(1-4), 23–112. doi: 10.1007/s11214-012-9872-6

Pinto, V. A., Keesee, A. M., Coughlan, M., Mukundan, R., Johnson, J. W., Ngwira, C. M., & Connor, H. K. (2022). Revisiting the Ground Magnetic Field Perturbations Challenge: A Machine Learning Perspective. *Frontiers in Astronomy and Space Sciences*, *9*. doi: 10.3389/fspas.2022.869740

Poblet, F. L., & Azpilicueta, F. (2018). 27-day variation in solar-terrestrial parameters: Global characteristics and an origin based approach of the signals. *Advances in Space Research*, *61*(9), 2275–2289. doi: 10.1016/j.asr.2018.02.016

Poppe, B. B. (2000). New scales help public, technicians understand space weather. *Eos, Transactions American Geophysical Union*, *81*(29), 322. doi: 10.1029/00EO00247

Price, C. (2016). ELF electromagnetic waves from lightning: The schumann resonances. *Atmosphere*, *7*(9), 116. doi: 10.3390/atmos7090116

Primdahl, F. (1979). The fluxgate magnetometer. *Journal of Physics E: Scientific Instruments*, *12*(4), 241–253. doi: 10.1088/0022-3735/12/4/001

Proakis, J., & Manolakis, D. (2006). *Digital Signal Processing* (4th ed.). Pearson.

Pulkkinen, A., Lindahl, S., Viljanen, A., & Pirjola, R. (2005). Geomagnetic storm of 29-31 October 2003: Geomagnetically induced currents and their relation to problems in the Swedish high-voltage power transmission system. *Space Weather*, *3*(8), n/a–n/a. doi: 10.1029/2004SW000123

Raouafi, N. E., Matteini, L., Squire, J., Badman, S. T., Velli, M., Klein, K. G., … Woolley, T. (2023). Parker Solar Probe: Four Years of Discoveries at Solar Cycle Minimum. *Space Science Reviews*, *219*(1), 8. doi: 10.1007/s11214-023-00952-4

Rastogi, R. G., Crandra, H., & James, M. E. (1996). On the Disintegration of the Vortex Structure of Ionospheric Current System along Asian Longitude Sector. *Journal of geomagnetism and geoelectricity*, *48*(12), 1481–1488. doi: 10.5636/jgg.48.1481

Réville, V., Poirier, N., Kouloumvakos, A., Paul Rouillard, A., Pinto, R., Fargette, N., … Scoul, C. (2023). HelioCast: heliospheric forecasting based on white-light observations of the solar corona. I. Solar minimum conditions. *Journal of Space Weather and Space Climate*, *13*, 11. doi: 10.1051/swsc/2023008

Roscher, R., Bohn, B., Duarte, M. F., & Garcke, J. (2020). Explainable Machine Learning for Scientific Insights and Discoveries. *IEEE Access*, *8*, 42200–42216. doi: 10.1109/ACCESS.2020.2976199

Rostoker, G., Akasofu, S.-I., Foster, J., Greenwald, R., Kamide, Y., Kawasaki, K., … Russell, C. (1980). Magnetospheric substorms—definition and signatures. *Journal of Geophysical Research*, *85*(A4), 1663. doi: 10.1029/ja085ia04p01663

Rudin, C. (2019). Stop explaining black box machine learning models for high stakes decisions and use interpretable models instead. *Nature Machine Intelligence*, *1*(5), 206–215. doi: 10.1038/s42256-019-0048-x

Rumelhart, D. E., Hinton, G. E., & Williams, R. J. (1986). Learning representations by back-propagating errors. *Nature 1986 323:6088*, *323*(6088), 533–536. doi: 10.1038/323533a0

Runov, A., Angelopoulos, V., Artemyev, A. V., Weygand, J. M., Lu, S., Lin, Y., & Zhang, X. J. (2021). Global and local processes of thin current sheet formation during substorm growth phase. *Journal of Atmospheric and Solar-Terrestrial Physics*, *220*, 105671. doi: 10.1016/j.jastp.2021.105671

Sandhu, J. K., Rae, I. J., & Walach, M. T. (2021). Challenging the Use of Ring Current Indices During Geomagnetic Storms. *Journal of Geophysical Research: Space Physics*, *126*(2). doi: 10.1029/2020JA028423

Sarker, I. H. (2021). Deep Learning: A Comprehensive Overview on Techniques, Taxonomy, Applications and Research Directions. *SN Computer Science*, *2*(6), 420. doi: 10.1007/s42979-021-00815-1

Schlapp, D. M. (1968). World-wide morphology of day-to-day variability of Sq. *Journal of Atmospheric and Terrestrial Physics*, *30*(10), 1761–1776. doi: 10.1016/0021-9169(68)90096-2

Schunk, R., & Nagy, A. (2009). *Ionospheres* (2nd ed.). Cambridge: Cambridge University Press. doi: 10.1017/cbo9780511635342

Serrano, L. G. (2021). *Grokking Machine Learning* (K. Hales, Ed.). Manning Publications Co.

Shinbori, A., Koyama, Y., Nosé, M., Hori, T., & Otsuka, Y. (2017). Characteristics of Seasonal Variation and Solar Activity Dependence of the Geomagnetic Solar Quiet Daily Variation. *Journal of Geophysical Research: Space Physics*, *122*(10), 10,796–10,810. doi: 10.1002/2017JA024342

Siciliano, F., Consolini, G., Tozzi, R., Gentili, M., Giannattasio, F., & De Michelis, P. (2021). Forecasting SYM-H Index: A Comparison Between Long Short-Term Memory and Convolutional Neural Networks. *Space Weather*, *19*(2), e2020SW002589. doi: 10.1029/2020SW002589

SILSO World Data Center. (2023). The International Sunspot Number. *International Sunspot Number Monthly Bulletin and online catalogue*, 1947–2023. Retrieved from `http://www.sidc.be/silso/`

Stening, R. J. (2008). The shape of the Sq current system. *Annales Geophysicae*, *26*(7), 1767–1775. doi: 10.5194/angeo-26-1767-2008

Stening, R. J., Reztsova, T., & Minh, L. H. (2005). Day-to-day changes in the latitudes of the foci of the Sq current system and their relation to equatorial electrojet strength. *Journal of Geophysical Research: Space Physics*, *110*(A10). doi: 10.1029/2005JA011219

Stening, R. J., & Winch, D. E. (2013). The ionospheric Sq current system obtained by spherical harmonic analysis. *Journal of Geophysical Research: Space Physics*, *118*(3), 1288–1297. doi: 10.1002/jgra.50194

Stevens, A., De Smedt, J., & Peeperkorn, J. (2022). Quantifying Explainability in Outcome-Oriented Predictive Process Monitoring. In *Lecture notes in business information processing* (Vol. 433 LNBIP, pp. 194–206). doi: 10.1007/978-3-030-98581-3

Sucksdorff, C., Pirjola, R., & Häkkinen, L. (1991). Computer Production of K-Indices based on Linear Elimination. *Geophysical Transactions*, *36*(3-4), 333–345.

Sugiura, M. (1964). Hourly values of equatorial Dst for the IGY. *Annals of the International Geophysical Year*.

Sugiura, M., & Chapman, S. (1960). *The Average Morphology of Geomagnetic Storms with Sudden Commencement.* V&r Academic.

Takeda, M. (1999). Time variation of global geomagnetic Sq field in 1964 and 1980. *Journal of Atmospheric and Solar-Terrestrial Physics*, *61*(10), 765–774. doi: 10.1016/S1364-6826(99)00028-0

Takeda, M., & Araki, T. (1985). Electric conductivity of the ionosphere and nocturnal currents. *Journal of Atmospheric and Terrestrial Physics*, *47*(6), 601–609. doi: 10.1016/0021-9169(85)90043-1

Tan, Y., Hu, Q., Wang, Z., & Zhong, Q. (2018). Geomagnetic Index Kp Forecasting With LSTM. *Space Weather*, *16*(4), 406–416. doi: 10.1002/2017SW001764

Tapping, K. F. (2013). The 10.7 cm solar radio flux (F10.7). *Space Weather*, *11*(7), 394–406. doi: 10.1002/swe.20064

Taylor, P. T., & Frawley, J. J. (1987). Magsat anomaly data over the Kursk region, U.S.S.R. *Physics of the Earth and Planetary Interiors*, *45*(3), 255–265. doi: 10.1016/0031-9201(87)90014-8

Thébault, E., Vigneron, P., Langlais, B., & Hulot, G. (2016). A Swarm lithospheric magnetic field model to SH degree 80. *Earth, Planets and Space*, *68*(1), 126. doi: 10.1186/s40623-016-0510-5

Tibshirani, R. (1996). Regression Shrinkage and Selection via the Lasso. *Journal of the Royal Statistical Society. Series B (Methodological)*, *58*(1), 267–288.

Tozzi, R., Mandea, M., & De Michelis, P. (2016). Unmodelled magnetic contributions in satellite-based models Swarm Science Results after two years in Space 1. Geomagnetism. *Earth, Planets and Space*, *68*(1), 1–14. doi: 10.1186/s40623-016-0484-3

Trask, A. W. (2019). *Grokking Deep Learning.*

Troshichev, O., Dmitrieva, N., & Kuznetsov, B. (1979). Polar cap magnetic activity as a signature of substorm development. *Planetary and Space Science*, *27*(3), 217–221. doi: 10.1016/0032-0633(79)90063-1

Troshichev, O., & Janzhura, A. (2012). Space weather monitoring by groundbased means: PC index. , 287.

Tsyganenko, N. A. (1989). A magnetospheric magnetic field model with a warped tail current sheet. *Planetary and Space Science*, *37*(1), 5–20. doi: 10.1016/0032-0633(89)90066-4

Tsyganenko, N. A., & Stern, D. P. (1996). Modeling the global magnetic field of the large-scale Birkeland current systems. *Journal of Geophysical Research: Space Physics*, *101*(A12), 27187–27198. doi: 10.1029/96ja02735

Van De Kamp, M. (2013). Harmonic quiet-day curves as magnetometer baselines for ionospheric current analyses. *Geoscientific Instrumentation, Methods and Data Systems*, *2*(2), 289–304. doi: 10.5194/gi-2-289-2013

Vasyliunas, V. M. (1983). Large-Scale Morphology of the Magnetosphere. In R. Carovillano & J. Forbes (Eds.), *Solar-terrestrial physics* (pp. 243–254). Springer, Dordrecht. doi: 10.1007/978-94-009-7194-3

Verbanac, G., Mandea, M., Bandic, M., & Subasic, S. (2015). Magnetic observatories: Biases over CHAMP satellite mission. *Solid Earth*, *6*(2), 775–781. doi: 10.5194/se-6-775-2015

Walach, M. T., & Grocott, A. (2019). SuperDARN Observations During Geomagnetic Storms, Geomagnetically Active Times, and Enhanced Solar Wind Driving. *Journal of Geophysical Research: Space Physics*, *124*(7), 5828–5847. doi: 10.1029/2019JA026816

Wanliss, J. A., & Showalter, K. M. (2006). High-resolution global storm index: Dst versus SYM-H. *Journal of Geophysical Research*, *111*(A2), A02202. doi: 10.1029/2005JA011034

Weygand, J. M., & McPherron, R. L. (2006). Dependence of ring current asymmetry on storm phase. *Journal of Geophysical Research*, *111*(A11), A11221. doi: 10.1029/2006JA011808

Williams, R., & Zipser, D. (1995). Gradient-based learning algorithms for recurrent networks and their computational complexity. *taylorfrancis.com.*

Wolfert, S., Ge, L., Verdouw, C., & Bogaardt, M. J. (2017). Big Data in Smart Farming – A review. *Agricultural Systems*, *153*, 69–80. doi: 10.1016/j.agsy.2017.01.023

Wright, J. M., Lewis, F. P., Corell, R. W., Thomas, A. R., Huntress, W. T., Devine, J. F., . . . Stailey, J. (1997). *National Space Weather Program: The Implementation Plan* (Tech. Rep.). Washington, DC: National Space Weather Program Council.

Wu, C. C., Liou, K., Lepping, R. P., Hutting, L., Plunkett, S., Howard, R. A., & Socker, D. (2016). The first super geomagnetic storm of solar cycle 24: "the St. Patrick's day event (17 March 2015)" Global Data Systems for the Study of Solar-Terrestrial Variability 3. Space science. *Earth, Planets and Space*, *68*(1), 151. doi: 10.1186/s40623-016-0525-y

Yamazaki, Y., Häusler, K., & Wild, J. A. (2016). Day-to-day variability of midlatitude ionospheric currents due to magnetospheric and lower atmospheric forcing. *Journal of Geophysical Research: Space Physics*, *121*(7), 7067–7086. doi: 10.1002/2016JA022817

Yamazaki, Y., & Kosch, M. J. (2014). Geomagnetic lunar and solar daily variations during the last 100 years. *Journal of Geophysical Research: Space Physics*, *119*(8), 6732–6744. doi: 10.1002/2014JA020203

Yamazaki, Y., Matzka, J., Stolle, C., Kervalishvili, G., Rauberg, J., Bronkalla, O., … Jackson, D. R. (2022). Geomagnetic Activity Index Hpo. *Geophysical Research Letters*, *49*(10), e2022GL098860. doi: 10.1029/2022GL098860

Yamazaki, Y., & Maute, A. (2017). Sq and EEJ—A Review on the Daily Variation of the Geomagnetic Field Caused by Ionospheric Dynamo Currents. *Space Science Reviews*, *206*(1-4), 299–405. doi: 10.1007/s11214-016-0282-z

Yamazaki, Y., & Richmond, A. D. (2013). A theory of ionospheric response to upward-propagating tides: Electrodynamic effects and tidal mixing effects. *Journal of Geophysical Research: Space Physics*, *118*(9), 5891–5905. doi: 10.1002/jgra.50487

Yamazaki, Y., Richmond, A. D., Maute, A., Liu, H. L., Pedatella, N., & Sassi, F. (2014). On the day-to-day variation of the equatorial electrojet during quiet periods. *Journal of Geophysical Research: Space Physics*, *119*(8), 6966–6980. doi: 10.1002/2014JA020243

Yamazaki, Y., Richmond, A. D., Maute, A., Wu, Q., Ortland, D. A., Yoshikawa, A., … Tsugawa, T. (2014). Ground magnetic effects of the equatorial electrojet simulated by the TIE-GCM driven by TIMED satellite data. *Journal of Geophysical Research: Space Physics*, *119*(4), 3150–3161. doi: 10.1002/2013JA019487

Yang, Z., Morton, Y. T., Zakharenkova, I., Cherniak, I., Song, S., & Li, W. (2020). Global View of Ionospheric Disturbance Impacts on Kinematic GPS Positioning Solutions During the 2015 St. Patrick's Day Storm. *Journal of Geophysical Research: Space Physics*, *125*(7). doi: 10.1029/2019JA027681

Yu, L., Qu, J., Gao, F., & Tian, Y. (2019). A Novel Hierarchical Algorithm for Bearing Fault Diagnosis Based on Stacked LSTM. *Shock and Vibration*, *2019*, 1–10. doi: 10.1155/2019/2756284

Zakharenkova, I., Astafyeva, E., & Cherniak, I. (2016). GPS and GLONASS observations of large-scale traveling ionospheric disturbances during the 2015 St. Patrick's Day storm. *Journal of Geophysical Research: Space Physics*, *121*(12), 12,138–12,156. doi: 10.1002/2016JA023332

Zinkova, M. (2020). A possible role of space weather in the events surrounding the Titanic disaster. *Weather*, *75*(11), 360–364. doi: 10.1002/wea.3817

Introduction (FR)

La météorologie de l'espace et le champ géomagnétique

Au cours du siècle dernier, la technologie et la numérisation ont accéléré le progrès humain, ce qui a conduit à ce qu'une part croissante de notre culture existe sous forme numérique (Hodson, 2018). La révolution numérique a permis à l'humanité d'accéder à un large éventail de nouvelles possibilités, notamment la communication et la navigation à l'échelle mondiale, ainsi qu'à une vaste base de données de connaissances en ligne. Tout cela est alimenté par l'électricité et exige donc l'expansion et le développement des infrastructures de réseau électrique tout autour du globe. Le ciel n'étant pas la limite, nous avons commencé à peupler notre environnement spatial proche de la Terre de technologies destinées à soutenir notre infrastructure et à explorer le système solaire afin de mieux comprendre le monde dans lequel nous vivons. Nous sommes devenus dépendants de ces infrastructures et, par conséquent, nous avons également appris à connaître les menaces auxquelles elles sont confrontées. Au cours des dernières décennies, l'expression *Météorologie de l'Espace* est apparue pour décrire les effets de l'interaction entre notre Soleil et la Terre sur le fonctionnement technologique et le bien-être humain. La National Science Foundation des États-Unis définit la météorologie de l'espace comme suit (Wright et al., 1997), traduit en français:

> *"Conditions sur le Soleil et dans le vent solaire, la magnétosphère, l'ionosphère et la thermosphère qui peuvent influencer la performance et la fiabilité des systèmes technologiques spatiaux et terrestres et peuvent mettre en danger la vie ou la santé humaine".*

Au fur et à mesure que l'humanité s'étend et favorise ses avancées technologiques, la météorologie de l'espace est en mesure d'avoir un impact sur une grande variété de domaines. De nombreuses conséquences socio-économiques sont bien documentées dans la littérature (voir par exemple Koskinen et al. (2001); Desmaris (2015); Wolfert et al. (2017); Eastwood et al. (2017)), y compris les exemples sélectionnés suivants:

- **Charge utile scientifique des missions spatiales**
  Lors des missions spatiales, les satellites et leur charge utile constituée d'électronique sensible doivent résister à l'environnement hostile de l'espace tout en accomplissant leurs tâches. Les particules hautement énergétiques sont capables de pénétrer les couches extérieures des satellites et d'endommager les composants fragiles en corrompant les données ou, dans le pire des cas, en détruisant les composants électriques et les instruments essentiels.

- **Systèmes de communication et de positionnement**
  L'ionosphère module la propagation des signaux de radiofréquence. Les variations de la densité d'électrons dues à l'augmentation de l'activité solaire peuvent entraîner une perte de signaux, affectant ainsi des systèmes de communication et de positionnement essentiels. Cela peut entraîner, par exemple, des erreurs de positionnement importantes dans l'agriculture de précision et une diminution de la précision des forages directionnels (ex : pétroliers).

- **Dommages au réseau électrique**
  Les courants magnétosphériques et ionosphériques sont renforcés lors des perturbations géomagnétiques et entraînent des variations magnétiques rapides et intenses. Accompagnés de champs géoélectriques, ils sont responsables de courants induits dans la croûte terrestre ou GIC dans les systèmes électriques. Les GICs peuvent entraîner des dommages et des dysfonctionnements sur le réseau électrique, provoquant d'importantes coupures de courant sur de vastes étendues.

Un autre aperçu plus récent et plus complet des effets de la météorologie de l'espace est présenté dans Coster et al. (2021). En particulier, les événements météorologiques spatiaux violents appelés orages solaires représentent un risque important. L'un des premiers événements extrêmes documentés est l'événement de Carrington qui s'est produit en 1859. Richard Carrington a observé d'intenses éruptions de lumière blanche au-dessus d'un grand groupe de taches solaires à la surface du Soleil. Seulement 18 heures plus tard, de fortes aurores étaient visibles dans le ciel nocturne mondial, y compris aux latitudes moyennes et basses. À l'époque, la communication reposait sur les télégraphes, qui reliaient les différentes stations par des câbles électriques de plusieurs kilomètres de long. À l'échelle mondiale, si certains opérateurs télégraphiques ont signalé la perte de leurs services de messagerie, d'autres avaient la possibilité d'envoyer des messages sans alimentation électrique active. C'était à une époque où la technologie n'en était qu'à ses débuts. Une étude récente sur un autre événement intense, la superorage de mars 1940 par Love et al. (2023), résume les impacts des variations exceptionnellement rapides du champ géomagnétique comme, traduit en français, *sévères pour les champs géoélectriques induits sur les infrastructures de communication et de réseau électrique à l'époque.*

Bien qu'aucun événement d'une intensité comparable ne se soit produit dans un passé proche, de nombreux enregistrements d'impacts météorologiques spatiaux témoignent de la menace actuelle. En 2003, les événements dits d'Halloween étaient une série de orages accompagnées de magnifiques aurores boréales, mais qui ont entraîné d'importantes pannes d'électricité en Laponie (Pulkkinen et al., 2005). Un exemple récent montre que les orages très intenses ne sont pas les seules à pouvoir perturber nos activités: En 2022, un lot de satellites de communication a été lancé mais n'a pas pu atteindre son orbite en raison de réserves de carburant insuffisantes. La cause en était une orage solaire modérée qui a très probablement entraîné un réchauffement et donc une expansion de l'atmosphère neutre suffisants pour que la traînée des satellites soit plus forte que la poussée maximale de leurs moteurs (Fang et al., 2022). Une autre étude intéressante porte sur les conséquences possibles des conditions météorologiques spatiales lors de la tragédie du Titanic, qui ont affecté les systèmes de navigation et de communication (Zinkova, 2020).

Ce ne sont là que quelques exemples de l'impact de la météorologie de l'espace, qui illustrent son importance et la nécessité de mieux la comprendre et d'améliorer les capacités de prévision. Notre société étant devenue plus dépendante à la technologie, une perturbation globale des communications et des infrastructures constitue une menace mondiale importante. La discipline de la météorologie de l'espace est consacrée à l'origine de ces effets et traite de l'étude des phénomènes qui se produisent sur le Soleil et de leurs interactions et effets sur la Terre et dans l'environnement de l'espace proche de la Terre. Par nature, elle englobe une grande variété de domaines, de l'héliophysique à la géophysique. La figure 10.2 présente une vue d'ensemble des principaux acteurs et des phénomènes liés à la météorologie de l'espace.

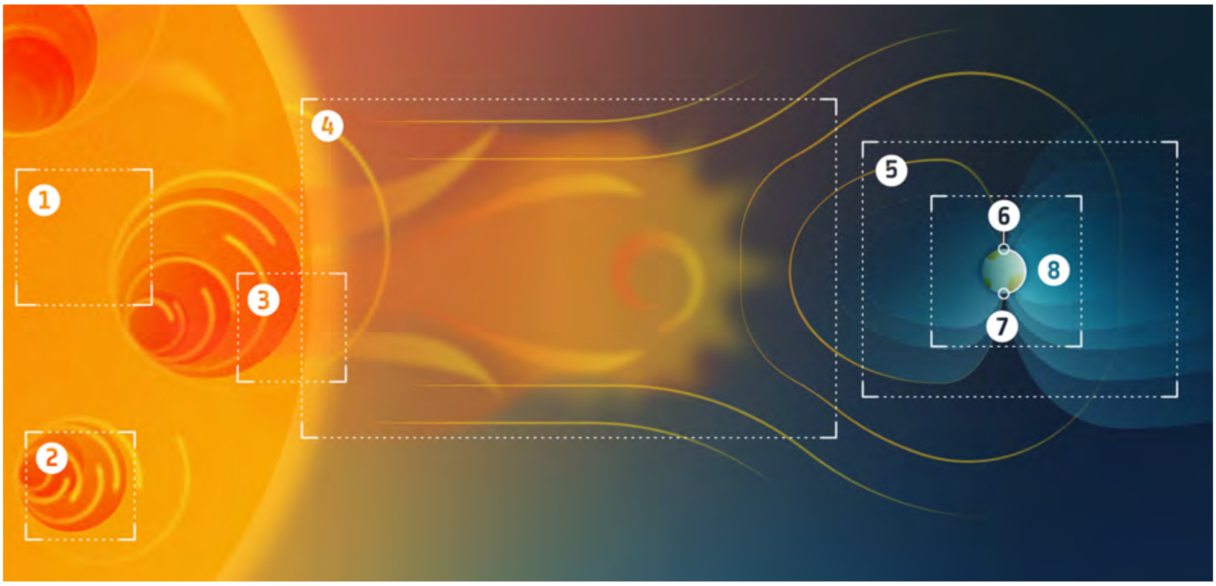

Figure 10.2: Une vue d'ensemble de la météorologie de l'espace décrivant les principaux acteurs et les phénomènes associés, le Soleil ①-③ et la Terre ⑤-⑧, et leur interconnexion via le vent solaire ④. Image reproduite avec l'aimable autorisation de l'ESA.

① **Le Soleil** est notre étoile la plus proche et est le principal moteur et fournisseur d'énergie pour les phénomènes météorologiques spatiaux.

② **Les éruptions solaires** sont de fortes explosions d'énergie électromagnétique qui prennent naissance à la surface du Soleil.

③ **Les éjections de masse coronale** (CME) sont des éruptions à grande échelle de matériaux solaires qui sont éjectés dans l'espace.

④ **Le vent solaire** est un flux continu de particules provenant de l'atmosphère du Soleil et entraînant avec lui le champ magnétique solaire, qui est à l'origine de l'environnement magnétique particulier de la Terre.

⑤ **La magnétosphère** se forme lorsque le vent solaire comprime le champ magnétique interne de la Terre du côté diurne et l'allonge du côté nocturne. Sa morphologie et les systèmes de courant associés sont décrits dans le chapitre 2.2

⑥ **Les sous-orages** sont des perturbations à plus petite échelle du champ géomagnétique dont les conséquences sont principalement confinées aux régions polaires et sont associées à des manifestations aurorales.

⑦ **L'ionosphère** est une couche de particules ionisées autour de la Terre qui coexiste avec la haute atmosphère neutre de la Terre, appelée thermosphère.

⑧ **Les orages géomagnétiques**, accompagnés de sous-orages, induisent de fortes perturbations du champ géomagnétique qui ont des conséquences à l'échelle mondiale, en particulier dans les régions équatoriales et les ceintures de radiation.

Les acteurs et les phénomènes associés liés à la météorologie de l'espace peuvent être principalement décrits par la physique des plasmas, comme présenté dans le chapitre 1. Le détails du Soleil sont présentés en détail dans chapitre 2.1. La magnétosphère en tant que structure à grande échelle est introduite et les systèmes de courant importants qui soutiennent sa morphologie sont décrits en chapitre 2.2. Dans cette introduction condensée, une discussion détaillée sur l'ionosphère est présentée, en mettant l'accent sur les latitudes moyennes, étant donné que les phénomènes qui y sont associés sont d'une grande importance pour ce travail. Puis, le champ géomagnétique et ses sources sont ensuite décrits. Enfin, des mesures importantes dans le domaine de la météorologie de l'espace sont introduites : les indices d'activité magnétique. Ceux-ci condensent les informations géomagnétiques en un (ou plusieurs) indicateur(s) unique(s) qui caractérise(nt) l'état du champ géomagnétique et agisse(nt) comme d'importants indicateurs de la météorologie de l'espace. Le dernier chapitre de l'introduction traite des données de référence géomagnétiques nécessaires pour déterminer l'effet net des facteurs externes sur le champ géomagnétique, ce qui représente le cœur du travail présenté.

L'ionosphère

L'atmosphère neutre de la Terre peut être décrite à partir de profil de température distincts en fonction de l'altitude. La troposphère, qui s'étend du sol à environ 12 km, est la couche dans laquelle nous vivons et pour laquelle les températures diminuent avec l'augmentation de l'altitude. La stratosphère, située entre 12 et 50 km d'altitude, se caractérise par une élévation de la température due à l'absorption des UV solaires par l'ozone. Entre 50 et 85 km, la mésosphère présente des températures qui chutent rapidement avec l'augmentation de l'altitude en raison d'un refroidissement efficace par le CO_2. Au-dessus de 85 km, les températures augmentent rapidement dans la thermosphère car le rayonnement solaire UV et les rayons X mous peuvent pénétrer facilement à ces hauteurs, ce qui entraîne un chauffage efficace (de Pater & Lissauer, 2015). Le rayonnement solaire ne se contente pas d'augmenter les températures, il est suffisamment énergétique pour provoquer l'ionisation et joue un rôle important dans la création de l'ionosphère. Comme l'atmosphère neutre est caractérisée par son profil de température, l'ionosphère peut l'être par son profil de densité électronique, comme illustré dans figure 10.3. La haute atmosphère neutre se superpose à la basse ionosphère, ce qui entraîne des interactions plasma-neutre, en particulier dans les régions D et E. On trouvera des études détaillées sur la chimie et les mécanismes de transport dans l'ionosphère, ainsi qu'un traitement de sa production et de ses variations, par exemple dans Kelley (1989) et Schunk and Nagy (2009). Dans ce qui suit, les principaux processus d'ionisation et de perte qui sont responsables du profil de densité distinct de l'ionosphère sont brièvement décrits.

- **Ionisation UV solaire**
  La principale source de production d'électrons dans l'ionosphère est l'irradiation directe du Soleil. Les hautes énergies nécessaires pour ioniser les atomes et les molécules de l'atmosphère, c'est-à-dire pour retirer des électrons de l'enveloppe de l'atome, proviennent d'une source supérieure au régime UV du spectre de rayonnement solaire. Plus le rayonnement est puissant, plus il peut pénétrer profondément dans l'atmosphère, comme le montre la figure 10.3. Lorsqu'un atome ou une molécule est ionisé, le rayonnement incident diminue son intensité car il dépense de l'énergie pour l'ionisation. L'ampleur de cette diminution dépend de l'intensité initiale de la densité du gaz neutre, de la section efficace d'absorption et de la longueur

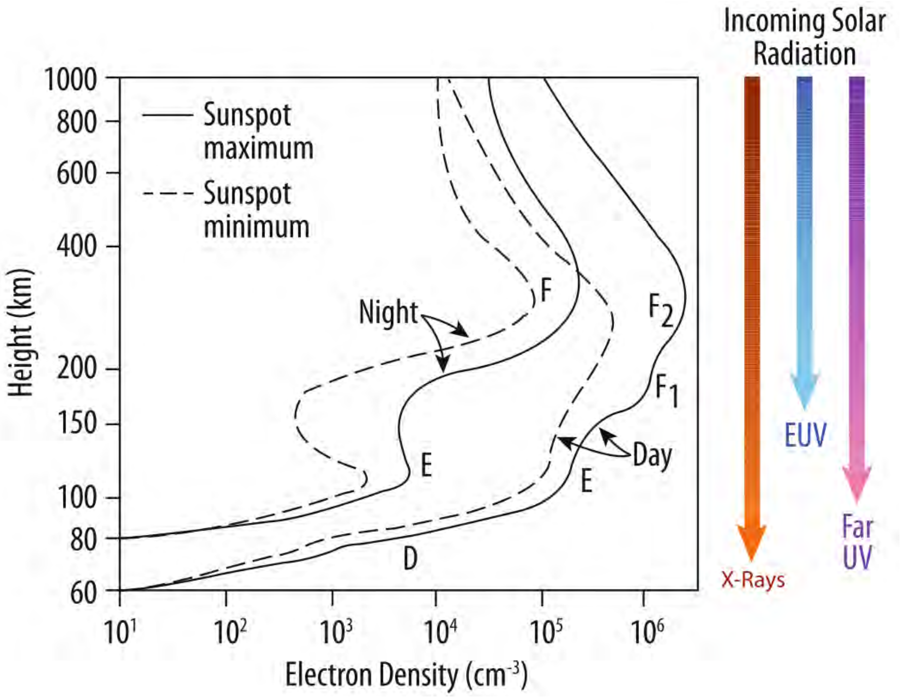

Figure 10.3: Le profil de densité électronique de l'ionosphère avec des indications sur les profondeurs de pénétration du rayonnement solaire. Les profils distincts pour la nuit et le jour pendant le maximum et le minimum solaire sont indiqués. (extrait de Pfaff (2012))

du trajet du rayonnement dans le milieu. Selon la loi barométrique, la densité neutre diminue avec l'altitude et l'intensité du rayonnement est plus intense avec l'altitude. Cela conduit à un pic prononcé de densité électronique autour de 400 km, formant ce que l'on appelle le profil de Chapman (Chapman, 1931).

- **Ionisation par les particules énergétiques**
  Les particules énergétiques provenant essentiellement de la magnétopause et de la queue qui pénètrent dans l'atmosphère par les lignes de champ magnétique ont suffisamment d'énergie pour ioniser les atomes et les molécules. Ce processus de production domine pendant la nuit, lorsque la principale source d'ionisation, le rayonnement solaire, cesse. Ce processus est capable de maintenir le profil général de l'ionosphère, mais dans une moindre mesure. La profondeur de pénétration marque la hauteur à laquelle la particule entrante dépose la majorité de son énergie dans l'atmosphère, ce qui conduit aux pics nocturnes. Ce processus est particulièrement important aux hautes latitudes où l'ionisation et la conductivité sont renforcées par la précipitation de particules provenant du vent solaire via la reconnexion côté jour et la reconnexion côté queue.

- **Recombinaison**
  Un processus de perte important est la recombinaison au cours de laquelle un ion positif gagne un électron et forme un atome neutre. Le taux de recombinaison dépend des densités d'ions et d'électrons, ainsi que de la fréquence de collisions. Dans la basse ionosphère, la recombinaison est dominante lorsque les fréquences de collision augmentent en raison de la forte densité d'atomes et de molécules neutres.

- **Échange de charges**

Le processus d'échange d'électrons entre des particules en interaction et en collision (par exemple, entre des atomes neutres et des ions) est appelé échange de charges. Ce processus modifie la nature des ions et est proportionnel au nombre d'électrons. Il s'agit d'un processus chimique important dans la région F de haute altitude de l'ionosphère, qui convertit les ions hydrogène en ions oxygène et vice-versa.

La combinaison de ces processus forme le profil de densité caractéristique de l'ionosphère, tel qu'il est esquissé pour les latitudes moyennes dans la figure 10.3. Selon ce profil, il est courant de diviser l'ionosphère en trois couches principales: les régions D, E et F.

- **La région D**
  La région D est située à une altitude d'environ 60 à 90 km. Le principal processus d'ionisation est le rayonnement X solaire de haute énergie, qui peut pénétrer à ces profondeurs. En raison de la densité relativement élevée d'atomes et de molécules neutres de l'atmosphère, les fréquences de collision sont élevées, ce qui conduit à un gaz qui n'est que faiblement ionisé. Dans cette région, la chimie domine et des ions négatifs et complexes peuvent être formés. Pendant la nuit, la source de production de l'irradiation solaire cesse et les processus de perte dominent, de sorte que la région D disparaît. Temporairement, le niveau d'ionisation dans la région D peut être remarquablement augmenté lors d'événements tels que les éruptions solaires. Même si elle n'est que faiblement ionisée, la région D est un important atténuateur pour les signaux de communication, des taux d'ionisation plus élevés entraînant une plus grande atténuation.

- **La région E**
  À des altitudes comprises entre 90 et 150 km, la couche E se forme en raison de l'absorption des rayonnements EUV à UV solaires lointains, avec des densités maximales autour de 110 km. À ces hauteurs, des densités substantielles de neutres sont encore présentes et le gaz est partiellement ionisé. Cela permet de fortes interactions dues au mouvement différentiel entre les particules ionisées et neutres, donnant lieu à la dynamo de la région E qui est la source d'importants systèmes de courant dans l'ionosphère. En général, cette couche est en équilibre entre les processus de production, d'échange de charge et de perte, et donc en équilibre chimique. Les précipitations de particules aurorales sont capables de maintenir la région E pendant la nuit aux latitudes plus élevées.

- **La région F**
  La région F peut être classée en deux sous-régions pendant la journée : la région F1 se forme par absorption du rayonnement UV court à environ 200 km suivie par la formation chimique d'ions NO^+ qui possèdent un potentiel d'ionisation très faible. Elle disparaît au cours de la nuit lorsque cette source de production cesse. La région F2 située à une altitude d'environ 300 km est principalement peuplée d'ions Oxygène. Pendant la journée, O^+ est produit localement dans l'ionosphère et transporté vers le haut le long du champ magnétique jusqu'à la plasmasphère. Celle-ci agit comme un réservoir et les particules sont transportées vers le bas, maintenant la région F pendant la nuit, car les effets de recombinaison sont également réduits en raison des faibles densités.

Chacune de ces couches dépend en grande partie du rayonnement solaire, ce qui crée les profils de densité distincts jour et nuit sur la figure 10.3. L'intensité du rayonnement solaire varie en fonction du cycle solaire, tout comme le profil d'ionisation. Pendant le maximum solaire (et donc le maximum de taches solaires), la densité d'électrons est nettement plus élevée en raison de l'augmentation du rayonnement solaire que pendant le minimum solaire (et donc le minimum de taches solaires). La différence est de l'ordre d'un à deux ordres de grandeur. En outre, comme l'illumination solaire varie en fonction des saisons, les densités sont plus élevées en été qu'en hiver.

La dynamique ionosphérique de la région E

Aux altitudes de la région E, les particules chargées et neutres coexistent en abondance et permettent de fortes interactions entre ces populations, créant ainsi ce que l'on appelle la dynamo ionosphérique. À son tour, cette dynamo donne naissance à d'importants systèmes de courants dans l'ionosphère. La région E est également appelée région de la dynamo ionosphérique. À ces altitudes, les constituants neutres et ionisés coexistent en abondance et le mouvement différentiel entre les électrons et les ions donne lieu à des courants ionosphériques, voir les courants Sq ci-dessous. Dans cette région, le plasma peut être considéré comme partiellement ionisé et magnétisé avec des densités permettant des collisions abondantes. La fréquence cyclotron électronique est plus élevée que la fréquence de collision électron-neutre pour les électrons qui sont plus légers. En revanche, la fréquence cyclotronique des ions, plus lourds, est inférieure à leur fréquence de collision avec les neutres. Les électrons sont donc figés dans le champ magnétique, tandis que les ions sont régis par les vents et les marées de l'atmosphère neutre. Par conséquent, dans la loi d'Ohm (1.25), le tenseur de conductivité devient anisotrope comme dans (1.28) et s'écrit comme suit

$$\mathbf{j} = \sigma(\mathbf{E} + \mathbf{U} \times \mathbf{B}) , \tag{10.3}$$

avec $\mathbf{U}$ la vitesse du vent neutre et le tenseur de conductivité anisotrope σ avec la conductivité de Pedersen σ_P, la conductivité de Hall σ_H et la conductivité parallèle $\sigma_{||}$. Les conductivités dépendent de la densité électronique et des fréquences de collision ions-électrons et ions-neutres. Les expressions exactes sont dérivées dans K.-I. Maeda (1977) et Takeda and Araki (1985). La figure 10.4 illustre un profil de conductivité typique dans l'ionosphère diurne aux latitudes moyennes, tel qu'il est généré par le IPIM (Marchaudon & Blelly, 2015).

La conductivité de Hall σ_H (en bleu) culmine à des altitudes plus basses avec des valeurs plus élevées que la conductivité de Pedersen σ_P (en rouge). La conductivité parallèle $\sigma_{||}$ (en noir) est toujours supérieure à σ_P et σ_H. Ces conductivités sont à la base des systèmes de courants ionosphériques, car les courants parallèles (alignés sur le champ), de Pedersen et de Hall sont générés et coexistent dans ce système. Le mouvement différentiel entre les ions et les électrons crée un courant de Hall à travers le mouvement des électrons perpendiculaires aux champs électriques et magnétiques, puisque les ions sont fortement ralentis par les collisions avec les neutres. À des altitudes plus élevées, où la fréquence cyclotronique et la fréquence de collision des ions deviennent comparables, les ions commencent à se déplacer dans la direction du champ électrique et sont porteurs d'un courant de Pedersen. Dans l'ionosphère des hautes latitudes, les courants de Pedersen ont pour rôle de fermer les courants alignés au champ magnétique ou Field-Aligned Currents (FAC) dans l'ovale auroral et sont associés aux processus auroraux (Baker, 2019).

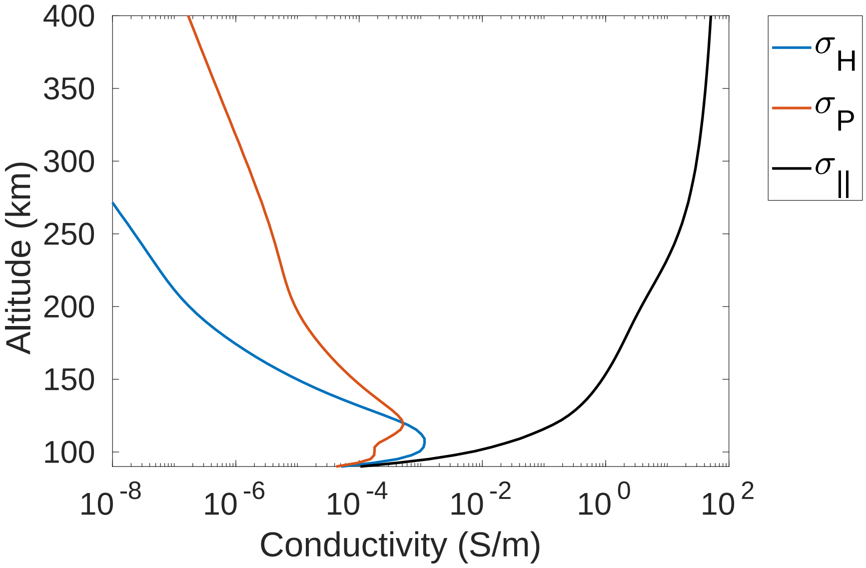

Figure 10.4: Profil de conductivité de la région E et F dans l'ionosphère latitudinale moyenne à l'aide de IPIM. (Marchaudon & Blelly, 2015).

Systèmes de courant Solar Quiet

Aux latitudes basses et moyennes, la dynamo de la région E alimente un important système de courants : le système de courants dit Soleil Calme ou Solar Quiet (Sq). Le nom de courant solaire calme vient de leur empreinte sur les mesures du champ géomagnétique, car ils induisent des variations diurnes très douces et caractéristiques en l'absence de orages solaires, c'est-à-dire pendant les périodes géomagnétiquement calmes.

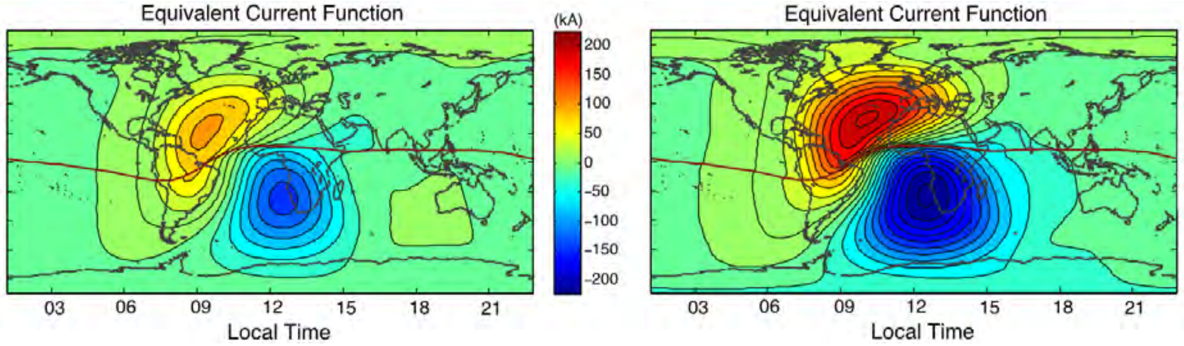

Figure 10.5: Simulation de l'intensité globale des systèmes de courant solaire calme en cas de faible activité solaire (à gauche) et de forte activité solaire (à droite). (Tiré de Yamazaki and Maute (2017))

La forme globale des systèmes de courant Sq est représentée sur la figure 10.5 et forme deux vortex, un dans chaque hémisphère. La direction des courants est inversée dans les deux hémisphères, c'est-à-dire que dans l'hémisphère nord (NH), la cellule de courant suit le sens inverse des aiguilles d'une montre et dans l'hémisphère sud (SH), elle suit le sens des aiguilles d'une montre. À l'équateur géomagnétique, où les deux cellules se rencontrent, un courant zonal très fort circule, renforcé par la configuration magnétique spécifique de cette région : l'électrojet équatorial ou EEJ, voir le chapitre 2.3.3.1. Les courants Sq ne peuvent pas être mesurés directement, mais sont indirectement dérivés des données du champ magnétique (voir chapitre 2.6.1). La figure 10.6 illustre les schémas typiques induits par les cellules de courant Sq dans les relevés des magnétomètres pour un grand ensemble de stations magnétiques réparties en latitude et alignées sur un secteur de longitude. Le champ magnétique est indiqué en coordonnées géographiques, N pointant vers le Nord, E vers l'Est et Z verticalement vers le bas. La composante Nord indique la position par rapport au foyer de la cellule actuelle. Dans le NH, elle est négative lorsque la station est située au-dessus du foyer et positive lorsqu'elle est située en dessous du foyer. Dans le SH, c'est l'inverse car la cellule de courant circule dans la direction opposée. La composante Est présente un signal sinusoïdal régulier qui change de signe entre NH et SH. La composante Z ne semble pas affectée. Dans les trois composantes, les empreintes de l'électrojet équatorial sont clairement visibles autour de l'équateur magnétique.

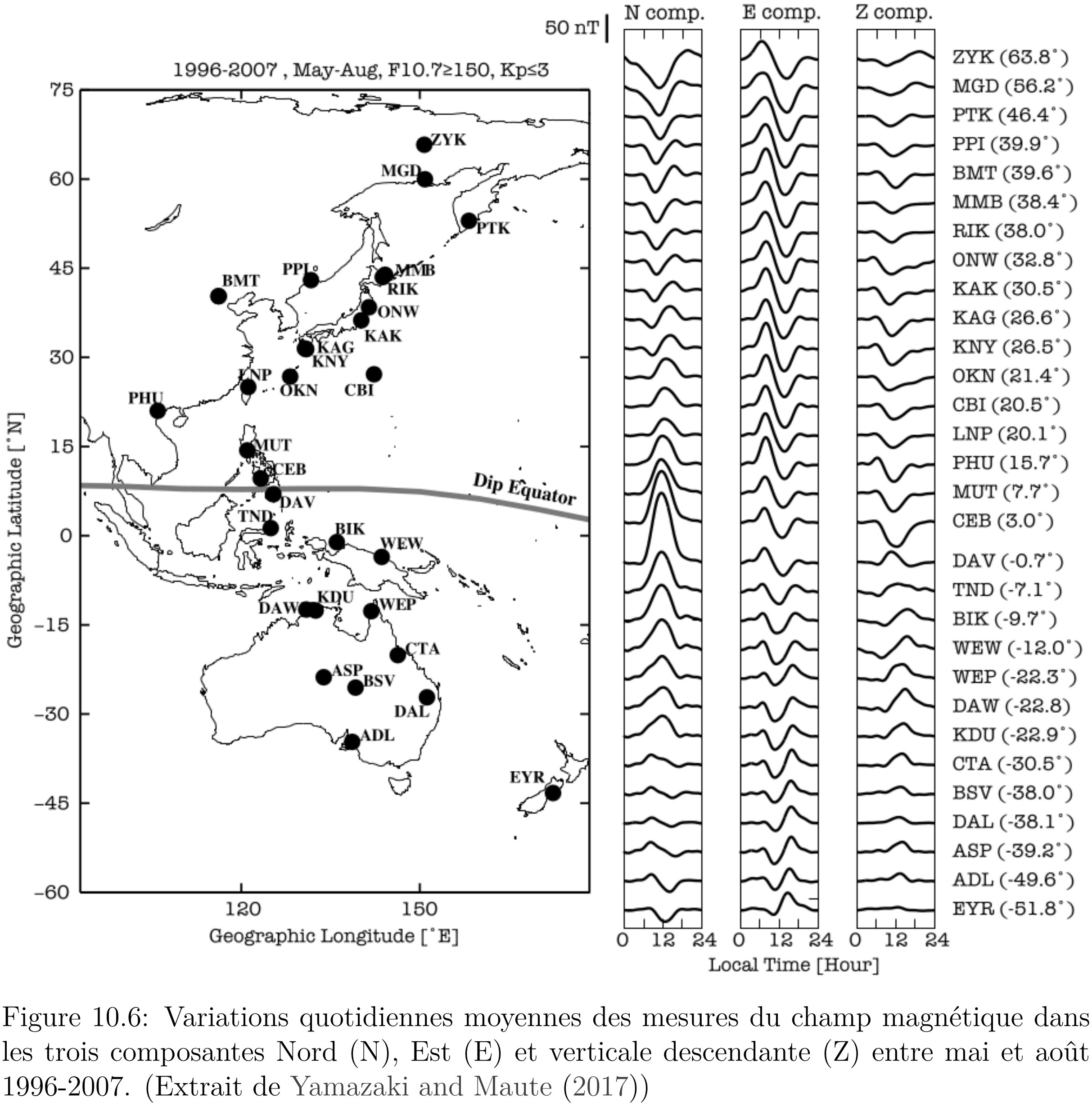

Figure 10.6: Variations quotidiennes moyennes des mesures du champ magnétique dans les trois composantes Nord (N), Est (E) et verticale descendante (Z) entre mai et août 1996-2007. (Extrait de Yamazaki and Maute (2017))

Comme ces cellules sont alimentées par la dynamo de la région E, qui dépend de l'irradiation solaire directe, ces systèmes de courant sont concentrés sur le côté jour. En raison du couplage avec l'atmosphère neutre dans la région dynamo, les courants Sq sont fortement modulés par les marées atmosphériques. Ces marées sont des oscillations à l'échelle mondiale avec des périodes harmoniques d'un jour, c'est-à-dire 24 heures, 12 heures, 8 heures, 6 heures et ainsi de suite, dont la marée de 24 heures est le principal moteur des courants Sq (H. Maeda, 1955; Kato, 1957; Lindzen & Chapman, 1969). Grâce à l'absorption du rayonnement infrarouge dans la troposphère et à l'absorption par l'ozone dans la stratosphère, la chaleur latente libérée génère des marées qui se propagent vers le haut. En se propageant vers le haut, elles croissent de manière exponentielle et, lorsqu'elles atteignent la région dynamo, elles ont des amplitudes de plusieurs dizaines de mètres par seconde dans le vent horizontal. Un tiers des courants totaux Sq de la planète est entraîné par de telles marées se propageant vers le haut (Yamazaki & Richmond, 2013; Yamazaki, Richmond, Maute, Wu, et al., 2014). En analysant les mesures des magnétomètres des latitudes moyennes, les spectres montrent des pics distincts à 24h, 12h, 8h et 6h qui sont un indicateur clair du système de courant Sq (Campbell, 1989).

Comme indiqué précédemment et comme le montre la figure 10.3, la densité d'électrons et donc la conductivité varient en fonction du cycle solaire et modulent par conséquent le système de courants solaires calmes. Les variations distinctes du cycle solaire, saisonnières et journalières des courants Sq sont bien documentées et décrites dans ce qui suit. Un aperçu et une description détaillés des courants Sq et de l'électrojet équatorial figurent dans Yamazaki and Maute (2017).

- **Dépendance du cycle solaire**
  La conductivité de l'ionosphère est étroitement liée à l'activité solaire. Cela affecte l'amplitude et la position du foyer des cellules de courant Sq. L'amplitude est généralement deux fois plus importante pendant le maximum solaire que pendant le minimum (Takeda, 1999). Diverses études suggèrent que l'amplitude est fortement corrélée de manière linéaire avec des indicateurs solaires tels que $F10.7$ (Yamazaki & Kosch, 2014; Yamazaki & Maute, 2017). Des études ont montré que l'amplitude des composantes de Fourier de 24h, 12h et 8h dépend fortement de $F10.7$, tandis qu'il en va de même pour la phase des composantes de 24h et 12h et donc pour l'emplacement du foyer qui se déplace vers des heures locales plus tardives à mesure que l'activité solaire augmente (Olsen, 1988; Yamazaki & Kosch, 2014; Yamazaki & Maute, 2017).
- **Dépendance saisonnière**
  En général, l'amplitude du Sq est plus élevée en été qu'en hiver aux latitudes moyennes en raison d'une irradiation solaire prolongée. Les amplitudes maximales sont observées lors des deux équinoxes aux latitudes basses et équatoriales, ce qui peut être lié aux influences de l'électrojet équatorial et à d'éventuels effets équinoctiaux. Les amplitudes en été sont environ trois fois plus élevées qu'en hiver (Takeda, 1999; Yamazaki & Maute, 2017). En hiver notamment, les courants peuvent devenir si faibles que la cellule elle-même peut disparaître (Campbell et al., 1993; Rastogi et al., 1996; Stening & Winch, 2013). La saison a également un effet significatif sur l'emplacement du foyer. En été, le foyer est déplacé vers des heures locales plus précoces qu'en hiver, ce qui est vrai pour les deux hémisphères (Campbell & Schiffmacher, 1987, 1988).
- **Variabilité d'un jour à l'autre**
  Les systèmes de courant Sq présentent une forte variabilité journalière (D2D) en termes de forme, d'amplitude et de phase. Cette variabilité D2D est bien documentée, mais ses mécanismes d'entraînement ne sont pas entièrement compris, voir par exemple Hasegawa (1960); Stening (2008). La figure 2.13 est un exemple de

ces variations pour quatre stations du secteur indien, réparties sur une petite bande longitudinale, couvrant les latitudes moyennes à basses, voir le panneau a. Le panneau b illustre la variation journalière moyenne ΔH de la composante horizontale du champ géomagnétique entre mars et avril 2009. De même, la forme de cette variation renseigne sur la localisation de l'observatoire par rapport au foyer de la cellule. Kashi (KSH) est proche du foyer, de sorte que lorsque la cellule est exactement au-dessus de la station, ΔH est nul avec des signes changeants avant et après la traversée. Novossibirsk (NVS) est au nord de la cellule actuelle et est donc influencé par la partie supérieure, vers l'ouest, du courant Sq. Jaipur (JAI) et Alibag (ABG) sont au sud du foyer et sont donc influencés par la partie est. Enfin, le pic observé à Tirunelveli (TIR) est induit par la partie la plus forte de l'EEJ. Le panneau c montre les valeurs de ΔH à midi pendant la même période pour chaque station et chaque jour. Les amplitudes peuvent varier de façon très irrégulière d'un jour à l'autre à toutes les latitudes. Il s'agit d'une caractéristique persistante du système de courant solaire calme qui est également présente pendant les périodes magnétiquement très calmes, comme c'est le cas pour la période de la figure 2.13 qui se situe pendant l'année très calme de 2009 (pendant le minimum solaire). Cela suggère que la variation intrinsèque de D2D a ses racines dans les vents et les marées de l'atmosphère neutre. De nombreuses études et simulations ont été menées pour souligner l'importance des facteurs de la basse atmosphère, comme par exemple Kawano-Sasaki and Miyahara (2008); Jin et al. (2011); Fang et al. (2013); Yamazaki, Richmond, Maute, Liu, et al. (2014). D'autres études et recherches sont nécessaires pour mieux comprendre les causes de la variabilité de D2D.

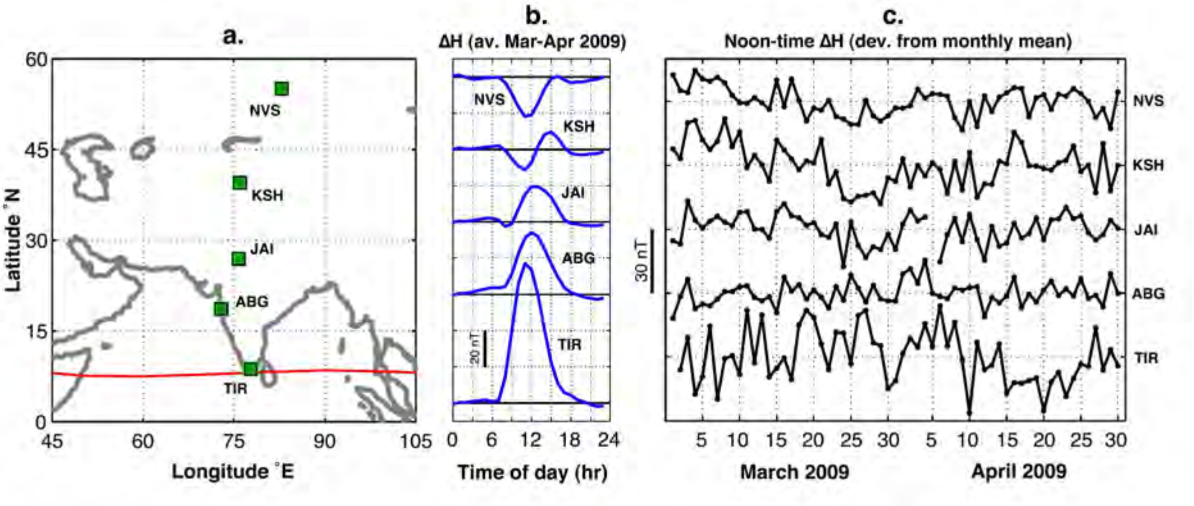

Figure 10.7: Variations journalières de la cellule nord du système de courant solaire calme. Le panneau a indique l'emplacement des observatoires magnétiques. Le panneau b montre la variation journalière moyenne de la composante horizontale H. Le panneau c montre la valeur de la composante H à midi chaque jour durant 2 mois. (Tiré de Yamazaki and Maute (2017))

Orages géomagnétiques

Si le champ magnétique interplanétaire (IMF) du vent solaire pointe vers le nord, le taux de reconnexion avec le champ géomagnétique est considérablement réduit (voir chapitre 2.2). Si cette condition se maintient pendant une longue période, la magnétosphère peut être considérée comme étant dans un état calme (Moretto et al., 2021). Cependant, si le vent solaire entrant a un IMF dirigé vers le sud (B_z négatif), favorisant la reconnexion côté jour, des quantités considérables d'énergie et de particules provenant du vent solaire sont injectées dans le système magnétosphère-ionosphère. Cela entraîne une augmentation de la convection et des taux de reconnexion, renforce les systèmes de courant et conduit à d'autres phénomènes qui jouent un rôle important dans la météorologie de l'espace : les orages géomagnétiques.

Un orage géomagnétique est une perturbation magnétique observée dans le monde entier, qui dure de plusieurs heures à plusieurs jours et ne se limite pas aux hautes latitudes, mais affecte également les basses et moyennes latitudes. On dit donc qu'il est géo-effectif. Ces perturbations du champ géomagnétique à l'échelle mondiale sont induites par de puissants événements transitoires solaires tels que les CME, accompagnés d'un IMF B_z prolongé vers le sud pendant plusieurs heures. La quantité d'énergie déposée dans le système magnétosphère-ionosphère et donc le niveau de géo-efficacité dépendent fortement des paramètres du vent solaire tels que la vitesse, la densité ainsi que la force et l'orientation de l'IMF. En raison du dépôt accru d'énergie pendant les orages géomagnétiques, les processus pré-existants sont considérablement renforcés. Cela se traduit par une activité accrue des sous-orages et une intensification des électrojets auroraux. La caractéristique la plus marquante est l'augmentation du courant annulaire qui subit une injection élevée de particules en raison de l'augmentation de la reconnexion depuis la queue magnétosphérique (Kistler et al., 2016). Sa signature la plus claire se trouve dans les mesures du champ géomagnétique. Lorsque le courant annulaire, qui s'écoule vers l'ouest dans le plan équatorial, s'intensifie pendant un orage, son champ magnétique induit est en sens inverse au champ dipolaire terrestre, ce qui entraîne une nette dépression de la composante horizontale H, comme l'indique la figure 10.8.

Les orages géomagnétiques peuvent être divisés en trois phases : la phase initiale, la phase principale et la phase de rétablissement. La phase initiale est marquée par une augmentation positive associée à la compression du champ magnétique côté jour en raison de l'augmentation de la pression du vent solaire. Lorsque la compression est particulièrement forte, un Storm Sudden Commencement (SSC) peut être observé sous la forme d'une forte déviation positive, toujours dans les doonées de magnétomètres au sol. La phase principale est indiquée par une forte déviation négative due à l'augmentation du courant annulaire. La phase de rétablissement englobe le retour à la normale du courant annulaire après l'orage (Hutchinson et al., 2011). Le champ magnétique des perturbations aux latitudes basses et moyennes n'est généralement pas axisymétrique. Pendant la phase principale de l'orage, le courant annulaire est généralement asymétrique car les ions injectés sont principalement présents dans les secteurs soir et après-midi. Lorsque l'injection se termine et que la phase de rétablissement commence, le courant annulaire devient plus symétrique (Sugiura & Chapman, 1960; Akasofu & Chapman, 1964; Weygand & McPherron, 2006).

Il est courant de caractériser les orages géomagnétiques en fonction de la déviation globale de la composante magnétique H induite par le courant annulaire renforcé. Cette déviation est résumée par l'indice de perturbation temporelle (Dst) dérivé des quatre

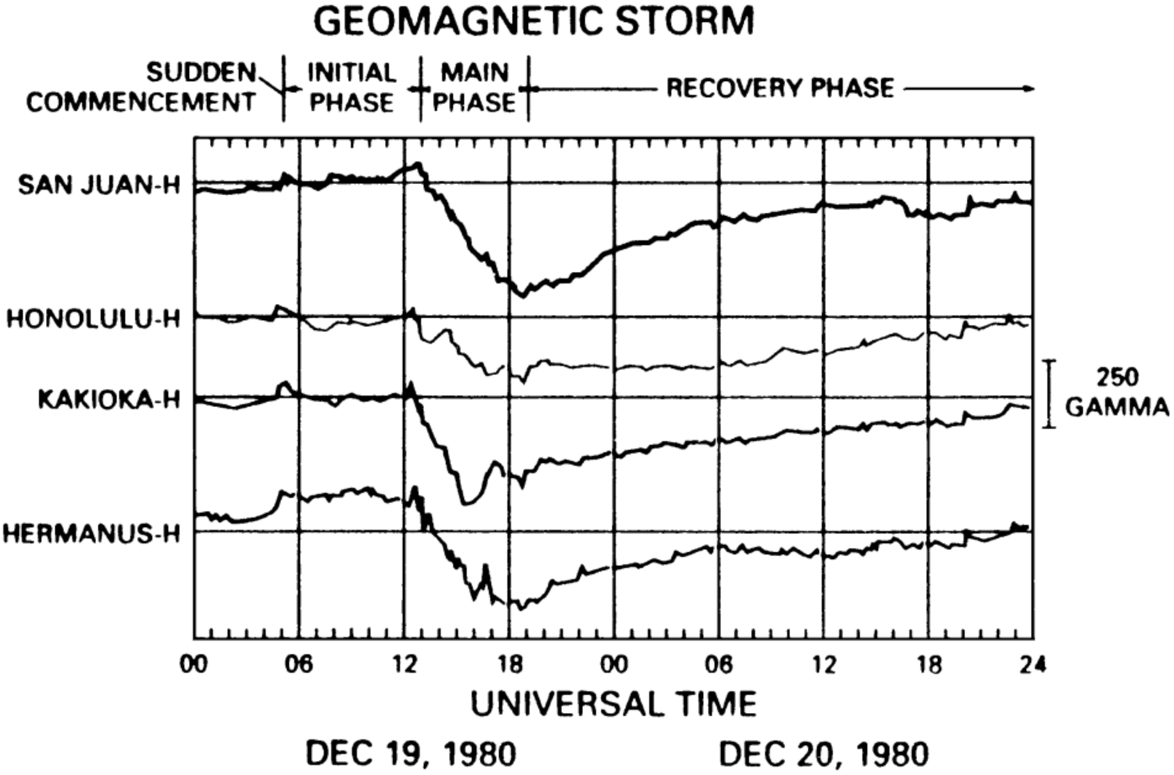

Figure 10.8: Les effets des orages magnétiques sur la composante horizontale des mesures du champ géomagnétique dans quatre observatoires des basses latitudes. Les phases typiques de l'orage sont indiquées. 1γ correspond à 1 nT. (Tiré de Campbell (2003))

observatoires magnétiques de la figure 10.8. Gonzalez et al. (1994) définit les orages géomagnétiques comme suit, traduit en français :

> *"... un intervalle de temps pendant lequel un champ électrique de convection interplanétaire suffisamment intense et durable conduit, par le biais d'une énergisation substantielle du système magnétosphère-ionosphère, à un courant annulaire intensifié suffisamment fort pour dépasser un certain seuil clé de l'indice de quantification de la durée de l'orage Dst."*

C'est pourquoi l'indice Dst sur 1 heure et, de nos jours, sa version sur 1 minute, l'indice SYM-H, ont été utilisés dans de nombreuses études pour définir et classer les orages géomagnétiques (voir le chapitre IV pour plus de détails sur ces indices). Alors que les CME fortes peuvent provoquer de très forts orages avec des valeurs Dst associées bien inférieures à $-100\,\text{nT}$, les Régions d'interaction en corotation (CIR) peuvent provoquer des orages modérés, en particulier pendant les phases de déclin et de faible activité solaire (Allen et al., 2020).

Les orages géomagnétiques à l'échelle mondiale et les sous-orages à l'échelle locale peuvent avoir des effets indésirables et néfastes sur nos technologies et constituer une menace pour la santé et la sécurité humaines, comme nous l'avons vu dans l'introduction de ce chapitre. L'amélioration de nos capacités à les prévoir avec précision est un domaine important et actif qui a également commencé à exploiter les méthodes d'intelligence artificielle (Camporeale, 2019; Nitti et al., 2022).

Les effets directs des orages comprennent le réchauffement de la haute atmosphère en raison de l'augmentation de la convection des particules chargées, responsable d'une friction ions-neutres ainsi que des précipitations de particules, ce qui entraîne un frottement supplémentaire sur les satellites en orbite basse. La convection et les précipitation de particules provoquent également des modifications chimiques importantes de l'ionosphère qui entraînent des changements de densité et une déviation des signaux radio la traversant, ainsi que des erreurs de positionnement GNSS, perturbant les systèmes mondiaux de navigation par satellite. L'intensification des courants ionosphériques provoquent également des courants géomagnétiques induits dans la croûte nuisibles pour les réseaux électriques et les pipelines.

Champ géomagnétique

Le champ géomagnétique est une superposition de nombreuses sources magnétiques, le champ magnétique interne de la Terre étant le principal contributeur, communément appelé champ principal. La création de l'ionosphère via le rayonnement solaire et l'interaction du vent solaire avec le champ principal de la Terre dans la magnétosphère entraîne un système complexe et couplé de courants au sein de ces régions. Selon la loi d'Ampère (équation (1.35), chacun de ces courants induit un champ magnétique et contribue ainsi au champ géomagnétique global.

La figure 10.9 illustre quelques sources importantes du champ géomagnétique. Elles sont classées en deux catégories: les sources externes et les sources internes. Les sources externes comprennent les différents systèmes de courants déjà mentionnés ci-dessus tels que : courant annulaire, Sq, FAC et EEJ. Les sources internes comprennent entre autre le champ principal et sont abordées ci-après.

Champ magnétique principal de la Terre

En première approche, le champ principal peut être approximé par un champ dipolaire au sol. Cependant, cette approximation reste grossière. En effet, le champ magnétique interne contient des longueurs d'onde spatiales plus courtes non seulement de son champ principal mais aussi de son champ crustal. Les mesures, acquises à la surface ou à l'altitude des satellites, contiennent des contributions de diverses sources internes et externes couvrant de larges gammes d'échelles spatiales et temporelles (Mandea et al., 2019). Dans les profondeurs de notre Terre, les niveaux de pression et de température sont si élevés que la roche, le fer et le nickel fondent, constituant le noyau externe fluide. Ces fluides sont en mouvement par convection et, avec la rotation de la Terre, génèrent un courant électrique qui induit un puissant champ magnétique. Ce processus est appelé dynamo géomagnétique et serait à l'origine du champ magnétique intrinsèque de la Terre (Gauss, 1877; Landeau et al., 2022). Dans un rayon d'environ $6R_E$, ce champ peut être approximé par un champ magnétique dipolaire avec des intensités de ~60 000 nT aux pôles et ~25 000 nT à l'équateur. La géométrie dipolaire est à l'origine des miroirs magnétiques qui conduisent à la formation des ceintures de radiation et du courant annulaire, comme détaillé dans le chapitre 2.2. L'axe du dipôle est incliné par rapport à l'axe de rotation de la Terre d'environ 11° et le pôle sud magnétique est situé dans l'hémisphère nord, tandis que le pôle nord magnétique est situé dans l'hémisphère sud.

Le processus dynamo n'est pas stable, de sorte que l'intensité et la direction du champ magnétique changent lentement mais continuellement. Les échelles de temps impliquées

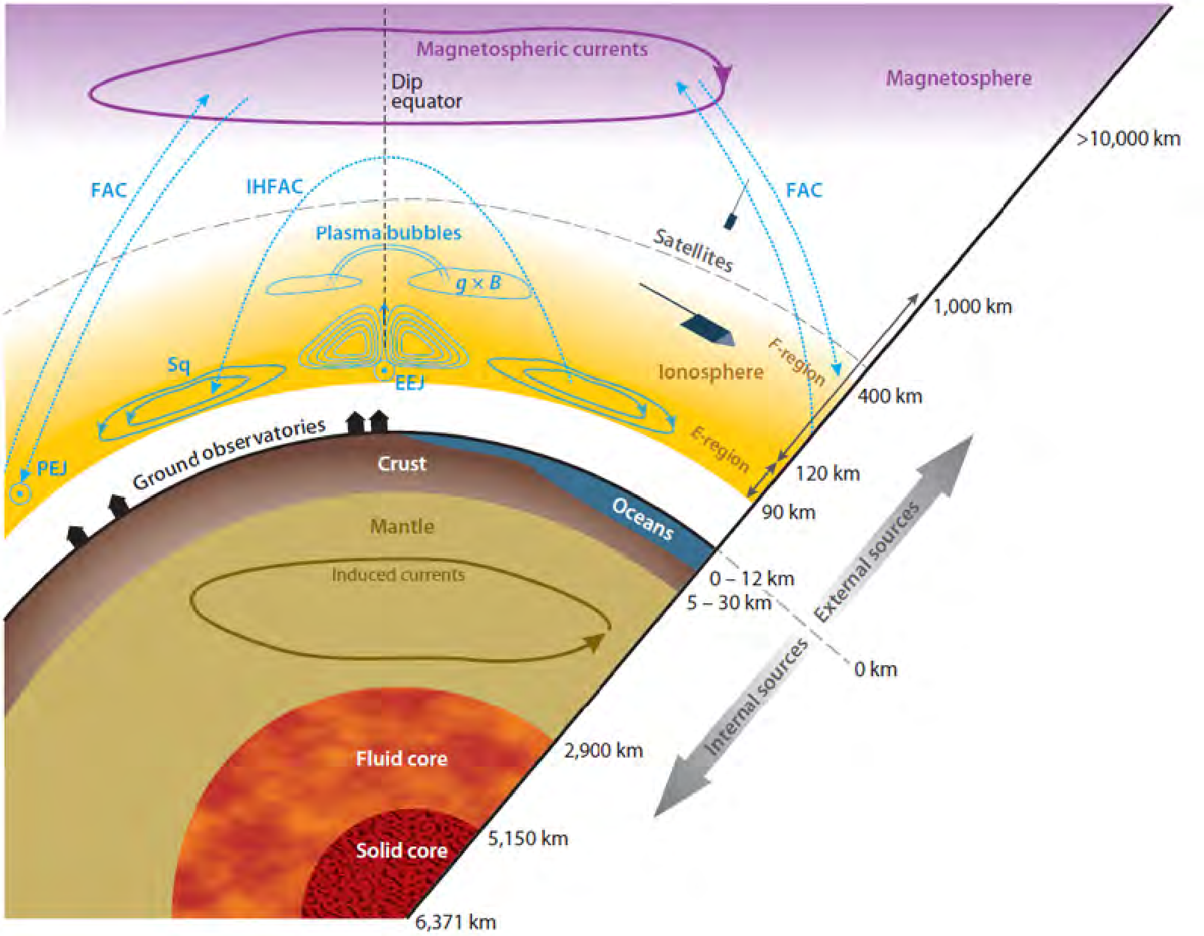

Figure 10.9: Vue d'ensemble des sources internes et externes du champ géomagnétique. (Tiré de (Olsen, 2016))

dans cette dérive régulière vont de quelques années à des millénaires. Le paléomagnétisme est le domaine d'étude qui utilise des techniques spécialisées pour extraire des informations sur le champ magnétique à partir d'échantillons très anciens afin de comprendre ces changements à long terme du champ principal. Les événements les plus spectaculaires sont les inversions de pôles, au cours desquelles l'intensité du champ diminue pendant quelques milliers d'années jusqu'à ce que l'inversion ait lieu, suivie d'un renforcement du champ au cours des milliers d'années suivantes (Gubbins, 2008). Actuellement, le pôle sud magnétique se déplace à raison de 60 km par an du Canada vers la Sibérie et le pôle nord magnétique à raison d'environ 5 km par an de l'Antarctique vers l'Australie (Olsen & Mandea, 2007). Ces changements progressifs sont appelés variations séculaires et constituent un domaine d'étude actif (Bloxham & Gubbins, 1985; Finlay et al., 2016, 2020). Bien que graduelles, elles sont des facteurs importants pour la météorologie de l'espace, car la modification des configurations du champ peut directement accentuer ses effets (Mandea & Chambodut, 2020).

Afin de décrire le champ magnétique en constante évolution, des modèles sophistiqués sont générés sur la base des mesures du champ géomagnétique. Le modèle du champ géomagnétique international de référence (IGRF) est produit et mis à jour par l'Association Internationale de Géomagnétisme et d'Aéronomie (IAGA). Le modèle représente le champ géomagnétique en termes d'harmoniques sphériques dont les coefficients sont déterminés tous les cinq ans pour tenir compte des changements temporels de la variation séculaire. L'expansion des harmoniques sphériques montre que la contribution du premier degré (la partie dipolaire) représente 93 % du champ magnétique total. Le modèle le plus récent est IGRF-13 et il est valable pour les années 1990 à 2025 (Alken et al., 2021).

Autres sources internes

Dans la croûte terrestre, l'aimantation rémanente et induite de minéraux magnétiques tels que la magnétite et le titane se trouve dans la lithosphère. L'ère spatiale a permis de cartographier le champ lithosphérique grâce à des études par satellite (Thébault et al., 2016). Les intensités de champ associées dépendent de l'emplacement et ne dépassent généralement pas 100 nT, mais peuvent atteindre plusieurs centaines de nanotesla pour des anomalies majeures dans des régions comme Koursk et Bangui (Taylor & Frawley, 1987; Njiteu Tchoukeu et al., 2021). Les moyennes du biais crustal et les variances respectives pour les observatoires géomagnétiques sont données par exemple dans Verbanac et al. (2015) dont une sélection est résumée dans le tableau 2.1. La variation autour de la moyenne est de nature oscillatoire et peut être liée à des erreurs dans les données d'entrée et à des influences provenant de champs externes. Une autre source interne est la circulation océanique qui génère un champ magnétique qui peut être détecté à proximité des océans et des régions côtières. Le courant électrique associé est généré par des ions de sel qui sont déviés par la force de Lorentz dans différentes directions en raison de leur polarité (Petereit et al., 2022).

Variabilité du champ géomagnétique

Lors de l'enregistrement du champ géomagnétique, le signal résultant est une composition de toutes les sources internes et externes, ce qui se traduit par un large spectre d'amplitude et de fréquence, comme le montre la figure 10.10. Le champ crustal est pratiquement constant et n'est pas représenté dans le spectre. Les variations induites par le champ magnétique interne sont progressives et s'étalent sur de longues périodes. Elles sont associées à des changements de grande amplitude dans la partie basse fréquence du spectre. Il s'agit notamment des inversions de pôles qui s'étendent sur des millions d'années et de la variation séculaire qui modifie constamment l'amplitude, reconnaissable en quelques mois ou années. Les sources externes agissent sur des échelles de temps plus courtes et sont associées à des variations d'amplitude plus faibles. Le cycle solaire, avec sa période d'environ 11 ans, induit des amplitudes de l'ordre de 10-20 nT. Aux latitudes moyennes, les systèmes de courants solaires calmes peuvent induire des variations diurnes et subdiurnes de 20-50 nT. Les sous-orages sont responsables de variations du champ pouvant atteindre 1000 nT dans les régions polaires pendant plusieurs heures, tandis que les orages géomagnétiques peuvent perturber le champ géomagnétique mondial de l'ordre de centaines de nanotesla, même aux latitudes moyennes pendant plusieurs jours. La foudre induit des résonances électromagnétiques entre la surface de la Terre et l'ionosphère. Ces résonances sont appelées résonances de Schumann et se situent dans le régime des hautes fréquences (Price, 2016). À l'extrémité du spectre des hautes fréquences, on trouve des générateurs de bruit d'origine humaine, notamment le bruit des lignes électriques et les émissions radio (Mandea et al., 2019).

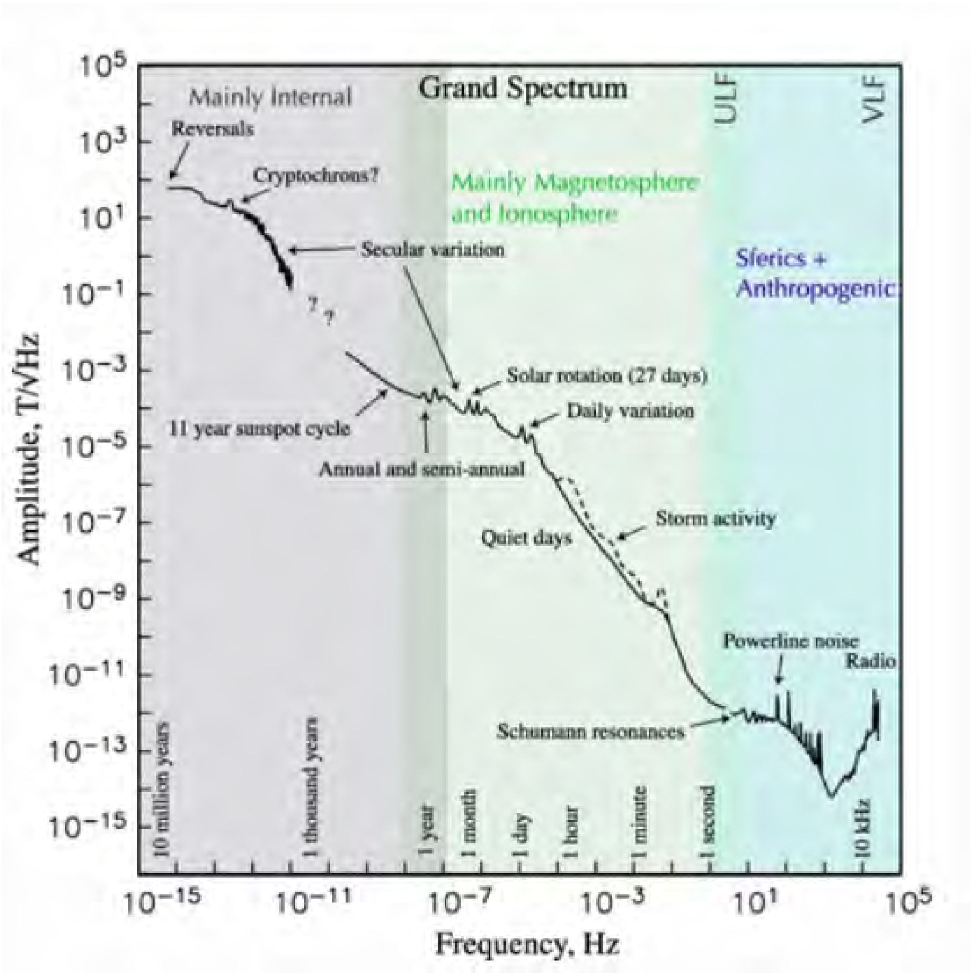

Figure 10.10: Le spectre amplitude-fréquence du champ géomagnétique avec des indications sur les sources associées. (Tiré de Constable (2016))

Mesures du champ géomagnétique

Les sources du champ géomagnétique sont très variées dans l'espace et dans le temps, comme l'indique la figure 10.10. Les variations du champ géomagnétique qui se produisent à l'échelle des temps géologiques, comme les inversions de pôles, sont déterminées à l'aide de techniques de paléomagnétisme (Gilder & Lhuillier, 2019). Pour d'autres variations plus courtes, on utilise des instruments spécialisés qui enregistrent les champs magnétiques ambiants. Avec l'avènement de l'ère spatiale, il est non seulement possible de collecter des données depuis le sol, mais aussi de mesurer la configuration du champ magnétique dans l'espace (Marchaudon, 2019).

À la surface de la Terre, les observatoires magnétiques sont des installations situées sur des sites géographiques stables qui hébergent des magnétomètres et fournissent des mesures absolues du champ géomagnétique de haute qualité, sur de longues séquences, les enregistrements continus les plus longs remontant à plus de 150 ans. Aujourd'hui, un nombre croissant d'observatoires magnétiques sont en mesure de fournir des données de haute qualité sur le champ magnétique avec une résolution temporelle pouvant atteindre quelques secondes. Une liste de ces observatoires est tenue à jour par le IAGA, avec leur désignation officielle en trois lettres. Par exemple, l'observatoire français de Chambon-la-Forêt est désigné par l'abréviation CLF. Le INTERMAGNET[1], garantit la qualité des données à la résolution minute de ses observatoires membres et facilite l'échange gratuit de données entre les nations et la création de produits de données géomagnétiques. Les données du réseau INTERMAGNET sont fournies en format vectoriel avec une résolution de 0.1 nT et une cadence de 1 minute. 41 observatoires magnétiques ont participé à la création de ce réseau en 1991. Depuis, le nombre d'observatoires membres n'a cessé d'augmenter, bien que certaines stations se soient retirées complètement ou pour une durée limitée en raison de dysfonctionnements ou de l'arrêt de la production de données (Kerridge, 2001; Gilder & Lhuillier, 2019). L'annexe A fournit des détails sur les observatoires INTERMAGNET entre 1991 et 2019. La distribution mondiale des observatoires est également illustrée dans la figure 4.1.

D'autres installations au sol comprennent des réseaux de magnétomètres qui peuvent être déployés de manière flexible. Ils sont généralement utilisés dans le cadre de campagnes de mesure visant à étudier des phénomènes magnétiques spécifiques sur une courte période.

Si ces options fonctionnent bien sur les sols solides, elles sont moins adaptées aux mesures magnétiques sur les étendues d'eau. Les deux tiers de notre planète étant recouvert d'océans, les mesures du champ magnétique sont soumises à d'importantes restrictions. Des études magnétiques marines et aéroportées sont menées sur l'eau et dans l'espace aérien afin de couvrir ces parties du monde sur une distance et pendant une durée limitées.

Systèmes de coordonnées

Les systèmes de coordonnées sont utilisés pour localiser les objets dans l'espace et pour donner un cadre de référence aux champs de vecteurs. En général, les systèmes de coordonnées sont adaptés aux phénomènes et aux conditions qui nous intéressent. Pour le champ géomagnétique, plusieurs systèmes de coordonnées magnétiques adaptés sont en place. Un examen approfondi, y compris les définitions des systèmes les plus utilisés, est disponible dans Laundal and Richmond (2016).

Les mesures du champ géomagnétique au sol sont généralement effectuées dans un système de coordonnées géographiques locales (NED) dont l'axe x pointe vers le nord géographique, l'axe y vers l'est géographique et l'axe z vers le bas, d'où l'appellation de système NED. Les composantes $B = (X, Y, Z)$ sont illustrées sur la figure 10.11. Les données du réseau INTERMAGNET sont fournies dans ce repère NED. Les éléments magnétiques dérivés sont la déclinaison D, qui est l'angle entre le Nord géographique et le Nord magnétique, l'inclinaison I, qui est l'angle entre le plan horizontal local et le vecteur champ, et les intensités du champ totale et horizontale, F et H. L'expression de ces quantités et leur visualisation sont présentées dans la figure 10.11.

Jusqu'à présent, nous avons utilisé des expressions telles que polaire, latitudes moyennes et équatoriale pour désigner certaines régions latitudinales de la Terre. Comme l'axe du dipôle magnétique est incliné d'environ 11° par rapport à l'axe de rotation de la Terre, ces régions ne coïncident pas dans les repères magnétique et géographique. Pour décrire les phénomènes qui dépendent du champ magnétique, il est plus pratique de choisir un repère de référence magnétique plutôt que géographique. Un tel système de coordonnées dépend du champ magnétique généré en interne par la Terre, ce qui implique que ses coordonnées magnétiques changent en même temps que la variation séculaire. En première approximation, le champ magnétique peut être décrit par un dipôle incliné par rapport à l'axe

---

[1] https://intermagnet.github.io, consulté le 2023-07

$$D = arctan\left(\frac{Y}{X}\right)$$

$$I = arctan\left(\frac{Z}{H}\right)$$

$$F = \sqrt{X^2 + Y^2 + Z^2}$$

$$H = \sqrt{X^2 + Y^2}\,.$$

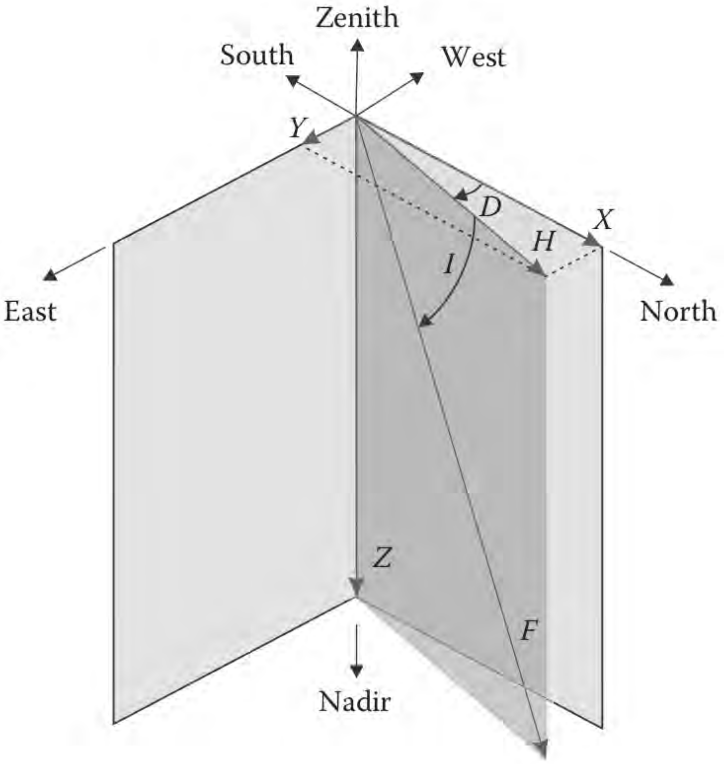

Figure 10.11: Système de coordonnées locales NED avec les éléments magnétiques X, Y, Z et définition des éléments dérivés déclinaison D, inclinaison I, intensité du champ F et intensité horizontale H. (Tiré de Olsen (2016))

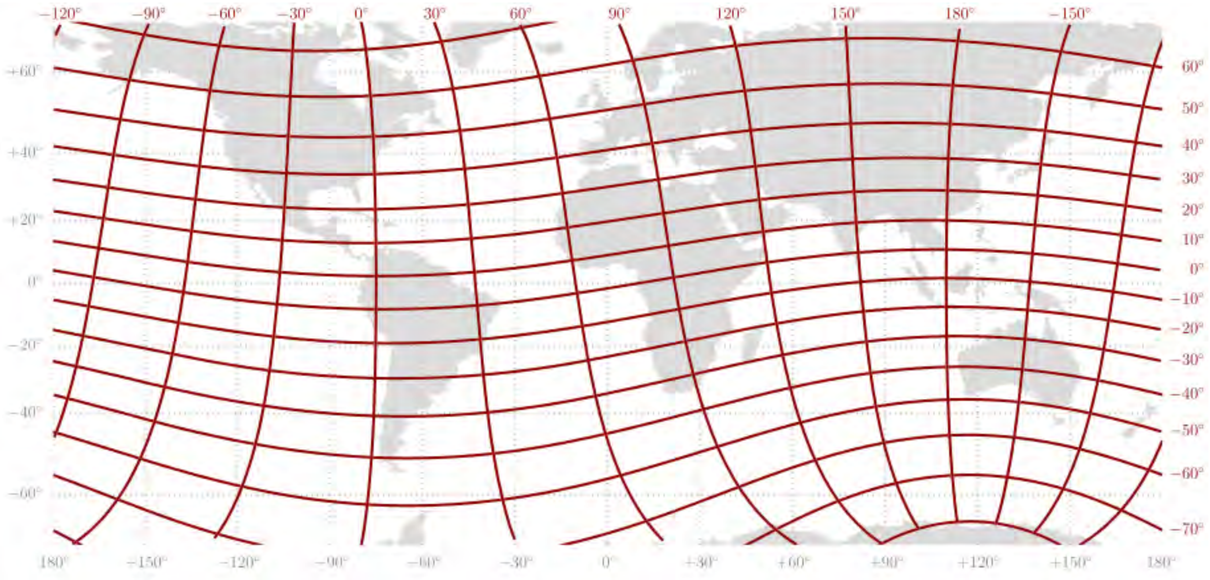

Figure 10.12: Coordonnées dans le repère du dipôle excentré projetées sur la carte de la surface géographique de la Terre. (Tiré de Laundal and Richmond (2016))

de rotation de 11° et qui prend naissance au centre de la Terre en utilisant le système de coordonnées du dipôle centré (CD). Pour une description plus précise, le système de coordonnées ED (Eccentric Dipole) est basé sur la représentation d'un dipôle dont l'origine est décalée par rapport au centre de la Terre. Son axe cartésien z est aligné sur l'axe du dipôle, positivement vers le Nord, et est décalé d'environ 500 km du centre de la Terre, d'où le nom dipôle *excentré*. Son axe y est perpendiculaire au plan contenant l'axe du dipôle et l'axe de rotation de la Terre. L'axe x complète le trièdre. Les coordonnées du dipôle excentré peuvent être exprimées en coordonnées sphériques (r, θ, ϕ) avec r correspondant au rayon de la Terre, θ à la latitude magnétique et ϕ à la longitude magnétique. La figure 10.12 illustre la manière dont ce système de coordonnées magnétiques se place à la surface géographique de la Terre. Pour les phénomènes plus éloignés de la Terre, le champ géomagnétique lui-même en tant que repère de référence peut ne plus être idéal. Le système de coordonnées géocentriques de la magnétosphère solaire (GSM) est particulièrement pratique pour l'observation du vent solaire. Son axe x pointe du centre de la Terre (qui est aussi son origine) vers le Soleil. L'axe y est perpendiculaire à l'axe du dipôle magnétique et à la ligne Terre-Soleil. L'axe z complète le trièdre. L'angle μ, parfois appelé angle d'inclinaison du dipôle, est l'angle entre l'axe du dipôle géomagnétique et l'axe z dans le repère géocentrique de la magnétosphère solaire (GSM). Cet angle varie en fonction de l'heure de la journée (en raison de l'inclinaison de l'axe du dipôle) et de la saison (en raison de l'inclinaison du plan équatorial de la Terre). Dans l'hémisphère nord, μ a son maximum au solstice d'été et son minimum au solstice d'hiver, et inversement dans l'hémisphère sud. Aux équinoxes, il est égal à zéro (Cnossen et al., 2012). Dans ce qui suit, le *tilt* fait référence à l'angle d'inclinaison variable du dipôle μ (à ne pas confondre avec l'inclinaison entre l'axe du dipôle et l'axe de rotation de la Terre avec ses 11°, qui ne varie qu'à l'échelle des temps géologiques). Une autre grandeur pratique est la longitude solaire L qui décrit la position de la Terre autour du Soleil et fournit des informations sur la saison. Elle est définie comme étant 0° à l'équinoxe de printemps, et donc 90° au solstice d'été, 180° à l'équinoxe d'automne et 270° au solstice d'hiver. Pour les phénomènes induits par l'illumination solaire directe, on peut utiliser l'angle zénithal χ qui est de 90° lorsque le Soleil est directement au-dessus de l'endroit considéré. L'heure locale magnétique (MLT) combine les informations relatives à la longitude magnétique et à la position solaire. Le méridien magnétique minuit est défini comme le méridien situé à 180° de longitude magnétique du point subsolaire. Une heure, où 1 h correspond à 15° de longitude magnétique, est positive vers l'est magnétique. Le système MLT/latitude magnétique tourne par rapport à la Terre à la vitesse à laquelle le point subsolaire traverse les méridiens magnétiques.

Indices d’activité géomagnétique

L’identification et la quantification des signatures de orages dues au forçage solaire est un sujet important dans le domaine de la météorologie de l’espace. Il est reconnu depuis longtemps que les signatures des orages sont clairement présentes dans les mesures du champ géomagnétique et peuvent donc être utilisées pour caractériser les perturbations qui en résultent. Les indices géomagnétiques ou indices d’activité magnétique basés sur les mesures du champ magnétique sont des mesures toutes désignées pour quantifier l’activité magnétique. Les indices sont traditionnellement dérivés de données provenant d’un réseau d’observatoires terrestres stables et représentent généralement des sources de perturbation externes du champ géomagnétique. La stratégie commune de dérivation consiste à diviser le signal en contributions provenant de sources calmes et perturbées. Lorsque l’on observe le champ géomagnétique au-dessus du régime de basse fréquence et en l’absence de facteurs solaires externes puissants (voir la figure 10.10) le champ géomagnétique présente des variations lisses au cours d’une journée, en plus d’une tendance plus longue induite par des sources telles que le système de courants solaires calmes et la variation séculaire. En revanche, les perturbations induisent des variations non périodiques et, dans une certaine mesure, de plus courte durée, comme la dépression H proéminente des orages géomagnétiques, voir la figure 10.8. La détermination des sources calmes conduit à un signal théorique de champ magnétique calme, appelé ligne de base géomagnétique. Cette ligne de base est ensuite soustraite du signal magnétique enregistré, laissant l’information sur les perturbations dans le résidu.

L’un des premiers indices dérivés de cette manière est l’indice K introduit par Bartels en 1939. À cette époque, des observateurs qualifiés identifiaient les lignes de base sur des magnétogrammes imprimés sur papier. L’idée générale de ces indices a perduré jusqu’à aujourd’hui. Cependant, depuis cette première tentative, des améliorations significatives ont été apportées à notre compréhension du champ géomagnétique et des effets associés à la météorologie de l’espace. En particulier, au cours des dernières décennies, l’entrée dans l’ère numérique a facilité l’accès aux données sur le champ géomagnétique et la possibilité d’utiliser des ordinateurs pour analyser et manipuler les signaux du champ géomagnétique. Cette avancée a conduit à la définition de nouveaux indices qui jouent un rôle crucial dans la description des relations Soleil-Terre et agissent comme un important proxy pour les modèles et les prévisions de météorologie de l’espace (Liemohn et al., 2018). Des efforts considérables ont été déployés pour créer et dériver des indices magnétiques dans le but d’améliorer notre compréhension des impacts solaires sur le champ géomagnétique. Alors que certains indices sont créés dans le but d’évaluer l’état global du champ géomagnétique, d’autres sont dédiés à la quantification de phénomènes physiques spécifiques tels que les systèmes de courant et les processus associés à certaines régions. De nos jours, les indices magnétiques sont largement utilisés et un aspect important de la météorologie de l’espace concerne la prévision de ces indices. Le Service International des Indices Magnétiques (ISGI), en tant que service de IAGA, a pour mission de valider les indices géomagnétiques qui répondent à certaines normes de qualité et d’en permettre l’accès. Étant donné que la dérivation des indices magnétiques peut prendre beaucoup de temps et afin de fournir des valeurs le plus rapidement possible, ils peuvent être marqués comme quick-look ou provisoires. Cela indique que la valeur de l'indice n'est pas finale et peut différer de sa valeur dite définitive. Les paragraphes suivants donnent des exemples d'indices géomagnétiques bien établis et largement utilisés, ainsi que leurs méthodes de calcul. Des discussions approfondies sur les indices géomagnétiques sont disponibles dans Menvielle et al. (2011). Comme on le verra, la détermination de la ligne de base est un élément important, car elle définit les contributions des sources contenues dans un indice. Des méthodes de dérivation de la ligne de base pour certains indices sont présentées, ainsi que d'autres méthodologies permettant d'extraire les variations calmes des mesures du champ géomagnétique. La dernière partie de ce chapitre porte sur les limites et les possibilités d'amélioration des lignes de base géomagnétiques existantes et motive le présent travail.

Exemples

Comme nous l'avons déjà mentionné, l'un des tout premiers indices introduits est l'indice K. Plusieurs indices planétaires destinés à décrire l'état général du champ géomagnétique sont basés sur ces premières versions et sont encore utilisés de nos jours. Nous commençons par l'introduction de ces indices et poursuivons avec ceux qui ont été proposés plus récemment et qui ont évolué en raison de notre meilleure compréhension du champ géomagnétique et de la disponibilité des données.

Indices K et indices dérivés de K

Les indices K ont été introduits par Bartels et al. (1939) dans le but de quantifier les variations irrégulières dans les mesures du champ géomagnétique. En général, ils sont calculés et fournis par les observatoires magnétiques eux-mêmes, conformément aux normes recommandées par l'IAGA. Pour leur dérivation, les variations irrégulières pour chacune des deux composantes horizontales X et Y du champ géomagnétique sont déterminées. Pour ce faire, on élimine des mesures les variations dites "non-K". Les variations non-K sont définies comme comprenant toutes les contributions de sources calmes du champ géomagnétique. Pour chaque intervalle de 3 heures UT, 0-3 UT, 3-6 UT, etc., et pour chacune des deux composantes X, Y, la différence maximale des variations irrégulières déterminées est calculée. A partir de ces deux valeurs, le maximum est utilisé pour quantifier le niveau d'irrégularité en chiffres de 0 à 9. Un niveau de 0 correspond à un état très calme du champ géomagnétique, tandis que 9 indique un état extrêmement perturbé. La correspondance entre la valeur maximale en nanotesla et la classe 0-9 a été fixée pour l'observatoire de Niemegk (NGK) dans une échelle non linéaire, voir le tableau 3.1. Comme les amplitudes des perturbations magnétiques dépendent fortement de l'emplacement à la surface du globe, cette échelle ne peut pas être appliquée directement à d'autres observatoires, en supposant que la même perturbation produit la même classe dans chaque observatoire. C'est pourquoi des grilles sont utilisées pour définir la proportionnalité appropriée par observatoire. Ces grilles dépendent de ce que l'on appelle le K9 lower limit (K9LL) qui est déterminé pour chaque observatoire par l'ISGI (Mayaud, 1968). Ainsi, les indices K locaux sont utilisés pour définir des indices plus globaux, appelés indices géomagnétiques dérivés de K. Ceci est nécessaire pour garantir la comparabilité des indices K entre stations.

Kp Index

L'un des indices les plus utilisés est l'indice Kp (K-planétaire). L'idée de l'indice Kp est de quantifier l'activité à l'échelle planétaire globale du champ géomagnétique et a été introduite par Bartels en 1949. Il est dérivé d'indices K standardisés, les indices Ks, provenant de 13 observatoires géomagnétiques. Le processus de normalisation est nécessaire pour éliminer les artefacts saisonniers et temporels locaux des indices K pour lesquels des tables de conversion empiriques et complexes sont utilisées (Bartels, 1957a, 1957b). Le Kp lui-même est défini comme la moyenne simple des indices K des 13 stations et, en tant que tel, a une résolution temporelle de 3 heures et une échelle de 0 à 9. Les classes et donc l'indice Kp ne sont pas linéaires, bien que la linéarité soit une caractéristique souhaitable pour les indices en général. C'est pourquoi l'indice *ap* a été introduit en *unités ap*, 1 unité ap correspondant à environ 2 nT (Bartels & Veldkamp, 1954). L'indice Kp est utilisé dans de nombreux modèles de météorologie de l'espace et est populaire auprès du grand public, où il est utilisé pour les prévisions d'aurores. Il est généralement admis qu'un Kp inférieur à 2 est considéré comme une activité géomagnétique faible à calme, tandis qu'un Kp supérieur à 7 est considéré comme une activité très forte. Il convient de souligner ici que les observatoires utilisés pour le Kp sont situés à des latitudes moyennes et sont fortement pondérés vers l'Europe, voir la figure 3.4 dans le panneau supérieur gauche. Par conséquent, les indices Kp constituent une approximation plus appropriée pour ces régions. Ł'indice Kp est un indice historique approuvé par l'IAGA, voir Matzka et al. (2021) pour un examen récent. Depuis le début, la série temporelle Kp est dérivée par l'institut allemand en charge de l'observatoire de Niemegk, aujourd'hui le GeoForschungsZentrum (GFZ) Potsdam qui est aussi l'institut collaborateur de l'ISGI. L'ensemble des données est disponible sur `doi.org/10.5880/Kp.0001`.

Classification des jours perturbés et calmes D- et Q-days

Johnston (1943) a introduit les jours les plus calmes et les plus perturbés par mois sur la base de l'indice Kp. Chaque jour d'un mois se voit attribuer un nombre dérivé de la moyenne de :

1. la somme des huit valeurs Kp
2. la somme des carrés des huit valeurs Kp
3. le maximum des huit valeurs Kp

Cela permet de classer les jours : les dix jours Q les plus calmes sont ceux qui présentent les valeurs les plus faibles et les cinq jours D les plus perturbés sont ceux qui présentent les valeurs les plus élevées. Le principal problème de cette définition est que les jours Q et D sont définis de manière relative pour chaque mois. Cela signifie qu'au cours d'un mois très perturbé, même les jours calmes peuvent être perturbés et vice-versa pour les mois très calmes.

aa Index

L'indice *aa* a été introduit pour fournir des moyens simples de surveiller et de déterminer l'activité géomagnétique mondiale depuis 1868 (Mayaud, 1972). Il est produit à partir des indices K de deux observatoires magnétiques antipodaux en Angleterre et en Australie, voir Mayaud, Menvielle, and Chambodut (2023) pour un aperçu des anciens observatoires et la figure 3.4 au milieu du panneau de gauche pour les observatoires actuels. Les indices

K sont reconvertis en amplitudes en nanotesla et normalisés pour représenter l'activité à une latitude magnétique de 50° en utilisant les amplitudes de classe moyenne de la grille de Niemegk. Cet indice est une mesure approximative de l'activité géomagnétique avec une série homogénéisée sur le long terme. Il est officiellement approuvé par l'IAGA et dérivé par l'EOST. L'ensemble des données est disponible sur `doi:10.25577/9z05-v751`.

Classification des jours vraiment calmes

Les jours très calmes et calmes sur 24 heures et 48 heures (jours CK24 et CK48) ont été introduits par Mayaud (1972) pour indiquer les périodes magnétiquement très calmes. Elles sont basées sur 1) la moyenne des valeurs de l'indice *aa* et 2) la somme p qui est la somme transformée et pondérée des valeurs *aa*, centrée sur le jour UT. La clé de la somme p est indiquée dans le tableau 3.2.

La classification en jours 'C' et 'K' est la suivante :

- CK24: jours les plus calmes sur 24 heures avec moyenne(aa) $<$ 13 nT
  - 'C' indique un jour C très calme avec Sum(p) < 4
  - 'K' indique un jour K calme avec Sum(p) $>= 4$
- CK48: jours les plus calmes sur 48 heures avec moyenne(aa) $<$ 13 nT
  - 'C' indique un jour C très calme avec Sum(p) < 6
  - 'K' indique un jour K calme avec Sum(p) $>= 6$

Le nombre de jours CK24 et CK48 par an est représenté sur la figure 3.1 et n'est pas réparti uniformément car il suit l'activité solaire. Il est à noter que la période commence dès 1868, en raison de la disponibilité à long terme de l'indice *aa*.

Indices du courant annulaire

L'indice de perturbation (Dst) a été introduit par Sugiura (1964) pour surveiller la partie à symétrie axiale du courant annulaire qui induit la dépression de la composante magnétique horizontale du champ magnétique. Il est approuvé par le IAGA et est dérivé des quatre observatoires de la figure 10.8 qui sont suffisamment éloignés des zones EEJ et aurorales, voir la figure 3.4 au milieu du panneau de droite. L'ensemble des données est disponible sur `dx.doi.org/10.17593/14515-74000`. Sa dérivation de base prend en compte le champ principal et les variations du système de courant solaire calme dérivés pendant les cinq jours les plus calmes du mois, les Q-days. Cependant, avec sa résolution temporelle d'une heure, il ne permet pas d'étudier les phénomènes à plus courte durée de vie et les caractéristiques connexes. L'indice SYM-H provisoire avec une résolution temporelle d'une minute est basé sur 6 observatoires, voir la figure 3.4 en bas à droite, avec l'idée de fournir une meilleure description de la partie symétrique du courant annulaire. De la même façon, l'ASY-H est proposé pour suivre la partie asymétrique du courant annulaire. Leur dérivation est décrite dans Iyemori (1990) et dans le rapport technique Iyemori et al. (2010). La ligne de base comprend le champ principal et le champ Sq, comme pour l'indice Dst. Le SYM-H est communément accepté et utilisé comme indice Dst à haute résolution temporelle. Naturellement, certaines différences apparaissent et doivent être gardées à l'esprit, en particulier pour les perturbations les plus fortes (Wanliss & Showalter, 2006). Pour les deux indices, il n'est pas exclu qu'ils contiennent des contributions d'autres systèmes de courant. Comme ils sont moyennés en longitude, ils ne donnent pas non plus d'informations sur les variations locales. Lorsqu'il est utilisé comme indicateur de l'énergie des courants annulaires symétriques, le SYM-H surestime l'apport d'énergie d'un facteur pouvant aller jusqu'à 4 et décale le contenu énergétique maximal de 3 à 9 heures en raison des contributions incluses des courants de queue et de l'activité des sous-orages (Sandhu et al., 2021). Compte tenu de leur importance dans la caractérisation de l'activité des orages, la littérature montre un intérêt croissant pour la prévision des indices Dst et SYM-H, y compris avec des méthodes d'intelligence artificielle, voir par exemple Ji et al. (2012); Lu et al. (2016); Bhaskar and Vichare (2019); Laperre et al. (2020); Siciliano et al. (2021).

Lignes de base géomagnétiques

Qu'il s'agisse de suivre l'intensité d'un système de courant spécifique ou de décrire l'état général du champ géomagnétique, tous les indices ont en commun de caractériser les variations irrégulières correspondantes dans les mesures du champ. Pour ce faire, la contribution de la source d'intérêt doit être isolée dans le signal du champ géomagnétique. En général, on y parvient en supprimant la ligne de base géomagnétique. Cette ligne de base est censée contenir toutes les contributions des sources de champ magnétique stables et calmes et aucune contribution de la source d'intérêt. Ainsi, après suppression, les résidus contiennent uniquement des informations sur la source d'intérêt, par exemple les perturbations. En 1939, Bartels (1939) désignait cette séparation des sources sous le nom de variations K, qui contiennent les sources calmes, et de variations non-K, qui contiennent les contributions des sources perturbatrices - ou irrégulières. Bartels et al. (1939) définit la ligne de base géomagnétique comme suit, traduit en français :

> *"... une courbe lisse (une variation quotidienne régulière) à laquelle on peut s'attendre pour cet élément lors d'une journée magnétiquement calme, en fonction de la saison, du cycle des taches solaires et, dans certains cas, de la phase de la Lune".*

Elle est supposée englober la variation journalière solaire, la variation journalière lunaire et les conséquence de perturbations telles que les phases de rétablissement du courant annulaire. À l'époque, des observateurs qualifiés identifiaient à la main ces courbes calmes sur les magnétogrammes analogiques. Cette définition plutôt subjective a ensuite été concrétisée par un ensemble de 7 règles pratiques par Mayaud (1980) pour soutenir l'objectivité de la détermination de la ligne de base. L'identification des systèmes de courants calmes solaires pour les observatoires à latitude moyenne a été explicitement incluse dans ces règles. Grâce à l'ère spatiale, notre compréhension de l'environnement proche de la Terre et des systèmes de courants associés, ainsi que de leur couplage avec le vent solaire, nous a permis de mieux comprendre les sources contribuant au champ géomagnétique. Aujourd'hui, il est communément admis qu'une ligne de base géomagnétique comprend les variations séculaires, les variations induites par les cycles solaires et les variations solaires calmes. Cependant, à ce jour, il n'existe pas de vérité unique sur la forme des lignes de base géomagnétiques et les lignes directrices générales du passé sont encore largement utilisées pour justifier les dérivations des lignes de base actuelles. Comme nous l'avons brièvement indiqué, chacune des familles d'indices introduites utilise une méthode différente pour la détermination de la ligne de base. Cela implique également que chaque méthode produira des lignes de base différentes, ce qui entraînera des différences dans la dérivation des perturbations (c'est-à-dire les résidus après suppression de la ligne de base spécifique). En fin de compte, il en résulte des différences dans la classification réelle des perturbations, qui doivent être prises en compte lors de l'utilisation des indices. Quelques méthodes de référence fréquemment utilisées sont présentées ci-après.

Dérivation numérique de la ligne de base des indices K

Depuis leur introduction en 1939, les indices K constituent toujours la base de la production d'indices géomagnétiques dérivés K largement utilisés pour les latitudes basses et moyennes. Avec la numérisation croissante, le besoin d'une production plus rapide et assistée par ordinateur des indices K s'est fait sentir et, en réponse directe, une variété d'algorithmes a été introduite. En 1991, lors de la réunion de l'Union Géodésique et Géophysique Internationale (UGGI) à Vienne, les algorithmes disponibles ont été systématiquement étudiés du point de vue de leur précision dans la production des indices K et des lignes de base correspondantes (Menvielle et al., 1995). L'algorithme de Sucksdorff et al. (1991), appelé méthode FMI (abréviation de Finnish Meteorological Institute), a donné des résultats suffisamment bons pour que l'on puisse dériver des indices K numérisés [2]. La ligne de base selon la méthode IGF est basée sur une régression sur une fenêtre glissante centrée sur le jour UT de 24 heures. Pour chaque heure UT avec l'heure de début t_0 et l'heure de fin t_1, la moyenne sur l'intervalle $(t_0 - m, t_1 + n)$ est calculée, avec m et n étant des minutes. Les 24 valeurs résultantes (une par heure) sont ajustées par une courbe harmonique de 5ème ordre qui est la ligne de base.

m est un nombre fixe de minutes, qui dépend de l'heure locale (LT) : de 0 à 3 LT $m = 90$min, de 3 à 6 LT $m = 60$min, de 6 à 18 LT $m = 0$min, de 18 à 21 $m = 60$min et de 21 à 0LT $m = 90$min. n est calculé en deux étapes :

1. Étape 1 : pour chaque intervalle UT de 3 heures (0-3UT, 3-6UT, etc.), le maximum et le minimum des composantes horizontales sont utilisés pour obtenir une valeur K initiale K_{init}. Avec $n_{init} = K_{init}^{3.3}$, les valeurs horaires moyennes pour les intervalles $(t_0 - m, t_1 + n_{init})$ sont ajustées avec une harmonique de 5ème ordre qui donne la ligne de base préliminaire.
2. Étape 2 : la ligne de base préliminaire est ensuite retirée des mesures. Par intervalle de 3 heures, le maximum et le minimum des résidus sont utilisés pour déterminer l'indice K préliminaire K_{prelim}. La valeur finale n utilisée pour la longueur réelle de l'intervalle de dérivation de la ligne de base K est définie comme $n = K_{prelim}^{3,3}$.

Pour mettre en œuvre cette méthode, il faut disposer des mesures de l'ensemble de la journée UT. Pour chaque bloc de 3 heures (00:00-03:00, 03:00-06:00, etc.), la variation entre le maximum et le minimum des deux valeurs horizontales du champ B est comparée au tableau suivant pour obtenir un indice K initial n. Pour chaque heure de la journée, les valeurs horizontales moyennes pour cette heure +/- (n + m) minutes sont calculées, où n est l'indice K initial, et m une constante qui dépend de l'heure de la journée. Ensemble, ces points donnent une estimation approximative de la variation du courant calme solaire. Cette estimation approximative de la variation du courant calme solaire est ensuite lissée, puis retirée des données brutes. Les étapes 3 à 5 sont ensuite répétées en utilisant l'indice K secondaire pour calculer le troisième et dernier indice K. Ce dernier indice K est celui qui est utilisé pour calculer les données finales et qui est affiché sur la page web à l'adresse suivante : `https://www.magie.ie/fmi-method/`.

---

[2] Le script informatique en C est disponible à l'adresse `https://space.fmi.fi/MAGN/K-index/FMI_method/K_index.h`

Dérivation de la ligne de base de l'indice Dst

La ligne de base de l'indice Dst final est dérivée de la composante H de quatre observatoires de basse latitude qui sont suffisamment éloignés des électrojets auroraux et équatoriaux pour minimiser leur influence. La dérivation est détaillée dans Sugiura, M., et T. Kamei (1991). Elle tient compte de la variation séculaire $H_{secular}$ et de la variation de l'indice Sq H_{sq}. Les deux valeurs sont basées sur les variations correspondantes des cinq jours les plus calmes de chaque mois, les Q-days.

$H_{secular}$ est estimé par ajustement des moindres carrés des valeurs moyennes annuelles de tous les jours Q, pendant l'époque τ qui comprend également les quatre dernières années comme suit :

$$H_{secular}(\tau) = A + B\tau + C\tau^2 \,. \tag{10.4}$$

Pour chaque mois, une moyenne Sq est calculée sur la base des 5 jours Q par mois. Pour une année, cet ensemble de 12 moyennes Sq est développé dans une double série de Fourier en tenant compte de l'heure locale LT et du mois M, comme suit :

$$H_{sq}(\mathrm{LT}, \mathrm{M}) = \sum_j \sum_k A_{jk} \cos\left(j\mathrm{LT} + \alpha_j\right) \cos\left(k\mathrm{M} + \beta_k\right) \,. \tag{10.5}$$

Par conséquent, pour calculer l'indice Dst final au pas de temps t, les mesures des 4 années précédentes t doivent être disponibles. Cela entraîne des retards importants dans la production des Dst. Le Centre Mondial de Données pour le Géomagnétisme de Kyoto fournit des valeurs Dst provisoires et en temps réel (quicklook). Il faut garder à l'esprit que ces valeurs sont dérivées de données brutes non vérifiées et qu'elles peuvent donc contenir des inexactitudes.

Détermination de la ligne de base pour les indices PC

Janzhura and Troshichev (2008) a introduit une méthode automatique pour la détermination de la ligne de base pour les deux stations de la calotte polaire utilisées pour les indices PC. Ils utilisent les données des jours calmes pour générer une variation statistique des jours calmes H_q qui est basée sur une fenêtre de 30 jours. Par heure UT, 120 échantillons de minutes calmes sont identifiés à partir de la fenêtre courante et la moyenne de ces minutes représente H_q. Les échantillons calmes sont déterminés par deux critères :

1. $dB/dt < \gamma$ pour chaque intervalle de 20 minutes
2. $|B(dt) - \overline{B(dt)}| < \beta$ pour la moyenne des 20 minutes $B(dt)$ et la moyenne des intervalles de 20 minutes $\overline{B(dt)}$ au cours des 3 heures précédentes.

La détermination des seuils γ et β dépend du nombre de points disponibles pour déterminer H_q. En commençant par $\gamma = 2\,\mathrm{nT/min}$ et $\beta = 2\,\mathrm{nT}$, γ et β sont augmentés de manière itérative jusqu'à ce que 120 échantillons calmes soient trouvés. La moyenne finale est pondérée en fonction du nombre d'itérations nécessaires pour atteindre le seuil de 120 échantillons. Cette moyenne est utilisée comme référence pour les jours à partir desquels elle est générée. Pour les autres jours, donc perturbés, la ligne de base des jours calmes identifiés est interpolée. Cette approche permet de projeter la ligne de base jusqu'à 20 jours à l'avance en extrapolant H_q en amplitude. La phase est considérée comme constante, car aucun changement de phase important n'a été constaté dans leurs observations. Par conséquent, la méthode PC peut être utilisée comme méthode courante pour fournir des lignes de base en temps quasi-réel pour les deux stations de la calotte polaire.

Méthode IMAGE

Van De Kamp (2013) a introduit une dérivation de la ligne de base pour les observatoires qui font partie de l'International Monitor for Auroral Geomagnetic Effects (IMAGE) en Scandinavie dans le but d'étudier les courants ionosphériques des hautes latitudes, en particulier les électrojets auroraux. Le réseau comprend un total de 32 magnétomètres dont les latitudes géographiques s'étendent de 58° à 79° et qui fournissent des données avec une résolution de 10 secondes. Cette base ne comprend pas seulement la tendance à long terme et les variations diurnes, mais aussi les discontinuités dans les mesures des magnétomètres. Lorsque les données magnétométriques ne proviennent pas d'instruments stables et bien contrôlés, des discontinuités artificielles occasionnelles peuvent se produire et affecter la ligne de base. Dans la première étape de la méthode IMAGE, les sauts identifiés automatiquement sont examinés et supprimés manuellement en conséquence. La tendance à long terme et les variations quotidiennes sont basées sur les jours calmes et perturbés identifiés. La première étape de la méthode IMAGE consiste à surmonter ce problème en présentant à l'utilisateur une liste de sauts potentiels et en lui permettant de décider si un saut est artificiel. La ligne de base des sauts ainsi générée est ensuite soustraite des données du magnétomètre. Pour identifier les jours calmes, chaque heure UT est ajustée par une ligne droite qui est retirée des mesures. L'écart-type σ est calculé à partir de ces résidus. Le maximum σ_{max} de tous les σ horaires est utilisé pour décrire le niveau de perturbation pour le jour UT correspondant. Le jour où le σ_{max} est le plus petit est considéré comme le jour le plus calme du mois. Pour garantir un calme réel, le σ_{max} le plus petit doit en outre être inférieur à un seuil identifié de manière empirique. Le seuil optimal est dérivé par inspection visuelle de la station Abisko (ABK), près de Kiruna en Suède, puis ajusté empiriquement pour d'autres stations par rapport à ABK. La ligne de base diurne pour un jour calme est constituée des 7 harmoniques les plus basses de la transformée de Fourier rapide (FFT) appliquée aux données du jour calme. Pour les jours non calmes, les courbes des jours calmes adjacents sont interpolées. Cette méthode peut également être appliquée lorsqu'il n'y a pas de jour calme au cours d'un mois ou pour des périodes plus longues. La ligne de base à long terme est la simple médiane du jour UT si le jour n'est pas perturbé. La catégorisation des jours perturbés se fait de manière analogue à la détermination des jours calmes : σ_{max} doit être supérieur à un seuil empirique. Dans ce cas, la tendance à long terme pour le jour UT est interpolée à partir des jours adjacents non perturbés. Les écarts types horaires déterminent également si les variations à long terme déterminées peuvent être utilisées ou si elles doivent être interpolées. Les variations calmes sont déterminées en utilisant les 7 harmoniques les plus basses extraites avec la FFT sur les jours calmes et sont interpolées pour générer la ligne de base diurne. La ligne de base complète est alors la superposition des lignes de base à long terme et diurne. La ligne de base est dérivée pour chaque station et chaque composante séparément, et donc chacune des étapes manuelles énumérées ci-dessus (vérification des sauts, détermination des seuils) doit être effectuée pour chaque station et chaque composante. La détermination de la ligne de base prend donc beaucoup de temps et n'est applicable que pour l'intervalle de temps considéré. Elle n'est donc pas applicable aux applications en temps réel. Cependant, en supprimant le saut de ligne de base, la méthode IMAGE permet d'accéder à des données provenant d'équipements éloignés et donc plus difficiles à entretenir, ce qui est une situation courante aux latitudes aurorales. Cela permet d'améliorer la distribution spatiale des mesures pour les études de météorologie de l'espace.

Méthode SuperMAG

Gjerloev (2012) a présenté une méthode de dérivation de la ligne de base utilisée pour les indices SuperMAG. La toute première étape de cette méthode consiste à faire pivoter les mesures du magnétomètre dans un système de coordonnées magnétiques local spécifique. L'angle de rotation est déterminé par un angle de déclinaison arbitrairement défini en fonction du temps et basé sur les composantes horizontales du champ, lissées sur 17 jours. La méthode définit une valeur typique comme le mode, c'est-à-dire la valeur la plus fréquente, sur une certaine période de temps.

La tendance à long terme et les variations diurnes sont incluses dans la ligne de base. Pour les variations diurnes, le mode (c'est-à-dire la valeur ayant le taux d'occurrence le plus élevé) pour chaque jour est retiré des mesures. Pour chaque intervalle de 30 minutes, le mode des résidus du jour en question, ainsi que des jours précédents et suivants, est déterminé. Le nombre de jours entourant le jour en question dépend des fluctuations des composantes X, Y, Z et de la latitude magnétique du magnétomètre utilisé. Une méthode d'interpolation par convolution cubique est appliquée aux valeurs pondérées du mode semi-horaire pour obtenir les variations diurnes. Les poids dépendent du nombre de jours utilisés. Pour la tendance annuelle, le mode des 17 derniers jours est généré pour chaque jour. Une procédure de lissage pondéré est ensuite appliquée à la série de modes pour déterminer la tendance à long terme. La procédure de lissage pondéré dépend des fluctuations des mesures instantanées et des huit jours précédents et diffère pour chacune des composantes. Enfin, à partir des résidus (différence entre les mesures et les variations diurnes et la tendance annuelle), un offset spécifique à la station est déterminé. Ce décalage est dérivé comme le mode des résidus pendant les jours Q et montre des dépendances claires avec la latitude magnétique.

La ligne de base finale de SuperMAG est composée des variations diurnes, de la tendance annuelle et du décalage résiduel. Pour la méthode SuperMAG, aucune étape manuelle n'est nécessaire. Cependant, comme elle nécessite des informations sur les jours environnants, elle ne peut pas être appliquée en temps réel, et on ne sait pas non plus combien de jours suivants sont nécessaires pour produire le mode pour l'intervalle de 30 minutes. En outre, la connaissance des coordonnées magnétiques des mesures est une condition préalable.

Motivation pour cette Thèse

Chacune des méthodes de base présentées ci-dessus est activement utilisée et présente ses propres avantages et inconvénients. Compte tenu de la définition assez floue de ce qu'est une ligne de base géomagnétique, il n'est pas trivial de quantifier les différentes lignes de base et de dire si l'une est plus correcte que l'autre. L'une des justifications d'une ligne de base est donnée par Van De Kamp (2013) qui compare la méthode IMAGE à la méthode SuperMAG et soutient que les deux sont très similaires et peuvent donc être employées l'une et l'autre. Le consensus commun qui semble s'être établi au cours des dernières années est cependant qu'une ligne de base est constituée des sources calmes qui constituent la tendance à long terme et de certaines variations diurnes typiques. Cette approche est explicitement suivie par les méthodes Dst, IMAGE et SuperMAG. Bien que chacune d'entre elles motive sa propre méthode de dérivation pour contenir les sources calmes, les études détaillées des sources réellement contenues sont largement absentes. Gjerloev (2012) et Van De Kamp (2013) montrent les spectres de la ligne de base et soutiennent que les harmoniques de 24 heures sont suffisamment représentées et incluent donc les variations calmes diurnes. De nombreuses méthodes utilisent en fait une sorte de moyenne statistique pour décrire les variations calmes. Dans le cas des méthodes appliquées aux latitudes moyennes, cela conduit à une moyenne des empreintes du courant Sq, en négligeant totalement sa variabilité D2D intrinsèque. Un défi commun à toutes les méthodes est l'identification des mesures des variations calmes qui sont utilisées comme approximations de la ligne de base. L'utilisation des jours Q officiels dérivés des indices K décrits dans le chapitre 3.1.1.2 ou de tout autre jour calme UT choisi arbitrairement s'accompagne d'une série de limitations et de mises en garde qui ont été largement discutées dans Mayaud (1980); Joselyn (1989); Menvielle et al. (1995); Janzhura and Troshichev (2008); Gjerloev (2012); Van De Kamp (2013), par exemple. En voici quelques-unes :

- Les perturbations peuvent être localement et temporellement confinées, de sorte qu'elles ne sont pas prises en compte lors de l'examen de la journée UT.
- Les jours calmes qui sont basés sur des indices qui nécessitent une sorte de critère de calme sont basés sur un raisonnement causal circulaire
- L'utilisation de la moyenne d'un nombre quelconque de jours UT calmes dans une certaine fourchette afin de dériver des propriétés statistiques des variations calmes est arbitraire.

Ainsi, les méthodes qui utilisent et produisent des lignes de base par jour UT, telles que les méthodes K-, Dst et PC, peuvent ne pas être en mesure de décrire avec précision les influences des perturbations. Ł'idée d'une dérivation informatisée des lignes de base pour les indices K est née de la nécessité de les fournir le plus rapidement possible et de manière automatique, sans intervention manuelle. Il est certain que pour toute application en temps quasi-réel, cette exigence doit également être respectée. Cela implique que l'utilisation de mesures futures ou de paramètres d'entrée supplémentaires tels que les positions magnétiques ne peut pas être incorporée dans la dérivation de la ligne de base, comme c'est le cas pour les méthodes K, Dst et SuperMAG. Toute intervention manuelle nécessaire pour les étapes de dérivation de la ligne de base, comme l'élimination des valeurs aberrantes ou la dérivation des seuils, n'est pas non plus adaptée aux applications en temps réel. Le but ultime de ce travail est de présenter une ligne de base qui contient les sources du champ géomagnétique calme et dont la mise en œuvre est entièrement automatisée et peut donc être utilisée en temps quasi réel, en surmontant les lacunes mentionnées. Pour une telle dérivation de la ligne de base, les chapitres suivants :

1. décrivent la dérivation automatique de la ligne de base pendant les périodes calmes
2. étudient et analysent les sources associées qui contribuent à la ligne de base calme
3. introduisent un algorithme pour déduire les variations calmes pendant les périodes perturbées pour la ligne de base.
4. étudient le déploiement de l'intelligence artificielle pour la dérivation de la ligne de base.

Conclusion et Perspective (FR)

Conclusion finale et perspectives pour les travaux futurs

Au tout début de cette thèse, j'ai formulé deux questions de recherche que j'ai motivées et auxquelles j'ai essayé de répondre tout au long de cette thèse. Dans ce qui suit, je résume les réponses trouvées.

1. La ligne de base dérivée reflète-t-elle les variations calmes du champ géomagnétique ?

Les indices magnétiques condensent les informations sur le champ géomagnétique en quelques valeurs qui visent à décrire l'état complexe du système Terre sous l'effet de la météorologie de l'espace (chapitres 2 et 3). La réaction du champ géomagnétique aux phénomènes météorologiques spatiaux est un indicateur important de leur gravité. Le champ géomagnétique étant une superposition de sources, les signatures des orages doivent être extraites des autres variations calmes. Cette séparation de sources est réalisée par des lignes de base géomagnétiques, qui décrivent les variations calmes et constituent la base des indices magnétiques. Il existe plusieurs méthodes de lignes de base, mais elles ne sont pas applicables aux applications en temps (quasi) réel (chapitre 3.2). En outre, si les étapes de la dérivation de la ligne de base pour la plupart des méthodes sont bien décrites, l'identification des sources incluses fait largement défaut.

Dans le chapitre 4, je présente une méthodologie pour extraire les variations calmes du champ géomagnétique de manière automatique et efficace en utilisant des filtres temporels avec des caractéristiques de fréquence appropriées. Dans le chapitre 5, les réponses des filtres qui en résultent sont analysées en détail en ce qui concerne la contribution des sources du champ géomagnétique et l'identification des sources calmes. Trois modèles analytiques sont proposés pour décrire les variations observées. Grâce à des discussions détaillées et à une analyse physique, j'ai conclu que la méthode de filtrage est appropriée pour capturer les sources calmes du champ géomagnétique. Je me réfère à cette ligne de base préliminaire comme la ligne de base du filtre.

À ce stade, la réponse à la première question de recherche a été présentée. L'analyse approfondie et l'interprétation physique de la ligne de base du filtre ont montré qu'elle est capable d'extraire et de décrire automatiquement les sources qui contribuent au champ géomagnétique calme aux latitudes moyennes, les principales étant la variation séculaire et les systèmes de courants solaires calmes. Un résultat important de l'analyse est que la ligne de base du filtre est capable de capturer la variabilité journalière intrinsèque des systèmes de courant Sq, ce qui n'est pas le cas de la majorité des méthodes de ligne de base existantes. En outre, les modèles dérivés et l'étude de la variabilité journalière améliorent notre compréhension de la climatologie des systèmes de courants solaires calmes.

Cependant, la ligne de base du filtre n'est que préliminaire, car les filtres temporels contiennent des contributions de perturbations pendant les périodes non calmes, comme indiqué au chapitre 5.3. L'utilisation directe de la ligne de base du filtre conduirait donc à une sous-estimation des perturbations dans les résidus. Je traite cette question au chapitre 6. La solution comprend deux étapes : l'étape 1 identifie les périodes pendant lesquelles une perturbation est sous-estimée et à l'étape 2, je déduis les variations calmes possibles pendant la période de perturbation identifiée. La ligne de base initiale du filtre est adaptée pendant les périodes de perturbation pour aboutir à la proposition de plusieurs lignes de base finales. Dans le chapitre 6.4, je compare les résultats de la méthode de base introduite avec ceux des méthodes existantes.

La principale conclusion que je peux tirer de ce travail est que la ligne de base introduite peut être utilisée pour la dérivation d'indices magnétiques spécifiques, car elle décrit de manière satisfaisante les variations du champ géomagnétique calme. En outre, la dérivation de la ligne de base proposée ne repose pas sur d'autres paramètres d'entrée que les mesures du champ magnétique elles-mêmes et peut donc être utilisée dans des applications en temps quasi6réel. Néanmoins, il reste plusieurs aspects qui pourraient être intéressants pour des travaux futurs :

1. **Applications en temps réel.**
   La méthode de filtrage est basée sur une fenêtre centrée sur trois jours et la ligne de base finale ne sera donc disponible qu'avec un délai d'un jour et demi. Dans un contexte opérationnel, cela conduit à deux produits : 1) la ligne de base rapide, qui est basée sur le filtrage des trois jours précédents ou qui prend en compte une sorte de propagation vers l'avant des valeurs de filtrage et 2) la ligne de base finale qui est disponible après un jour et demi. Des études quantifiant les différences entre l'aperçu rapide et le niveau de référence final confirmeraient l'applicabilité d'une telle approche.

2. **Séparation des sources dans les mesures du champ géomagnétique.**
   Pour décrire et comprendre le champ géomagnétique, on utilise des modèles très complexes qui tiennent compte d'une multitude de mesures du champ magnétique effectuées tout autour du globe, y compris des données satellitaires. Ces modèles sont très efficaces pour la séparation des sources et la détermination des différentes contributions, mais ils ne peuvent pas être déployés en temps quasi-réel en raison de leur complexité. Bien que la méthode de filtrage permette d'extraire suffisamment bien les sources calmes, elle n'est pas en mesure d'effectuer une séparation complète des sources. Avec la disponibilité croissante de flux de données fiables provenant de plusieurs observatoires, il pourrait être possible d'améliorer la méthode de filtrage avec une composante spatiale, par exemple en comparant le signal entre des stations voisines afin d'améliorer la séparation des sources en temps quasi-réel.

3. **Détection des perturbations.**
   La détection des perturbations introduite bénéficierait également d'une composante spatiale. Cela permettrait d'identifier et de propager les événements perturbateurs ou de permettre la détection d'anomalies locales. En outre, d'autres paramètres permettraient d'identifier les périodes complètes pendant lesquelles la ligne de base du filtre doit être remplacée, par exemple pour inclure entièrement les débuts d'événements. En tout état de cause, la détection des perturbations introduite peut être exploitée pour d'autres applications nécessitant l'identification automatique des signatures des orages et des perturbations.

4. **L'influence de l'atmosphère neutre.**
   Il est bien connu, et nous l'avons également constaté lors de l'élaboration des modèles, que l'atmosphère neutre joue un rôle important dans la variabilité quotidienne

des systèmes de courants calmes solaires, car elle influence directement la région dynamo par le biais des marées et des vents. Plusieurs efforts de modélisation très sophistiqués sont activement poursuivis pour décrire l'atmosphère neutre et pour mieux comprendre la dynamo ionosphérique, ce qui permettrait de mieux décrire les variations quotidiennes et le moteur des systèmes de courants solaires calmes. Des paramètres supplémentaires décrivant et caractérisant les vents et les marées dans l'atmosphère neutre peuvent également être exploités pour améliorer la description de base et le remplacement. Une première étape utile consisterait à étudier la densité, la température et les vents thermosphériques à l'emplacement des observatoires magnétiques. Une telle approche peut être réalisée en équipant les observatoires d'instruments appropriés tels que l'interféromètre de Fabry-Perot.

5. **L'implication de la communauté.**
   Comme mentionné tout au long de cette thèse, l'identification de la ligne de base n'a pas de vérité absolue (du moins au moment de ce travail). À l'avenir, des modèles de champ géomagnétique sophistiqués et les progrès de la recherche liés aux relations Soleil-Terre et aux variations du champ géomagnétique pourront aider à identifier une ligne de base idéale. D'ici là, il est important d'impliquer la communauté, y compris les utilisateurs intéressés par la ligne de base (et les indices dérivés) au cours du processus de dérivation de la ligne de base. Il convient de discuter et d'introduire ensemble des critères réalisables et mesurables pour les niveaux de référence et les procédures connexes de test des niveaux de référence.

6. **Dérivation des indices magnétiques.**
   Les options de base présentées peuvent être utilisées pour la dérivation des indices géomagnétiques. Ces indices ne sont pas limités dans leur dérivation en temps réel lorsqu'on utilise la ligne de base introduite. D'autres études devraient être menées pour démontrer le comportement et les caractéristiques des lignes de base, ainsi que pour décrire les sources contenues dans les observatoires géomagnétiques supplémentaires dans différentes gammes longitudinales et latitudinales. Une telle étude peut également aider les utilisateurs à choisir la ligne de base idéale pour leur application spécifique et mettre en lumière les avantages et les inconvénients qu'il faut garder à l'esprit. Ces aspects sont idéalement discutés avec la communauté spécifique (par exemple, la modélisation du champ interne bénéficierait de propriétés différentes de celles des prévisions de météorologie de l'espace).

2. Dans quelle mesure l'IA peut-elle contribuer à la détermination de la ligne de base par rapport aux méthodes traditionnelles ?

Cette thèse est principalement axée sur la détermination de la ligne de base à l'aide de méthodes traditionnelles. Cependant, dans la deuxième partie, j'ai exploré des méthodologies d'apprentissage automatique et d'apprentissage profond bien établies pour déterminer les variations calmes, avec un succès limité. Comme c'est souvent le cas, le réseau de neurones a eu du mal à décrire les variations de la composante X, alors que la composante Y a été assez bien décrite. Bien que limitée, la substitution de la ligne de base par le modèle LSTM préliminaire est un début prometteur et les résultats ouvrent la voie à des améliorations futures qui offrent une variété de possibilités :

1. **Un modèle par composante.**
   Comme X est beaucoup plus compliqué que Y, il convient d'utiliser un modèle par composante, l'un plus complexe et l'autre plus simple. En outre, un modèle pour la troisième composante Z, qui n'a pas été prise en compte dans ce travail, pourrait permettre de cartographier les effets de l'induction.

2. **Comprendre la boîte noire.**
   Une fois qu'un modèle approprié a été trouvé pour les perturbations au sol ou les variations calmes, il convient de déployer des méthodologies d'importance des caractéristiques basées sur le type de modèle. D'autres paramètres décrivant l'atmosphère neutre devraient être pris en compte dans ces modèles. Cela nous permettra de mieux comprendre les principaux moteurs des résultats et donc des variations diurnes.

3. **Détection des perturbations.**
   Le chapitre 6 est consacré à l'identification des intervalles de perturbation. Il serait intéressant de savoir dans quelle mesure l'apprentissage automatique est capable d'identifier de tels intervalles. Dans un premier temps, un modèle supervisé peut être utilisé pour reproduire la méthodologie déployée dans cette thèse, qui peut ensuite être améliorée. Une autre possibilité serait de déployer des méthodes non supervisées pour lesquelles l'ordinateur dériverait ses propres classifications des perturbations.

4. **Capacités actuelles et prévisionnelles.**
   Les résultats de cette thèse motivent la génération de lignes de base (analytiques ou IA) pour un certain nombre d'observatoires dans un délai très court, car cela est possible dès que les mesures du champ magnétique sont disponibles. Comme un nombre croissant d'observatoires fournit des données de haute qualité en temps quasi-réel, la projection de l'état du champ géomagnétique devient de plus en plus possible et précise. En ajoutant les données sur le vent solaire, des modèles d'IA sophistiqués peuvent être dérivés et exploités pour améliorer les capacités de prévision.

Au final, cette thèse introduit une nouvelle dérivation de la ligne de base pour des applications en temps quasi-réel dont les résultats sont largement discutés et présentés. Pour la première fois, l'application de l'IA pour la dérivation de la ligne de base a été déployée et a donné des résultats prometteurs. Néanmoins, cette thèse soulève plus de questions qu'elle n'en résout. Chacune des perspectives énumérées ci-dessus mériterait à elle seule une étude doctorale pour laquelle j'espère que le présent travail pourra être utile. En particulier, les travaux futurs qui dérivent de nouvelles familles d'indices magnétiques à l'aide des concepts de base introduits, constituent une partie passionnante à laquelle je serais heureuse de contribuer. L'application de l'IA donne des résultats prometteurs et je suis impatiente de voir d'autres applications, en particulier dans le cadre de la dérivation de la ligne de base ou du calcul des indices magnétiques. Avec cette thèse, je suis fière d'avoir contribué à améliorer la compréhension de la météorologie de l'espace.

Acronyms

R_E	Earth-radii
AARI	Arctic and Antarctic Research Institute
AI	Artificial Intelligence
ANN	Artificial Neural Network
CNN	Convolutional Neural Network
D2D	day-to-day
DL	Deep Learning
DTU Space	National Space Institute at the Technical University of Denmark
EEJ	Equatorial Electrojet
EOST	École et Observatoire des Sciences de la Terre
ESA	European Space Agency
GIC	geomagnetically induced currents
GRU	Gated Recurrent Unit
IAGA	International Association of Geomagnetism and Aeronomy
ICME	Interplanetary Coronal Mass Ejection
INTERMAGNET	Real-time Magnetic Observatory Network
IPIM	IRAP plasmasphere-ionosphere model
ISGI	International Service of Geomagnetic Indices
IUGG	International Union of Geodesy and Geophysics
K9LL	K9 lower limit
KB	kilobyte
LSTM	Long-Short Term Memory
MAE	mean absolute error
MHD	Magnetohydrodynamics
ML	Machine Learning
MLP	Multilayer Perceptron
MSE	mean square error
NN	Neural Network

RMSE	Root Mean Square Error
RNN	Recurrent Neural Networks
SC	Solar Cycle
SEA	superposed epoch analysis
Sq	Solar Quiet
SSC	Storm Sudden Commencement

Acknowledgments

The work conducted during and the writing of this PhD thesis was not done in solitude, as is the case for any successful activity. An extensive list of favourable conditions allowed me to contribute to space weather research with the present work. I hereby would like to give a non-exhaustive list of the conditions and people I owe my deep gratitude to.

This work would not have been possible without the availability of geomagnetic field measurements. First and foremost, I would like to hereby express my sincere gratitude and respect for all the people and institutes involved in maintaining magnetic observatory operations around the globe and providing access to high-quality geomagnetic field data.

I would like to acknowledge INTERMAGNET for promoting high standards of magnetic observatory practices and providing access to the data (doi.org/10.17616/R3XK82). I would like to acknowledge ISGI for the elaboration and dissemination of geomagnetic indices (doi.org/10.17616/R3WS49). Additionally, I would like to thank all the people and entities that generate and provide access to model data and space data including the WDC SILSO (doi.org/10.17616/R38322), the NASA/GSFC's Space Physics Data Facility's OMNIWeb service (doi.org/10.17616/R3TH0D), the NOAA National Centers for Environmental Information (doi.org/10.17616/R3362J) and the LASP Interactive Solar Irradiance Datacenter (LISIRD, lasp.colorado.edu/lisird/).

I would like to thank the providers of magnetic indices for the easy accessibility of their data:

- All the observatories who provide their K index
- Kp index: doi.org/10.5880/Kp.0001
- *am*, *an*, *as* indices: doi.org/10.25577/et43-6h78
- $a\sigma$ indices: isgi.unistra.fr/indices_asigma.php
- *aa* index: doi:10.25577/9z05-v751
- Hpo indices: doi.org/10.5880/Hpo.0002
- AE indices: dx.doi.org/10.17593/15031-54800
- PCN index: doi.org/10.11581/DTU:00000057
- Dst index: dx.doi.org/10.17593/14515-74000
- SYM-H index: https://wdc.kugi.kyoto-u.ac.jp/wdc/Sec3.html
- SuperMAG indices: supermag.jhuapl.edu/indices

Most importantly I would like to express my gratitude to my supervisors Aurélie Marchaudon and Aude Chambodut for giving me the possibility to conduct this work. I would like to especially thank them for their constant guidance, motivation and understanding they offered me throughout the whole PhD. I would also like to thank my inofficial shadow-supervisor Pierre-Louis Blelly for his teaching and constant support. Without you three this PhD would not have been as prosperous. I would like to thank interesting office mates including Rungployphan Kieokaew, Thomas Simon, Mathias Rojo, Sandra Wiersma, Julian Eisenbeis, Florent Castellani and many more for their continuos assistance, making my every-day at the lab and in Toulouse a little brighter. I would also like to thank my PhD defense jury for their relevant and interesting questions and discussions.

Last but not least, I would like to thank my family and friends for their constant support. I consider myself extremely lucky to have you folks around me and I hope you are aware of how much I appreciate every single of you.

Part V

Appendix

Appendix A

Magnetic Observatories

The magnetic data used for this thesis comes from magnetic observatories which are members of the INTERMAGNET network during the period of 1991 to 2019. Table A.1 provides a list of these stations with their magnetic latitude θ and longitude ϕ (in eccentric dipole coordinates, taken at the 30th June of the first year of membership) and the years in which they delivered data together with their geographic coordinates and the responsible institute. Figure 4.1 visualises the geographic distribution of these magnetic observatories. Observatories in blue are located in the northern hemisphere within the sub-auroral range of $\theta \in [20°, 60°]$, observatories in red in the southern hemisphere within $\theta \in [-60°, -20°]$, grey corresponds to stations outside of the studied region of low and mid-latitudes.

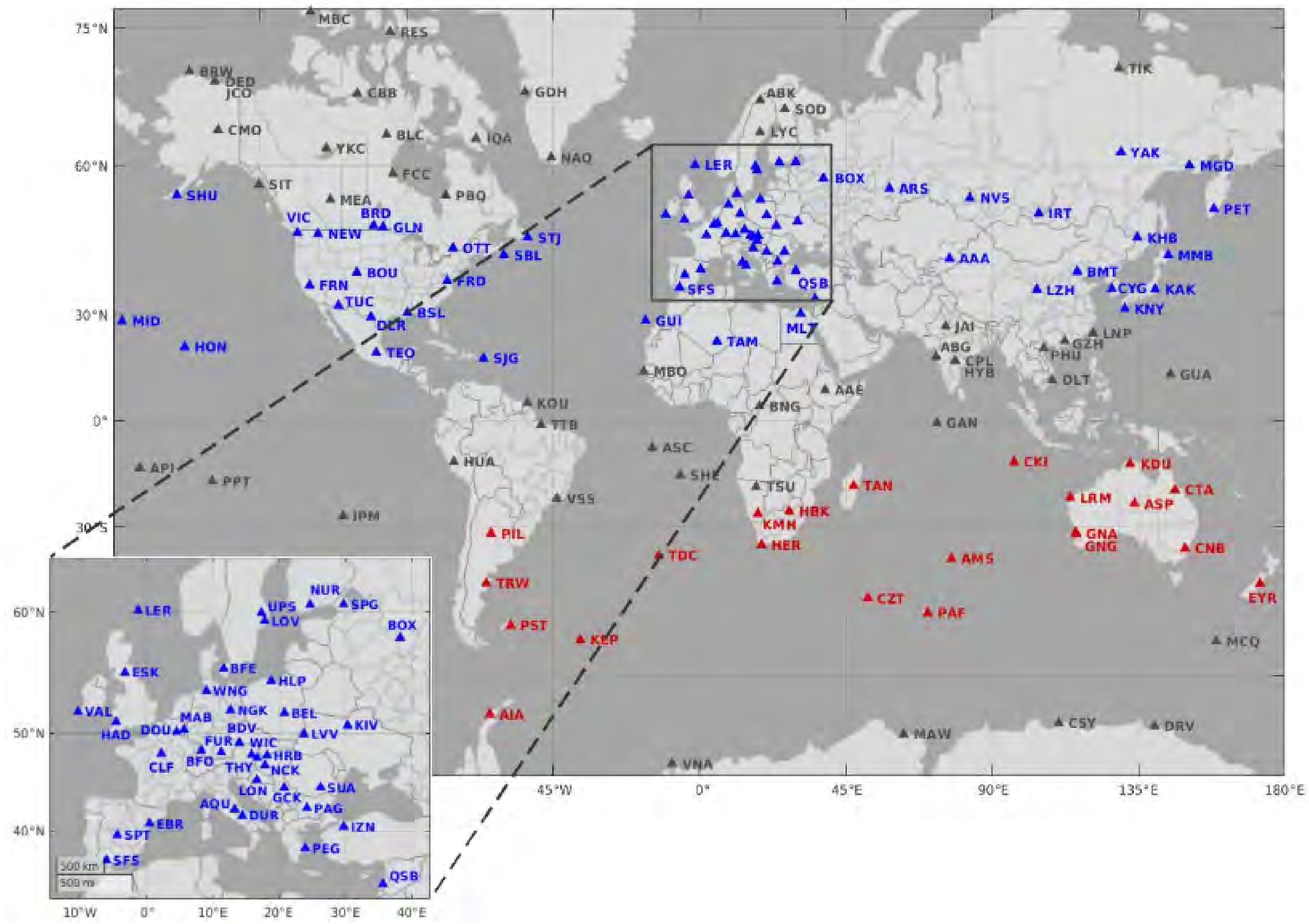

Figure A.1: The same geographic map as figure 4.1 enlarged showing INTERMAGNET stations which delivered data for at least one year between 1991 - 2019. Blue and red corresponds to stations with absolute magnetic ED latitude between 20° and 60° in the northern (blue) and southern (red) hemispheres, respectively. Grey corresponds to stations outside of these boundaries, i.e. equatorial and polar regions.

Table A.1: List of magnetic observatories (OBS) from the INTERMAGNET network during 1991 - 2019, together with the geographic latitude (LAT) and longitude (LON), the magnetic ED latitude θ and longitude ϕ (computed on the 30th June of the station's first year in period), the period of INTERMAGNET membership and the responsible institute. Blue and red corresponds to stations with absolute magnetic ED latitude between 20° and 60° in the northern hemisphere (blue) and the southern hemisphere (red), while black indicates stations outside of these boundaries, i.e. equatorial and polar regions.

OBS	LAT	LON	θ	ϕ	Period	Responsible Institute
AAA	**43.18**	**76.95**	**34.41**	**147.51**	**2005 - 2015**	**Institute of the Ionosphere Republic of Kazak**
AAE	9.02	38.77	4.05	106.95	1998-1999, 2001-2013	University of Addis Ababa
ABG	18.62	72.87	9.02	141.37	1997 - 2019	Indian Institute of Geomagnetism
ABK	68.36	18.82	64.38	104.35	1994 - 2018	Geological Survey of Sweden
AIA	**-65.25**	**295.73**	**-52.09**	**8.69**	**2004 - 2017**	**Lviv Centre of Institute of Space Research**
ALE	82.5	297.6	86.19	82.33	1992, 1995-1997, 2002	Geological Survey of Canada
AMS	**-37.8**	**77.57**	**-48.22**	**136.78**	**1991-2009, 2012-2013**	**Ecole et Observatoire des Sciences de la Terre**
API	-13.81	188.23	-17.24	-93.57	1999 - 2018	Department of Agriculture, Forestry, Fisherie
AQU	**42.38**	**13.32**	**39.87**	**89.03**	**2000 - 2009**	**Instituto Nazionale di Geofisica**
ARS	**56.43**	**58.57**	**49.58**	**132.57**	**2014-2015, 2018**	**Ural Branch Russian Academy of Sciences**
ASC	-8	345.6	-3.18	54.64	2003 - 2018	British Geological Survey
ASP	**-23.76**	**133.88**	**-36.7**	**-152.51**	**1999 - 2019**	**Geoscience Australia**
BDV	**49.08**	**14.02**	**46.28**	**91.68**	**1994 - 2018**	**Academy of Sciences of the Czech Republic**
BEL	**51.84**	**20.8**	**48.07**	**98.69**	**1993 - 2018**	**Polish Academy of Sciences**
BFE	**55.63**	**11.67**	**52.96**	**91.8**	**1991 - 2008**	**Danish Meteorological Institute**
BFO	**48.33**	**8.33**	**46.18**	**85.69**	**2006-2011, 2014-2018**	**Black Forest Observatory**
BLC	64.3	264	71.34	-25.85	1991 - 2017	Geological Survey of Canada
BMT	**40.3**	**116.2**	**30.88**	**-175.8**	**1998 - 2019**	**Chinese Academy of Sciences**
BNG	4.33	18.57	3.1	86.97	1993-2003, 2005-2007, 2010	Institut de Physique du Globe de Paris
BOU	**40.1**	**254.8**	**46.79**	**-34.01**	**1991 - 2018**	**United States Geological Survey**
BOX	**58.07**	**38.23**	**52.4**	**115.4**	**2004 - 2019**	**Russian Academy of Sciences**
BRD	**49.87**	**260.03**	**55.25**	**-26.43**	**2014 - 2018**	**Geological Survey of Canada**
BRW	71.3	203.4	72.45	-107.27	1991 - 2019	United States Geological Survey
BSL	**30.4**	**270.4**	**37.94**	**-16.4**	**1991-2005, 2007-2018**	**United States Geological Survey**
CBB	69.1	255	75.86	-40.19	1991-2012, 2014-2017	Geological Survey of Canada
CKI	**-12.19**	**96.83**	**-24.39**	**164.93**	**2013 - 2018**	**Geoscience Australia**

OBS	LAT	LON	θ	ϕ	Period	Responsible Institute
CLF	**48.02**	**2.27**	**46.95**	**80.52**	**1991 - 2019**	**Institut de Physique du Globe de Paris**
CMO	64.9	212.2	67.38	-91.02	1991 - 2018	United States Geological Survey
CNB	**-35.32**	**149.36**	**-46.92**	**-131.83**	**1991 - 2018**	**Geoscience Australia**
CPL	17.29	78.92	7.72	148.11	2015 - 2019	Indian Institute of Geomagnetism
CSY	-66.28	110.53	-80.48	171.74	2010 - 2019	Geoscience Australia
CTA	**-20.09**	**146.26**	**-31.45**	**-138.31**	**2000 - 2019**	**Geoscience Australia**
CYG	**36.37**	**126.85**	**28.15**	**-163.78**	**2014 - 2017**	**Korean Meteorological Administration**
CZT	**-46.43**	**51.86**	**-50.97**	**105.11**	**1991 - 2015**	**Ecole et Observatoire des Sciences de la Terre**
DED	70.36	211.21	72.73	-91.84	2011 - 2017	United States Geological Survey
DLR	**29.3**	**259.2**	**36.42**	**-28.26**	**1991 - 2008**	**United States Geological Survey**
DLT	11.95	108.48	0.83	178.24	2012 - 2016	Vietnamese Academy of Science and Technology
DMC	-75.25	124.17	-88.57	-82.04	1999-2001, 2003-2017	Ecole et Observatoire des Sciences de la Terre
DOU	**50.1**	**4.6**	**48.42**	**82.86**	**2002 - 2019**	**Royal Meterological Institute of Belgium**
DRV	-66.67	140.01	-79.15	-120.7	1991 - 2013	Ecole et Observatoire des Sciences de la Terre
DUR	**41.65**	**14.47**	**38.83**	**89.68**	**2016 - 2019**	**Instituto Nazionale di Geofisica e Vulcanolog**
EBR	**40.82**	**0.49**	**40.08**	**76.59**	**2002 - 2019**	**Observatori de l'Ebre**
ESK	**55.3**	**356.8**	**54.67**	**77.94**	**1991 - 2019**	**British Geological Survey**
EYR	**-43.4**	**172.4**	**-50.38**	**-101.32**	**1994 - 2019**	**Institute of Geological and Nuclear Sciences**
FCC	58.8	265.9	65.84	-22.78	1991 - 2019	Geological Survey of Canada
FRD	**38.2**	**282.6**	**45.54**	**-3.26**	**1991 - 2019**	**United States Geological Survey**
FRN	**37.1**	**240.3**	**42.66**	**-49.51**	**1991 - 2018**	**United States Geological Survey**
FUR	**48.17**	**11.28**	**45.75**	**88.88**	**1995 - 2019**	**Ludwig Maximilians University Munich**
GAN	-0.69	73.15	-10.37	140.34	2012 - 2017	ETH Zürich
GCK	**44.63**	**20.77**	**41.05**	**96.3**	**2005-2005, 2007-2013, 2015-2018**	**Geomagnetic Institute Yugoslavia**
GDH	69.25	306.47	74.28	34.2	1991-2006, 2009-2018	Danish Meteorological Institute
GLN	**49.6**	**262.9**	**56.53**	**-25.6**	**1992 - 1997**	**Geological Survey of Canada**
GNA	**-31.78**	**115.95**	**-45.92**	**-174.52**	**1994 - 2012**	**Geoscience Australia**
GNG	**-31.36**	**115.72**	**-45.1**	**-173.42**	**2012 - 2018**	**Geoscience Australia**
GUA	13.6	144.9	4.03	-144.82	1991 - 2019	United States Geological Survey
GUI	**28.32**	**343.56**	**30.77**	**58.03**	**1997 - 2017**	**Instituto Geografico Nacional**
GZH	22.97	112.45	12.32	-178.54	2003-2006, 2008-2009	Seismologicial Bureau of Guangdong Province
HAD	**51**	**355.5**	**50.74**	**75.09**	**1991 - 2019**	**British Geological Survey**

OBS	LAT	LON	θ	ϕ	Period	Responsible Institute
HBK	**-25.88**	**27.71**	**-26.83**	**89.6**	**1999 - 2019**	**National Research Foundation**
HER	**-34.43**	**19.23**	**-32.88**	**79.41**	**1995 - 2019**	**National Research Foundation**
HLP	**54.6**	**18.81**	**51.01**	**97.52**	**1998 - 2018**	**Polish Academy of Sciences**
HON	**21.3**	**202**	**21.35**	**-86.82**	**1991 - 2018**	**United States Geological Survey**
HRB	**47.88**	**18.19**	**44.55**	**95.04**	**1997 - 2019**	**Slovak Academy of Sciences**
HRN	77	15.37	73.12	108.92	2002 - 2018	Polish Academy of Sciences
HUA	-12.05	284.67	-2.56	-1	2002 - 2017	Instituto Geofisico del Peru
HYB	17.41	78.56	7.63	147.36	2009-2012, 2014-2019	National Geophysical Research Institute
IPM	-27.17	250.59	-19.32	-30.17	2010 - 2017	Institut de Physique du Globe de Paris
IQA	63.8	291.5	69.91	11.24	1996-2005, 2007-2019	Geological Survey of Canada
IRT	**52.17**	**104.45**	**43.22**	**172.63**	**1998 - 2019**	**Russian Academy of Sciences**
IZN	**40.5**	**29.72**	**35.91**	**103.7**	**2007 - 2019**	**Bogazici University**
JAI	26.9	75.8	17.76	145.49	2011 - 2016	Indian Institute of Geomagnetism
JCO	70.36	211.2	72.74	-90.68	2014 - 2019	United States Geological Survey
KAK	**36.23**	**140.18**	**27.88**	**-152.47**	**1991 - 2019**	**Japan Meterological Agency**
KDU	**-12.69**	**132.47**	**-25.1**	**-155.25**	**2000 - 2019**	**Geoscience Australia**
KEP	**-54.28**	**323.51**	**-43.31**	**29.59**	**2013 - 2019**	**British Geological Survey**
KHB	**47.61**	**134.69**	**40.77**	**-157.66**	**2012 - 2018**	**Institute of Cosmophysical Researches**
KIV	**50.7**	**30.3**	**45.92**	**106.36**	**2009 - 2018**	**National Academy of Sciences of Ukraine**
KMH	**-26.54**	**18.11**	**-25.79**	**81.04**	**2009 - 2019**	**National Research Foundation**
KNY	**31.42**	**130.88**	**22.31**	**-160.51**	**2001 - 2018**	**Japan Meterological Agency**
KOU	5.21	307.27	13.17	20.4	1996 - 2018	Institut de Physique du Globe de Paris
LER	**60.1**	**358.8**	**58.98**	**82.02**	**1991 - 2019**	**British Geological Survey**
LNP	25	121.17	14.48	-170.13	1995, 1997-2000	Directorate General of Telecommunications
LON	**45.41**	**16.66**	**42.24**	**92.58**	**2014 - 2019**	**University of Zagreb**
LOV	**59.34**	**17.82**	**55.76**	**98.81**	**1991 - 2004**	**Geological Survey of Sweden**
LRM	**-22.22**	**114.1**	**-35.79**	**-176.21**	**2004 - 2019**	**Geoscience Australia**
LVV	**49.9**	**23.75**	**45.84**	**100.32**	**2004 - 2018**	**National Academy of Sciences of Ukraine**
LYC	64.61	18.75	60.87	100.75	2008 - 2019	Geological Survey of Sweden
LZH	**36.09**	**103.84**	**26.19**	**172.57**	**2001 - 2019**	**Lanzhou Institute of Seismology**
MAB	**50.3**	**5.7**	**48.43**	**83.81**	**2005 - 2019**	**Royal Meterological Institute of Belgium**
MAW	-67.6	62.88	-72	95.09	2005 - 2019	Geoscience Australia

OBS	LAT	LON	θ	ϕ	Period	Responsible Institute
MBC	76.2	240.6	81.71	-73.01	1991 - 1997	Geological Survey of Canada
MBO	14.38	343.03	18.08	55.29	1993 - 2018	Institut de Physique du Globe de Paris
MCQ	-54.5	158.95	-63.98	-109.86	2001 - 2019	Geoscience Australia
MEA	54.6	246.7	60.74	-45.7	1991 - 2018	Geological Survey of Canada
MGD	**60.05**	**150.73**	**55.54**	**-145.33**	**2012 - 2018**	**Institute of Cosmophysical Researches**
MID	**28.21**	**182.7**	**25.37**	**-107.27**	**2000 - 2002**	**United States Geological Survey**
MLT	**30.2**	**31.22**	**25.65**	**103.24**	**2003**	**National Research Institute of Geophysics and**
MMB	**43.9**	**144.2**	**36.62**	**-149.61**	**1993 - 2019**	**Japan Meterological Agency**
NAQ	61.18	314.57	65.68	37.63	1991-2008, 2011-2019	Danish Meteorological Institute
NCK	**47.63**	**16.72**	**44.53**	**93.77**	**1993, 1995-2018**	**Hungarian Academy of Sciences**
NEW	**48.3**	**242.9**	**54.12**	**-48.68**	**1991 - 2019**	**United States Geological Survey**
NGK	**52.07**	**12.68**	**49.34**	**91.35**	**1995 - 2019**	**GeoForschungsZentrum Potsdam**
NUR	**60.51**	**24.66**	**56.07**	**105.26**	**1991 - 2017**	**Finnish Meteorological Institute**
NVS	**54.85**	**83.23**	**46.36**	**153.92**	**2003 - 2019**	**Russian Academy of Sciences**
OTT	**45.4**	**284.4**	**52.49**	**-0.91**	**1991 - 2018**	**Geological Survey of Canada**
PAF	**-49.35**	**70.26**	**-57.81**	**123.04**	**1991 - 2013**	**Ecole et Observatoire des Sciences de la Terre**
PAG	**42.52**	**24.18**	**38.56**	**98.98**	**2007 - 2016**	**Bulgarian Academy of Science**
PBQ	55.3	282.2	62.2	-2.54	1992 - 2007	Geological Survey of Canada
PEG	**38.08**	**23.93**	**34.25**	**97.9**	**2012 - 2013**	**Institute of Geology and Mineral Exploration**
PET	**52.97**	**158.25**	**48.51**	**-136.75**	**2007 - 2019**	**Institute of Cosmophysical Researches**
PHU	21.03	105.95	9.88	174.58	1996 - 2018	Vietnam National Centre for Science and Techn
PIL	**-31.67**	**296.12**	**-21.2**	**9.62**	**2012 - 2019**	**Servicio Meteorologico Nacional**
PPT	-17.57	210.42	-16.31	-70.75	1991, 1993-2017	Institut de Physique du Globe de Paris
PST	**-51.7**	**302.1**	**-39.41**	**13.42**	**2003 - 2018**	**British Geological Survey**
QSB	**33.87**	**35.64**	**28.64**	**108**	**2000 - 2007**	**National Centre for Geophysical Research**
RES	74.7	265.1	81.85	-26.38	1992 - 2018	Geological Survey of Canada
SBA	-77.85	166.76	-79.01	-44.27	1996 - 2018	Institute of Geological Nuclear Sciences
SBL	**43.93**	**299.99**	**48.77**	**16.9**	**2013 - 2019**	**British Geological Survey**
SFS	**36.67**	**354.06**	**36.92**	**69.52**	**2005 - 2019**	**Real Observatorio de la Armada**
SHE	-15.96	354.25	-12.01	61.59	2010 - 2019	GeoForschungsZentrum Potsdam
SHU	**55.35**	**199.54**	**56.1**	**-96.52**	**2005 - 2018**	**United States Geological Survey**
SIT	57.1	224.7	61.13	-72.26	1991 - 2019	United States Geological Survey

OBS	LAT	LON	θ	ϕ	Period	Responsible Institute
SJG	**18.1**	**293.8**	**26.1**	**7.7**	**1991 - 2016**	**United States Geological Survey**
SOD	67.37	26.36	62.58	110.11	1991 - 2017	Finnish Academy of Science
SPG	**60.54**	**29.72**	**55.88**	**108.22**	**2015 - 2016**	**Russian Academy of Sciences**
SPT	**39.55**	**355.65**	**39.66**	**71.88**	**1997 - 2017**	**Instituto Geografico Nacional**
STJ	**47.6**	**307.3**	**53.32**	**24.88**	**1991 - 2018**	**Geological Survey of Canada**
SUA	**44.68**	**26.25**	**40.41**	**101.51**	**1999 - 2019**	**Geological Survey of Romania**
TAM	**22.79**	**5.53**	**22.53**	**77.93**	**1993 - 2019**	**Centre National d'Astrophysique et Geophysique**
TAN	**-18.92**	**47.55**	**-24.26**	**110.22**	**1993 - 2007**	**University of Antananarivo**
TDC	**-37.07**	**347.69**	**-30.15**	**51.96**	**2009 - 2016**	**GeoForschungsZentrum Potsdam**
TEO	**19.75**	**260.82**	**26.64**	**-25.18**	**2002 - 2008**	**Instituto Geofisica UNAM**
THL	77.48	290.83	83.59	28.19	1991 - 2019	Danish Meteorological Institute
THY	**46.9**	**17.89**	**43.69**	**94.67**	**1991 - 2018**	**Hungarian Geological Survey**
TIK	71.58	129	64.45	-170.84	1991	Arctic and Antarctic Research Institute
TRW	**-43.27**	**294.62**	**-31.37**	**7.71**	**2000-2011, 2013-2014**	**Facultad de Ciencias Astronomicas y Geofisica**
TSU	-19.2	17.58	-18.78	81.88	2004-2008, 2010-2019	National Research Foundation
TTB	-1.21	311.49	5.69	24.67	2018	Observatorio Nacional
TUC	**32.2**	**249.2**	**38.59**	**-39.22**	**1991 - 2018**	**United States Geological Survey**
UPS	**59.9**	**17.35**	**56.38**	**97.81**	**2003 - 2018**	**Geological Survey of Sweden**
VAL	**51.94**	**349.75**	**52.09**	**69.37**	**2002 - 2017**	**The Irish Meteorological Service**
VIC	**48.5**	**236.6**	**53.74**	**-55.87**	**1991 - 2018**	**Geological Survey of Canada**
VNA	-70.68	351.72	-61.14	42.12	2014 - 2019	Alfred Wegener Institute
VOS	-78.46	106.84	-86.35	45.23	2011-2012, 2015-2018	Arctic and Antarctic Research Institute
VSS	-22.4	316.35	-12.92	26.83	1999 - 2019	Observatorio Nacional
WIC	**47.93**	**15.86**	**44.79**	**92.38**	**2015 - 2019**	**Zentralanstalt für Meteorologie und Geodynamik**
WNG	**53.74**	**9.07**	**51.44**	**88.65**	**1994 - 2018**	**GeoForschungsZentrum Potsdam**
YAK	**61.96**	**129.66**	**55.57**	**-165.52**	**2009, 2011-2018**	**Institute of Cosmophysical Research and Aeronomy**
YKC	62.5	245.5	68.57	-49.59	1992 - 2015	Geological Survey of Canada

Appendix B

(Sub-)Diurnal Filter Responses between 1991-2019

The analogues of figures 5.3 and 5.4 for the entire period 1991-2019 are given in figures B.1 and B.2. The figures present the 24h, 12h, 8h and 6h filter responses together with combined daily signal as the sum of the four filters with respect to local time and day of year, alongside the $F10.7$ index in the first panel to facilitate comparisons with solar cycle phases. The occurrence of sunrise and sunset at 110 km altitude is superposed on corresponding panels as (lower and upper) black dashed lines.

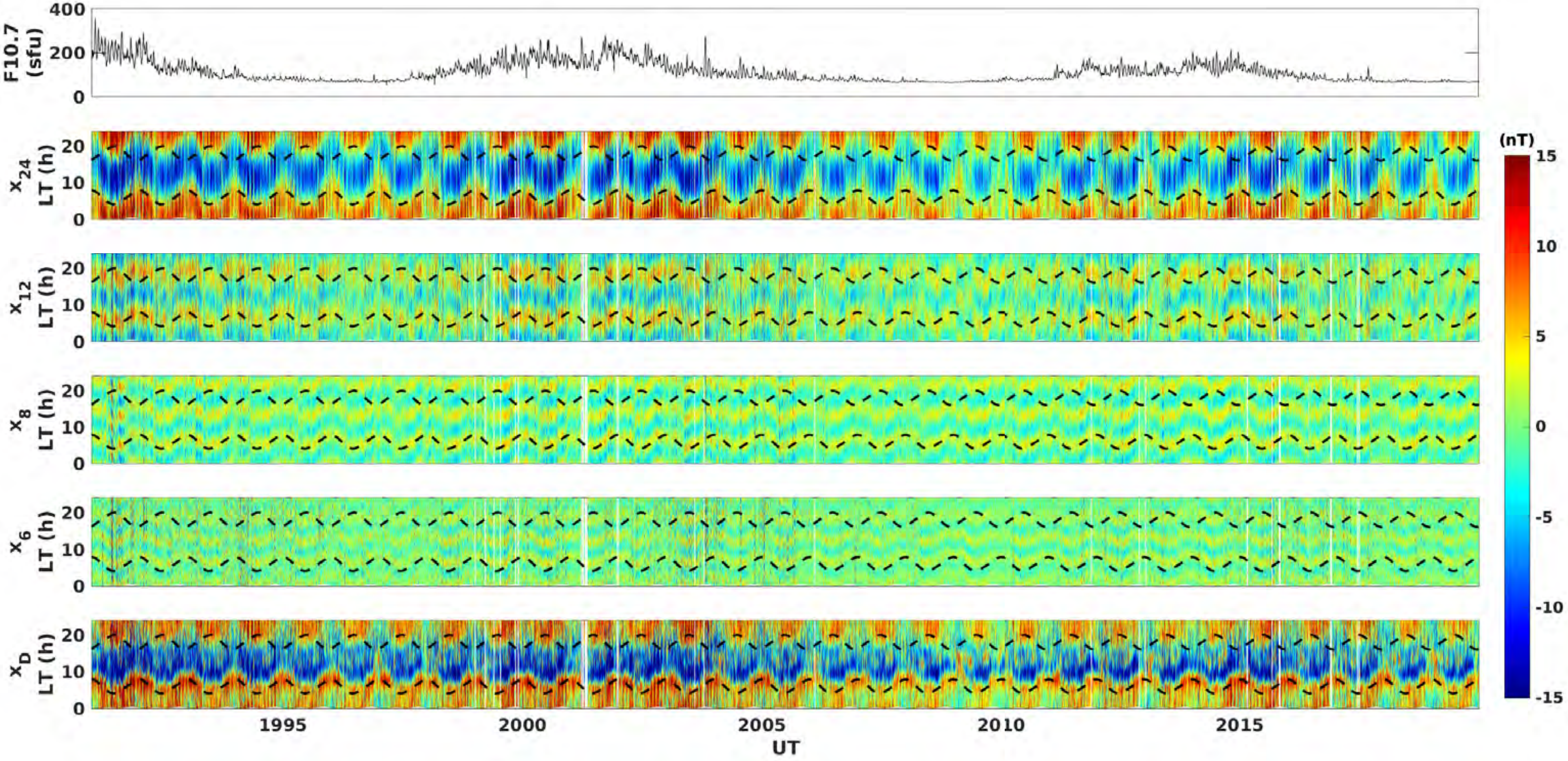

Figure B.1: Filter outputs for the entire period between 1991 and 2019 as function of solar local time (LT) for the X component of CLF. From top to bottom: the F10.7 daily values in sfu; x_{24}; x_{12}; x_8; x_6 and x_D. Dashed black lines indicate local time for sunrise (morning hours) and sunset (evening hours). Periods with unavailable data are not represented and appear as white vertical stripes. Note that the limits of the colour-scale range from -15nT to 15nT.

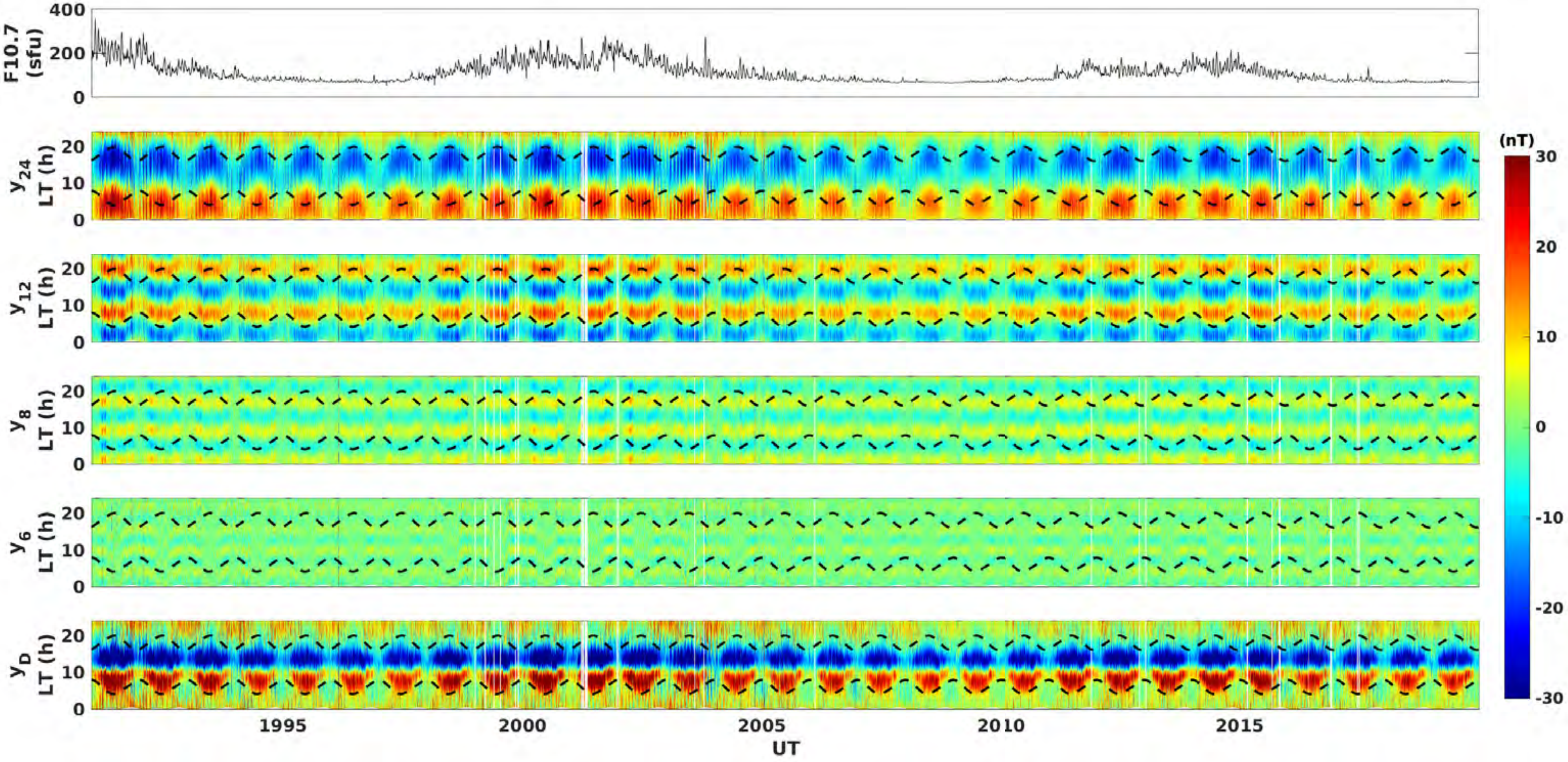

Figure B.2: Analog to Figure B.1 for the Y component of CLF. Note that the limits of the colour-scale range from -30nT to 30nT.

Appendix C

Coefficients

C.1 Coefficients for the Seasonal and Local Time Model

The tables C.1 and C.2 list the coefficients for the model taking into account the season and local time $\hat{x}_{L+LT}$ and $\hat{y}_{L+LT}$ as derived by equation (5.5). The provided coefficients represent the following:

$$\begin{aligned}
\hat{z}_{L+LT} &= \left(\sum_{i=0}^{k} \alpha_i \cos(iL) + \beta_i \sin(iL)\right) \left(\sum_{j=0}^{k} \gamma_j \cos(jLT) + \delta_j \sin(jLT)\right) && \text{(C.1)} \\
&= \sum_{i=0}^{k} \sum_{j=0}^{k} \quad \underbrace{\alpha_i \gamma_j}_{c_1} \cos(iL) \cos(jLT) + \underbrace{\alpha_i \delta_j}_{c_2} \cos(iL) \sin(jLT) && \text{(C.2)} \\
&\qquad + \underbrace{\beta_i \gamma_j}_{c_3} \sin(iL) \cos(jLT) + \underbrace{\beta_i \delta_j}_{c_4} \sin(iL) \sin(jLT)
\end{aligned}$$

Table C.1: Coefficients of equation (C.2) for the combined diurnal and semi-diurnal SEA model $\hat{x}_{L+LT}$

$\mathbf{c_1}$	γ_0	γ_1	γ_2	γ_3	γ_4	$\mathbf{c_2}$	δ_1	δ_2	δ_3	δ_4
α_0	-0.0263	0.5794	0.0714	0.0388	0.0286	α_0	0.5794	0.0714	0.0388	0.0286
α_1	-0.0108	0.9172	-0.8563	-0.0125	-0.0027	α_1	0.9172	-0.8563	-0.0125	-0.0027
α_2	-0.0311	0.2577	0.2100	0.0008	0.0004	α_2	0.2577	0.2100	0.0008	0.0004
α_3	-0.0095	0.3200	-0.5050	-0.0335	-0.0153	α_3	0.3200	-0.5050	-0.0335	-0.0153
α_4	0.0037	-0.0296	0.1304	-0.0063	-0.0061	α_4	-0.0296	0.1304	-0.0063	-0.0061
$\mathbf{c_3}$	γ_0	γ_1	γ_2	γ_3	γ_4	$\mathbf{c_4}$	δ_1	δ_2	δ_3	δ_4
β_1	0.0182	2.9392	0.5291	0.0129	-0.0007	β_1	-2.1186	1.2508	-0.0315	-0.0203
β_2	0.0027	0.3747	-0.5330	-0.0217	-0.0104	β_2	0.3444	-0.5847	-0.0150	-0.0062
β_3	0.0081	-0.3688	0.6905	-0.0099	-0.0050	β_3	-0.9466	0.6956	-0.0064	-0.0112
β_4	0.0047	0.4800	-0.7203	0.0058	0.0044	β_4	0.6183	-0.4768	-0.0227	-0.0199

Table C.2: Coefficients of equation (C.2) for the combined diurnal and semi-diurnal SEA model $\hat{y}_{L+LT}$

$\mathbf{c_1}$	γ_0	γ_1	γ_2	γ_3	γ_4	$\mathbf{c_2}$	δ_1	δ_2	δ_3	δ_4
α_0	-0.0150	9.7131	-7.9364	-0.0052	-0.0041	α_0	9.7131	-7.9364	-0.0052	-0.0041
α_1	-0.0063	-0.9451	0.2759	0.0005	0.0016	α_1	-0.9451	0.2759	0.0005	0.0016
α_2	0.0122	0.4188	-0.8574	-0.0110	-0.0067	α_2	0.4188	-0.8574	-0.0110	-0.0067
α_3	0.0106	-0.0033	-0.2664	0.0237	0.0122	α_3	-0.0033	-0.2664	0.0237	0.0122
α_4	0.0033	0.3732	-0.2935	-0.0066	-0.0001	α_4	0.3732	-0.2935	-0.0066	-0.0001
$\mathbf{c_3}$	γ_0	γ_1	γ_2	γ_3	γ_4	$\mathbf{c_4}$	δ_1	δ_2	δ_3	δ_4
β_1	-0.0323	1.6090	-5.0157	-0.0084	0.0067	β_1	7.2651	-2.8793	-0.0054	-0.0058
β_2	0.0074	-0.4048	0.3428	-0.0095	-0.0050	β_2	0.3113	-1.1593	0.0210	0.0078
β_3	-0.0082	0.6047	-1.1074	0.0025	0.0087	β_3	-0.2510	0.2633	0.0048	0.0034
β_4	-0.0208	-0.5754	0.7115	0.0082	0.0079	β_4	0.3641	-0.9636	0.0100	0.0073

C.2 Coefficients for the Solar Activity and Seasonal Model

The coefficients α_i for $i = 0, 1, 2$ and β_i for $i = 1, 2$ from (5.7) and (5.8) are produced per component, i.e. one set of coefficients per x_{24}, x_{12}, y_{24}, y_{12}. The corresponding coefficients for $a(L)$, $b(L)$, $c(L)$, $d(L)$ from equation (5.10) are given in tables C.3 and C.4.

Table C.3: Coefficients α, β from equation (5.10) for $\hat{x}_{24,L+F10.7}$ and $\hat{x}_{12,L+F10.7}$ models in (5.9). Recall from (5.7) and (5.8) that b and d describe the linear dependence of the amplitude and phase on $F10.7$, respectively.

$\hat{x}_{24,L+F10.7}$	a	b	c	d
α_0	5.3364	0.0389	32.3355	-0.0863
α_1	0.0560	-0.0161	19.5602	-0.0421
β_1	1.9733	-0.0061	-47.8145	0.0699
α_2	-1.3116	0.0189	-6.8263	0.0580
β_2	-0.8604	0.0064	-13.1357	0.0590

$\hat{x}_{12,L+F10.7}$	a	b	c	d
α_0	2.8252	0.0183	-10.2856	0.0092
α_1	0.1543	-0.0055	-20.3110	-0.0441
β_1	-0.5147	0.0038	37.0176	0.1298
α_2	-0.2379	0.0040	13.3312	-0.1100
β_2	-0.3209	0.0030	-2.6032	-0.0821

Table C.4: Coefficients α, β from equation (5.10) for $\hat{y}_{24,L+F10.7}$ and $\hat{y}_{12,L+F10.7}$ models in (5.9). Recall from (5.7) and (5.8) that b and d describe the linear dependence of the amplitude and phase on $F10.7$, respectively.

$\hat{y}_{24,L+F10.7}$	a	b	c	d
α_0	9.0574	0.0513	23.9721	0.1454
α_1	0.9103	-0.0059	-3.4816	0.0437
β_1	4.8206	0.0109	42.4548	-0.1489
α_2	-0.5270	0.0081	5.6243	-0.0266
β_2	-0.7912	0.0044	-0.4685	-0.0011

$\hat{y}_{12,L+F10.7}$	a	b	c	d
α_0	6.8981	0.0398	-114.9332	0.0522
α_1	-0.1134	-0.0027	7.3996	-0.0281
β_1	2.2607	0.0201	-19.8060	-0.0690
α_2	0.5140	0.0048	-2.7156	-0.0098
β_2	-0.3712	0.0072	-3.1790	-0.0012

C.3 Coefficients for the Day-to-Day Variability

The amplitude A of the D2D variability is fitted in dependence of solar longitude L with a 4th order polynomial in figure 5.14, 5.17 and 5.18. The resulting coefficients from

$$p(L) = p_0 + p_1 L + p_2 L^2 + p_3 L^3 + p_4 L^4 \tag{C.3}$$

are given in table C.5.

Table C.5: Coefficients of the polynomial fit in equation (C.3) for the amplitude variations in season L for the diurnal and semi-diurnal filters, as well as the combined (sub-)diurnal filter.

	p_0	p_1	p_2	p_4	p_5
x_{24}	6.3043	-0.0009	0.0003	-1.9001e-06	2.8413e-09
x_{12}	19.8149	0.3905	-0.0024	7.7867e-07	8.5360e-09
y_{24}	23.0659	0.0945	2.6951e-05	-5.7946e-06	1.3724e-08
y_{12}	5.2257	0.1525	-0.0004	-1.9931e-06	5.7889e-09
x_D	-9.0889	-0.0616	-0.0003	4.3415e-06	-8.0766e-09
y_D	56.1542	-0.0615	0.0033	-2.6301e-05	4.8366e-08

Appendix D

Storm Parameters

D.1 Storm Signature in Dst

The moderate storm that is identified on 27th July 1999 in Li and Yao (2020) with a minimum Dst of $-38\,\mathrm{nT}$ does not have a strong signature in the X and Y measurements from CLF. Using residuals derived from the filter baseline during this storm event in figure D.1 in orange would not lead to a significant underestimation of the storm. In fact, the filter baseline smoothly follows the day-to-day variation during this day for both components, suggestion no need to replace it.

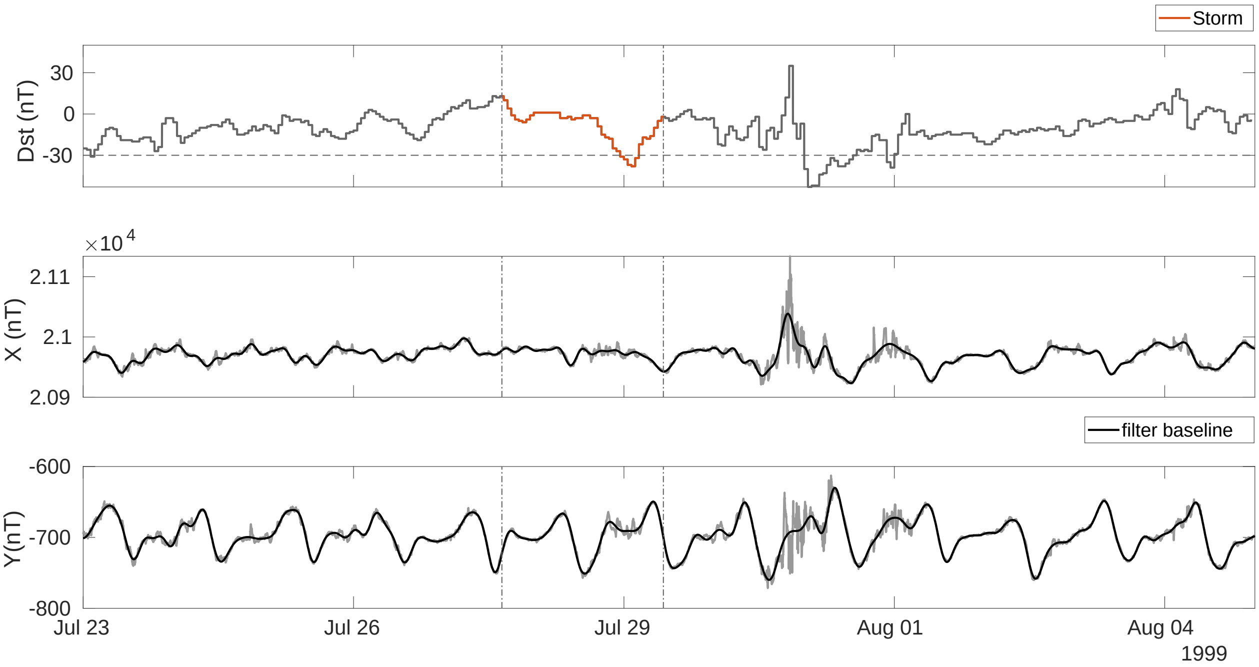

Figure D.1: The storm event in orange from 27th July 1999 from the storm list of Li and Yao (2020). From top to bottom: Dst index, X component and Y component at CLF.

D.2 Details of the De-trended Long-term Horizontal Intensity

Figure D.2 shows several magnetic observatories and their relation between SYM-H and the de-trended long-term horizontal intensity $\bar{h}_{>24}$.

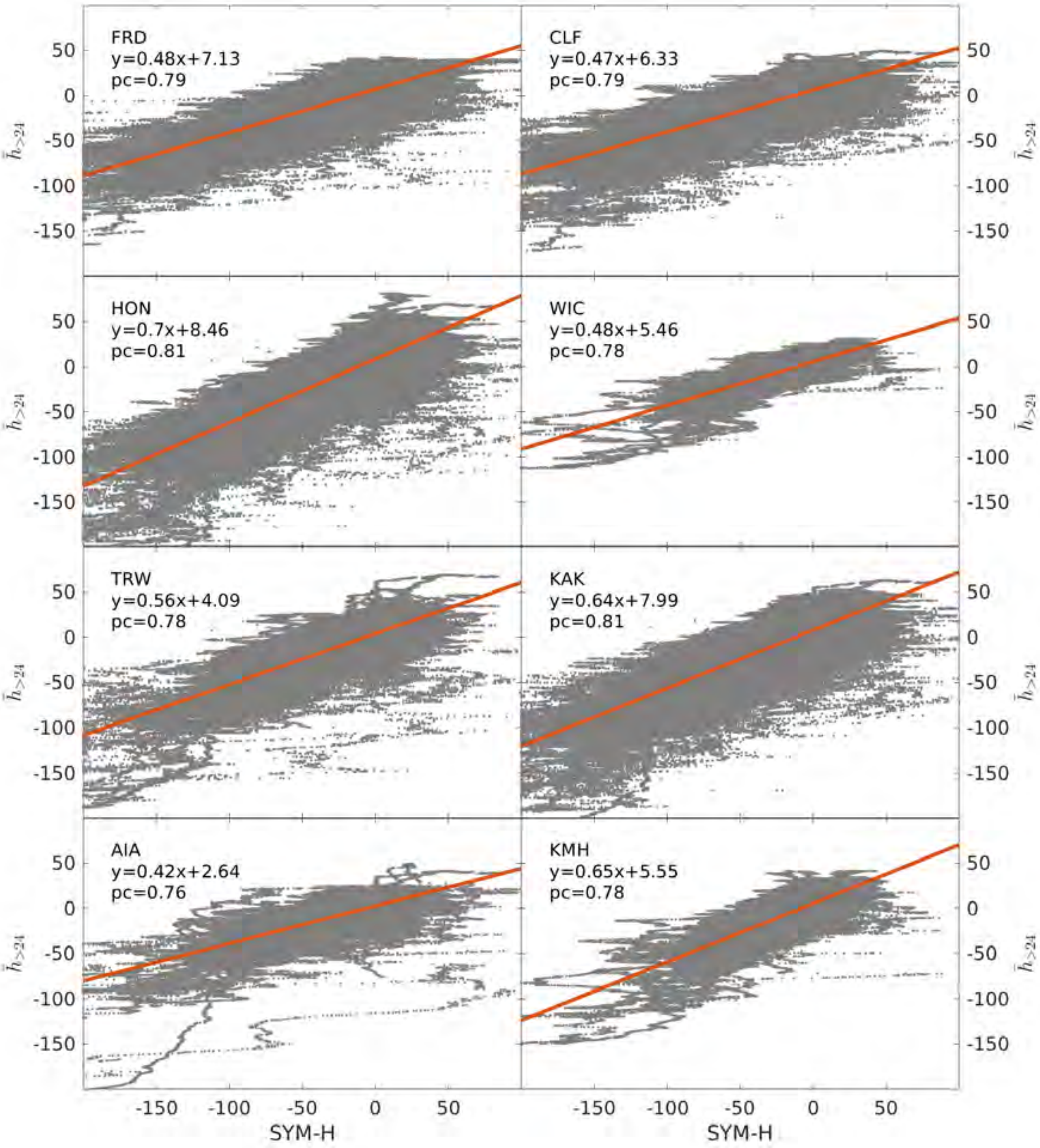

Figure D.2: Correlation with SYM-H for the de-trended long-term horizontal intensity $\bar{h}_{>24}$ for several magnetic observatories in mid-latitudes.

D.3 Disturbance List for CLF

Table D.1 lists disturbance events for the magnetic observatory Chambon-la-Fôret. Figures D.3 to D.7 illustrate the X and Y components, together with the filter baseline during these events.

#	**Start Time**	**End Time**	**Dst$_{min}$**	**Flag**
1	10-Mar-1998 10:00:00	14-Mar-1998 10:00:00	-116	0
2	25-Jun-1998 18:30:00	26-Jun-1998 10:30:00	-101	1
3	08-Nov-1998 20:30:00	11-Nov-1998 08:30:00	-142	1
4	18-Feb-1999 03:30:00	21-Feb-1999 09:30:00	-123	0
5	30-Jul-1999 12:00:00	01-Aug-1999 10:00:00	-53	1
6	22-Sep-1999 10:00:00	23-Sep-1999 10:00:00	-173	1
7	01-Mar-2000 03:30:00	03-Mar-2000 00:30:00	-43	1
8	26-Jun-2000 02:00:00	27-Jun-2000 08:00:00	-76	0
9	28-Oct-2000 20:30:00	30-Oct-2000 18:30:00	-127	1
10	23-Jan-2001 12:00:00	25-Jan-2001 06:00:00	-61	1
11	27-May-2001 17:30:00	29-May-2001 08:30:00	-42	1
12	31-Oct-2001 14:30:00	02-Nov-2001 21:30:00	-106	1
13	28-Feb-2002 05:30:00	01-Mar-2002 21:30:00	-71	1
14	01-Aug-2002 05:30:00	03-Aug-2002 07:00:00	-51	1
15	14-Dec-2002 06:00:00	15-Dec-2002 15:00:00	-42	0
16	01-Feb-2003 17:00:00	03-Feb-2003 08:00:00	-68	0
17	10-Jul-2003 18:00:00	13-Jul-2003 06:00:00	-105	0
18	20-Nov-2003 08:30:00	24-Nov-2003 03:30:00	-422	1
19	22-Jan-2004 04:00:00	24-Jan-2004 04:00:00	-130	0
20	22-Jul-2004 14:30:00	24-Jul-2004 01:30:00	-99	1
21	05-Dec-2004 09:00:00	07-Dec-2004 04:12:00	-44	0
22	17-Jan-2005 06:30:00	19-Jan-2005 12:00:00	-103	1
23	10-Jul-2005 11:30:00	11-Jul-2005 09:30:00	-92	1
24	31-Oct-2005 04:30:00	02-Nov-2005 05:30:00	-74	1
25	23-Jan-2006 00:00:00	24-Jan-2006 11:00:00	-21	0
26	27-Jul-2006 19:00:00	28-Jul-2006 10:00:00	-48	0
27	30-Sep-2006 03:30:00	02-Oct-2006 03:00:00	-51	1
28	23-Mar-2007 10:00:00	24-Mar-2007 18:00:00	-72	0
29	22-May-2007 10:00:00	24-May-2007 08:00:00	-58	0
30	19-Nov-2007 21:30:00	22-Nov-2007 07:30:00	-59	1
31	08-Mar-2008 12:00:00	10-Mar-2008 09:00:00	-86	0
32	14-Jun-2008 06:00:00	15-Jun-2008 08:00:00	-41	0
33	11-Oct-2008 07:00:00	12-Oct-2008 09:00:00	-54	0
34	03-Feb-2009 18:30:00	06-Feb-2009 05:24:00	-42	1
35	22-Jul-2009 01:00:00	23-Jul-2009 10:00:00	-83	0
36	29-Oct-2009 14:00:00	31-Oct-2009 09:03:00	-34	0
37	14-Feb-2010 19:00:00	17-Feb-2010 06:00:00	-59	0
38	03-Aug-2010 19:30:00	06-Aug-2010 22:30:00	-74	1
39	28-Dec-2010 09:00:00	29-Dec-2010 20:30:00	-43	1

Table D.1: Disturbance list for CLF with start and end-times, minimum Dst value Dst$_{min}$. The last column Flag indicates if the respective event is found in the storm list of Li and Yao (2020).

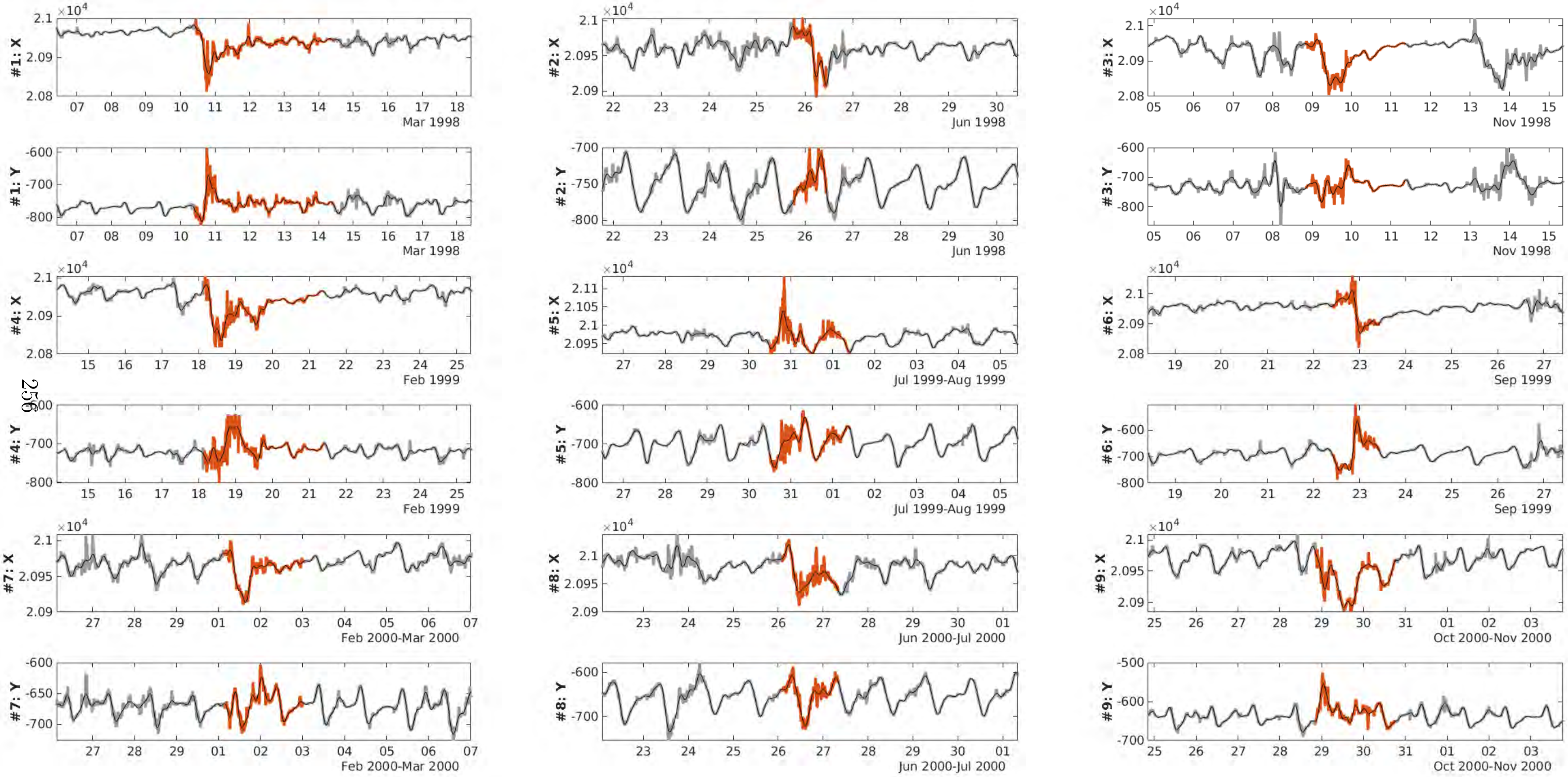

Figure D.3: The components X and Y for each of the events between 1998-2000 from the storm list of CLF. The components are in grey, the initial filter baseline in black and the events are indicated in orange.

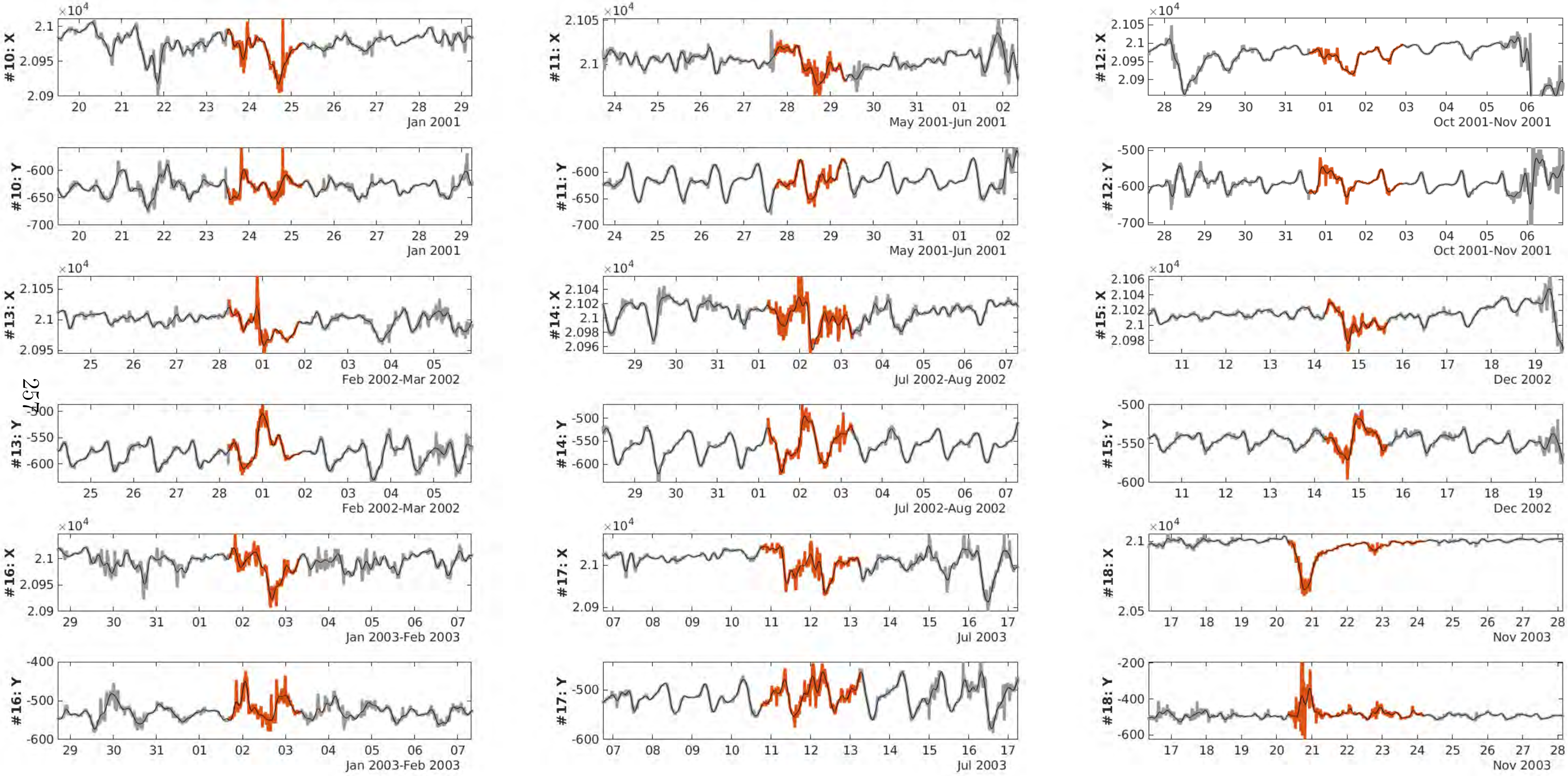

Figure D.4: The components X and Y for each of the events between 2001-2003 from the storm list of CLF. The components are in grey, the initial filter baseline in black and the events are indicated in orange.

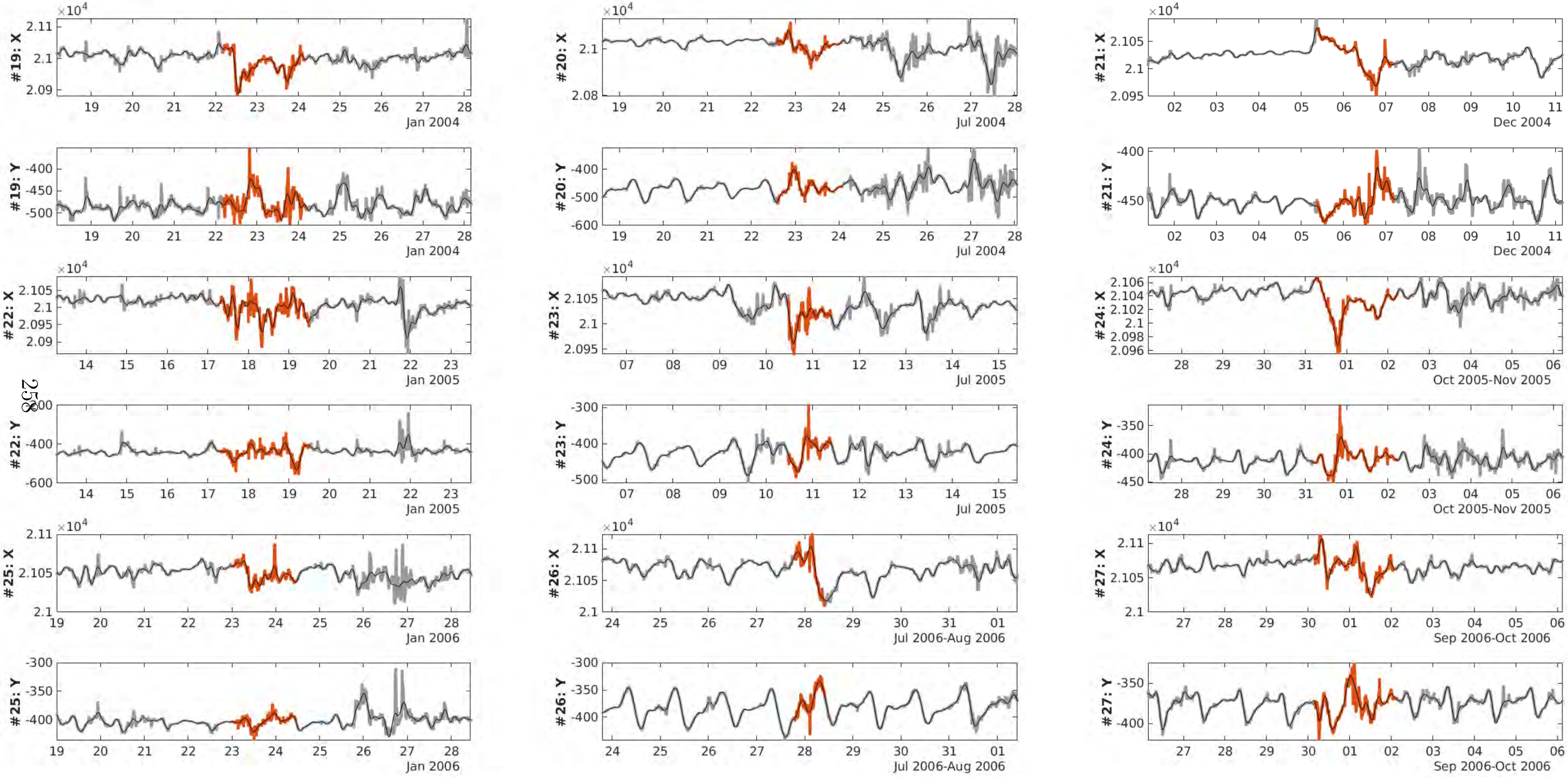

Figure D.5: The components X and Y for each of the events between 2004-2006 from the storm list of CLF. The components are in grey, the initial filter baseline in black and the events are indicated in orange.

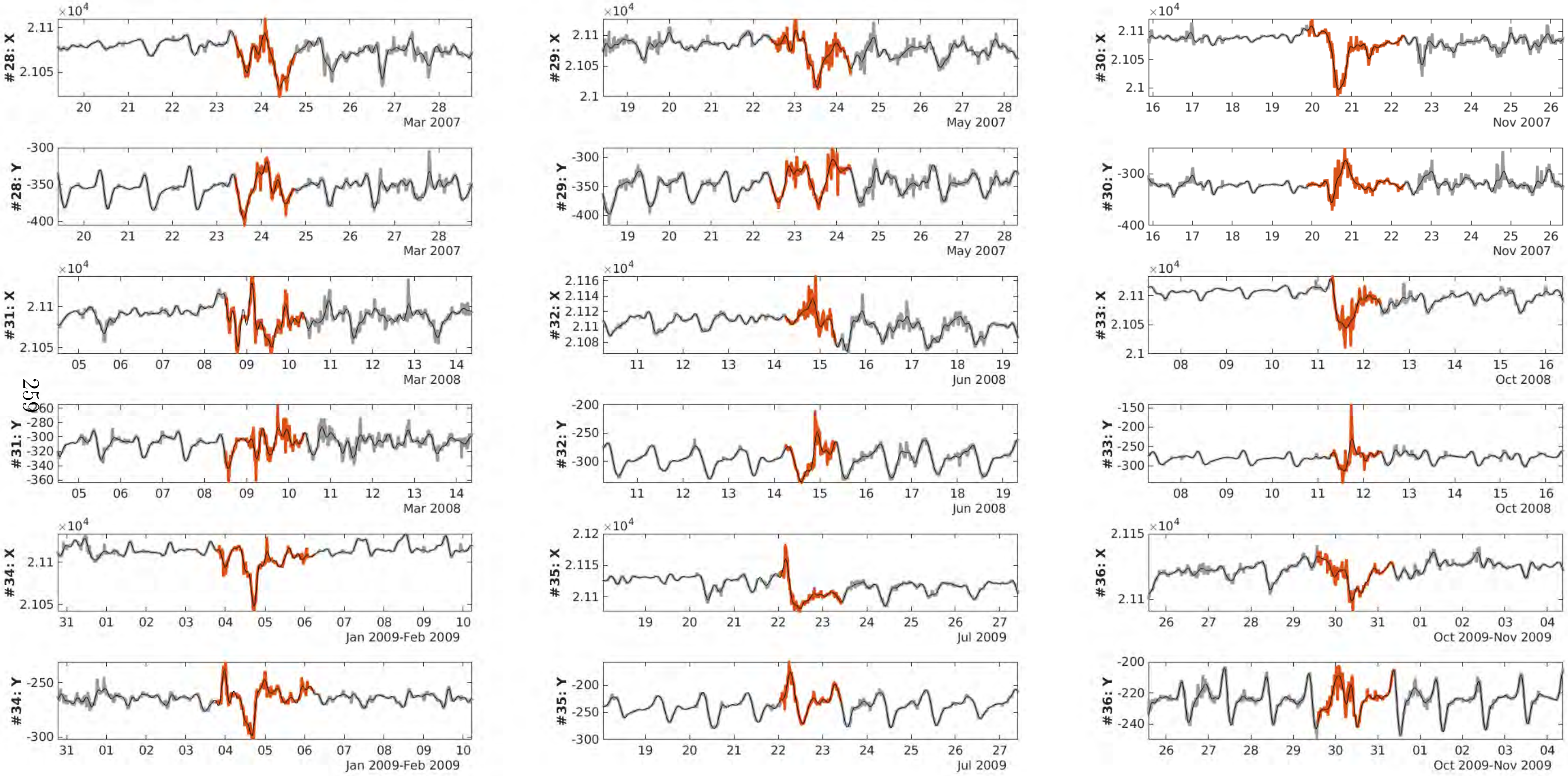

Figure D.6: The components X and Y for each of the events between 2007-2009 from the storm list of CLF. The components are in grey, the initial filter baseline in black and the events are indicated in orange.

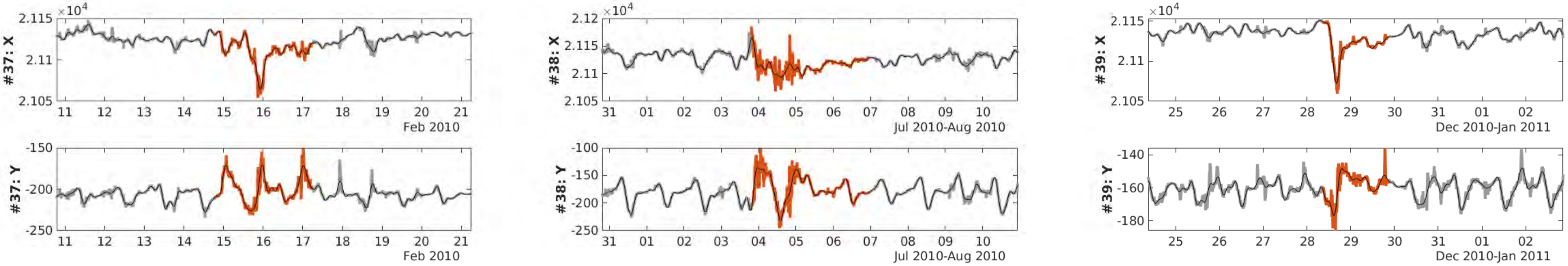

Figure D.7: The components X and Y for each of the events for 2010 from the storm list of CLF. The components are in grey, the initial filter baseline in black and the events are indicated in orange.

Appendix E

Results for further Observatories

During the course of this thesis most of the results were presented for the magnetic observatory Chambon-la-Forêt as motivated in 4.1. Still, it is of high interest, and after fruitful discussions with the jury, the present manuscript profits from adding results of further observatories which this appendix is dedicated to.

E.1 Solar Quiet Current Patterns

Using the superposed epoch analysis (SEA) as introduced in chapter 5.2.1 reveals the solar quiet current footprints within the combined (sub-)diurnal filter responses. Figure E.1 presents the patterns of further stations, together with the idealised Sq current geometry and the expected related signals for the horizontal components X and Y (taken from Amory-Mazaudier (1983)). For all stations located in the northern hemisphere, the y_D component describes the expected maximum during morning hours and minimum during afternoon hours, while the y_D component at stations located in the southern hemisphere describes the inverse with minimum during morning and maximum during afternoon. The x_D component follows the expected Sq patterns at all stations with stations that are closely below the Sq focus showing less pronounced amplitudes.

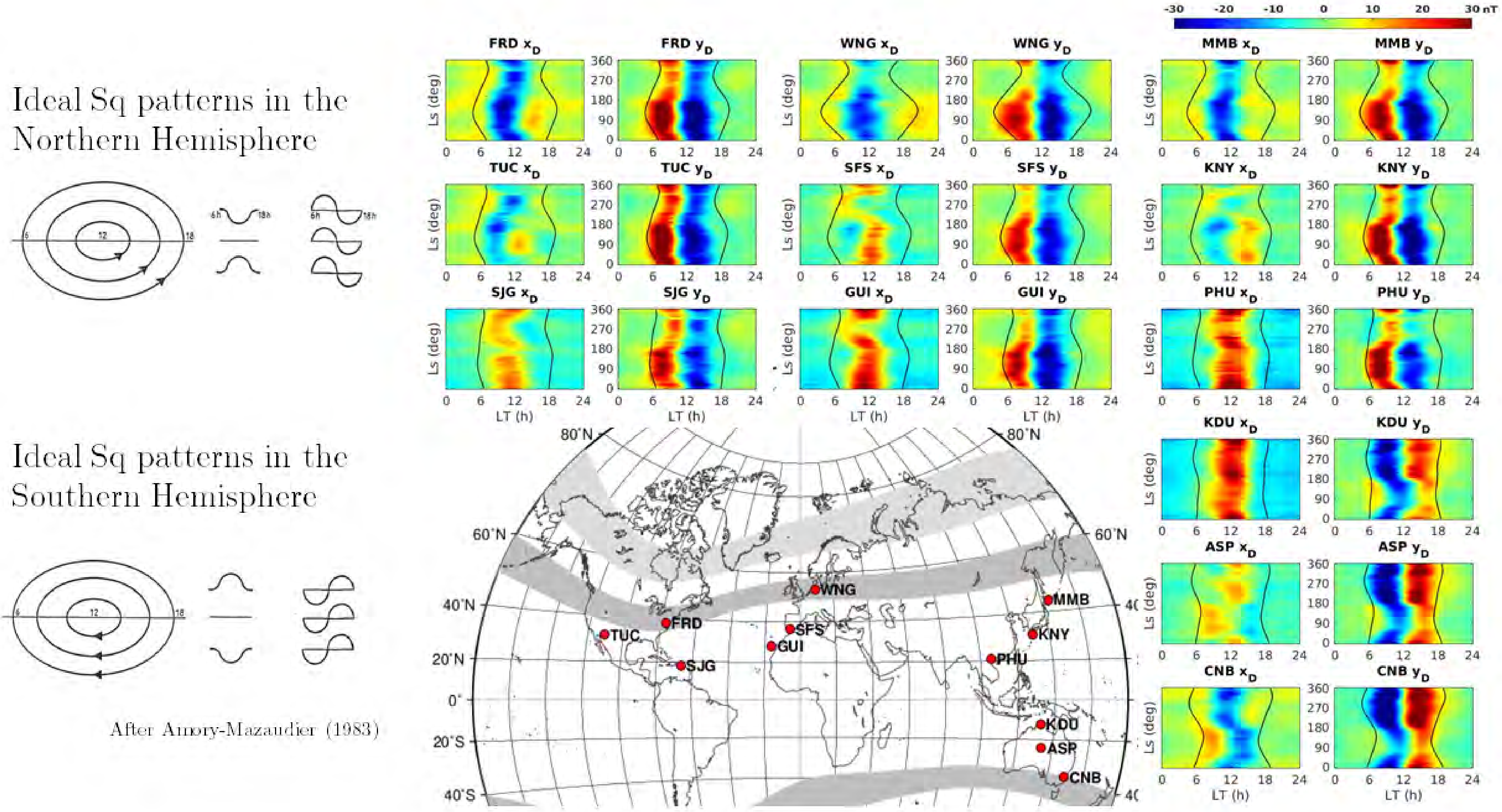

Figure E.1: Results of the SEA of the combined (sub-)diurnal filter responses x_D and y_D of further geomagnetic observatories for geographic sectors North America, Europe, Asia and Australia. On the left the ideal solar quiet current patterns are indicated, together with the expected horizontal components X and Y responses.

E.2 Geomagnetic Baselines for a Moderate Geomagnetic Storm

In chapter 6.3, the results of the full baseline algorithm are presented for the geomagnetic observatory Chambon-la-Foret. Figure E.2 illustrates the resulting baselines $\tilde{x}_B$ and $\tilde{y}_B$ for the moderate geomagnetic storm of mid-December 2002 for several geomagnetic observatories on a global scale. In general, the final baseline describes quiet variations well. The algorithm did not replace the filter baseline for the magnetic observatory Tuckson (TUC), and the X components of Phuthuy (PHU) and Kakadu (KDU).

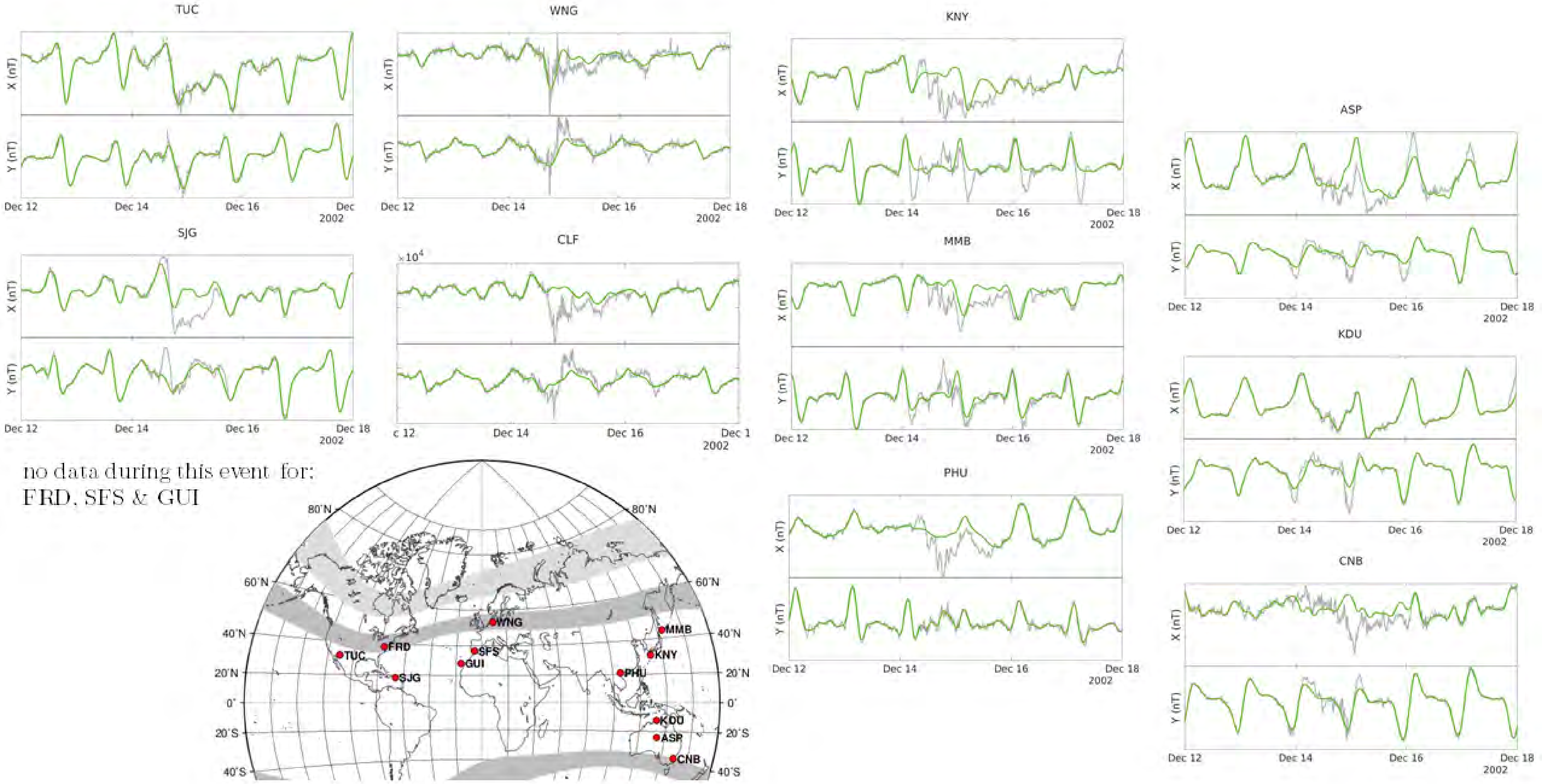

Figure E.2: Final geomagnetic baselines for further geomagnetic observatories located in geographic sectors North America, Europe, Asia and Australia during a moderate geomagnetic storm.

List of Figures

List of Tables

List of Publications

Veronika Haberle, Aurélie Marchaudon, Aude Chambodut & Pierre-Louis Blelly, (2022). Direct Determination of Geomagnetic Baselines During Quiet Periods for Low- and Mid-Latitude Observatories. *Journal of Geophysical Research: Space Physics*, 127 (8), e2022JA030407
DOI: 10.1029/2022JA030407

Veronika Haberle; Aurélie Marchaudon; Aude Chambodut; Pierre-Louis Blelly, Extraction of solar forcing signatures in ground magnetometer data from sub-auroral regions, Preprint, 2023,
DOI: 10.5194/egusphere-egu23-7835

Veronika Haberle; Aurélie Marchaudon; Aude Chambodut; Pierre-Louis Blelly, Extraction of ground magnetic signatures from solar quiet current systems in sub-auroral regions, Preprint, 2022
DOI: 10.5194/egusphere-egu22-1416

Veronika Haberle; Aurélie Marchaudon; Pierre-Louis Blelly; Aude Chambodut, Local diurnal variations of the geomagnetic field during magnetically quiet conditions, Preprint, 2021
DOI: 10.5194/egusphere-egu21-2169

Gopika Prasannakumara Pillai Geethakumari; Anita Aikio; Lei Cai; Heikki Vanhamaki; Marcus Pedersen; Anthea Coster; Aurelie Marchaudon; Pierre-Louis Blelly; **Veronika Haberle**; Astrid Maute et al., HSS/CIR driven storm effects on the ionosphere-thermosphere system, Preprint, 2023,
DOI: 10.5194/egusphere-egu23-9293

Gopika Prasannakumara Pillai Geethakumari; Anita Aikio; Lei Cai; Heikki Vanhamaki; Marcus Pedersen; Anthea Coster; Aurelie Marchaudon; Pierre-Louis Blelly; **Veronika Haberle**; Astrid Maute et al., Total Electron Content Variations during an HSS/CIR driven storm at high and middle latitudes, Preprint, 2022
DOI: 10.5194/egusphere-egu22-8194

Alexandros Adamis, Astrid Veronig, Tatiana Podladchikova, Karin Dissauer, Rositsa Miteva, Jingnan Guo, **Veronika Haberle**, Mateja Dumbovic, Manuela Temmer, Kamen Kozarev, Jasmina Magdalenic, and Christina Kay, Statistical study of CMEs, lateral overexpansion and SEP events, Preprint, 2021
DOI: 10.5194/egusphere-egu21-3216

ADVANCING EARTH AND SPACE SCIENCE

JGR Space Physics

RESEARCH ARTICLE

10.1029/2022JA030407

Direct Determination of Geomagnetic Baselines During Quiet Periods for Low- and Mid-Latitude Observatories

V. Haberle[1,2], **A. Marchaudon**[1], **A. Chambodut**[2], **and P.-L. Blelly**[1]

[1]Institut de Recherche en Astrophysique et Planétologie, Université de Toulouse, CNRS, CNES, Toulouse, France, [2]Institut Terre et Environnement de Strasbourg, UMR7063, Université de Strasbourg/EOST, CNRS, Strasbourg Cedex, France

Key Points:

- A basic signal filtering approach is used to determine geomagnetic baselines during quiet periods
- The baselines capture the secular variation and solar quiet current systems accurately
- The baseline method is applicable for low- and mid-latitude magnetic observatories and does not require any apriori information

Supporting Information:

Supporting Information may be found in the online version of this article.

Correspondence to:

V. Haberle,
veronika.haberle@irap.omp.eu

Citation:

Haberle, V., Marchaudon, A., Chambodut, A., & Blelly, P.-L. (2022). Direct determination of geomagnetic baselines during quiet periods for low- and mid-latitude observatories. *Journal of Geophysical Research: Space Physics*, *127*, e2022JA030407. https://doi.org/10.1029/2022JA030407

Received 18 FEB 2022
Accepted 12 JUL 2022

Abstract

The geomagnetic field is composed of a variety of sources that act on a wide range of timescales and amplitudes. The separation of magnetic storm effects from quiet variations is needed to accurately quantify impacts of space weather events. The extraction of such quiet contributions within geomagnetic measurements is achieved by the determination of baselines, which, ideally, is done by a simple algorithm which captures quiet sources suitably well, while being applicable to an extensive network of magnetic observatories independent of the period of time. In this work, we apply signal filtering techniques on the horizontal components of geomagnetic field measurements from low- and mid-latitude observatories to determine baselines. The variations within the baseline are investigated for magnetically quiet periods between 1991 and 2019, focusing on long-term trends, seasonal and local time dependencies, and day-to-day variability. The analysis confirms that the contributing quiet sources include the secular variation and the solar quiet (Sq) current system. The non-negligible day-to-day variability, that is typical for Sq in low- and mid-latitudes, is embedded within the baseline. Thus, the filter approach extracts quiet magnetic field variations well. Comparisons with other baseline methods show good agreements. We conclude that the filter approach can be used to determine baselines automatically during magnetically quiet periods without the need of further apriori information and is applicable on a wide network of magnetic observatories. It marks the first step for deriving magnetic indices for (near) real-time space weather applications.

Plain Language Summary

The Earth's intrinsic magnetic field is generated by the motion of molten rock within its interior and interacts with the constant flow of charged particles coming from the Sun. Measurements of the geomagnetic field strength on the surface not only include the intrinsic magnetic field but also phenomena that arise due to this interaction. Some of these phenomena show regular variations without major effects and some, like solar storms, are able to disrupt the geomagnetic field, affecting technological systems. In order to quantify how harmful disruptive events are, it is important to determine the regular variations first. In this paper, we determine the regular variations within the signal (baselines) by applying signal filtering techniques on geomagnetic field measurements. Our analysis shows that regular variations during undisturbed days in low- and mid-latitude ranges are captured accurately.

1. Introduction

Ground magnetic observatories continuously monitor the evolution of Earth's magnetic field, producing high quality magnetic field measurements at stable locations. These measurements display a high degree of variability as the geomagnetic field is a superposition of various sources spanning a wide amplitude-frequency spectrum (Constable & Constable, 2004). These sources can operate on overlapping frequencies and their spatial and temporal separation is an active field of research requiring sophisticated modeling techniques (Wardinski & Thébault, 2019, and references therein). Internal sources comprise the main field that is generated within the fluid outer core by geodynamo processes; the lithospheric field as a result of the superposition of induced and remnant magnetisation of the Earth's sub-surface rocks; and the oceanic circulation, tidal and induction effects. The most prominent temporal feature of the internal part is the variation of the main field, the so-called secular variation, noticeable over periods exceeding a month. The main magnetic field accounts for over 93% of the magnetic field measured at the Earth's surface. The rest may be attributed to external sources with origins in the magnetosphere and ionosphere which temporal variations range from shorter than a few seconds to decades (Finlay et al., 2017). Among them, the Sun with its solar cycle induces variations with periods of around 11 years, as well as periods of 27 days due to its rotation (Kunagu et al., 2013; Ma et al., 2012; Shinbori et al., 2014). Disturbance events like solar flares and coronal mass ejections that hit Earth's magnetic field are able to induce sudden changes, within minutes to days, reaching relatively high amplitudes of over 100 nT within geomagnetic field measurements at low-to mid-latitudes (Cliver & Dietrich, 2013; Kozyreva et al., 2018). On days with no significant external influences, known as quiet days, the magnetic field, measured at a stable location on Earth's surface, features daily variations in the sense of a smooth curve. These variations have distinct contributions with periods of 24, 12, 8 and 6 hr (Campbell, 2003) and are mainly associated with the solar quiet (Sq) current systems at mid-latitudes. These systems feature two current cells, one in the northern hemisphere (NH) flowing anti-clockwise and one in the southern hemisphere (SH) flowing clockwise within the sunlit ionospheric dynamo region which are the result of ionisation by solar radiation (Campbell, 1989). They show peculiar seasonal and local time dependencies, being most intense during summer months in mid-latitudinal regions and reaching lowest amplitudes during the night when irradiation ceases (Hitchman et al., 1998; Shinbori et al., 2017; Takeda, 1999; Yamazaki & Maute, 2016).

Thus, magnetic field measurements are a rich source of information on various physical phenomena and processes affecting Earth. An important application of magnetic observatory measurements is the derivation of magnetic indices which quantify the overall geomagnetic activity or idealised physical processes like ionospheric and magnetospheric current systems (see Menvielle et al. (2011) for a comprehensive review). The three indices *Kp*, *aa* and *am* are sub-auroral magnetic activity indices endorsed by IAGA, the International Association of Geomagnetism and Aeronomy (https://www.iaga-aiga.org/). These indices rely on intermediate data-products of magnetic observatory time series, the so-called *K*-indices, having a temporal resolution of 3 hr. One of the main challenges when deriving magnetic indices is to separate the contributions of relevant sources from the rest of the magnetic field signal in an effective and timely manner. Generally, this is achieved by determining a so-called "baseline" which is extracted from the measurements. This definition of "baseline" is used throughout the present paper. As such, it should not be confused with the baseline used in other contexts, for example, in the calibration of magnetic observatory data. The first qualitative description of a baseline was given by Bartels et al. (1939) who defined it as a smooth and to-be-expected curve during a magnetically quiet day. At this epoch, its derivation included hand-scaling of such regular daily variation curves as identified by trained observers. Mayaud (1967) concretised this description to rules which act as guidelines. With the raise of the digital age and the increasing availability of magnetic data, the need for automatic determination of baselines has become imperative. In 1991, IAGA endorsed four algorithms to automatically determine the quiet baseline for *K*-indices (Menvielle et al., 1995) which includes the Finnish Meteorological Institute (FMI) method (Sucksdorff et al., 1991). The FMI method uses the observatory's magnetic latitude as input to derive baselines. The main geomagnetic field changes over time, thus magnetic coordinates evolve. They have to be calculated and adjusted following the time frame of availability of the international reference model (IGRF updated every 5-years).

With the potential of improvement given by data accessibility, many other techniques and methodologies have been developed during the past years. Some prominent examples include the baseline calculation for the PC index as introduced by Janzhura and Troshichev (2008), the method used by the International Monitor for Auroral Geomagnetic Effects (IMAGE) as described by Van De Kamp (2013) and the one used by SuperMAG as described by Gjerloev (2012).

In this paper, we introduce a direct and easily reproducible method to determine such magnetic field baselines for ground magnetic observatory measurements. It is based on fundamental signal treatment techniques and we investigate its applicability to produce baselines between 1991 and 2019. We limit our study to magnetic observatories located at low- and mid-latitudes and present physical analysis and interpretation of contributing sources during magnetically quiet periods.

The geomagnetic field data and derivation of the baselines are described in Section 2. Section 3 analyses observed variations within the different frequency regimes, which are related to physical phenomena during magnetically quiet periods in Section 4. Section 5 demonstrates the baseline and compares it to other methods, followed by the conclusion (Section 6).

2. Data

Vectorial geomagnetic field measurements from magnetic observatories between 1991 and 2019, covering more than two solar cycles, are used. The measurements have a temporal resolution of 1 min, that is, one day comprises 1440 data points. They are made available through the International Real-time Magnetic Observatory

Table 1
Finite Impulse Response (FIR) Filters, Corresponding Passing Frequencies and Their Notation

Signal contribution	Pass frequencies	Notation	
Long-term	below 7.716×10^{-6} Hz	$x_{>24}$	$y_{>24}$
Diurnal	7.716×10^{-6}–1.1574×10^{-5} Hz	x_{24}	y_{24}
Semi-diurnal	1.1574×10^{-5}–2.3148×10^{-5} Hz	x_{12}	y_{12}
8 hr	2.3148×10^{-5}–3.4722×10^{-5} Hz	x_8	y_8
6 hr	3.4722×10^{-5}–4.6296×10^{-5} Hz	x_6	y_6

Note. The sum of the five filter outputs forms the baselines x_B and y_B.

Network (INTERMAGNET, https://intermagnet.github.io/) data repository which ensures high quality data with consistent observing practices regarding modern standard specifications for measurement procedures and recording equipment. The use of definitive data, that is, fully calibrated magnetic observatory data, rather than variational data issued from direct outputs of instruments, allows to fully assess the magnitude of the various contributions and to take advantage of the homogeneous and continuous time series.

In the following, we consider the horizontal components of the magnetic field in the local spherical frame, namely X towards the geographic North and Y towards the geographic East (H being the intensity of the magnetic field in the horizontal plane, i.e., $H = \sqrt{X^2 + Y^2}$). We concentrate on observatories in regions with magnetic latitudes between $\pm 10°$ and $\pm 60°$ in eccentric dipole coordinates (Laundal & Richmond, 2016). This constraint allows to mitigate influences from equatorial and auroral electrojets at equatorial and high magnetic latitudes.

To illustrate our results, we primarily use data from the magnetic observatory Chambon-la-Forêt (CLF) located in France, Europe, with geographic latitude 48.025°. It is located in mid-latitudes and can thus be considered a representative example. Other observatories are used when applicable.

A list of all used observatories (location and used data) is enclosed as Supporting Information S1.

2.1. Baseline Derivation

Magnetic field measurements may be viewed as discrete time signals consisting of the superposition of various sources. In order to extract specific frequency contributions, a finite impulse response (FIR) filter is applied. For the truncation, we make use of the Hamming window function to smooth the convolution operation in the frequency domain with a window-size of 3 days, that is, 3 days correspond to 4320 min/data-points. These filtering techniques and window functions are standard tools in signal processing described in corresponding books, for example, Proakis and Manolakis (2006). Similar numerical filters have been used to remove diurnal components from ground magnetic measurements, see for example, Behannon and Ness (1966a); Behannon and Ness (1966b); Ness and Williams (1966); Bhargava and Yacob (1970); Jadhav et al. (2002).

The main contributions to the quiet daily variations are to be found within the periods of 24, 12, 8 and 6 hr in low- and mid-latitudinal regions. Additionally to these (sub-) diurnal variations, a smooth change of the geomagnetic field is induced by sources acting above the 24 hr timescales (like the secular variation). These considerations result in a total of five filters. To extract long-term variations, we use a low-pass filter with cut-off frequency of 7.716×10^{-6} Hz corresponding to variations above 36 hr within the signal. For the four (sub-) diurnal frequencies, we eventually use band-pass filters that are implemented with the help of low-pass filters. To extract the 24-hr variations, we apply a low-pass filter with cut-off frequency of $1/24\text{hr} = 1.1574 \times 10^{-5}$ Hz on the signal, from which we subtract the output of the long-term filter. The 12-hr variations are then computed as the difference between the low-pass filter with cut-off frequency of $1/12\text{hr} = 2.3148 \times 10^{-5}$ Hz applied on the signal and the sum of the outputs of the 24 hr band-pass and the long-term filter. The 8 and 6 hr band-pass filters are implemented analogously. The filters are applied to the horizontal components X and Y of the geomagnetic field measurements. In the following, we label the magnetic observatory measurements in capital X, Y, and the filter outputs in lower-case x, y with the corresponding period range as subscript, as summarised in Table 1. The sources of the quiet geomagnetic field superpose each other and accordingly the baseline per component is defined as the sum of the five filter outputs, that is, the baseline for X is $x_B = x_{>24} + x_{24} + x_{12} + x_8 + x_6$ and for Y is $y_B = y_{>24} + y_{24} + y_{12} + y_8 + y_6$. These baselines are direct filter outputs and thus totally independent of any apriori information regarding the position of the considered magnetic observatory or of the local time. Figure 1 shows an example of the decomposition of X and Y from CLF by each of the filters in the five upper panels. The baseline is demonstrated in the sixth panel (in red) plotted together with the measurements (in black). The residuals are calculated as the difference between the magnetic observatory measurements and the defined baseline, visualised in the bottom panel.

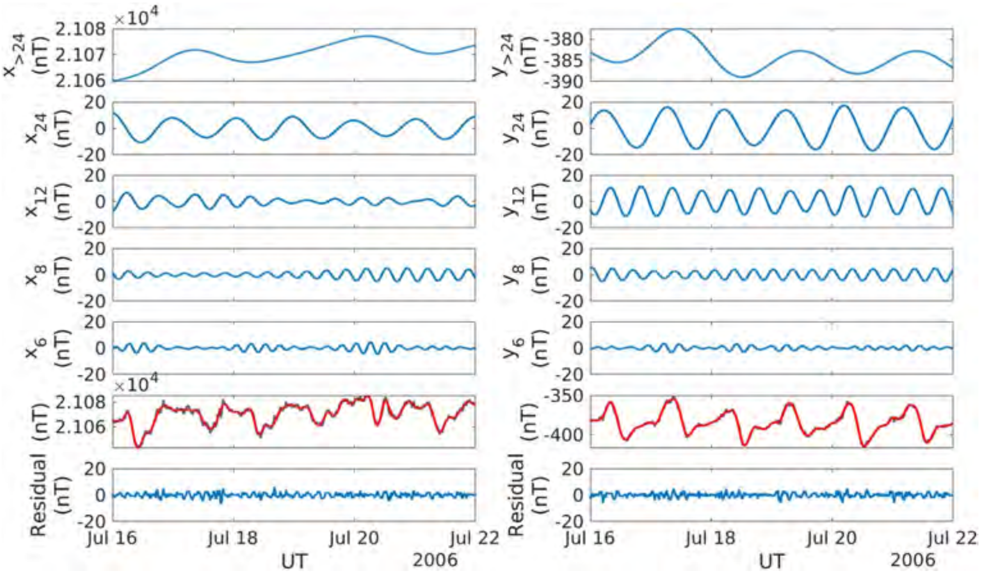

Figure 1. Decomposition of *X* (left) and *Y* (right) measurements at Chambon-la-Forêt over 6 quiet days. From top to bottom: the five consecutive finite impulse response filters; comparison of measured magnetic field component (black) with the determined quiet baseline (red); residuals calculated as difference between measurements and baseline.

2.2. Selection of Magnetically Quiet Days

In order to understand which quiet sources are contained within our filter baseline, we have to study its variations during geomagnetically quiet periods. Therefore, we select time intervals for which the contribution of disturbance events from external sources like geomagnetic storms is minimised. To do so, we need to use an independent indicator regarding the quietness of the considered days. The quietest CK-days ("Really Quiet (C)" and "Quiet (K)", http://isgi.unistra.fr/events_ckdays.php) are IAGA-endorsed data products provided by the International Service of Geomagnetic Indices (ISGI, http://isgi.unistra.fr/). They indicate magnetically quietest days by using the *aa* index (Mayaud, 1972), with a mean lower than 13 nT. Two data products exist: the quietest days over 24-hr (CK24) and over 48-hr (CK48) centered on the UT day. We thus choose the CK48 days in order to be as strict as possible in ensuring the minimisation of external disturbance contributions within the magnetic field measurements. Indeed, between 1991 and 2019, there is a total of 3 040 CK48 days. The amount of quiet days per year is not evenly distributed (see bottom panel of Figure 2) and clearly anti-correlated with solar activity (top panel). To quantify solar cycle and solar activity, we use the well defined daily F10.7 index, measured in solar flux units (sfu), see Tapping (2013) for an overview.

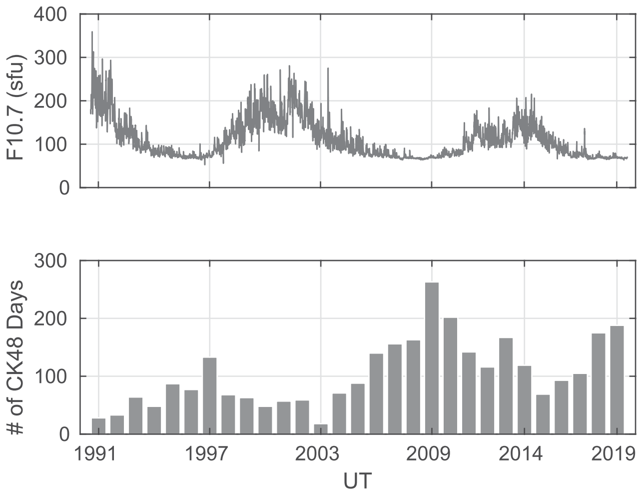

Figure 2. Solar activity and quiet days between 1991 and 2019. The upper panel depicts the F10.7 daily values in solar flux units, while the lower panel indicates the amount of magnetically really quiet (CK48) days per year.

3. Variations of the Filter Outputs

In this section, we first present the filter outputs during the entire considered period, revealing their global variations. These results lead us to deeper investigate the variations within the combined daily filter outputs during magnetically quiet periods only.

3.1. Filter Outputs

3.1.1. Long-Term Filters

The long-term filters preserve all contributions with periods above 36 hr. Their outputs $x_{>24}$ and $y_{>24}$ are shown in Figure 3 for CLF. The upper panels show variations over 29 years (1991–2019), whereas the lower panels focus on a three month period (October–December 2007) comparing long-term filters (blue) with the magnetic observatory measurements *X*, *Y* (grey). The

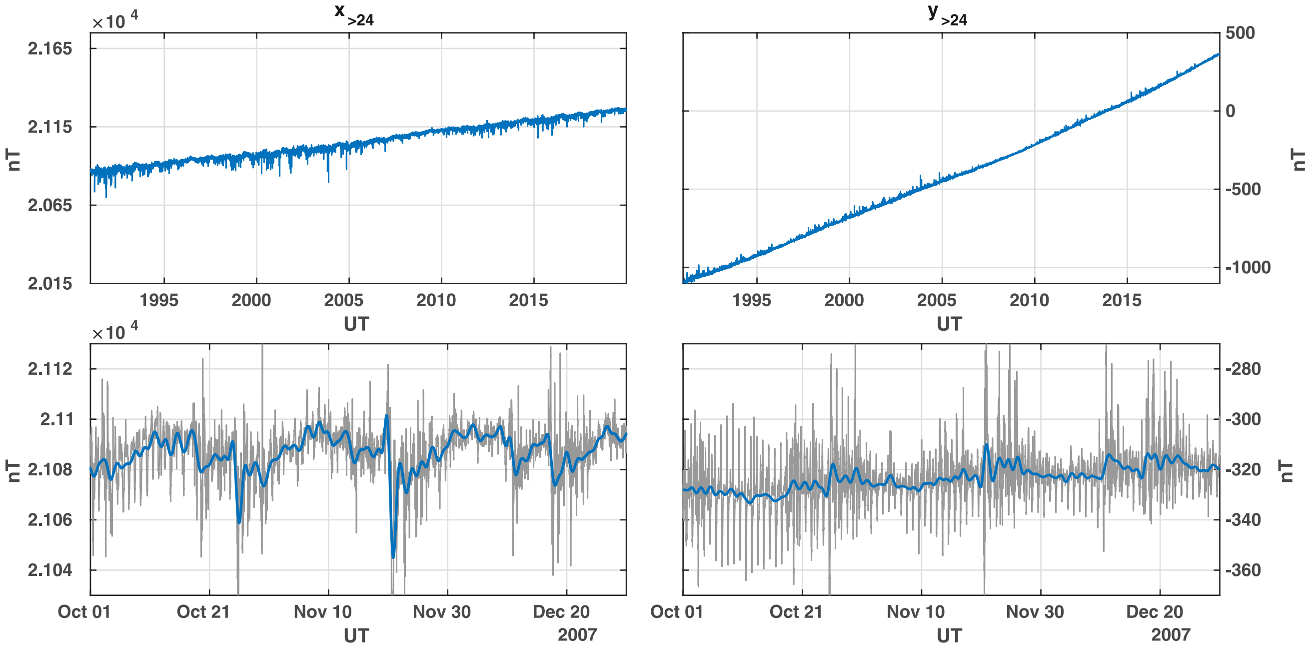

Figure 3. Variations within the long-term contributions $x_{>24}$ (left panels) and $y_{>24}$ (right panels) in blue for Chambon-la-Forêt. Upper panels demonstrate the long-term trend over 29 years, while the lower panels present a zoomed-in view of 3 months whereby the magnetic components X, Y are indicated in grey.

upper left panel shows a steady increase in $x_{>24}$ of about 570 nT, with shorter fluctuations of up to 300 nT during the considered time-interval. Similarly, the right upper panel shows a steady, but steeper increase of $y_{>24}$ (around 1500 nT), transitioning from negative to positive values around 2014, with shorter fluctuations in the order of tens of nanotesla. The lower panels illustrate variations in the 27-days regime which are very clear for $x_{>24}$ and less clear, but still present, for $y_{>24}$. Physical processes that are responsible for these variations are discussed in Section 4.1.

3.1.2. 24h, 12h, 8h and 6h Filters

In this subsection, we look at the global patterns of the 24, 12, 8 and 6 hr filter outputs of the X and Y components at CLF and the combined daily signal containing the sum of the four filter outputs: $x_D = x_{24} + x_{12} + x_8 + x_6$ and $y_D = y_{24} + y_{12} + y_8 + y_6$. They are presented in Figures 4 and 5 with respect to local time and day of year, alongside the F10.7 index to facilitate comparisons with solar cycle phases. For demonstration purposes, we illustrate dependencies on local time, season and solar activity corresponding to variable solar irradiation conditions over approximately one solar cycle between 2000 and 2012. The analog figures for the entire period 1991–2019 can be found in Supporting Information S1.

We first focus on the individual filter outputs which are presented in the four central panels of Figure 4 for X and of Figure 5 for Y. Comparisons to F10.7 (top panels) show that the level of magnetic activity of each filter output, especially the 24 hr ones, is higher during the maximum phase of the solar cycle. Periodical patterns can be observed with respect to day-of-year and, more specifically, season and local time with diurnal, semi-diurnal, 8 and 6 hr recurrence for each individual filter output. These patterns can be disturbed from 1 day to the other by magnetospheric processes enhancing the level of magnetic activity, especially during the maximum of the solar cycle. Finally, the filter outputs contributing to the X component are in general twice as less intense as the ones contributing to the Y component. More specifically, for the X component, the 24 hr filter is by far the most intense, the 12, 8 and 6 hr filter contributions being secondary, while for the Y component the 24 and 12 hr filters are more comparable in intensity.

Second, we look at the combined daily signals x_D and y_D presented in the lowest panels of Figures 4 and 5. Similar to the individual filter outputs, y_D is twice as intense as x_D. For both, the periodical patterns remain clear and highlight solar cycle, seasonal and daily variations with enhanced activity during solar maximum (around 2002), summer periods and daylight hours. x_D has a seasonal-dependent minimum around local noon which is surrounded

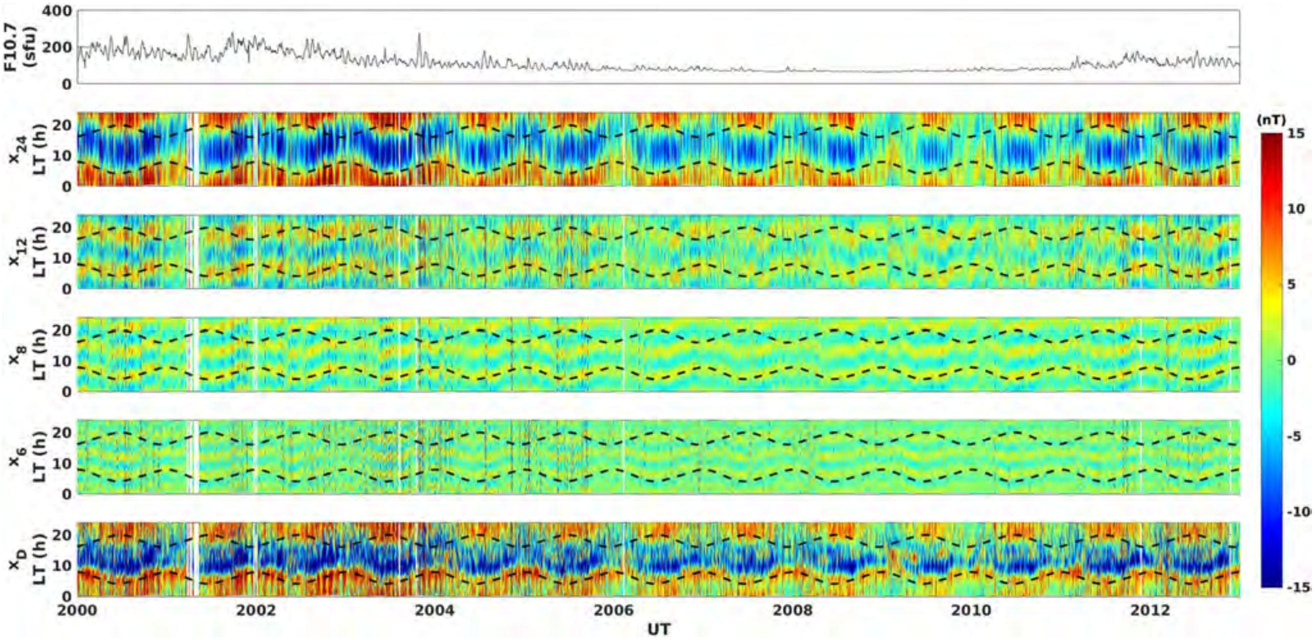

Figure 4. Filter outputs between 2000 and 2012 as function of solar local time (LT) for the *X* component of Chambon-la-Forêt. From top to bottom: the F10.7 daily values in solar flux units; x_{24}; x_{12}; x_8; x_6 and x_D in nT. Dashed black lines indicate local time for sunrise (morning hours) and sunset (evening hours). Periods with unavailable data are not represented and appear as white vertical stripes. Note that the limits of the colour-scale range from −15 to 15 nT.

by two positive crests of activity around dawn and dusk (at least during summer). y_D has a maximum followed by a minimum of activity, with the zero-crossing centred around local noon, which shows no clear dependency on season. We superimposed the occurrence of sunrise and sunset at 110 km altitude on corresponding panels in Figures 4 and 5 (black dashed lines). The activity increase is well phased with sunrise for both combined signals, while the activity decrease is more complex to associate with sunset. A clear reduction of the activity is observed in the night time for y_D where it almost reaches zero, implying that all filter outputs added together cancel out,

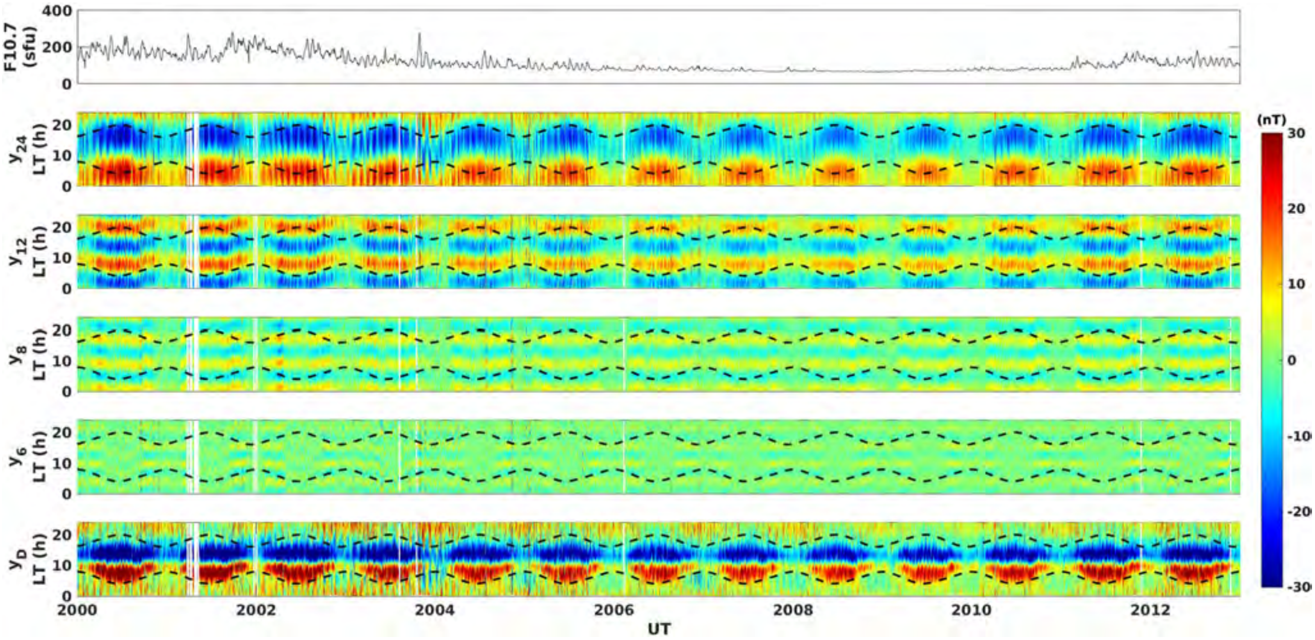

Figure 5. Analog to Figure 4 for the *Y* component of Chambon-la-Forêt. Note that the limits of the colour-scale range from −30 to 30 nT.

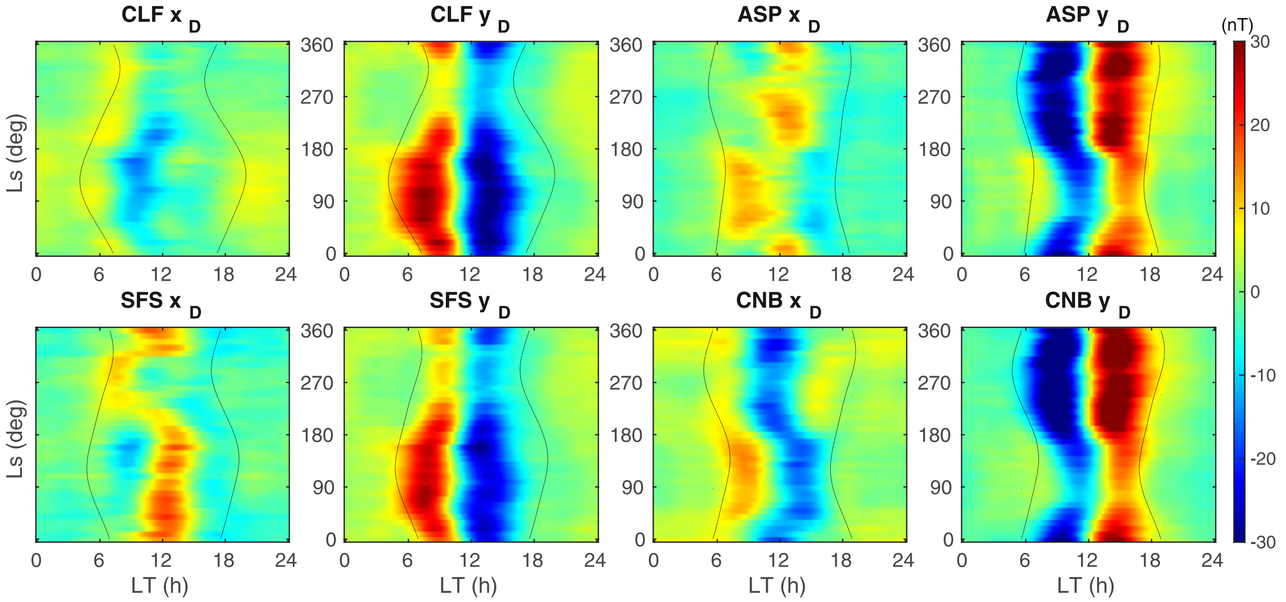

Figure 6. Super-posed epoch analysis of the combined signals x_D and y_D, depending on local time and season for two European observatories (CLF, SFS) and two Australian observatories (ASP, CNB), during magnetically quiet days. Black lines indicate local sunrise (morning hours) and sunset (evening hours). Note that the colour-scale is the same for all panels.

showing that only the combination of the individual filters is physically meaningful. The combined signal x_D still displays night-side activity especially during solar maximum, but also in summer nights during solar minimum.

3.2. Variations of the Combined Daily Filters During Magnetically Quiet Periods

The previous section showed a clear trend within the long-term filters that follows secular variation (see Section 4.1). There are evident dependencies of the combined daily filters on season and local time. However, all filter outputs also contain obvious storm signatures which potentially mask out the quiet magnetic variations. As we would like to better understand the quiet sources that contribute to the combined daily filters, we need to avoid storm signatures as much as possible and thus, we constrain the following analysis to magnetically quiet periods only.

3.2.1. Seasonal and Local Time Patterns

To gain a better understanding of the variations within the combined daily filter outputs, we focus on their local time and seasonal dependencies. We show examples for several observatories at low and mid-latitudes, where the signatures of equatorial and auroral electrojets are minimized, and during magnetically quiet periods as defined in Section 2.2. Per magnetic observatory, we conduct a super-posed epoch analysis (SEA) of x_D and y_D in dependence of solar local time and day of year (season) for CK48 days between 1991 and 2019 (see Figure 2). The season can be described by the solar longitude $Ls \in (0°, 360°)$ which is derived from the position of Earth around the Sun, whereby $Ls = 0°$ defines spring equinox in the NH. The data is arranged into bins of $\Delta Ls = 10°$ (vertical axis) and $\Delta LT = 10$ min (horizontal axis). The value per bin is derived as the average of all values that belong to the specific bin. Here we present four representative stations in detail. The SEA of further stations may be found in Supporting Information S1. The selection of specific observatories presented in this study is motivated by the need to examine the baseline properties in both hemispheres and in different geographic sectors while ensuring that the length of considered time series is sufficient to produce meaningful statistics. The period for which data is available at each observatory can be found in Supporting Information S1. Nevertheless, an exhaustive examination of the baselines obtained shows consistent results, indicating that the filtering method is applicable for all INTERMAGNET observatories at low and mid-latitudes.

Figure 6 presents the resulting SEA for two European observatories: CLF and San Fernando (SFS), and two Australian observatories: Alice Springs (ASP) and Canberra (CNB). Note that they are located in latitude from

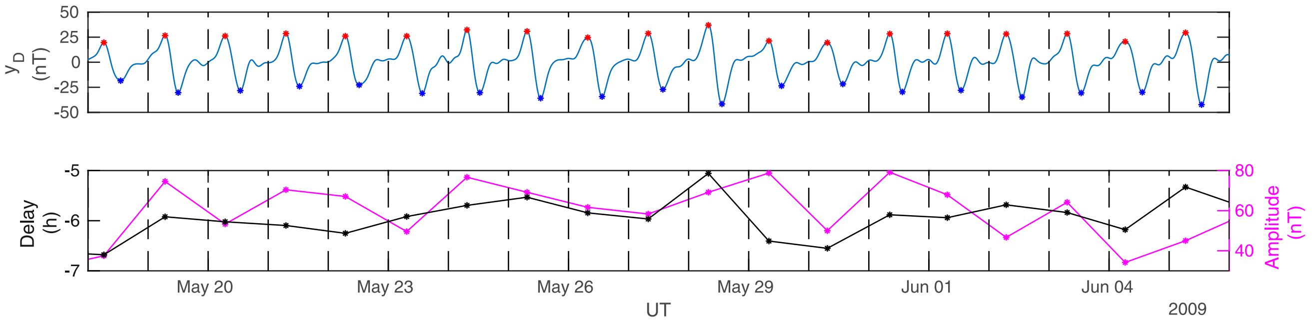

Figure 7. Day-to-day variability of y_D at Chambon-la-Forêt. The upper panel depicts the daily evolution of y_D (blue) with daily maximum/minimum marked by red/blue dots. The lower panel presents the variations in delay (black) and amplitude (magenta) between maxima and consecutive minima.

North to South in this order. The black lines indicate the mean local sunrise (morning hours) and sunset (evening hours) at an altitude of 110 km between 1991 and 2019. The upper left panels show the SEA for CLF. The combined filter output y_D describes a maximum during morning and a minimum during afternoon hours, almost vanishing during night times throughout the year. The increase in activity during morning hours strictly follows local sunrise, appearing earlier during summer than during winter, while the activity decreases rather constantly in the afternoon around 15 hr LT, except during winter solstice. In addition to the prolonged activity, the signal intensity is stronger during summer (in NH $Ls = 90°$) than during winter (in NH $Ls = 270°$). One of the most striking features is the relatively constant zero-crossing of the activity around noon for y_D. The pattern of x_D is less clear. As noted in the global patterns before, the dawn crest of activity is well phased with sunrise and is present throughout the solar longitude, while the minimum and the dusk crest that extends into the pre-midnight hours, are mainly observed during summer and autumn.

SFS is located South of CLF and its SEA is presented in the lower left panels of Figure 6. Its y_D shows a remarkably similar pattern as CLF, being well phased with sunrise and to a lesser extent with sunset. The main difference to CLF lies within its x_D which describes a maximum around local noon from spring to autumn. Around autumn equinox ($Ls = 180°$), the maximum abruptly shifts to morning hours and returns to noon hours shortly after winter solstice ($Ls = 270°$). On the other hand, no clear activity is observed during night, at dawn, or at dusk and only a rather limited minimum is observed after dawn during summer.

The solar longitude describes the season reversely in each hemisphere, for example, summer in SH is at $Ls = 270°$ and winter at $Ls = 90°$. ASP is located in the SH and its SEA is presented in the top right panels of Figure 6. The combined signal y_D describes a minimum in the morning hours and a maximum during afternoon hours, as opposed to NH stations, with stronger amplitudes during summer. As for NH observatories, y_D is well phased with sunrise and additionally with sunset. The only exception is during winter at sunrise, when a local and fainter maximum can be observed. The combined signal x_D is not as clearly phased with sunrise. During spring ($Ls = 180°$) and autumn equinox ($Ls = 0°$), x_D shows a maximum around noon. Similar to SFS in the NH, the maximum shifts to morning hours shortly after autumn equinox and returns to noon hours at spring equinox.

CNB is situated south of ASP and analogously shows a remarkably similar behaviour in y_D. x_D has a minimum during day-light hours that shifts to later LT between autumn and spring equinox. During local winter, x_D shows also a local maximum in the morning hours.

These global patterns may be interpreted as magnetic footprints of current cells flowing anti-clockwise in the NH and clockwise in the SH, following the apparent motion of the sun. The focus would be located between CLF and ASP for the northern cell and between CNB and ASP for the southern one. More physical interpretation of these results are given in subsection 4.2.

3.2.2. Day-To-Day Variability

The combined filter outputs x_D and y_D not only vary on seasonal timescales but also on a day-to-day basis, even during quiet periods. This behaviour can be followed on the top panel of Figure 7 where CLF's y_D is plotted over consecutive CK48 days during summer 2009. We see a recurrent sinusoidal pattern during sunlit hours which amplitude and occurrence times of maxima (red stars) and minima (blue stars) vary from one day to the other.

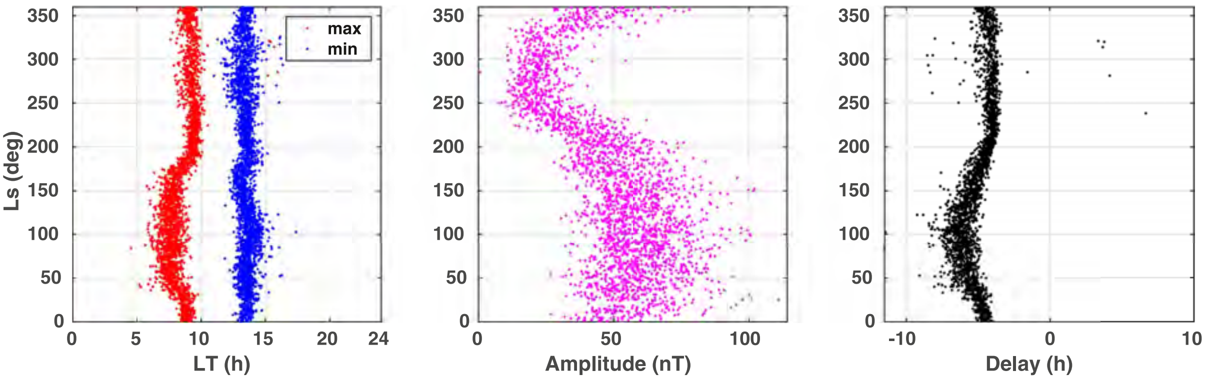

Figure 8. Statistics of seasonal and day-to-day variability of y_D at Chambon-la-Forêt during quiet days between 1991 and 2019. From left to right, the panels show local time occurrence of extrema, amplitude and delay between them.

To illustrate this variability quantitatively, we first determine the local time occurrence of the maximum and minimum for each day during sunlit hours. Then, the amplitude is derived as the difference between the values at maximum and at the consecutive minimum (given in nanoteslas) and finally, the delay is given as the time in hours that has passed to reach the consecutive minimum from the maximum. The bottom panel of Figure 7 illustrates these amplitudes (magenta) and delays (black) from 1 day to the next. The amplitude varies significantly on a daily basis between 20 and 80 nT, as does the delay between 5 and 8 hr in this example.

We compute the day-to-day parameters, that is, the occurrence times of extrema, peak-to-peak ampitudes and delays, for y_D at CLF for all quiet days between 1991 and 2019. They are presented as a scatter-plot against solar longitude in Figure 8 and from which it is clear that the day-to-day variability has a strong seasonal dependency. For the maximum, two regimes can be distinguished: during summer months the maxima occur around 06–09 hr LT, while they occur later at around 09–10 hr LT during winter, which is directly related to the LT sunrise shift with season as already seen in the previous section. The transition between these two regimes happens abruptly around $Ls = 10°$ and $Ls = 180°$. On the other hand, the timing of the minimum is more constant over time, which, too, is related to the decrease of activity observed constantly around 15 hr LT in Figure 6. The central panel shows a clear sinusoidal dependency of the amplitude on the season. This dependency can be described by a 4th order polynomial fit which summer maximum is 63 nT and winter maximum 23 nT, indicating that the amplitude during summer is about 3 times larger than during winter. Finally, the right panel shows that the delay between maximum and consecutive minimum is longer during summer (around 6–7 hr) than during winter (around 5 hr).

For x_D, the definition of a maximum and minimum (and successively delay and amplitude) during sunlit hours is not applicable. Its trend generally has only one extremum during the day (see Figure 6) which visualisation analog to Figure 8 can be found in Supporting Information S1. The timing of its minimum at CLF shows a distinct shift of approximately 2 hr around equinox (starting around 08 hr LT between spring and summer and around 10 hr LT during autumn and winter) which is comparable to the shift observed in y_D. The amplitude of the minimum has a similar trend to what is observed for the peak-to-peak amplitude of y_D: a polynomial fit of order 3 can be used to describe its variations. The summer minimum is around -15 nT and the spring minimum is around -5 nT, indicating that the summer amplitude is 3 times larger than during spring.

Returning to the day-to-day variability of the signal, it is clear from Figure 8 that, for any given Ls, a spread is observed in all three parameters of interest: local time occurrence of extrema, amplitude and delay for y_D. This spread is higher during solstices than during equinoxes, and is also doubled during summer with respect to winter. For the amplitude, the standard deviation is 12.17 nT for the summer period ($45° < Ls < 135°$) and 7.8 nT during winter ($225° < Ls < 315°$), suggesting that the spread during summer increases by over 60% compared to winter. For x_D amplitude, the standard deviation, however, is rather constant, with maximum differences of 20%.

Overall, we see a total day-to-day variability in amplitude for y_D of about 20%–30% and for x_D of about 20%.

4. Physical Sources Within the Baseline

In this section, we relate the characteristic variations of the filter outputs, that is, the baseline elements, to sources that are known to contribute to the quiet geomagnetic field.

4.1. Secular Variation

The secular variation is the evolution of Earth's intrinsic magnetic field over time that induces a smooth shift within geomagnetic field measurements at stable ground locations. The magnetic pole configuration is such that the magnetic North Pole moves closer to Europe (Olsen & Mandea, 2007) and thus CLF is slowly drifting to higher magnetic latitudes, enhancing the magnetic field intensity at its location. This increase in field strength can be observed in each component of the magnetic field measured at CLF and in particular here in both $x_{>24}$ and $y_{>24}$ (see the upper panels of Figure 3). The magnitude of $y_{>24}$ is lower than that of $x_{>24}$ as the magnetic meridian is close to geographic North (equal in 2014 when $Y = 0$ and thus declination was zero at that point). Furthermore, $y_{>24}$ shows less short-time variability than $x_{>24}$, as it is proportionally less affected by fluctuations from external sources. The observed 27-day variation is in agreement with Briggs (1984) and Van De Kamp (2013) who attribute these to either the solar rotation period or tidal variations that arise from the interaction between solar-quiet and lunar tides. However, we cannot exclude the possibility that these variations are a superposition of sources enhancing each other within the same frequency range. Here we would like to point out, that signatures of geomagnetic storms are identifiable within the long-term filters. For example, the famous Halloween storms in 2003 can be clearly identified in both, $x_{>}$ 24 and $y_{>}$ 24.

4.2. Seasonal and Local Time Patterns of the Quiet Daily Variations

The analysis presented in Figure 6 is in good agreement with the magnetic footprints one expects from the solar quiet current cells flowing at an altitude of about 110 km above the magnetic observatories, that is, the increase of activity at sunrise, the inversion of the x_D variations for locally close observatories (e.g., CLF vs. SFS, ASP vs. CNB) and the inversion of the y_D variations between observatories located in different hemispheres (e.g., CLF vs. CNB). This implies that the combined filter output from the 24, 12, 8 and 6 hr filters are the major contributors to the Sq currents.

While the overall day-side patterns of x_D and y_D are clearly related to the Sq currents, some specific details in Figure 6 demand further discussion. When useful and applicable, we refer to additional stations which can be found in Supporting Information S1. First, x_D of CLF and CNB, and to a lesser extent y_D, show some remnant activity in the night-side, which is in contrast to stations located closer to the equator (SFS and ASP). This feature is also observed for stations over Northern America and Northern Asia (see Supporting Information S1). The night-side enhancements may be related to the closer proximity of the stations to the auroral electrojets. These currents essentially flow azimuthally (i.e., affecting mainly the magnetic X component), increasing in intensity during summer and are modulated by substorm activity with recurrence rates of about 2–4 hr (Smith et al., 2017). Nevertheless, the level of night-side activity remains generally very weak (below 5 nT), as expected for quiet days. For disturbed days, this activity is enhanced as seen on Figures 4 and 5.

On the day-side, y_D is remarkably stable from one station to the other, having opposite signs between hemispheres. For all stations, the intensification is phased with season, being higher during summer when solar illumination is stronger. The activity follows the local sunrise smoothly, but decreases drastically before sunset, around 15 hr LT, at least in NH. While it is easy to understand that solar illumination is the primary factor triggering the Sq current flow by enhancing locally neutral winds and electron density, it is less evident why the current should decrease before sunset. As for the neutral atmosphere, we looked at various critical parameters given by empirical state-of-the-art models during the same very quiet periods, such as neutral winds (HWM-14, see Drob et al. (2015)), neutral densities, temperature and pressure (NRLMSISE-00, see Picone et al. (2002)). No relationship between the variations of these parameters and the observed constant decrease around 15 hr LT was evident. This analysis was conducted with empirical models which may explain the difficulty to correlate the Sq magnetic variations with thermospheric parameters. More investigations on this topic are necessary and could invoke some kind of saturation of the atmosphere.

Whereas y_D has a clear pattern, x_D shows a more complex day-side behaviour. The *X* component of the Sq current, and thus the x_D filter, indicates the position of the observatory with respect to the current cell's focus location. For an ideal current cell with a circular shape, a negative (positive) x_D component indicates that the station is located above (below) the focus. When x_D is close to zero, the station is beneath the cell's focus. A stable pattern with smooth variations in x_D (apart from the expected decrease of the activity during winter when solar illumination decreases) is observed for stations located far of the Sq current cell focus (for examples see Supporting Information S1 SEA for: MMB and PHU over Asia, FRD and SJG over North America, WNG and GUI over Europe, KDU over Australia). However, stations South of the Sq current focus in Europe show less smooth and stable patterns with respect to SJG and PHU. This may be related to the tilted position of the magnetic equator, deforming the southern part of the Sq cell. Stations close to the Sq cell focus show a more complex pattern, particularly for CLF, SFS (and KNY in Supporting Information S1) in NH and ASP and CNB in SH. First, the overall x_D component is weaker, confirming the proximity of the Sq cell focus. Second, variations of the minimum/maximum of x_D in local time with respect to season reflects variations either of the Sq focus position and/or of the Sq cell shape and size (Stening, 2008; Stening et al., 2007).

As shown by Yamazaki et al. (2011), the local time of the cell's focus shifts to earlier times during summer compared to winter months, which is in agreement with the morning shift of the minimum occurrence of x_D observed at CLF and CNB (see blue feature of x_D in Figure 6), situated at slightly higher latitudes than the Sq focus. CLF is closer to this Sq focus than CNB, as its minimum almost disappears during winter. This may be an indication that the Sq focus also moves to higher latitudes during winter and that the Sq cell almost disappears (which is in agreement with Soloviev et al. (2019)). This behaviour is also confirmed at SFS, when between summer and fall equinox, a minimum is followed by a maximum, showing that the Sq focus is likely to be very close to SFS and moves from above to beneath the focus during the course of a day, as proposed by Anad et al. (2016). This behaviour is also seen at KNY and less clearly at TUC (see Supporting Information S1). The x_D component at ASP behaves similarly to SFS, but presumably never crosses the Sq focus during summer, since no real minimum is observed during morning hours.

A last intriguing feature is observed in y_D just before sunrise during local winter, when a local minimum is observed at CLF and SFS and a local maximum at ASP and CNB (see again Figure 6). This behaviour is difficult to explain from the Sq current cell system alone. Considering the possibility of inter-hemispheric field-aligned-currents (IHFACs), as analysed by for example, Olsen (1997) and Park et al. (2011), such currents should flow at dawn. As Shinbori et al. (2017) stated, the *Y* component of the magnetic field is the most susceptible to be perturbed by the presence of IHFACs. Thus, this local minimum/maximum before sunrise could encompass magnetic variations associated with such dawn IHFACs. The dawn minimum is fainter above North America (see Supporting Information S1), which is consistent with the findings of Lühr et al. (2015), that IHFACs are more intense above Europe and almost disappear above North America. Again, the level of activity of this feature is low. The x_D component also has a local maximum centred just after sunrise during local winter at ASP, SFS, CNB (and KNY). The cause of this structure still remains unclear but may also be related to such IHFACs.

Overall, it is clear from this section that x_D and y_D capture the Sq current cell properties well.

4.3. Day-To-Day Variability

Figures 7 and 8 demonstrate a non-negligible day-to-day variability of the combined filter outputs x_D and y_D which is more pronounced during summer. This phenomenon has been observed in the majority of physical and electro-dynamical parameters of the ionosphere for more than 40 years and is well documented for Sq currents in the literature (see e.g., Brown and Williams (1969); Greener and Schlapp (1979); Schlapp (1968); Takeda (1984); Yamazaki and Maute (2016)). Simulations from Yamazaki et al. (2016) showed that variations within the Sq current can be attributed to 75% to solar illumination and to 25% to atmospheric and magnetospheric drivers. Forbes et al. (2000) found that around 25%–30% of the plasma peak density variations in the 1–2 hr to days range in the F-region can be attributed to meteorological phenomena. The day-to-day variabilities found in our study are in the order of 20%–30% for the amplitude of x_D and y_D, which is consistent with these previous studies. Additionally, the results presented in Figure 8 reveal two intriguing properties of the day-to-day variability:

- The occurrence in local time of the maxima and minima, as well as the delay among them has a clear dependency on season.

- The spread of the amplitude is clearly dependent on season.

Our analysis minimises magnetospheric influences by taking into account only very quiet magnetic conditions. However, on such quiet days, solar flares may still occur and disturb the signal. To investigate on this, we excluded all quiet days on which X and M class solar flares were recorded during daylight hours and re-ran our analysis. Expectably, the percentages of day-to-day variability did not change significantly. Flares can have very strong effects on the ionospheric ionization and thus on the associated currents, but their influences are only present for a very limited time (Liu et al., 1996).

These considerations lead us to conclude that the majority of the observed day-to-day variability may be attributed to atmospheric drivers only, which underlying processes become stronger with increasing solar illumination, confirming the neutral atmosphere as a key role.

Gravity waves and tides within the neutral atmosphere are known to exhibit complex interference behaviour that can drastically change from 1 day to another (Liu et al., 2018; Stening et al., 2005). For example, the lunar tide induced by the revolution of the moon around Earth has a period of 12.4 hr which is very close to that of the solar semi-diurnal one. The small difference in period may lead to a smooth drift of the contributions of x_D and y_D, leading to amplification or reduction of the global signal over a course of a few days. Attempts to model such a lunar tide effect did not reproduce the variations of amplitude within the combined daily contributions x_D and y_D. This tends to conclude that several sources of tides and waves are involved in this phenomenon which remains challenging to model.

5. Comparison of Baselines During Magnetically Quiet Days

On days without major external influences, the magnetic field measurements follow regular daily variations that Bartels et al. (1939) describes as a to-be-expected smooth curve which philosophy persists till the present day. This definition implies that there is no quantitative way to evaluate the performance of baselines. We can, however, compare our baseline with existing and widely accepted counterparts like the FMI method and SuperMAG method. The mentioned PC index and IMAGE methods are designed for polar stations and auroral Scandinavian magnetometers respectively and thus are out of range for low- and mid-latitudes considered in this work.

To determine the baseline, the FMI method performs a 5th degree harmonic fit to hourly means, which are determined taking into account apriori information such as magnetic latitude and local time (Sucksdorff et al., 1991). The original software written in C is made available through the long-term ISGI repository. The method used by the SuperMAG service consists of determining its own field orientation, followed by a daily baseline, annual trend and residual offset that differs for each of the magnetic field vector components (Gjerloev, 2012). Their baseline data is not directly accessible and several steps had to be executed to make them available for this work. SuperMAG provides the actual and baseline removed data in a magnetic local frame that uses an arbitrary declination. In order to compare them to the original data as provided by observatories from INTERMAGNET, SuperMAG data needs to be transformed to the local geographic frame first, followed by subtracting the baseline removed data from the measurements in order to retrieve the baseline. Hereafter we compare our method to the FMI method, referred to as x_K, y_K; and to the SuperMAG method, referred to as x_S, y_S. As such, Figure 9 demonstrates our baseline (red) in comparison with the X, Y components (grey), the FMI (blue) and the SuperMAG (green) baselines, whereby grey shaded time intervals indicate non-CK48 days.

During magnetically quiet days (white background), our and FMI baselines closely follow the magnetic activity, capturing the day-to-day variability smoothly and showing little discrepancies between them. The SuperMAG baseline x_S, y_S shows some distinct differences, especially for the X component. The actual measurements are not always followed closely, for example, there is a clear positive and negative offset between the magnetic observatory data and SuperMAG estimation of the quiet baseline for the X component during the afternoon/night of 10 and 13th December. In general, the SuperMAG method follows a rather steady pattern showing minor differences from 1 day to another. As shown before, there is a non-negligible day-to-day variation within the signal, which is most likely induced by atmospheric drivers. These variations are well captured by x_B, y_B and x_K, y_K, but less with x_S, y_S indicating that it may tend to overestimate magnetospheric drivers during quiet days. To be able to qualitatively compare baselines, we calculate the difference between ours and each of the two other methods for all CK48 days of 2009. We make the simple assumption that this difference can be described by a Gaussian

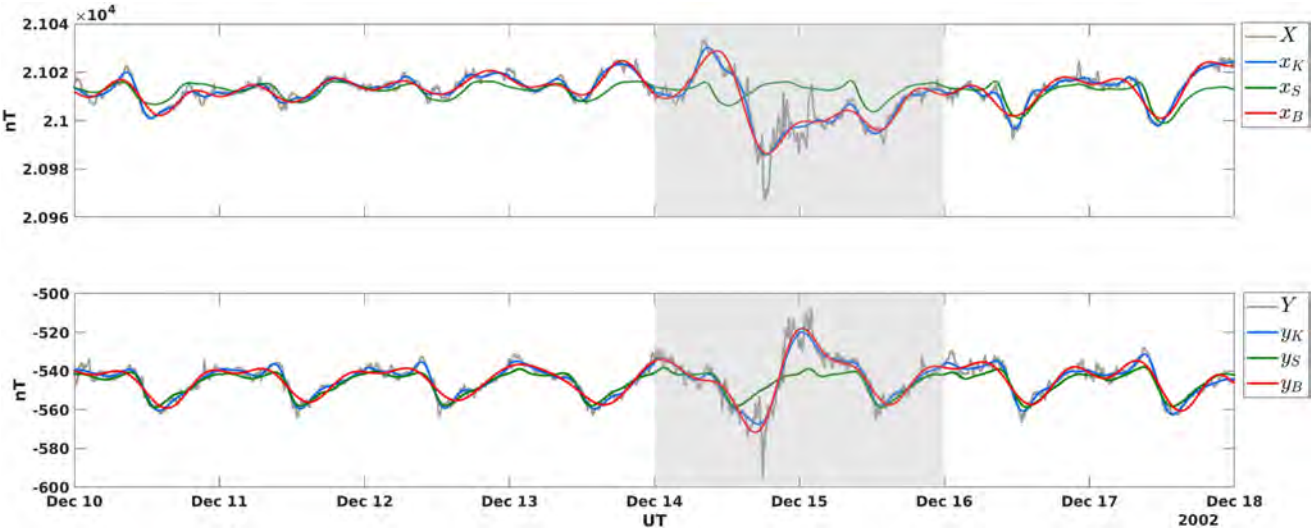

Figure 9. Comparison of baseline methods. The methods of the introduced baseline (red), Finnish Meteorological Institute (blue) and SuperMAG (green) for *X*, *Y* components (grey) at Chambon-la-Forêt during winter 2002 are presented. The grey shaded areas indicate non-CK48 days.

distribution, using its variance to quantify deviations. For the *X* component, we find a variance of 1.6 nT, and for the *Y* component 1.7 nT between our baselines and the FMI ones; and 6.2 nT, and 4.6 nT between our baselines and SuperMAG ones. This implies that our determination of baselines can be used instead of the FMI method without causing major changes in the baseline reconstruction during magnetically quiet days. Additionally, the filtering method produces baselines without any further information than the magnetic measurements themselves, whereas the FMI method needs the magnetic latitude as an input, which is evolving over time and not trivial to be determined in real-time. This property gives the filtering method the main advantage of being directly applicable, that is, as soon as the geomagnetic field data is available.

Giving a detailed analysis of our filtering method during disturbed magnetic periods would far exceed the scope of the present paper. However, we would like to add a few thoughts on the application of our method during non-quiet days. During non-CK48 days, indicated by the grey shaded area in Figure 9, clear differences between all three baseline methods are evident. Our filter method follows the activity very closely, including the depression and the following fluctuations on 14th December. These features are followed to a lesser extend by the FMI method. Contrarily, the SuperMAG baseline is insensitive to any of these storm effects in this example and follows a smooth curve from the last quiet day to the next quiet day. This may suggest that our filter and the FMI methods underestimate, whereas the SuperMAG may overestimate the actual storm activity and its effects. The implication for our filter approach is, that it is not directly applicable during disturbed periods, and thus quiet and storm time need to be treated separately (which is true for the SuperMAG and IMAGE methods as well). The discrimination between quiet and disturbed periods may be done by statistical measures, as has been done by Gjerloev (2012) and Van De Kamp (2013), and by additionally taking into account dependencies on season or solar activity. Furthermore, the fact that there is no quantitative way to validate quiet curves remains especially true during storm times. For example, in Figure 9 the SuperMAG baselines x_S and y_S during the two disturbed days are very similar to their quiet curve of the preceding day, which can be interpreted physically as a fully developed Sq current cell. However such a full system does not necessarily form during a disturbance event (Le Huy & Amory-Mazaudier, 2008) which may be even the case in this example, as the actual measurements are very different from the expected Sq current signature.

Another important observation is that signatures of storms, are also contained within the long-term filter as described in Section 4.2. This shows that all level of filters can be strongly modified during non-quiet periods, making our filter baseline not directly applicable outside quiet periods.

Future work will address the application of our filter method baseline for magnetically disturbed periods, focusing on the aforementioned considerations.

6. Conclusion

This paper introduces a method to directly determine baselines of geomagnetic field measurements during magnetically quiet periods in low- and mid-latitudinal regions. The method is based upon signal filtering techniques to extract long-term (with periods above 36 hr) and (sub-) diurnal (with periods of 24, 12, 8 and 6 hr) variations within the time-series of each magnetic component.

We conducted an exhaustive analysis of the contribution's variations, relating it to physical sources that are known to constitute the quiet geomagnetic field. The long-term filter includes the contributions induced by the secular variation, as well as tidal effects. The combined diurnal contributions have a strong dependency on local time and season and show the typical day-to-day variability which lets us confirm that the Sq current system is strongly modified by the underlying atmosphere. Furthermore, the results for the day-to-day variability as extracted by the filtering technique suggest that the amplitude and its spread around an expected value, as well as the occurrence of extrema, have a clear seasonal dependency. The filtering technique provides promising preliminary results and may be used for more thorough analysis of quiet Sq current systems in future works.

The baseline is then made up of the superposition of the long-term and the combined daily contributions. During magnetically quiet conditions our filter baseline smoothly follows the variations in the X and Y component. It produces remarkably similar baselines as the ones calculated with the FMI method with the advantage of not needing apriori information. We conclude that our approach characterises the quiet magnetic field well and is suitable to be used during magnetically quiet periods. The filtering method tends to follow the activity very closely, risking to under-estimate potential storm effects and thus is not directly applicable during magnetically disturbed periods.

As the introduced filtering method is a standard signal-treatment approach that does not need any apriori information for its application, it is directly applicable to any magnetic observatory in low and mid-latitudes independent of the time period. Therefore, the limiting factor for its real-time application is the discrimination of quiet versus non-quiet periods and the determination of the baseline during non-quiet periods. Once these challenges are overcome, it has the capability of being used in (near) real-time applications that make use of low- and mid-latitude magnetic observatories, like space weather severeness estimations and index derivations.

Acknowledgments
The results presented in this paper rely on: (a) data collected at magnetic observatories. We thank the national institutes that support them and INTERMAGNET (International Real-time Magnetic Observatory Network) for promoting high standards of magnetic observatory practice (www.intermagnet.org). (b) Magnetic activity indices, and related data products, calculated and made available by ISGI (International Service of Geomagnetic Indices) Collaborating Institutes from data collected at magnetic observatories. We thank the involved national institutes and ISGI (www.isgi.unistra.fr). This work was supported by the PNST (*Programme National Soleil Terre*), from CNRS-INSU (*Institut des Sciences de l'Univers* of *Centre National de la Recherche Scientifique*) co-funded by CNES (*Centre National d'Etudes Spatiales*) and CEA (*Commissariat à l'Energie Atomique et aux Energies Alternatives*), and by TOSCA committee from CNES focused on Space weather and Geomagnetism. This work was supported by CNES. Veronika Haberle is sponsored by Thales Alenia Space, Toulouse. The authors acknowledge the support of the French ANR (*Agence Nationale de la Recherche*), under grant ANR-20-ASTC-0030 (project ASTRID PRISMS).

Data Availability Statement

The magnetic observatory data are available from INTERMAGNET data repository: http://doi.org/10.17616/R3XK82. The magnetic activity indices are available from ISGI data repository: http://doi.org/10.17616/R3WS49.

References

Anad, F., Amory-Mazaudier, C., Hamoudi, M., Bourouis, S., Abtout, A., & Yizengaw, E. (2016). Sq solar variation at Medea Observatory (Algeria), from 2008 to 2011. *Advances in Space Research*, *58*(9), 1682–1695. https://doi.org/10.1016/J.ASR.2016.06.029

Bartels, J., Heck, N. H., & Johnston, H. F. (1939). The three-hour-range index measuring geomagnetic activity. *Journal of Geophysical Research*, *44*(4), 411. https://doi.org/10.1029/TE044I004P00411

Behannon, K. W., & Ness, N. F. (1966). *The design of numerical filters for geomagnetic data analysis (NASA Technical Note No. NASA-TN-D-3341)*. Goddard Space Flight Center NASA.

Behannon, K. W., & Ness, N. F. (1966). Magnetic storms in the earth's magnetic tail. *Journal of Geophysical Research*, *71*(9), 2327–2351. https://doi.org/10.1029/JZ071I009P02327

Bhargava, B. N., & Yacob, A. (1970). The secular variation of the magnetic field and its cyclic components. *Journal of Atmospheric and Terrestrial Physics*, *32*(3), 365–372. https://doi.org/10.1016/0021-9169(70)90008-5

Briggs, B. (1984). The variability of ionospheric dynamo currents. *Journal of Atmospheric and Terrestrial Physics*, *46*(5), 419–429. https://doi.org/10.1016/0021-9169(84)90086-2

Brown, G., & Williams, W. (1969). Some properties of the day-to-day variability of Sq (H). *Planetary and Space Science*, *17*(3), 455–470. https://doi.org/10.1016/0032-0633(69)90076-2

Campbell, W. H. (1989). An introduction to quiet daily geomagnetic fields. *Pure and Applied Geophysics*, *131*(3), 315–331. https://doi.org/10.1007/BF00876831

Campbell, W. H. (2003). *Introduction to geomagnetic fields*. Cambridge University Press. https://doi.org/10.1017/cbo9781139165136

Cliver, E. W., & Dietrich, W. F. (2013). The 1859 space weather event revisited: Limits of extreme activity. *Journal of Space Weather and Space Climate*, *3*, A31. https://doi.org/10.1051/SWSC/2013053

Constable, C. G., & Constable, S. C. (2004). Satellite magnetic field measurements: Applications in studying the deep Earth. In *Geophysical monograph series* (Vol. 150, pp. 147–159). Blackwell Publishing Ltd. https://doi.org/10.1029/150GM13

Drob, D. P., Emmert, J. T., Meriwether, J. W., Makela, J. J., Doornbos, E., Conde, M., et al. (2015). An update to the Horizontal Wind Model (HWM): The quiet time thermosphere. *Earth and Space Science*, *2*(7), 301–319. https://doi.org/10.1002/2014EA000089

Finlay, C. C., Lesur, V., Thébault, E., Vervelidou, F., Morschhauser, A., & Shore, R. (2017). Challenges handling magnetospheric and ionospheric signals in internal geomagnetic field modelling. *Space Science Reviews*, *206*(1), 157–189. https://doi.org/10.1007/s11214-016-0285-9

Forbes, J. M., Palo, S. E., & Zhang, X. (2000). Variability of the ionosphere. *Journal of Atmospheric and Solar-Terrestrial Physics*, *62*(8), 685–693. https://doi.org/10.1016/S1364-6826(00)00029-8

Gjerloev, J. W. (2012). The SuperMAG data processing technique. *Journal of Geophysical Research*, *117*(A9), 9213. https://doi.org/10.1029/2012JA017683

Greener, J. G., & Schlapp, D. M. (1979). A study of day-to-day variability of Sq over Europe. *Journal of Atmospheric and Terrestrial Physics*, *41*(2), 217–223. https://doi.org/10.1016/0021-9169(79)90014-X

Hitchman, A. P., Lilley, F. E. M., & Campbell, W. H. (1998). The quiet daily variation in the total magnetic field: Global curves. *Geophysical Research Letters*, *25*(11), 2007–2010. https://doi.org/10.1029/98GL51332

Jadhav, G., Rajaram, M., & Rajaram, R. (2002). A detailed study of equatorial electrojet phenomenon using Ørsted satellite observations. *Journal of Geophysical Research*, *107*(A8), 12–1. https://doi.org/10.1029/2001JA000183

Janzhura, A., & Troshichev, O. (2008). Determination of the running quiet daily geomagnetic variation. *Journal of Atmospheric and Solar-Terrestrial Physics*, *70*(7), 962–972. https://doi.org/10.1016/j.jastp.2007.11.004

Kozyreva, O. V., Pilipenko, V. A., Belakhovsky, V. B., & Sakharov, Y. A. (2018). Ground geomagnetic field and GIC response to March 17, 2015, storm. *Earth Planets and Space*, *70*(1), 1–13. https://doi.org/10.1186/S40623-018-0933-2

Kunagu, P., Balasis, G., Lesur, V., Chandrasekhar, E., & Papadimitriou, C. (2013). Wavelet characterization of external magnetic sources as observed by CHAMP satellite: Evidence for unmodelled signals in geomagnetic field models. *Geophysical Journal International*, *192*(3), 946–950. https://doi.org/10.1093/GJI/GGS093

Laundal, K. M., & Richmond, A. D. (2016). Magnetic coordinate systems. *Space Science Reviews*, *206*(1–4), 27–59. https://doi.org/10.1007/s11214-016-0275-y

Le Huy, M., & Amory-Mazaudier, C. (2008). Planetary magnetic signature of the storm wind disturbance dynamo currents: D_{dyn}. *Journal of Geophysical Research*, *113*(2). https://doi.org/10.1029/2007JA012686

Liu, H. L., Bardeen, C. G., Foster, B. T., Lauritzen, P., Liu, J., Lu, G., et al. (2018). Development and validation of the Whole Atmosphere Community Climate Model with thermosphere and ionosphere extension (WACCM-X 2.0). *Journal of Advances in Modeling Earth Systems*, *10*(2), 381–402. https://doi.org/10.1002/2017MS001232

Liu, J. Y., Chiu, C. S., & Lin, C. H. (1996). The solar flare radiation responsible for sudden frequency deviation and geomagnetic fluctuation. *Journal of Geophysical Research*, *101*(A5), 10855–10862. https://doi.org/10.1029/95JA03676

Lühr, H., Kervalishvili, G., Michaelis, I., Rauberg, J., Ritter, P., Park, J., et al. (2015). The interhemispheric and F region dynamo currents revisited with the Swarm constellation. *Geophysical Research Letters*, *42*(9), 3069–3075. https://doi.org/10.1002/2015GL063662

Ma, R., Xu, J., Wang, W., & Lei, J. (2012). The effect of 27 day solar rotation on ionospheric F2 region peak densities (N_mF_2). *Journal of Geophysical Research*, *117*(A3), 3303. https://doi.org/10.1029/2011JA017190

Mayaud, P.-N. (1967). *Atlas of K Indices (vol. IAGA bull No. 21)*. IUGG Publication Office.

Mayaud, P.-N. (1972). The aa indices: A 100-year series characterizing the magnetic activity. *Journal of Geophysical Research*, *77*(34), 6870–6874. https://doi.org/10.1029/JA077I034P06870

Menvielle, M., Iyemori, T., Marchaudon, A., & Nosé, M. (2011). *Geomagnetic observations and models*. Springer Netherlands. https://doi.org/10.1007/978-90-481-9858-0

Menvielle, M., Papitashvili, N., Häkkinen, L., & Sucksdorff, C. (1995). Computer production of K indices: Review and comparison of methods. *Geophysical Journal International*, *123*(3), 866–886. https://doi.org/10.1111/J.1365-246X.1995.TB06895.X

Ness, N. F., & Williams, D. J. (1966). Correlated magnetic tail and radiation belt observations. *Journal of Geophysical Research*, *71*(1), 322–325. https://doi.org/10.1029/JZ071I001P00322

Olsen, N. (1997). Ionospheric F region currents at middle and low latitudes estimated from Magsat data. *Journal of Geophysical Research*, *102*(A3), 4563–4576. https://doi.org/10.1029/96JA02949

Olsen, N., & Mandea, M. (2007). Will the magnetic North Pole move to Siberia? *Eos, Transactions American Geophysical Union*, *88*(29), 293. https://doi.org/10.1029/2007EO290001

Park, J., Lühr, H., & Min, K. W. (2011). Climatology of the inter-hemispheric field-aligned current system in the equatorial ionosphere as observed by CHAMP. *Annales Geophysicae*, *29*(3), 573–582. https://doi.org/10.5194/angeo-29-573-2011

Picone, J. M., Hedin, A. E., Drob, D. P., & Aikin, A. C. (2002). NRLMSISE-00 empirical model of the atmosphere: Statistical comparisons and scientific issues. *Journal of Geophysical Research*, *107*(A12), 15–1. https://doi.org/10.1029/2002JA009430

Proakis, J., & Manolakis, D. (2006). *Digital signal processing* (4th edn). Pearson.

Schlapp, D. M. (1968). World-wide morphology of day-to-day variability of Sq. *Journal of Atmospheric and Terrestrial Physics*, *30*(10), 1761–1776. https://doi.org/10.1016/0021-9169(68)90096-2

Shinbori, A., Koyama, Y., Nosé, M., Hori, T., & Otsuka, Y. (2017). Characteristics of seasonal variation and solar activity dependence of the geomagnetic solar quiet daily variation. *Journal of Geophysical Research: Space Physics*, *122*(10), 796–10. https://doi.org/10.1002/2017JA024342

Shinbori, A., Koyama, Y., Nose, M., Hori, T., Otsuka, Y., & Yatagai, A. (2014). Long-term variation in the upper atmosphere as seen in the geomagnetic solar quiet daily variation. *Earth Planets and Space*, *66*(1), 1–20. https://doi.org/10.1186/S40623-014-0155-1

Smith, A. R., Beggan, C. D., Macmillan, S., & Whaler, K. A. (2017). Climatology of the auroral electrojets derived from the along-track gradient of magnetic field intensity measured by POGO, Magsat, CHAMP, and Swarm. *Space Weather*, *15*(10), 1257–1269. https://doi.org/10.1002/2017SW001675

Soloviev, A., Smirnov, A., Gvishiani, A., Karapetyan, J., & Simonyan, A. (2019). Quantification of Sq parameters in 2008 based on geomagnetic observatory data. *Advances in Space Research*, *64*(11), 2305–2320. https://doi.org/10.1016/J.ASR.2019.08.038

Stening, R. (2008). The shape of the Sq current system. *Annales Geophysicae*, *26*(7), 1767–1775. https://doi.org/10.5194/angeo-26-1767-2008

Stening, R., Reztsova, T., & Le Huy, M. (2005). Day-to-day changes in the latitudes of the foci of the Sq current system and their relation to equatorial electrojet strength. *Journal of Geophysical Research*, *110*(A10), A10308. https://doi.org/10.1029/2005JA011219

Stening, R., Reztsova, T., & Le Huy, M. (2007). Variation of Sq focus latitudes in the Australian/Pacific region during a quiet sun year. *Journal of Atmospheric and Solar-Terrestrial Physics*, *69*(6), 734–740. https://doi.org/10.1016/j.jastp.2006.12.002

Sucksdorff, C., Pirjola, R., & Häkkinen, L. (1991). Computer production of K-indices based on linear elimination. *Geophysical Transactions*, *36*(3–4), 333–345.

Takeda, M. (1984). Day-to-day variation of equivalent sq current system during March 11–26, 1970. *Journal of Geomagnetism and Geoelectricity*, *36*(5), 215–228. https://doi.org/10.5636/jgg.36.215

Takeda, M. (1999). Time variation of global geomagnetic Sq field in 1964 and 1980. *Journal of Atmospheric and Solar-Terrestrial Physics*, *61*(10), 765–774. https://doi.org/10.1016/S1364-6826(99)00028-0

Tapping, K. F. (2013). The 10.7 cm solar radio flux (F10.7). *Space Weather*, *11*(7), 394–406. https://doi.org/10.1002/swe.20064

Van De Kamp, M. (2013). Harmonic quiet-day curves as magnetometer baselines for ionospheric current analyses. *Geoscientific Instrumentation, Methods and Data Systems*, *2*(2), 289–304. https://doi.org/10.5194/GI-2-289-2013

Wardinski, I., & Thébault, E. (2019). Modelling internal and external geomagnetic fields using satellite data. *Geomagnetism, Aeronomy and Space Weather: A Journey from the Earth's Core to the Sun*, 84–97. https://doi.org/10.1017/9781108290135.008

Yamazaki, Y., Häusler, K., & Wild, J. A. (2016). Day-to-day variability of midlatitude ionospheric currents due to magnetospheric and lower atmospheric forcing. *Journal of Geophysical Research: Space Physics*, *121*(7), 7067–7086. https://doi.org/10.1002/2016JA022817

Yamazaki, Y., & Maute, A. (2016). Sq and EEJ—A review on the daily variation of the geomagnetic field caused by ionospheric dynamo currents. *Space Science Reviews*, *206*(1–4), 299–405. https://doi.org/10.1007/s11214-016-0282-z

Yamazaki, Y., Yumoto, K., Cardinal, M. G., Fraser, B. J., Hattori, P., Kakinami, Y., et al. (2011). An empirical model of the quiet daily geomagnetic field variation. *Journal of Geophysical Research*, *116*(A10), 10312. https://doi.org/10.1029/2011JA016487